frontiers | Research Topics

Medicinal and pharmaceutical chemistry editor's pick 2024

Edited by
Michael Kassiou

Published in
Frontiers in Chemistry

ISSN 1664-8714
ISBN 978-2-8325-5940-6
DOI 10.3389/978-2-8325-5940-6

About Frontiers

Frontiers is more than just an open access publisher of scholarly articles: it is a pioneering approach to the world of academia, radically improving the way scholarly research is managed. The grand vision of Frontiers is a world where all people have an equal opportunity to seek, share and generate knowledge. Frontiers provides immediate and permanent online open access to all its publications, but this alone is not enough to realize our grand goals.

Frontiers journal series

The Frontiers journal series is a multi-tier and interdisciplinary set of open-access, online journals, promising a paradigm shift from the current review, selection and dissemination processes in academic publishing. All Frontiers journals are driven by researchers for researchers; therefore, they constitute a service to the scholarly community. At the same time, the *Frontiers journal series* operates on a revolutionary invention, the tiered publishing system, initially addressing specific communities of scholars, and gradually climbing up to broader public understanding, thus serving the interests of the lay society, too.

Dedication to quality

Each Frontiers article is a landmark of the highest quality, thanks to genuinely collaborative interactions between authors and review editors, who include some of the world's best academicians. Research must be certified by peers before entering a stream of knowledge that may eventually reach the public - and shape society; therefore, Frontiers only applies the most rigorous and unbiased reviews. Frontiers revolutionizes research publishing by freely delivering the most outstanding research, evaluated with no bias from both the academic and social point of view. By applying the most advanced information technologies, Frontiers is catapulting scholarly publishing into a new generation.

What are Frontiers Research Topics?

Frontiers Research Topics are very popular trademarks of the *Frontiers journals series*: they are collections of at least ten articles, all centered on a particular subject. With their unique mix of varied contributions from Original Research to Review Articles, Frontiers Research Topics unify the most influential researchers, the latest key findings and historical advances in a hot research area.

Find out more on how to host your own Frontiers Research Topic or contribute to one as an author by contacting the Frontiers editorial office: frontiersin.org/about/contact

Medicinal and pharmaceutical chemistry editor's pick 2024

Topic editor
Michael Kassiou — The University of Sydney, Australia

Citation
Kassiou, M., ed. (2025). *Medicinal and pharmaceutical chemistry editor's pick 2024*. Lausanne: Frontiers Media SA. doi: 10.3389/978-2-8325-5940-6

Table of contents

frontiers | Frontiers in Chemistry

TYPE Review
PUBLISHED 17 January 2023
DOI 10.3389/fchem.2023.1098331

OPEN ACCESS

EDITED BY
Mi Wang,
Michigan Medicine, University of Michigan,
United States

REVIEWED BY
Benedict-Tilman Berger,
Goethe University Frankfurt, Germany
Xie Zhouling,
Hefei University of Technology, China
Jun Wan,
Genentech Inc., United States
Bing Feng,
Pennington Biomedical Research Center,
United States
Jianli Zhang,
SOURCE, Johns Hopkins University,
United States

*CORRESPONDENCE
Shuang-Xi Gu,
shuangxigu@163.com
Mingliang Wang,
wangmingliang@simm.ac.cn

†These authors have contributed equally to this work

SPECIALTY SECTION
This article was submitted to Medicinal and Pharmaceutical Chemistry,
a section of the journal
Frontiers in Chemistry

RECEIVED 14 November 2022
ACCEPTED 06 January 2023
PUBLISHED 17 January 2023

CITATION
Jiang H, Xiong H, Gu S-X and Wang M (2023), E3 ligase ligand optimization of Clinical PROTACs.
Front. Chem. 11:1098331.
doi: 10.3389/fchem.2023.1098331

E3 ligase ligand optimization of Clinical PROTACs

Hanrui Jiang[1,2†], Huan Xiong[2,3†], Shuang-Xi Gu[1*] and Mingliang Wang[2,3*]

[1]Key Laboratory for Green Chemical Process of Ministry of Education, School of Chemical Engineering & Pharmacy, Wuhan Institute of Technology, Wuhan, China, [2]Zhongshan Institute for Drug Discovery, Shanghai Institute of Materia Medica, Chinese Academy of Sciences, Zhongshan, China, [3]Department of Medicinal Chemistry, Shanghai Institute of Materia Medica, Chinese Academy of Sciences, Shanghai, China

Proteolysis targeting chimeras (PROTACs) technology can realize the development of drugs for non-druggable targets that are difficult to achieve with traditional small molecules, and therefore has attracted extensive attention from both academia and industry. Up to now, there are more than 600 known E3 ubiquitin ligases with different structures and functions, but only a few have developed corresponding E3 ubiquitin ligase ligands, and the ligands used to design PROTAC molecules are limited to a few types such as VHL (Von-Hippel-Lindau), CRBN (Cereblon), MDM2 (Mouse Doubleminute 2 homolog), IAP (Inhibitor of apoptosis proteins), etc. Most of the PROTAC molecules that have entered clinical trials were developed based on CRBN ligands, and only **DT2216** was based on VHL ligand. Obviously, the structural optimization of E3 ubiquitin ligase ligands plays an instrumental role in PROTAC technology from bench to bedside. In this review, we review the structure optimization process of E3 ubiquitin ligase ligands currently entering clinical trials on PROTAC molecules, summarize some characteristics of these ligands in terms of druggability, and provide some preliminary insights into their structural optimization. We hope that this review will help medicinal chemists to develop more druggable molecules into clinical studies and to realize the greater therapeutic potential of PROTAC technology.

KEYWORDS

PROTACs, E3 ubiquitin ligase ligand, structure optimization, clinical trials, CRBN

1 Introduction

The degradation of most damaged and soluble misfolded proteins is achieved by the 26S proteasome through ubiquitin-proteasome system (UPS)-mediated protein degradation (Paiva et al., 2019; Pohl et al., 2019; Kawahata et al., 2020). In the UPS, the proteasome conjugated to a protein substrate through enzymatic cascade (Hershko et al., 1983; Hershko et al., 1992; Komander et al., 2012). First, E1 (Ub activating enzyme) binds Ub (ubiquitin) *via* an ATP-dependent mechanism and then transfers Ub to E2 (Ubconjugating enzyme) by forming an E2 ubiquitin conjugate (Schulman et al., 2009; Ye et al., 2009). Next, the E3 (Ub ligase) mediates the transfer of the ubiquitin from E2 to the substrate protein, followed by 26S proteasome-induced degradation or post-translational modification of the substrate protein (Zheng et al., 2017). E3 ligase mediates the specificity of protein substrates through a non-covalent or covalent mechanism, and the type of E3 ligase determines the outcome of the substrate protein. For instance, TRAF6 (tumor necrosis factor receptor-associated factor 6) interacts with YAP (Yes-associated protein) and promotes its ubiquitination to enhance YAP stability (Liu et al., 2020). c-Cbl (Casitas B lymphoma) binds to the intracytoplasmic tail of PD-1 and targets it for ubiquitination-proteasomal degradation

TABLE 1 PROTAC degraders in clinical development.

Company	Degrader	Target	E3 ligase	ROA	Highest phase	Clinical trial no. (if applicable)
Arvinas	ARV-110	AR	CRBN	Oral	Phase II	NCT03888612
Arvinas	ARV-766	AR	Undisclosed	Oral	Phase I	NCT05067140
Arvinas/Pfizer	ARV-471	ER	CRBN	Oral	Phase II	NCT04072952
Accutar Biotech	AC682	ER	CRBN	Oral	Phase I	NCT05080842
Bristol Myers Squibb	CC-94676	AR	CRBN	Oral	Phase I	NCT04428788
Dialectic Therapeutics	DT2216	BCL-X_L	VHL	I.v	Phase I	NCT04428788
Foghorn Therapeutics	FHD-609	BRD9	Undisclosed	Oral	Phase I	NCT04965753
Kymera	KT-413	IRAK4	CRBN	I.v	Phase I	NA
Kymera	KT-333	STAT3	Undisclosed	Undisclosed	Phase I	NA
Kymera/Sanofi	KT-474	IRAK4	Undisclosed	Oral	Phase I	NCT04772885
Nurix Therapeutics	NX-2127	BTK	CRBN	Oral	Phase I	NCT04830137
Nurix Therapeutics	NX-5948	BTK	CRBN	Oral	Phase I	NCT04830137
C4 Therapeutics	CFT8634	BRD9	CRBN	Oral	IND- e	NA
C4 Therapeutics	CFT8919	$EGFR^{L858R}$	CRBN	Oral	IND- e	NA
Cullgen	CG001419	TRK	CRBN	Oral	IND- e	NA

NA, not applicable.

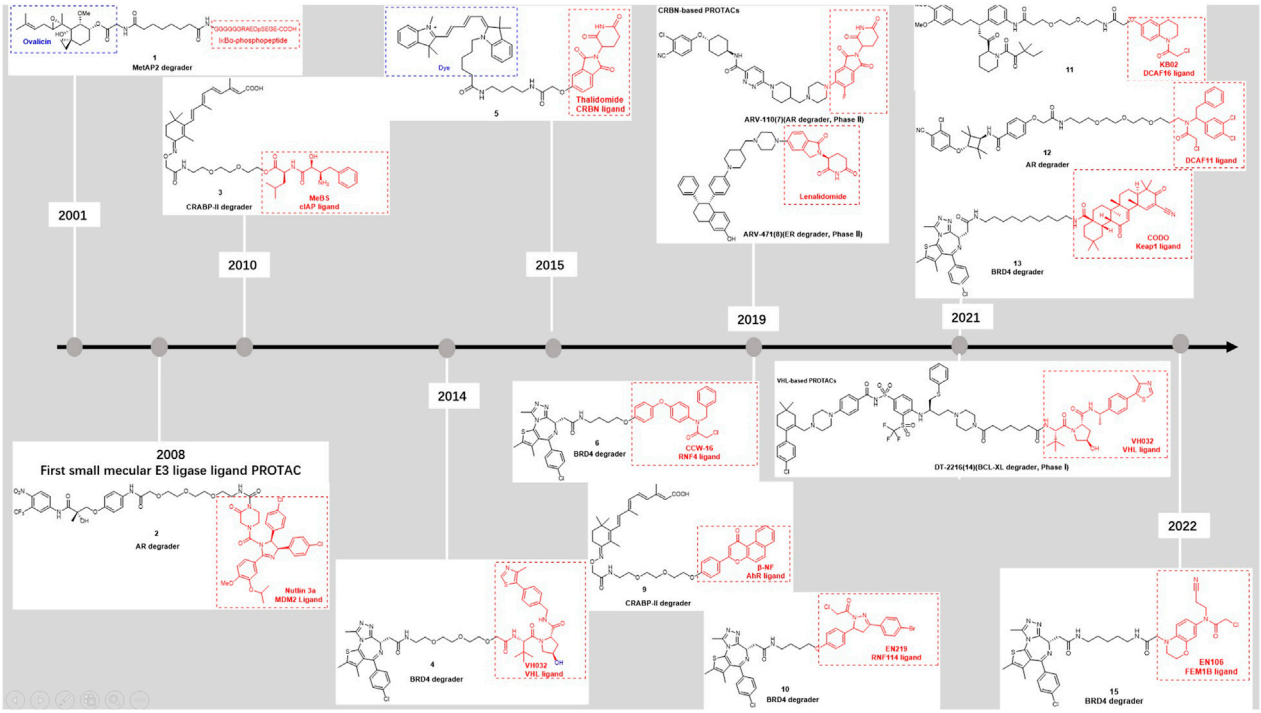

FIGURE 1
Timeline of E3 ligases ligands discoveries.

in macrophages, resulting in downregulation of PD-1 and reduced surface expression leading to increased tumor phagocytosis and tumor suppression (Lyle et al., 2019).

Proteolysis targeting chimeras (PROTACs) is based on proteasomes (Schapira et al., 2019). These bifunctional molecules consist of three parts: An E3-recruiting ligand, a POI (protein of

interest) targeting warhead, and a linker connecting the two ligands (Sun et al., 2019). PROTAC degraders mediate their own formation of POI-PROTAC-E3 complexes with substrate proteins and E3 ubiquitin ligases, which lead to the degradation of the substrate protein *via* UPS (Wang et al., 2020; Yang et al., 2021). There are many target-based POI warheads and linkers available for the design and optimization of PROTAC degraders for medicinal chemists, but only a few E3 ubiquitin ligases ligands have been developed (Sun et al., 2019).

Arvinas is the first company to clinically implement two PROTAC degraders, the androgen receptor (AR) degrader **ARV-110** and the estrogen receptor (ER) degrader **ARV-471** (Mullard, 2019). The safety and effectiveness of **ARV-110** has been demonstrated in the treatment of metastatic castrated prostate cancer (mCRPC) (Neklesa et al., 2018; Neklesa et al., 2019; Gao et al., 2022), and **ARV-471** also has shown great potential in the treatment of breast cancer (Snyder et al., 2021). Since **ARV-110** and **ARV-471** entered clinic trials, an increasing number of protein targets have emerged to develop clinical degraders of PROTACs, such as BRD9 and IRAK4 (Table 1), while antitumor is currently the most concentrated field of research for PROTACs, except for KYMERA's degrader **KT-474**, which is the only clinical degrader for autoimmune-disease (Békés et al., 2022). These PROTACs degraders are based on different E3 ligands, but mainly on CRBN-based ligands.

The first PROTAC was discovered in 2001 by Craig Crews, founder of Arvinas (Sakamoto et al., 2001) (Figure 1). This compound consists of a covalent small molecule inhibitor of MetAP-2, and IκBα-phosphopeptide, enabling the ligase to ubiquitylate METAP2. As the first attempt to explore PROTACs, this compound exposed the poor cell permeability prevented it from being widely used, and the structure of phosphopeptides in this type of PROTAC is easily hydrolyzed by intracellular phosphatase, which reduces its stability. Therefore, the desired small molecule E3 ligase ligand, must have good membrane permeability, be stable *in vitro* environment and have strong affinity to E3 ubiquitin ligase, on the basis of which PROTACs will have stronger druggability.

In the past 2 decades, various E3 ligase ligands based on different functions have been reported. Such as MDM2 ligand (Honda et al., 1997; Schneekloth et al., 2008; Saadatzadeh et al., 2017), cIAP ligands (Sato et al., 2008; Itoh et al., 2011; Ohoka et al., 2017), VHL ligand (Schneekloth et al., 2004; Rodriguez-Gonzalez et al., 2008), CRBN ligand (Winter et al., 2015), AhR (Aryl hydrocarbon receptor) ligand (Ohtake et al., 2007; Ohoka et al., 2019), DCAF (DDB1- And CUL4-Associated Factor) 11 and 15 and 16 ligands (Han et al., 2017; Zhang et al., 2019; Zhang et al., 2021), RNF (RING finger protein) 4 and 114 ligands (Kumar et al., 2019; Ward et al., 2019; Luo et al., 2021), FEM1B (Fem-1 Homolog B) ligand (Henning et al., 2022), KEAP1 (Kelch Like ECH Associated Protein 1) ligand (Tong et al., 2020; Wei et al., 2021; Pei et al., 2022) (Figure 1). They were developed based on the function of different E3 ligases thus have different properties. For instance, VHL is the substrate receptor of CRL2VHL E3 ubiquitin ligase.

The Pro564 residue of HIF-1α (Hypoxia-Inducible Factor-1α) is hydroxylated by prolyl hydroxylase (also the hydroxyl group in the VHL ligands), bound to VHL proteins and subsequently ubiquitinated by CRL2VHL E3 (Ivan et al., 2001; Schneekloth et al., 2004). HIF-1α protects cells during hypoxia, and VHL-based PROTAC shows good degradation activity in most cases, and VHL ligands even reduce side effects in some cases (Jaakkola et al., 2001). However, in subsequent studies, the poor membrane permeability and low oral delivery rate of VHL ligands limited their application. The E3 ubiquitin ligase ligands are like a toolbox for PROTACs, and the appropriate "tool" is selected based on the different properties of E3 ligands for the purpose of the researchers.

In this review, we will summarize the experience of small molecule PROTACs currently entering clinical trials in optimizing E3 ligase ligands for degraders from the perspective of chemical structure. It is expected to shed light on the optimization of E3 ligase ligands for degraders of PROTACs in the future.

2 E3 ligase ligands optimization of PROTACs for clinical application

2.1 E3 ligase ligands optimization of AR PROTACs

Annually, more than 350,000 deaths are associated with prostate cancer, making the disease one of the leading causes of cancer-related death in men, and the androgen receptor (AR) is believed to drive hormone dependency of prostate cancer (Rebello et al., 2021). Key AR gene alterations contribute to castration-resistant prostate cancer (CRPC) (de Bono et al., 2020). Both enzalutamide and abiraterone have shown good results as AR antagonists in the treatment of prostate cancer. However, the drug resistance is inevitable when mutations occur in the ligand-binding domain (Teo et al., 2019). Therefore, the development of AR degraders based on PROTACs technology has become a new strategy (Pan et al., 2007).

The earlier AR PROTAC was designed using enzalutamide as the AR antagonist and VHL-b ligands as E3 ligase ligand. In 2019, Wang et al. selected **Ari-16** as the antagonist of the degrader by screening various VHL-based E3 ligase ligands **(compounds 16–24)** to build different AR degraders (Kregel et al., 2020; Zhao et al., 2020) (Figure 2). During E3 ligase ligand optimization process, they found that the (*S*)-methyl group in **VHL-b** exposed to the solvent environment could serve as a possible tethering point for the design of AR degraders (Han et al., 2019). Subsequently, they reported that **ARD-61** is an AR degrader with DC_{50} (concentration that resulted in a 50% targeted protein degradation) values of 7.2 nM and 1.0 nM in LNCaP and VCaP cells, respectively. Apparently, the large molecular weight of the VHL ligand makes ARD-61 too large (MW = 1095.8) for its degradation activity to be significant. In their following work, the E3 ligase ligand part of **ARD-61** was replaced with a VHL ligand and the optimized degrader **ARD-69** showed AR DC_{50} values of 0.86 nM and 0.76 nM in LNCaP and VCaP cells, respectively. However, the molecular weight of **ARD-69** was still too large as an AR degrader. Subsequently, they shortened the linker length and modified the VHL ligand to decrease its molecular weight. Thus, led to degrader **ARD-266** with similar degradation activity, the AR DC_{50} values were 0.5 nM and 1.0 nM in LNCaP and VCaP cells, respectively (Han et al., 2019). The poor membrane permeability and low oral availability of VHL ligands led to its eventual replacement by CRBN ligands which is also used in Bristol Myers Squibb's ER clinical degrader **CC-94676**. On the basis of the above three molecules, they discovered that **ARD-2128** showed the same degradation activity as **ARD-61** (MW = 820.4), but its molecular weight was significantly reduced and its bioavailability in mice reached 67% (Han et al., 2021). Finally, on the basis of CRBN ligand, they re-optimized the linker and the antagonist and disclosed **ARD-2585**, which has 51% oral bioavailability in mice and with AR

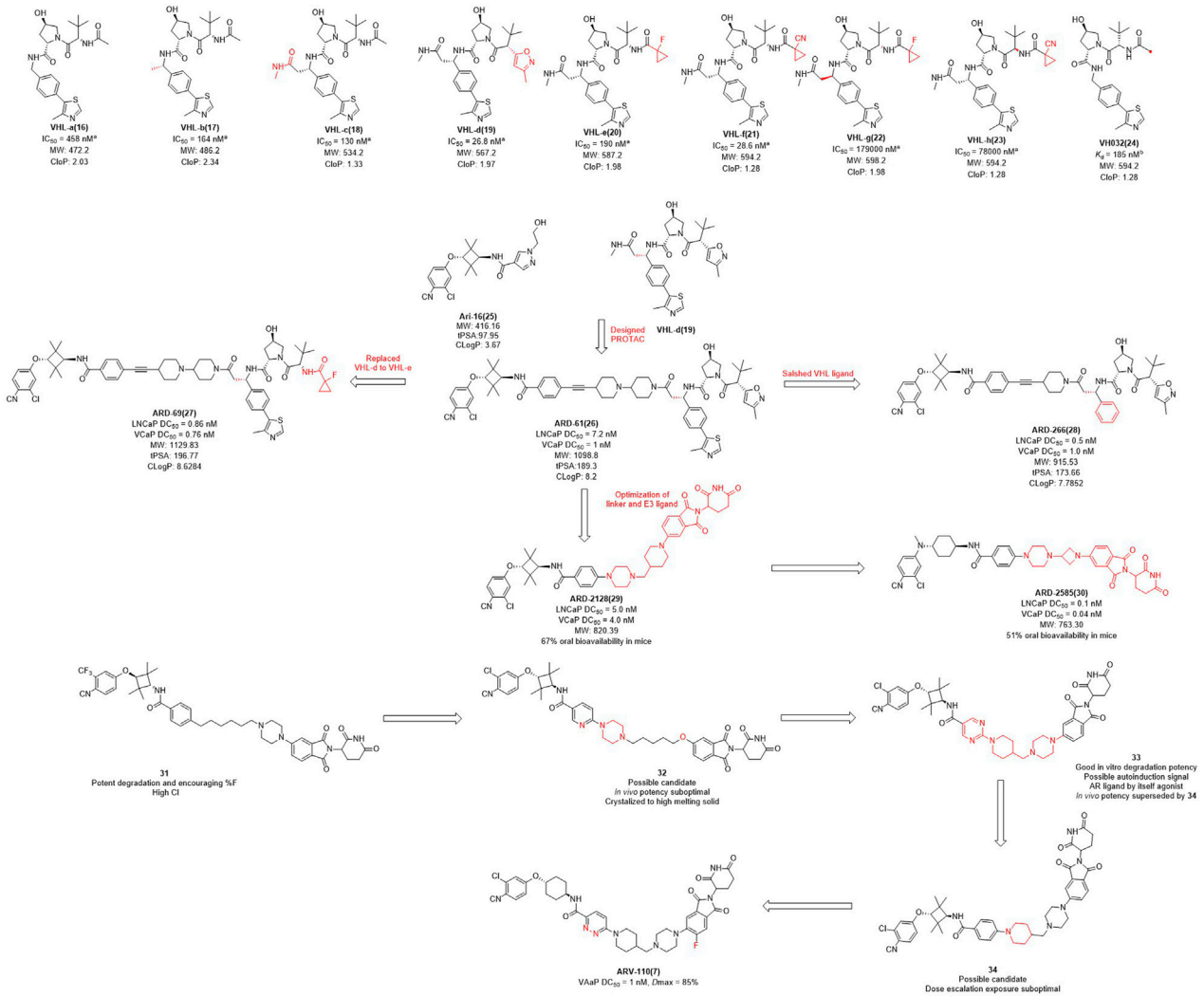

FIGURE 2
Chemical structures of VHL ligands and their binding affinities to VHL protein and the design and optimization of AR PROTACs. [a]Inhibitory activity (IC50) of E3 ligands on their substrates. [b]inding affinity (Kd) of E3 ligands to their respective substrates MW, molecular weight; tPSA, total polar surface area; cLog P, calculated Log P; *The arrows in the figure do not mean progressive relationship between these compounds.

DC_{50} of 0.10 nM and 0.04 nM in LNCaP and VCaP cells, respectively (Xiang et al., 2021).

In the pharmaceutical industry, AR degraders have also received the attention of Arvinas, whose CRBN-based AR degrader **ARV-110** (Figure 2) is currently in phase II clinical trials (Snyder et al., 2021). Arvinas has also performed many optimizations for AR degradation. First of all, compounds **31** and **32** showed good degradation abilities *in vitro*, but also with a high clearance rate *in vivo*. Subsequently, they disclosed that bi-functional compound **33** showed strong degradation activity *in vitro*, however, poor activity *in vivo*, perhaps due to the metabolism of **33**. The structure of compound **34** was optimized on the basis of compound **33** with improved activity *in vivo*, but it was dose dependent and needed further optimization. Finally, the H at position 3 of the benzene ring of the CRBN ligand of **34** was replaced with fluorine to obtain degrader **ARV-110** which improved the druggability. **ARV-110** was highly efficient in VCaP cells with a DC_{50} value with 1 nM and *D*max (maximal levels of protein degradation) of 85% (Snyder et al., 2021). Above all, the E3 ubiquitin ligand functions as the promoter of the degradation process, and optimizing the E3 ligand and modifying its molecular structure is expected to improve the activity and oral delivery rate of the degraders.

2.2 E3 ligase ligands optimization of ERα PROTACs

The importance of estrogen regulates (ER) for female breast cancer is similar to AR for male prostate cancer. ER targets are associated with 70%–80% of breast cancer profiles, and become the primary therapeutic target for this disease (Ohoka et al., 2018; Waks et al., 2019; Criscitiello et al., 2022). ERα is a member of the nuclear receptor family and plays a crucial role in mediating the estrogen signaling pathway within the mammary glands and female reproductive tract (Arnal et al., 2017). In contrast to the high expression of ERα in breast tumors, the ERα expression is low in

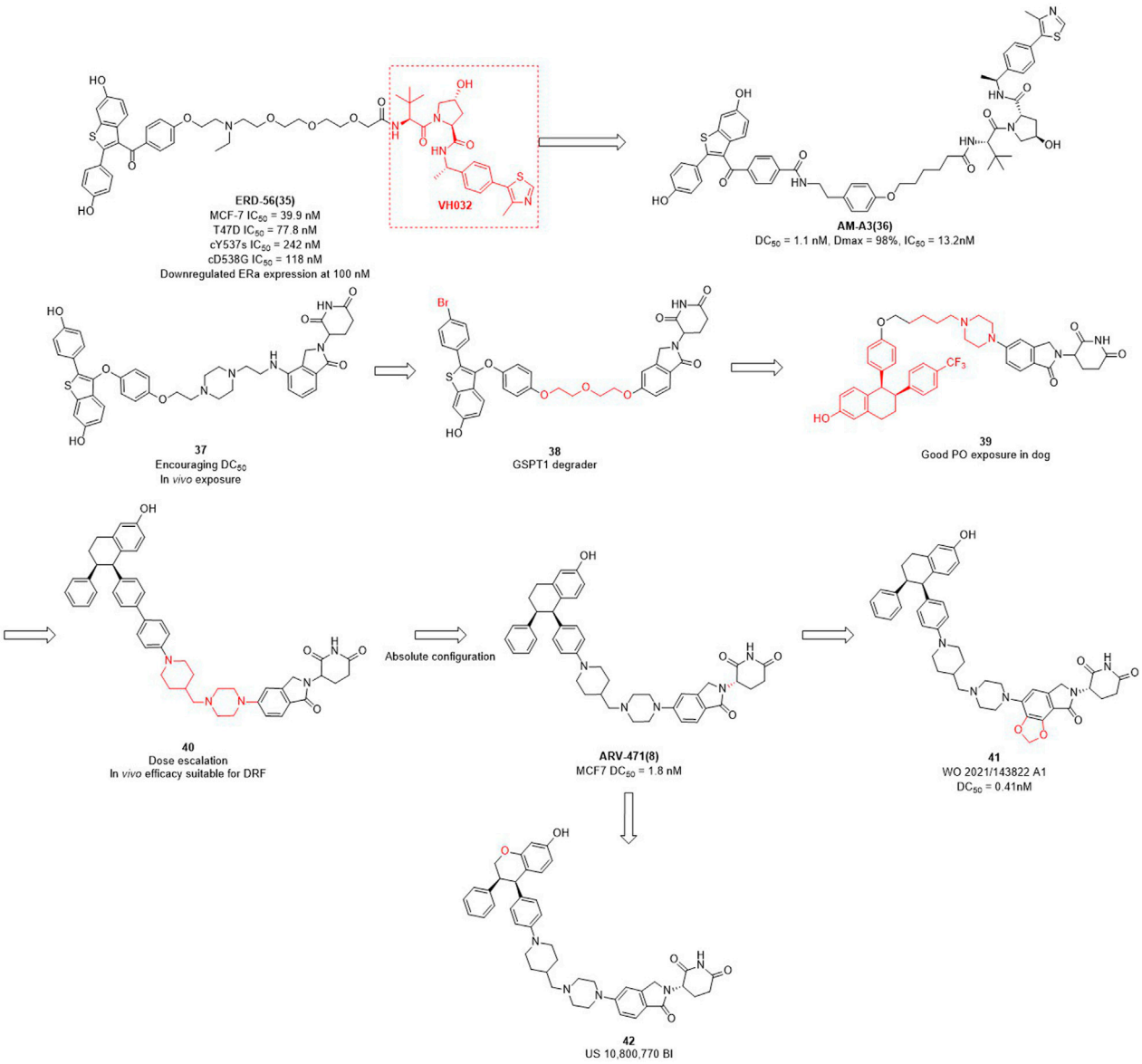

FIGURE 3
Design and optimization process of ER PROTACs.

normal breast epithelium cells (Huang et al., 2014). ERα knockout experiments in rats demonstrated that ERα plays an important role in promoting the formation of breast cancer cells in the mammary gland (Zhang et al., 2011). In addition to ERα knockout, PROTAC can also reduce the expression levels of ERα in breast. Wang et al. focused not only on AR degraders but also on ERα degraders. In their initial studies of ERα degradation, they singled out raloxifene as ERα-binding ligand and CRBN and VHL as E3 ligase ligands, respectively. Interestingly, the VHL-based PROTACs were shown to induce significant degradation of the target protein, whereas no obvious protein degradation was observed for CRBN-based molecules. Therefore, they synthesized a series of PROTACs based on raloxifene and **VH032** (Figure 3). Among them, **ERD-56** showed significant degradation properties of ERα protein at 100 nM, and also showed good anti-proliferative activity in MCF-7 and T47D cells with IC_{50} (half maximal inhibitory concentration) of 39.9 nM and 77.8 nM (Gonzalez et al., 2020). In order to improve the potency of **ERD-56**, they optimized the linker and **ERD-308** showed the best efficacy with DC_{50} of 0.17 nM (Hu et al., 2019). Interestingly, the ER protein degraders reported above were all designed based on **VH032** as an E3 ligase ligand. Due to the poor druggability of **VH032** itself, the druggability of ER protein degraders developed based on it was also generally poor. Different from the above studies, Arvinas has also been working on the development of ERα degraders based on CRBN. First, they designed ERα degraders based on raloxifene and lenalidomide, and found that degrader **37** (Figure 3) showed good degradation activity. Based on **37**, they optimized the linker and ERα ligands to obtain the degrader **38** targeting GSPT1. Then they modified the structure of raloxifene to obtain degrader **39**, due to the poor druggability of the long-chain linker, they decided to use the same linker that existed in **ARV-110** to obtain degrader **40**. From the activity screening

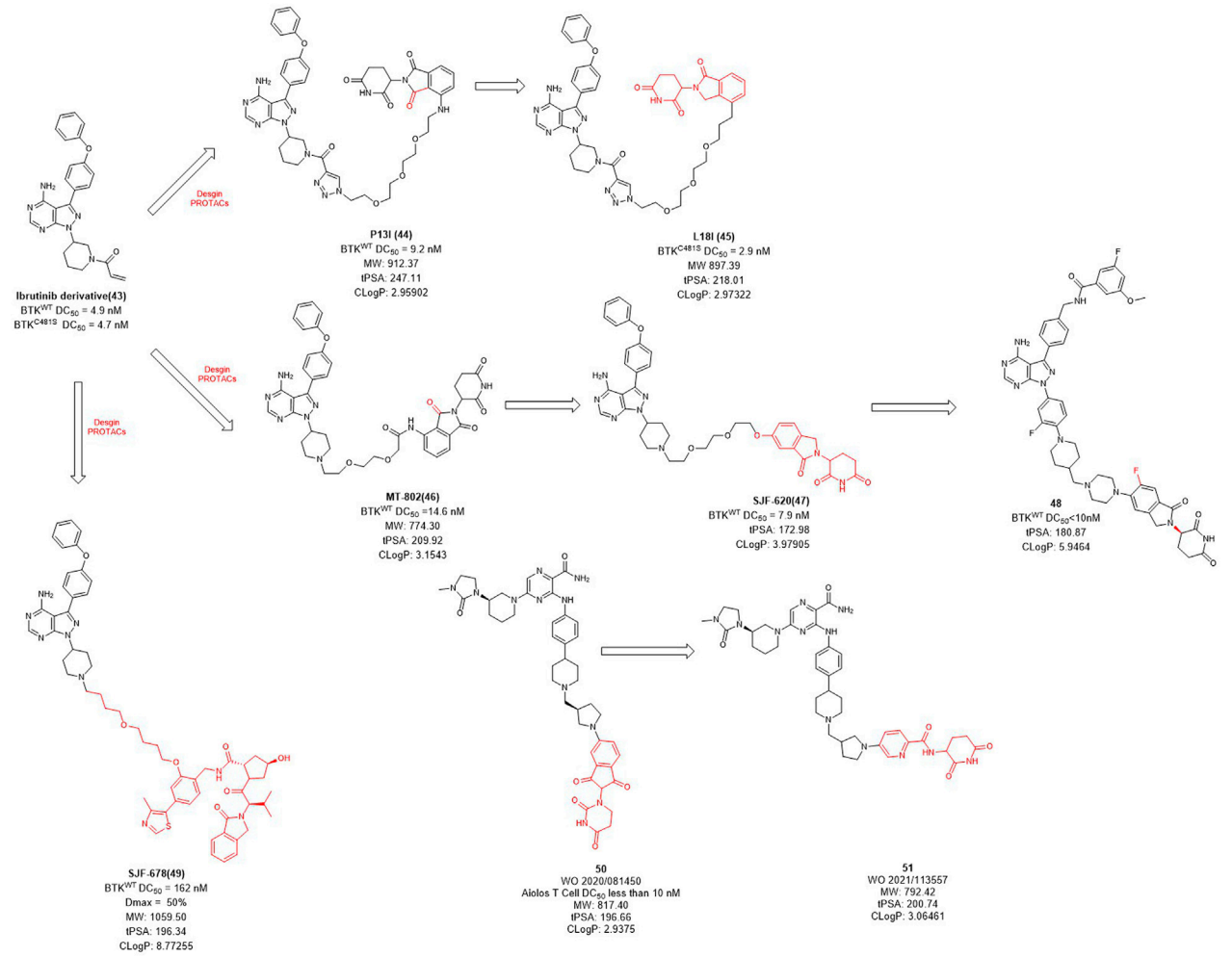

FIGURE 4
Design and optimization of BTK PROTACs.

experiment, it was found that the chiral degrader **ARV-471** had better degradation activity than **40**. The ERα degradation activity DC_{50} in MCF-7 cells was 1.8 nM and thus **ARV-471** became another clinical degrader of Arvinas (Snyder et al., 2021). Hengrui Medicine further optimized CRBN E3 ligase ligand and improve the degradation activity of ER degraders, and found compound **41** with DC_{50} value of 0.41 nM in MCF-7 cells (Yang et al., 2021). Accutar Biotech undisclosed their structure of ER clinical degrader (AC682) (NCT05080842), in their research they found that the compound **42** with DC_{50} value of 0.3 nM in MCF-7 cells (Fan et al., 2021). In summary, the optimization of E3 ubiquitin ligase ligand is the key to improve the oral availability and potency of PROTACs.

2.3 E3 ligase ligands optimization of BTK PROTACs

Bruton's tyrosine kinase (BTK) is highly expressed in various of lymphoma cells and plays an essential role in B-cell receptor (BCR) signal and B cell activation (Davis et al., 2010). Since the ATP binding site of BTK is highly conserved, how to achieve kinase selectivity of BTK inhibitors becomes the key issue. Ibrutinib is the first approved BTK covalent inhibitor with high selectivity, strong activity and good oral bioavailability (Pan et al., 2007). The acrylamide warhead of ibrutinib forms a covalent bond with the sulfhydryl group of the cysteine residue 481 in BTK, which is irreversible and thus permanently inactivates BTK kinase with an IC_{50} value of 0.5 nM after 2 h (Pan et al., 2007). However, the C481S BTK mutation (cysteine to serine mutation at position 481) prevents the formation of the critical covalent bond with ibrutinib, leading to drug resistance (Woyach et al., 2014). In order to overcome this challenge, in 2018, Rao et al. applied the PROTAC technology for ibrutinib-resistant BTK degradation and reported **P13I** (Figure 4) which is an ibrutinib and pomalidomide-linked degrader with DC_{50} value of 9.2 nM for wild-type and DC_{50} value of 30 nM for ibrutinib-resistant C481S BTK in Mino cells (Sun et al., 2018). While ibrutinib has difficulty inhibiting the autophosphorylation of C481S mutant BTK, **P13I** is effective at low concentrations. For HBL-1 cells expressing the C481S mutant BTK, the GI_{50} (50% growth inhibitory concentration) of **P13I** was about 28 nM compared to about 700 nM for ibrutinib, a 20-fold decrease in potency. In

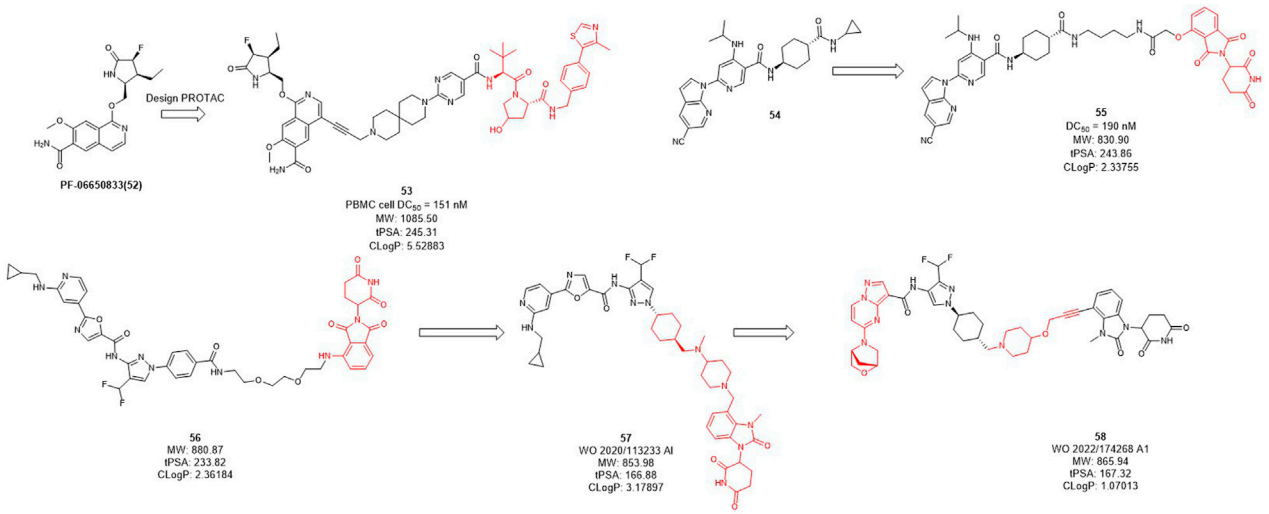

FIGURE 5
Design and optimization of IRAK4 PROTACs.

addition, **P13I** showed no effect on ITK, EGFR and TEC family kinases that cause side effects. Subsequently, in order to improve the aqueous solubility of **P13I** for both *in vitro* and *in vivo* evaluations, Rao et al. further optimized the E3 ligase ligand of **P13I** with lenalidomide and to obtain a new degrader **L18I** (Sievers et al., 2018; Sun et al., 2019). **L18I** exhibited good solubility in phosphate buffered saline (PBS), and inhibit C481S BTK in DLBCL tumors growth *in vivo*. These efforts suggest that PROTACs may provide a new treatment strategy for ibrutinib-resistant tumors.

Unlike the usually used ibrutinib-based BTK PROTACs (In this section we only discuss the reversible non-covalent BTK PROTACs), Crews et al. reported another non-covalent analog of ibrutinib, and developed a novel CRBN-recruiting BTK PROTAC, **MT-802** (Figure 4), which induced the efficient degradation of both wild-type (DC_{50} = 14.6 nM) and C481S mutation (DC_{50} = 14.9 nM) BTK (Buhimschi et al., 2018). Meanwhile, they found that the degradation efficiency of VHL-recruited BTK PROTAC degrader **SJF678** was significantly weaker than that of CRBN-recruited BTK PROTACs. They then developed a BTK degrader **49** based on the E3 ligand of **ARV-110** with DC_{50} value less than 10 nM treated in RAMOS cell lines for 6 h. Nurix Therapeutics discovered two BTK degraders, NX-2127 and NX-5948, currently in Phase I clinical trials and their structures have not been disclosed. In recent years, they have disclosed oral PROTAC degraders **50** and **51** with good activities both *in vitro* and *in vivo*, as well as oral bioavailability (Robbins et al., 2020; Sands et al., 2020). The druggability of BTK degraders was significantly improved after modifying the linker to make it more rigid and reducing the molecular weight of the E3 ligand.

2.4 E3 ligase ligands optimization of IRAK4 PROTACs

Interleukin-1 receptor-associated kinase 4 (IRAK4) is a serine/threonine kinase that not only performs phosphorylation but also functions as a scaffold role in Toll-like receptor (TLR) and interleukin-1 receptor (IL-1R) signaling pathways (Brzezinska et al., 2009; Lim et al., 2013; Vollmer et al., 2017). As a promising therapeutic target for diffusing large B-cell lymphoma driven by the MYD88 L265P mutant, the IRAK4 target receives significant attention. While Previous inhibitors had only moderate effects on IRAK4 target because they inhibited kinase function but had no effect on scaffold function. Unlike traditional small molecule inhibitors, which only inhibit kinase activity, PROTACs for protein degradation may offer a solution to block both IRAK4 kinase activity and scaffold capabilities. In 2019, Anderson et al. selected **PF-06650833** as IRAK4 inhibitor and synthesized a series of compounds based on VHL, CRBN, and IAP ligands. Among them, only the degrader **53** (Figure 5) based on VHL showed degradation activity of IRAK, with the DC_{50} value of 151 nM in PBMC cell (Nunes et al., 2019). In 2020, Dai et al. designed and synthesized a series of CRBN-based IRAK4 degraders and compound **55** showed DC_{50} value of 190 nM *in vitro* (Zhang et al., 2020). However, its degradation activity may be weaker than that of inhibitors **54**. It may be due to the weak affinity between the inhibitor and the target protein, and replacing the E3 ligand will not obtain the desired potency.

Kymera has two IRAK4 degraders, KT-474 and KT-413 in phase I clinical trial while their structures are undisclosed (Kymera, 2022). From their published patent (WO 2020/113233 Al), they obtained a series of IRAK4 degraders based on CRBN in combination with different IRAK4 inhibitors, most of which such as compound **56** (Figure 5) showed more than 50% degradation of IRAK4 at 0.01 nM in PMBC cells (Kargbo, 2019) (e.g., compound **57**). Subsequently, the E3 ligase ligand part of **56** was replaced with the CRBN ligand, and the linker-optimized degrader **57** also showed DC_{50} less than 0.01 nM in PMBC cells (Mainolfi et al., 2020). Recently, they disclosed the structure of compound **58** which is also based on CRBN ligand and showed excellent *in vitro* and *in vivo* activity, as well as oral bioavailability (Gollob et al., 2022).

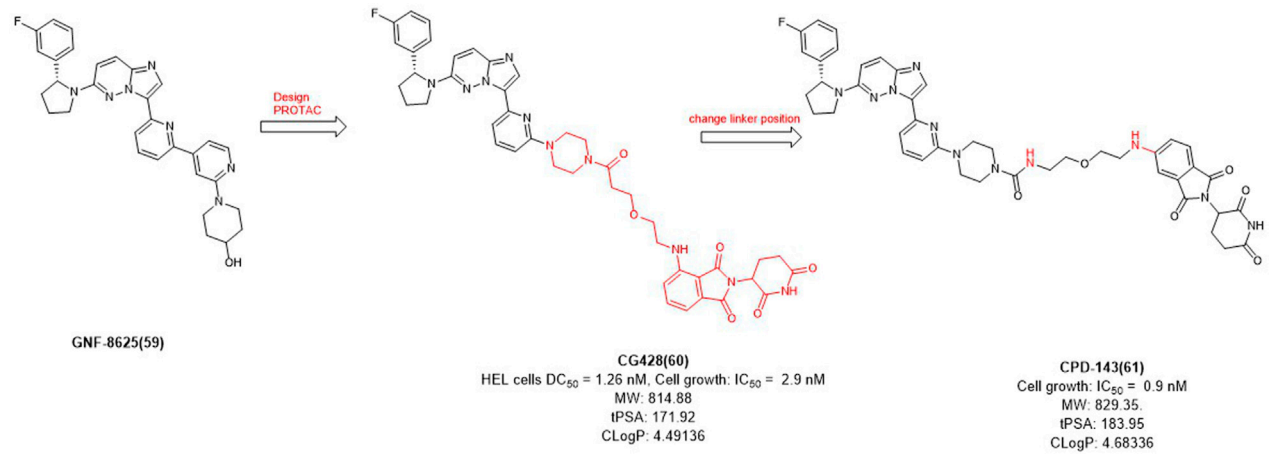

FIGURE 6
Design and optimization of TRK PROTACs.

2.5 E3 ligase ligands optimization of TRK PROTACs

The tropomyosin receptor kinase (TRK) receptor family comprises three members: TRKA, TRKB, and TRKC that are encoded by the NTRK1, NTRK2, and NTRK3 genes, respectively, which plays an important role in regulating cell differentiation, proliferation, pain, and survival (Pulciani et al., 1982; Martin-Zanca et al., 1986; Klein et al., 1989). TRKs are tyrosine kinases receptors and their main implication is the development and function of neuronal tissues (Kargbo, 2020). Although the targeted treatment of TRK1 and TRK2 shows an overall good safety profile in the clinic trials, this strategy could also be improved because currently available pan-TRK kinase inhibitors may induce off-target adverse effects by modulating TRK family members present in the CNS. Currently, moderate off-target adverse effects have been observed, such as dizziness/ataxia, paresthesia, and weight gain (Drilon, 2019). Non-specific side effects and drug resistance to TRK kinase inhibitors remain great challenges for effective treatment (Kargbo, 2020). In contrast, PROTACs technology keep the target protein in the periphery without penetrating the blood-brain barrier, thus avoid the side effects of off-targeting to the CNS.

In 2020, Cullgen et al. selected **GNF-8625** (Figure 6) as TRK inhibitor and linked with CRBN to obtain a series of TRK degraders and **CG428** proved to be the most promising degrader. It demonstrated that **CG428** can induce the degradation of wild-type TRKA in HEL cells with DC_{50} value of 1.26 nM and also inhibit cell growth with IC_{50} value of 2.9 nM (Chen et al., 2020). They then changed the connect position of pomalidomide with linker and obtained compound **CPD-143** with an increased activity which the cell growth IC_{50} was 0.9 nM (Kargbo, 2020). It can be seen that when optimizing PROTACs, once the POI and E3 ligands were identified, changing the linker position on the E3 ligase ligand could be considered to improve the potency of PROTACs.

2.6 E3 ligase ligands optimization of BRD9 PROTACs

The BRD9 (bromodomain-containing protein 9) has gained special attention as a component of the human ATP-dependent chromatin remodeling BAF (BRG1/BRM-associated factor) complex (also known as mammalian SWI/SNF (SWItch Sucrose Non-Fermentable)) (Kadoch et al., 2013; Theodoulou et al., 2016). Studies have shown that BRD9 is preferentially used by cancers harboring SMARCB1 abnormalities, such as malignant rhabdoid tumors and several specific types of sarcomas (Kim et al., 2014). BRD9-containing complexes bind to active promoters and enhancers where they contribute to gene expression (Gatchalian et al., 2018). Loss of BRD9 leads to changes in gene expression related to apoptosis regulation, translation and development regulation. BRD9 is essential for the proliferation of SMARCB1-deficient cancer cell lines and is therefore a therapeutic target for these lethal cancers, and it is also a key target for causing acute myeloid leukemia (Hohmann et al., 2016; Michel et al., 2018). Despite the early discovery of BRD9 inhibitors, there is limited understanding of the function of BRD9 beyond acetyl lysine recognition based on early chemical probes.

Therefore, Bradner et al. designed the first BRD9 degrader **63** in 2017 to provide a tool compound (Figure 7) (Remillard et al., 2017). Compound **63** was designed by using **BI-7273** as inhibitor of BRD9 and CRBN ligand pomalidomide as E3 ligase ligand, it turned out to be valuable for exploring the biological and therapeutic potential of degrading BRD9. C4 Therapeutics (C4T) started with **64** and optimized both BRD9 inhibitors and E3 ligands and finally obtained the tool degrader **65** with DC_{50} value of 5 nM.

Compound **66** was optimized based on the structure of compound **65** with fewer hydrogen bond donors and its bioavailability (F %) in mice was increased to 100%, thus improving the druggability of the degrader. Subsequently, they made minor modifications of the POI and linker of compound **65**, more importantly, for the E3 ligase ligand part, they replaced the F to trifluoromethyl group of the pomalidomide to obtain the degrader **CFT8634** with high oral bioavailability (Jackson et al., 2022). Finally, Food and drug

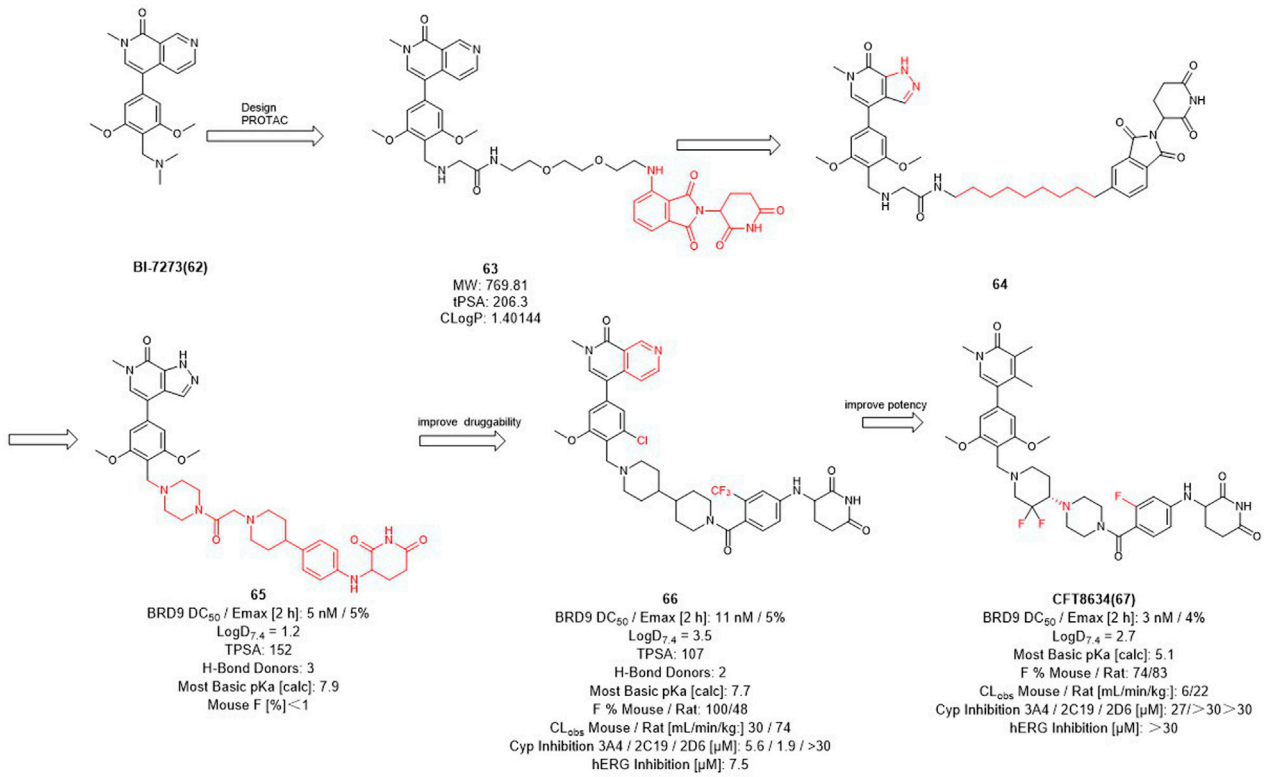

FIGURE 7
Design and optimization of BRD9 PROTACs.

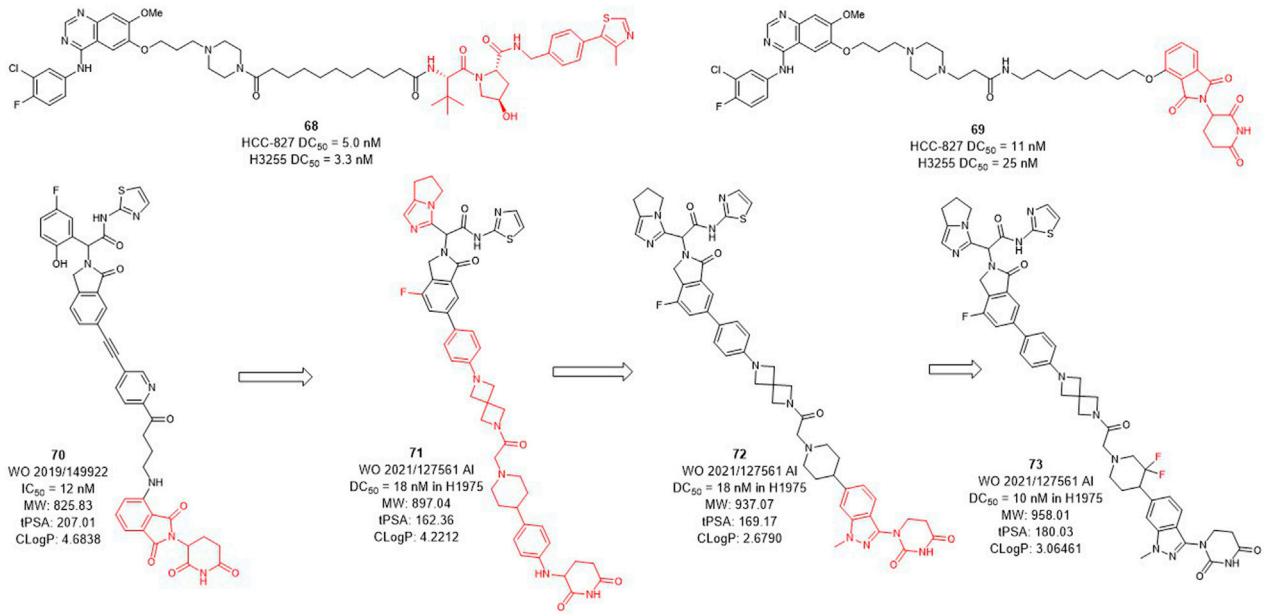

FIGURE 8
Design and optimization of EGFR L858R PROTACs.

Administration (FDA) has granted orphan drug designation (ODD) to **CFT8634** (Figure 7) for the treatment of soft tissue sarcoma which is an orally bioavailable, selective degrader of BRD9 (DC_{50} = 3 nM) (Sabnis, 2021). In summary, the optimization process from **64** to **CFT8634** indicates that the dramatic change in their E3 ligands fraction improves their treatment potential.

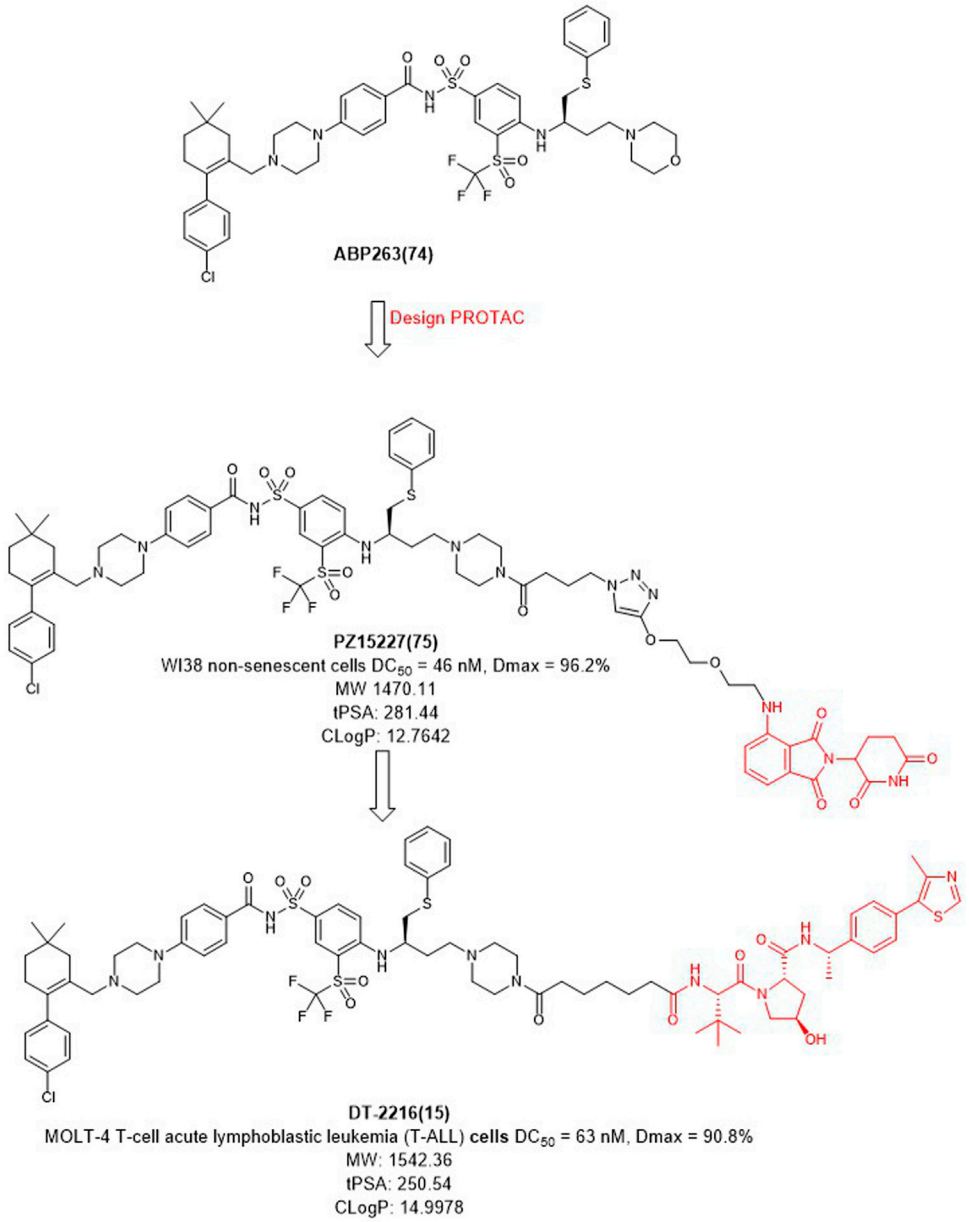

FIGURE 9
Design and optimization of BCL-X_L PROTACs.

2.7 E3 ligase ligands optimization of EGFR L858R PROTACs

Several epidermal growth factor receptor (EGFR) tyrosine kinase inhibitors have been developed and approved by the FDA for the treatment of non-small-cell lung cancer, but their efficacy may be compromised by drug resistance in EGFR-mutant variants (Sharma et al., 2007; Hirsch et al., 2017). Activating mutations, mainly in-frame deletions in exon 19 and L858R mutations, the former occurring in the αC-helix domain and the latter in the adenosine triphosphate (ATP) binding domain of the EGFR kinase. The EGFR L858R variant leads to poor prognosis and high incidence of malignant pleural effusion in non-small cell lung cancer, and the current small molecule drugs are only moderately effective against this variant (Kohno et al., 2021; Matsui et al., 2021). The development of EGFR L858R degraders based on PROTACs technology has become a new strategy. In 2020, Jin et al. designed and synthesized EGFR degraders with gefitinib and VHL or CRBN-recruited E3 ligands. The DC_{50} values of VHL-based degrader **68** (Figure 8) were 5.0 nM in HCC-827 cells and 3.3 nM in H3255 cells. The DC_{50} values of compound **69** which was based on CRBN ligand were 11 nM and 25 nM, respectively. In addition, they also showed good plasma exposure in mice.

C4T discovered the CRBN-based EGFR L858R degrader **70** (Figure 8) with an IC_{50} (BaF3 EGFR T790M/L858R/C797S degradation) value of 12 nM (Duplessis et al., 2019). After the optimization of the linker and the CRBN ligand, compounds **71** and **72** were subsequently synthesized, both showed a DC_{50} value

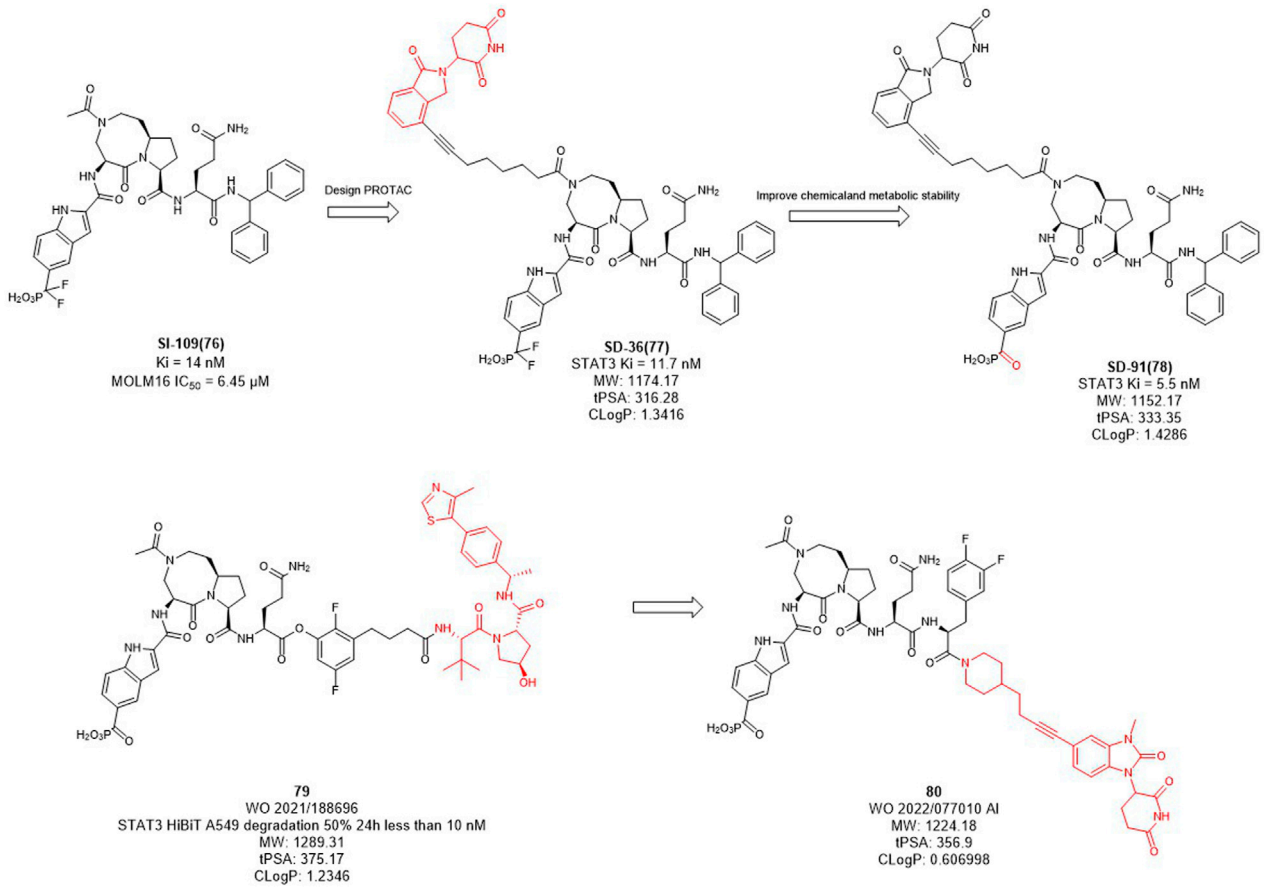

FIGURE 10
Design and optimization of STAT3 PROTACs.

TABLE 2 Summary of the chemical properties of E3 ligase ligands in clinical trials.

E3 ligase ligand	E3 ligase	MW	ROA	tPSA	cLog P
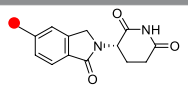	CRBN	244.08	Oral	66.48	0.305
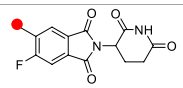	CRBN	276.05	Oral	83.55	0.747
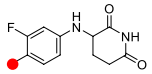	CRBN	222.08	Oral	58.2	1.184
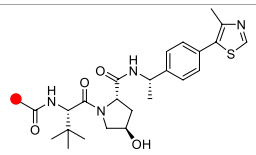	VHL	486.23	I.v	111.1	2.343

Red spot: Linking site.

of 18 nM in H1975 cells. Based on the structure of **72**, compound **73** was further identified, which improved the DC_{50} value to 10 nM in H1975 cells. C4T replaced the lenalidomide ligand with a new CRBN-based derivative ligand, resulted in a better activity of compound **73** than compound **70** on the basis of structural optimization (Nasveschuk et al., 2021).

2.8 E3 ligase ligands optimization of BCL-X_L PROTACs

BCL-X_L belongs to the anti-apoptotic BCL-2 protein family and plays a key role in determining cell life and death by regulating the intrinsic apoptotic pathway (Czabotar et al., 2014). The anti-apoptotic function of BCL-X_L protects cancer cells and induces drug resistance, which also promotes tumor progression (Igney et al., 2002). Inhibition of BCL-X_L has been of great interest as a potential cancer therapeutic strategy. However, traditional BCL-X_L inhibitors, such as **ABT263** (Figure 9), exhibit targeted and dose-limited platelet toxicity (Zhang et al., 2019). Since the tissue distribution studies of VHL and CRBN have shown that its expression in platelets is minimal, degraders of BCL-X_L could be developed through PROTAC technology.

In 2019, Zheng et al. selected **ABT263** (Figure 9) as BCL-X_L inhibitor connected with CRBN to obtain the degrader **PZ15227** with DC_{50} value of 46 nM and *D*max of 96.2% in WI38 non-senescent cells (NCs) (He et al., 2020). Compared with **ABT263**, **PZ15227** showed reduced toxicity to platelets but remained toxicity against senescent cells because CRBN was less expressed in platelets. Subsequently, they found that CRBN-based PROTACs were highly potent against other cancer cell lines, but less potent in MOLT-4 cells, possibly due to the low expression of CRBN (Zhang et al., 2020).

In 2021, Zheng *et al.* discovered **DT2216** (NCT04886622) as an effective BCL-X_L degrader based on VHL E3 ligase with a DC_{50} value of 63 nM and *D*max of 90.8% in MOLT-4 cells. Compared with **ABT263** (EC_{50} = 0.191 μM, half max effective concentration) and **DT2216** (EC_{50} = 0.052 μM), the latter showed increased cytotoxicity to MOLT-4 cells. More importantly, **DT2216** exerted almost no effect on the viability of platelets up to a concentration of 3 μM which showed better effect than **PZ15227**. **DT2216** was found to have enhanced efficacy against a variety of BCL-X_L-dependent leukemia cell lines and exhibited much less toxic to platelets than **ABT263** (Khan et al., 2019). Therefore, **DT2216** was approved by FDA to enter phase I clinical trials for the treatment of advanced liquid and solid tumors. These findings demonstrated the potential of using PROTAC to reduce the toxicity of targeted drugs.

2.9 E3 ligase ligands optimization of STAT3 PROTACs

In mammalian cells, the signal transducer and activator of transcription 3 (STAT3) is an essential component of the seven members of the STAT family (STAT1, 2, 3, 4, 5a, 5b, 6). STAT3 is widely expressed in a variety of cells and tissues and activates the expression of downstream genes in response to various cytokines, growth factors and other signals (Yu et al., 2009). Under normal physiological conditions, STAT3 activation is rapid and transient, mainly due to the presence of negative regulators in cells. However, STAT3 is continuously activated and expressed at high levels in tumor cells. Overexpression of STAT3 is strongly associated with cancer cell survival, proliferation, invasion, metastasis, drug resistance, and immune evasion, among other related genes. Since STAT3 dysregulation contributes to many human cancers and other human diseases (Wang et al., 2018). Inhibition or downregulation of STAT3 expression has become a main strategy for cancer therapy. However, to date, no drugs based on STAT3 targets have been approved in the market. Wang et al. designed several STAT3 degraders based on **SI-109** (Figure 10) and lenalidomide, and discovered that degrader **SD-36** exhibited good degradation activity (Zhou et al., 2019). In the subsequent studies, they converted the difluoro methylene group of **SD-36** to a ketone group to obtain degrader **SD-91** with improved potency both *in vitro* and *in vivo* (Zhou et al., 2021). Kymera Therapeutics chose the similar inhibitor, **SI-109** (Figure 10), but changed the linker attachment site and synthesized a series of degraders based on VHL ligand or CRBN ligand derivatives (Yang et al., 2022). From their disclosed data, the degradation activity of VHL-based degraders was generally better than that of CRBN-based derivatives. However, their recent patent selected CRBN-based ligands for further optimization may due to the large molecular of VHL ligand. It is hypothesized that reducing the molecular weight and the hydrogen bond receptors of E3 ligands may be the trend for PROTACs to be more druggable.

3 Conclusions and perspectives

Since PROTAC technology was first identified as a clinical therapeutic strategy, both academia and industry have shown great interest in PROTACs technology. However, PROTACs degraders have relatively more complex chemical structures and biological mechanisms than traditional small molecule drugs, which require efforts in the fields of organic synthetic chemistry and medicinal chemistry.

Although PROTACs technology has shown many advantages over traditional small molecule drugs for antitumor therapy, unlike traditional small molecule drugs, they are mostly regarded as "beyond rule-of-five". PROTACs molecules have more hydrogen bond donors and acceptors and larger molecular weights, mostly around 1,000 Da. Therefore, the poor membrane permeability and low bioavailability of PROTACs molecules limit its clinical application. In the process of optimizing E3 ligase ligands by medicinal chemists, it is important to ensure a high affinity between the E3 ligase ligands and E3 ubiquitin ligases. The excessive molecular weight of E3 ligands leads to poor membrane permeability. Based on the suitable molecular weight size of CRBN ligand, **ARV-110** and **CFT8634** were rationally designed. In addition, they both introduced F in the aromatic ring of CRBN ligands, probably to improve their druggability. Most of the other CRBN ligands modifications are designed to improve the affinity with E3 ligases or to improve the druggability properties of these degraders in oral PROTACs.

Typically, the POIs based on agonists or antagonists of target proteins, as well as the traditional pharmacological optimization of these small molecules, have been studied in the design and optimization of PROTACs. The optimization of linkers tends to have more rigid structures. However, although more than 600 E3 ligases have been identified, the number of small molecule ligands available to design PROTAC molecules for E3 ligands is rather limited, and only CRBN-based PROTACs have been clinically achieved for oral application (Table 2).

It is believed that advances in artificial intelligence techniques (protein structure prediction), virtual drug screening, and other technologies will facilitate the discovery of E3 ligands and provide more tools for PROTAC design. These advances will greatly facilitate the transition of PROTACs degraders from being considered as tool molecules to small molecule clinical drug candidates.

Author contributions

Concept, writing, review, and revision of the manuscript: MW, S-XG, HJ, and HX; all authors have approved the final version of the manuscript.

Funding

This work was supported by Highlevel new R&D institute (2019B090904008), and High-level Innovative Research Institute (2021B0909050003) from Department of Science and Technology of Guangdong Province.

Conflict of interest

The authors declare that the research was conducted in the absence of any commercial or financial relationships that could be construed as a potential conflict of interest.

Publisher's note

All claims expressed in this article are solely those of the authors and do not necessarily represent those of their affiliated organizations, or those of the publisher, the editors and the reviewers. Any product that may be evaluated in this article, or claim that may be made by its manufacturer, is not guaranteed or endorsed by the publisher.

References

Arnal, J. F., Lenfant, F., Metivier, R., Flouriot, G., Henrion, D., Adlanmerini, M., et al. (2017). Membrane and nuclear estrogen receptor alpha actions: From tissue specificity to medical implications. *Physiol. Rev.* 97, 1045–1087. doi:10.1152/physrev.00024.2016

Békés, M., Langley, D. R., and Crews, C. M. (2022). PROTAC targeted protein degraders: The past is prologue. *Nat. Rev. Drug Discov.* 21, 181–200. doi:10.1038/s41573-021-00371-6

Brzezinska, A. A., Johnson, J. L., Munafo, D. B., Ellis, B. A., and Catz, S. D. (2009). Signalling mechanisms for toll-like receptor-activated neutrophil exocytosis: Key roles for interleukin-1-receptor-associated kinase-4 and phosphatidylinositol 3-kinase but not toll/IL-1 receptor (TIR) domain-containing adaptor inducing IFN-beta (TRIF). *Immunology* 127, 386–397. doi:10.1111/j.1365-2567.2008.02980.x

Buhimschi, A. D., Armstrong, H. A., Toure, M., Jaime-Figueroa, S., Chen, T. L., Lehman, A. M., et al. (2018). Targeting the C481S ibrutinib-resistance mutation in bruton's tyrosine kinase using PROTAC-mediated degradation. *Biochemistry* 57, 3564–3575. doi:10.1021/acs.biochem.8b00391

Chen, L., Chen, Y., Zhang, C., Jiao, B., Liang, S., Tan, Q., et al. (2020). Discovery of first-in-class potent and selective tropomyosin receptor kinase degraders. *J. Med. Chem.* 63, 14562–14575. doi:10.1021/acs.jmedchem.0c01342

Criscitiello, C., Guerini-Rocco, E., Viale, G., Fumagalli, C., Sajjadi, E., Venetis, K., et al. (2022). Immunotherapy in breast cancer patients: A focus on the use of the currently available biomarkers in oncology. *Anticancer Agents Med. Chem.* 22, 787–800. doi:10.2174/1871520621666210706144112

Czabotar, P. E., Lessene, G., Strasser, A., and Adams, J. M. (2014). Control of apoptosis by the BCL-2 protein family: Implications for physiology and therapy. *Nat. Rev. Mol. Cell Biol.* 15, 49–63. doi:10.1038/nrm3722

Davis, R. E., Ngo, V. N., Lenz, G., Tolar, P., Young, R. M., Romesser, P. B., et al. (2010). Chronic active B-cell-receptor signalling in diffuse large B-cell lymphoma. *Nature* 463, 88–92. doi:10.1038/nature08638

De Bono, J., Mateo, J., Fizazi, K., Saad, F., Shore, N., Sandhu, S., et al. (2020). Olaparib for metastatic castration-resistant prostate cancer. *N. Engl. J. Med.* 382, 2091–2102. doi:10.1056/NEJMoa1911440

Drilon, A. (2019). TRK inhibitors in TRK fusion-positive cancers. *Ann. Oncol.* 30, viii23–viii30. viii23-viii30. doi:10.1093/annonc/mdz282

Duplessis, M., Jaeschke, G., Kuhn, B., Lazarski, K., Liang, Y. N., Alice, Yvonne, et al. (2019). Preparation of substituted isoindoline compounds which cause degradation of EGFR and are useful as anticancer agents. U.S. patent NO WO2019149922. Watertown: United States Patent Application Publication.

Fan, J., Qian, Y., He, W., and Liu, K. (2021). Bicyclic imide derivative, preparation method thereof, and application thereof in medicine. CN patent NO WO 2021/143822 Al. Shanghai: World Intellectual Property Organization.

Gao, X., Iii, H. a. B., Vuky, J., Dreicer, R., Sartor, A. O., Sternberg, C. N., et al. (2022). Phase 1/2 study of ARV-110, an androgen receptor (AR) PROTAC degrader, in metastatic castration-resistant prostate cancer (mCRPC). *J. Clin. Oncol.* 40, 17. doi:10.1200/JCO.2022.40.6_suppl.017

Gatchalian, J., Malik, S., Ho, J., Lee, D. S., Kelso, T. W. R., Shokhirev, M. N., et al. (2018). A non-canonical BRD9-containing BAF chromatin remodeling complex regulates naive pluripotency in mouse embryonic stem cells. *Nat. Commun.* 9, 5139. doi:10.1038/s41467-018-07528-9

Gollob, J., Davis, J., Mcdonald, A., and Rong, H. (2022). Irak4 degraders and uses thereof. U.S. patent NO WO 2022/174268 Al. Watertown: World Intellectual Property Organization.

Gonzalez, T. L., Hancock, M., Sun, S., Gersch, C. L., Larios, J. M., David, W., et al. (2020). Targeted degradation of activating estrogen receptor alpha ligand-binding domain mutations in human breast cancer. *Breast Cancer Res. Treat.* 180, 611–622. doi:10.1007/s10549-020-05564-y

Han, T., Goralski, M., Gaskill, N., Capota, E., Kim, J., Ting, T. C., et al. (2017). Anticancer sulfonamides target splicing by inducing RBM39 degradation via recruitment to DCAF15. *Science* 356, eaal3755. doi:10.1126/science.aal3755

Han, X., Wang, C., Qin, C., Xiang, W., Fernandez-Salas, E., Yang, C.-Y., et al. (2019a). Discovery of ARD-69 as a highly potent proteolysis targeting chimera (PROTAC) degrader of androgen receptor (AR) for the treatment of prostate cancer. *J. Med. Chem.* 62, 941–964. doi:10.1021/acs.jmedchem.8b01631

Han, X., Zhao, L., Xiang, W., Qin, C., Miao, B., Mceachern, D., et al. (2021). Strategies toward discovery of potent and orally bioavailable proteolysis targeting chimera degraders of androgen receptor for the treatment of prostate cancer. *J. Med. Chem.* 64, 12831–12854. doi:10.1021/acs.jmedchem.1c00882

Han, X., Zhao, L., Xiang, W., Qin, C., Miao, B., Xu, T., et al. (2019b). Discovery of highly potent and efficient PROTAC degraders of androgen receptor (AR) by employing weak binding affinity VHL E3 ligase ligands. *J. Med. Chem.* 62, 11218–11231. doi:10.1021/acs.jmedchem.9b01393

He, Y., Zhang, X., Chang, J., Kim, H. N., Zhang, P., Wang, Y., et al. (2020). Using proteolysis-targeting chimera technology to reduce navitoclax platelet toxicity and improve its senolytic activity. *Nat. Commun.* 11, 1996. doi:10.1038/s41467-020-15838-0

Henning, N. J., Manford, A. G., Spradlin, J. N., Brittain, S. M., Zhang, E., Mckenna, J. M., et al. (2022). Discovery of a covalent FEM1B recruiter for targeted protein degradation applications. *J. Am. Chem. Soc.* 144, 701–708. doi:10.1021/jacs.1c03980

Hershko, A., and Ciechanover, A. (1992). The ubiquitin system for protein degradation. *Annu. Rev. Biochem.* 61, 761–807. doi:10.1146/annurev.bi.61.070192.003553

Hershko, A., Heller, H., Elias, S., and Ciechanover, A. (1983). Components of ubiquitin-protein ligase system. Resolution, affinity purification, and role in protein breakdown. *J. Biol. Chem.* 258, 8206–8214. doi:10.1016/s0021-9258(20)82050-x

Hirsch, F. R., Scagliotti, G. V., Mulshine, J. L., Kwon, R., Curran, W. J., Wu, Y.-L., et al. (2017). Lung cancer: Current therapies and new targeted treatments. *Lancet* 389, 299–311. doi:10.1016/s0140-6736(16)30958-8

Hohmann, A. F., Martin, L. J., Minder, J. L., Roe, J. S., Shi, J., Steurer, S., et al. (2016). Sensitivity and engineered resistance of myeloid leukemia cells to BRD9 inhibition. *Nat. Chem. Biol.* 12, 672–679. doi:10.1038/nchembio.2115

Honda, R., Tanaka, H., and Yasuda, H. (1997). Oncoprotein MDM2 is a ubiquitin ligase E3 for tumor suppressor p53. *FEBS Lett.* 420, 25–27. doi:10.1016/s0014-5793(97)01480-4

Hu, J., Hu, B., Wang, M., Xu, F., Miao, B., Yang, C. Y., et al. (2019). Discovery of ERD-308 as a highly potent proteolysis targeting chimera (PROTAC) degrader of estrogen receptor (ER). *J. Med. Chem.* 62, 1420–1442. doi:10.1021/acs.jmedchem.8b01572

Huang, B., Omoto, Y., Iwase, H., Yamashita, H., Toyama, T., Coombes, R. C., et al. (2014). Differential expression of estrogen receptor α, β1, and β2 in lobular and ductal breast cancer. *Proc. Natl. Acad. Sci. U. S. A.* 111, 1933–1938. doi:10.1073/pnas.1323719111

Igney, F. H., and Krammer, P. H. (2002). Death and anti-death: Tumour resistance to apoptosis. *Nat. Rev. Cancer* 2, 277–288. doi:10.1038/nrc776

Itoh, Y., Ishikawa, M., Kitaguchi, R., Sato, S., Naito, M., and Hashimoto, Y. (2011). Development of target protein-selective degradation inducer for protein knockdown. *Bioorg Med. Chem.* 19, 3229–3241. doi:10.1016/j.bmc.2011.03.057

Ivan, M., Kondo, K., Yang, H., Kim, W., Valiando, J., Ohh, M., et al. (2001). HIFα targeted for VHL-mediated destruction by proline hydroxylation: Implications for O_2 sensing. *Science* 292, 464–468. doi:10.1126/science.1059817

Jaakkola, P., Mole, D. R., Tian, Y. M., Wilson, M. I., Gielbert, J., Gaskell, S. J., et al. (2001). Targeting of HIF-alpha to the von Hippel-Lindau ubiquitylation complex by O2-regulated prolyl hydroxylation. *Science* 292, 468–472. doi:10.1126/science.1059796

Jackson, K. L., Agafonov, R. V., Carlson, M. W., Chaturvedi, P., Cocozziello, D., Cole, K., et al. (2022). Abstract ND09: The discovery and characterization of CFT8634: A potent and selective degrader of BRD9 for the treatment of SMARCB1-perturbed cancers. *Cancer Res.* 82, ND09. doi:10.1158/1538-7445.Am2022-nd09

Kadoch, C., Hargreaves, D. C., Hodges, C., Elias, L., Ho, L., Ranish, J., et al. (2013). Proteomic and bioinformatic analysis of mammalian SWI/SNF complexes identifies extensive roles in human malignancy. *Nat. Genet.* 45, 592–601. doi:10.1038/ng.2628

Kargbo, R. B. (2020). PROTAC compounds targeting TRK for use in cancer therapeutics. *ACS Med. Chem. Lett.* 11, 1090–1091. doi:10.1021/acsmedchemlett.0c00235

Kargbo, R. B. (2019). PROTAC degradation of IRAK4 for the treatment of neurodegenerative and cardiovascular diseases. *ACS Med. Chem. Lett.* 10, 1251–1252. doi:10.1021/acsmedchemlett.9b00385

Kawahata, I., and Fukunaga, K. (2020). Degradation of tyrosine hydroxylase by the ubiquitin-proteasome system in the pathogenesis of Parkinson's disease and dopa-responsive dystonia. *Int. J. Mol. Sci.* 21, 3779. doi:10.3390/ijms21113779

Khan, S., Zhang, X., Lv, D., Zhang, Q., He, Y., Zhang, P., et al. (2019). A selective BCL-XL PROTAC degrader achieves safe and potent antitumor activity. *Nat. Med.* 25, 1938–1947. doi:10.1038/s41591-019-0668-z

Kim, K. H., and Roberts, C. W. (2014). Mechanisms by which SMARCB1 loss drives rhabdoid tumor growth. *Cancer Genet.* 207, 365–372. doi:10.1016/j.cancergen.2014.04.004

Klein, R., Parada, L. F., Coulier, F., and Barbacid, M. (1989). trkB, a novel tyrosine protein kinase receptor expressed during mouse neural development. *EMBO J.* 8, 3701–3709. doi:10.1002/j.1460-2075.1989.tb08545.x

Kohno, T., Matsui, T., and Enatsu, S. (2021). Differences between EGFR exon 19 deletion and exon 21 L858R point mutation, frequently detected EGFR mutations in patients with non-small cell lung cancer, from a molecular biology viewpoint. *Gan Kagaku Ryoho* 48, 1463–1467.doi:10.1038/srep31636

Komander, D., and Rape, M. (2012). The ubiquitin code. *Annu. Rev. Biochem.* 81, 203–229. doi:10.1146/annurev-biochem-060310-170328

Kregel, S., Wang, C., Han, X., Xiao, L., Fernandez-Salas, E., Bawa, P., et al. (2020). Androgen receptor degraders overcome common resistance mechanisms developed during prostate cancer treatment. *Neoplasia* 22, 111–119. doi:10.1016/j.neo.2019.12.003

Kumar, R., and Sabapathy, K. (2019). RNF4-A paradigm for SUMOylation-mediated ubiquitination. *Proteomics* 19, e1900185. doi:10.1002/pmic.201900185

Kymera (2022). https://investors.kymeratx.com/news-releases/news-release-details/kymera-announces-positive-results-phase-1-clinical-trial (Accessed Dec 14, 2022).

Kymera (2022). https://investors.kymeratx.com/news-releases/news-release-details/kymera-therapeutics-doses-first-patients-phase-1-oncology-trials (Accessed Jun 15, 2022).

Lim, K. H., and Staudt, L. M. (2013). Toll-like receptor signaling. *Cold Spring Harb. Perspect. Biol.* 5, a011247. doi:10.1101/cshperspect.a011247

Liu, M., Yan, M., Lv, H., Wang, B., Lv, X., Zhang, H., et al. (2020). Macrophage K63-linked ubiquitination of YAP promotes its nuclear localization and exacerbates atherosclerosis. *Cell Rep.* 32, 107990. doi:10.1016/j.celrep.2020.107990

Luo, M., Spradlin, J. N., Boike, L., Tong, B., Brittain, S. M., Mckenna, J. M., et al. (2021). Chemoproteomics-enabled discovery of covalent RNF114-based degraders that mimic natural product function. *Cell Chem. Biol.* 28, 559–566.e15. e515. doi:10.1016/j.chembiol.2021.01.005

Lyle, C., Richards, S., Yasuda, K., Napoleon, M. A., Walker, J., Arinze, N., et al. (2019). c-Cbl targets PD-1 in immune cells for proteasomal degradation and modulates colorectal tumor growth. *Sci. Rep.* 9, 20257. doi:10.1038/s41598-019-56208-1

Mainolfi, N., Ji, N., Kluge, A. F., Weiss, M. M., Zhang, Y., and Zheng, X. (2020). Preparation of bifunctional compounds as IRAK degraders and uses thereof. U.S. patent NO WO 2020/113233 Al. Cambridge: World Intellectual Property Organization.

Martin-Zanca, D., Hughes, S. H., and Barbacid, M. (1986). A human oncogene formed by the fusion of truncated tropomyosin and protein tyrosine kinase sequences. *Nature* 319, 743–748. doi:10.1038/319743a0

Matsui, T., Tanizawa, Y., and Enatsu, S. (2021). [Exon 19 Deletion and Exon 21 L858R Point Mutation in EGFR Mutation—Positive Non—Small Cell Lung Cancer]. *Gan To Kagaku Ryoho* 48 (5), 673–676.

Michel, B. C., D'avino, A. R., Cassel, S. H., Mashtalir, N., Mckenzie, Z. M., Mcbride, M. J., et al. (2018). A non-canonical SWI/SNF complex is a synthetic lethal target in cancers driven by BAF complex perturbation. *Nat. Cell Biol.* 20, 1410–1420. doi:10.1038/s41556-018-0221-1

Mullard, A. (2019). First targeted protein degrader hits the clinic. *Nat. Rev. Drug Discov.* 21 doi:10.1038/d41573-019-00043-6

Nasveschuk, C. G., Duplessis, M., Ahn, J. Y., Hird, A. W., Michael, R. E., Lazarski, K., et al. (2021). Preparation of isoindolinone and indazole compounds for the degradation of EGFR. U.S. patent NO WO2021127561 A1. Watertown: World Intellectual Property Organization.

Neklesa, T., Snyder, L. B., Willard, R. R., Vitale, N., Pizzano, J., Gordon, D. A., et al. (2019). ARV-110: An oral androgen receptor PROTAC degrader for prostate cancer. *J. Clin. Oncol.* 37, 259. doi:10.1200/JCO.2019.37.7_suppl.259

Neklesa, T., Snyder, L. B., Willard, R. R., Vitale, N., Raina, K., Pizzano, J., et al. (2018). Abstract 5236: ARV-110: An androgen receptor PROTAC degrader for prostate cancer. *Cancer Res.* 78, 5236. doi:10.1158/1538-7445.Am2018-5236

Nunes, J., Mcgonagle, G. A., Eden, J., Kiritharan, G., Touzet, M., Lewell, X., et al. (2019). Targeting IRAK4 for degradation with PROTACs. *ACS Med. Chem. Lett.* 10, 1081–1085. doi:10.1021/acsmedchemlett.9b00219

Ohoka, N., Morita, Y., Nagai, K., Shimokawa, K., Ujikawa, O., Fujimori, I., et al. (2018). Derivatization of inhibitor of apoptosis protein (IAP) ligands yields improved inducers of estrogen receptor α degradation. *J. Biol. Chem.* 293, 6776–6790. doi:10.1074/jbc.RA117.001091

Ohoka, N., Okuhira, K., Ito, M., Nagai, K., Shibata, N., Hattori, T., et al. (2017). *In vivo* knockdown of pathogenic proteins via specific and nongenetic inhibitor of apoptosis protein (IAP)-dependent protein erasers (SNIPERs). *J. Biol. Chem.* 292, 4556–4570. doi:10.1074/jbc.M116.768853

Ohoka, N., Tsuji, G., Shoda, T., Fujisato, T., Kurihara, M., Demizu, Y., et al. (2019). Development of small molecule chimeras that recruit AhR E3 ligase to target proteins. *ACS Chem. Biol.* 14, 2822–2832. doi:10.1021/acschembio.9b00704

Ohtake, F., Fujii-Kuriyama, Y., and Kato, S. (2007). Transcription factor AhR is a ligand-dependcnt E3 ubiquitin ligase. *Tanpakushitsu kakusan Koso. Protein, nucleic Acid. enzyme* 52, 1973–1979. doi:10.1038/nature05683

Paiva, S. L., and Crews, C. M. (2019). Targeted protein degradation: Elements of PROTAC design. *Curr. Opin. Chem. Biol.* 50, 111–119. doi:10.1016/j.cbpa.2019.02.022

Pan, Z., Scheerens, H., Li, S. J., Schultz, B. E., Sprengeler, P. A., Burrill, L. C., et al. (2007). Discovery of selective irreversible inhibitors for Bruton's tyrosine kinase. *ChemMedChem* 2, 58–61. doi:10.1002/cmdc.200600221

Pei, J., Xiao, Y., Liu, X., Hu, W., Sobh, A., Yuan, Y., et al. (2022). Identification of Piperlongumine (PL) as a new E3 ligase ligand to induce targeted protein degradation. *bioRxiv*.12 doi:10.1101/2022.01.21.474712

Pohl, C., and Dikic, I. (2019). Cellular quality control by the ubiquitin-proteasome system and autophagy. *Science* 366, 818–822. doi:10.1126/science.aax3769

Pulciani, S., Santos, E., Lauver, A. V., Long, L. K., Aaronson, S. A., and Barbacid, M. (1982). Oncogenes in solid human tumours. *Nature* 300, 539–542. doi:10.1038/300539a0

Rebello, R. J., Oing, C., Knudsen, K. E., Loeb, S., Johnson, D. C., Reiter, R. E., et al. (2021). Prostate cancer. *Nat. Rev. Dis. Prim.* 7, 9. doi:10.1038/s41572-020-00243-0

Remillard, D., Buckley, D. L., Paulk, J., Brien, G. L., Sonnett, M., Seo, H.-S., et al. (2017). Degradation of the BAF complex factor BRD9 by heterobifunctional ligands. *Angew. Chem. Int. Ed.* 56, 5738–5743. doi:10.1002/anie.201611281

Robbins, D. W., Sands, A. T., Mcintosh, J., Mihalic, J., Wu, J., Kato, D., et al. (2020). Bifunctional compounds for degrading BTK via ubiquitin proteolytic pathway and their preparation. U.S. patent NO WO2020081450 A1. San Francisco: World Intellectual Property Organization.

Rodriguez-Gonzalez, A., Cyrus, K., Salcius, M., Kim, K., Crews, C. M., Deshaies, R. J., et al. (2008). Targeting steroid hormone receptors for ubiquitination and degradation in breast and prostate cancer. *Oncogene* 27, 7201–7211. doi:10.1038/onc.2008.320

Saadatzadeh, M. R., Elmi, A. N., Pandya, P. H., Bijangi-Vishehsaraei, K., Ding, J., Stamatkin, C. W., et al. (2017). The role of MDM2 in promoting genome stability versus instability. *Int. J. Mol. Sci.* 18, 2216. doi:10.3390/ijms18102216

Sabnis, R. W. (2021). BRD9 bifunctional degraders for treating cancer. *ACS Med. Chem. Lett.* 12, 1879–1880. doi:10.1021/acsmedchemlett.1c00580

Sakamoto, K. M., Kim, K. B., Kumagai, A., Mercurio, F., Crews, C. M., and Deshaies, R. J. (2001). Protacs: Chimeric molecules that target proteins to the skp1-cullin-F box complex for ubiquitination and degradation. *Proc. Natl. Acad. Sci. U. S. A.* 98, 8554–8559. doi:10.1073/pnas.141230798

Sands, A. T., and Kelly, A. (2020). Bifunctional compounds for degrading btk via ubiquitin proteosome pathway. U.S. patent NO WO2021113557. San Francisco: World Intellectual Property Organization.

Sato, S., Aoyama, H., Miyachi, H., Naito, M., and Hashimoto, Y. (2008). Demonstration of direct binding of cIAP1 degradation-promoting bestatin analogs to BIR3 domain: Synthesis and application of fluorescent bestatin ester analogs. *Bioorg Med. Chem. Lett.* 18, 3354–3358. doi:10.1016/j.bmcl.2008.04.031

Schapira, M., Calabrese, M. F., Bullock, A. N., and Crews, C. M. (2019). Targeted protein degradation: Expanding the toolbox. *Nat. Rev. Drug Discov.* 18, 949–963. doi:10.1038/s41573-019-0047-y

Schneekloth, A. R., Pucheault, M., Tae, H. S., and Crews, C. M. (2008). Targeted intracellular protein degradation induced by a small molecule: En route to chemical proteomics. *Bioorg Med. Chem. Lett.* 18, 5904–5908. doi:10.1016/j.bmcl.2008.07.114

Schneekloth, J. S., Jr., Fonseca, F. N., Koldobskiy, M., Mandal, A., Deshaies, R., Sakamoto, K., et al. (2004a). Chemical genetic control of protein levels: Selective *in vivo* targeted degradation. *J. Am. Chem. Soc.* 126, 3748–3754. doi:10.1021/ja039025z

Schneekloth, J. S., Jr., Fonseca, F. N., Koldobskiy, M., Mandal, A., Deshaies, R., Sakamoto, K., et al. (2004b). Chemical genetic control of protein levels: Selective *in vivo* targeted degradation. *J. Am. Chem. Soc.* 126, 3748–3754. doi:10.1021/ja039025z

Schulman, B. A., and Harper, J. W. (2009). Ubiquitin-like protein activation by E1 enzymes: The apex for downstream signalling pathways. *Nat. Rev. Mol. Cell Biol.* 10, 319–331. doi:10.1038/nrm2673

Sharma, S. V., Bell, D. W., Settleman, J., and Haber, D. A. (2007). Epidermal growth factor receptor mutations in lung cancer. *Nat. Rev. Cancer* 7, 169–181. doi:10.1038/nrc2088

Sievers, Q. L., Petzold, G., Bunker, R. D., Renneville, A., Słabicki, M., Liddicoat, B. J., et al. (2018). Defining the human C2H2 zinc finger degrome targeted by thalidomide analogs through CRBN. *Science* 362, eaat0572. doi:10.1126/science.aat0572

Snyder, L. B., Flanagan, J. J., Qian, Y., Gough, S. M., Andreoli, M., Bookbinder, M., et al. (2021a). Abstract 44: The discovery of ARV-471, an orally bioavailable estrogen receptor degrading PROTAC for the treatment of patients with breast cancer. *Cancer Res.* 81, 44. doi:10.1158/1538-7445.Am2021-44

Snyder, L. B., Neklesa, T. K., Chen, X., Dong, H., Ferraro, C., Gordon, D. A., et al. (2021b). Abstract 43: Discovery of ARV-110, a first in class androgen receptor degrading PROTAC for the treatment of men with metastatic castration resistant prostate cancer. *Cancer Res.* 81, 43. doi:10.1158/1538-7445.Am2021-43

Sun, X., Gao, H., Yang, Y., He, M., Wu, Y., Song, Y., et al. (2019). PROTACs: Great opportunities for academia and industry. *Signal Transduct. Target Ther.* 4, 64. doi:10.1038/s41392-019-0101-6

Sun, Y., Ding, N., Song, Y., Yang, Z., Liu, W., Zhu, J., et al. (2019). Degradation of Bruton's tyrosine kinase mutants by PROTACs for potential treatment of ibrutinib-resistant non-Hodgkin lymphomas. *Leukemia* 33, 2105–2110. doi:10.1038/s41375-019-0440-x

Sun, Y., Zhao, X., Ding, N., Gao, H., Wu, Y., Yang, Y., et al. (2018). PROTAC-induced BTK degradation as a novel therapy for mutated BTK C481S induced ibrutinib-resistant B-cell malignancies. *Cell Res.* 28, 779–781. doi:10.1038/s41422-018-0055-1

Teo, M. Y., Rathkopf, D. E., and Kantoff, P. (2019). Treatment of advanced prostate cancer. *Annu. Rev. Med.* 70, 479–499. doi:10.1146/annurev-med-051517-011947

Theodoulou, N. H., Bamborough, P., Bannister, A. J., Becher, I., Bit, R. A., Che, K. H., et al. (2016). Discovery of I-BRD9, a selective cell active chemical probe for bromodomain containing protein 9 inhibition. *J. Med. Chem.* 59, 1425–1439. doi:10.1021/acs.jmedchem.5b00256

Tong, B., Luo, M., Xie, Y., Spradlin, J. N., Tallarico, J. A., Mckenna, J. M., et al. (2020). Bardoxolone conjugation enables targeted protein degradation of BRD4. *Sci. Rep.* 10, 15543. doi:10.1038/s41598-020-72491-9

Vollmer, S., Strickson, S., Zhang, T., Gray, N., Lee, K. L., Rao, V. R., et al. (2017). The mechanism of activation of IRAK1 and IRAK4 by interleukin-1 and Toll-like receptor agonists. *Biochem. J.* 474, 2027–2038. doi:10.1042/BCJ20170097

Waks, A. G., and Winer, E. P. (2019). Breast cancer treatment: A review. *JAMA* 321, 288–300. doi:10.1001/jama.2018.19323

Wang, Y., Jiang, X., Feng, F., Liu, W., and Sun, H. (2020). Degradation of proteins by PROTACs and other strategies. *Acta Pharm. Sin. B* 10, 207–238. doi:10.1016/j.apsb.2019.08.001

Wang, Y., Shen, Y., Wang, S., Shen, Q., and Zhou, X. (2018). The role of STAT3 in leading the crosstalk between human cancers and the immune system. *Cancer Lett.* 415, 117–128. doi:10.1016/j.canlet.2017.12.003

Ward, C. C., Kleinman, J. I., Brittain, S. M., Lee, P. S., Chung, C. Y. S., Kim, K., et al. (2019). Covalent ligand screening uncovers a RNF4 E3 ligase recruiter for targeted protein degradation applications. *ACS Chem. Biol.* 14, 2430–2440. doi:10.1021/acschembio.8b01083

Wei, J., Meng, F., Park, K. S., Yim, H., Velez, J., Kumar, P., et al. (2021). Harnessing the E3 ligase KEAP1 for targeted protein degradation. *J. Am. Chem. Soc.* 143, 15073–15083. doi:10.1021/jacs.1c04841

Winter, G. E., Buckley, D. L., Paulk, J., Roberts, J. M., Souza, A., Dhe-Paganon, S., et al. (2015). Phthalimide conjugation as a strategy for *in vivo* target protein degradation. *Science* 348, 1376–1381. doi:10.1126/science.aab1433

Woyach, J. A., Furman, R. R., Liu, T. M., Ozer, H. G., Zapatka, M., Ruppert, A. S., et al. (2014). Resistance mechanisms for the Bruton's tyrosine kinase inhibitor ibrutinib. *N. Engl. J. Med.* 370, 2286–2294. doi:10.1056/NEJMoa1400029

Xiang, W., Zhao, L., Han, X., Qin, C., Miao, B., Mceachern, D., et al. (2021). Discovery of ARD-2585 as an exceptionally potent and orally active PROTAC degrader of androgen receptor for the treatment of advanced prostate cancer. *J. Med. Chem.* 64, 13487–13509. doi:10.1021/acs.jmedchem.1c00900

Yang, B., Zheng, X., and Zhu, X. (2022). Preparation of peptidomimetics as STAT degraders and their uses for treating diseases. CN. patent NO WO2022077010 A1. Watertown: World Intellectual Property Organization.

Yang, F., Jia, M., He, W., Chen, G., He, F., and Tao, W. (2021a). Bicyclic imide derivative, preparation method thereof, and application thereof in medicine. CN. patent NO WO 2021/143822 A1. Shanghai: World Intellectual Property Organization.

Yang, Q., Zhao, J., Chen, D., and Wang, Y. (2021b). E3 ubiquitin ligases: Styles, structures and functions. *Mol. Biomed.* 2, 23. doi:10.1186/s43556-021-00043-2

Ye, Y., and Rape, M. (2009). Building ubiquitin chains: E2 enzymes at work. *Nat. Rev. Mol. Cell Biol.* 10, 755–764. doi:10.1038/nrm2780

Yu, H., Pardoll, D., and Jove, R. (2009). STATs in cancer inflammation and immunity: A leading role for STAT3. *Nat. Rev. Cancer* 9, 798–809. doi:10.1038/nrc2734

Zhang, J., Fu, L., Shen, B., Liu, Y., Wang, W., Cai, X., et al. (2020a). Assessing IRAK4 functions in ABC DLBCL by IRAK4 kinase inhibition and protein degradation. *Cell Chem. Biol.* 27, 1500–1509 e1513. doi:10.1016/j.chembiol.2020.08.010

Zhang, X., Crowley, V. M., Wucherpfennig, T. G., Dix, M. M., and Cravatt, B. F. (2019a). Electrophilic PROTACs that degrade nuclear proteins by engaging DCAF16. *Nat. Chem. Biol.* 15, 737–746. doi:10.1038/s41589-019-0279-5

Zhang, X., Luukkonen, L. M., Eissler, C. L., Crowley, V. M., Yamashita, Y., Schafroth, M. A., et al. (2021). DCAF11 supports targeted protein degradation by electrophilic proteolysis-targeting chimeras. *J. Am. Chem. Soc.* 143, 5141–5149. doi:10.1021/jacs.1c00990

Zhang, X., Thummuri, D., He, Y., Liu, X., Zhang, P., Zhou, D., et al. (2019b). Utilizing PROTAC technology to address the on-target platelet toxicity associated with inhibition of BCL-XL. *Chem. Commun. (Camb)* 55, 14765–14768. doi:10.1039/c9cc07217a

Zhang, X., Thummuri, D., Liu, X., Hu, W., Zhang, P., Khan, S., et al. (2020b). Discovery of PROTAC BCL-XL degraders as potent anticancer agents with low on-target platelet toxicity. *Eur. J. Med. Chem.* 192, 112186. doi:10.1016/j.ejmech.2020.112186

Zhang, X. T., Kang, L. G., Ding, L., Vranic, S., Gatalica, Z., and Wang, Z. Y. (2011). A positive feedback loop of ER-α36/EGFR promotes malignant growth of ER-negative breast cancer cells. *Oncogene* 30, 770–780. doi:10.1038/onc.2010.458

Zhao, L., Han, X., Lu, J., Mceachern, D., and Wang, S. (2020). A highly potent PROTAC androgen receptor (AR) degrader ARD-61 effectively inhibits AR-positive breast cancer cell growth *in vitro* and tumor growth *in vivo*. *Neoplasia* 22, 522–532. doi:10.1016/j.neo.2020.07.002

Zheng, N., and Shabek, N. (2017). Ubiquitin ligases: Structure, function, and regulation. *Annu. Rev. Biochem.* 86, 129–157. doi:10.1146/annurev-biochem-060815-014922

Zhou, H., Bai, L., Xu, R., Mceachern, D., Chinnaswamy, K., Li, R., et al. (2021). SD-91 as A Potent and selective STAT3 degrader capable of achieving complete and long-lasting tumor regression. *ACS Med. Chem. Lett.* 12, 996–1004. doi:10.1021/acsmedchemlett.1c00155

Zhou, H., Bai, L., Xu, R., Zhao, Y., Chen, J., Mceachern, D., et al. (2019). Structure-based discovery of SD-36 as a potent, selective, and efficacious PROTAC degrader of STAT3 protein. *J. Med. Chem.* 62, 11280–11300. doi:10.1021/acs.jmedchem.9b01530

frontiers | Frontiers in Chemistry

TYPE Original Research
PUBLISHED 26 January 2023
DOI 10.3389/fchem.2023.1128859

OPEN ACCESS

EDITED BY
Kailin Yang,
Cleveland Clinic, United States

REVIEWED BY
Xiang Liu,
Nankai University, China
Hongfei Wang,
Shanxi University, China

*CORRESPONDENCE
María Eugenia Castro,
mareug.castro@correo.buap.mx
Enrique González-Vergara,
enrique.gonzalez@correo.buap.mx

SPECIALTY SECTION
This article was submitted to Medicinal and Pharmaceutical Chemistry, a section of the journal Frontiers in Chemistry

RECEIVED 21 December 2022
ACCEPTED 17 January 2023
PUBLISHED 26 January 2023

CITATION
Vazquez-Rodriguez S, Ramírez-Contreras D, Noriega L, García-García A, Sánchez-Gaytán BL, Melendez FJ, Castro ME, de Azevedo WF Jr and González-Vergara E (2023), Interaction of copper potential metallodrugs with TMPRSS2: A comparative study of docking tools and its implications on COVID-19. *Front. Chem.* 11:1128859. doi: 10.3389/fchem.2023.1128859

Interaction of copper potential metallodrugs with TMPRSS2: A comparative study of docking tools and its implications on COVID-19

Sergio Vazquez-Rodriguez[1], Diego Ramírez-Contreras[1], Lisset Noriega[2,3], Amalia García-García[1,4], Brenda L. Sánchez-Gaytán[1], Francisco J. Melendez[2], María Eugenia Castro[1]*, Walter Filgueira de Azevedo Jr[5] and Enrique González-Vergara[1]*

[1]Centro de Química del Instituto de Ciencias, Benemérita Universidad Autónoma de Puebla, Puebla, Mexico, [2]Laboratorio de Química Teórica, Depto. de Fisicoquímica, Facultad de Ciencias Químicas, Benemérita Universidad Autónoma de Puebla, Puebla, Mexico, [3]Departamento de Física Aplicada, Centro de Investigación y de Estudios Avanzados del Instituto Politécnico Nacional, Mérida, Mexico, [4]Departamento de Química Inorgánica, Facultad de Ciencias, Universidad de Granada, Granada, Spain, [5]Escola de Ciências da Saúde, Pontifícia Universidade Católica do Rio Grande do Sul (PUCRS), Porto Alegre, Rio Grande do Sul, Brazil

SARS-CoV-2 is the virus responsible for the COVID-19 pandemic. For the virus to enter the host cell, its spike (S) protein binds to the ACE2 receptor, and the transmembrane protease serine 2 (TMPRSS2) cleaves the binding for the fusion. As part of the research on COVID-19 treatments, several Casiopeina-analogs presented here were looked at as TMPRSS2 inhibitors. Using the DFT and conceptual-DFT methods, it was found that the global reactivity indices of the optimized molecular structures of the inhibitors could be used to predict their pharmacological activity. In addition, molecular docking programs (AutoDock4, Molegro Virtual Docker, and GOLD) were used to find the best potential inhibitors by looking at how they interact with key amino acid residues (His296, Asp 345, and Ser441) in the catalytic triad. The results show that in many cases, at least one of the amino acids in the triad is involved in the interaction. In the best cases, Asp435 interacts with the terminal nitrogen atoms of the side chains in a similar way to inhibitors such as nafamostat, camostat, and gabexate. Since the copper compounds localize just above the catalytic triad, they could stop substrates from getting into it. The binding energies are in the range of other synthetic drugs already on the market. Because serine protease could be an excellent target to stop the virus from getting inside the cell, the analyzed complexes are an excellent place to start looking for new drugs to treat COVID-19.

KEYWORDS

TMPRSS2, COVID-19, molecular docking, Casiopeina-like metallodrugs, copper, DFT, Casiopeina analogs

1 Introduction

In December 2019, a new respiratory sickness called coronavirus disease 2019 (COVID-19) was found in Wuhan, China. Due to its rapid spread, COVID-19 was declared a global pandemic by the World Health Organization (WHO) on 11 March 2020. The causative virus was identified as the severe acute respiratory syndrome coronavirus 2 (SARS-CoV-2) (Hoffmann et al., 2020). Until December 2022, SARS-CoV-2 and its variants have almost infected 650 million people worldwide,

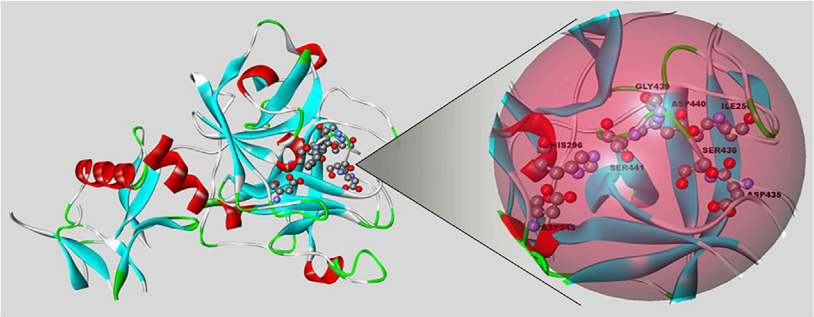

FIGURE 1
Representation of the TMPRSS2 protein (PDB code: 7MEQ) using Biovia/Discovery Studio v. 20.1. On the right side is the active site of the protein, where the triad of amino acids is located (His296, Asp345, Ser441).

and 6.6 million people have died as a result (Dong et al., 2020; World Health Organization, 2022). Even though effective drugs have not been found yet, the disease has been treated with antiviral and anti-inflammatory drugs, antibodies, corticosteroids, and plasma from people who have recovered from the disease (Ni et al., 2022).

The structure of SARS-CoV-2 has an external spike (S) glycoprotein that is needed to get into host cells. One of the methods for the virus to infect a cell (the other one is by endocytosis) begins with binding the viral S glycoprotein to the host receptor angiotensin-converting enzyme-2 (ACE2). Then, some viral glycoproteins go through activation by the transmembrane protease serine 2 (TMPRSS2), which proteolytically cleaves the binding for fusion between viral and host cells and allows membrane fusion and subsequent viral genome release (Wettstein et al., 2022). Although ACE2 is needed for SARS-CoV-2 infection, it may be hard to target it therapeutically because it plays a key role in metabolism, such as how the heart works. On the other hand, TMPRSS2 could be a more suitable target (Baughn et al., 2020). TMPRSS2 is expressed, depending on age, in epithelial cells of lung tissue, heart, liver, gastrointestinal tract, respiratory tract, prostate gland, and even the human corneal epithelium. It is involved in normal and abnormal processes like digestion, blood clotting, fertility, inflammatory responses, tumor growth, cell death, and pain (Thunders and Delahunt, 2020). In this way, TMPRSS2, which is found in human airways, helps activate important respiratory viruses like influenza and coronaviruses (Wettstein et al., 2022).

The first published report about TMPRSS2 was in 1997, when its structure was described (Paoloni-Giacobino et al., 1997). This enzyme contains 492 amino acids, or 37 more in isoform 1 (Zmora et al., 2015), divided among an N-terminal intracellular domain, a hydrophobic transmembrane domain, and the stem region. The last one is made up of a low-density lipoprotein receptor class A domain (which is responsible for tethering the protease to the plasma membrane), a scavenger receptor cysteine-rich domain (that plays a role in protein-protein interactions and substrate recognition), and the C-terminal serine protease domain, which contains the amino acid triad essential for proteolytic activity (His296, Asp345, and Ser441) (Figure 1). The serine protease domain possesses the main proteolytic activity: It cleaves after Arg or Lys residues since it contains Asp435 at the base of the specificity pocket (S1 subsite) that binds to the substrate (Fraser et al., 2022). Because SARS-CoV-2 infection depends on TMPRSS2, protease inhibitors could be used to treat the disease. Some of the most studied serine protease inhibitors are camostat and nafamostat. Both inhibit the TMPRSS2 protease activity in human bronchial epithelial cells *in vitro*, but nafamostat shows higher efficiency.

Furthermore, studies *in vivo* in transgenic mice expressing the human *ACE2* gene show that nafamostat, delivered *via* intranasal, effectively reduces SARS-CoV-2 infection. Since nafamostat has been approved for decades as a treatment for other medical conditions, it could also be a good choice for treating COVID-19 (Li et al., 2021). In addition, some clinical studies on a few people have been done (Jang and Rhee, 2020; Takahashi et al., 2021), and although nafamostat appears to be effective against COVID-19, it could cause hyperkalemia and should be administered with heparin to compensate for its antifibrinolytic effect (Takahashi et al., 2021).

In searching for safe and effective drugs to treat the COVID-19 pandemic disease, metallodrugs, widely used in medicine, could be good candidates because coordination compounds have unique reactivity properties that cannot be achieved using only organic compounds (Cirri et al., 2021). Some metal ions, including selenium, iron, zinc, and copper, are known to block the interaction between the virus and the host cell, preventing the infection, inhibiting viral replication, destroying the viral structure, or inhibiting the activity of critical enzymes (Ni et al., 2022). In this regard, Casiopeinas® are well-known planar copper(II) compounds with phenanthroline or bipyridine ligands. Even though these compounds are important because they fight cancer, parasites, and bacteria, new research has been done to explore their inhibitory effect against the main protease, M^{pro}, which is responsible for the replication and primary transcription of the SARS-CoV-2 virus's genetic material. It was concluded that most studied Casiopeinas® could inhibit M^{pro} more efficiently than free monochelates, bioactive ligands, and boceprevir (a recognized inhibitor) (Reina et al., 2022).

Molecular docking is an *in silico* technique for determining the most stable configuration in which a specific molecule will connect to a receptor active site (Mhatre et al., 2021). Docking has become crucial in drug development, easing the burdensome process of finding functional therapeutic molecules (Tanveer et al., 2022). A scoring function that assigns a numerical fit value to a calculated protein/molecule configuration and a search algorithm that finds the molecule posture with the highest fit score in the protein binding site are the two critical components of every docking method (Halperin et al., 2002). Good docking is measured by two factors: The type of interaction and the docking score. Non-covalent bonds, Van der Waals interactions, π-stacking, and, in some cases, ionic bonds are examples of typical interactions (Mhatre et al., 2021).

Currently, there are only three approved drugs for COVID-19, Remdesivir, Molnupiravir, and Paxlovid, that inhibit viral replication (Gandhi et al., 2022; Jiang et al., 2022). However, several researchers have turned to drug repositioning to find quick and effective treatments. Also, molecular docking-based virtual screening seems to be a key way to find new antiviral drugs. Researchers can use this method as a different way to assign the synthesis of new compounds or the repositioning of drugs (Milite et al., 2019).

Following the research of drugs against SARS-CoV-2, in this work, seven Casiopeina analogs containing amino acids have been subjected to comparative *in silico* studies to determine their binding modes against the TMPRSS2 enzyme. Nafamostat and two Casiopeinas®, Cas III-ia (currently in clinical phase I trials in Mexico; Serment-Guerrero et al., 2011) and Cas IX-gly (Becco et al., 2014), have been used as comparative inhibitors.

2 Experimental section

2.1 Computational methods

The optimized molecular structures of the cationic complexes were calculated using the DFT method with the functional mPW1PW91 (Adamo and Barone, 1998) from the crystal structures already reported (Tovar-Tovar et al., 2004; Patra et al., 2009; García-Ramos et al., 2014; Martínez-Valencia et al., 2020; Rodrigues et al., 2020; Corona-Motolinia et al., 2021; Sánchez-Lara et al., 2021; Ramírez-Contreras et al., 2022) or modeled from them using Spartan'20 (Wavefunction Inc.). The basis set 6-311G(d) (Krishnan et al., 1980) was used for C, N, and O atoms, and 6-31G (Ditchfield et al., 1971) was used for H atoms. A valence double zeta with polarization on all atoms' VDZP basis set (Wachters, 1970) was used for the Cu atom. These basis sets were used to achieve a well-balanced complete basis set. For aqueous solutions, the conductor-like polarizable continuum model (CPCM) (Cossi et al., 2003) was used to consider the solvent's effect. The global reactivity indices, such as chemical potential (μ), electronegativity (χ), hardness (η), softness (s), and electrophilicity index (ω), were evaluated using the vertical Self-Consistent Field (ΔSCF) approach (Balawender and Geerlings, 2005). The vertical ionization potential (I) and the vertical electron affinity (A) were obtained from the energy difference between the ground state geometry and their corresponding ionized species from the optimized structures in an aqueous solution. All calculations were carried out in the Gaussian16 package (Frisch et al., 2016).

2.2 Molecular docking analysis

For molecular docking, copper(II) coordination compounds with bidentate ligands were used. The ligands are of type diimine (N, N), 2,2′-bipyridine, and (N, O) L-aminoacidatos of arginine, citrulline, asparagine, glycine, lysine, ornithine, glutamine, and theanine. Casiopeina III-ia and Casiopeina IX-gly were used for comparative purposes.

Three different molecular docking programs were employed to evaluate protein-complex interactions of the copper compounds with the transmembrane protease serine 2 (TMPRSS2): AutoDock4 (Morris et al., 2009), Molegro Virtual Docker (MVD) (Thomsen and Christensen, 2006), and GOLD software from the CCDC Mercury suite (Jones et al., 1997). To carry out the docking simulations, the protein TMPRSS2 with the protease inhibitor nafamostat (PDB code: 7MEQ) was used (Fraser et al., 2022). In addition, two sets of copper compounds were prepared, one with water molecules coordinated to copper(II) (named **System 1**) and the second one without water molecules (**System 2**). The nafamostat's coordinates were taken out so that docking simulations for copper compounds could be done.

2.2.1 Docking studies with AutoDock4

The docking process consists of two key steps; the first one is related to the conformation of the coordination complex and its orientation to the protein binding site, while the second key step consists of the prediction of the affinity of the complex to the protein using a scoring function.

To make a random search of the conformation of the copper complexes, the Lamarckian genetic algorithm was used. This algorithm considers the different complex poses and then interchanges between them, leading to a new generation of structures. Each member of the generation is evaluated with the scoring function, and only those values that meet the requirements (conformation, rotation, and orientation with respect to the protein) continue to the next-generation and so on until finding the best ligand conformations (Morris et al., 1998).

The force field used in AutoDock4 is a semiempirical free energy scoring function that considers the contribution of the hydrogen bonds and the electrostatic interactions. This scoring function discriminates the suitable poses from the wrong ones and estimates the affinity between the complex and the protein.

The protein and complexes were prepared through AutoDockTools4 by removing water molecules and polar hydrogens and adding Gasteiger charges. The receptor grid box was centered at x = 9.3, y = −5.9, and z = 19.993 Å. The box size was 40 $Å^3$. Docking studies were done with 150 individuals in the population, a maximum energy evaluation of 2,500,000, and a maximum generation of 27,000 to result in 50 docking poses. The parameters for the copper(II) atom were the sum of the Van der Waals radii of two similar atoms (3.50 Å), the Van der Waals well depth (0.005 kmol mol^{-1}), the atomic solvation volume (12.0 $Å^3$), and the atomic solvation parameter (−0.00110). The hydrogen bond radius of the heteroatom in contact with hydrogen (0.0 Å), the well depth of the hydrogen bond (0.0 kcal mol^{-1}), and various integers indicate the type of hydrogen bonding atom and indexes for the generation of the autogrid map (0, −1, −1, 1, respectively).

2.2.2 Docking studies with molegro (MVD)

The MolDock scoring function implemented in MVD is the sum of the intermolecular energy (E_{inter}) and the internal energy of the copper complex (E_{intra}). The intermolecular interaction is calculated as follows:

$$E_{inter} = \sum_i \sum_j \left[332.0 \frac{q_i q_j}{4 r_{ij}^2} + PLP(r_{ij}) \right]$$

Subscripts i and j represent all the non-hydrogen atoms in the complex and protein. The first term is a Coulomb potential for charges q_i and q_j. The variable r_{ij} represents the interatomic distance involving complex (i) and protein (j) atoms.

On the other hand, MVD defines intramolecular energy as follows:

$$E_{intra} = \sum_i \sum_j PLP(r_{ij}) + \sum_{FB} A[1 - cos(m \cdot \theta - \theta_0)] + E_{clash}$$

Summations are between all atom pairs in the complex except the atom pairs connected by two bonds or less. The term FB refers to the

flexible bonds in the copper complex, and θ is the torsional angle of the bond. The last term (E_{clash}) is a penalty of 1,000 applied if the distance between two atoms is less than 2.0 Å. The *PLP* is the piecewise linear potential in both equations. *PLP* uses two sets of parameters, one based on the Van der Waals interactions and the other for the hydrogen bonds (Thomsen and Christensen, 2006). Compared to other scoring functions, the MolDock score showed superior predictive performance (Thomsen and Christensen, 2006; Bitencourt-Ferreira and de Azevedo Jr., 2019).

The REDUCE program was employed for docking simulations with MVD to add hydrogens to the protein structure (Word et al., 1999). Atomic charges were assigned using the MVD program for all complexes and protein (Bitencourt-Ferreira and de Azevedo Jr., 2019). During docking simulation, the Ant Colony Optimization (Heberlé and de Azevedo Jr., 2011) search algorithm was combined with the MolDock scoring function (Thomsen and Christensen, 2006; Dias and de Azevedo Jr., 2008). To reproduce the results, 1123581321 was used as a random seed in all docking simulations, and the simulations were limited to a 12 Å radius sphere centered at the coordinates x = −9.17, y = −6.55, and z = 20.08 Å. After running docking simulations, the Nelder-Mead algorithm in MVD (Nelder and Mead, 1965) was used to find the protein-complex structures with the least energy.

2.2.3 Docking studies with GOLD (genetic optimization for ligand docking)

The Goldscore function is a scoring function used to rank different ways of binding. It is based on molecular mechanics and has four terms:

GOLD Fitness = *Shb_ext* + *Svdw_ext* + *Shb_int* + *Svdw_int*

Shb_ext is the hydrogen-bond score between the protein and complex, and *Svdw_ext* is the Van der Waals score between them. *Shb_int* is the contribution to fitness from intramolecular hydrogen bonds in the complex. This term is turned off in all calculations (Verdonk et al., 2003) (this is the GOLD default and usually gives the best results). *Svdw_int* is the contribution from intramolecular strain in the complex. GOLD uses a genetic algorithm (GA) to change or improve parameters such as rotatable bonds, ring geometries, protein groups, and binding sites.

The Hermes software was used to carry out the protein preparation, which included removing water molecules before adding polar hydrogens and removing the nafamostat inhibitor. For the simulation, a maximum of 125,000 GA operations were carried out on a single population of 100 GA runs for each of the 10 independent GA runs. Crossover, mutation, and migration operator weights were left at their default values. The docking study was performed in the area comprising the active sites and the closest residues and constricted to a 10 Å radius sphere centered at the coordinates x = −6.04, y = −3.15, and z = 15.65 Å. The compounds were ranked by their GOLDscore.

3 Results and discussion

3.1 Global reactivity indices of the cationic complexes

Several reactivity indices have been analyzed to shed light on the structure-reactivity relationship of copper complexes. Firstly, in Figure 2, the optimized molecular structures for the seven complexes containing the amino acid residues Arg, Orn, Lys, Citr, Asn, The, Gln, and two Casiopeinas, Cas III-ia and Cas IX-Gly, containing acetylacetonato and Gly, respectively, are shown. Additionally, complexes containing Arg, Orn, Lys, Citr, Cas III-ia, and Cas IX-Gly have also been optimized with one water molecule in the apical position of Cu(II), while Asn and Cas IX-Gly also have two water molecules in both apical positions. In Table 1, the relevant parameters of the optimized molecular structures are compared with those reported crystal structures of compounds involving Bipy or Phen and aminoacidatos.

In most cases, the RMSD for these parameters are between 0.005 and 0.045 Å for the bond length, while the bond angles are between 0.69 and 2.42°. Furthermore, it indicates that the reliability of the DFT calculations is adequate, and the predicted geometrical parameters are a reliable source for predicting the chemical reactivity of the copper complexes.

In total, seventeen structures were calculated to analyze their global reactivity indices such as chemical potential ($\boldsymbol{\mu}$), electronegativity ($\boldsymbol{\chi}$), hardness ($\boldsymbol{\eta}$), softness ($\boldsymbol{s}$), electrophilicity index ($\boldsymbol{\omega}$), ang gap energy (E_{gap}), that were obtained with the following equations:

$\mu = -\frac{(I+A)}{2}$; $\chi = \frac{(I+A)}{2}$; $\eta = \frac{(I-A)}{2}$; $s = \frac{1}{2\eta}$; $\omega = \frac{\mu^2}{2\eta}$; and $E_{gap} = I - A$; from the vertical ionization potential $I = E_{N+1} - E_N$, and the vertical electron affinity $A = E_N - E_{N-1}$, where E_N is the electronic energy of the ground state, and E_{N+1} and E_{N-1} are the electronic energies of the system with one less electron and one more electron, respectively, according to the ΔSCF approach.

The global reactivity indices for all compounds are collected in Supplementary Table S1; Figure 3. In Figure 3A the results show that the complexes with higher values of electronegativity χ (or lower chemical potential) are the copper complexes with Arg, Orn, Lys, The, Gln, and Gly, without water. These values of χ in the range of 5.11–5.20 eV indicate greater resistance to electron density loss or greater ability to attract electron density towards itself (Sert et al., 2014). Concerning the value of hardness η, $[Cu(Bipy)(Arg)(H_2O)]^{2+}$, $[Cu(Bipy)(Orn)(H_2O)]^{2+}$, $[Cas\ IX\text{-}Gly(H_2O)]^{1+}$, and $[Cas\ IX\text{-}Gly(H_2O)_2]^{2+}$ are the hardest species. It means these complexes resist exchanging electron density with the environment and could be good nucleophiles. On the other hand, $[Cu(Bipy)(Citr)]^{1+}$, $[Cu(Bipy)(Citr)(H_2O)]^{1+}$, $[Cas\ III\text{-}ia]^{1+}$, and $[Cas\ III\text{-}ia(H_2O)]^{1+}$ have the smallest values of η; thus they could be good electrophiles. Regarding the electrophilicity index, the complexes with values of 6.48–6.65 eV can also be considered good electrophiles, including the complexes with Arg, Orn, Lys, Citr, The, Gln, and Gly, without water. The gap energy values E_{gap}, *i.e.*, the energy gained or lost in an electron donor-acceptor transfer, show that the most reactive complexes could be $[Cu(Bipy)(Citr)]^{1+}$, $[Cu(Bipy)(Citr)(H_2O)]^{1+}$, $[Cas\ III\text{-}ia]^{1+}$, and $[Cas\ III\text{-}ia(H_2O)]^{1+}$. Finally, in Figure 3B, it is possible to observe that the smallest softness values s, corresponding to $[Cu(Bipy)(Arg)(H_2O)]^{2+}$, $[Cu(Bipy)(Orn)(H_2O)]^{2+}$, $[Cas\ IX\text{-}Gly(H_2O)]^{1+}$, and $[Cas\ IX\text{-}Gly(H_2O)_2]^{1+}$ could be the least toxic (Siddiqui and Javed, 2021).

3.2 Docking analysis

Molecular docking is a powerful tool for accelerating drug discovery to treat many diseases (Adelusi et al., 2022). For this

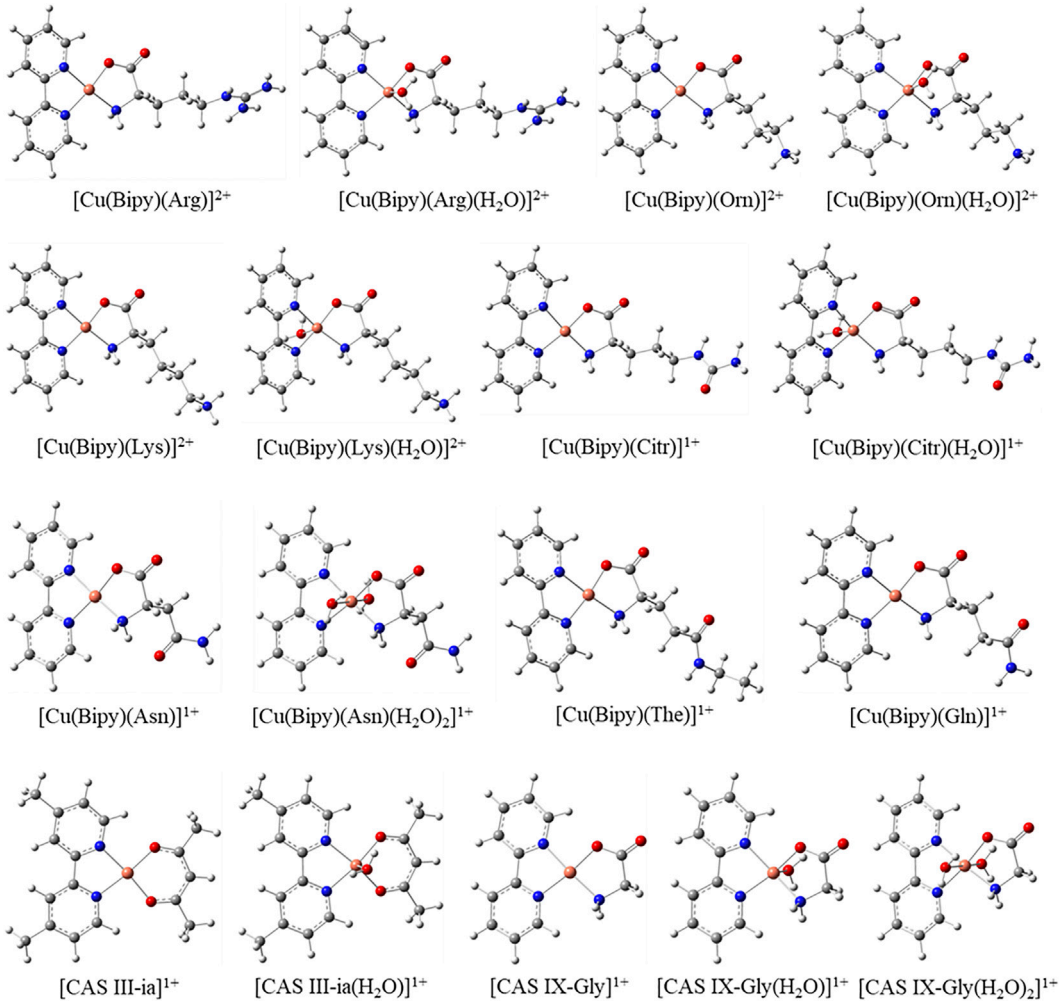

FIGURE 2
Optimized molecular structures of the copper complexes calculated with the mPW1PW91 functional in an aqueous solution.

reason, this technique was used to explore the possible interactions between TMPRSS2 and the copper compounds. To compare their results, three different docking programs were used (AutoDock4, Molegro Virtual Docker, and GOLD). The docked binding energies of the seven copper complexes, Cas III-ia and Cas IX-gly, with coordinated water molecules (**System 1**) and without them (**System 2**), along with the inhibitor nafamostat, are collected in Tables 2, 3.

Many potential metallodrugs have been investigated against different target proteins of SARS-CoV-2 (Karges and Cohen, 2021). Two proteases are considered the most essential for SARS-CoV-2 replication: The papain-like protease (PL^{pro}) and the 3-chymotrypsin-like "main" protease ($3CL^{pro}$ or M^{pro}). This makes them attractive targets for potential therapies against COVID-19. Currently, some SARS-CoV-2 protease inhibitors are being studied, such as Lopinavir and Ritonavir, two already-approved Human Immunodeficiency Virus treatments (Tao et al., 2022). In this regard, coordination compounds have emerged as new candidates for PL^{pro} or M^{pro} inhibitors, including Zn(II) (DeLaney et al., 2021; Tao et al., 2022), Au(I) (Gil-Moles et al., 2020), Bi(III) (Yuan et al., 2020; Tao et al., 2021), Re(I) complexes (Karges et al., 2021), and other metals (Gandhimathi and Anbuselvi, 2022). Other inhibitory studies on the host receptor ACE2 with transition metal-based compounds (Al-Harbi, 2022) or against the spike protein with decavanadate (Favre et al., 2022) have also been conducted. Only a few compounds, however, have been studied against TMPRSS2, including some organic molecules such as nafamostat, camostat, and gabexate, all of them possessing a guanidinium group that interacts with Asp435 and an ester group pointing into Ser441 of the triad catalytic site, in a similar way to the small molecules here reported (Hu et al., 2021). In addition, polyoxotungstates have been examined, where $[SiW_{12}O_{40}]^{-4}$ has a binding free energy of −9.4 kcal mol^{-1} toward the TMPRSS2, but none of the amino acids of the catalytic triad are present in the interactions (Shahabadi et al., 2022). Among coordination compounds, only two complexes based on Co(II) and Zn(II) have been studied, showing binding energies of −6.2 and −6.3 kcal mol^{-1}, respectively, but again without interactions with the catalytic triad (Öztürkkan et al., 2022).

TABLE 1 Selected crystal structure and optimized parameters of the copper complexes calculated with the mPW1PW91 functional in an aqueous solution. Bond lengths in (Å) and bond angles in (°).

Complex	Crystal structure				Calculated			
	Cu–N	Cu–O	N–Cu–N	O–Cu–N	Cu–N	Cu–O	N–Cu–N	O–Cu–N
$[Cu(Bipy)(Arg)]^{2+}$ Patra et al. (2009)	2.019[a]	1.939[c]	81.41[d]	91.10[f]	1.996[a]	1.914[c]	81.10[d]	92.87[f]
	2.038[a]		100.41[e]	83.63[g]	2.015[a]		102.79[e]	83.28[g]
	1.993[b]				2.014[b]			
$[Cu(Bipy)(Orn)]^{2+}$ Martínez-Valencia et al. (2020)	1.997[a]	1.945[c]	80.59[d]	91.40[f]	1.994[a]	1.912[c]	81.20[d]	93.45[f]
	2.006[a]		99.52[e]	84.29[g]	2.013[a]		101.92[e]	83.82[g]
	2.001[b]				2.016[b]			
$[Cu(Bipy)(Lys)]^{2+}$ Sánchez-Lara et al. (2021)	1.990[a]	1.936[c]	81.46[d]	91.41[f]	1.995[a]	1.911[c]	81.13[d]	93.04[f]
	2.002[a]		102.24[e]	83.57[g]	2.015[a]		102.24[e]	83.87[g]
	1.994[b]				2.014[b]			
$[Cu(Bipy)(Citr)]^{1+*}$	2.001[a]	1.915[c]	82.31[d]	91.52[f]	1.996[a]	1.913[c]	81.06[d]	93.01[f]
Ramírez-Contreras et al. (2022)	2.008[a]		99.11[e]	85.93[g]	2.017[a]		102.72[e]	83.37[g]
	1.997[b]				2.011[b]			
$[Cu(Bipy)(Asn)]^{1+}$	1.960[a]	1.980[c]	81.54[d]	92.95[f]	1.997[a]	1.919[c]	81.04[d]	93.09[f]
Rodrigues et al. (2020)	2.063[a]		102.59[e]	82.91[g]	2.014[a]		101.91[e]	83.98[g]
	1.976[b]				2.003[b]			
$[Cu(Bipy)(The)]^{1+}$	—	—	—	—	1.996[a]	1.911[c]	81.07[d]	92.83[f]
					2.017[a]		102.49[e]	83.67[g]
					2.014[b]			
$[Cu(Bipy)(Gln)]^{1+}$	2.005[a]	1.909[c]	81.78[d]	90.46[f]	1.996[a]	1.911[c]	81.07[d]	92.77[f]
Corona-Motolinia et al. (2021)	2.015[a]		101.25[e]	84.62[g]	2.016[a]		102.64[e]	83.69[g]
	2.018[b]				2.015[b]			
[Cas III-ia]$^{1+}$ Tovar-Tovar et al. (2004)	1.973[a]	1.896[c]	81.43[d]	94.68[h]	2.000[a]	1.915[c]	80.93[d]	93.56[h]
	1.983[a]	1.885[c]			2.000[a]	1.915[c]		
[Cas IX-Gly]$^{1+}$ García-Ramos et al. (2014)	1.992[a]	1.942[c]	81.22[d]	91.98[f]	1.995[a]	1.913[c]	81.08[d]	92.92[f]
	2.013[a]		99.80[e]	84.54[g]	2.016[a]		101.87[e]	84.34[g]
	2.003[b]				2.017[b]			

[a]Cu–N bond length with N of Bipy or Phen.
[b]Cu–N bond length with N of aminoacidato.
[c]Cu–O bond length with O of aminoacidato.
[d]N–Cu–N bond angle with both N of Bipy or Phen.
[e]N–Cu–N bond angle with one N of Bipy or Phen, and one N of aminoacidato.
[f]O–Cu–N bond angle with one N of Bipy or Phen, and one O of aminoacidato.
[g]O–Cu–N bond angle with both N and O of aminoacidato.
[h]O–Cu–O bond angle with both O of acetylacetonato for CAS III-ia complexes.
*The data corresponds to the D-citrullinato complex.

3.2.1 Docking simulations with AutoDock4

The redocking results with the inhibitor nafamostat conserved the interactions with the amino acids of the catalytic site His296, Asp345, and Ser441. It presented an energy of −6.3 kcal mol^{-1}. The compound that held the best binding free energy when compared to nafamostat and Casiopeinas® was $[Cu(Bipy)(Lys)]^{2+}$, followed by $[Cu(Bipy)(Orn)]^{2+}$, and $[Cu(Bipy)(Arg)]^{2+}$ in both Systems. The water molecule forms an extra hydrogen bond (Arg470), which is why there is a small increase in binding free energy when water is present in the complexes. Dicationic complexes of $[Cu(Bipy)(Lys)(H_2O)]^{2+}$, $[Cu(Bipy)(Orn)(H_2O)]^{2+}$, and $[Cu(Bipy)(Arg)(H_2O)]^{2+}$ form several hydrogen bonds that include the amino acids Ser436 and Gly464, and one salt bridge with Asp435. Although they do not present hydrogen bonds with the triad of interest, they present hydrophobic interactions with His296 and Ser441 (Figure 4).

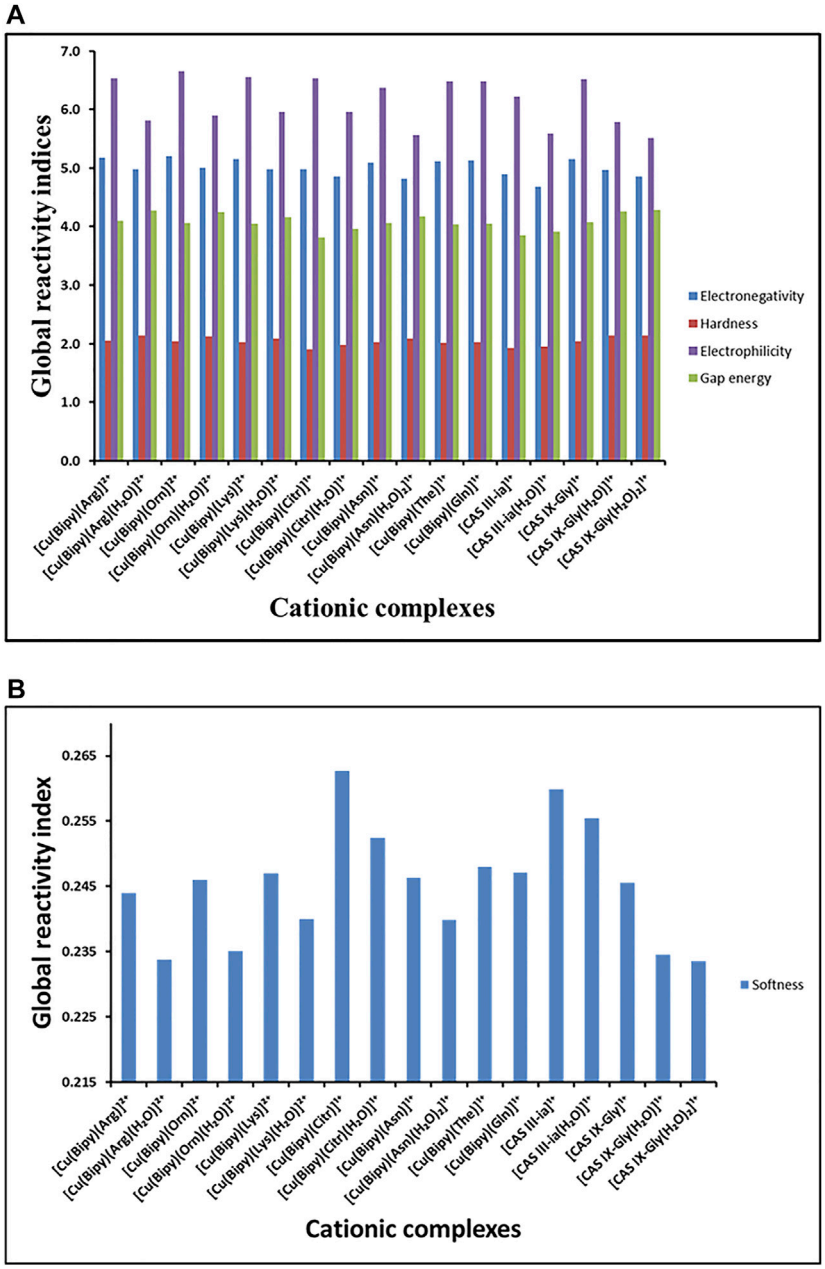

FIGURE 3
(A) Reactivity global indices χ, η, ω, and E_{gap}; and **(B)** Reactivity global index s of the copper complexes calculated with the mPW1PW91 functional in an aqueous solution.

The results obtained with AutoDock4 for **Systems 1**, **2** are found to be similar in the complexes with Arg, whereas for the complexes $[Cu(Bipy)(Orn)(H_2O)]^{2+}$ and $[Cu(Bipy)(Lys)(H_2O)]^{2+}$ the presence of the water molecule slightly changes the disposition of the complexes when they are interacting with the protein. Furthermore, this water molecule interacts with other amino acids of the protein, which explains the changes in binding free energies found in these complexes.

The binding affinity of $[Cu(Bipy)(Lys)]^{2+}$ with AutoDock is similar to that shown by a Cu(II)-phenanthroline compound against M^{pro} (−9.0 kcal mol^{-1}) (Aprajita and Choudhary, 2022). In addition, when compared to previous docking analyses of anti-SARS-CoV-2 drugs like remdesivir (−6.77 kcal mol^{-1}), chloroquine (−6.93 kcal mol^{-1}), and dexamethasone (−7.77 kcal mol^{-1}), all the calculated binding affinities are relatively higher (Shivanika et al., 2022).

3.2.2 Docking simulations with MVD

The docking approach is validated with the atomic coordinates of the structure 7MEQ. The lowest energy pose generated a docking root-mean-squared deviation (RMSD) of 0.58 Å, as shown in Figure 5. Docking simulations of the structures of **System 1** pointed out the

TABLE 2 Results of docking simulations of System 1.

Compound	AutoDock (kcal·mol^{-1})	MolDock score (au)[a]	GOLDscore (au)[a]
$[Cu(Bipy)(Arg)(H_2O)]^{2+}$	−8.4	−140.881	54.792
$[Cu(Bipy)(Orn)(H_2O)]^{2+}$	−8.4	−135.100	55.903
$[Cu(Bipy)(Lys)(H_2O)]^{2+}$	−9.6	−133.086	55.124
$[Cu(Bipy)(Citr)(H_2O)]^{1+}$	−7.6	−124.847	51.513
$[Cu(Bipy)(Asn)(H_2O)]^{1+}$	−7.8	−117.995	45.626
$[Cu(Bipy)(The)(H_2O)]^{1+}$	−7.2	−127.699	51.685
$[Cu(Bipy)(Gln)(H_2O)]^{1+}$	−8.2	−111.124	49.352
$[Cas\ III\text{-}ia(H_2O)]^{1+}$	−7.3	−114.753	49.457
$[Cas\ XI\text{-}Gly(H_2O)]^{1+}$	−6.8	−99.1762	43.014
GBS[b]	−6.3	−87.8000	43.973

[a]Arbitrary units (au).
[b]Nafamostat.

TABLE 3 Results of docking simulations of System 2.

Compound	AutoDock (kcal·mol^{-1})	MolDock score (au)[a]	GOLDscore (au)[a]
$[Cu(Bipy)(Arg)]^{2+}$	−8.3	−129.865	52.247
$[Cu(Bipy)(Orn)]^{2+}$	−8.6	−129.439	56.716
$[Cu(Bipy)(Lys)]^{2+}$	−8.6	−125.484	54.234
$[Cu(Bipy)(Citr)]^{1+}$	−7.0	−125.296	49.403
$[Cu(Bipy)(Asn)]^{1+}$	−8.2	−115.534	46.670
$[Cu(Bipy)(The)]^{1+}$	−6.7	−121.692	51.717
$[Cu(Bipy)(Gln)]^{1+}$	−7.7	−111.094	49.352
$[Cas\ III\text{-}ia]^{1+}$	−6.4	−105.918	46.933
$[CAS\ IX\text{-}Gly]^{1+}$	−5.8	−95.9585	41.827
GBS[b]	6.3	−87.8000	43.973

[a]Arbitrary units (au).
[b]Nafamostat.

copper compound $[Cu(Bipy)(Arg)(H_2O)]^{2+}$ with the lowest binding energy (Figure 6), lower than nafamostat and Casiopeinas®. Analysis of this compound's intermolecular interactions (Figure 7) indicates 14 hydrogen bonds, three involving the water coordinating the Cu(II). The following residues in the hydrogen bonds were found: His296, Asp434, Ser436, Cys437, Gly439, Ser441, Ser460, Gly464, and Pro471. Analysis of the intermolecular hydrogen bonds for the complex involving nafamostat shows the conservation of the interactions involving the following amino acids: Asp435, Ser436, Gly439, Ser441, and Gly464. The overall network of hydrogen bonds is conserved in the structure $[Cu(Bipy)(Arg)(H_2O)]^{2+}$. Only residues His296, Cys437, and Pro471 are specific for the copper compound. These additional interactions observed for $[Cu(Bipy)(Arg)(H_2O)]^{2+}$ contribute to the lowest energy determined for the complex.

Docking simulations for **System 2** revealed $[Cu(Bipy)(Arg)]^{2+}$ to be the lowest energy complex. Although this complex has no water molecule coordinating with the copper, most intermolecular interactions are conserved.

3.2.3 Docking simulations with GOLD

For both Systems, the Orn compound was the one that obtained the highest score, followed by the complexes of Lys and Arg, compared to nafamostat and Casiopeinas®. The compound $[Cu(Bipy)(Orn)(H_2O)]^{2+}$ formed a total of six hydrogen bonds with His296 in addition to Ser436, Ser441, Ser460, Gly462, and Gly464. Also, this complex formed a salt bridge with Asp435, a π-π interaction with His296, a π-bond with His296, and hydrogen bonds with Pro471, Gly464, and Ser436 residues, as shown in Figure 8, as well as a salt bridge with Asp435. On the other hand, $[Cu(Bipy)(Orn)]^{2+}$ formed five hydrogen bonds. In both Systems, there are interactions with the residues of the triad; in the case of **System 1**, water coordination helps to form hydrogen bonds with the residues of amino acids, contributing to the final ligand interaction.

The Lysine compound was discovered to form four hydrogen bonds with the residues Gly464, Pro471, Ser441, and Ser436, as well as a salt bridge with Asp435 and a π-sulfide interaction with Cys281. The water, in this case, had no interaction with any amino acid residue. In

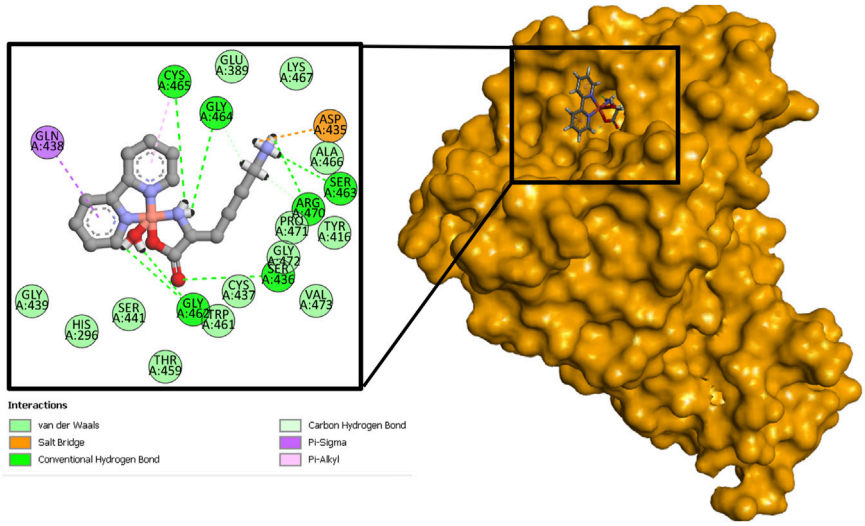

FIGURE 4
Binding interactions between $[Cu(Bipy)(Lys)(H_2O)]^{2+}$ and the protein (7MEQ).

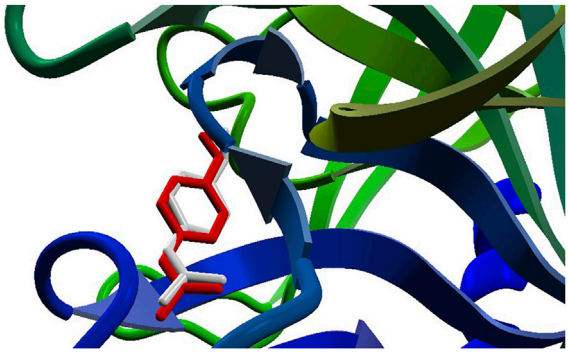

FIGURE 5
The re-docking result of the structure 7MEQ. MVD generated an RMSD of 0.58 Å. The pose structure of the nafamostat is indicated in red, whereas the inhibitor's crystallographic coordinates are light gray—an image generated by the MVD program.

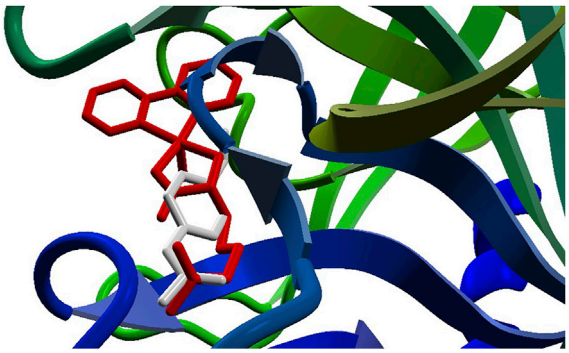

FIGURE 6
Docking results for the compounds $[Cu(Bipy)(Arg)(H_2O)]^{2+}$ (red) and nafamostat (light gray).

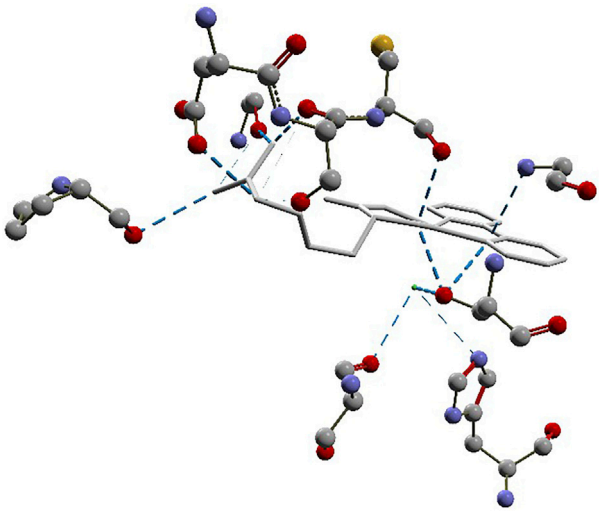

FIGURE 7
Intermolecular hydrogen bonds (dashed blue lines) between the $[Cu(Bipy)(Arg)(H_2O)]^{2+}$ compound and the protein.

System 2, the lysine complex formed three hydrogen bonds with the amino acids Gly464, Gly439, and Ser 436, as well as a salt bridge with Asp435, a π-π interaction with His296, and a π-alkyl interaction with Cys281.

For the Arginine compound, eleven hydrogen bonds were observed with the residues of Asp435, Gly464, Ser460, Gly439, Ser441, Asp440, Gly462, and Ser436, a π-π interaction with His296, and a π-alkyl with Cys281 for the **System 1**. For **System 2**, the Arginine compound presented ten hydrogen bonds with the residues Asp435, Gly462, Ser436, Asp440, Ser441, Gly439, Ser460, and Gly464, a π-π interaction with His296, and a π-alkyl with Cys281. In both compounds (Lysine and Arginine) in **System 1**, it was not observed that the water coordinate had some interaction with some

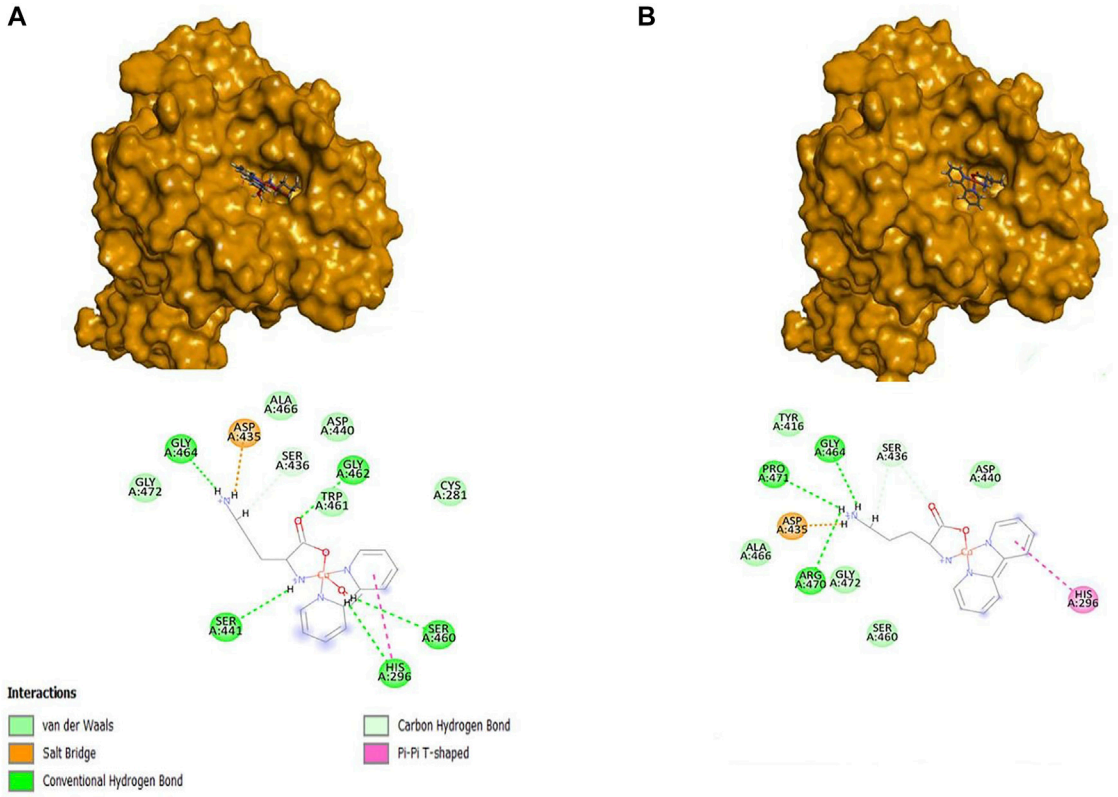

FIGURE 8
Representations 3D and 2D of the $[Cu(Bipy)(Orn)(H_2O)]^{2+}$ **(A)** and $[Cu(Bipy)(Orn)]^{2+}$ **(B)** with 7MEQ.

residue; however, in both **Systems**, bonds were formed with the amino acids of the catalytic triad.

Finally, the correlation between the scores (binding energies) calculated using MolDock and those determined using GOLDscore and AutoDock4 was also analyzed. We have a positive Pearson correlation of 0.761 between MolDock and AutoDock4 for both **Systems**. The correlation between the MolDock score and the GOLDscore is −0.911 and −0.878 for **Systems 1** and **2**, respectively. There is a negative correlation since GOLDscore assigns the highest values for the best hits. For all scoring functions, the three best hits found in **System 1** are the compounds $[Cu(Bipy)(Arg)(H_2O)]^{2+}$, $[Cu(Bipy)(Orn)(H_2O)]^{2+}$, and $[Cu(Bipy)(Lys)(H_2O)]^{2+}$, and for **System 2**, all three scoring functions identified the same three best compounds with differences in the order: $[Cu(Bipy)(Arg)]^{2+}$, $[Cu(Bipy)(Orn)]^{2+}$, and $[Cu(Bipy)(Lys)]^{2+}$.

COVID-19 still stresses healthcare systems and causes a high mortality rate worldwide 3 years after the outbreak. Remdesivir, Paxlovid, and molnupiravir, three oral antivirals, have been licensed in several countries. However, the best treatment option is still required, so new drugs and novel uses for current ones are expected in 2023. People who cannot access vaccines, whose immune systems do not fully respond to immunization, or who develop intercurrent infections need new medicines. Furthermore, Philippe Guérin, head of the Oxford University Infectious Diseases Data Observatory, pointed out that many clinical trials focus on therapies that would be too expensive or difficult to use in many countries, creating a division between research and low- and middle-income nations (Ledford, 2022). Currently, most efforts are focused on antibodies, organic molecules, or already approved drugs for other diseases, such as chloroquine, favipiravir, remdesivir, molnupiravir, nirmatrevir, paxlovid (Akhtar, 2020), or the M^{pro} inhibitor in phase 3 trial, S-217622 (ensitrelvir) (Sasaki et al., 2022). As an alternative, metal-based compounds have also been explored as anti-SARS-CoV-2 agents (Cirri et al., 2021; Gil-Moles et al., 2021; Karges and Cohen, 2021; Vlasiou and Pafti, 2021; Li et al., 2022; Ni et al., 2022).

Coronaviruses and influenza viruses rely heavily on TMPRSS2 for host entry and dissemination (Stopsack et al., 2020; Wettstein et al., 2022). This includes SARS-CoV, the agent responsible for the 2003 SARS outbreak, and influenza H1N1, the virus responsible for the 1918 and 2009 influenza pandemics (Chaipan et al., 2009; Matsuyama et al., 2010; Hoffmann et al., 2020). These examples illustrate the central and conserved function of TMPRSS2 in the pathogenesis of diseases caused by coronaviruses and influenza viruses. The inhibitor, Camostat mesylate, partially prevented the entry of SARS-CoV-2 into lung epithelial cells in an *in vitro* investigation involving cell lines and primary pulmonary cells (Hoffmann et al., 2020). In a TMPRSS2 deletion model, mice infected with the H1N1 influenza virus exhibited a significantly reduced illness course, with protection from pulmonary pathology, weight loss, and death, compared to wild-type control mice (Hatesuer et al., 2013). Given its prominent role in beginning SARS-CoV-2 and

other respiratory viral infections, it is believed that regulating TMPRSS2 expression or activity represents a suitable target for prospective COVID-19 treatments. Key functional residues of TMPRSS2 (His296, Ser441, and Ser460) interacted with nearby residues of SARS-CoV-2 spike protein cleavage sites. The TMPRSS2 region interacts with the C-terminal cleavage site (Arg815/Ser816) of the SARS-CoV-2 spike protein. This site was considered more druggable than the N-terminal cleavage site (Arg685/Ser686). Therefore, a complex made up of human TMPRSS2 and SARS-CoV-2 spike protein is suggested as a potential drug target that could be used to guide structure-based drug design (Hussain et al., 2020).

Molecular docking has demonstrated that copper(II) complexes can interact with crucial SARS–CoV–2 targets such as M^{pro}, PL^{pro}, spike protein, and ACE2 (Al-Harbi, 2022; Viola et al., 2022). Among them, the square planar complex $[Cu(L)_2]$, where L = 2-(4-morpholinobenzylideneamino)phenol (Sakthikumar et al., 2022), shows binding energy of −7.8 kcal mol^{-1} against M^{pro} with Autodock Vina (interactions are not specified), higher than the results of the copper complexes with Arg, Orn, and Lys, here studied. In addition, fifty Casiopeinas® and related Cu(II) compounds were also investigated as M^{pro} inhibitors with AutoDock (Reina et al., 2022). Some Casiopeinas®, such as CasII-5Clsa, CasII-ambz, or CasII-tyr, show promising results with binding energies between −8.58 and −9.25 and kcal·mol^{-1}, lower than the references boceprevir and N3 peptide, and they interact with His41, Asn142, Cys145, Glu166, and Gln189, which are part of the catalytic site cavity of M^{pro} (Kneller et al., 2020). However, as TMPRSS2 inhibitors, Cas III-ia and Cas IX-gly exhibit high binding energies with values between −5.8 and −7.3 kcal mol^{-1}.

Here we have shown that copper(II) complexes derived from amino acids, analogs of Casiopeinas®, could be considered good candidates for potential metallodrugs against COVID-19, as compared with Casiopeinas® already in phase I clinical trials and nafamostat. The cationic nature of the analogs and the basic terminal nature of the side chains of the amino acids are responsible for anchoring them close to the active site by interacting with Asp495, a key amino acid residue for interacting with arginine or lysine residues of target proteins.

4 Conclusion

The optimized molecular structures of seven complexes containing the amino acid residues: Arg, Orn, Lys, Citr, Asn, The, and Gln; and two Casiopeinas: Cas III-ia and Cas IX-gly, containing acetylacetonato and Gly, respectively, were investigated using DFT methodology, and the global reactivity indices were determined. The highest gap energy values between 4.17 and 4.28 eV suggest that the complexes with Arg, Orn, and Lys with a molecule of water and for Asn with two molecules of water are the most stable and can present bioactivity, with comparable values to Casiopeinas®. Additionally, the softness index appeared to have the smallest values between 0.234–0.240 eV for the same complexes with Arg, Orn, and Lys with a molecule of water and Asn with two molecules of water, comparable with the values for CAS IX-Gly with one and two water molecules (0.234 and 0.235 eV, respectively). A low value of the softness index is related to low toxicity through electrophilic-nucleophilic interactions, and it can be used as a descriptor of their biological activity with the TPMRSS2 protein.

AutoDock4, MVD, and GOLD have different scoring functions and search algorithms to carry out docking simulations. Nevertheless, they identified the same top three compounds for both systems, indicating the convergence of our docking approaches. Also, in the three Docking methodologies, the following similarities were found: i) An improvement in the binding energy/score when only one water molecule is in the structure of the studied complexes; ii) the binding energy/docking score is better for the studied complexes than for the nafomastat inhibitor; and iii) the compounds that interact best with the protein are the complexes with the amino acid residues Orn, Lys, and Arg, though the order of these amino acid residues varies between them.

Since the copper compounds localize just above the catalytic triad, they could stop substrates from getting into it. The binding energies are in the range of other expensive synthetic drugs already on the market. Because serine protease could be an excellent target to stop the virus from getting inside the cell, the analyzed complexes are an excellent place to start looking for new drugs to treat COVID-19.

Data availability statement

The original contributions presented in the study are included in the article/Supplementary Material, further inquiries can be directed to the corresponding authors.

Author contributions

SV-R, DR-C, LN, and WA carried out the docking simulations. DFT calculations were carried out by FM and MC. SV-R, DR-C, LN, EG-V, MC, AG-G, and BS-G wrote and revised the manuscript. SV-R, DR-C, and EG-V conceived and designed this study. All authors contributed extensively to the work presented in this paper. All authors have read and agreed to the published version of the manuscript.

Funding

Projects funded for this research include 100108444-VIEP, 100256733-VIEP, and 100233622-VIEP; the PRODEP Academic Group BUAP-CA-263 (SEP, Mexico); and the Ministerio de Universidades and Funds Next-Generation for the Margarita Salas contract 401 (Spain); this work was supported by a grant from CNPq (Brazil) (309029/2018-0).

Acknowledgments

SV-R, DR-C and LN thank CONACyT for their M.Sc and PhD fellowship support numbers 1143792, 774653, and postdoctoral fellowship. MC and FM wish to thank Laboratorio Nacional de Supercómputo del Sureste de México (LNS-BUAP) and the CONACyT network of national laboratories for the computer resources and support provided. AG-G thanks the Ministerio de Universidades and funding Next-Generation (Spain).

Conflict of interest

The authors declare that the research was conducted in the absence of any commercial or financial relationships that could be construed as a potential conflict of interest.

Publisher's note

All claims expressed in this article are solely those of the authors and do not necessarily represent those of their affiliated organizations, or those of the publisher, the editors and the reviewers. Any product that may be evaluated in this article, or claim that may be made by its manufacturer, is not guaranteed or endorsed by the publisher.

Supplementary material

The Supplementary Material for this article can be found online at: https://www.frontiersin.org/articles/10.3389/fchem.2023.1128859/full#supplementary-material

References

Adamo, C., and Barone, V. (1998). Exchange functionals with improved long-range behavior and adiabatic connection methods without adjustable parameters: The MPW and MPW1PW models. *J. Chem. Phys.* 108, 664–675. doi:10.1063/1.475428

Adelusi, T. I., Oyedele, A.-Q. K., Boyenle, I. D., Ogunlana, A. T., Adeyemi, R. O., Ukachi, C. D., et al. (2022). Molecular modeling in drug discovery. *Inf. Med. Unlocked* 29, 100880. doi:10.1016/j.imu.2022.100880

Akhtar, M. J. (2020). COVID-19 inhibitors: A prospective therapeutics. *Bioorg. Chem.* 101, 104027. doi:10.1016/j.bioorg.2020.104027

Al-Harbi, S. A. (2022). Synthesis and characterization of violurate-based Mn(II) and Cu(II) complexes nano-crystallites as DNA-binders and therapeutics agents against SARS-CoV-2 virus. *J. Saudi Chem. Soc.* 26, 101528. doi:10.1016/j.jscs.2022.101528

Aprajita and Choudhary, M. (2022). Structural and computational studies of cobalt(II) and copper(II) complexes with aromatic heterocyclic ligand. *Polycycl. Aromat. Compd.* 42, 1–27. doi:10.1080/10406638.2022.2061530

Balawender, R., and Geerlings, P. (2005). DFT-based chemical reactivity indices in the Hartree-Fock method. II. Fukui function, chemical potential, and hardness. *J. Chem. Phys.* 123, 124103–124116. doi:10.1063/1.2012330

Baughn, L. B., Sharma, N., Elhaik, E., Sekulic, A., Bryce, A. H., and Fonseca, R. (2020). Targeting TMPRSS2 in SARS-CoV-2 infection. *Mayo Clin. Proc.* 95, 1989–1999. doi:10.1016/J.MAYOCP.2020.06.018

Becco, L., García-Ramos, J. C., Azuara, L. R., Gambino, D., and Garat, B. (2014). Analysis of the DNA interaction of copper compounds belonging to the Casiopeínas® antitumoral series. *Biol. Trace Elem. Res.* 161, 210–215. doi:10.1007/s12011-014-0098-1

Bitencourt-Ferreira, G., and de Azevedo, W. F., Jr. (2019). Molegro virtual docker for docking. *Methods Mol. Biol.* 2053, 149–167. doi:10.1007/978-1-4939-9752-7_10

Chaipan, C., Kobasa, D., Bertram, S., Glowacka, I., Steffen, I., Tsegaye, T. S., et al. (2009). Proteolytic activation of the 1918 influenza virus hemagglutinin. *J. Virol.* 83, 3200–3211. doi:10.1128/JVI.02205-08

Cirri, D., Pratesi, A., Marzo, T., and Messori, L. (2021). Metallo therapeutics for COVID-19. Exploiting metal-based compounds for the discovery of new antiviral drugs. *Expert Opin. Drug Discov.* 16, 39–46. doi:10.1080/17460441.2020.1819236

Corona-Motolinia, N. D., Martínez-Valencia, B., Noriega, L., Sánchez-Gaytán, B. L., Mendoza, A., Meléndez-Bustamante, F. J., et al. (2021). Ternary copper complex of L-glutamine and phenanthroline as counterions of cyclo-tetravanadate anion: Experimental-theoretical characterization and potential antineoplastic activity. *Metals* 11, 1541. doi:10.3390/met11101541

Cossi, M., Rega, N., Scalmani, G., and Barone, V. (2003). Energies, structures, and electronic properties of molecules in solution with the C-PCM solvation model. *J. Comput. Chem.* 24, 669–681. doi:10.1002/jcc.10189

DeLaney, C., Sheng, Y., Pectol, C., Vantansever, E., Zhang, H., Bhuvanesh, N., et al. (2021). Zinc thiotropolone combinations as inhibitors of the SARS-CoV-2 main protease. *Dalton Trans.* 50, 12226–12233. doi:10.1039/d1dt02499j

Dias, R., and de Azevedo, W. F., Jr. (2008). Molecular docking algorithms. *Curr. Drug Targets* 9, 1040–1047. doi:10.2174/138945008786949432

Ditchfield, R., Hehre, W. J., and Pople, J. A. (1971). Self-Consistent molecular-orbital methods. IX. An extended Gaussian-type basis for molecular-orbital studies of organic molecules. *J. Chem. Phys.* 54, 724–728. doi:10.1063/1.1674902

Dong, E., Du, H., and Gardner, L. (2020). An interactive web-based dashboard to track COVID-19 in real-time. *Lancet Infect. Dis.* 20, 533–534. doi:10.1016/S1473-3099(20)30120-1

Favre, D., Harmon, J. F., Zhang, A., Miller, M. S., and Kaltashov, I. A. (2022). Decavanadate interactions with the elements of the SARS-CoV-2 spike protein highlight the potential role of electrostatics in disrupting the infectivity cycle. *J. Inorg. Biochem.* 234, 111899. doi:10.1016/j.jinorgbio.2022.111899

Fraser, B. J., Beldar, S., Seitova, A., Hutchinson, A., Mannar, D., Li, Y., et al. (2022). Structure and activity of human TMPRSS2 protease implicated in SARS-CoV-2 activation. *Nat. Chem. Biol.* 18, 963–971. doi:10.1038/s41589-022-01059-7

Frisch, M. J., Trucks, G. W., Schlegel, H. B., Scuseria, G. E., Robb, M. A., Cheeseman, J. R., et al. (2016). *Gaussian 16, revision B.O1*. Wallingford: Gaussian, Inc.

Gandhi, R. T., Malani, P. N., and Del Rio, C. (2022). COVID-19 therapeutics for nonhospitalized patients. *JAMA* 327, 617–618. doi:10.1001/jama.2022.0335

Gandhimathi, R., and Anbuselvi, S. (2022). *In silico* molecular docking, ADMET property, molecular dynamic simulation evaluation of *N,N'*-bis(2-hydroxybenzylidene)-1,2-diaminobenzene and its metal complexes against SARS-CoV-2. *Asian J. Chem.* 34, 2573–2582. doi:10.14233/ajchem.2022.23883

García-Ramos, J. C., Galindo-Murillo, R., Tovar-Tovar, A., Alonso-Saenz, A. L., Gómez-Vidales, V., Flores-Álamo, M., et al. (2014). The π-back-bonding modulation and its impact in the electronic properties of Cu(II) antineoplastic compounds: An experimental and theoretical study. *Chem.* 20, 13730–13741. doi:10.1002/chem.201402775

Gil-Moles, M., Basu, U., Büssing, R., Hoffmeister, H., Türck, S., Varchmin, A., et al. (2020). Gold metallodrugs to target coronaviruses proteins: Inhibitory effects on the spike-ACE2 interaction and on PL^{pro} protease activity by auranofin and gold organometallics. *Chem. Eur. J.* 26, 15140–15144. doi:10.1002/chem.202004112

Gil-Moles, M., Türck, S., Basu, U., Pettenuzzo, A., Bhattacharya, S., Rajan, A., et al. (2021). Metallodrug profiling against SARS-CoV-2 target proteins identifies highly potent inhibitors of the S/ACE2 interaction and the papain-like protease PL^{pro}. *Chem. – Eur. J.* 27, 17928–17940. doi:10.1002/chem.202103258

Halperin, I., Ma, B., Wolfson, H., and Nussinov, R. (2002). Principles of docking: An overview of search algorithms and a guide to scoring functions. *Proteins Struct. Func. Genet.* 47, 409–443. doi:10.1002/PROT.10115

Hatesuer, B., Bertram, S., Mehnert, N., Bahgat, M. M., Nelson, P. S., Pöhlman, S., et al. (2013). Tmprss2 is essential for influenza H1N1 virus pathogenesis in mice. *PLoS Pathog.* 9, e1003774. doi:10.1371/journal.ppat.1003774

Heberlé, G., and de Azevedo, W. F., Jr. (2011). Bio-inspired algorithms applied to molecular docking simulations. *Curr. Med. Chem.* 18, 1339–1352. doi:10.2174/092986711795029573

Hoffmann, M., Kleine-Weber, H., Schroeder, S., Krüger, N., Herrler, T., Erichsen, S., et al. (2020). SARS-CoV-2 cell entry depends on ACE2 and TMPRSS2 and is blocked by a clinically proven protease inhibitor. *Cell* 181, 271–280. doi:10.1016/J.CELL.2020.02.052

Hu, X., Shrimp, J. H., Guo, H., Xu, M., Chen, C. Z., Zhu, W., et al. (2021). Discovery of TMPRSS2 inhibitors from virtual screening as a potential treatment of COVID-19. *ACS Pharmacol. Transl. Sci.* 4, 1124–1135. doi:10.1021/acsptsci.0c00221

Hussain, M., Jabeen, N., Amanullah, A., Baig, A. A., Aziz, B., Shabbir, S., et al. (2020). Molecular docking between human TMPRSS2 and SARS-CoV-2 spike protein: Conformation and intermolecular interactions. *AIMS Microbiol.* 6, 350–360. doi:10.3934/microbiol.2020021

Jang, S., and Rhee, J.-Y. (2020). Three cases of treatment with nafamostat in elderly patients with COVID-19 pneumonia who need oxygen therapy. *Int. J. Infect. Dis.* 96, 500–502. doi:10.1016/J.IJID.2020.05.072

Jiang, Y., Rubin, L., Zhou, Z., Zhang, H., Su, Q., Hou, S.-T., et al. (2022). Pharmacological therapies and drug development targeting SARS-CoV-2 infection. *Cytokine Growth Factor Rev.* 68, 13–24. doi:10.1016/j.cytogfr.2022.10.003

Jones, G., Willet, P., Glen, R. C., Leach, A. R., and Taylor, R. (1997). Development and validation of a genetic algorithm for flexible docking. *J. Mol. Biol.* 267, 727–748. doi:10.1006/JMBI.1996.0897

Karges, J., and Cohen, S. (2021). Metal complexes as antiviral agents for SARS-CoV-2. *ChemBioChem* 22, 2600–2607. doi:10.1002/CBIC.202100186

Karges, J., Kalaj, M., Gembicky, M., and Cohen, S. M. (2021). Re^{I} tricarbonyl complexes as coordinate covalent inhibitors for the SARS-CoV-2 main cysteine protease. *Angew. Chem. Int. Ed.* 60, 10716–10723. doi:10.1002/anie.202016768

Kneller, D. W., Phillips, G., O'Neill, H. M., Jedrzejczak, R., Stols, L., Langan, P., et al. (2020). Structural plasticity of SARS-CoV-2 3CL M^{pro} active site cavity revealed by room temperature X-ray crystallography. *Nat. Commun.* 11, 3202. doi:10.1038/s41467-020-16954-7

Krishnan, R., Binkley, J. S., Seeger, R., and Pople, J. A. (1980). Self-consistent molecular orbital methods. XX. A basis set for correlated wavefunctions. *J. Chem. Phys.* 72, 650–654. doi:10.1063/1.438955

Ledford, H. (2022). Hundreds of COVID trials could provide a deluge of new drugs. *Nature* 603, 25–27. doi:10.1038/D41586-022-00562-0

Li, H., Yuan, S., Wei, X., and Sun, H. (2022). Metal-based strategies for the fight against COVID-19. *ChemComm* 58, 7466–7482. doi:10.1039/d2cc01772e

Li, K., Meyerholz, D. K., Bartlett, J. A., and McCray, P. B. (2021). The TMPRSS2 inhibitor nafamostat reduces SARS-CoV-2 pulmonary infection in mouse models of COVID-19. *mBio* 12, 00970211–e97111. doi:10.1128/mBio.00970-21

Martínez-Valencia, B., Corona-Motolinia, N. D., Sánchez-Lara, E., Noriega, L., Sánchez-Gaytán, B. L., Castro, M. E., et al. (2020). Cyclo-tetravanadate bridged copper complexes as potential double bullet pro-metallodrugs for cancer treatment. *J. Inorg. Biochem.* 208, 111081. doi:10.1016/J.JINORGBIO.2020.111081

Matsuyama, S., Nagata, N., Shirato, K., Kawase, M., Takeda, M., and Taguchi, F. (2010). Efficient activation of the severe acute respiratory syndrome coronavirus spike protein by the transmembrane protease TMPRSS2. *J. Virol.* 84, 12658–12664. doi:10.1128/JVI.01542-10

Mhatre, S., Naik, S., and Patravale, V. (2021). A molecular docking study of EGCG and theaflavin digallate with the druggable targets of SARS-CoV-2. *Comput. Biol. Med.* 129, 104137–104139. doi:10.1016/j.compbiomed.2020.104137

Milite, C., Amendola, G., Nocentini, A., Bua, S., Cipriano, A., Barresi, E., et al. (2019). Novel 2-substituted-benzimidazole-6-sulfonamides as carbonic anhydrase inhibitors: Synthesis, biological evaluation against isoforms I, II, IX and XII and molecular docking studies. *J. Enzyme Inhib. Med. Chem.* 34, 1697–1710. doi:10.1080/14756366.2019.1666836

Morris, G. M., Goodsell, D. S., Halliday, R. S., Huey, R., Hart, W. E., Belew, R. K., et al. (1998). Automated docking using a Lamarckian genetic algorithm and an empirical binding free energy function. *J. Comput. Chem.* 19, 1639–1662. doi:10.1002/(sici)1096-987x(19981115)19:14<1639::aid-jcc10>3.0.co;2-b

Morris, G. M., Huey, R., Lindstrom, W., Sanner, M. F., Belew, R. K., Goodsell, D. S., et al. (2009). AutoDock4 and AutoDockTools4: Automated docking with selective receptor flexibility. *J. Comput. Chem.* 30, 2785–2791. doi:10.1002/jcc.21256

ViolaMuhammad, N., Khan, I. N., Ali, Z., Ibrahim, M., Shujah, S., Ali, S., et al. (2022). Synthesis, characterization, antioxidant, antileishmanial, anticancer, DNA, and theoretical SARS-CoV-2 interaction studies of copper(II) carboxylate complexes. *J. Mol. Struct.* 1253, 132308. doi:10.1016/j.molstruc.2021.132308

Nelder, J., and Mead, R. (1965). A simplex method for function minimization. *Comput. J.* 7, 308–313. doi:10.1093/COMJNL/7.4.308

Ni, Y.-Q., Zeng, H.-H., Song, X.-W., Zheng, J., Wu, H.-Q., Liu, C.-T., et al. (2022). Potential metal-related strategies for prevention and treatment of COVID-19. *Rare Met.* 41, 1129–1141. doi:10.1007/s12598-021-01894-y

Öztürkkan, F. E., Özdemir, M., Akbaba, G. B., Sertçelik, M., Yalçın, B., Necefoglu, H., et al. (2022). Synthesis, crystal structure, potential drug properties for Coronavirus of Co(II) and Zn(II) 2-chlorobenzoate with 3-cyanopyridine complexes. *J. Mol. Struct.* 1250, 131825. doi:10.1016/j.molstruc.2021.131825

Paoloni-Giacobino, A., Chen, H., Peitsch, M. C., Rossier, C., and Antonarakis, S. E. (1997). Cloning of the TMPRSS2 gene, which encodes a novel serine protease with transmembrane, LDLRA, and SRCR domains and maps to 21q22.3. *Genomics* 44, 309–320. doi:10.1006/GENO.1997.4845

Patra, A. K., Bhowmick, T., Roy, S., Ramakumar, S., and Chakravarty, A. R. (2009). Copper(II) complexes of L-arginine as netropsin mimics showing DNA cleavage activity in red light. *Inorg. Chem.* 48, 2932–2943. doi:10.1021/IC8017425

Ramírez-Contreras, D., García-García, A., Sánchez-Gaytán, B. L., Serrano-de la Rosa, L. E., Melendez, F. J., Choquesillo-Lazarte, D., et al. (2022). Bis-citrullinato copper(II) complex: Synthesis, crystal structure, and non-covalent interactions. *Crystals* 12, 1386. doi:10.3390/cryst12101386

Reina, M., Talavera-Contreras, L. G., Figueroa-DePaz, Y., Ruiz-Azuara, L., and Hernández-Ayala, L. F. (2022). Casiopeinas® as SARS-CoV-2 main protease (Mpro) inhibitors: A combined DFT, molecular docking and ONIOM approach. *New J. Chem.* 46, 12500–12511. doi:10.1039/D2NJ01480G

Rodrigues, J. A. O., Neto, J. G. O., de Barros, A. O. S., Ayala, A. P., Santos-Oliveira, R., de Menezes, A. S., et al. (2020). Copper(II): Phenanthroline complexes with L-asparagine and L-methionine: Synthesis, crystal structure, and *in-vitro* cytotoxic effects on prostate, breast, and melanoma cancer cells. *Polyhedron* 191, 114807. doi:10.1016/J.POLY.2020.114807

Sakthikumar, K., Krause, R. W. M., Isamura, B. K., Raja, J. D., and Athimoolam, S. (2022). Spectro-electrochemical, fluorometric and biothermodynamic evaluation of pharmacologically active morpholine scaffold single crystal ligand and its metal(II) complexes: A comparative study on *in-vitro* and *in-silico* screening towards DNA/BSA/SARS-CoV-2. *J. Inorg. Biochem.* 236, 111953. doi:10.1016/j.jinorgbio.2022.111953

Sánchez-Lara, E., García-García, A., González-Vergara, E., Cepeda, J., and Rodríguez-Diéguez, A. (2021). Magneto-structural correlations of *cyclo*-tetravanadates functionalized with mixed-ligand copper(II) complexes. *New J. Chem.* 45, 5081–5092. doi:10.1039/D0NJ06004F

Sasaki, M., Tabata, K., Kishimoto, M., Itakura, Y., Kobayashi, H., Ariizumi, T., et al. (2022). S-217622, a SARS-CoV-2 main protease inhibitor, decreases viral load and ameliorates COVID-19 severity in hamsters. *Sci. Transl. Med.* 15, eabq4064. doi:10.1126/scitranslmed.abq4064

Serment-Guerrero, J., Cano-Sanchez, P., Reyes-Perez, E., Velazquez-Garcia, F., Bravo-Gomez, M. E., and Ruiz-Azuara, L. (2011). Genotoxicity of the copper antineoplastic coordination complexes casiopeinas®. *Toxicol. Vitro* 25, 1376–1384. doi:10.1016/J.TIV.2011.05.008

Sert, Y., Sreenivasa, S., Dogan, H., Mohan, N. R., Suchetan, P. A., and Ucun, F. (2014). Vibrational frequency analysis, FT-IR and Laser-Raman spectra, DFT studies on ethyl (2E)-2-cyano-3-(4-methoxyphenyl)-acrylate. *Spectrochim. Acta, Part A* 130, 96–104. doi:10.1016/j.saa.2014.03.061

Shahabadi, N., Mahdavi, M., and Zendehcheshm, S. (2022). Can polyoxometalates (POMs) prevent of coronavirus 2019-nCoV cell entry? Interaction of POMs with TMPRSS2 and spike receptor domain complexed with ACE2 (ACE2-RBD): Virtual screening approaches. *Inf. Med. Unlocked* 29, 100902. doi:10.1016/j.imu.2022.100902

Shivanika, C., Deepak, S. K., Ragunathan, V., Tiwari, P., Sumitha, A., and Brindha, P. D. (2022). Molecular docking, validation, dynamics simulations, and pharmacokinetic prediction of natural compounds against the SARS-CoV-2 main-protease. *J. Biomol. Struct. Dyn.* 40, 585–611. doi:10.1080/07391102.2020.1815584

Siddiqui, N., and Javed, S. (2021). Quantum computational, spectroscopic investigations on ampyra (4-aminopyridine) by DFT/TD-DFT with different solvents and molecular docking studies. *J. Mol. Struct.* 1224, 129021. doi:10.1016/j.molstruc.2020.129021

Stopsack, K. H., Mucci, L. A., Antonarakis, E. S., Nelson, P. S., and Kantoff, P. W. (2020). TMPRSS2 and COVID-19: Serendipity or opportunity for intervention? *Cancer Discov.* 10, 779–782. doi:10.1158/2159-8290.CD-20-0451

Takahashi, W., Yoneda, T., Koba, H., Ueda, T., Tsuji, N., Ogawa, H., et al. (2021). Potential mechanisms of nafamostat therapy for severe COVID-19 pneumonia with disseminated intravascular coagulation. *Int. J. Infect. Dis.* 102, 529–531. doi:10.1016/j.ijid.2020.10.093

Tanveer, F., Anwar, M. F., Siraj, B., and Zarina, S. (2022). Evaluation of anti-EGFR potential of quinazoline derivatives using molecular docking: An *in silico* approach. *Biotechnol. Appl. Biochem.* 69, 1226–1237. doi:10.1002/BAB.2199

Tao, X., Zhang, L., Du, L., Liao, R., Cai, H., Lu, K., et al. (2021). Allosteric inhibition of SARS-CoV-2 3CL protease by colloidal bismuth subcitrate. *Chem. Sci.* 12, 14098–14102. doi:10.1039/d1sc03526f

Tao, X., Zhang, L., Du, L., Lu, K., Zhao, Z., Xie, Y., et al. (2022). Inhibition of SARS-CoV-2 replication by zinc gluconate in combination with hinokitiol. *J. Inorg. Biochem.* 231, 111777. doi:10.1016/j.jinorgbio.2022.111777

Thomsen, R., and Christensen, M. H. (2006). MolDock: A new technique for high-accuracy molecular docking. *J. Med. Chem.* 49, 3315–3321. doi:10.1021/jm051197e

Thunders, M., and Delahunt, B. (2020). Gene of the month: TMPRSS2 (transmembrane serine protease 2). *J. Clin. Pathol.* 73, 773–776. doi:10.1136/jclinpath-2020-206987

Tovar-Tovar, A., Ruiz-Ramírez, L., Campero, A., Romerosa, A., Moreno-Esparza, R., and Rosales-Hoz, M. J. (2004). Structural and reactivity studies on 4,4'-dimethyl-2,2'-bipyridine acetylacetonate copper(II) nitrate (CASIOPEINA III-ia®) with methionine, by UV-visible and EPR techniques. *J. Inorg. Biochem.* 98, 1045–1053. doi:10.1016/j.jinorgbio.2004.02.023

Verdonk, M. L., Cole, J. C., Hartshorn, M. J., Murray, C. W., and Taylor, R. D. (2003). Improved protein-ligand docking using GOLD. *Proteins* 52, 609–623. doi:10.1002/prot.10465

Vlasiou, M. C., and Pafti, K. S. (2021). Screening possible drug molecules for Covid-19. The example of vanadium (III/IV/V) complex molecules with computational chemistry and molecular docking. *Comput. Toxicol.* 18, 100157. doi:10.1016/j.comtox.2021.100157

Wachters, A. J. H. (1970). Gaussian basis set for molecular wavefunctions containing third-row atoms. *J. Chem. Phys.* 52, 1033–1036. doi:10.1063/1.1673095

Wettstein, L., Kirchhoff, F., and Münch, J. (2022). The transmembrane protease TMPRSS2 as a therapeutic target for COVID-19 treatment. *Int. J. Mol. Sci.* 23, 1351–1427. doi:10.3390/ijms23031351

Word, J. M., Lovell, S. C., Richardson, J. S., and Richardson, D. C. (1999). Asparagine and glutamine: Using hydrogen atom contacts in the choice of side-chain amide orientation. *J. Mol. Biol.* 285, 1735–1747. doi:10.1006/JMBI.1998.2401

World Health Organization (2022). *WHO coronavirus (COVID-19) dashboard*. Available at: https://covid19.who.int/ (Accessed December 13, 2022).

Yuan, S., Wang, R., Chan, J. F.-W., Zhang, A. J., Cheng, T., Chik, K. K.-H., et al. (2020). Metallodrug ranitidine bismuth citrate suppresses SARS-CoV-2 replication and relieves virus-associated pneumonia in Syrian hamsters. *Nat. Microbiol.* 5, 1439–1448. doi:10.1038/s41564-020-00802-x

Zmora, P., Moldenhauer, A.-S., Hofmann-Winkler, H., and Pöhlmann, S. (2015). TMPRSS2 isoform 1 activates respiratory viruses and is expressed in viral target cells. *PLoS ONE* 10, 01383800–e138414. doi:10.1371/JOURNAL.PONE.0138380

frontiers | Frontiers in Chemistry

TYPE Original Research
PUBLISHED 14 March 2023
DOI 10.3389/fchem.2023.1126427

OPEN ACCESS

EDITED BY
Anton V. Dolzhenko,
Monash University, Australia

REVIEWED BY
Mohammed Salah Ayoup,
Alexandria University, Egypt
Clemens Zwergel,
Sapienza University of Rome, Italy

*CORRESPONDENCE
Sveva Pelliccia,
sveva.pelliccia@unina.it
Margherita Brindisi,
margherita.brindisi@unina.it

†These authors have contributed equally to this work

SPECIALTY SECTION
This article was submitted to Medicinal and Pharmaceutical Chemistry, a section of the journal Frontiers in Chemistry

RECEIVED 17 December 2022
ACCEPTED 02 March 2023
PUBLISHED 14 March 2023

CITATION
Pelliccia S, Alfano AI, Gomes Da Assunção BR, Turco L, Lembo F, Summa V, Buommino E and Brindisi M (2023), Rejuvenating the [1, 2, 3]-triazolo [1,5-a]quinoxalin-4(5*H*)-one scaffold: Synthesis and derivatization in a sustainable guise and preliminary antimicrobial evaluation. *Front. Chem.* 11:1126427. doi: 10.3389/fchem.2023.1126427

Rejuvenating the [1, 2, 3]-triazolo [1,5-a]quinoxalin-4(5*H*)-one scaffold: Synthesis and derivatization in a sustainable guise and preliminary antimicrobial evaluation

Sveva Pelliccia[1*†], Antonella Ilenia Alfano[1†], Beatriz Ramos Gomes Da Assunção[2], Luigia Turco[1,3], Francesca Lembo[1], Vincenzo Summa[1], Elisabetta Buommino[1] and Margherita Brindisi[1*]

[1]Department of Pharmacy, University of Naples Federico II, Naples, Italy, [2]ESTeSL- Lisbon School of Health Technology, Polytechnic Institute of Lisbon, Lisbon, Portugal, [3]Department of Precision Medicine, University of Campania "Luigi Vanvitelli", Naples, Italy

The [1,2,3]-triazolo [1,5-a] quinoxalin-4(5*H*)-one scaffold and its analogues triazole-fused heterocyclic compounds are relevant structural templates in both natural and synthetic biologically active compounds. However, their medicinal chemistry applications are often limited due to the lack of synthetic protocols combining straightforward generation of the central core while also allowing extensive decoration activity for drug discovery purposes. Herein, we report a "refreshed" synthesis of the [1,2,3]-triazolo [1,5-*a*]quinoxalin-4(5*H*)-one core, encompassing the use of eco-compatible catalysts and reaction conditions. We have also performed a sustainable and extensive derivatization campaign at both the endocyclic amide nitrogen and the ester functionality, comprehensively exploring the reaction scope and overcoming some of the previously reported difficulties in introducing functional groups on this structural template. Finally, we unveiled a preliminary biological investigation for the newly generated chemical entities. Our assessment of the compounds on different bacterial species (two *S. aureus* strains, three *P. aeruginosa* strains, *K. pneumonia*), and two fungal *C. albicans* strains, as well as the evaluation of their activity on *S. epidermidis* biofilm formation, foster further optimization for the retrieved hit compounds **9**, **14**, and **20**.

KEYWORDS

[1,2,3]-triazolo [1,5-a] quinoxalin-4(5H)-one, privileged scaffold, sustainable synthesis, green chemistry, drug discovery, antimicrobial agents

1 Introduction

The triazoloquinoxaline scaffold is considered a versatile moiety, and an important structural template for the design and synthesis of novel biologically relevant compounds such as antibacterial, anti-HIV, antitrypanosomal, antiallergic, antifungal, cardiovascular, antileishmanial, and chemotherapeutic agents (Amer et al., 2010; El-Sagheer and Brown,

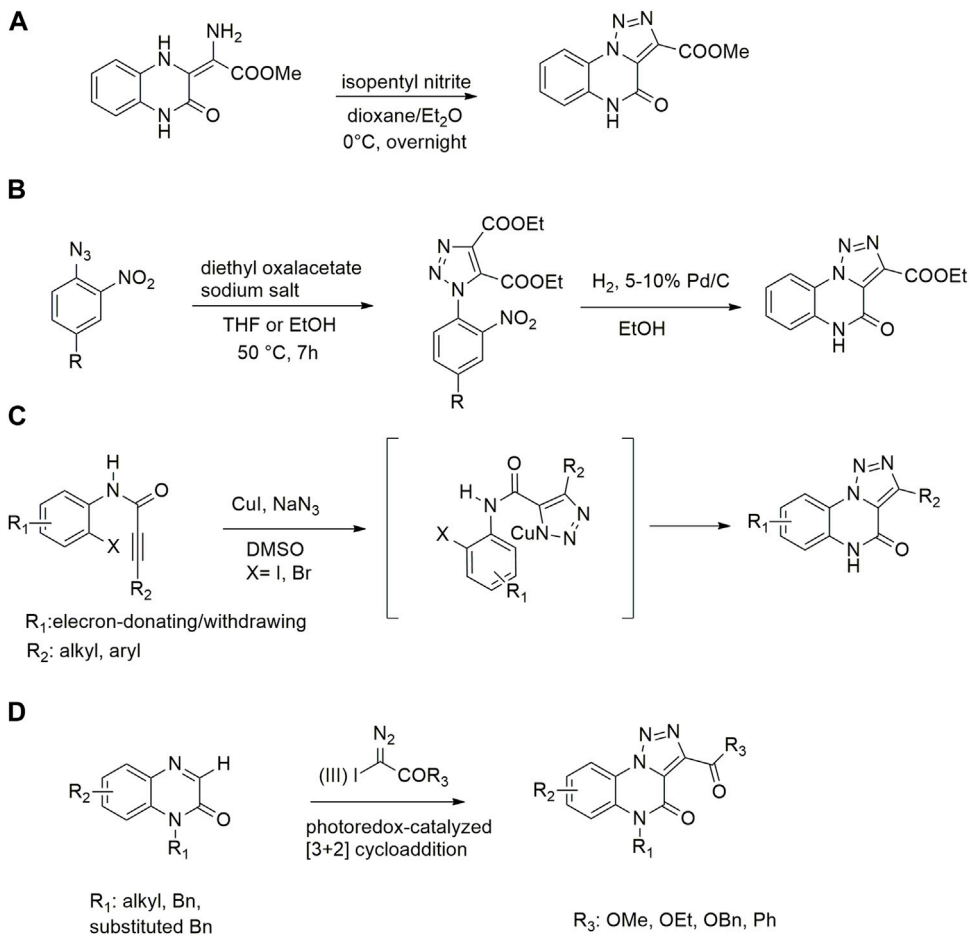

SCHEME 1
Previously reported approaches for [1,2,3]-triazolo [1,5-*a*] quinoxalin-4(5*H*)-ones synthesis **(A–D)**.

2012; Ayoup et al., 2016; Nagavelli et al., 2016; Zhang et al., 2017; Ayoup et al., 2022). Despite several applications of this scaffold in medicinal chemistry and its special features and potentiality of derivatization, little has been done with respect to the search of versatile and potentially ecofriendly synthetic protocols (Baashen et al., 2016).

Accordingly, compared to the more largely explored and synthetically accessible 1,2,4-triazoloquinoxalines (Alswah et al., 2018; El-Attar et al., 2018; Houa et al., 2020; Wesseler et al., 2022), only few applications on the 1,2,3-triazoloquinoxaline counterpart have been reported in literature, most probably due to the available somewhat outdated synthetic protocols that lack versatility for quick scaffold decoration and derivatization.

Typically [1,2,3]-triazolo [1,5-*a*] quinoxalin-4(5*H*)-ones were prepared through cyclization of methyl 2-amino-2-(3,4-dihydro)-2-(3,4-dihydro-2(1*H*)-quinoxalinylidene) acetate with amyl nitrite in presence of 2,2,2- trichloroacetic acid and dioxane/diethyl ether as solvents (Scheme 1A) (Ager et al., 1988).

More recent methodologies for the generation of this tricyclic system require multiple steps involving the preparation of the suitable triazole intermediates followed by cycloamidation. Accordingly, substituted 2-nitrophenyl azides can react with diethyl oxalacetate, ethyl benzoyl pyruvate and ethyl 2-furoyl pyruvate in form of their sodium salts producing triazoles diesters in a complex mixture of triazole byproducts, corresponding aniline of the azide and substituted benzofurazan-*N*-oxide (Scheme 1B) (Biagi et al., 2002). 2-Nitrophenyl triazoles subsequently undergo catalytic hydrogenation with Pd/C thus providing the corresponding 1,2,3-triazoloquinoxalin-4-one scaffold, further functionalized on its amide moiety mainly through alkylation reactions. However, these methodologies suffer from poor yields, the use of volatile and polluting solvents, highly toxic chemicals (*e.g.* diethyl oxalacetate for the triazole formation and dimethyl sulphate for the subsequent amide methylation step) and require the preparation of the appropriate starting compounds (*e.g.* the diamine or ethyl benzoyl- and 2-furoyl pyruvate sodium salts) (Biagi et al., 2002).

In 2012, Cai and Ding explored a strategy for the synthesis of [1,2,3]-triazolo [1,5-*a*]quinoxalin-4(5*H*)-ones starting from *N*-(2-iodophenyl)propiolamides, following a tandem azide-alkyne cycloaddition/Ullmann C-N coupling process. The exploration of the scope through the use of different alkyl and aryl substituents on the alkyne moieties (R_2) as well as electron-donating and -withdrawing substituents (R_1) on the 1-(2-iodoaryl) ring

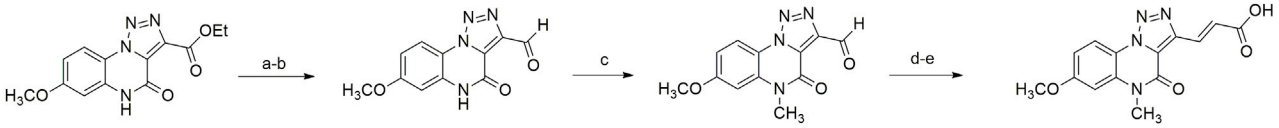

SCHEME 2
Previously reported approach for [1,2,3]-triazolo [1,5-*a*] quinoxalin-4(5*H*)-one derivatization. [a]Reaction and conditions: **(A)** $LiBH_4$, THF, 65°C; **(B)** Dess Martin reagent, CH_2Cl_2, rt, 84% over two steps; **(C)** MeI, K_2CO_3, DMF, 80°C, 15%; **(D)** $MeO_2CCH_2P(O)(OMe)_2$, *n*-BuLi, THF, 0°C to rt; **(E)** LiOH, THF/MeOH/H_2O, rt, 81% over two steps.

(Scheme 1C). However, these linear approaches are generally not convenient for scaffold diversification; moreover, no further functionalization steps were carried out on the amide functionality in the same paper (Yan et al., 2012).

Very recently, Li and coworkers reported a photoredox-catalyzed [3 + 2] cyclization reaction for the synthesis of [1,2,3]-triazolo-[1,5-*a*]quinoxalin-4(5*H*)-ones through quinoxalinones and hypervalent iodine (III) reagents, thus witnessing the renewed interest for innovative synthetic procedures towards this scaffold (Wen et al., 2022). Despite the simple proposed strategy for the preparation of 1*H*-quinoxalinones, starting from *o*-phenylenediamine and ethyl 2-oxoacetate and the subsequent alkylation with halogenoalkanes in DMF as solvent, it is important to highlight that the disclosed protocol required the preparation of the α-aryliodonio diazo compounds starting from ethyl diazoacetate (EDA) and bis(onio)-substituted aryliodine (III) salts or (diacetoxyiodo) benzene (Weiss et al., 1994; Xu et al., 2021). Furthermore, this method displays several drawbacks, lacking variability of substitutions on the triazoloquinoxaline scaffold, only reporting halo/methyl substitutions on the phenyl ring and envisaging the use of DMF and DCE as solvents. In addition, *N*-free quinoxalinone could not promote the reaction to generate the desirable product, making necessary the upstream *N*-alkylation step, thus affecting protocol versatility and product diversification (Scheme 1D).

Only few examples of direct derivatization of the triazole esters have been previously reported, probably due to the low solubility of the deriving carboxylic acids and lengthy purification steps required; among them, it is reported conversion into aldehyde, without isolation of the alcohol intermediate and providing a long chain connected to the triazole ring with multiple synthetic steps using toxic reagents [9] (Scheme 2) (HongShen et al., 2009).

For these reasons, the development of new methodologies for an easy access to this heterocyclic scaffold in a sustainable guise would be a nice and useful add-on to the currently limited armamentarium. As reported before, compared to the previous syntheses, we reasoned to plan a new ecofriendly methodology able to rejuvenate the chemical path toward [1, 2, 3]-triazolo [1,5-a] quinoxalin-4(5*H*)-one in a green and sustainable declination exploring for the first time on this scaffold a catalytic direct amidation and demonstrating the scope through the use of aliphatic, benzylic and aromatic amines. During our investigation, we used eco-sustainable reagents and catalysts for all the synthetic steps, performing reactions, whenever possible, through neat conditions, avoiding the hydrolysis of the esters and the pre-activation of the carboxylic acid with coupling agents and, thus, improving both yields and total atom economy of the synthesis (Scheme 3).

2 Results and discussion

2.1 Chemistry

In order to perform our 1,2,3-triazoloquinoxaline synthesis in a green declination and to expand the final library with focused structural modifications, our devised protocol started from in-house synthesized (through a sustainable Suzuki coupling protocol) (**2a-b**) or commercially available (**2c-i**) substituted 2-nitro anilines. Anilines were then converted into their corresponding 2-nitro azides (**3a-i**) using *tert*-butyl nitrite and trimethyl silyl azide that, compared to the reported procedures using sodium nitrite and sodium azide, could be considered as non-toxic and inert reagents (Barral et al., 2007) (Scheme 3). The resulting azides were then engaged in the click reaction with dimethyl acetylene dicarboxylate as the alkyne, without the need of catalysts or halogenated solvents providing the corresponding dimethyl carboxylate triazoles (**4a-i**) and avoiding the formation of previously described byproducts when using diethyl oxalacetate, ethyl benzoyl pyruvate and ethyl 2-furoyl pyruvate sodium salts. It is worth of note that for the generation of 1,4,5-trisubstituted 1,2,3-triazole moieties, only 2 references for the click reaction of 2-nitrophenyl azides and dimethyl acetylenedicarboxylate have been reported in literature, using copper nanoparticles immobilized on silk fibroin (Mirzaei et al., 2021) or regular stirring and microwave irradiation in dichloromethane (Souad et al., 2011). A relevant part of this project was then devoted to the exploration of different eco-compatible reaction conditions, using 2-nitrophenyl azide and dimethyl acetylene dicarboxylate as the starting materials in combination with different solvents, ionic liquids and catalysts, and also through the use of microwave and ultrasound bath (Table 1). When the reaction was performed in acetonitrile/water using copper sulphate and sodium ascorbate in order to generate Cu(I) required for the azyde/alkyne cycloaddition (Table 1, entry 1) a disappointing 4% yield of the desired compound was obtained. We then sought to explore ethanol both in the presence or not of Cu(I) (Table 1, entries 2 and 3), thus obtaining the triazole derivative in 44% and 40% yields, respectively. A further investigation using acetonitrile (Table 1, entry 4) and 2-Me-THF (Table 1, entry 5) for 12 h at reflux temperature, provided the desired compound in 28% and 61% yield, respectively. Surprisingly, when performed using 2-Me-THF as green solvent (Table 1, entry 6) under microwave condition, the reaction yield dropped to 17%. Also, the use of a ionic liquid as BMIM PF_6 did not bring significant benefits, leading to the desired compound in 36% yield (Table 1, entry 7). We then sought to investigate the neat reaction conditions

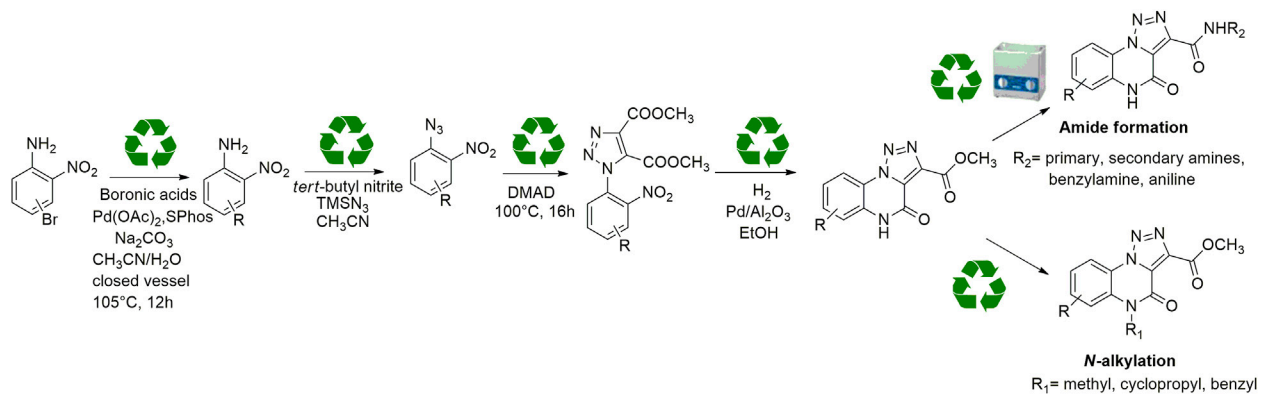

SCHEME 3
General scheme for the newly conceived sustainable approach for the synthesis and derivatization of [1,2,3]-triazolo [1,5-a] quinoxalin-4(5*H*)-ones.

TABLE 1 Optimization of reaction conditions for triazoles synthesis.

Entry	DMAD (eq)	Solvent	Catalyst	Temperature	Yield
1	1 eq	CH_3CN/H_2O (0.24M)10:1	$CuSO_4$/sodium ascorbate	Rt	4%
2	1 eq	EtOH (0.2M)	-	reflux	44%
3	1 eq	EtOH (0.2M)	CuI 5% mol	reflux	40%
4	1 eq	CH_3CN (0.2M)	-	reflux	28%
5	1 eq	2-Me-THF	-	reflux	61%
6	1 eq	2-Me-THF	-	MW; 100°C, 300W	17%
7	2 eq	0.25 eq BMIM PF_6	-	MW; 100°C, 300W	36%
8	2 eq	neat	-	MW; 100°C, 300W	52%
9	2 eq	neat	-	MW; 120°C, 300W	54%
10	2 eq	neat	-	100°C	80%
11	2 eq	neat	-	ultrasound, rt	traces
12	2 eq	neat	-	ultrasound, 50 °C	traces

using microwave irradiation (entries 8 and 9), oil bath traditional heating (entry 10) and ultrasound bath (entries 11 and 12), monitoring the reaction through TLC. We found the best conditions driving a neat reaction at 100°C for 16 h (entry 10) with 80% yield.

Once optimized the reaction conditions for the cycloaddition step, we then explored the reaction scope through the synthesis of differently substituted 1-aryl 1,2,3-triazole derivatives, bearing electron withdrawing, donating and biphenyl groups, with yields ranging from 40% to 98% (Table 2). Interestingly, only few of the synthesized triazoles were reported in literature, in lower yields when compared to our protocol; most of them were not previously described, highlighting the importance of this procedure also for the effective aryl triazole moiety generation.

Synthesized triazoles were then converted into the corresponding [1,2,3]-triazolo [1,5-*a*]quinoxalin-4(5*H*)-ones (**5a-e**) through nitro group reduction and following spontaneous cyclization, using hydrogen gas generator that produces hydrogen in a safe and convenient way, through electrolysis of water with a sustainable palladium on alumina catalyst 5% wt (Scheme 4). Reaction scope was also investigated, exploring different substituents on the phenyl ring, thus generating [1,2,3]-triazolo [1,5-*a*] quinoxalin-4(5*H*)-ones **5a-e**. As expected, when submitted to these reaction conditions, triazoles **4f, g, h**, only provided their de-halogenated counterpart **5c** (Table 3).

With our [1,2,3]-triazolo [1,5-*a*] quinoxalin-4(5*H*)-ones in hand, we started our campaign for its sustainable derivatization. First of all, we performed a simple alkaline hydrolysis of the ester group of compound **5c** with sodium hydroxide in a mixture of methanol and water, which provided the corresponding carboxylic acid derivative **6** (Scheme 5).

Regarding the *N*-methylation step for the [1,2,3]-triazolo [1,5-*a*] quinoxalin-4(5*H*)-one scaffold, the reported protocol encompassed the use of dimethyl sulfate and iodomethane as methylating agents,

TABLE 2 1,2,4-Triazoles formation scope using optimized conditions.

Cmp	Triazoles	Yield (%)
4a	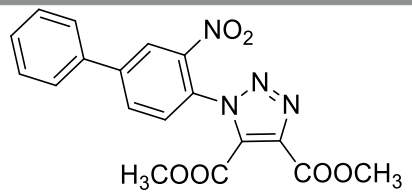	84
4b	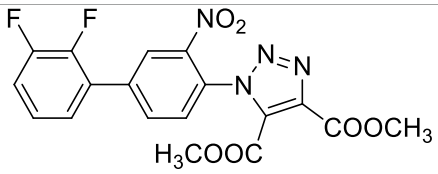	65
4c	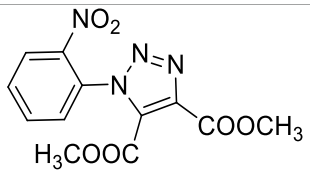	80[15]
4d	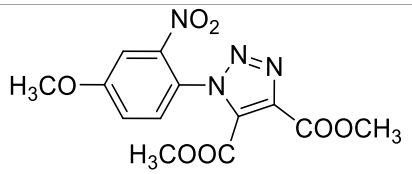	98
4e	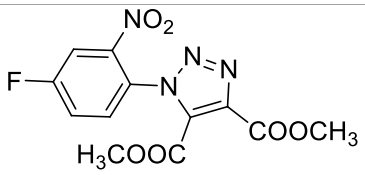	89
4f	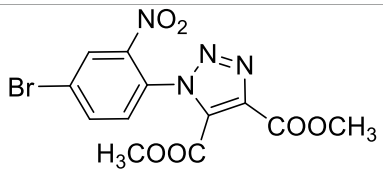	66
4g	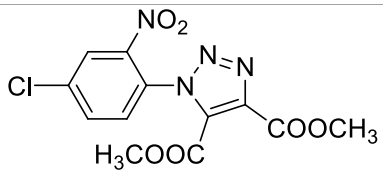	51
4h	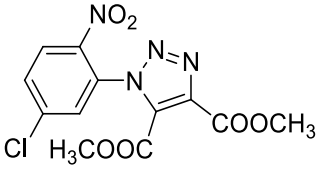	50

(Continued in next column)

TABLE 2 (*Continued*) 1,2,4-Triazoles formation scope using optimized conditions.

Cmp	Triazoles	Yield (%)
4i	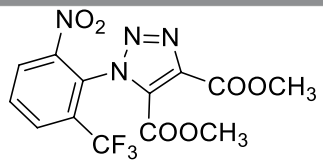	40

obtaining the *N*-methylated derivative with yields of 64% and 15%, respectively [13]. In our quest for a more sustainable protocol, we decided to carry on compound **5c** using the greener dimethyl carbonate, taking advantage of its dual role as both solvent and electrophilic reagent (Fiorani et al., 2018), and potassium carbonate as the base in a closed vessel at 140 °C for 12 h. This protocol allowed to obtain derivative **7** with a satisfying 78% yield (Scheme 5).

We then shifted to interrogate a benzyl substitution on the endocyclic amide nitrogen. After a small investigation of reaction conditions, we carried out the reaction in the presence of benzyl bromide and potassium carbonate, using cyclopentyl methyl ether (CPME), a versatile eco-friendly solvent with high boiling point and a low peroxide formation rate (Watanabe et al., 2007), thus almost quantitatively obtaining the desired compound **9** with only traces of the disubstituted derivative **8** (Scheme 5). Noteworthy, the same reaction carried out using dimethylformamide as the solvent, gave the *N*-benzylated compound **9** in 34% yield due to the concomitant formation of higher amounts of the disubstituted counterpart **8** (40% yield).

Likewise, compound **10** was obtained using cyclopropyl methyl bromide and potassium carbonate in CPME (Scheme 5).

Our further efforts were devoted to the functionalization of the ester moiety on the 1,2,3-triazole ring. To this aim, we explored an unprecedented direct amidation reaction on this scaffold (Scheme 5 and Table 3). For this protocol, we first treated compound **5c** with benzylamine using toluene as the solvent. The reaction proceeded quantitatively both in absence (Table 3, entry 1) and in the presence of sustainable amidation catalysts such as dichlorobis (cyclopentadienyl)zirconium (Cp_2ZrCl_2) (Table 3, entry 2) and calcium iodide (Table 3, entry 3). Gratifyingly, the reaction provided a quantitative outcome even under neat conditions at room temperature (Table 1, entry 4). Finally, we found the best condition by direct irradiation with an ultrasound bath for 15 min without any catalyst (Table 3, entry 5) and we applied the same conditions to both an aliphatic primary amine (cyclohexylamine, Table 3, entry 6) and a secondary amine (pyrrolidine, Table 3, entry 7) obtaining quantitative conversions for all the starting materials, thus confirming the broad scope of this amidation protocol. However, when trying to extend the procedure to anilines we did not observe product formation (Table 3, entry 8). Our previous results with eco-sustainable catalysts prompted us to test the coupling with aniline using calcium iodide (Table 3, entry 9) and Cp_2ZrCl_2 dichlorobis (cyclopentadienyl) zirconium (Table 3, entry 10) in toluene at 110°C overnight. Only when using Cp_2ZrCl_2 as the

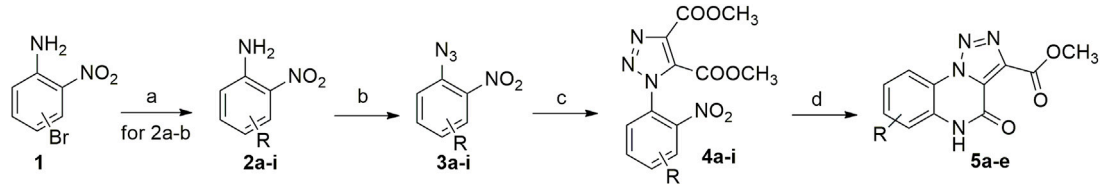

SCHEME 4
Eco-sustainable syntheses of triazoloquinoxalines. [a]Reagents and conditions: **(A)** boronic acids, $Pd(OAc)_2$, SPhos, Na_2CO_3, CH_3CN/H_2O (0.30 M; 3:1), 105°C; **(B)** *tert*-butyl nitrite, $TMSN_3$, CH_3CN, rt; **(C)** Dimethyl acetylenedicarboxylate; **(D)** H_2, 5% loading Pd/Al_2O_3, rt.

TABLE 3 Optimized conditions for the direct amidation of methyl 4-oxo-4,5-dihydro [1,2,3]triazolo [1,5-*a*]quinoxaline-3-carboxylate.

Entry	Amine	Solvent	Catalyst	Temperature/time	Yield
1	Benzylamine (1.3 eq)	Toluene	-	110°C, 12 h	quantitative
2	Benzylamine (1.3 eq)	Toluene	Cp_2ZrCl_2 10% mol	110°C, 12 h	quantitative
3	Benzylamine (1.3 eq)	Toluene	CaI_2 10% mol	110 °C, 12 h	quantitative
4	Benzylamine (2.6 eq)	-	-	rt, 2 h	quantitative
5	Benzylamine (2.6 eq)	-	-	Ultrasound, 15′	quantitative
6	Cyclohexylamine (2.6 eq)	-	-	Ultrasound, 15′	97%
7	Pyrrolidine (2.6 eq)	-	-	Ultrasound, 15′	99%
8	Aniline (2.6 eq)	-	-	Ultrasound, 15′	Nd
9	Aniline (1.3 eq)	Toluene (4 M)	CaI_2	110 °C, 12 h	traces
10	Aniline (1.3 eq)	Toluene (4 M)	Cp_2ZrCl_2 10% mol	110 °C, 12 h	80%
11	Aniline (1.3 eq)	CPME	Cp_2ZrCl_2 10% mol	110 °C, 12 h	81%

catalyst, we were able to obtain the desired benzamide in 80% yield (Table 3, entry 10). Gratifyingly, replacement of toluene with CPME, was successful for the conversion into amide with a sustainable protocol (Table 3, entry 11) and in 81% yield.

The full library of 20 derivatives synthesized within this study is reported in Table 4.

2.2 Biological evaluation as antimicrobial agents

According to previous reports highlighting antibacterial properties for some triazoloquinoxalinone derivatives, we decided to perform a preliminary biological investigation for evaluating the antimicrobial potential in multiple bacterial and fungal species of our newly synthesized derivatives. Polymicrobial infections, caused by a simultaneous infection of viruses, bacteria, fungi, and parasites, represent an emerging and quickly increasing phenomenon, due to the possibility of one pathogen to predispose the host to colonization by other pathogens. These infections are more tolerant to antibiotic therapy, thus rendering necessary the search for broad-spectrum antimicrobials, which would display several advantages with respect to a therapy with multiple antibiotics. Another relevant issue to be taken into account when dealing with polymicrobial infections is the biofilm formation, which can be reasonably considered as a resistance mechanism adopted by some bacterial species, able to generate a self-produced extracellular polymeric substance (EPS) to form a matrix. Biofilm provides a survival strategy and protection against antibiotics, acting as a reservoir for the cellular exchange of plasmids encoding for resistance to antibiotics. In this context, the discovery of new compounds able to counteract both Gram-positive and Gram-negative bacteria or yeasts, while reducing at the same time biofilm formation, is of crucial importance.

To assess the antimicrobial properties of compounds **5a**, **5d**, **5e**, **6-9**, **11-18**, and **20**, the minimal inhibitory concentrations (MIC) were determined by broth microdilution assay. The assay was preliminarily performed against different pathogenic bacteria strains to verify if the compounds were able to inhibit cell growth. The examined strains were two Gram-positive, *S. aureus* ATCC 29213 and *S. aureus* ATCC 43300 (MRSA), and three Gram-negative, *P. aeruginosa* ATCC 27853, *K. pneumoniae* ATCC 13883, and *K. pneumonia* ATCC BAA-1705. The antibiotics OXA, VAN, TOB, and IPM were used as a control against *S. aureus*, *P. aeruginosa*, and *K. pneumoniae*, according to European Committee on Antimicrobial Susceptibility Testing (EUCAST version 12.0, 2022). As reported in Figures 1, 2 none of the compounds was able to produce a MIC value at the tested concentrations (up to 100 μM). However, three compounds were able to slightly affect the growth of the microorganisms studied. Compounds **9** (SL69) and **20** (QNX55) were able to reduce the

10.3389/fchem.2023.1126427

TABLE 4 Full library of synthesized [1,2,3]-triazolo [1,5-a] quinoxalin-4(5*H*)-ones within this work.

Cmp	[1,2,3]-triazolo [1,5-a] quinoxalin-4(5*H*)-ones	Yield
5a	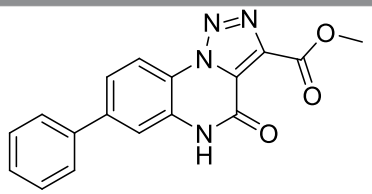	20%
5b	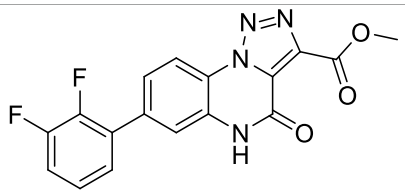	27%
5c	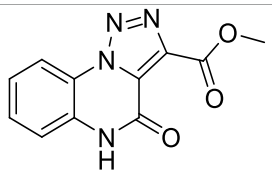	65%
5d	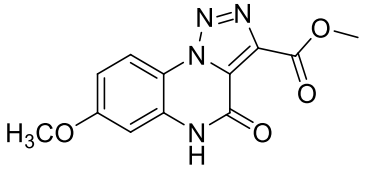	56%
5e	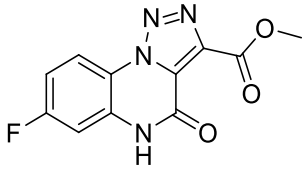	35%
6	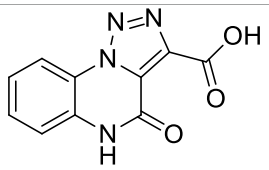	quantitative
7	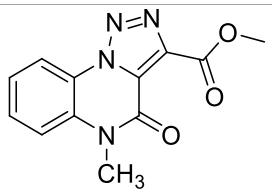	78%
8	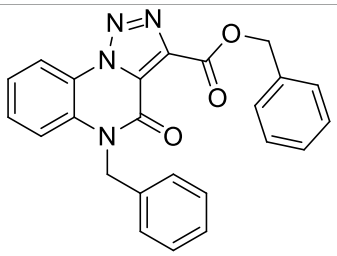	traces

(Continued on following page)

TABLE 4 (*Continued*) **Full library of synthesized [1,2,3]-triazolo [1,5-a] quinoxalin-4(5*H*)-ones within this work.**

Cmp	[1,2,3]-triazolo [1,5-a] quinoxalin-4(5*H*)-ones	Yield
9	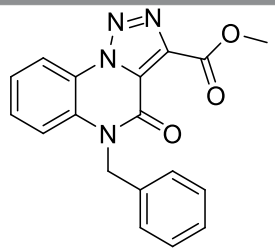	quantitative
10	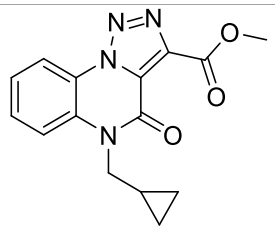	86%
11	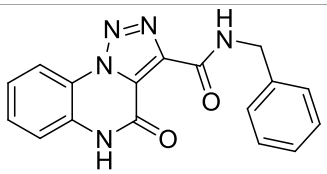	quantitative
12	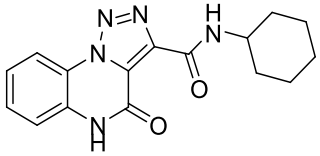	97%
13	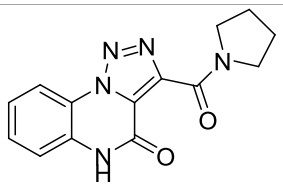	99%
14	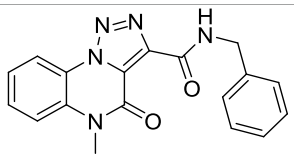	94%
15	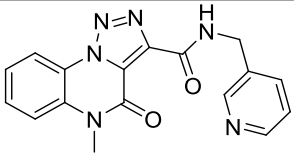	95%

(Continued on following page)

TABLE 4 (*Continued*) **Full library of synthesized [1,2,3]-triazolo [1,5-a] quinoxalin-4(5*H*)-ones within this work.**

Cmp	[1,2,3]-triazolo [1,5-a] quinoxalin-4(5*H*)-ones	Yield
16	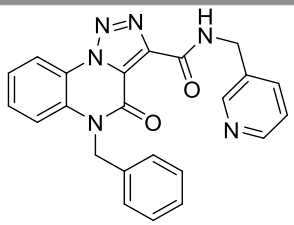	96%
17	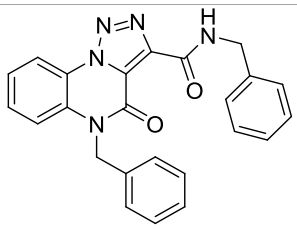	quantitative
18	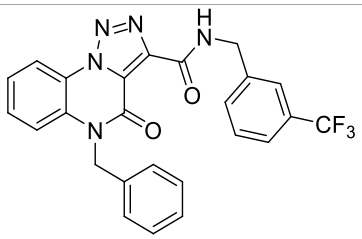	89%
19	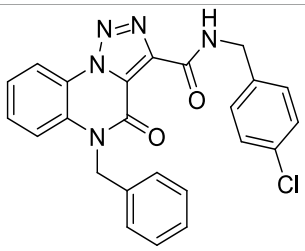	93%
20	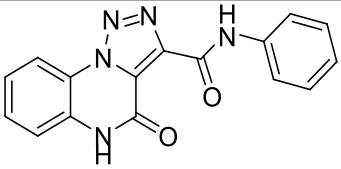	81%

growth of both *S. aureus* ATCC strains at the highest concentration with a percentage of reduction ranging between 15%-18% (Figures 1A, B). Compound **14** (SL66) was able to reduce by 22% also the growth of *S. aureus* ATCC 29213. The same compounds **9**, **14** and **20** (SL66, SL69, QNX55) were able to affect the growth of *P. aeruginosa* (Figure 2), but not *K. pneumoniae* (data not shown). The best activity was observed with compound **14** (SL66), able to cause about a 23% reduction in *P. aeruginosa* cell growth.

The compounds showing the best results in the antimicrobial assay were also tested for their antifungal properties against the yeast *C. albicans*. Among the three compounds, only compound **9** (SL69) was able to contrast the growth of both strains of *C. albicans*, the control strain and the azole-resistant one (Figures 3A, B).

Finally, we tested the activity of derivatives **9**, **14** and **20** (L66, SL69, and QNX55) to affect the growth of *S. epidermidis* ATCC 35984 and to contrast its ability to form biofilm (Vollaro et al., 2019; Alfano et al., 2021). As shown in Figure 4A only compound **7** (SL69) slightly affected the growth of *S. epidermidis* at the highest concentration (100 μM), while at 50 μM we did not observe cell growth inhibition. Consequently, since 50 μM compound **9**, **14** and **20** (SL66, SL69, and QNX55) did not produce a bacteriostatic effect the latter was chosen as the

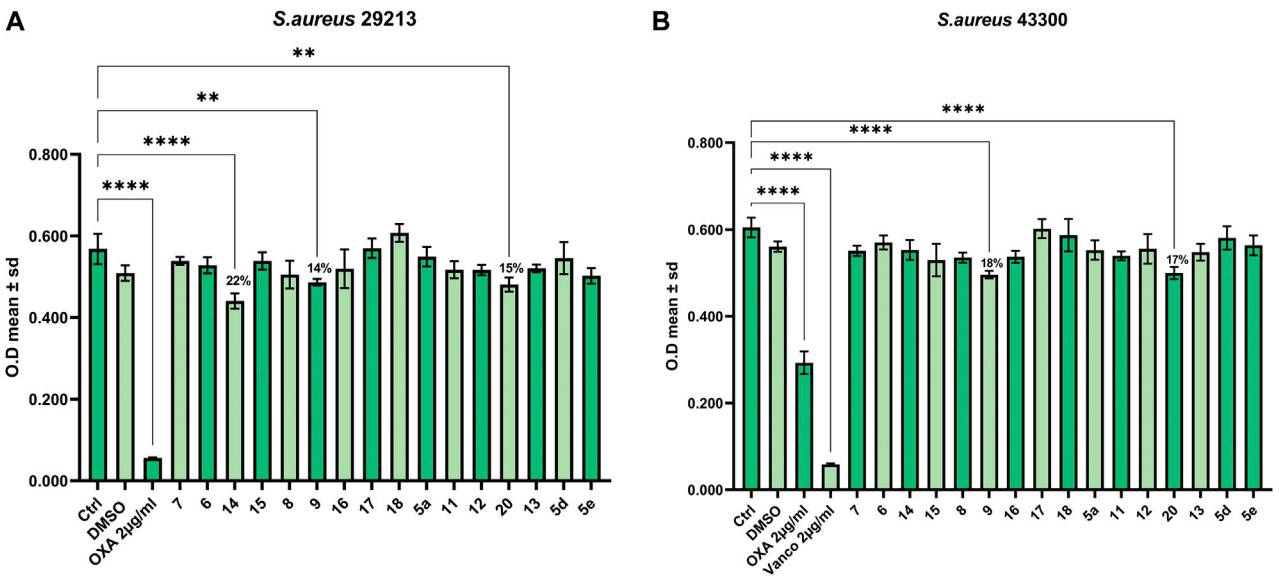

FIGURE 1
Antibacterial effect against Gram-positive **(A)** *S. aureus* ATCC 29213 and **(B)** *S. aureus* ATCC 43300.

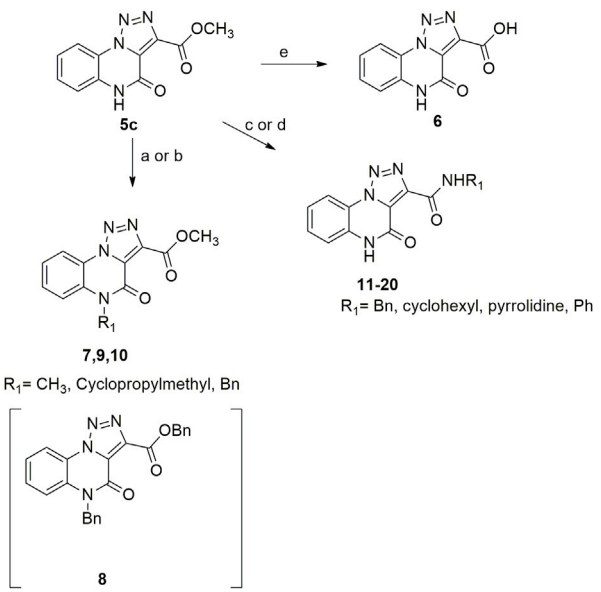

SCHEME 5
Hydrolysis, *N*- derivatization and direct amidation of [1,2,3]-triazolo [1,5-*a*]quinoxalin-4(5*H*)-one scaffold. [a]Reagents and conditions: **(A)** dimethyl carbonate, K_2CO_3, closed vessel, 140°C, 16 h; **(B)** benzyl bromide or cyclopropyl methyl bromide, K_2CO_3, cyclopentylmethylether (0.1 M), 115°C, reflux, 12 h; **(C)** cyclohexylamine, pyrrolidine or benzyl amines, ultrasound bath, rt, 15′; **(D)** aniline, cyclopentylmethylether (4M), Cp_2ZrCl_2 10 mol%, 110°C, 12 h; **(E)** NaOH, MeOH/H_2O (0.25 M, 3:1), 1.5 h.

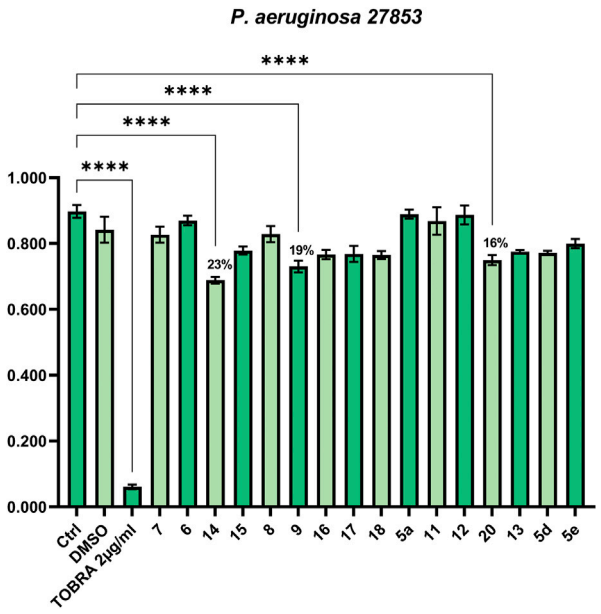

FIGURE 2
Antibacterial effect against Gram-negative *P. aeruginosa* 27853.

concentration useful to perform the biofilm assay. As reported in Figure 4B, compounds **9** and **14** (SL66 and SL69) were both able to contrast the biofilm formation by 18% and 23%, respectively.

The results here obtained are encouraging since three out of 16 compounds displayed a limited antimicrobial property, but compound **9** (SL69) reduced the growth of different bacterial strains and the yeast *Candida*, also affecting biofilm formation in *S. epidermidis*. Taken together, these data foster further optimization of the compounds and the synthetic protocol herein developed guarantees straightforward and sustainable scaffold morphing and derivatization.

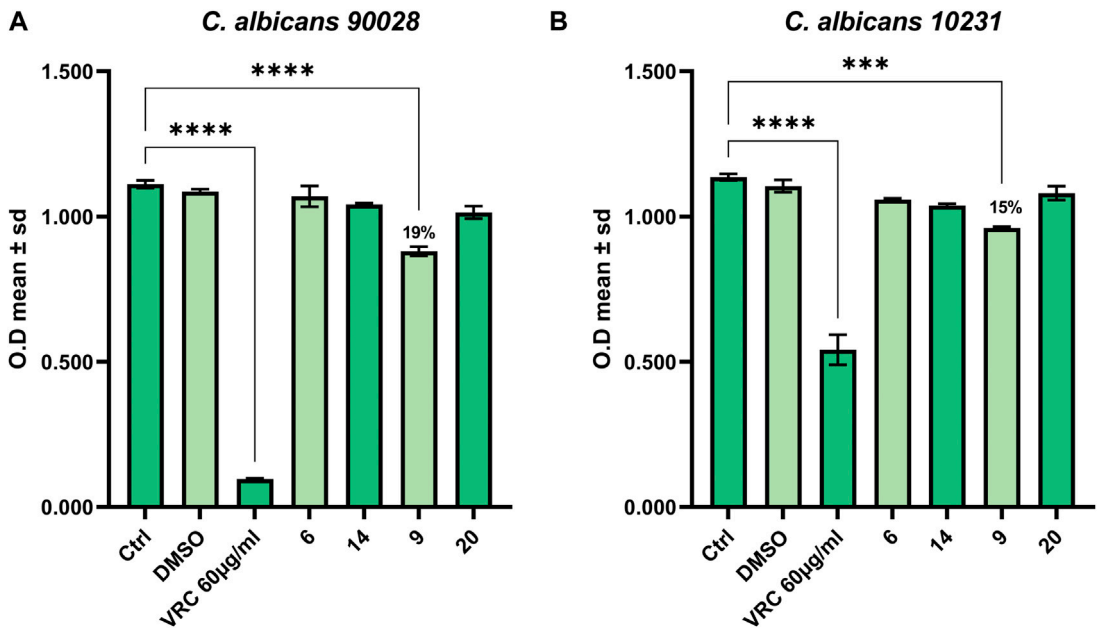

FIGURE 3
Antifungal activity against **(A)** *C. albicans* 90028 and **(B)** *C. albicans* azole-resistant 10231.

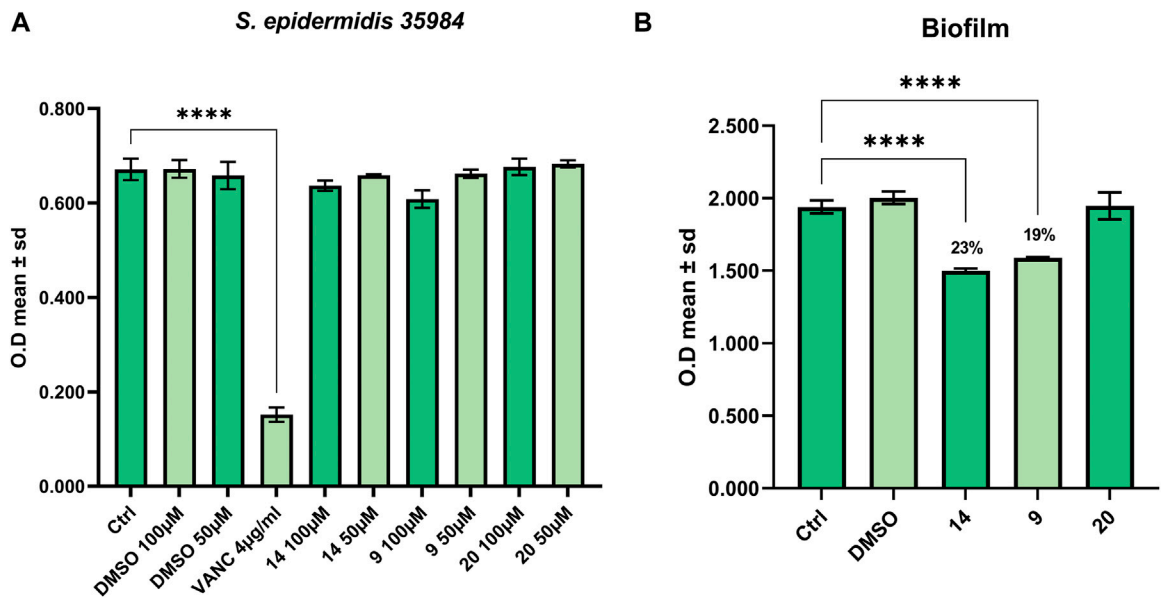

FIGURE 4
Antibacterial activity against **(A)** S. *Epidermidis* 35984 and **(B)** inhibition of biofilm formation.

3 Materials and methods

3.1 Chemistry

3.1.1 General methods

Commercially available reagents and solvents were used without further purification. When necessary, the reactions were performed in oven-dried glassware under a positive pressure of dry nitrogen. Melting points were determined in open glass capillaries and are uncorrected. All the compounds were characterized by ^{1}H and ^{13}C APT NMR that were recorded at a Bruker Avance NEO instruments (400 and 700 MHz). Mass spectra of final products were performed on LTQ Orbitrap XL™Fourier transform mass spectrometer (FTMS) equipped with an ESI ION MAX™ (Thermo Fisher, San

José, USA) source operating in positive mode. The spectra were recorded by infusion into the ESI source using MeOH as the solvent. Chemical shifts (δ) are reported in part per million (ppm) relative to the residual solvent peak. Column chromatography was performed on silica gel (70–230 mesh ASTM) using the reported eluents. Thin layer chromatography (TLC) was carried out on 5 × 20 cm plates with a layer thickness of 0.25 mm (Silica gel 60 F254). The purity of all compounds was confirmed by NMR and analytic HPLC-UV as ε 92%-95%.

3.1.2 General preparation of substituted anilines

A microwave vial was charged under argon with the corresponding halo-derivative (0.92 mmol), the corresponding phenylboronic acid (1.2 equiv.), $Pd(OAc)_2$ (10% mol), Sphos (20%mol) Na_2CO_3 (3.0 equiv.) and a mixture of acetonitrile: water (0.30M; 2:1). The vial was capped properly, flushed with argon and heated to 105 °C until complete conversion of the starting material. After it was cooled, the reaction mixture was concentrated under vacuum. The crude residue was diluted in water. The organic phase was extracted 3 times with EtOAc. The organic layers were combined, washed with brine, dried over Na_2SO_4, filtered, concentrated and purified by silica gel chromatography column, eluting with the appropriate *n*-hexane: ethylacetate mixture.

3-Nitrobiphenyl-4-amine (2a). The crude material was purified by column chromatography (*n*-hexane/EtOAc 80:20) to give the product as a red-brown crystals (172 mg, 87% yield).

^{1}H NMR (DMSO-d_6, 400 MHz): δ 8.22 (s, 1H), δ 7.79 (d, *J* = 8.8 Hz, 1H), δ 7.63 (d, *J* = 8 Hz, 2H), δ 7.54 (s, 2H), δ 7.44 (t, *J* = 7.6 Hz, 2H), δ 7.33 (t, *J* = 7.2 Hz, 1H), δ 7.13 (d, *J* = 8.8 Hz, 1H). ^{13}C APT (DMSO-d_6; 176 MHz): δ 146.01, 138.74, 134,73, 130.91, 129.48, 127.83, 127.50, 126.23, 122,84,120.49.

2′,3′-Difluoro-3-nitrobiphenyl-4-amine (2b). ^{1}H NMR (DMSO-d_6, 400 MHz): δ 8.18 (s, 1H), δ 7.67-7.64 (m, 3H), δ 7.43-7.36 (m, 2H), δ 7.31-7.25 (m, 1H), δ 7.14 (d, *J* = 9.2 Hz, 1H). ^{13}C APT (DMSO-d_6; 176 MHz): δ 151.4, 150.1, 148.2, 146,8, 146.42, 136.30, 130.54, 129.18, 125.8, 125.6, 125.5, 121.16, 120.22, 116.6.

3.1.3 General preparation of azides

4-Azido-3-nitrobiphenyl (3a). The crude material was purified by column chromatography (*n*-hexane/EtOAc 98:1) to give the product as an orange solid (97% yield).

^{1}H NMR ($CDCl_3$, 400 MHz): δ 8.1 (s, 1H), δ 7.76 (d, *J* = 8.8 Hz, 1H), δ 7.51 (d, *J* = 8.0 Hz, 2H), δ 7.41 (t, *J* = 7.6 Hz, 2H) δ, 7.37-7.32 (m, 2H). ^{13}C APT ($CDCl_3$; 176 MHz): δ 138.52, 137.69, 133.54, 132. 28, 129.26, 128.61, 126.85, 124.37, 121.26.

4′-Azido-2,3-difluoro-3′-nitrobiphenyl (3b). The crude material was purified by column chromatography (*n*-hexane/EtOAc 98:1) to give the product as an orange solid (90% yield). ^{1}HNMR ($CDCl_3$, 400 MHz): δ 8.06 (s, 1H), δ 7.74 (d, *J* = 8.4 Hz, 1H) δ,7.36 (d, *J* = 8.4 Hz, 1H), δ 7.17-7.13 (m, 3H). ^{13}C APT ($CDCl_3$; 176 MHz): δ 151.89, 150.46, 148.76, 147.25, 140.86, 134.59, 134.26, 131.77, 127.85, 126.31, 124.78, 121.07, 118.19, 117.49.

1-Azido-2-nitrobenzene (3c). 2-Nitroaniline (280 mg, 2.02 mmol) was dissolved in acetonitrile (4 ml) in a 25 ml round-bottomed flask and cooled to 0°C in an ice bath. *t*-BuONO (312 mg, 360 μL, 3.03 mmol) was then added followed by $TMSN_3$ (279 mg, 322 μL, 2.42 mmol) dropwise. The resulting solution was stirred at room temperature for 1 h. The reaction mixture was concentrated under vacuum and the crude product was purified by silica gel chromatography (*n*-hexane) to give the product, as a pale yellow solid (327 mg, 98%).

^{1}H NMR ($CDCl_3$, 400 MHz): δ 7.87 (d, *J* = 8.0 Hz, 1H), δ 7.55 (t, *J* = 8.0 Hz, 1H), δ 7.27 (d, *J* = 8.8 Hz, 1H), δ 7.19 (t, *J* = 8.4, 1H). ^{13}C APT ($CDCl_3$; 176 MHz): δ 140.92, 134.84, 126.13, 124.93, 120.79.

1-Azido-4-methoxy-2-nitrobenzene (3d). The crude material was purified by column chromatography (*n*-hexane/EtOAc 98:2) to give the product as a yellow solid (265 mg, 82% yield). ^{1}H NMR ($CDCl_3$, 400 MHz): δ 7.39 (s, 1H), δ 7.17 (d, 1H, *J* = 8.8 Hz), δ 7.12-7.09 (m, 1H), δ 3.79 (s, 3H). ^{13}C APT ($CDCl_3$; 176 MHz): δ 156.49, 141.11, 127.22, 121.95, 121.26, 110.14, 56.12.

1-Azido-4-fluoro-2-nitrobenzene (3e). The crude material was purified by column chromatography (*n*-hexane/EtOAc 98:1) to give the product as an orange oil (269 mg, 89% yield).

^{1}H NMR ($CDCl_3$, 400 MHz): δ 7.64-7.62 (m, 1H), δ 7.32-7.23 (m, 2H). ^{13}C APT ($CDCl_3$; 176 MHz): δ 159.07, 157.65, 131.06, 122.32, 121.68/121.55, 113.66/113.50.

1-Azido-4-bromo-2-nitrobenzene (3f). The crude material was purified by column chromatography (*n*-hexane/EtOAc 99:1) to give the product as a yellow solid (360 mg, 89% yield).

^{1}H NMR ($CDCl_3$, 400 MHz): δ 8.01 (s, 1H), δ 7.65 (d, *J* = 8.4 Hz, 1H), δ 7.15 (d, *J* = 8.8 Hz, 1H).

^{13}C APT ($CDCl_3$; 176 MHz): δ 141.08, 136.91, 134.05, 128.96, 122.20, 117.15.

1-Azido-4-chloro-2-nitrobenzene (3g). The crude material was purified by column chromatography (*n*-hexane/EtOAc 98:1) to give the product as a yellow solid (96% yield).

^{1}H NMR ($CDCl_3$, 400 MHz): δ 7.97 (s, 1H),7.61 (d, *J* = 8.4, 1H), δ 7.30 (d, *J* = 8.4 Hz, 1H). ^{13}C APT ($CDCl_3$; 176 MHz): δ 134.04, 133.54, 130.30, 126.14, 121.95.

2-Azido-4-chloro-1-nitrobenzene (3h). The crude material was purified by column chromatography (*n*-hexane/EtOAc 98:1) to give the product as a yellow solid (94% yield).

^{1}H NMR ($CDCl_3$, 400 MHz): δ 7.95 (d, *J* = 8.8 Hz, 1H), δ 7.34 (s, 1H), δ 7.25 (d, *J* = 8.8, 1H). ^{13}C APT ($CDCl_3$; 176 MHz): δ 140.42, 136.40, 127.45, 125.19, 120.89.

3.1.4 General preparation of triazoles

Dimethyl 1-(3-nitrobiphenyl-4-yl)-1*H*-1,2,3-triazole- 4, 5-dicarboxylate (4a).

^{1}H NMR ($CDCl_3$, 400 MHz): δ 8.42 (s, 1H), δ 7.96 (d, *J* = 8.0 Hz, 1H), δ 7.62-7.56 (m, 3H), δ 7.50-7.42 (m, 3H), δ 3.97 (s, 3H), δ 3.81 (s, 3H). ^{13}C APT ($CDCl_3$; 176 MHz): δ 160.07, 158.10, 145.70, 144.57, 139.81, 137.02, 132.26, 132.03, 130.23, 129.59, 129.49, 127.89, 127.30, 124.14, 53.68, 53.00.

Dimethyl 1-(2′, 3′-difluoro-3-nitrobiphenyl-4-yl)-1*H*-1, 2, 3-triazole-4, 5-dicarboxylate (4b). Sticky solid, 65% yield. ^{1}H NMR ($CDCl_3$, 400 MHz): δ 8.40-8.39 (m, 1H), δ 7.97-7.94 (m, 1H), δ 7.61 (d, *J* = 8.0 Hz, 1H), δ 7.27-7.21 (m, 3H), δ 3.98 (s, 3H), δ 3.82 (s, 3H). ^{13}C APT ($CDCl_3$; 176 MHz): δ 160.01, 158.03, 151.92 (151.85), 150.50 (150.43), 148.83 (148.75), 147.40 (147.32), 144.39, 139.89, 139.10, 134.42, 131.95, 130.13, 128.79, 127.22 (127.17), 126.06 (126.05), 125.10 (125.07,125.02, 125.00), 118.61, 118.52, 53.72, 53.04.

Dimethyl 1-(2-nitrophenyl)-1*H*-1,2,3-triazole-4,5-dicarboxylate (4c). Dimethyl acetylene dicarboxylate (2 equivalents) was then added to the 1-azido-2-nitrobenzene and the reaction was stirred 12 h at 85°C. The product was obtained after silica gel chromatography column (7:3 *n*-hexane/Ethyl acetate). ^{1}H NMR ($CDCl_3$, 400 MHz): δ 8.24 (d, *J* = 7.6 Hz, 1H), δ 7.82-7.72 (m, 2H), δ 7.52 (d, *J* = 7.6 Hz, 1H), δ 3.97 (s, 3H), δ 3.78 (s, 3H). ^{13}C APT ($CDCl_3$; 176 MHz): δ 160.04, 157.96, 144.37, 139.80, 134.37, 132.15, 131.98, 129.91, 129.43, 125.86, 53.63, 52.99.

Dimethyl 1-(4-methoxy-2-nitrophenyl)-1*H*-1,2,3-triazole-4,5-dicarboxylate (4d).

^{1}H NMR ($CDCl_3$, 400 MHz): δ 7.70 (s, 1H), δ 7.41 (d, *J* = 8.8 Hz, 1H), δ 7.24-7.21 (m, 1H), δ 3.96 (s, 3H), δ 3.91 (s, 3H), δ 3.78 (s, 3H). ^{13}C APT ($CDCl_3$; 176 MHz): δ 161.72, 160.11, 158.14, 145.18, 139.60, 132.20, 130.87, 121.69, 119,53, 110.96, 56.47, 53.59, 52.93.

Dimethyl 1-(4-fluoro-2-nitrophenyl)-1*H*-1, 2, 3-triazole-4, 5-dicarboxylate (4e).

^{1}H NMR ($CDCl_3$, 400 MHz): δ 7.97-7.95 (m, 1H), δ 7.56-7.47 (m, 2H), δ 3.97 (s, 3H), δ 3.80 (s, 3H). ^{13}C APT ($CDCl_3$; 176 MHz): δ 163.85, 162.38, 159.94, 157.93, 145.26, 139,92, 131.90, 131.78, 125.64, 121.54, 121.42, 114.03, 113.87, 53.70, 53.04.

Dimethyl 1-(4-bromo-2-nitrophenyl)-1*H*-1, 2, 3-triazole-4, 5-dicarboxylate (4f).

^{1}H NMR ($CDCl_3$, 400 MHz): δ 8.36 (s. 1H), δ 7.91 (d, *J* = 8.4 Hz, 1H), δ 7.40 (d, *J* = 8.4 Hz, 1H), δ 3.96 (s, 3H), δ 3.80 (s, 3H). ^{13}C APT ($CDCl_3$; 176 MHz): δ 159.88, 157.89, 144.54, 139.98, 137.41, 131.77, 131.03, 128.99, 128.35, 125.92, 53.72, 53.02.

Dimethyl 1-(4-chloro-2-nitrophenyl)-1*H*-1, 2, 3-triazole-4, 5-dicarboxylate (4g). Yellow solid, 51% yield. ^{1}H NMR ($CDCl_3$, 400 MHz): δ 8.31 (s, 1H), δ 7.85 (dd, 1H, *J* = 8.4 and 2.4 Hz), δ 7.57 (d, 1H, *J* = 8.4 Hz), δ 4.06 (s, 3H), δ 3.89 (s, 3H). ^{13}C APT ($CDCl_3$; 176 MHz): δ 159.91, 157.91, 144.59, 139.97, 138.40, 134.35, 131.81, 130.92, 127.86, 126.15, 53.74, 53.06.

Dimethyl 1-(5-chloro-2-nitrophenyl)-1*H*-1, 2, 3-triazole-4, 5-dicarboxylate (4h). Yellow solid, 50% yield. ^{1}H NMR ($CDCl_3$, 400 MHz): δ 8.29 (d, 1H, *J* = 8.8 Hz), δ 7.80 (dd, 1H, *J* = 8.8 Hz and 2.0 Hz), δ 7.62 (s, 1H), δ 4.06 (s, 3H), δ 3.90 (s, 3H). ^{13}C APT ($CDCl_3$; 176 MHz): δ 159.86, 157.81, 142. 59, 140.85, 139.96, 132.14, 131.75, 130.48, 130.13, 126.98, 53.75, 53.08.

Dimethyl 1-(2-nitro-6-(trifluoromethyl)phenyl)-1*H*-1, 2, 3-triazole-4, 5-dicarboxylate (4i). Light yellow oil, 40% yield. ^{1}H NMR ($CDCl_3$, 400 MHz): δ 8.42 (d, 1H, *J* = 8.4 Hz), δ 8.11 (d, 1H, *J* = 7.6 Hz), δ 7.92 (t, 1H, *J* = 8.0 Hz), δ 3.98 (s, 3H), δ 3.79 (s, 3H).

^{13}C APT ($CDCl_3$; 176 MHz): δ 159.72, 157,63, 146,10, 139.57, 132.57, 131.94, 129.89. 129.23, 128.06, 122.24, 120.68, 53.62, 53.07.

3.1.5 General procedure for [1, 2, 3]-triazolo [1,5-*a*] quinoxalin-4(5*H*)-one scaffold

To a solution of the corresponding triazole diester in EtOH (0.036M), 10% Pd/Al_2O_3 (5% loading) was added and the mixture was hydrogenated at room temperature overnight. Ethanol was evaporated and the crude was purified by silica gel chromatography column (dichloromethane/methanol).

Methyl 4-oxo-7-phenyl-4,5-dihydro-[1,2,3]triazolo[1,5-*a*] quinoxaline-3-carboxylate (5a). White solid, 20% yield. ^{1}H NMR (DMSO-d_6, 400 MHz): δ 12.32 (s, 1H), δ 8.45 (d, *J* = 8.8 Hz, 1H), δ 7.72-7.68 (m, 4H), δ 7.55 (t, *J* = 7.6 Hz, 2H), δ 7.47 (t, *J* = 6.8 Hz, 1H), δ 3.95 (s, 3H). ^{13}C APT (DMSO-d_6; 176 MHz): δ 160.70, 152.69, 142.09, 139.06, 138.08, 130.65, 129.77, 128.93, 127.60, 127.32, 122.77. 120.49, 117.16, 114.75, 53.02. ESI-MS (m/z): 321.2 [M + H]$^+$, 343.1 [M + Na]$^+$, 359.2 [M + K] $^+$

Methyl 7-(2,3-difluorophenyl)-4-oxo-4,5-dihydro-[1,2,3] triazolo[1,5-*a*]quinoxaline-3-carboxylate (5b). White solid, 27% yield. ^{1}H NMR (DMSO-d_6, 400 MHz): δ 12.35 (s, 1H), δ 8.50 (d, *J* = 8.4 Hz, 1H), δ 7.63-7.61 (m, 2H), δ 7.58-7.51 (m, 1H), δ 7.46-7.36 (m, 2H), δ 3.95 (s, 3H). ^{13}C APT (DMSO-d_6; 176 MHz): δ 160.65, 152.64,151.39, 149.99, 148.19, 146.82, 138, 11, 135.53, 130. 33, 129.35, 127.84, 126.24, 125.99, 124.66, 121.04, 118.03, 117.93, 117.07, 53.04. ESI-MS (m/z): 357.2 [M + H]$^+$, 379.2 [M + Na]$^+$, 395.3 [M + K] $^+$

Methyl 4-oxo-4, 5-dihydro-[1, 2, 3]triazolo[1,5-*a*] quinoxaline-3-carboxylate (5c). White solid, 65% yield. ^{1}H NMR (DMSO-d_6, 400 MHz): δ 12.18 (s, 1H), δ 8.38 (d, *J* = 8.0 Hz, 1H), δ 7.50 (t, *J* = 7.6 Hz, 1H), δ 7.46 (d, *J* = 8.0 Hz, 1H), δ 7.41 (t, *J* = 8.4 Hz, 1H), δ 3.94 (s, 3H). ^{13}C APT (DMSO-d_6; 176 MHz): δ 160.69, 152.52, 138.06, 130.33, 129.98, 127.68, 124.19, 121.10, 117.13, 116.54, 52.99. ESI-MS (m/z): 254.0 [M + H]$^+$, 267.1 [M + Na]$^+$, 283.1 [M + K] $^+$.

Methyl 7-methoxy-4-oxo-4, 5-dihydro-[1, 2, 3]triazolo[1,5-*a*] quinoxaline-3-carboxylate (5d). White solid, 56% yield. ^{1}H NMR (DMSO-d_6, 400 MHz): δ 12.16 (s, 1H), δ 8.29 (d, *J* = 8.8 Hz, 1H), δ 7.01 (d, *J* = 9.2 Hz, 1H), δ 6.94 (s, 1H), δ 3.93 (s, 3H), δ 3.85 (s, 3H). ^{13}C APT (DMSO-d_6; 176 MHz): δ 160.72, 160.53, 152.71, 137.92, 131.49, 126.62, 117.91, 115.26, 111.41, 100.61, 56.24, 52.94. ESI-MS (m/z): 275.2 [M + H]$^+$, 297.2 [M + Na]$^+$, 313.3 [M + K] $^+$.

Methyl 7-fluoro-4-oxo-4, 5-dihydro-[1, 2, 3]triazolo[1,5-*a*] quinoxaline-3-carboxylate (5e). White solid, 35% yield. ^{1}H NMR (DMSO-d_6, 400 MHz) δ: 12.33 (s, 1H), δ 8.45-8.41 (m, 1H), δ 7.28 (t, *J* = 8.4 Hz, 1H), δ 7.21 (d, *J* = 9.6 Hz, 1H), δ 3.93 (s, 3H). ^{13}C APT (DMSO-d_6; 176 MHz): δ 162.98, 161.59, 160.59, 152.65, 138.08, 131.75, 127.29, 118.90 (118.84) 118.18, 111.63 (111.49), 103.54 (103.38), 53.02. ESI-MS (m/z): 263.1 [M + H]$^+$, 285.1 [M + Na]$^+$, 301.1 [M + K] $^+$.

4-Oxo-4, 5-dihydro-[1, 2, 3]triazolo[1,5-*a*]quinoxaline-3-carboxylic acid (6). Compound **5c** (12 mg, 0.05 mmol) was dissolved in a mixture of tetrahydrofuran and water (0.25M, 3:1) and sodium hydroxide (4 mg, 0.1 mmol) was added. Reaction mixture was stirred at room temperature for 1.5 h. One drop of concentrated HCl was then added and the solvent was evaporated under vacuum and the crude product was triturated using dichloromethane, giving compound **6** as white solid (11 mg, quantitative). ^{1}H NMR (DMSO-d_6, 400 MHz): δ 13.12 (s, 1H), δ 8.45 (d, 1H, *J* = 8.0 Hz), δ 7.68 (t, 1H, *J* = 7.6 Hz), δ 7.61 (d, 1H, *J* = 8.0 Hz), δ 7.53 (t, 1H, *J* = 8.0 Hz). ^{13}C APT (DMSO-d_6; 176 MHz): δ 159.50, 156.03, 138.64, 130.51, 127.21, 125.46, 121.71, 116.47. ESI-MS (m/z): 231.1 [M + H]$^+$, 253.1 [M + Na]$^+$.

Methyl 5-methyl-4-oxo-4,5-dihydro-[1, 2, 3]triazolo[1,5-*a*] quinoxaline-3-carboxylate (7). Methyl 4-oxo-4,5-dihydro-[1,2,3] triazolo [1,5-a]quinoxaline-3-carboxylate (10 mg, 0.04 mmol), dimethyl carbonate (1.6 mmol; 40 equivalents) and potassium carbonate (0.12 mmol; 3 equivalents) were charged in a closed vessel and the reaction was left at 140 °C for 16 h. The mixture was then cooled at room temperature and purified by silica gel chromatography column with dichloromethane/methanol (98:2), to obtain methyl 5-methyl-4-oxo-4,5-dihydro-[1,2,3]triazolo [1,5-a]quinoxaline-3-carboxylate **7** as off white solid (8.3 mg;

78% yield). ^{1}H NMR (DMSO-d$_6$, 400 MHz): δ 8.49 (d, *J* = 8.0 Hz, 1H), δ 7.76-7.70 (m, 2H), δ 7.51 (t, *J* = 8.0, 1H), δ 3.94 (s, 3H), δ 3.65 (s, 3H). ^{13}C APT (DMSO-d$_6$; 176 MHz): δ 160.74, 152.20, 138.27, 131.09, 130.59. 126.62, 125.53, 121.55, 117.13, 116.70, 53.06, 29.61. ESI-MS (m/z): 259.1 [M + H]$^+$, 281.1 [M + Na]$^+$, 297.1 [M + K] $^+$.

Benzyl 5-benzyl-4-oxo-4,5-dihydro-[1,2,3]triazolo[1,5-a] quinoxaline-3-carboxylate (8). ^{1}H NMR (DMSO-d$_6$, 400 MHz): δ 8.51 (d, J = 8.0 Hz, 1 H), δ 7.59-7.24 (m, 13 H), δ 5.52 (s, 2 H), δ 5.46 (s, 2 H). ^{13}C APT (DMSO-d$_6$; 176 MHz): δ 160.11, 152.71, 138.43, 136.12, 130.44, 130.26, 129.08, 128.95, 128.71, 127.76, 127.11, 126.91, 124.67, 121.96, 117.41, 116.98. 67.35, 45.42. ESI-MS (m/z): 411.2 [M + H]$^+$, 433.2 [M + Na]$^+$, 449.2 [M + K] $^+$.

Methyl 5-benzyl-4-oxo-4, 5-dihydro-[1, 2, 3]triazolo[1,5-*a*] quinoxaline-3-carboxylate (9). To a suspension of methyl 4-oxo-4,5-dihydro-[1,2,3]triazolo [1,5-a]quinoxaline-3-carboxylate (5 mg, 0.02 mmol) in cyclopentyl methyl ether (0.1M) in a closed vessel, benzyl bromide (0.03 mmol, 3.6 μL) and potassium carbonate (0.06 mmol, 8.3 mg) were charged and the reaction was left at 130 °C for 12 h. The mixture was then cooled at room temperature and purified by silica gel chromatography column with dichloromethane/methanol (98: 2), to obtain methyl 5-benzyl-4-oxo-4,5-dihydro-[1,2,3]triazolo [1,5-a]quinoxaline-3-carboxylate as light yellow solid (6.6 mg, quantitative) and traces of the di-substituted compound **8**. ^{1}H NMR (DMSO-d$_6$, 400 MHz): δ 8.51 (d, *J* = 8.4 Hz, 1H), δ 7.59 (t, *J* = 8.0Hz, 1H), δ 7.52-7.46 (m, 2H), δ 7.37-7.24 (m, 5H), δ 5.54 (s, 2H), δ 3.95 (s, 3H). ^{13}C APT (DMSO-d$_6$; 176 MHz): δ 160.73, 152.66, 138.45, 136.08, 130.45, 130.26, 129.07, 127.75, 127.09, 126.75, 124.68, 121.94, 117.49, 116.98, 53.05, 45.42. ESI-MS (m/z): 335.2 [M + H]$^+$, 357.2 [M + Na]$^+$, 373.1 [M + K] $^+$.

Methyl 5-(cyclopropylmethyl)-4-oxo-4,5-dihydro-[1,2,3] triazolo[1,5-*a*]quinoxaline-3-carboxylate (10). To a suspension of methyl 4-oxo-4,5-dihydro-[1,2,3]triazolo [1,5-*a*]quinoxaline-3-carboxylate (5 mg, 0.02 mmol) in cyclopentyl methyl ether (0.1M) in a round-bottom flask, cyclopropyl methyl bromide (0.03mmol, 3.0 μL) and potassium carbonate (0.06 mmol, 8.3 mg) were added and the reaction was left at reflux for 12 h. The mixture was then cooled at room temperature and purified by silica gel chromatography column with *n*-hexane/ethyl acetate (80:20), to obtain **8** as white solid, 86% yield. ^{1}H NMR (DMSO-d$_6$, 400 MHz): δ 8.52 (dd, J = 8.0, 1.2 Hz, 1H), δ 7.88 (d, *J* = 8.0 Hz, 1H), δ 7.73 (t, 1H, *J* = 8.4 Hz), δ 7.52 (t, 1H, *J* = 8.0 Hz), δ 4.22 (d, *J* = 6.8 Hz, 2H), δ 3.94 (s, 3H) δ, 1.31-1.26 (m, 1H), δ 0.51-0.49 (m, 4H). ^{13}C APT (DMSO-d$_6$; 176 MHz): δ 160.71, 152,34, 138,37, 130.65, 130.34, 126.47, 124.56, 121.64, 117.36, 117.03, 53.05, 45.94, 10.02, 4.37. ESI-MS (m/z): 299.2 [M + H]$^+$, 321.2 [M + Na]$^+$, 337.2 [M + K] $^+$.

3.1.6 General procedures for coupling reactions

3.1.6.1 **Method A** (for primary, secondary and benzylamines)

To Methyl 4-oxo-4,5-dihydro-[1, 2, 3]triazolo [1,5-*a*] quinoxaline-3-carboxylate or Methyl 5-methyl-4-oxo-4,5-dihydro-[1, 2, 3]triazolo [1,5-*a*] quinoxaline-3-carboxylate or Methyl 5-benzyl-4-oxo-4,5-dihydro-[1, 2, 3]triazolo [1,5-*a*] quinoxaline-3-carboxylate, the corresponding amines were added (benzylamine, 3-picolylamine, cyclohexylamine, pyrrolidine). Reaction was performed under ultrasound bath at room temperature for 15 min. The mixture was then purified by silica gel chromatography column with dichloromethane/methanol (98:2), to obtain the corresponding amides.

***N*-benzyl-4-oxo-4, 5-dihydro-[1,2,3]triazolo[1,5-*a*] quinoxaline-3-carboxamide (11).** White solid, quantitative yield. ^{1}H NMR (DMSO-d$_6$, 400 MHz): δ 10.74 (s, 1H), δ 8.42 (d, *J* = 8.4 Hz, 1H), δ 7.62 (t, *J* = 8.4 Hz, 1H), δ 7.52-7.34 (m, 6H), δ 7.28 (t, *J* = 6.8 Hz, 1H), δ 4.62 (d, *J* = 5.6 Hz, 2H). ^{13}C APT (DMSO-d$_6$; 176 MHz): δ 158.64, 156.10, 140.90, 139.18, 130.16, 128.92, 127.80, 127.50, 125.68, 124.72, 121.64, 118.10, 116.42, 42.90. ESI-MS (m/z): 320.2 [M + H]$^+$, 342.2 [M + Na]$^+$, 358.2 [M + K] $^+$.

***N*-cyclohexyl-4-oxo-4, 5-dihydro-[1,2,3]triazolo[1,5-*a*] quinoxaline-3-carboxamide (12).** White solid, 97% yield. ^{1}H NMR (DMSO-d$_6$, 400 MHz): δ 10.24 (d, *J* = 7.2 Hz, 1H), δ 8.41 (d, *J* = 8.0 Hz, 1H), δ 7.62 (t, *J* = 8.0 Hz, 1H), δ 7.53-7.45 (m, 2H), δ 3.92-3.85 (m, 1H), δ 1.91-1.85 (m, 2H), δ 1.78–1.72 (m, 2H), δ 1.59-1.53 (m, 1H), δ 1.44-1.29 (m, 5H). ^{13}C APT (DMSO-d$_6$; 176 MHz): δ 157.44, 156.04, 141.37, 130.19, 125.39, 124.89, 121.63, 117.79, 116.47, 47.81, 32.51, 25.69, 24.29. ESI-MS (m/z): 312.3 [M + H]$^+$, 334.2 [M + Na]$^+$, 350.2 [M + K] $^+$.

3-(Pyrrolidine-1-carbonyl)-[1,2,3]triazolo[1,5-*a*]quinoxalin-4(5*H*)-one (13). White solid, 99% yield. ^{1}H NMR (DMSO-d$_6$, 400 MHz): δ 12.16 (s, 1H), δ 7.36 (d, *J* = 8.4 Hz, 1H), δ 7.59 (t, *J* = 8.0 Hz, 1H), δ 7.48-7.40 (m, 2H), δ 3.56-3.51 (m, 2H), δ 3.30-3.28 (m, 2H), δ 1.95-1.88 (m, 2H), δ 1.86-1.79 (m, 2H). ^{13}C APT (DMSO-d$_6$; 176 MHz): δ 159.53, 153.57, 142.52, 130.07, 129.89, 124.59, 124.25, 121.31, 117.39, 116.38, 47.84, 46.02, 25.81, 24.45. ESI-MS (m/z): 284.2 [M + H]$^+$.

***N*-benzyl-5-methyl-4-oxo-4,5-dihydro-[1,2,3]triazolo[1,5-*a*] quinoxaline-3-carboxamide (14).** White solid, 94% yield. ^{1}H NMR (DMSO-d$_6$, 400 MHz): δ 10.48 (t, *J* = 5.6 Hz, NH, 1H), δ 8.53 (d, *J* = 8 Hz, 1H), δ 7.81 (d, *J* = 8.4 Hz, 1H), δ 7.75 (t, *J* = 7.6 Hz, 1H), δ 7.57 (t, *J* = 8.0 Hz, 1H), δ 7.42-7.35 (m, 4H), δ 7.29 (t, *J* = 7.2 Hz, 1H), δ 4.63 (d, *J* = 6.0 Hz, 2H), δ 3.69 (s, 3H). ^{13}C APT (DMSO-d$_6$; 176 MHz): δ 158.48, 155.28, 141.23, 139.15, 130.51, 130.44, 128.98, 127.89, 127.57, 125.35, 124.82, 122.00, 117.53, 116.68, 42.95, 30.12. ESI-MS (m/z): 334.2 [M + H]$^+$.

5-Methyl-4-oxo-*N*-(pyridin-3-yl methyl)-4, 5-dihydro-[1, 2, 3] triazolo[1,5-*a*]quinoxaline-3-carboxamide (15). White solid, 95% yield. ^{1}H NMR (DMSO-d$_6$, 400 MHz): δ 10.49 (t, *J* = 5.2 Hz, 1H), δ 8.64 (s, 1H), δ 8.54-8.49 (m, 2H), δ 7.81 (d, *J* = 8.4 Hz, 2H), δ 7.75 (t, *J* = 7.6, 1H), δ 7.58 (t, *J* = 7.6 Hz, 1H), δ 7.42-7.38 (m, 1H), δ 4.66 (d, *J* = 6.0 Hz, 2H), δ 3.70 (s, 3H). ^{13}C APT (DMSO-d$_6$; 176 MHz): δ 158.72, 155.20, 149.33, 148.85, 141.09, 135.76, 134.81, 130.54, 130.45, 125.36, 124.91, 124.09, 121.97, 117.54, 116.68, 40.63, 30.12. ESI-MS (m/z): 335.2 [M + H]$^+$.

5-Benzyl-4-oxo-*N*-(pyridin-3-yl methyl)-4, 5-dihydro-[1, 2, 3] triazolo[1,5-*a*]quinoxaline-3-carboxamide (16). White solid, 96% yield. ^{1}H NMR (DMSO-d$_6$, 400 MHz): δ 10.39 (t, *J* = 6.0Hz, 1H), δ 8.62 (s, 1H), δ 8.55 (d, *J* = 8.0 Hz, 1H), δ 8.47 (d, *J* = 4.4 Hz, 1H), δ 7.81 (d, *J* = 7.6 Hz, 1H), δ 7.63-7.51 (m, 3H), δ 7.39-7.25 (m, 6H), δ 5.59 (s, 2H), δ 4.65 (d, *J* = 5.8 Hz, 2H). ^{13}C APT (DMSO-d$_6$; 176 MHz): δ 158.85, 156.65, 149.31, 148.80, 141.39, 135.81, 135.70, 134.85, 130.39, 129.63, 129.12, 127.86, 127.04, 125.46, 124.09, 122.34,117.78, 116.94, 45.87, 40.64. ESI-MS (m/z): 411.2 [M + H]$^+$

***N*-5-Dibenzyl-4-oxo-4, 5-dihydro-[1,2,3]triazolo[1,5-*a*] quinoxaline-3-carboxamide (17).** White solid, quantitative. ^{1}H NMR (DMSO-d$_6$, 400 MHz): δ 10.38 (t, *J* = 5.6 Hz, 1H, NH), δ

8.55 (d, J = 7.6 Hz, 1H), δ 7.63-7.51 (m, 3H), δ 7.41-7.25 (m, 10H), δ 5.58 (s, 2H), δ 6.62 (d, J = 5.6 Hz, 2H). ^{13}C APT (DMSO-d_6; 176 MHz): δ 158.60, 155.73, 141.52, 139.15, 135.70, 130.37, 129.62, 129,12, 128.96, 127.92, 127.85, 127.57, 127.03, 125.45, 124.97, 122.37, 117.78, 116.94, 45.87, 42.96. ESI-MS (m/z): 410.3 [M + H]$^+$.

5-Benzyl-4-oxo-*N*-(3-(trifluoromethyl)benzyl)-4, 5-dihydro-[1,2,3]triazolo[1,5-*a*]quinoxaline-3-carboxamide (18). White solid, 89% yield. ^{1}H NMR (DMSO-d_6, 400 MHz): δ 10.42 (t, J = 6.0 Hz, 1H), δ 8.55 (d, J = 8.0 Hz, 1H), δ 7.78 (s, 1H), δ 7.72 (d, J = 7.6 Hz, 1H), δ 7.65-7.51 (m, 5H), δ 7.39 (d, J = 7.2 Hz, 2H), δ 7.34-7.25 (m, 3H), δ 5.59 (s, 2H), δ 4.72 (d, J = 6.0 Hz, 2H). ^{13}C APT (DMSO-d_6; 176 MHz): δ 158.90, 155.65, 141.42, 140.93, 135.78, 132.05, 130.37, 129.99, 129.67, 129.08, 127.85, 127.14, 125.41, 125.13, 124.38, 124.26, 122.38, 117.78, 116.94, 45.85, 42.47. ESI-MS (m/z): 478.3 [M + H]$^+$.

5-Benzyl-*N*-(4-chlorobenzyl)-4-oxo-4, 5-dihydro-[1, 2, 3] triazolo[1,5-*a*]quinoxaline-3-carboxamide (19). White solid, 93% yield. ^{1}H NMR (DMSO-d_6, 400 MHz): δ 10.37 (t, J = 6.0 Hz, 1H, NH), δ 8.55 (d, J = 8.0 Hz, 1H), δ 7.64-7.51 (m, 3H), δ 7.42 (s, 3H), δ 7.39-7.25 (m, 6H), δ 5.59 (s, 2H), δ 4.62 (d, J = 6.0 Hz, 2H). ^{13}C APT (DMSO-d_6; 176 MHz): δ 158.68, 155.70, 141.45, 138.37, 135.75, 132.10, 130.36, 129.82, 129.66, 129.10, 128.88, 127.83, 127.07, 125.42, 125.05, 122.39, 117.81, 116.93, 45.87, 42.27. ESI-MS (m/z): 444.3 [M + H]$^+$.

3.1.6.2 **Method B** (for anilines)

4-Oxo-*N*-phenyl-4, 5-dihydro-[1,2,3]triazolo[1,5-*a*] quinoxaline-3-carboxamide (20). To a solution of Methyl 4-oxo-4,5-dihydro-[1,2,3]triazolo [1,5-a]quinoxaline-3-carboxylate (7.3 mg; 0.03 mmol) in cyclopentyl methyl ether (0.3 M), aniline (0.039 mmol, 3.55 μL) and Cp_2ZrCl_2 (10 mol%, 0.003 mmol, 0.9 mg) were added. The mixture was refluxed for 12 h, then cooled and purified by silica gel chromatography column with dichloromethane/methanol (98:2), to obtain compound **20** as white solid, 81% yield. ^{1}H NMR (DMSO-d_6, 400 MHz): δ 12.45 (s, 1H), δ 8.46 (d, J = 8.0 Hz, 1H), δ 7.76 (d, J = 8.0 Hz, 2H), δ 7.67 (t, J = 7.6 Hz, 1H), δ 7.57 (d, J = 8.0 Hz, 1H), δ 7.51 (t, J = 7.6 Hz, 1H), δ 7.44 (t, J = 7.6 Hz, 2H), δ 7.17 (t, J = 7.2 Hz, 1H). ^{13}C APT (DMSO-d_6; 176 MHz): δ 156.60, 156.37, 141.30, 138.93, 130.38, 129.69, 125.65, 125.13, 124.59, 121.67, 119.84, 116.53. ESI-MS (m/z): 306.2 [M + H]$^+$

3.2 Biological procedures

3.2.1 Antibiotics and strains

Vancomycin (VAN), oxacillin (OXA), imipenem (IPM), tobramycin (TOB), amphotericin B (AMB), and voriconazole (VRC) were purchased from Sigma-Aldrich (Milan, Italy). *Staphylococcus aureus* ATCC 29213, ATCC 43300 (methicillin-resistant *S. aureus*, MRSA), *S. epidermidis* ATCC 35984, *Pseudomonas aeruginosa* ATCC 27853, *Klebsiella pneumoniae* ATCC 13883, *K. pneumonia* ATCC BAA-1705 (carbapenem-resistant) *Candida albicans* ATCC 90028, and *Candida albicans* ATCC 10231 (voriconazole resistant strain) were obtained from the American Type Culture Collection (Rockville, MD).

3.2.2 Antimicrobial susceptibility testing

Minimal inhibitory concentrations (MIC) of all the compounds were determined in Mueller–Hinton medium (MH) by the broth microdilution assay, following the procedure already described (Fiorani et al., 2018). The compounds were added to the bacterial suspension in each well yielding a final cell concentration of 1 × 10^6 CFU/ml and a final compound concentration ranging from 3,1–100 μM. Negative control wells were set to contain bacteria in Mueller–Hinton broth plus the amount of vehicle (DMSO) used to dilute each compound. Positive controls included VAN (2 μg/ml), OXA (2 μg/ml), IPM (2 μg/ml), and TOB (2 μg/ml), the MIC was defined as the lowest concentration of drug that caused a total inhibition of microbial growth after 24 h incubation time at 37°C

The antifungal activity of compounds was determined using a standardized broth microdilution method (Clinical and Laboratory Standards Institute. Reference method for broth dilution antifungal susceptibility testing of yeasts. M27—4th Ed. Pennsylvania (US): Clinical and Laboratory Standards Institute; 2017.) Briefly, the cell suspension was adjusted to 3 × 10^3 CFU/ml in RPMI 1640 medium (Sigma) supplemented with 0.2% (w/v) glucose. One hundred microliter aliquots of these cell suspensions were dispensed into 96-well microtiter plates. Compounds were serially diluted using RPMI 1640 medium and added to the wells at a final concentration ranging from 0.4 to 100 μM, and the plate was incubated for 48 h at 37°C. Voriconazole (30 μg/ml for ATCC 10231 and 0.25 μg/ml for ATCC 90028) and AMB (0.12 μg/ml) were chosen as positive controls.

All the tests were conducted at least three times using independent cell suspensions.

3.2.3 Biofilm formation assay

Biofilm formation was evaluated by measuring the ability of cells to adhere to a sterile 96-well polystyrene flat-bottom microtiter plate (BD Falcon, Mississauga, Ontario Canada) as described previously 18. Briefly, a suspension of *S. epidermidis* (MH supplemented with 1% glucose) at the final density of 10^5 CFU ml-1 was treated with compounds **9**, **14**, and **20** 50 mM. After 24 h at 37°C, planktonic cells were removed, and the wells washed twice with phosphate-buffered saline (PBS) and dried at 60°C for 30 min. Crystal violet solution (150 ml at 0.1%) was added to each well and the plates were incubated at room temperature for 30 min. The wells were then washed with PBS and discolored with 200 ml of 96% ethanol for 20 min. Absorbance was measured at 620 nm using a microtiter plate reader. The percentage of biofilm mass reduction was calculated using the formula [(Ac-At)/Ac] ×100, where Ac is the absorbance value (OD) for control wells and At is the OD value in the presence of a compound.

3.2.4 Statistical analysis

Statistical analyses for biological assays were performed using GraphPad Prism 9 (GraphPad Software, San Diego, CA, USA). Analysis of variance (ANOVA) for multiple comparisons followed by Dunnett's *post hoc* test was used to compare the treated and control groups. *p-value* < 0.01 was considered significant for all the *in vitro* experiments.

4 Conclusion

We reported the discovery of a novel eco-sustainable protocol for both the synthesis and decoration of the [1,2,3]-triazolo [1,5-*a*] quinoxalin-4(5*H*)-one scaffold, a so far poorly explored moiety for medicinal chemistry purposes. Our conceived procedure rejuvenated the chemical path toward this scaffold by using eco-sustainable reagents, catalysts and neat conditions for the majority of the required synthetic steps. Notably, in the case of aliphatic amines and benzylamines the amidation products were obtained under neat conditions. Furthermore, catalytic direct amidation with anilines was explored for the first time on this scaffold, using dichlorobis (cyclopentadienyl)zirconium (Cp_2ZrCl_2) and CPME as eco-friendly catalyst and solvent, respectively.

The results of the antimicrobial assay obtained against *S. aureus* ATCC 29213 and *S. aureus*, *P. aeruginosa*, *K. pneumoniae*, *C. albicans*, and also the inhibition of *S. epidermidis* biofilm formation foster a further optimization campaign, since three out of 16 compounds, namely compounds **9**, **14** and **20**, displayed a limited antimicrobial property. Interestingly compound **9** reduced the growth of different bacteria and the yeast *Candida*, also affecting biofilm formation in *S. epidermidis*, thus proving to be a promising hit compound for the discovery of novel agents against polymicrobial infections.

Data availability statement

The original contributions presented in the study are included in the article/Supplementary Material, further inquiries can be directed to the corresponding authors.

Author contributions

SP and MB contributed to conception and design of the study and wrote the paper; AA and SP were involved in all experimental synthetic work and performed all data analyses. BG contributed to perform the synthetic experimental work; LT and EB performed the microbiological assays; FL and EB designed the microbiological studies and analyzed the data; MB and VS cured manuscript review and editing. All authors contributed to manuscript revision, read, and approved the submitted version.

Acknowledgments

The MIUR Grant "Dipartimento di Eccellenza 2018–2022" to the Department of Pharmacy of the University of Naples "Federico II" is gratefully acknowledged. SP and MB acknowledge MUR (Ministero dell'Università e della Ricerca), PON R&I 2014-2020- Asse IV "Istruzione e Ricerca per il recupero-REACT-EU", Azione IV.6 "Contratti di Ricerca su tematiche Green". This research was supported by EU funding within the MUR PNRR Extended Partnership initiative on Emerging Infectious Diseases (Project no. PE00000007, INF-ACT).

Conflict of interest

The authors declare that the research was conducted in the absence of any commercial or financial relationships that could be construed as a potential conflict of interest.

Publisher's note

Supplementary material

The Supplementary Material for this article can be found online at: https://www.frontiersin.org/articles/10.3389/fchem.2023.1126427/full#supplementary-material

References

Ager, I. R., Barnes, A. C., Danswan, G. W., Hairsine, P. W., Kay, D. P., Kennewell, P. D., et al. (1988). Synthesis and oral antiallergic activity of carboxylic acids derived from imidazo[2,1-c] [1,4]benzoxazines, imidazo[1,2-a]quinolines, imidazo[1,2-a] quinoxalines, imidazo[1,2-a]quinoxalinones, pyrrolo[1,2-a]quinoxalinones, pyrrolo [2,3-a]quinoxalinones, and imidazo[2,1-b]benzothiazoles. *J. Med. Chem.* 31 (6), 1098–1115. doi:10.1021/jm00401a009

Alfano, A. I., Buommino, E., Ferraro, M. G., Irace, C., Zampella, A., Lange, H., et al. (2021). Coupling interrupted fischer and multicomponent joullié-ugi to chase chemical diversity: From batch to sustainable flow synthesis of peptidomimetics. *ChemMedChem* 16 (24), 3795–3809. doi:10.1002/cmdc.202100474

Alswah, M., Bayoumi, A. H., Kamal Elgamal, K., Elmorsy, A., Saleh Ihmaid, S., and Ahmed, H. E. A. (2018). Design, synthesis and cytotoxic evaluation of novel chalcone derivatives bearing triazolo[4,3-a]- quinoxaline moieties as potent anticancer agents with dual EGFR kinase and tubulin polymerization inhibitory effects. *Molecules* 23, 48. doi:10.3390/molecules23010048

Amer, A., Ayoup, M. S., Khattab, S. N., Hassan, S. Y., Langer, V., Senior, S., et al. (2010). A regio- and stereo-controlled approach to triazoloquinoxalinyl C-nucleosides. *Carbohydr. Res.* 345, 2474–2484. doi:10.1016/j.carres.2010.08.010

Ayoup, M. S., Ahmed, H. E. A., El Massry, A. M., Senior, S., Khattab, S. N., Hassan, S. Y., et al. (2016). Synthesis, docking, and evaluation of antimicrobial activity of a new series of acyclo C-nucleosides of 1, 2, 4-triazolo[4, 3-a]quinoxaline derivatives. *J. Heterocycl. Chem.* 53, 153–163. doi:10.1002/jhet.2396

Ayoup, M. S., Rabee, A. R., Abdel-Hamid, H., Harras, M. F., El Menofy, N. G., and Ismail, M. M. F. (2022). Exploration of nitroaromatic antibiotics via sanger's reagent: Synthesis, in silico, and antimicrobial evaluation. *ACS Omega* 7 (6), 5254–5263. doi:10.1021/acsomega.1c06383

Baashen, M. A., Abdel-Wahab, B. F., and El-Hiti, G. A. (2016). Syntheses of triazoloquinoxalines. *Heterocycles* 92, 1931–1952. doi:10.3987/rev-16-847

Barral, K., Moorhouse, D., and Moses, J. E. (2007). Efficient conversion of aromatic amines into Azides: A one-pot synthesis of triazole linkages. *Org. Lett.* 9, 1809–1811. doi:10.1021/ol070527h

Biagi, G., Giorgi, I., Livi, O., Scartoni, V., Betti, L., Giannaccini, G., et al. (2002). New 1,2,3-triazolo[1,5-a]quinoxalines: Synthesis and binding to benzodiazepine and adenosine receptors. II. *II Eur. J. Med. Chem.* 37, 565–571. doi:10.1016/s0223-5234(02)01376-4

El-Attar, M. A. Z., Elbayaa, R. Y., Shaaban, O. G., Habib, N. S., Abdel Wahab, A. E., Abdelwahab, I. A., et al. (2018). Synthesis of pyrazolo-1,2,4-triazolo[4,3-a]quinoxalines

as antimicrobial agents with potential inhibition of DHPS enzyme. *Future Med. Chem.* 10, 2155–2175. doi:10.4155/fmc-2018-0082

El-Sagheer, A. H., and Brown, T. (2012). Click nucleic acid ligation: Applications in biology and nanotechnology. *Acc. Chem. Res.* 45, 1258–1267. doi:10.1021/ar200321n

Fiorani, G., Perosa, A., and Selva, M. (2018). Dimethyl carbonate: A versatile reagent for a sustainable valorization of renewables. *Green Chem.* 20, 288–322. doi:10.1039/c7gc02118f

HongShen, C. H. C., Ding, F. X., Deng, Q., Wilsie, L. C., Krsmanovic, M. L., Taggart, A. K., et al. (2009). Discovery of novel tricyclic full agonists for the G-protein-coupled niacin receptor 109A with minimized flushing in rats. *J. Med. Chem.* 52, 2587–2602. doi:10.1021/jm900151e

Houa, H., Yangb, R., Liub, X., Wub, X., Zhangb, S., Chenb, K., et al. (2020). Discovery of triazoloquinoxaline as novel STING agonists via structure-based virtual screening. *Bioorg. Chem.* 100, 103958. doi:10.1016/j.bioorg.2020.103958

Mirzaei, H., Eshghi, H., and Seyedi, S. M. (2021). Cu Nano particles immobilized on silk-fibroin as a greenand biodegradable catalyst for copper catalyzed azide-terminal, internal alkynes cycloaddition. *Appl. Organomet. Chem.* 35, e6019. doi:10.1002/aoc.6019

Nagavelli, V. R., Nukala, S. K., Narsimha, S., Battula, K. S., Tangeda, S. J., and Reddy, Y. N. (2016). Synthesis, characterization and biological evaluation of 7-substituted-4-((1-aryl-1H-1,2,3-triazol-4-yl) methyl)-2H- benzo[b] [1,4]oxazin-3(4H)-ones as anticancer agents. *Med. Chem. Res.* 25, 1781–1793. doi:10.1007/s00044-016-1616-9

Souad, B., Fatmi, C. E., and Mabrouk, T. (2011). Synthesis of some 1,4,5-trisubstituted 1,2,3-triazoles by 1,3-dipolar cycloaddition of 2-substituted phenyl azides to dimethyl acetylene dicarboxylate (DMAD), regular stirring versus microwave irradiation: A comparative study. *Rasayan J. Chem.* 4, 806–809.

Vollaro, A., Catania, M. R., Iesce, M. R., Sferruzza, R., D'Abrosca, B., Donnarumma, G., et al. (2019). Antimicrobial and anti-biofilm properties of novel synthetic lignan-like compounds. *New Microbiol.* 42, 21–28.

Watanabe, K., Yamagiwa, N., and Torisawa, Y. (2007). Cyclopentyl methyl ether as a new and alternative process solvent. *Org. Process Res. Dev.* 11 (2), 251–258. doi:10.1021/op0680136

Weiss, R., Seubert, J., and Hampel, F. (1994). α-Aryliodonio diazo compounds: SN reactions at theα-C atom as a novel reaction Type for diazo compounds. *Angew. Chem. Int. Ed.* 33 (19), 1952–1953. doi:10.1002/anie.199419521

Wen, J., Zhao, W., Gao, X., Ren, X., Dong, C., Wang, C., et al. (2022). Synthesis of [1,2,3]Triazolo-[1,5-a]quinoxalin-4(5H)-ones through photoredox-catalyzed [3 + 2] cyclization reactions with hypervalent iodine(III) reagents. *J. Org. Chem.* 87, 4415–4423. doi:10.1021/acs.joc.2c00135

Wesseler, F., Lohmann, S., Riege, D., Halver, J., Roth, A., Pichlo, C., et al. (2022). Phenotypic discovery of triazolo[1,5-c]quinazolines as a first-in- class bone morphogenetic protein amplifier chemotype. *J. Med. Chem.* 65 (22), 15263–15281. doi:10.1021/acs.jmedchem.2c01199

Xu, J., Yang, H., He, L., Huang, L., Shen, J., Li, W., et al. (2021). Synthesis of (E)-quinoxalinone oximes through a multicomponent reaction under mild conditions. *Org. Lett.* 23, 195–201. doi:10.1021/acs.orglett.0c03918

Yan, J., Zhou, F., Qin, D., Cai, T., Ding, K., and Cai, Q. (2012). Synthesis of [1,2,3] Triazolo- [1,5-a]quinoxalin-4(5H)-ones through copper-catalyzed tandem reactions of N-(2-Haloaryl)propiolamides with sodium azide. *Org. Lett.* 14, 1262–1265. doi:10.1021/ol300114w

Zhang, S., Xu, Z., Gao, C., Ren, Q.-C., Chang, L., Lv, Z.-S., et al. (2017). Triazole derivatives and their anti-tubercular activity. *Eur. J. Med. Chem.* 138, 501–513. doi:10.1016/j.ejmech.2017.06.051

frontiers | Frontiers in Chemistry

TYPE Original Research
PUBLISHED 24 May 2023
DOI 10.3389/fchem.2023.1185224

OPEN ACCESS

EDITED BY
Xuben Hou,
Shandong University, China

REVIEWED BY
Silvia Gervasoni,
University of Cagliari, Italy
Pasquale Linciano,
University of Pavia, Italy

*CORRESPONDENCE
Fang Yu,
fang.yu@lnpu.edu.cn
Xingzhou Li,
lixz@bmi.ac.cn
Junhai Xiao,
xiaojunhai@139.com

†These authors have contributed equally to this work and share first authorship

RECEIVED 13 March 2023
ACCEPTED 09 May 2023
PUBLISHED 24 May 2023

CITATION
Shi Q, Wen H, Xu Y, Zhao X, Zhang J, Li Y, Meng Q, Yu F, Xiao J and Li X (2023), Virtual screening–based discovery of AI-2 quorum sensing inhibitors that interact with an allosteric hydrophobic site of LsrK and their functional evaluation. *Front. Chem.* 11:1185224. doi: 10.3389/fchem.2023.1185224

Virtual screening–based discovery of AI-2 quorum sensing inhibitors that interact with an allosteric hydrophobic site of LsrK and their functional evaluation

Qianqian Shi[1,2†], Huiqi Wen[3†], Yijie Xu[2,4†], Xu Zhao[5], Jing Zhang[6], Ye Li[7], Qingbin Meng[4], Fang Yu[1,2]*, Junhai Xiao[2,4]* and Xingzhou Li[2,4]*

[1]School of Petrochemical Engineering, Liaoning Petrochemical University, Fushun, China, [2]National Engineering Research Center for the Emergency Strategic Drug, Beijing Institute of Pharmacology and Toxicology, Beijing, China, [3]State Key Laboratory of Pathogen and Biosecurity, Institute of Microbiology and Epidemiology, Academy of Military Medical Sciences, Beijing, China, [4]State Key Laboratory of Toxicology and Medical Countermeasures, Beijing Institute of Pharmacology and Toxicology, Beijing, China, [5]Department of Hepatology, Fifth Medical Center of Chinese PLA General Hospital, Beijing, China, [6]Qionglai Medical Center Hospital, Chengdu, China, [7]The No 968 Hospital of PLA, Jinzhou, China

Introduction: Quorum sensing (QS) is a bacterial intracellular and intercellular communication system that regulates virulence factor production, biofilm formation, and antibiotic sensitivity. Quorum-sensing inhibitors (QSIs) are a novel class of antibiotics that can effectively combat antibiotic resistance. Autoinducer-2 (AI-2) is a universal signaling molecule that mediates inter- and intraspecies QS systems among different bacteria. Furthermore, LsrK plays an important role in regulating the activity and stability of the intracellular AI-2 signaling pathway. Thus, LsrK is considered an important target for the development of QSIs.

Methods: We designed a workflow integrating molecular dynamic (MD) simulations, virtual screening, LsrK inhibition assays, cell-based AI-2-mediated QS interference assays, and surface plasmon resonance (SPR)-based protein affinity assays to screen for potential LsrK kinase inhibitors.

Results: MD simulation results of the LsrK/ATP complex revealed hydrogen bonds and salt bridge formation among four key residues, namely, Lys 431, Tyr 341, Arg 319, and Arg 322, which are critical for the binding of ATP to LsrK. Furthermore, MD simulation results indicated that the ATP-binding site has an allosteric pocket that can become larger and be occupied by small molecule compounds. Based on these MD simulation results, a constraint of forming at least one hydrogen bond with Arg 319, Arg 322, Lys 431, or Tyr 341 residues was introduced when performing virtual screening using Glide's virtual screening workflow (VSW). In the meantime, compounds with hydrophobic group likely to interact with the allosteric hydrophobic pocket are preferred when performing visual inspection. Seventy-four compounds were selected for the wet laboratory assays based on virtual screening and the absorption, distribution, metabolism, and excretion (ADME) properties of these compounds. LsrK inhibition assays revealed 12 compounds inhibiting LsrK by more than 60% at a 200 μM concentration; four of these (Y205-6768, D135-0149, 3284–1358, and N025-0038) had IC_{50}

values below 50 μM and were confirmed as ATP-competitive inhibitors. Six of these 12 LsrK inhibitors exhibited high AI-2 QS inhibition, of which, Y205-6768 had the highest activity with IC_{50} = 11.28 ± 0.70 μM. The SPR assay verified that compounds Y205-6768 and N025-0038 specifically bound to LsrK. MD simulation analysis of the docking complexes of the four active compounds with LsrK further confirmed the importance of forming hydrogen bonds and salt bridges with key basic amino acid residues including Lys 431, Tyr 341, Arg 319, and Arg 322 and filling the allosteric hydrophobic pocket next to the purine-binding site of LsrK.

Discussion: Our study clarified for the first time that there is an allosteric site near the ATP-binding site of Lsrk and that it enriches the structure–activity relationship information of Lsrk inhibitors. The four identified compounds showed novel structures, low molecular weights, high activities, and novel LsrK binding modes, rendering them suitable for further optimization for effective AI-2 QSIs. Our work provides a valuable reference for the discovery of QSIs that do not inhibit bacterial growth, thereby avoiding the emergence of drug resistance.

KEYWORDS

ATP competitive inhibitors, LsrK, antibacterial agents, quorum sensing, virtual screening, molecular dynamics

1 Introduction

Quorum sensing (QS) is an intercellular and intracellular communication system that allows bacteria to regulate many bacterial phenotypes by sensing interspecific or intraspecific populations (Antunes et al., 2010; Eickhoff and Bassler, 2018; Papenfort and Bassler, 2016). QS is involved in regulating various pathological processes, such as the induction of many bacteria density-dependent responses, including the synchronous production and secretion of virulence factors (Zhu et al., 2002; J. Li et al., 2021; Bansal et al., 2008; Antunes et al., 2010), bioluminescence, biofilm formation (Gu et al., 2020; Sun et al., 2020), changes in motility (Laganenka et al, 2016), cellular differentiation, and modification of antibiotic susceptibility (Grillo-Puertas et al., 2012; Patzelt et al., 2013). QS is mediated by signaling molecules called autoinducers (AIs). There are three main types of AIs: acylated homoserine lactones (AHL) utilized by gGram-negative bacteria; autoinducer peptides (AIPs) utilized by Gram-positive bacteria; and AI-2 identified in both Gram-positive and Gram-negative bacteria (Papenfort and Bassler, 2016). Other AIs include the *Pseudomonas* quinolone signal (PQS) (Hodgkinson et al., 2016; Dandela et al., 2018), diffusible signal factor (DSF) (He et al., 2022; Barber et al., 1997; Ryan et al., 2015), and *γ*-butyrolactone (Hur, Jang, and Sim, 2021; Takano, 2006). AI-2 is a unique AI that facilitates inter- and intraspecies communication and is thus defined as a "common language" of microbes (Federle and Bassler, 2003; Pereira, Thompson, and Xavier, 2013). Inter- and intraspecies communication through AI-2 QS has been demonstrated to coordinate critical features such as coaggregation, biofilm formation, and virulence (Duan et al., 2003). For instance, the synthesis of AI-2 by *Enterococcus faecalis* enhances *Escherichia coli (E. coli)* aggregation, coaggregation, and biofilm development (Laganenka, Colin, and Sourjik, 2016; Laganenka and Sourjik, 2018). Patients with cystic fibrosis and other diseases are often co-infected with *Pseudomonas aeruginosa* and Al-2 producing bacterial species such as *Staphylococcus aureus, Klebsiella pneumoniae,* and *Streptococcus mitis* (Laganenka and Sourjik, 2018; H. Li et al., 2015; Hotterbeekx et al., 2017; H. Li et al., 2017).

AI-2 is a set of (4*S*)-4,5-dihydroxy-2,3-pentanedione (*S*)-DPD derivatives that can rapidly convert to one another in solution (Stotani et al., 2019; Globisch et al., 2012). *S-ribosylhomocysteinase* (LuxS), which is found in more than 80 evolutionarily different bacterial species, may degrade *S-ribosylhomocysteine* (SRH) into adenine and (*S*)-DPD, the precursor of AI-2 (Lowery, Dickerson, and Janda, 2008; Zhu et al., 2013). Outside of the bacterial cytoplasmic membrane, linear (S)-DPD spontaneously rearranges into the cyclic isomers *S*-DHMF and *R*-DHMF. (Figure 1). Two cyclic tetrahydrated isomers, *S*-THMF and *R*-THMF, can be formed in the aqueous environment by hydration at C_3 (Figure 1). X-ray crystallography revealed that *S*-THMF (Wang et al., 2018; Medarametla et al., 2021), in the form of S-THMF-borate, binds to the periplasmic protein LuxP (Chen et al., 2002), thereby activating QS in *Vibrio harveyi*. When the extracellular medium has an adequate amount of AI-2 in enteric bacteria, R-THFM is imported via the LsrBACD transporter, and its linear form (i.e., *S*-THP) is phosphorylated by LsrK, a member of the FGGY family of carbohydrate kinases (Hooshangi and Bentley, 2011) Finally, LsrG and LsrF process the resultant S-THP-phosphate [phospho-DPD (P-DPD, Figure 1)], to end the AI-2 signaling cycle (Ha et al., 2018).

P-DPD can bind to LsrR and undo the suppression of the LuxS-regulated (Lsr) promoter, thereby increasing the expression level of the transporter and positively regulating the AI-2-induced QS (Xavier and Bassler, 2005; Xavier et al., 2007). LsrK is the only known kinase that can phosphorylate DPD, and AI-2-induced QS has been reported to be markedly less intense in LsrK deletion–deficient strains than in wild-type strains (Zhu et al., 2013). Thus, using selective LsrK inhibitors to suppress QS could represent a valuable strategy for obtaining new antibiotics.

As LsrK is a relatively new potential target, research on it is limited and mostly aided by computer-aided drug design. One type of LsrK inhibitor (such as compound 1, Figure 2) was identified through virtual screening using the LsrK homology model

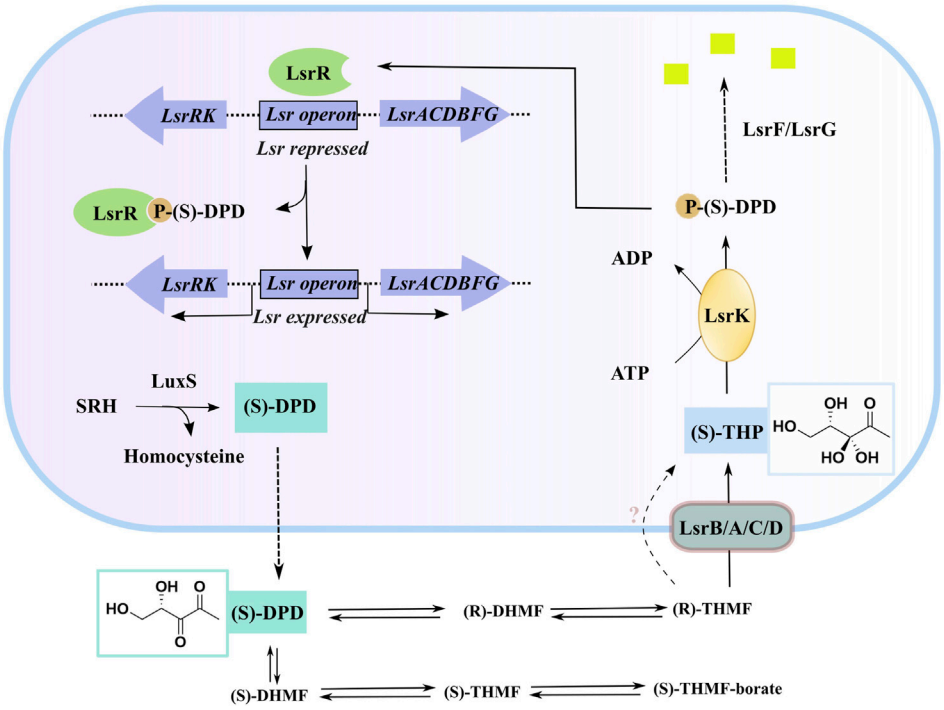

FIGURE 1
AI-2 mediated QS cascade—biosynthesis, transport, and degradation of AI-2 signal (Linciano et al., 2020). ("Equilibrium species of AI-2 in an aqueous environment" are shown in Supplementary Figure S1).

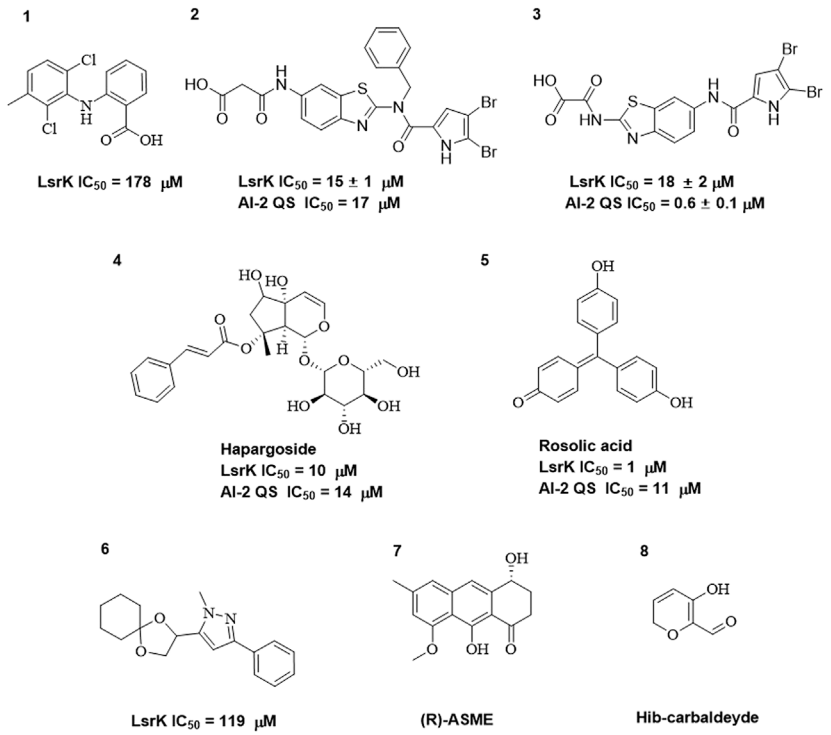

FIGURE 2
Chemical structure, LsrK inhibitory activity, and AI-2 QS inhibitory activity of the representative LsrK inhibitors.

(Medarametla et al., 2018). The homology model demonstrates good structural agreement with the recently reported crystal structure of LsrK. Medarametla used molecular dynamics simulations to provide details of structural flexibility of these structures and variations in binding-site volumes, which indicates the LsrK binding site can accommodate ligands of different sizes. This study contributed to structure-based drug design targeting LsrK and provides a foundation for further research on phosphorylation of the active site of LsrK.

A cell-based assay for identifying AI-2-mediated QSIs has been developed, and several hits (such as compounds 2 and 3, Figure 2) were discovered as ATP-competitive LsrK inhibitors (Gatta et al., 2020). Natural products (such as compound 4, harpagoside, compound 5, and rosolic acid, Figure 2) identified via high-throughput screening (Gatta et al., 2019), and compound 6 (Figure 2), designed using a structure-based approach (Stotani et al., 2019), were identified to have LsrK and AI-2 QS inhibitory activities. Recently, Listro et al. used tryptophan fluorescence spectroscopy as a simple and reliable analytical method to identify promising LsrK inhibitor candidates [such as compound 7, (*R*)-ASME, ((*R*)-(−)-aloesaponol III 8-methyl ether), and 8, Hib-carbaldehyde, Figure 2], which can suppress biofilm production (Listro et al., 2023).

Nevertheless, these reported ATP-competitive LsrK inhibitors have limitations such as poor activity, low ligand efficiency, and ambiguous structure–activity relationships (SARs). Therefore, it is necessary to find new active and druggable LsrK inhibitors to combat antibiotic resistance. In this study, we first identified key interactions between LsrK and ATP using MD simulations then performed *in silico* virtual screening of large-scale commercial compound libraries using a glide-based docking approach with constrained search criteria. Next, wet laboratory assays identified four compounds with novel structures and explicit binding modes to LsrK, which were suitable for optimization as leads for effective AI-2 QSIs.

2 Materials and methods

All chemicals were purchased from Sigma-Aldrich (St. Louis, MO, United States) unless otherwise stated. DPD was purchased from the SHANGHAI ZZBIO Co., LTD. (Shanghai, China). The Kinase-Glo Max Luminescent Kinase Assay Kit was purchased from Promega (Madison, WI, United States). NTA sensor chips were purchased from GE Healthcare (Chicago, IL, United States). All compounds used as potential inhibitors of LsrK were purchased from Topscience Biotechnology Co. Ltd. (Shanghai, China). The QS reporter strain WHQ02 (*E. coli* BL21 ΔTolC pWHQ01) was donated by Huiqi Wen (Institute of Microbiology and Epidemiology, Academy of Military Sciences, Beijing, China). The plasmid pWHQ01 was constructed by cloning the *lsr* promoter and the *lux*CDABE luminescent gene. *Bam*HI and *Xho*I were purchased from New England Biolabs (Ipswich, MA, United States). pET-28a was purchased from Novagen (Madison, WI, United States). *Escherichia coli* BL21 (DE3) cells were purchased from TransGen Biotech Co., LTD. (Beijing, China). A Ni-NTA column was purchased from Sangon Biotech (Shanghai, China). Sodium dodecyl sulfate-polyacrylamide gel electrophoresis (SDS-PAGE) and the Bradford Protein Assay Kit were purchased from Thermo Fisher Scientific (Waltham, MA, United States).

2.1 Molecular docking, molecular dynamics, and binding free energy calculation

2.1.1 Molecular docking

Three-dimensional conformations of the small molecules were generated using the LigPrep module (Schrödinger 2020.3). An OPLS3 force field was applied to produce low-energy conformers. Possible ionization states and tautomers were generated at pH 7.0 ± 2.0. The protein structure (PDB:5YA1) was prepared using Protein Preparation Wizard (Schrödinger 2020.3). Specifically, hydrogen atoms were added, the loop regions were refined, H-bond assignments were optimized, and restrained energy minimization (only the hydrogens) was then executed using the OPLS3 force field with default settings. Protein _chain_A (LsrK) and ATP were extracted from the protein complex for MD simulations. The receptor grid was generated using the Receptor Grid Generation module (Schrödinger 2020.3). The center of ATP (28.06(X), 26.37(Y), and 13.84(Z)) was designated as the grid center, and the grid box size was set to 1.2′, 1.2′, and 1.2 nm for x, y, and z, respectively.

2.1.2 Molecular dynamics simulations

All MD simulations were performed using GROMACS 2021.3 (Páll et al., 2020). The LsrK/ligand complexes were simulated using the AMBER ff99SB-ILDN force field (Lindorff-Larsen et al., 2010) for the protein and GAFF force field for the ligands. The programs Acpype (Sousa da Silva and Vranken, 2012) and Ambertools were used to generate the ligand topologies for GROMACS. The B3LYP-D3(BJ)/ma-TZVP level was used to derive the partial atomic charges of ligands using the restrained electrostatic potential (RESP) method using Multiwfn in the gas phase and the IEFPCM solvation model (water environment). The RESP2 (0.5) charges (Schauperl et al., 2020) used in the MD simulations were derived based on the RESP charges for both environments. The octahedron box dimensions for periodic boundary condition (while keeping a minimum distance from any atom to the boundary of the box at 1 nm) were calculated as 6.9 nm × 5.2 nm × 7.4 nm. The TIP4P water model was used to conduct MD simulations in explicit solvation condition. Sodium ions (Na^+) were added to the system for neutralization. The steepest descent algorithm was used for energy minimization, and the maximum force (Fmax) was set to not exceed 1,000 kJ/mol/nm. A Berendsen thermostat (Berendsen et al., 1984) and Parrinello-Rahman barostat (Parrinello and Rahman, 1981) were used for the temperature and pressure coupling, respectively. The system was equilibrated at 300 K and 1 bar using two consecutive 1,000 ps simulations with canonical NVT ensembles and isobaric NPT ensembles, respectively. MD simulations were then conducted under stable temperature and pressure conditions, with a 2 fs time step, LINCS algorithm for constraint handling, and a 1 nm cutoff for long-range interactions. After simulation completion, the GROMACS package was used to calculate the root-mean-square deviation (RMSD) and root-mean-square fluctuation (RMSF) relative to the crystal structure. To ensure the reliability and reproducibility of our results, we performed the experiment with

three independent replicates of MD simulations using the same parameters. Similar results were obtained for all the three replicates, indicating the robustness and stability of our simulations.

2.1.3 Estimation and decomposition of binding free energy by gmx_MMPBSA

The molecular mechanics/Poisson-Boltzmann surface area (MM/PBSA) in the gmx_MMPBSA tools (Valdés-Tresanco et al., 2021) was used to determine the thermodynamic stability of ligands inside the binding sites of the targets and to inspect the contribution of each residue in the binding pocket. In total, 100,000 frames of the LsrK/ATP complex were produced after equilibrium, and 20,000 frames for 200–400 ns were selected to calculate the binding energy and free energy decomposition. A total of 10,000 frames of LsrK/Y205-6768, LsrK/N025-0038, LsrK/D135-0149, and LsrK/3284-1358 complexes were produced after equilibrium, and 5,000 frames for 50–100 ns from each complex were selected to calculate the binding free energy and free energy decomposition, respectively. Default parameters were applied for all calculations.

2.1.4 MD trajectory clustering analysis and volume calculation of the hydrophobic allosteric pocket

The MD trajectories of the LsrK/Y205-6768, LsrK/N025-0038, LsrK/D135-0149, and LsrK/3284-1358 complexes from 50 to 100 ns were selected for clustering analysis. Clustering analysis was conducted using the Gromos algorithm based on the RMSD values of the ligands, and the cutoff value was set at 0.25. One cluster for each complex was generated and superimposed for visual inspection by PyMOL 2.5 (The PyMOL Molecular Graphics System, Version 2.5 Schrödinger, LLC.)

To better determine the volume changes in the allosteric hydrophobic pocket, the corresponding residue set was extracted with a radius of 1 nm, centered on the Glu 345 residue in the crystal structure, using PyMOL 2.5 software, and the volume of the pocket was calculated using SiteMap (Schrödinger 2020.3). For the conformation at 20 ns during MD simulation, the same residue set centered on the Glu 345 residue was extracted, and the volume of the pocket was calculated using SiteMap. The difference in volume between the two conformations provided a relative quantitative measure of the conformational changes in the hydrophobic pocket.

2.1.5 Virtual screening

The receptor grid was generated as described in Section 1.1. Nearly three million molecules from commercial compound libraries (Chemdiv and Enamine) were processed using the LigPrep module (Schrödinger suite) to develop the new compound 3D structure database described in Section 1.1.

According to the MD simulation of the LsrK/ATP complex, restrictions were introduced in the virtual screening to form at least one hydrogen bond with Arg 319, Arg 322, Lys 431, or Tyr 341 residues. The 3D structure database of newly generated compound was subjected to Glide VSW module (Schrödinger Suite) processing to obtain the initial hits. Glide-VSW is a hierarchical multi-precision docking protocol involving three levels of increasing docking precision: high-throughput virtual screening (HTVS), standard precision (SP), and extra precision (XP). The compounds were limited with an output score of the first 10% in each stage of HTVS and SP to the next round of docking, and the molecules with an output score of the first 10% in the XP stage were selected. Based on the XP Gscore, the top 400 molecules were selected and classified into 100 clusters by volume overlap. Compounds with hydrophobic groups that are likely to interact near the allosteric hydrophobic pocket were preferentially selected for visual inspection. Considering the structural diversity and ADME properties, 74 compounds were selected from the visually selected compounds and purchased for bioassay evaluation.

2.1.6 Molecular property prediction

The molecular properties of the four compounds were assessed using the Ligand-Based ADME of AMDE and Molecular Properties module (Schrödinger 2020.3). The values of MW, cLogP, and PSA were extracted as references for the lead-likeness of the compounds.

2.2 Biological assay

2.2.1 LsrK overexpression and purification

To express LsrK with a 6 × His-tag at the C-terminus, the LsrK encoding gene of *Salmonella typhimurium* was amplified using primers carrying restriction endonuclease sites *Bam*HI and *Xho*I. The amplified product was cloned into the expression vector pET-28a with a C-terminal 6 × His-tag and transfected into *E. coli* BL21 (DE3).

The transformed cells were selected on LB agar plates containing 50 μg/mL kanamycin. IPTG (0.5 mM) was added to induce protein synthesis. Then, the recombinant isolates were cultured at 37°C until mid-log exponential phase was reached. After overnight culturing, the cells were pelleted at 4°C 13,000 × *g* for 10 min, then resuspended in Lysis Buffer (50 mM NaH_2PO_4, 300 mM NaCl, pH 8.0), and sonicated on ice for 10 cycles with 30 s pulse and 30 s pause, and passed the supernatant through a 0.22 μm filter.

Then, the filtrate was loaded onto a Ni-NTA column, and proteins were eluted with 5 volumes of imidazole-containing buffer (50 mM NaH_2PO_4, 300 mM NaCl, 250 mM imidazole, pH 8.0) by way of a step gradient to recuperate the purified LsrK. The latter was then placed in a lysis buffer and dialyzing it overnight at 4°C using a 55 kDa molecular-mass-cutoff membrane bag. The molecular weight of lsrK was identified by utilizing sodium dodecyl sulfate 10% polyacrylamide gel electrophoresis (SDS-PAGE), followed by staining it with Coomassie blue. Subsequently, the Bradford Protein Assay Kit was used to quantify LsrK.

2.2.2 LsrK inhibition assay

This assay was performed as previously described (Gatta et al., 2019), and the conditions were optimized. The assay was carried out at a final concentration of 300 nM LsrK, 100 μM ATP, and 300 μM DPD in a reaction buffer (pH 7.4) containing 25 mM TEA, 800 μM $MgCl_2$, and 0.1 mg/mL BSA. 74 purchased compounds were dissolved in dimethyl sulfoxide (20% v/v DMSO in reaction buffer) at a concentration of 2 mM. Briefly, 10 μL DPD, 10 μL LsrK, and 5 μL compound were added to a 96-well plate, and 25 μL ATP or 25 μL reaction buffer was added after 30 min incubation. The plate was incubated for 10 min at 37°C, then 50 μL of kit reagent was added, and the plate was incubated at

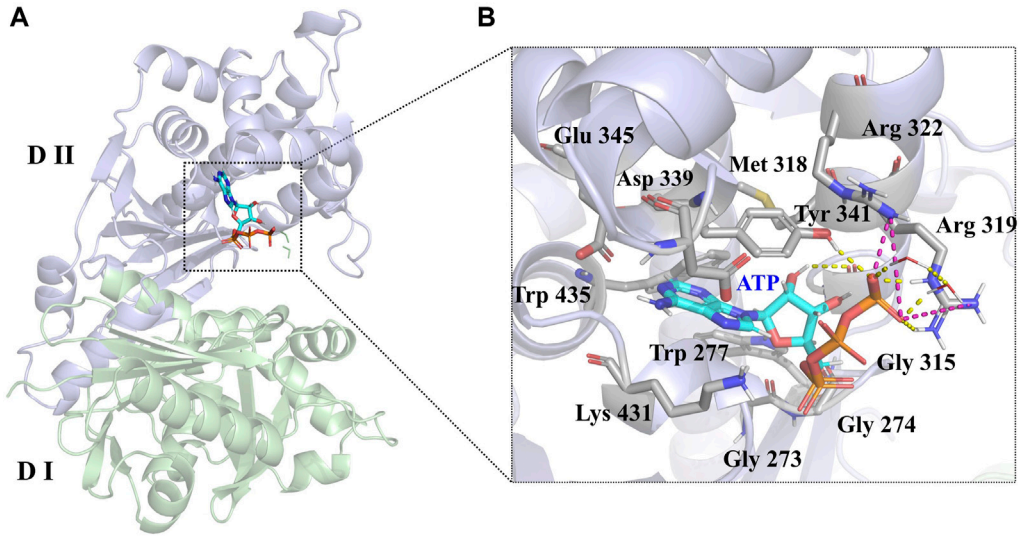

FIGURE 3
(A) Crystal structure of the LsrK/ATP complex (PDB: 5YA1). The two subunits of LsrK are shown as green cartoon (Domain I) and purple cartoon (Domain II). **(B)** A close-up of the interactions between ATP and LsrK (the involved residues are shown in gray stick). Key amino acid residues are represented in stick mode. Yellow dashed lines represent the hydrogen bonds, while purple dashed lines represent the salt bridges. Heteroatoms are color-coded (oxygen atoms in red, nitrogen atoms in dark blue, and phosphorus atoms in yellow).

37°C for 15 min. The luminescence signal was measured using an Enspire 2300 microplate reader (PerkinElmer). Dose-response tests were carried out to verify the activity of hits chosen by primary screening. (200 μM–6.25 μM) (Medarametla et al., 2018). The inhibition percentage of each tested compound was determined as previously described and IC_{50} was calculated using four logistic parameters.

2.2.3 Glycerol kinase inhibition assay

The nine compounds that had an IC_{50} < 100 μM were dissolved in DMSO at a final concentration of 100 μM. The assay was carried out as previously described (Medarametla et al., 2018) for LsrK using a reaction mixture including 0.3 U/mL glycerol kinase from *E. coli*, 100 μM ATP, and 300 μM glycerol.

2.2.4 SPR assay

His-tagged LsrK was immobilized in the NTA sensor chip (GE Healthcare) in Biacore 8 K using a running buffer consisting of 1 × PBS-T and 5% v/v DMSO. Serially diluted small molecules (concentration range: 50 to 1.56 μM) were injected. Intermediate concentration (12.5 μM) was set as a repeat, and 1 × PBS-T with 5% v/v DMSO was set as the control. The association time was set to 120 s; the dissociation time was set to 130 s; and the flow rate was set to 30 μL/min. The resulting data were fitted to the affinity binding model using Biacore Evaluation Software (GE Healthcare).

2.2.5 Cell-based AI-2-mediated QS interference assay

WHQ02 cultured overnight were diluted 1:100 in fresh LB supplemented with 100 μg/mL ampicillin and grown at 30°C and until the logarithmic phase (OD_{600} = 0.4–0.6). The bacterial culture was centrifuged at 4,000 × *g* for 5 min, and the pellet was resuspended in fresh LB medium to prepare a suspension of 2 McFarland standard and added to the 96-well plate. In the experimental group, 74 compounds (final concentrations ranging from 100 to 3.125 μM) were added to reach a total volume of 100 μL. In addition, 100 μL LB medium with an equal volume of DMSO (negative control) or 100 μL LB supplemented with 2% glucose and the same volume of DMSO (positive control) were added. Bacteria was cultured at 37°C with shaking for 3 h. The fluorescence intensity of WHQ02 is directly regulated by the *lsr* promoter, reflecting the strength of QS. The luminescence and OD_{600} were measured using an Enspire 2300 microplate reader (Perkin Elmer). To further study the effect of compounds on bacterial growth, overnight cultured WHQ02 was diluted 1:1,000 with LB medium and added to 96 well plate. Then, the compounds were added to a 96-well plate (final concentration: 100 μM) and diluted in a gradient. The same volume of DMSO was added to the control group. The plates were incubated at 37°C for 18 h. OD_{600} values were recorded using an Enspire 2300 microplate reader. The experiment was performed in triplicate.

3 Results and discussion

3.1 Analysis of LsrK/ATP complex and virtual screening

3.1.1 Analysis of LsrK/ATP dynamic interactions by MD simulation

LsrK consists of two domains (Figure 3A): an N-terminal domain (Domain I) and a C-terminal domain (Domain II). The ATP binding site consists of polar residues, such as Lys 341, Arg 319, and Arg 322, and a hydrophobic pocket composed of Tyr 341, Met 318, Trp 435, and Phe 394 residues. In the crystal structure (PDB:

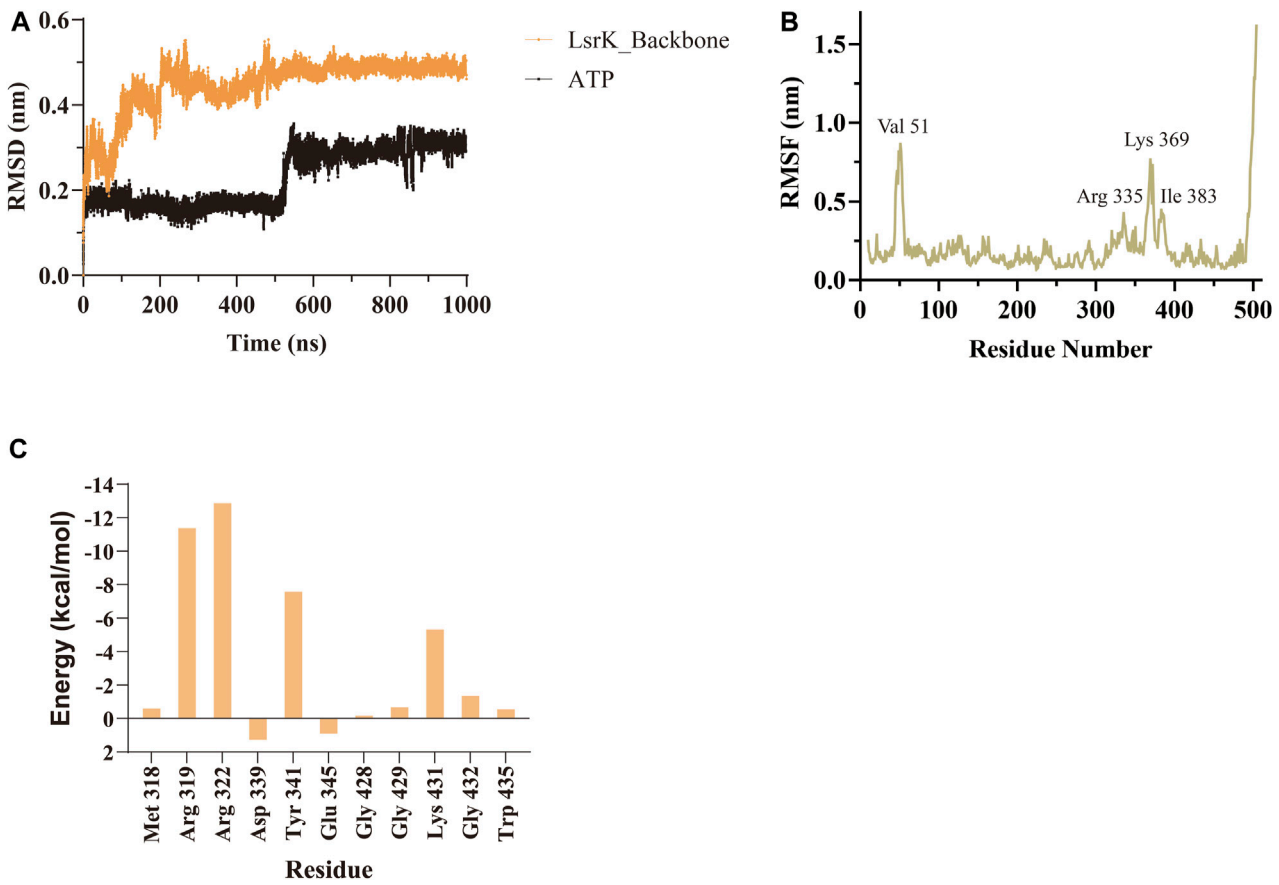

FIGURE 4
MD simulation results of LsrK/ATP complex. **(A)** RMSD values for LsrK backbone and ATP during 1000 ns MD simulations. **(B)** RMSF for the LsrK backbone residues during the 1000 ns simulation. **(C)** Calculated binding free energy and energy components of LsrK/ATP complex during 200–400 ns. ΔE_{vdw}: contribution of the van der Waals energy; ΔE_{ele}: contribution of the electrostatic energy; ΔE_{PB}: contribution of the polar solvation energies; ΔE_{nonPB}: contribution of the nonpolar solvation energies; ΔG_{gas}: contribution of $\Delta E_{vdw} + \Delta E_{ele}$; ΔG_{slov}: contribution of $\Delta E_{PB} + \Delta E_{nonPB}$; ΔG_{total}: the final estimated binding free energy of $\Delta G_{gas} + \Delta G_{slov}$.

5YA1), the phosphate group of ATPs is near the solvent region and forms hydrogen bonds with Arg 319, Arg 322, Tyr 431, and the two crystal water molecules. The phosphate group also forms salt bridges with Arg 319 and Arg 322 residues. The 4-hydroxyl group of ribose forms a hydrogen bond with the Gly 315 residue (Figure 3B). Unlike other kinases, the purine of ATP did not form hydrogen bonds with LsrK in this crystal structure, piquing our interest and prompting us to use an MD simulation approach to analyze the binding mode of LsrK to ATP and to investigate the key amino acid residues.

A 1,000 ns MD simulation of the LsrK/ATP complex was performed using GROMACS 2021.3. The trajectory data of the production simulations were used to calculate the RMSD and RMSF. The RMSD values of proteins and ligands are important parameters for assessing the stability of the interactions between proteins and ligands during MD simulations. The RMSD values of the LsrK backbone demonstrated that LsrK underwent large conformational changes during the first 200 ns of MD simulation, while the conformations were relatively stable during the last 800 ns of MD simulation (Figure 4A). The RMSD values of ATP over time revealed drastic conformational changes at approximately 550 ns in the MD simulation (Figure 4A). The stability of each amino acid residue during the simulation was observed from the RMSF values. The RMSF plot showed that the conformational variability of residues in the ATP binding site, mainly located within the range of residue numbers 300–400, was significant (Figure 4B). The results indicated that the LsrK/ATP complex was not very stable during the simulation. In particular, the conformation of ATP and the amino acid residues of the ATP binding site underwent significant changes, and there were two different binding modes between ATP and LsrK according to the drastic change in ATP RMSD values during MD simulations.

To gain a more comprehensive understanding of the conformational change process, we extracted a total of 201 averaged structures from MD simulated trajectories at 5 ns intervals and verified them by visual inspection. The process of the ATP phosphate group extending to the binding pocket of the assumed substrate (DPD) was completed by a clockwise rotation of the entire C-terminal lobe and the continuous conformational changes of the Tyr 341 residue and three key basic residues, Lys 431, Arg 319, and Arg 322 (Figure 5A). The conformational fluctuation of ATP was mainly caused by the phosphate group extending to the presumed substrate (DPD) binding site. Interestingly, a

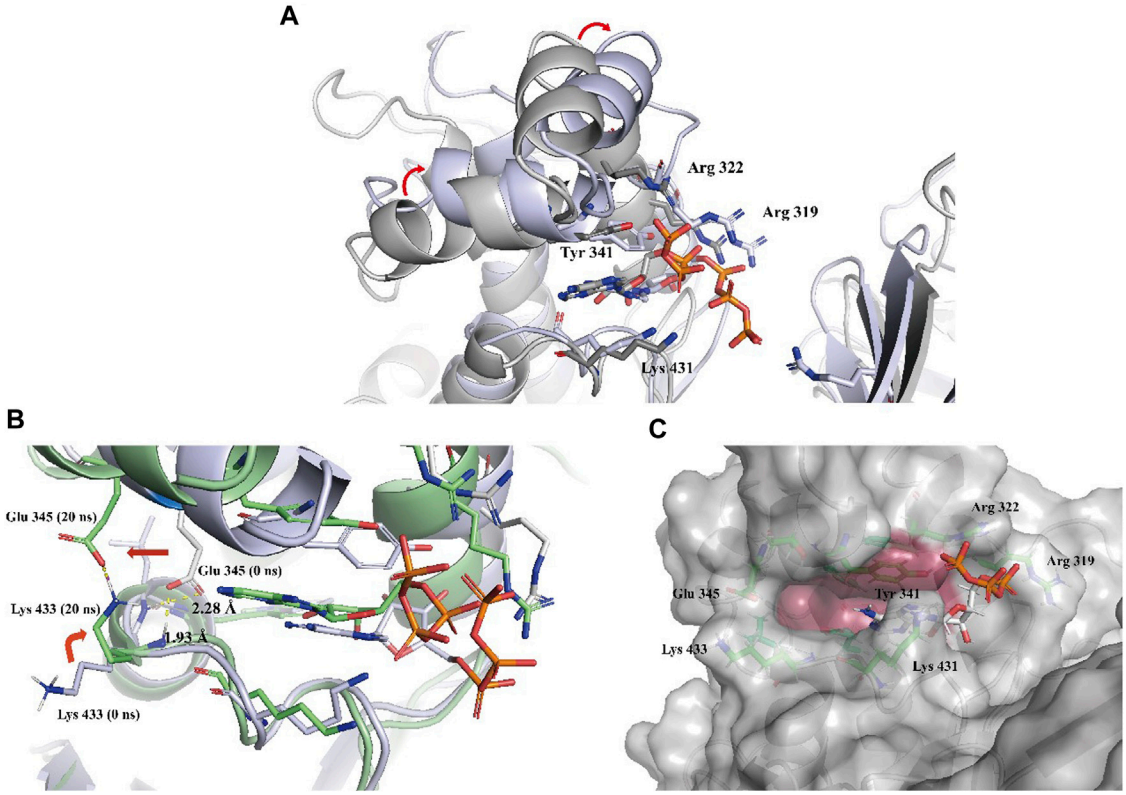

FIGURE 5
(A) Two representative conformations at 0 ns (the cartoon and C atoms of LsrK are in gray) and 850 ns (the cartoon and C atoms of LsrK are in purple) were selected to demonstrate the obvious conformational changes of the ATP binding site. **(B)** Conformational changes of Glu 345 and Lys 433 residues at 0 ns (the cartoon and C atoms of LsrK are in purple) and 20 ns (the cartoon and C atoms of LsrK are shown in green). **(C)**. Surface model of LsrK at 20 ns in the MD simulation. The surface of allosteric hydrophobic pocket residues is depicted in dark red.

conformational change in the hydrophobic pocket near the purine-binding site was observed during the MD simulation, which was significantly different from the crystal structure (Figure 5B). In the crystal structure, the side chain of the Glu 345 residue formed two hydrogen bonds with the main chain amide groups of Leu 434 and Trp 435 residues, with distances of 0.23 nm and 0.19 nm, respectively. Multiple MD simulations consistently showed that the deflection of the Glu 345 residue led to an increase in the volume of the hydrophobic pocket. Compared with the volume of the hydrophobic pocket in the crystal structure (0.119 nm^3), that of the hydrophobic pocket after the conformational change increased by approximately 0.5-fold (0.179 nm^3, Figure 5C). We believe that this potential conformational hydrophobic pocket is important for inhibitor design and could provide additional interaction sites for inhibitors to increase their affinity for LsrK.

Binding free energy calculations were used to analyze the affinity between ATP and LsrK, and free energy decomposition was used to analyze the hot amino acid residues that participate in ATP binding and induce conformational transformation of the ATP binding site. The binding free energy and free energy decomposition of each residue were calculated by selecting the stable binding period between ATP and LsrK (200–400 ns). The calculated binding free energy (ΔG_{total}) was −40.86 ± 8.54 kcal/mol. The free energy decomposition results showed that residues Arg 319, Arg 322, Tyr341, and Lys431 made significant contributions to the binding free energy (Figure 4C).

In summary, the MD simulations provided us with two valuable pieces of information: (1) four amino acid residues, Tyr 341, Lys 431, Arg 319, and Arg 322, play an important role in maintaining the stable binding of ATP to LsrK, and (2) an allosteric hydrophobic pocket larger than that in the crystal structure can be generated near the ATP binding site of LsrK. This information is beneficial for the discovery and design of LsrK inhibitors.

3.1.2 Structure-based virtual screening

Commercial compound libraries containing Chemdiv and Enamine, a total of approximately 3 million compounds, were processed and subjected to Glide-VSW module (Schrödinger suite) processing to obtain the initial hits. To improve the hit rate of virtual screening, a constraint search condition was added to form at least one hydrogen bond with the four key residues Arg319, Arg322, Tyr 341, and Lys 431. The presence of a potential allosteric hydrophobic pocket near the purine binding site is critical for the discovery of novel inhibitors, as it provides additional interaction sites for inhibitors for improving affinity. However, considering that the residue conformations of this allosteric site are very flexible, it would be risky to arbitrarily select a conformation obtained by MD simulation for virtual screening; therefore, we

TABLE 1 The IC_{50} values for the 12 positive hits tested against LsrK inhibition assay and cell-based AI-2 QS interference assay. Hits were tested at 200 μM with 100 μM ATP against LsrK inhibition assay. [A] Hits tested at 50 μM ATP against LsrK inhibition assay. [B] 100 μM ATP. [C] 150 μM ATP. [D] IC50 values for hits tested against cell-based QS interference assay. "N/A" means not applicable. IC50 values are represented as means ± SD of three independent experiments (n = 3).

Compound ID	Chemical structure	Inhibition (%)	IC50A (μM)	IC50B(μM)	IC50C(μM)	IC50D (μM)
Y205-6768	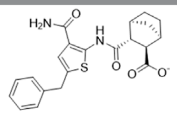	101.02 ± 8.39	8.73 ± 0.50	16.85 ± 0.76	26.05 ± 1.32	11.28 ± 0.70
3284–1358	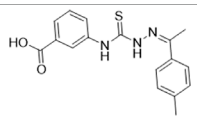	101.06 ± 3.82	29.89 ± 1.95	41.85 ± 2.57	88.09 ± 3.89	37.79 ± 3.18
Y204-6349	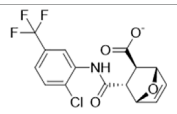	87.41 ± 2.60	N/A	75.14 ± 1.19	N/A	>100
D135-0149	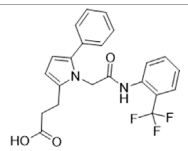	83.93 ± 6.33	21.80 ± 1.48	33.46 ± 2.52	80.10 ± 4.83	22.06 ± 1.66
N025-0038	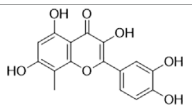	80.51 ± 2.31	26.64 ± 1.22	43.70 ± 4.31	67.98 ± 1.27	12.46 ± 0.99
3284–0335	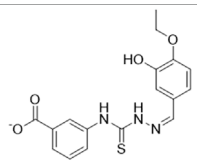	67.59 ± 4.88	N/A	84.86 ± 7.73	N/A	>100
2188–1861	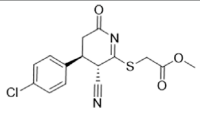	92.06 ± 6.68	N/A	128.76 ± 6.85	N/A	38.40 ± 3.35
5617–0915	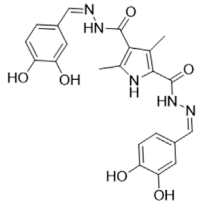	71.53 ± 4.33	N/A	79.42 ± 4.55	N/A	>100
Y040-9027	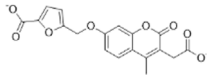	94.11 ± 6.72	N/A	90.04 ± 5.18	N/A	>100
3681–1274	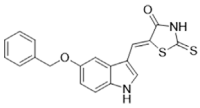	66.25 ± 3.54	N/A	133.20 ± 8.85	N/A	42.20 ± 2.15

(Continued on following page)

TABLE 1 (*Continued*) The IC_{50} values for the 12 positive hits tested against LsrK inhibition assay and cell-based AI-2 QS interference assay. Hits were tested at 200 μM with 100 μM ATP against LsrK inhibition assay. [A] Hits tested at 50 μM ATP against LsrK inhibition assay. [B] 100 μM ATP. [C] 150 μM ATP. [D] IC50 values for hits tested against cell-based QS interference assay. "N/A" means not applicable. IC50 values are represented as means ± SD of three independent experiments (n = 3).

Compound ID	Chemical structure	Inhibition (%)	IC50A (μM)	IC50B(μM)	IC50C(μM)	IC50D (μM)
4515–0182	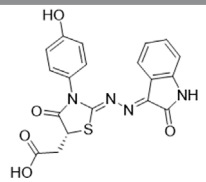	83.72 ± 9.63	N/A	52.06 ± 2.68	N/A	>100
Y502-2013	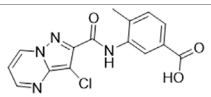	69.09 ± 8.64	N/A	139.91 ± 5.54	N/A	>100

conservatively selected the LsrK conformation in the crystal structure (PDB) for virtual screening. However, in visual inspection, we focused on compounds with hydrophobic groups near the hydrophobic pocket to identify compounds that may interact with this site.

VSW performed screening with different precision in three stages: HTVS precision, SP, and extra precision (XP) screening. The top 10% of the compounds in each stage were selected for subsequent screening. Total 3,872 compounds passed extra precision screening, and the top 400 compounds with XP G-score value below −6.5 kcal/mol were divided into 100 clusters based on the volume overlap by ligand clustering module (Schrödinger 2020–3). Compounds with hydrophobic groups near the allosteric hydrophobic pocket were selected for visual inspection. Considering the hydrophobic interactions with the allosteric hydrophobic pocket and the binding diversity with LsrK and ADME properties, 74 commercially available compounds were shortlisted from the visually selected compounds and purchased for wet laboratory assays (Supplementary Table S1).

3.2 Biochemical assays

3.2.1 LsrK inhibition assay

The 74 compounds were used in the LsrK inhibition assay at a final concentration of 200 μM with 100 μM ATP (Supplementary Table S1). [43,44] Twelve hits with inhibition levels above 60% were tested in a dose-response assay to determine their IC_{50} values (Table 1). Among these, four hits had IC_{50} values below 50 μM (Figure 6). Compound Y205-6768 had the highest inhibitory activity, with IC_{50} of 16.85 ± 0.76 μM, compounds 3284–1358, N025-0038, and D135-0149 also had good LsrK inhibition activities, with IC_{50} of 41.85 ± 2.57 μM, 43.70 ± 4.31 μM, and 33.46 ± 2.52 μM, respectively. The four hits with IC_{50} values below 50 μM were classified as ATP competitive inhibitors by measuring their IC_{50} values at different ATP concentrations (50, 100, and 150 μM). Considering that both glycerol kinase and LsrK belong to the FGGY family, glycerol kinase inhibition assays were performed to preliminarily verify the selectivity of the nine compounds with IC_{50} < 100 μM, and none showed obvious inhibition against glycerol kinase at 100 μM (results not shown).

3.2.2 Cell-based AI-2-mediated QS interference assay

The 12 hits showing >60% LsrK inhibition were tested for QS inhibition using cell-based AI-2-mediated QS interference assay, as previously described Baba et al., 2006). To ensure that lower luminescence was the result of QS inhibition not the chemical toxicity or antibacterial activity, strain growth inhibition was assessed concurrently. Since AI-2 QS mainly occurs at the end of the logarithmic bacterial growth and the bacteria count is stable, dosing at that time does not reflect the inhibitory effect of the compound on bacterial growth. Therefore, a parallel experiment to test the MIC of compounds at a low bacterial density was conducted, indirectly reflecting the potential growth inhibition to avoid false positives. Six compounds (Y205-6768, 3284–1358, D135–0149, N025-0038, 2188–1861, and 3681–1274), exhibited significant QS inhibitory activities (Figure 7 and Supplementary Figure S3), and three hits (Y205-6768, D135-0149, and 3284–1358) exhibited maximum growth inhibition (<40%) and maximum AI-2 QS inhibition (>80%) (Figure 7). Notably N025-0038 exhibited AI-2 QS inhibition at sub-minimum inhibitory concentrations (sub-MIC, Figure 7).

3.2.3 SPR assay

SPR assays were performed to further investigate the specific binding between active compounds and LsrK. Two compounds (Y205-6768 and N025-0038) with significant LsrK inhibitory effects were selected as the representative compounds for this assay. Considering that LsrK is easy to inactivate in the LsrK inhibition assay, the SPR assay was performed with the NTA chip rather than with the CM5 chip. The assay results demonstrated that Y205-6768 and N025-0038 exhibited LsrK specific binding, and the KD values were 8.49×10^{-6} M and 3.03×10^{-5} M, respectively (Figure 8). Although the KD values of Y205-6768 were close to those of N025-0038, the combination and dissociation curve of Y205-6768 had a more obvious trend of slow combination and dissociation compared to N025-0038.

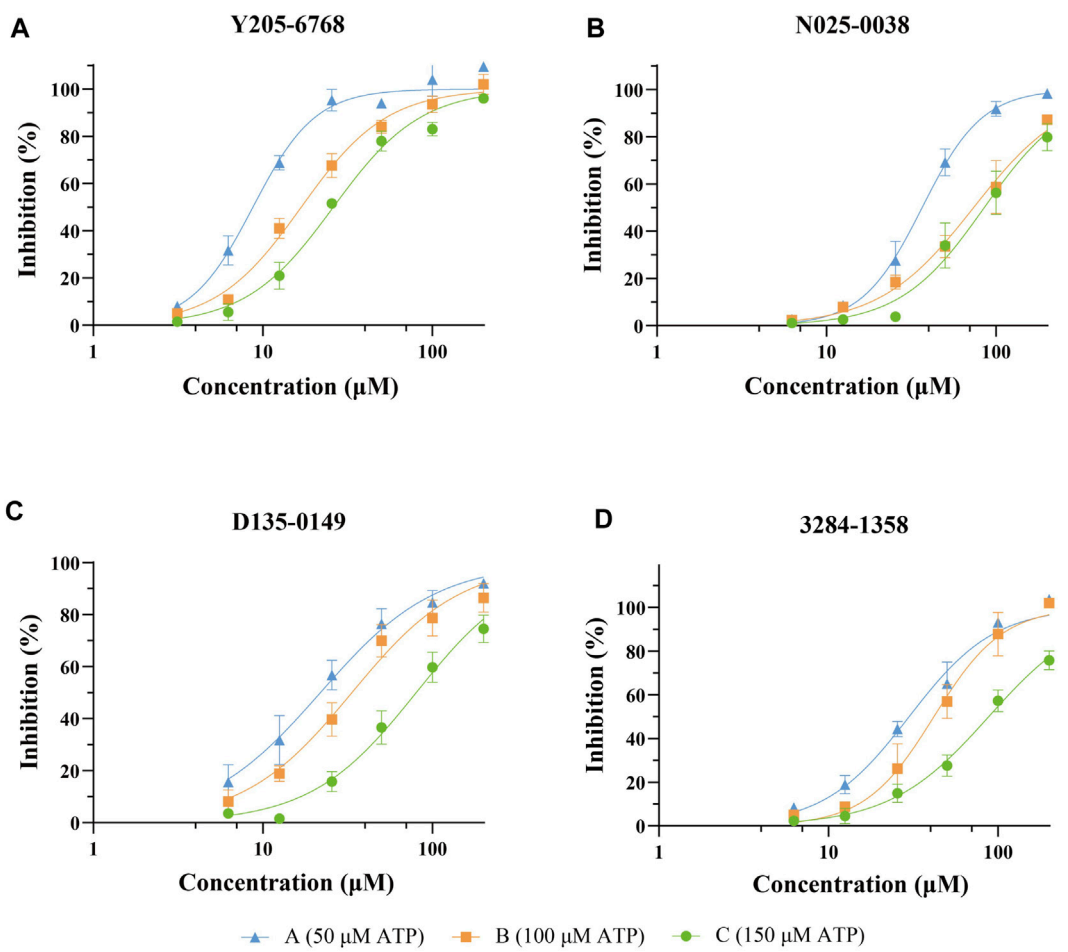

FIGURE 6
Dose-response curves against LsrK inhibition assay for compounds Y205-6768 **(A)**, N025-0038 **(B)**, D135-0149 **(C)**, and 3284–1358 **(D)** at different ATP (50, 100, and 150 μM). Data points are represented as the mean ± SD of three independent experiments (n = 3).

3.3 Binding mode analysis and SAR exploration of hit compounds

Considering the flexibility of the ATP binding pocket and the existence of an allosteric hydrophobic pocket, molecular docking based on the LsrK/ATP crystal structure could not accurately predict the LsrK binding modes of these hits. Therefore, the MD simulation approach was used to determine the most likely structure of LsrK in complex with the four compounds (N025-0038, Y205-6768, D135-0149, and 3284–1358) with the highest QS inhibitory activities. Specifically, considering the docking results of these four compounds under XP precision in virtual screening as the initial conformation of MD simulation, 100 ns MD simulations was carried out for these four protein-ligand complexes. The representative conformations obtained by cluster analysis of 100 ns MD simulated trajectories were considered the most likely conformations of our LsrK-bound compounds.

The protein backbones did not fluctuate much during the 100 ns MD simulations, indicating that the protein, as a whole, was in equilibrium (Figure 9A). Furthermore, the conformations of N025-0038, Y205-6768, and D135-0149 were relatively stable, and the conformation of 3284–1358 fluctuated greatly (Figure 9B); however, there was no major change overall. The calculated binding free energies of Y205–6768, N025-0038, D135-0149, and 3284–1358 were −26.62 ± 8.64, −22.29 ± 5.64, −25.41 ± 7.07, and −18.29 ± 4.83 kcal/mol, respectively, which were consistent with the bioassay results. These results indicate that these four compounds (N025-0038, Y205-6768, D135-0149, and 3284–1358) can form stable complexes with LsrK.

According to the representative conformations of the four complexes in the MD simulation (Figures 9C–E, and F), all four compounds occupied the allosteric hydrophobic pocket via benzene rings, with or without substituent groups, which was not observed in the molecular docking results. Inhibitors (Gatta et al., 2020) with additional benzene rings exhibited higher LsrK inhibitory activities in the LsrK inhibition assay, which cannot be well explained by molecular docking. In the representative conformation, Y205-6768 formed hydrogen bonds or salt bridges with Gly 315, Tyr 341, and Arg 322. D135-0149 formed hydrogen bonds or salt bridges with Lys 431 and Arg 322; whereas 3284–1358 formed hydrogen bonds with Gly 315 and Arg 319. These findings confirm the importance of hydrogen bonds and salt

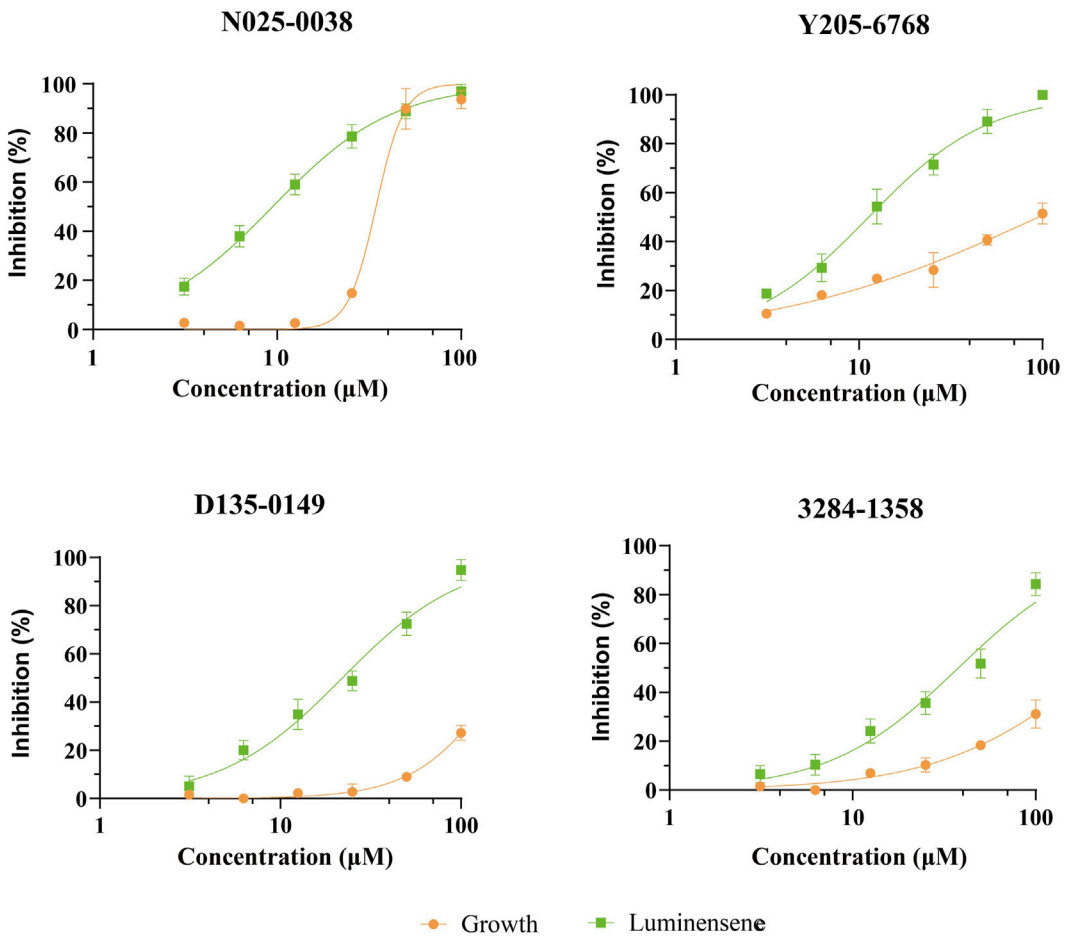

FIGURE 7
The QS inhibition and growth inhibition of N025-0038, Y205-6768, D135-0149, and 3681–1274 with concentrations ranging from 100 μM to 3.13 μM. The green and yellow curves represent the luminescence inhibition and the growth inhibition, respectively. Data points are represented as the mean ± SD of three independent experiments (n = 3).

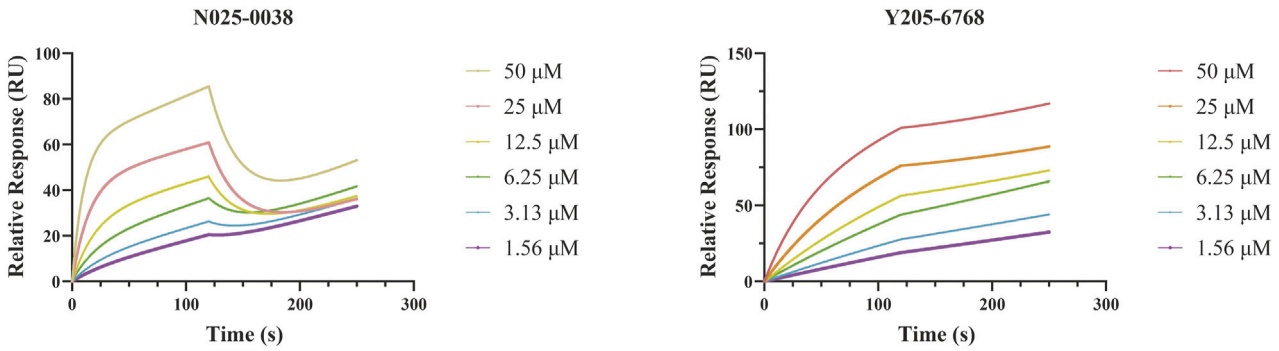

FIGURE 8
SPR Analysis of N025-0038 and Y205-6768. The graph depicts the binding curve (0–120 s) and dissociation curve (120–250 s) of the compounds used in concentrations ranging from 50 to 1.56 μM.

bridges with key basic amino acid residues, such as Gly 315, Tyr 341, Arg 322, and Arg 319. This information is valuable for designing novel LsrK inhibitors in the future.

The rule of five (RO5; molecular weight <500 (MW), logP <5 (milog), hydrogen bond acceptors <10, hydrogen bond donors <5, and rotatable bonds) is a rule of thumb to

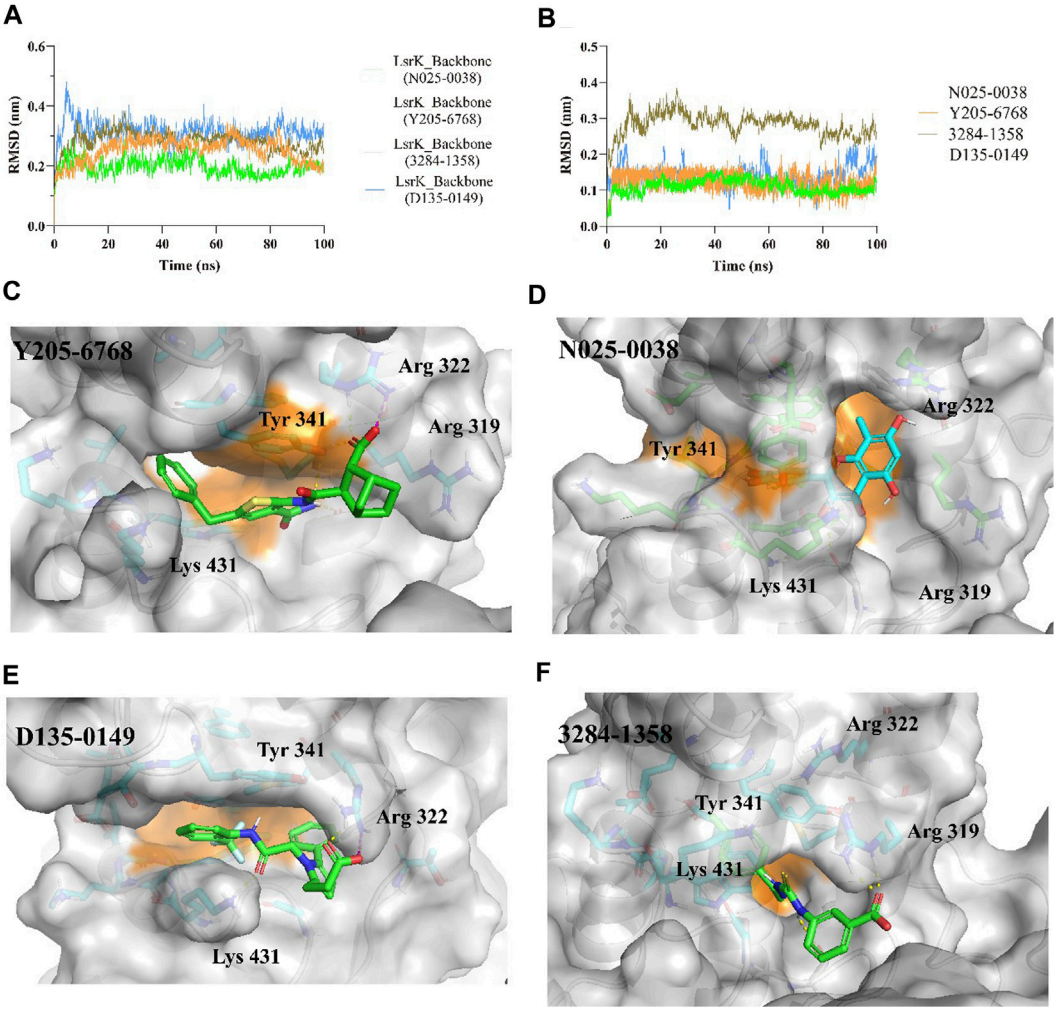

FIGURE 9
MD simulation results of LsrK/Y205-6768, LsrK/N025-0038, LsrK/D135-0149, and LsrK/3284–1358 complexes. **(A)** RMSD values *versus* time for LsrK backbone in four complexes during 100 ns MD simulations. **(B)** RMSD values *versus* time for N025-0038, Y205-6768, D135-0149, and 3284–1358 in four complexes during 100 ns MD simulations. **(C)** Representative conformation of LsrK/Y205-6768 complex. **(D)** Representative conformation of LsrK/N025-0038 complex. **(E)** Representative conformation of LsrK/D135-0149 complex. **(F)** Representative conformation of LsrK/3284–1358 complex. In the representative conformation, the key residues are depicted as sticks and C atoms are in blue. The surface of the residues in the allosteric hydrophobic pocket is depicted in orange.

TABLE 2 Chemical and physical properties of the 4 active compounds.

Compound ID	MW[a]	PSA[a]	cLogP	HBD[a] count	HBA[a] count	RB[a] count	Lipinski #violations
Y205-6768	327.40	88.73	3.33	4	6	5	0
N025-0038	420.43	71.34	3.85	5	7	6	0
D135-0149	404.52	106.97	0.83	2	6	9	0
3284–1358	316.27	140.32	0.71	2	4	4	0

[a]PSA, polar surface area; MW, molecular weight; HBA, H-bond acceptor; HBD, H-bond donor; RB, rotatable bond; cLogP, calculated LogP.

evaluate drug likeness. When these rules are not violated, it means that the compound has better druggability. In this study, all four compounds were found to follow Lipinski's rule of five (Table 2). Furthermore, these four compounds were found to possess novel structures, low molecular weights, favorable biological activities, and high affinities for LsrK, making them suitable lead compounds for the development of novel LsrK inhibitors.

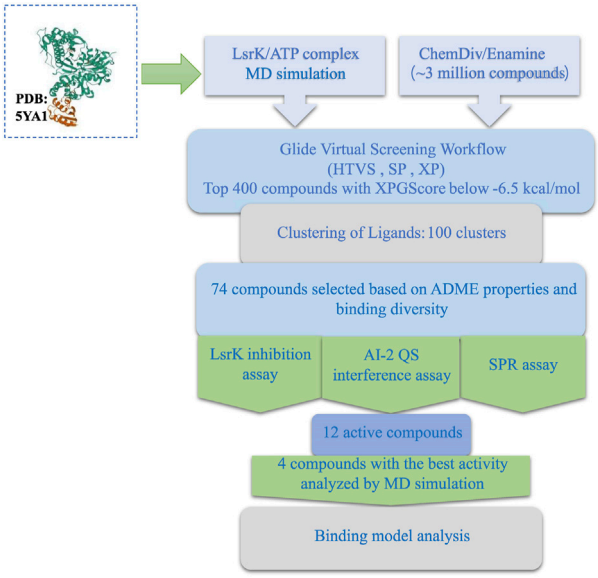

FIGURE 10
Stepwise flow diagram of the present work.

4 Conclusion

In this study, we developed a workflow for the virtual screening and bioassay-based evaluation of AI-2 QSIs against ATP binding site of LsrK. A stepwise flow diagram of the present work is illustrated in Figure 10.

We first analyzed the binding mode of ATP and LsrK by 1,000 ns MD simulations and obtained two valuable pieces of information: (1) Four amino acid residues (Arg 319, Arg 322, Tyr 341, and Lys 431) play an important role in maintaining a stable binding of ATP and LsrK; (2) Near the purine-binding site of LsrK, a significantly enlarged allosteric hydrophobic pocket, relative to that in the original crystal structure, was found, which can be occupied by small-molecule compounds.

In the following Glide-based virtual screening, we introduced the constraint of forming at least one hydrogen bond with these four key residues. Simultaneously, compounds with hydrophobic groups that are likely to interact near the allosteric hydrophobic pocket are preferred when performing a visual inspection. Considering the ligand efficiency, structural diversity, and ADME properties, 74 compounds were selected for wet laboratory assays. Twelve of the 74 purchased compounds inhibited the LsrK function, and six of these 12 compounds exhibited QS inhibition, with three of them (Y205-6768, D135-0149, and 3284–1358) exhibiting >80% QS inhibition% and <40% growth inhibition, while N025-0038 exhibited QS inhibition at sub-MIC concentrations. Our results confirmed that these AI-2 QSIs inhibited QS by specifically binding to the LsrK ATP-binding site and inhibiting LsrK phosphorylation. In addition, they have favorable characteristics such as a novel structure, low molecular weight, good biological activities, and druggability, and they are suitable as lead compounds for the development of new LsrK inhibitors, although partial compounds exhibited growth-inhibitory effects on bacteria. Binding mode analysis based on MD simulations confirmed the importance of the formation of hydrogen bonds and salt bridges with key basic amino acid residues and filling the allosteric hydrophobic pocket near the purine-binding site for LsrK inhibitors targeting the LsrK ATP-binding site. Our work provides a valuable reference for discovering QS inhibitors that are non-toxic and do not inhibit bacterial growth, thereby avoiding the emergence of drug resistance.

Data availability statement

The original contributions presented in the study are included in the article/Supplementary Material, further inquiries can be directed to the corresponding authors.

Author contributions

QS gathered the research materials and designed the study. QS performed the LsrK inhibition experiment using structure-based virtual screening. YX completed the dynamic simulation computation. QH completed the QS inhibition experiment. XZ, JZ, YL, and QM contributed to completing the experiments. QS, HW, and YC performed data analysis and manuscript drafting. FY, XL, and JX supplied funding support and experimental direction, and performed manuscript revision. All authors contributed to the article and approved the submitted version.

Acknowledgments

We thank Feng Lin (School of Life Sciences, Jilin University, Changchun, China) for her assistance with the design of the method. We also thank Guo Lei (State Key Laboratory of Toxicology and Medical Countermeasures, and Laboratory of Toxicant Analysis, Institute of Pharmacology and Toxicology, Academy of Military Medical Sciences, Beijing, China) for her guidance and assistance with the SPR assay.

Conflict of interest

The authors declare that the research was conducted in the absence of any commercial or financial relationships that could be construed as a potential conflict of interest.

Publisher's note

All claims expressed in this article are solely those of the authors and do not necessarily represent those of their affiliated organizations, or those of the publisher, the editors and the reviewers. Any product that may be evaluated in this article, or claim that may be made by its manufacturer, is not guaranteed or endorsed by the publisher.

Supplementary material

The Supplementary Material for this article can be found online at: https://www.frontiersin.org/articles/10.3389/fchem.2023.1185224/full#supplementary-material

References

Antunes, L. C. M., Ferreira, R. B. R., Buckner, M. M. C., and Brett Finlay, B. (2010). Quorum sensing in bacterial virulence. *Microbiology* 156 (8), 2271–2282. doi:10.1099/mic.0.038794-0

Baba, T., Ara, T., Hasegawa, M., Takai, Y., Okumura, Y., Baba, M., et al. (2006). Construction of Escherichia coli K-12 in-frame, single-gene knockout mutants: The keio collection. *Mol. Syst. Biol.* 2. doi:10.1038/msb4100050

Bansal, T., Jesudhasan, P., Pillai, S., Thomas, K., Jayaraman, A., and Jayaraman, A. (2008). Temporal regulation of enterohemorrhagic Escherichia coli virulence mediated by autoinducer-2. *Appl. Microbiol. Biotechnol.* 78 (5), 811–819. doi:10.1007/s00253-008-1359-8

Barber, C. E., Tang, J. L., Feng, J. X., Pan, M. Q., Wilson, T. J. G., Slater, H., et al. (1997). A novel regulatory system required for pathogenicity of xanthomonas campestris is mediated by a small diffusible signal molecule. *Mol. Microbiol.* 24 (3), 555–566. doi:10.1046/j.1365-2958.1997.3721736.x

Berendsen, H. J. C., Postma, J. P. M., van Gunsteren, W. F., DiNola, A., and Haak, J. R. (1984). Molecular dynamics with coupling to an external bath. *J. Chem. Phys.* 81 (8), 3684–3690. doi:10.1063/1.448118

Chen, X., Schauder, S., Potier, N., Van Dorsselaer, A., Pelczer, I., Bassler, B. L., et al. (2002). Structural identification of a bacterial quorum-sensing signal containing boron. *Nature* 415 (6871), 545–549. doi:10.1038/415545a

Dandela, R., Mantin, D., Cravatt, B. F., Rayo, J., and MichaelMeijler, M. (2018). Proteome-wide mapping of PQS-interacting proteins in *Pseudomonas aeruginosa*. *Chem. Sci.* 9 (8), 2290–2294. doi:10.1039/C7SC04287F

Duan, K., Dammel, C., Stein, J., Harvey, R., and MichaelSurette, G. (2003). Modulation of Pseudomonas aeruginosa gene expression by host microflora through interspecies communication. *Mol. Microbiol.* 50 (5), 1477–1491. doi:10.1046/j.1365-2958.2003.03803.x

Eickhoff, M. J., and Bassler, B. L. (2018). SnapShot: Bacterial quorum sensing. *Cell* 174 (5), 1328–1328.e1. doi:10.1016/j.cell.2018.08.003

Federle, M. J., and Bassler, B. L. (2003). Interspecies communication in bacteria. *J. Clin. Investigation* 112 (9), 1291–1299. doi:10.1172/JCI20195

Gatta, V., Ilina, P., Porter, A., McElroy, S., and Tammela, P. . (2019). Targeting quorum sensing: High-throughput screening to identify novel LsrK inhibitors. *Int. J. Mol. Sci.* 20 (12), 3112. doi:10.3390/ijms20123112

Gatta, V., Tomašič, T., Ilaš, J., Zidar, N., Mašič, L. P., Barančoková, M., et al. (2020). A new cell-based AI-2-mediated quorum sensing interference assay in screening of LsrK-targeted inhibitors. *ChemBioChem* 21 (13), 1918–1922. doi:10.1002/cbic.201900773

Globisch, D., Lowery, C. A., McCague, K. C., and Janda, K. D. (2012). Uncharacterized 4,5-dihydroxy-2,3-pentanedione (DPD) molecules revealed through NMR spectroscopy: Implications for a greater signaling diversity in bacterial species. *Angew. Chem.* 124 (17), 4280–4284. doi:10.1002/ange.201109149

Grillo-Puertas, M., Villegas, J. M., Rintoul, M. R., and Rapisarda, V. A. (2012). Polyphosphate degradation in stationary phase triggers biofilm formation via LuxS quorum sensing system in *Escherichia coli*. *PLoS ONE* 7 (11), e50368. doi:10.1371/journal.pone.0050368

Gu, Y., Wu, J., Tian, J., Li, L., Zhang, B., Zhang, Y., et al. (2020). Effects of exogenous synthetic autoinducer-2 on physiological behaviors and proteome of lactic acid bacteria. *ACS Omega* 5 (3), 1326–1335. doi:10.1021/acsomega.9b01021

Ha, J.-H., Hauk, P., Cho, K., Eo, Y., Ma, X., Stephens, K., et al. (2018). Evidence of link between quorum sensing and sugar metabolism in Escherichia coli revealed via cocrystal structures of LsrK and HPr. *Sci. Adv.* 4 (6), eaar7063. doi:10.1126/sciadv.aar7063

He, Ya-W., Deng, Y., Miao, Y., Chatterjee, S., Tran, T. M., Tian, J., et al. (2022). DSF-family quorum sensing signal-mediated intraspecies, interspecies, and inter-kingdom communication. *Trends Microbiol.*, 31, 36–50. doi:10.1016/j.tim.2022.07.006

Hodgkinson, J. T., Gross, J., Ysobel, R., Baker, D. R. S., and Welch, M. (2016). A new Pseudomonas quinolone signal (PQS) binding partner: MexG. *Chem. Sci.* 7 (4), 2553–2562. doi:10.1039/C5SC04197J

Hooshangi, S., and Bentley, W. E. (2011). LsrR quorum sensing "switch" is revealed by a bottom-up approach. *PLoS Comput. Biol.* 7 (9), e1002172. doi:10.1371/journal.pcbi.1002172

Hotterbeekx, A., Kumar-Singh, S., Goossens, H., and Malhotra-Kumar, S. (2017). *In vivo* and *in vitro* interactions between Pseudomonas aeruginosa and Staphylococcus spp. *Front. Cell. Infect. Microbiol.* 7. doi:10.3389/fcimb.2017.00106

Hur, J., Jang, J., and Sim, J. (2021). A review of the pharmacological activities and recent synthetic advances of γ-butyrolactones. *Int. J. Mol. Sci.* 22 (5), 2769. doi:10.3390/ijms22052769

Laganenka, L., Colin, R., and Sourjik, V. (2016). Correction: Corrigendum: Chemotaxis towards autoinducer 2 mediates autoaggregation in Escherichia coli. *Nat. Commun.* 7 (1), 13979. doi:10.1038/ncomms13979

Laganenka, L., and Sourjik, V. (2018). Autoinducer 2-dependent *Escherichia coli* biofilm formation is enhanced in a dual-species coculture. *Appl. Environ. Microbiol.* 84 (5), e02638. doi:10.1128/AEM.02638-17

Li, H., Li, X., Song, C., Zhang, Y., Wang, Z., Liu, Z., et al. (2017). Autoinducer-2 facilitates Pseudomonas aeruginosa PAO1 pathogenicity *in vitro* and *in vivo*. *Front. Microbiol.* 8, 1944. doi:10.3389/fmicb.2017.01944

Li, H., Li, X., Wang, Z., Fu, Y., Qing, A., Dong, Y., et al. (2015). Autoinducer-2 regulates Pseudomonas aeruginosa PAO1 biofilm formation and virulence production in a dose-dependent manner. *BMC Microbiol.* 15 (1), 192. doi:10.1186/s12866-015-0529-y

Li, J., Fan, Q., Jin, M., Mao, C., Zhang, H., Zhang, X., et al. (2021). Paeoniflorin reduce LuxS/AI-2 system-controlled biofilm formation and virulence in Streptococcus suis. *Virulence* 12 (1), 3062–3073. doi:10.1080/21505594.2021.2010398

Linciano, P., Cavalloro, V., Martino, E., Kirchmair, J., Listro, R., Rossi, D., et al. (2020). Tackling antimicrobial resistance with small molecules targeting LsrK: Challenges and opportunities. *J. Med. Chem.* 63 (24), 15243–15257. doi:10.1021/acs.jmedchem.0c01282

Lindorff-Larsen, K.S. P., Kim, P., Paul, M., Klepeis, J. L., Dror, R. O., Shaw, D. E., et al. (2010). Improved side-chain torsion potentials for the amber Ff99SB protein force field: Improved protein side-chain potentials. *Proteins Struct. Funct. Bioinforma.* 78 (8), 1950–1958. doi:10.1002/prot.22711

Listro, R., Milli, G., Pellegrini, A., Motta, C., Cavalloro, V., Martino, E., et al. (2023). Structural insights into the ligand-LsrK kinase binding mode: A step forward in the discovery of novel antimicrobial agents. *Mol. (Basel, Switz.* 28 (6), 2542. doi:10.3390/molecules28062542

Lowery, C. A., Dickerson, T. J., and Janda, K. D. (2008). Interspecies and interkingdom communication mediated by bacterial quorum sensing. *Chem. Soc. Rev.* 37 (7), 1337. doi:10.1039/b702781h

Medarametla, P., Gatta, V., Kajander, T., Laitinen, T., Tammela, P., and Poso, A. (2018). Structure-based virtual screening of LsrK kinase inhibitors to target quorum sensing. *ChemMedChem* 13 (22), 2400–2407. doi:10.1002/cmdc.201800548

Medarametla, P., Kronenberger, T., Laitinen, T., and Poso, A. (2021). Structural characterization of LsrK as a quorum sensing target and a comparison between X-ray and homology models. *J. Chem. Inf. Model.* 61 (3), 1346–1353. doi:10.1021/acs.jcim.0c01233

Páll, S., Zhmurov, A., Bauer, P., Abraham, M., Lundborg, M., Gray, A., et al. (2020). Heterogeneous parallelization and acceleration of molecular dynamics simulations in GROMACS. *J. Chem. Phys.* 153 (13), 134110. doi:10.1063/5.0018516

Papenfort, K., and Bassler, B. L. (2016). Quorum sensing signal–response systems in gram-negative bacteria. *Nat. Rev. Microbiol.* 14 (9), 576–588. doi:10.1038/nrmicro.2016.89

Parrinello, M., and Rahman, A. (1981). Polymorphic transitions in single crystals: A new molecular dynamics method. *J. Appl. Phys.* 52 (12), 7182–7190. doi:10.1063/1.328693

Patzelt, D., Wang, H., Buchholz, I., Rohde, M., Gröbe, L., Pradella, S., et al. (2013). You are what you talk: Quorum sensing induces individual morphologies and cell division modes in dinoroseobacter shibae. *ISME J.* 7 (12), 2274–2286. doi:10.1038/ismej.2013.107

Pereira, C. S., Thompson, J. A., and Xavier, K. B. (2013). AI-2-Mediated signalling in bacteria. *FEMS Microbiol. Rev.* 37 (2), 156–181. doi:10.1111/j.1574-6976.2012.00345.x

Ryan, R. P., Shi-qi, An, Allan, J. H., McCarthy, Y., and Maxwell Dow, J. (2015). The DSF family of cell–cell signals: An expanding class of bacterial virulence regulators. *PLOS Pathog.* 11 (7), e1004986. doi:10.1371/journal.ppat.1004986

Schauperl, M., Nerenberg, P. S., Jang, H., Wang, L.-P., Bayly, C. I., Mobley, D. L., et al. (2020). Non-bonded force field model with advanced restrained electrostatic potential charges (RESP2). *Commun. Chem.* 3 (1), 44. doi:10.1038/s42004-020-0291-4

Sousa da SilvaAlan, W., and Vranken, W. F. (2012). Acpype - AnteChamber PYthon parser InterfacE. *BMC Res. Notes* 5 (1), 367. doi:10.1186/1756-0500-5-367

Stotani, S., Gatta, V., Medarametla, P., Mohan, P., Anna, K., Giordanetto, F., et al. (2019). DPD-inspired discovery of novel LsrK kinase inhibitors: An opportunity to fight antimicrobial resistance. *J. Med. Chem.* 62 (5), 2720–2737. doi:10.1021/acs.jmedchem.9b00025

Sun, Y., Yu, L., Luo, Q., Huang, J., Chen, J., Zhang, R., et al. (2020). LuxS/AI-2 quorum sensing system in edwardsiella piscicida promotes biofilm formation and pathogenicity. *Infect. Immun.* 88 (5), e00907. doi:10.1128/IAI.00907-19

Takano, E. (2006). γ-Butyrolactones: Streptomyces signalling molecules regulating antibiotic production and differentiation. *Curr. Opin. Microbiol.* 9 (3), 287–294. doi:10.1016/j.mib.2006.04.003

Valdés-Tresanco, M. S., Valdés-Tresanco, M. E., Valiente, P. A., and Moreno, E. (2021). Gmx_MMPBSA: A new tool to perform end-state free energy calculations with GROMACS. *J. Chem. Theory Comput.* 17, 6281–6291. doi:10.1021/acs.jctc.1c00645

Wang, Y., Wang, Y., Sun, L., Grenier, D., and Yi, L. (2018). The LuxS/AI-2 system of Streptococcus suis. *Appl. Microbiol. Biotechnol.* 102 (17), 7231–7238. doi:10.1007/s00253-018-9170-7

Xavier, K. B., and Bassler, B. L. (2005). Regulation of uptake and processing of the quorum-sensing autoinducer AI-2 in Escherichia coli. *J. Bacteriol.* 187 (1), 238–248. doi:10.1128/JB.187.1.238-248.2005

Xavier, K. B., Miller, S. T., Lu, W., Kim, J. H., Rabinowitz, J., Pelczer, I., et al. (2007). Phosphorylation and processing of the quorum-sensing molecule autoinducer-2 in enteric bacteria. *ACS Chem. Biol.* 2 (2), 128–136. doi:10.1021/cb600444h

Zhu, J., Hixon, M. S., Globisch, D., Kaufmann, G. F., and Janda, K. D. (2013). Mechanistic insights into the LsrK kinase required for autoinducer-2 quorum sensing activation. *J. Am. Chem. Soc.* 135 (21), 7827–7830. doi:10.1021/ja4024989

Zhu, J., Miller, M. B., Vance, R. E., Dziejman, M., Bassler, B. L., and Mekalanos, J. J. (2002). Quorum-sensing regulators control virulence gene expression in Vibrio cholerae. *Proc. Natl. Acad. Sci.* 99 (5), 3129–3134. doi:10.1073/pnas.052694299

Glossary

QS	quorum sensing
QSIs	quorum sensing inhibitors
AIs	Autoinducers
AI-2	autoinducer-2
AIPs	autoinducer peptides
AI	autoinducer
MD	molecular dynamics
PQS	*pseudomonas* quinolone signal
DSF	diffusible signal factor
LuxS	S-ribosylhomocysteinase
R-DHMF	(2R,4S)-2,4-dihydroxy-2-methyldihydrofuran-3-one
R-THMF	(2R,4S)-2-methyl-2,3,3,4-tetrahydroxy-tetrahydrofuran
S-DHMF	(2S,4S)-2,4-dihydroxy-2-methyldihydrofuran-3-one
S-THMF	(2S,4S)-2-methyl-2,3,3,4-tetrahydroxytetrahydrofuran
S-THMF-borate	(2S,4S)-2-methyl-2,3,3,4-tetrahydroxytetrahydrofuranborate
BSA	bovine serum albumin
ATP	adenosine triphosphate
DPD	3,4,4-trihydroxy-2-pentanone-5-phosphate
S-THP	S-3,3,4,5-tetrahydroxy-2-pentanone
P-DPD	S-3,3,4,5-tetrahydroxy-2-pentanone-5-phosphate
S-DPD	S-4,5-dihydroxy-2,3-pentanedione
Lsr	LuxS regulated
$MgCl_2$	magnesium chloride
μM	micromolar
AHL	N-acyl homoserine lactones
SRH	S-ribosylhomocisteine
PDB	Protein Data Bank
VSW	virtual screening workflow
HTVS	high-throughput virtual screening
SP	standard precision
XP	extra-precision
Fmax	maximum force
RMSD	root-mean-square deviation
RMSF	root-mean-square fluctuation
MM/PBSA	Molecular mechanics/Poisson-Boltzmann surface area
SPR	surface plasmon resonance
HTS	high throughput screening
SARs	structure-activity relationships
SDS-PAGE	sodium dodecyl sulfate-polyacrylamide gel electrophoresis
PSA	polar surface area
MW	molecular weight
HBA	H-bond acceptor
HBD	H-bond donor
RB	Rotatable bond
cLogP	calculated LogP
TEA	Triethanolamine
DMSO	dimethyl sulfoxide
NTA	GE Healthcare
OD	optical density
PBS-T	phosphate buffer saline
MIC	minimum inhibitory concentration
sub-MIC	subminimum inhibitory concentration
ADME	Absorption, Distribution, Metabolism, Excretion.

frontiers | Frontiers in Chemistry

TYPE Original Research
PUBLISHED 04 August 2023
DOI 10.3389/fchem.2023.1231030

OPEN ACCESS

EDITED BY
Wagdy Mohamed Eldehna,
Kafrelsheikh University, Egypt

REVIEWED BY
Heba Allam,
Cairo University, Egypt
Rafael Gomes,
University of Lisbon, Portugal

*CORRESPONDENCE
Mariusz Jaremko,
mariusz.jaremko@kaust.edu.sa
Essa M. Saied,
essa.saied@science.suez.edu.eg

RECEIVED 14 June 2023
ACCEPTED 24 July 2023
PUBLISHED 04 August 2023

CITATION
Radwan EM, Abo-Elabass E, Abd El-Baky AE, Alshwyeh HA, Almaimani RA, Almaimani G, Ibrahim IAA, Albogami A, Jaremko M, Alshawwa SZ and Saied EM (2023), Unveiling the antitumor potential of novel N-(substituted-phenyl)-8-methoxycoumarin-3-carboxamides as dual inhibitors of VEGFR2 kinase and cytochrome P450 for targeted treatment of hepatocellular carcinoma. *Front. Chem.* 11:1231030. doi: 10.3389/fchem.2023.1231030

Unveiling the antitumor potential of novel N-(substituted-phenyl)-8-methoxycoumarin-3-carboxamides as dual inhibitors of VEGFR2 kinase and cytochrome P450 for targeted treatment of hepatocellular carcinoma

Eman M. Radwan[1], Eman Abo-Elabass[2], Atef E. Abd El-Baky[3], Hussah Abdullah Alshwyeh[4,5], Riyad A. Almaimani[6], Ghassan Almaimani[7], Ibrahim Abdel Aziz Ibrahim[8], Abdulaziz Albogami[9], Mariusz Jaremko[10]*, Samar Z. Alshawwa[11] and Essa M. Saied[12,13]*

[1]The Division of Organic Chemistry, Chemistry Department, Faculty of Science, Port-Said University, Port-Said, Egypt, [2]The Division of Biochemistry, Chemistry Department, Faculty of Science, Port-Said University, Port-Said, Egypt, [3]Biochemistry Department, Faculty of Pharmacy, Port-Said University, Port-Said, Egypt, [4]Department of Biology, College of Science, Imam Abdulrahman Bin Faisal University, Dammam, Saudi Arabia, [5]Basic and Applied Scientific Research Centre, Imam Abdulrahman Bin Faisal University, Dammam, Saudi Arabia, [6]Department of Biochemistry, Faculty of Medicine, Umm Al-Qura University, Makkah, Saudi Arabia, [7]Department of Surgery, Faculty of Medicine, Umm Al-Qura University, Makkah, Saudi Arabia, [8]Department of Pharmacology and Toxicology, Faculty of Medicine, Umm Al-Qura University, Makkah, Saudi Arabia, [9]Biology Department, Faculty of science, Al-Baha University, Al Aqiq, Saudi Arabia, [10]Division of Biological and Environmental Sciences (BESE) and Engineering, King Abdullah University of Science and Technology (KAUST), Thuwal, Saudi Arabia, [11]Department of Pharmaceutical Sciences, College of Pharmacy, Princess Nourah Bint Abdulrahman University, Riyadh, Saudi Arabia, [12]Chemistry Department, Faculty of Science, Suez Canal University, Ismailia, Egypt, [13]Institute for Chemistry, Humboldt Universität zu Berlin, Berlin, Germany

Being the sixth most diagnosed cancer and the fourth leading cause of cancer-related deaths worldwide, liver cancer is considered as a serious disease with a high prevalence and poor prognosis. Current anticancer drugs for liver cancer have drawbacks, such as limited efficacy in later stages of the disease, toxicity to healthy cells, and the potential for drug resistance. There is ample evidence that coumarin-based compounds are potent anticancer agents, with numerous analogues currently being investigated in preclinical and clinical studies. The current study aimed to explore the antitumor potency of a new class of 8-methoxycoumarin-3-carboxamides against liver cancer. Toward this aim, we have designed, synthesized, and characterized a new set of *N*-(substituted-phenyl)-8-methoxycoumarin-3-carboxamide analogues. The assessment of antitumor activity revealed that the synthesized class of compounds possesses substantial cytotoxicity toward Hep-G2 cells when compared to staurosporine, without significant impact on normal cells. Out of the synthesized compounds, compound **7** demonstrated the most potent cytotoxic effect against Hep-G2 cells with an IC_{50} of 0.75 μM, which was more potent than the drug staurosporine (IC_{50} = 8.37 μM). The investigation into the mechanism behind the antiproliferative

activity of compound **7** revealed that it interferes with DNA replication and induces DNA damage, leading to cell cycle arrest as demonstrated by a significant decrease in the percentage of cells in the G1 and G2/M phases, along with an increase in the percentage of cells in the S phase. Flow cytometric analysis further revealed that compound **7** has the ability to trigger programmed cell death by inducing necrosis and apoptosis in HepG-2 cells. Further explorations into the mechanism of action demonstrated that compound **7** displays a potent dual-inhibitory activity toward cytochrome P450 and vascular endothelial growth factor receptor-2 (VEGFR-2) proteins, as compared to sorafenib drug. Further, detailed computational studies revealed that compound **7** displays a considerable binding affinity toward the binding cavity of VEGFR2 and CYP450 proteins. Taken together, our findings indicate that the newly synthesized class of compounds, particularly compound **7**, could serve as a promising scaffold for the development of highly effective anticancer agents against liver cancer.

KEYWORDS

coumarin, hepatocellular carcinoma, cytotoxicity, cell arrest, apoptosis, cytochrome P450, VEGFR2

1 Introduction

Cancer continues to be a significant global health challenge, with millions of people affected by various types of cancer each year (Kocarnik et al., 2022; Tran et al., 2022). Among the many types of cancer, liver cancer stands out as a particularly concerning condition due to its high prevalence and poor prognosis. Liver cancer, also known as hepatocellular carcinoma (HCC), is a type of cancer that starts in the cells of the liver and can spread to other parts of the body. Liver cancer is a major public health issue worldwide. According to the World Health Organization (WHO), liver cancer is the sixth most commonly diagnosed cancer and the fourth leading cause of cancer-related deaths globally (Ferlay et al., 2019; Rumgay et al., 2022). Treatment options for liver cancer depend on the severity and stage of the disease. They may include surgery (such as liver resection or transplantation), radiation therapy, chemotherapy, targeted therapies, and immunotherapies. However, the effectiveness of treatment depends on the stage of liver cancer at the time of diagnosis, and the availability of resources and expertise for managing this complex condition (Liu et al., 2015; Medavaram and Zhang, 2018; Llovet et al., 2021).

VEGFR-2, also known as vascular endothelial growth factor receptor-2, is a protein that belongs to the family of receptor tyrosine kinases (RTKs) and involves in the progression and development of liver cancer, as angiogenesis is a crucial process in metastasis and tumor growth (Shibuya, 2011; Modi and Kulkarni, 2019). As a member of the VEGF receptor family, VEGFR-2 is a transmembrane receptor that is primarily expressed on the surface of endothelial cells, which are the cells that line blood vessels. In liver cancer, VEGFR-2 has been found to be overexpressed, meaning that there is an increased amount of this receptor present compared to normal liver tissue (Shibuya, 2011; Apte et al., 2019). Binding of the key angiogenic factor, vascular endothelial growth factor (VEGF), to VEGFR-2 triggers a cascade of intracellular events that promote capillary tube formation, migration, and endothelial cell proliferation. This leads to the formation of new blood vessels, which provide oxygen and nutrients to the growing tumor mass (Hicklin and Ellis, 2005; Schoenleber et al., 2009; Chen et al., 2016). In addition to angiogenesis, VEGFR-2 signaling can promote tumor cell survival, invasion, and metastasis, as well as modulate the tumor microenvironment by affecting immune cell recruitment and function. Targeting VEGFR-2 has emerged as a possible therapeutic strategy for liver cancer. Several anti-angiogenic drugs that specifically inhibit VEGFR-2 activity, such as regorafenib, lenvatinib, and sorafenib have been clinically approved for the advanced HCC treatment (Zhu et al., 2020; Niu et al., 2021). These drugs can block the binding of VEGF to VEGFR-2, thereby inhibiting angiogenesis and tumor vascularization, and potentially reducing tumor growth and metastasis (Bruix et al., 2017). While drugs that target VEGFR-2 have shown promise as a therapeutic approach for liver cancer, they also have some potential disadvantages, including, limited efficacy, adverse effects, off-target effects, development of resistance, cost and accessibility, and lack of long-term data. Therefore, finding potential antitumor agents against liver cancer that could target the intricate mechanisms of VEGFR-2 signaling with minor adverse effects is urgently needed (Huang et al., 2020; Luo et al., 2021).

Cytochrome P450 2D6 (CYP2D6) is an enzyme that plays a crucial role in drug metabolism and is primarily expressed in the liver. It is responsible for the metabolism of a wide range of drugs, including many commonly prescribed medications and other xenobiotics (Zanger and Schwab, 2013; Zhao et al., 2021). Multiple lines of evidence suggest that CYP2D6 may be involved in various mechanisms that could potentially contribute to the progression of liver cancer (Hu G. et al., 2021; Khamis et al., 2021). CYP2D6 is known to metabolize several drugs used in the treatment of liver cancer, such as tamoxifen, codeine, and oxycodone. Altered CYP2D6 activity due to genetic variations or other factors could impact the metabolism of these drugs, potentially affecting their efficacy or toxicity (Taylor et al., 2020; Dean and Kane, 2021). Further, CYP2D6 may interact with other enzymes involved in drug metabolism, such as CYP3A4 and CYP2C9, which are also expressed in the liver (Tarantino et al., 2009; Hakkola et al., 2020). Based on these facts, targeting CYP2D6 has emerged as a potential therapeutical approach for liver cancer.

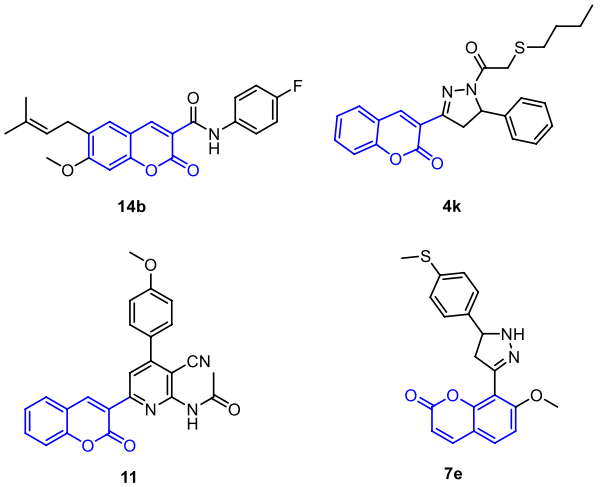

FIGURE 1
Representative reported coumarin analogues with potent antitumor activity against liver cancer cell line.

The discovery and development of potent drugs with minimal harmful side effects is a primary goal of modern medicinal chemistry. Coumarins are a class of bioactive molecules that are also known as *cis-O*-hydroxycinnamic lactones and possess a benzo-α-pyranone moiety in their basic structure (Küpeli Akkol et al., 2020; Salehian et al., 2021). They are secondary metabolites found in plants, bacteria, and fungi, with approximately 1,300 types of coumarins recognized so far (Stefanachi et al., 2018; Viana et al., 2021). Coumarin-based compounds have gained increasing attention due to their broad range of biological activities (Ahmed et al., 2020; Küpeli Akkol et al., 2020; Wu et al., 2020; Rawat and Vijaya Bhaskar Reddy, 2022). They have been reported to exhibit anticoagulant (Lu et al., 2022), antibacterial (Liu H. et al., 2020; Qin et al., 2020; Hu Y. et al., 2021), anti-inflammatory (Liang et al., 2020; Nayeli et al., 2020; Wang et al., 2020; Alfayomy et al., 2021), antioxidant (Sanches et al., 2019; Li et al., 2020; Ozalp et al., 2020; Parvin et al., 2021), antitumor (Kaur et al., 2015; Mohammed et al., 2020; Shahzadi et al., 2020; Konkoľová et al., 2021; Zhang et al., 2021; Rawat and Vijaya Bhaskar Reddy, 2022), antiviral (Liu G.-L. et al., 2020; Chidambaram et al., 2021; Shan et al., 2021; Özdemir et al., 2022), hyperlipidemia (Miao et al., 2021), anti-Alzheimer (Francisco et al., 2020), and enzyme inhibition effects (Zengin Kurt et al., 2019; Supuran, 2020; Xu et al., 2020; Meleddu et al., 2021). In the context of cancer treatment, coumarin analogues have been gaining increasing attention in recent years due to their potential as anticancer agents against liver cancer (Küpeli Akkol et al., 2020; Wu et al., 2020; Rawat and Vijaya Bhaskar Reddy, 2022). Coumarin derivatives (pyrazole, furan, sulfonyl, azoles, etc) have been found to promote cell cycle arrest, kinase inhibition, carbonic anhydrase inhibition, angiogenesis inhibition, and telomerase inhibition in different types of cancer cells. The specific substitution pattern on the coumarin ring governs its therapeutic applications and pharmacological properties (Küpeli Akkol et al., 2020; Wu et al., 2020; Rawat and Vijaya Bhaskar Reddy, 2022). As such, there is growing interest in the applications and future prospects of coumarin analogues as anticancer agents against liver cancer. For example, Phutdhawong *et al.* synthesized novel coumarin-3-carboxamides and found that compound **14b** possess potent anti-cancer potential against HepG-2 and HeLa cancer cell lines (Phutdhawong et al., 2021). Additionally, new coumarin derivatives have been synthesized and screened for anticancer potential against different cancer cell lines. Among synthesized compounds, compound **11** demonstrated a potential cytotoxic activity against HepG-2 cells with IC_{50} of 4.5 uM (Figure 1) (Fayed et al., 2019). A study conducted by Wu et al. investigated the effect of the introduction of the dihydropyrazole moiety in the coumarin skeleton. The authors showed that this class of coumarin analouges possesses considerable anticancer properties of coumarin analogs by inducing apoptosis and targeting telomerase activity e.g., compound **4k**). The findings of this study suggest that coumarin analogues may have potential therapeutic applications in the treatment of liver diseases. In a study by Fayed et al. (2019), it was shown that coumarin analogues with pyridine hybrids possess a wide range of anti-cancer properties. These compounds demonstrated the capacity to induce apoptosis and cell cycle arrest, along with a significant enhancement in caspase-3 activity (e.g., compound **11**).

Currently, there are several coumarin analogues that have been studied for their anti-liver cancer activity in preclinical or clinical, including furanocoumarin, umbelliprenin, scopoletin, fraxetin, esculetin, and dicoumarol (Figure 2) (Annunziata et al., 2020; Küpeli Akkol et al., 2020; Wu et al., 2020; Rawat and Vijaya Bhaskar Reddy, 2022). Furanocoumarins are a group of coumarin analogues found in certain plants, such as citrus fruits and herbs like *Angelica archangelica* (Bruni et al., 2019). Some furanocoumarins, such as psoralen and angelicin, have shown anti-liver cancer activity in preclinical studies by inducing cell cycle arrest and apoptosis in liver cancer cells (Ahmed et al., 2020). Scopoletin, also known as coumarin-7-hydroxy, is a coumarin analogue found in several medicinal plants (Antika et al., 2022). Some studies have shown that scopoletin exhibits anti-liver cancer activity by inhibiting cell proliferation, inducing apoptosis, and inhibiting angiogenesis in liver cancer cells (Wang et al., 2012; Sabeel et al., 2023). Dicoumarol is a naturally occurring coumarin analogue found in various plant species (Silva et al., 2022). It has been reported to possess anti-liver cancer activity by inhibiting the NAD(P)H:quinone oxidoreductase 1 (NQO1) enzyme, which is involved in tumor growth and survival pathways (Cullen et al., 2003). Esculetin is a coumarin analogue that has been shown to have anti-liver cancer properties. It has been reported to inhibit cell proliferation, induce apoptosis, and inhibit metastasis of liver cancer cells (Wang et al., 2015). Esculetin has also been shown to have anti-angiogenic effects in liver cancer, which can inhibit tumor growth and metastasis (Arora et al., 2016; Garg et al., 2022). Fraxetin is a coumarin analogue that has been studied for its potential anti-liver cancer activities. It has been reported to inhibit cell proliferation, induce apoptosis, and inhibit invasion and migration of liver cancer cells. Fraxetin has also been shown to modulate various signaling pathways involved in liver cancer development and progression (Figure 2) (Song et al., 2021). Accordingly, the diverse applications of coumarin analogues make them a promising avenue in future research for drug discovery and development (Annunziata et al., 2020; Küpeli Akkol et al., 2020; Wu et al., 2020; Rawat and Vijaya Bhaskar Reddy, 2022). In addition, the ease of synthesis and modifiability of the coumarin scaffold makes it a versatile platform for the design of novel compounds with improved pharmacological

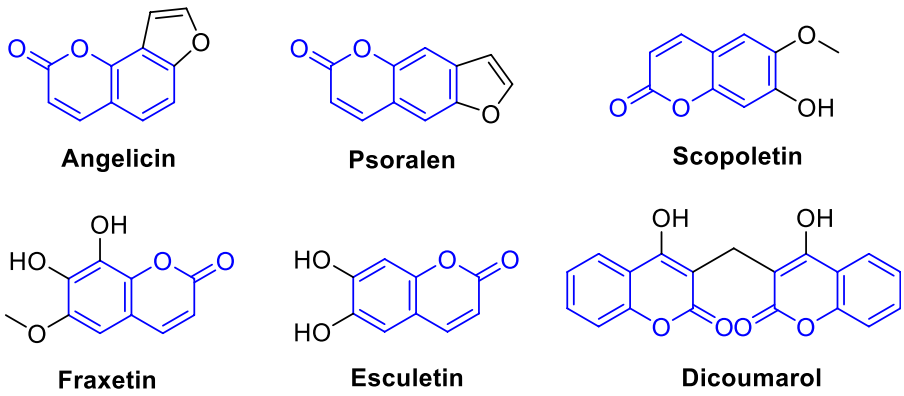

FIGURE 2
Representative coumarin analogues under preclinical or clinical investigations with anti-cancer activity against HCC.

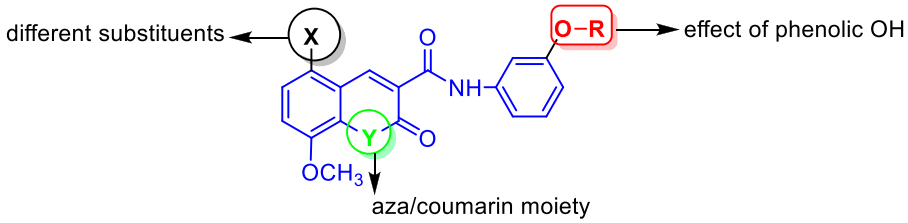

FIGURE 3
Representative structural features examined in the designed *N*-(substituted-phenyl)-8-methoxycoumarin-3-carboxamide analogues.

properties (Sarmah et al., 2021; Chaudhary et al., 2022; Sharma et al., 2022).

Based on the abovementioned facts and our continuous interest in discovering novel bioactive probes (Banhart et al., 2014; Saied et al., 2014; Saied et al., 2015; Saied et al., 2018; Gaber et al., 2020; El Azab et al., 2021; Saied and Arenz, 2021; Khirallah et al., 2022a; Khirallah et al., 2022b; Healey et al., 2022; Salem et al., 2022), the objective of this study was to design and synthesize a new series of *N*-(substituted-phenyl)-8-methoxycoumarin-3-carboxamides, and evaluate their cytotoxic activity against liver cancer cells (Figure 3). Additionally, the study aimed to explore the mechanism underlying the cytotoxic effects by assessing programmed cell death, cell cycle arrest, as well as inhibitory activity against CYP2D6 and VEGFR-2. Furthermore, *in silico* molecular modeling was performed to explore the binding potency of these compounds to the active site of VEGFR-2 and CYP2D6 proteins.

2 Results and discussion

2.1 Synthesis and characterization of 8-methoxycoumarin-3-carboxamides

In the present work, a series of *N*-(substituted)phenyl-8-methoxycoumarin-3-carboxamides, azacoumarin-3-carboxamide and their brominated derivatives (**3**–**8**) were synthesized from ethyl 8-methoxycoumarin-3-carboxylate (**1**) through a multi-step reaction sequence as shown in Scheme 1, 2. The synthesis of the target compounds involved several key steps, including cyclocondensation, hydrolysis, acid chloride formation, condensation, bromination, and acetylation, which were carefully designed and executed to obtain the desired products. The starting material, ethyl 8-methoxycoumarin-3-carboxylate (**1**), was synthesized in a satisfactory yield (86%) from 3-methoxy-2-hydroxybenzaldehyde and diethyl malonate through Knovanaegel condensation in the presence of piperidine as a base catalyst (Wu et al., 2014). The formation of compound **1** was affirmed by spectroscopic techniques such as ^{1}H nuclear magnetic resonance (NMR), ^{13}C NMR, infrared (IR), and mass spectrometry (EI-MS). Compound **1** was then converted to 8-methoxycoumarin-3-carboxylic acid (**2**) through hydrolysis with 4N HCl in acetic acid under reflux conditions to furnish compound **2** in 57% yield. The hydrolysis reaction was monitored by TLC and the formation of compound **2** was confirmed by spectroscopic techniques. Compound **2** was then used as a key intermediate for the synthesis of various derivatives. *N*-(3-hydroxy)phenyl 8-methoxycoumarin-3-carboxamide (**3**) was synthesized from compound **2** through the reaction with thionyl chloride to yield coumarin-3-acid chloride, followed by condensation with 3-aminophenol to afford compound **3** in a good yield (Healey et al., 2022). To obtain the brominated derivative, *N*-(3-hydroxy)

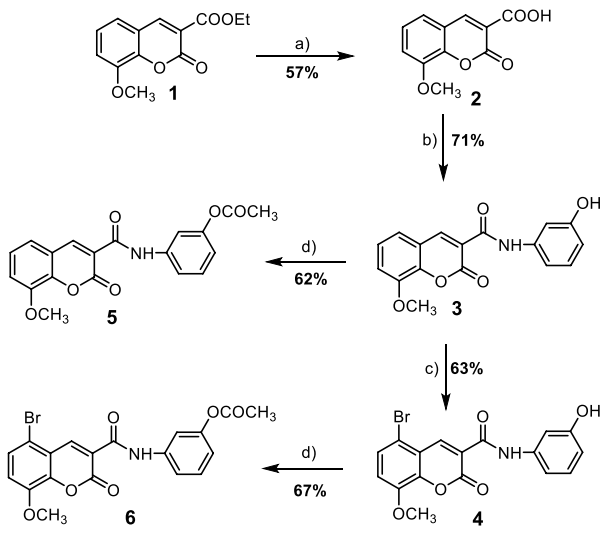

SCHEME 1
Synthesis of 8-methoxycoumarin-3-carboxamide derivatives **(3–6)**. Reagent and conditions: (a) 4N HCl, AcOH, reflux-rt., 18 h; (b) i- $SOCl_2$, reflux, 2 h, ii- 3-aminophenol, DMF, reflux-r.t., 12 h; (c) Br_2, AcOH, 60°C-r.t., 18 h; (d) Ac_2O, reflux-r.t., 16 h.

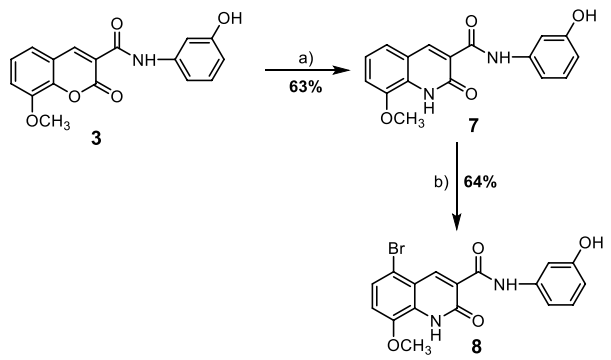

SCHEME 2
Synthesis of 8-methoxy-azacoumarin-3-carboxamide derivatives **(7 and 8)**. Reagent and conditions: (a) anhyd. K_2CO_3, NH_3 (soln.), reflux, 6 h; (b) Br_2, AcOH, 60°C-r.t., 18 h.

phenyl 5-bromo-8-methoxycoumarin-3-carboxamide (**4**), compound **3** was brominated with bromine in glacial acetic acid with stirring at 60°C to provide compound **4** in a moderate yield (63%) (Khirallah et al., 2022a). The bromination reaction was monitored by TLC and the formation of compound 4 was confirmed by spectroscopic techniques. To further support the structures of compounds **3** and **4**, they were transformed into *N*-(3-acetoxy)phenyl 8-methoxycoumarin-3-carboxamide (**6**) through acetylation with boiling acetic anhydride to give compound **6** in 67% yield (Khirallah et al., 2022b). The formation of compound **6** was also confirmed by spectroscopic techniques.

In addition to the coumarin derivatives, the synthesis of aza-coumarin analogues was also attempted (Scheme 2). *N*-(3-hydroxy) phenyl 8-methoxycoumarin-3-carboxamide (**3**) was converted to *N*-(3-hydroxy)phenyl-8-methoxy-azacoumarin-3-carboxamide (**7**) through aminolysis with ammonia solution in ethanol in the presence of anhydrous potassium carbonate under reflux to afford compound **7** in a good yield (63%). This was followed by halogenation of compound **7** with bromine in glacial acetic acid, resulting in the formation of *N*-(3-hydroxy)phenyl 5-bromo-8-methoxy-azacoumarin-3-carboxamide (**8**) in 64% yield, as shown in Scheme 2.

The successful synthesis of the targeted coumarin and aza-coumarin derivatives demonstrates the efficacy of the multi-step reaction sequence employed in this study (Bakare, 2021; Chaudhary et al., 2022; Szwaczko, 2022). The halogenation reactions leading to the formation of compounds **4** and **8** highlight the versatility of the synthetic route in introducing bromine substitution at the desired positions. The attempted synthesis of aza-coumarin analogues (compounds **7** and **8**) represents a novel approach in this study. The conversion of the coumarin scaffold to the corresponding aza-coumarin scaffold was successfully achieved through treatment with ammonia solution, followed by halogenation.

2.2 Characterization of synthesized compounds

The structures of compounds **3**-**6** were confirmed by various spectroscopic techniques including IR, ^{1}H-NMR, ^{13}C-NMR, and mass spectrometry (EI-MS) which provided evidence for their chemical identity and purity. In the IR spectra, characteristic absorption bands corresponding to specific functional groups such as carbonyl, amide, and bromine were observed, which supported the presence of these groups in the synthesized compounds. The ^{1}H-NMR and ^{13}C-NMR spectra provided detailed information about the chemical shifts of different protons and carbons in the molecules, which further confirmed the structures of the compounds. The mass spectrometry (EI-MS) data showed the expected molecular ion peaks and fragmentation patterns, which were consistent with the proposed structures. The ^{1}H-NMR spectrum of compound **3** exhibited several signals that provided information about its chemical structure. There were two singlet signals observed at δ 10.59 and 9.60 ppm, which can be attributed to the protons of the NH and OH groups, respectively. Another singlet signal at δ 8.87 ppm was observed, which can be assigned to the proton of H-4 in the coumarin ring. Furthermore, the absence of proton signals at δ 1.33 ppm suggests the absence of the acetoxy group (OCH_2CH_3) in compound **3**. This is supported by the appearance of a singlet signal at δ 3.96 ppm, which can be attributed to the protons of the methoxy group (OCH_3). The proton signals of the aromatic rings in compound **3** were observed within the expected chemical shifts in the region of δ 6.57–7.54 as multiplet signals. This confirms the presence of aromatic rings in the compound. The ^{13}C-NMR spectrum of compound **3** revealed several carbon signals that provide further information about its chemical structure. There were two carbon signals observed at δ 160.72 and 160.14 ppm, which can be attributed to the carbonyl groups of the amide and pyranone ring, respectively. Another carbon signal at δ 56.70 ppm was observed, which can be assigned to the carbon of the methoxy group (OCH_3). This is consistent with the presence of a methoxy group in compound **3**. The carbon signals detected within δ 158.28–107.32 ppm further confirm the presence of aromatic and coumarin rings in compound

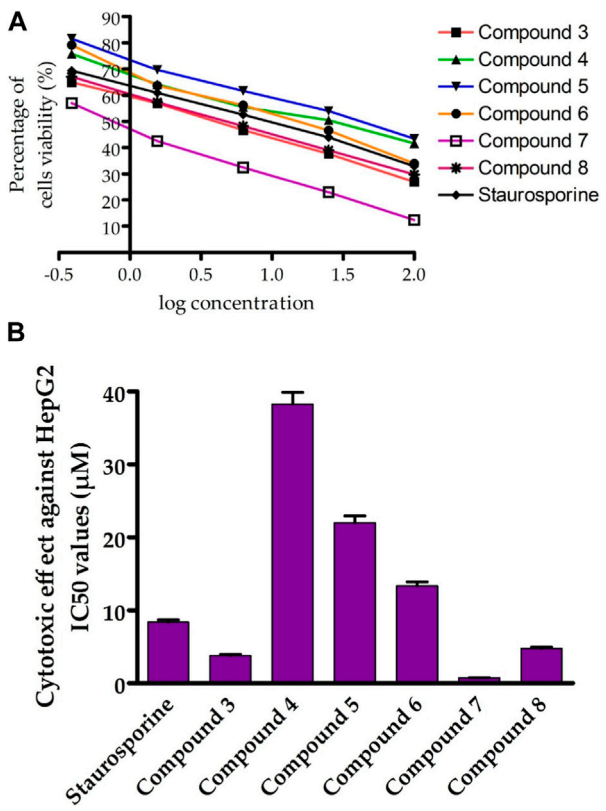

FIGURE 4
Assessment of cytotoxic activity of synthesized compounds toward Hep-G2 cells. **(A)** the dose-dependent cytotoxic activity of synthesized compounds. **(B)** Representative diagram for the IC_{50} (μM) values of synthesized compounds against Hep-G2 cells proliferation, as compared to STU. The data presented represents the mean ± SEM derived from the dose-response curve of a minimum of three independent experiments.

3. Overall, the ^{1}H NMR and ^{13}C NMR spectra of compound **3** provide clear evidence for its chemical structure. The detected signals corresponding to the OH and NH groups, H-4 of the coumarin ring, methoxy group, and aromatic rings are consistent with the expected chemical shifts, confirming the presence of these functional groups and rings in compound **3**.

The ^{1}H NMR spectra of compounds **5** and **6** provide important information about their chemical structures. The disappearance of a proton signal at δ 9.60 ppm suggests the absence of a hydroxyl group (OH) in both compounds. Instead, new singlet signals were observed at δ 2.30 and 2.38 ppm, which can be attributed to the three protons of the methyl group in the acetoxy group ($OCOCH_3$). This indicates that compounds **5** and **6** have undergone acetylation with acetic anhydride, resulting in the formation of acetoxy groups. Additionally, the NH and H-4 proton signals of the coumarin ring were still present in compounds **5** and **6**, observed at δ 10.77, 11.30 and 8.88, 9.01 ppm, respectively. This confirms that the coumarin ring is still present in these compounds. The methoxy (OCH_3) groups appeared as singlet signals at δ 3.98–3.96 ppm, indicating the presence of methoxy groups in compounds **5** and **6**. The aromatic protons were detected as multiplet signals within the expected chemical shifts, further supporting the presence of aromatic rings in compounds **5** and **6**. The ^{13}C NMR spectra of compounds **5** and **6** revealed the presence of two new carbon signals at δ 169.67, 168.64 ppm and 21.35, 20.98 ppm, which can be attributed to the carbonyl carbons of the acetoxy groups ($OCOCH_3$). This provides evidence for the acetylation of compounds **3** and **4**, resulting in the formation of compounds **5** and **6**. The ^{1}H and ^{13}C NMR spectra of compounds **5** and **6** provide important information about their chemical structures. The absence of a proton signal for the hydroxyl group and the appearance of singlet signals for the methyl group in the acetoxy group confirm the acetylation of compounds **3** and **4**. The presence of NH and H-4 proton signals of the coumarin ring, methoxy groups, and aromatic protons further support the chemical structures of compounds **5** and **6.** The ^{13}C NMR spectra provide additional evidence for the presence of acetoxy groups in compounds **5** and **6**.

The mass spectra of compounds **3** and **5** show prominent molecular ion peaks at *m/z* 311 and m/z 353, respectively. These peaks correspond to the molecular formula $C_{17}H_{13}NO_5$ for compound **3** and $C_{19}H_{15}NO_6$ for compound **5**. The molecular ion peak represents the intact molecular ion of the compound, and its *m/z* value provides information about the mass of the compound and its composition. The presence of molecular ion peaks at *m/z* 311 and *m/z* 353 in the mass spectra of compounds **3** and **5**, respectively, suggests that these compounds have relatively stable molecular ions. This indicates that the molecular ions of compounds **3** and **5** are less likely to undergo fragmentation or other chemical reactions during the ionization process. On the other hand, it was observed that the molecular ion peaks of compounds **4** and **6** are unstable. This means that the molecular ions of compounds **4** and **6** are not as stable as those of compounds **3** and **5**, and they may be prone to fragmentation or other chemical reactions during the ionization process (Supplementary Figures S1, S2). This instability could be due to the presence of labile functional groups or other structural features in compounds **4** and **6** that make their molecular ions less stable.

2.3 Evaluation of cytotoxic activity against liver cancer cells

We first screened the cytotoxicity of compounds against the proliferation of liver cancer cells (HepG-2) by using the MTT assay (Mohamed et al., 2022a). Toward this, the HepG-2 cells were cultured and treated with tested compounds at different concentrations for 24 h and subsequently 3-(4,5-dimethylthiazol-2-yl)-2,5-diphenyltetrazolium bromide (MTT) dye was added. The colorimetric measurement was assessed using an ELISA plate reader at a wavelength of 570 nm. In this assay, the activity of compounds was compared to the standard anticancer staurosporine (STU) drug under identical experimental conditions. As indicated in Figure 4; Table 1, the synthesized compounds exhibited considerable anti-proliferative activity against HepG-2 cells. The N-(3-hydroxy) phenyl 8-methoxycoumarin-3-carboxamide **3** exhibited a significant cytotoxic activity with IC_{50} of 3.81 uM. The bromine substitution at the 8-methoxycoumarin moiety of compound **3** provided a compound with lower inhibitory activity toward the growth of HepG-2 cells (compound 4, IC_{50} 38.28 uM). This result indicates that the introduction of the large bromine atom may

TABLE 1 Cytotoxic evaluation of compounds 3-8 against human liver carcinoma HepG2 cell line and HL-7702 normal cell line.

Comp no.	IC_{50} values (μM)	
	HepG2	HL-7702
3	3.81 ± 0.16	NT[a]
4	38.28 ± 1.62	NT[a]
5	22.03 ± 0.93	NT[a]
6	13.37 ± 0.56	NT[a]
7	0.75 ± 0.03	13.72 ± 1.8
8	4.79 ± 0.2	NT[a]
STU	8.37 ± 0.35	22.17 ± 2.1

[a]NT, not determined.

attenuate the binding affinity of the compound toward the targeted protein (s).

Further, acylation of the hydroxyl group at the phenyl 3-carboxamide moiety of compound **3** resulted in a considerable diminish in the cytotoxic activity (compound **5**, IC_{50} 22.03 μM), indicating the significance of the phenolic hydroxyl group in the antiproliferative activity of compound **3**. Conversely, acylation of 3-hydroxy-phenyl moiety in compound **5** led to a substantial improvement in the antiproliferative activity of the compound (compound **6**, IC_{50} 13.37 μM). Interestingly, shifting the 8-methoxycoumarin moiety in compound **3** into 8-methoxy-azacoumarin analogue (compound **7**) substantially improved the cytotoxic activity (IC_{50} 0.75 ± 0.03 μM), revealing the significance of the amine group in the cytotoxicity of this class of compounds. Similarly, bromination of compound **7** at the 8-methoxycoumarin-3-carboxamide moiety resulted in a dramatic diminish in the cytotoxic effect of the compound (IC_{50} 4.79 ± 0.2 μM). These results further demonstrate that the bromination of 8-methoxycoumarin-3-carboxamide moiety has a drastic effect on the antiproliferative of this class of compounds. Subsequently, we investigated the cytotoxic effects of these compounds on human normal liver cells (HL-7702). As indicated in Table 1, the synthesized compounds, except for compound **7**, did not show substantial cytotoxic activity toward human normal liver cells, demonstrating that this class of compounds exhibits a substantial and selective antiproliferative activity against HepG-2 cells, with a non-dramatic cytotoxic effect on normal liver cells. These findings align with previous studies that have demonstrated that methoxy-coumarin analogues exhibit potential anti-proliferative activity (Amin et al., 2015; Küpeli Akkol et al., 2020; Wu et al., 2020; Rawat and Vijaya Bhaskar Reddy, 2022). Among synthesized and investigated compounds, compound **7** demonstrated the most antiproliferative activity HepG-2 cells with IC_{50} of 0.75 ± 0.03 μM, as compared to STU drug (IC_{50} 8.37 ± 0.35 μM). In addition, compound **7** did not show a considerable cytotoxic activity against HL-7702 cells (IC_{50} 13.72 μM), as compared to STU drug with IC_{50} of 22.17 μM. Overall, these findings indicate that this class of 8-methoxycoumarin-3-carboxamide compounds could be considered for the development of promising antiproliferative lead compounds against hepatocellular carcinoma.

2.4 Cell cycle analysis

Among the compounds tested, our findings revealed that compound **7** displayed the highest level of cytotoxic activity against the liver carcinoma cell line (HepG-2). Based on this promising activity, compound **7** was selected for further evaluation to assess its effect on the cell cycle profile in HepG-2 cells. To evaluate the cell cycle, a biparametric cytofluorimetric analysis was conducted on HepG-2 cells treated with compound **7** at its IC_{50} concentration for a duration of 24 h. Propidium iodide (PI) was used as the staining agent for this analysis. (Figure 5). The analysis revealed that Compound 7 caused a significant decrease in the percentage of cells in the G1 and G2/M phases of the cell cycle. In the untreated control group, 46.35% of cells were in the G1 phase, while after treatment with compound **7**, the percentage decreased to 39.08%. Similarly, the percentage of cells in the G2/M phase decreased from 11.46% in the control group to 6.4% after treatment with compound **7**. In contrast, there was a notable increase in the percentage of cells in the S phase after treatment with Compound 7. The S phase, which is responsible for DNA synthesis, showed an increase from 42.19% in the untreated control group to 54.52% after treatment with Compound **7**. These findings indicate that the treatment of HepG-2 cells with compound **7** leads to cell cycle arrest specifically in the S phase. This is evident from the decrease in the proportion of cells in the G1 and G2/M phases, accompanied by an increase in the percentage of cells residing in the S phase. Cell cycle arrest is a widely recognized mechanism utilized by anticancer agents to impede the excessive proliferation of cancer cells. By inducing cell cycle arrest, these agents disrupt the normal progression of the cell cycle, preventing cancer cells from dividing and multiplying uncontrollably. This therapeutic strategy helps to halt tumor growth and promotes the effectiveness of cancer treatments. The observed effects of compound **7** on the cell cycle profile of HepG-2 cells are indicative of its potential as an antitumor agent. The decrease in the percentage of cells in the G1 phase suggests that compound **7** may inhibit the progression of cells from the G1 to S phase, which could lead to cell cycle arrest and subsequent inhibition of cell proliferation. Additionally, the decrease in the percentage of cells in the G2/M phase suggests that Compound **7** may also affect cell division and mitotic progression. Furthermore, the increase in the percentage of cells in the S phase upon treatment with Compound **7** may indicate DNA damage and activation of DNA repair mechanisms, which can contribute to the observed S phase arrest. This suggests that Compound **7** may interfere with DNA replication and induce DNA damage, leading to cell cycle arrest and inhibition of tumor cell growth. Overall, these results highlight the potential of Compound **7** as a promising antitumor agent against liver carcinoma, as it exhibits potent cytotoxic activity and induces S phase arrest in HepG-2 cells.

2.5 Flow cytometric analysis

The Annexin V-FITC/PI assay is a well-established flow cytometric method to evaluate the apoptotic potential of bioactive compounds. The assay allows differentiation between apoptotic cells and live cells by using fluorescent dyes that bind

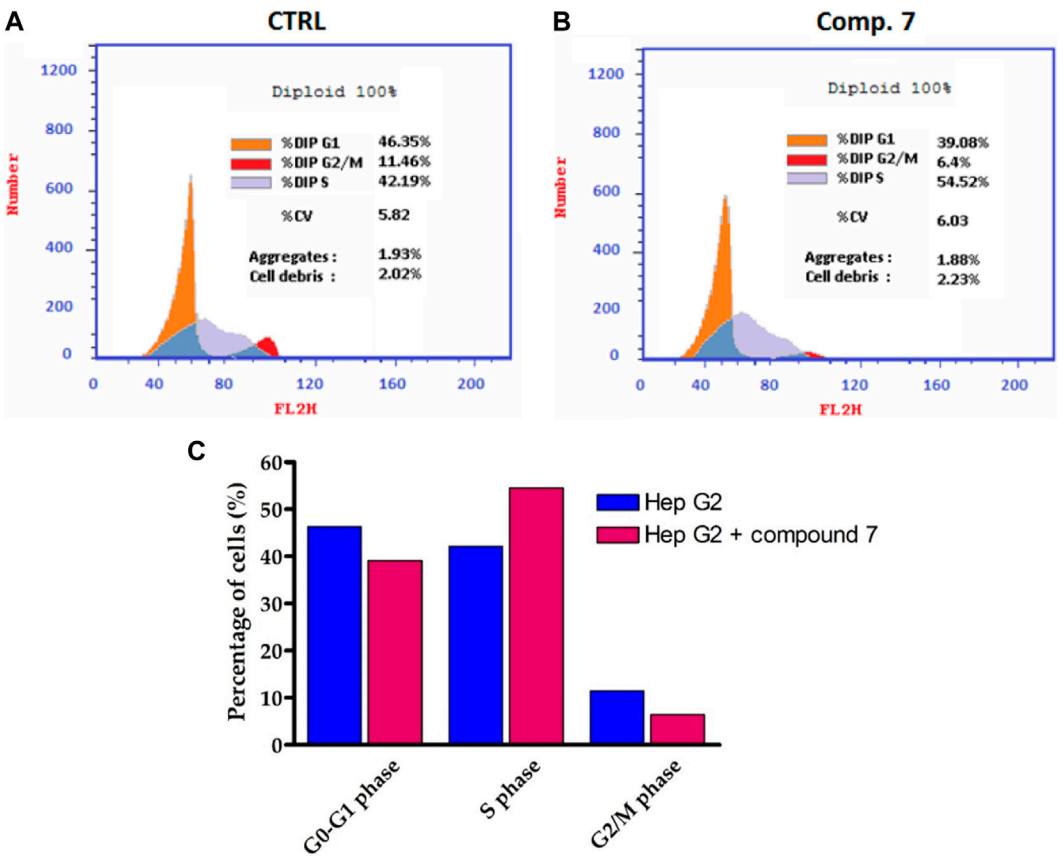

FIGURE 5
Influence of compound **7** at a concentration of 0.75 μM on Hep-G2 cell distribution. **(A,B)** Flow cytometry assessment of cell cycle stages in Hep-G2 cells of untreated and compound **7**-treated and cells. **(C)** Cell cycle distribution histograms of treated and untreated Hep-G2 cells.

to phosphatidylserine (PS) and DNA, respectively (Galluzzi et al., 2018; Pfeffer and Singh, 2018; Tong et al., 2022). In the present study, the assay was performed to explore the apoptotic effect of compound **7** (at its IC_{50} dose value) on HepG-2 cells. As indicated in Figure 6, the results revealed a substantial increase in the percentage of apoptotic cells at all stages (total, early, and late) compared to the control group. In this regard, compound **7** displayed the ability to increase the percentage of total apoptotic from (42.96%) by 23-fold compared to the control group (1.89%). At the early stage, the percentage of apoptotic cells increased from 0.55% in the control group to 24.72% in the compound **7**-treated group (45-fold increase). Similarly, at the late stage, the percentage of apoptotic cells increased from 0.21% in the control group to 15.34% in the compound **7**-treated group (73-fold increase). These results clearly demonstrate that compound **7** is able to induce apoptosis in these cells. Further, our results indicated that compound **7** exhibits a considerable ability to induce necrosis (2.5- fold increase) in HepG-2 cells, as compared to the control cells. The Annexin V-FITC/PI assay is a well-established method to evaluate the apoptotic potential of chemical compounds. Inducing apoptosis is an appealing therapeutic approach for cancer treatment as it is a vital cellular process essential for preserving tissue balance and removing impaired or unnecessary cells. Disruption in the regulation of apoptosis can contribute to various diseases, such as cancer, highlighting its significance. Hence, triggering apoptosis holds potential as an effective strategy to combat cancer (Galluzzi et al., 2018; Pfeffer and Singh, 2018; Tong et al., 2022). The presented results suggest that compound **7** may have potential as an anti-cancer agent by inducing apoptosis and necrosis cell death in HepG-2 cells. The observed increase in the percentage of apoptotic cells at all stages (total, early, and late) compared to the control group indicates that compound **7** is able to activate the apoptotic pathway in these cells. The early stage of apoptosis is characterized by the translocation of PS from the inner to the outer leaflet of the plasma membrane, which can be detected by Annexin V-FITC staining. In the present study, the percentage of Annexin V-FITC-positive cells significantly increased in the compound **7**-treated group, indicating that compound **7** induces early apoptosis in HepG-2 cells. Further, the late stage of apoptosis is characterized by DNA fragmentation, which can be detected by PI staining. Our findings revealed that the percentage of PI-positive cells significantly increased in the compound **7**-treated group, indicating that compound **7** induces late apoptosis in HepG-2 cells. According to these findings, there is a notable connection between the ability of compound **7** to induce programmed cell death in HepG-2 cells and its antiproliferative effects.

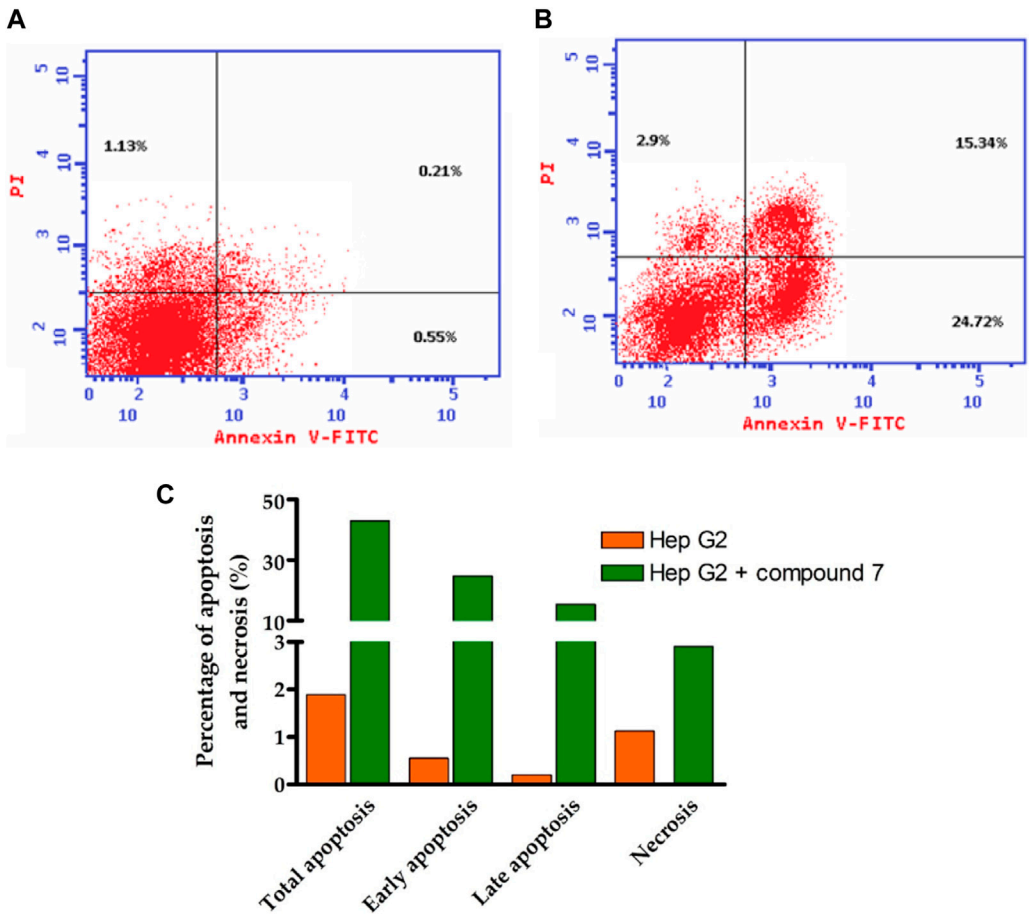

FIGURE 6
Illustrates the influence of compound 7 on programmed cell death in Hep-G2 cells. **(A)** The cytofluorometric analysis of untreated Hep-G2 cells was performed using the Annexin V FITC double labeling assay. **(B)** The Annexin V FITC double labeling assay was utilized to analyze Hep-G2 cells treated with compound 7 at a concentration of 0.75 μM. **(C)** A graphical representation is provided, demonstrating the different stages of programmed cell death in both untreated Hep-G2 cells and those treated with compound 7.

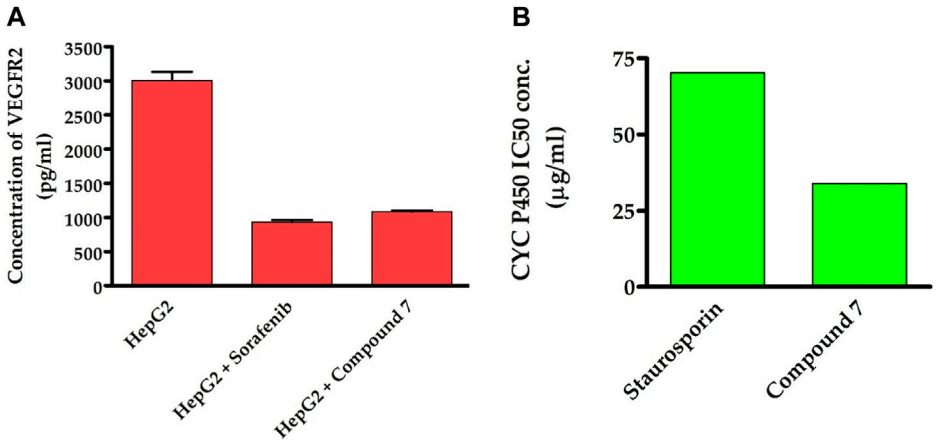

FIGURE 7
Dual-inhibitory activity of compound **7** toward VEGFR2 **(A)** and CYP450 **(B)** enzymes.

TABLE 2 Binding score and interactions of compound 7, as compared to the co-crystallized ligand Sorafenib, toward the active cavity of VEGFR2 protein.

Protein (PDB code)	Compound	Binding score (kcal/mol)	Hydrophobic interactions		Hydrophilic interactions	Distance (A)
VEGFR2 (*4asd*)	Sorafenib	−15.29	Leu840	Val848	Cys919	3.10
			Ala866	Ile888	Cys919	2.88
			Leu889	Ile892	Cys1045	3.32
			Val898	Val899	Asp1046	2.79
			Val916	Phe918	Glu885	3.34
			Leu1019	Ile1025	Glu885	2.58
			Leu1035	Ile1044		
			Phe1047			
	7	−14.71	Val846	Ile886	Glu883	3.35
			Leu887	Ile890	Glu833	2.71
			Val897	Val912	Asp1044	2.80
			Val914	Ile1023	Asp1044	3.57
			Ile1042	Phe1045	Cys1043	3.49
					Ile886	3.93

2.6 Assessment of VEGFR-2 inhibitory activity

To obtain additional mechanistic insights into the antitumor activity of compound **7**, we investigated whether it has the ability to suppress the activity of VEGFR2 enzyme. As previously discussed, VEGFR-2 is a crucial target among angiogenesis-related kinases as it plays a key role in controlling cellular responses to VEGF in various cancer cells (Goel and Mercurio, 2013). Targeting VEGFR-2 signaling has become a key strategy in the search for novel drugs to treat numerous cancers that rely on angiogenesis (Liu et al., 2022). In recent years, the FDA has approved a variety of VEGFR-2 inhibitors as anti-angiogenic drugs for treating various solid tumors. Including sorafenib, sunitinib, and regorafenib (Ayala-Aguilera et al., 2022). Toward this, we were curious to explore whether the antitumor activity of compound **7** is linked to its ability to target the VEGFR-2 receptor inHep-G2 cells. As indicated in Figure 7, compound **7** exhibited a substantial inhibitory activity toward VEGFR2 protein (1,086 pg/mL), as compared to the untreated Hep-G2 cells (3,007 pg/mL). Interestingly, the inhibitory activity of compound **7** was similar to that of the reference sorafenib drug (932.4 pg/mL). The results suggest that the ability of compound **7** to target VEGFR2 protein activity may be responsible for its antitumor effects on Hep-G2 cells.

2.7 Assessment of CYP inhibitory activity

Our findings motivated us to delve deeper into the underlying mechanisms responsible for the potent antitumor activity of this class of compounds. CYP2D6 is a key enzyme primarily found in the liver that plays a critical role in metabolizing numerous drugs, including commonly prescribed medications and other xenobiotics. Its altered activity due to factors such as genetic variations may affect drug metabolism and efficacy, and it may interact with other liver enzymes. Recent studies suggest targeting CYP2D6 as a potential therapeutic approach for liver cancer (Peter Guengerich et al., 2016). To investigate whether the antiproliferative effect of compound **7** is linked to its capacity to inhibit CYP2D6 activity, we have extended our studies. In this regard, we have assessed the dose-dependent inhibitory behavior of compound **7** toward the CYP2D6 activity and utilized the standard drug staurosporin. As indicated in Figure 7, the results revealed that compound **7** possesses a significant and dose-dependent inhibitory feature toward CYP2D6 activity with IC_{50} of 34 μg/mL. Interestingly, compound **7** exhibited an inhibitory activity toward CYP2D6 which was 2.1-fold more potent than that of the standard staurosporin drug (70.29 μg/mL). These findings imply that the antitumor activity of compound **7** might be explained by its dual inhibitory activity toward both VEGFR2 and CYP2D6 proteins.

2.8 In silico computational studies

2.8.1 *In silico* molecular modelling simulations

The technique of molecular docking simulation has been widely and effectively utilized to analyze how a bioactive ligand interacts with the active site of a specific protein, as well as to determine its binding score (Mohamed et al., 2021; Saied et al., 2021; Khirallah et al., 2022a; Mohamed et al., 2022a; Mohamed et al., 2022b; Healey et al., 2022). To further validate the potential of compound 7 as a dual-target inhibitor of VEGFR2 and CYP2D6 proteins, we employed *in silico* molecular docking analysis to evaluate its binding affinity towards the active sites of these proteins. Toward this, the crystal structure of the targeted proteins in complex with

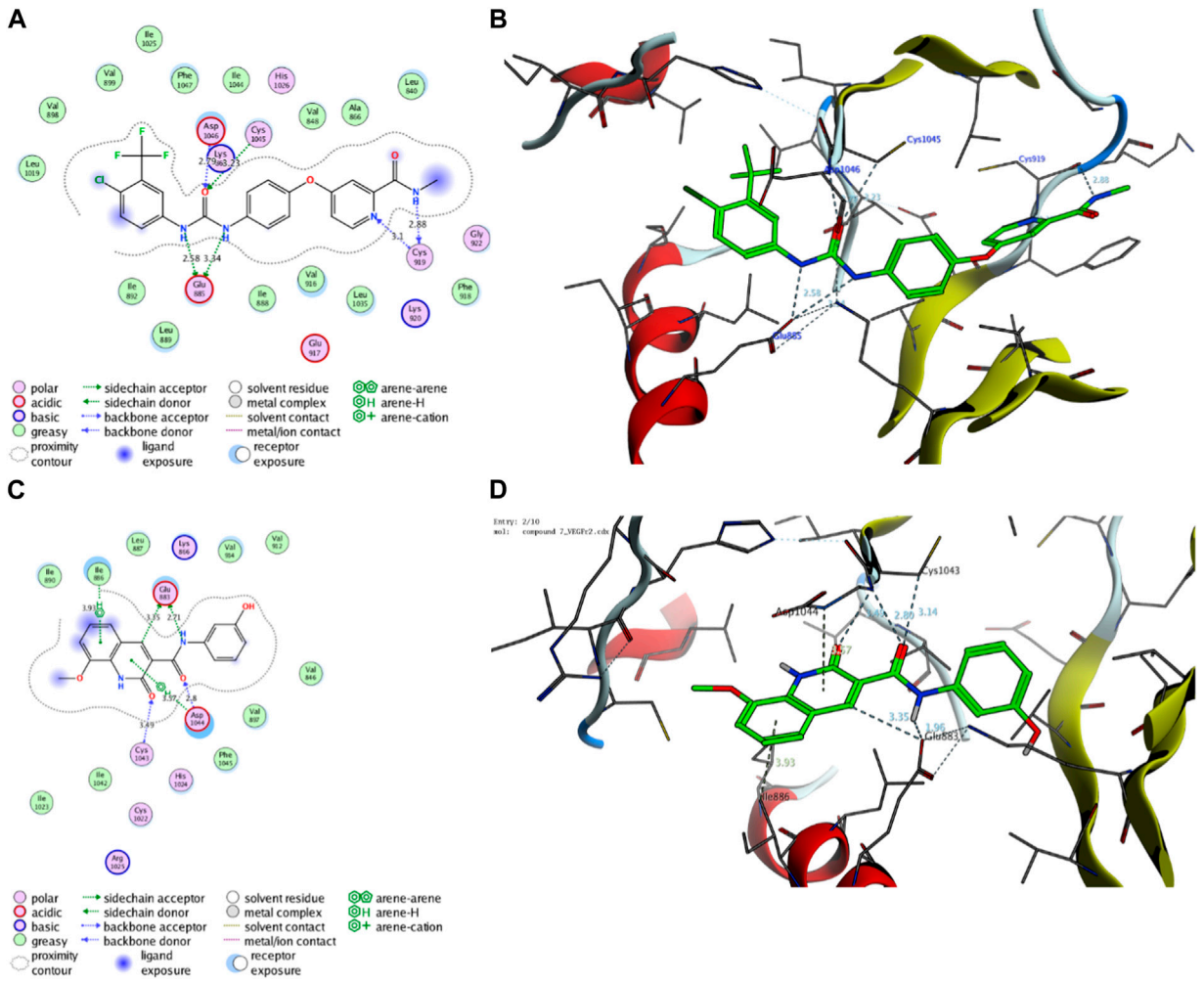

FIGURE 8
Representative binding modes of sorafenib **(A,B)** and compound **7 (C,D)** inside the active site of VEGFR2 (PDB code: *4asd*) protein through 2D and 3D molecular docking simulations.

their co-crystallized ligand was accessed from protein data bank (access 1/2/2023, https://www.rcsb.org/); VEGFR2 protein (PDB code: *4asd*) and CYP2D6 protein (PDB code: *4xrz*) (McTigue et al., 2012; Brodney et al., 2015). The acquired crystal structures were first prepared for molecular simulation by removing extra chains and water and other extra molecules. The docking protocol was adapted to ensure that the co-crystallized molecule interacts in similar mode as reported in the crystal structure with low RMSD values.

2.8.1.1 Molecular modelling simulation of compound **7** toward the active site of VEGFR2 protein

Initially, we investigated the binding affinity and mode of interaction between compound **7** and the function pocket of the VEGFR2 protein. In our study, we utilized the reported VEGFR2-crystal structure in complex with sorafenib as a co-crystallized ligand (PDB code: *4asd*) (McTigue et al., 2012). We modified and adapted the applied protocol to ensure that sorafenib forms the main interactions reported in the complex structure in the binding pocket. As shown in Table 2; Figure 8, the redocking process of sorafenib drug into the active site of VEGFR2 protein revealed a set of H-bonding and hydrophobic interactions with several amino acid residues in the pocket with binding score of −15.29 kcal/mol. The urea moiety of sorafenib formed four H-bonding interactions with Glu885, Asp1046, and Cys1045 amino acid residues. Further, Cys919 residue in the active site could form a dual H-bonding interactions with the *N*-methylnicotinamide moiety. The bind of sorafenib was further supported by a network of hydrophobic interactions with a set of grassy amino acid residues in the active site (Figure 8).

On the other hand, compound **7** exhibited a considerable binding affinity toward the active site of VEGFR2 pocket with score of −14.71 kcal/mol. Analysis of the binding mode revealed that compound **7** has the ability to interact and form four H-bonding with Glu883 and Asp1044 amino acid residues through its 3-hydroxyphenyl-acetamide moiety. Further, the azacoumarin scaffold participated in the stability of conformer by forming H-bonding with Cys1043 residue and interacting with Ile886 residue through H-arene bonding (Figure 8). The binding of compound **7** was further supported by a network of hydrophobic

TABLE 3 Binding score and interactions of compound 7, as compared to the co-crystallized ligand BACE1 inhibitor 6, toward the active cavity of CYP2D6 protein.

Protein (PDB code)	Ligand	Binding score (kcal/mol)	Hydrophobic interactions		Hydrophilic interactions	Distance (A)
CYP2D6 (*4xrz*)	**BACE1 Inhibitor 6**	−12.06	Phe120	Ala209	Asp301	3–50
			Leu213	Ala305	Cys443	4.28
			Val308	Val370		
			Phe483	Leu484		
	7	−12.97	Leu110	Phe112	Glu216	3.18
			Phe120	Leu121	Glu216	3.45
			Leu213	Ile297	Asp301	2.90
			Ala300	Ala305	Phe120	3.66
			Leu484			

amino acids in the pocket (Val846, Ile886, Leu887, Ile890, Val897, Val912, Val914, Ile1023, Ile1042, Phe1045). In agreement with our previous results, these findings affirm and explain the observed *in vitro* inhibitory activity of compound **7** toward VEGFR2 activity. Further, our results suggest that 8-methoxy-azacoumarin-3-carboxamide has the potential to serve as a primary structure for creating effective VEGFR2 inhibitors.

2.8.1.2 Molecular modelling simulation of compound **7** toward the active site of CYP2D6 protein

Next, an evaluation was conducted to determine the binding affinity and mode of interaction between compound 7 and the active site of the CYP2D6 protein. Toward this, we initially validated the docking protocol by re-docking the co-crystallized ligand (BACE1 inhibitor 6) into the pocket of CYP2D6 protein and affirmed the mode of interaction and binding score, as compared to the reported data (PDB code: *4xrz*) (Brodney et al., 2015). Our analysis revealed that BACE1 inhibitor 6 possesses a significant binding affinity (−12.06 kcal/mol) and binds mainly to two amino acid residues (Asp301, and Cys443) by H-bonding interaction (Table 3). In addition, BACE1 inhibitor 6 interacts hydrophobically with several amino acids (Phe120, Ala209, Leu213, Ala305, Val308, Val370, Phe483, and Leu484) in the active site to assure the conformer stability (Figure 9).

Regarding compound **7**, the docking simulation analysis demonstrated that compound **7** displays a significant binding affinity toward the active site of CYP2D6 protein with binding score of −12.97 kcal/mol (Table 3). Evaluation of the binding mode revealed that compound **7**, in the most stable conformer, displays the ability to interact with several amino acid residues in the active site by forming a network of hydrophobic and H-bonding interactions. As shown in Figure 9, compound **7** bound through its azacoumarin scaffold to Glu216 and Phe120 amino acid residues by H-bonding and arene-arene interaction, respectively. Further, the amino group of the acetamide moiety could also form a strong H-bonding with Glu216 residue, suggesting the beneficial role of 3-carboxamide-substitution at the azacoumarin ring. This finding was further supported by the ability of phenolic-OH to form H-binding to Asp301 residue. Similarly, compound **7** showed the ability to form a set of hydrophobic interactions with Leu110, Phe112, Phe120, Leu121, Leu213, Ile297, Ala300, Ala305, Leu484 amino acid residues. Together, our molecular docking simulation studies explain and affirm the *in vitro* inhibitory activity of compound **7** toward the CYP2D6 protein and further demonstrate the dual-inhibitory activity of this compound toward VEGFR2 and CYP2D6 proteins.

2.8.2 *In silico* toxicity and ADME prediction

Encouraged by our findings, we were interested in exploring the toxicity and drug likeness of the most active 8-methoxy-azacoumarin-3-carboxamide (compound **7**), as compared to the reference drugs sorafenib and staurosporine. Toward this, several computational analyses were *in silico* performed including SwissADME, Protox II, OSIRIS Property Explorer and pkCSM. As shown in Table 4, the analyses revealed that compound 7, sorafenib and staurosporine follow both of Lipinski rule and Veber rule without any violations (M.wt < 500 Da, TPSA<140 $Å^2$, HBA<10, HBD<5). The ratio of hybridized C-sp3 atoms to the total carbon number (fraction of Csp^3) indicated that both compound **7** and sorafenib exhibit a low saturation ratio (0.06–0.10), as compared to staurosporine (Csp^3 = 0.32). Furthermore, the evaluation of solubility with LogS indicated that compound **7** exhibits soluble behavior with ESOL value of −3.27, while sorafenib and staurosporine showed moderately soluble characteristic with ESOL range of −5.06 to −5.11. The prediction of lipophilicity for the compounds was realized by MLOGP (Moriguchi octanol–water partition coefficient) and XLogP3 (partition coefficient) estimation. The analysis indicated that all tested compounds possess acceptable MLogP (1.61–2.60) and XLogP3 (1.99–3.24) values.

The assessment of drug likeness parameters indicated that all evaluated compounds exhibit a considerable bioavailability score (0.55) with no PAIN violation in their structures. Interestingly, compound **7** exhibited a high drug-score value (0.86), as compared to sorafenib and staurosporine (0.2 and 0.37, respectively). In addition, compound 7 showed accessibility as a leadlikeness structure with an easy synthetic approachability (2.35), as compared to sorafenib and staurosporine (2.87 and 4.93, respectively). In addition, the assessment of pharmacokinetic parameters showed that all compounds have no ability to pass the blood–brain barrier (BBB), while they, except for

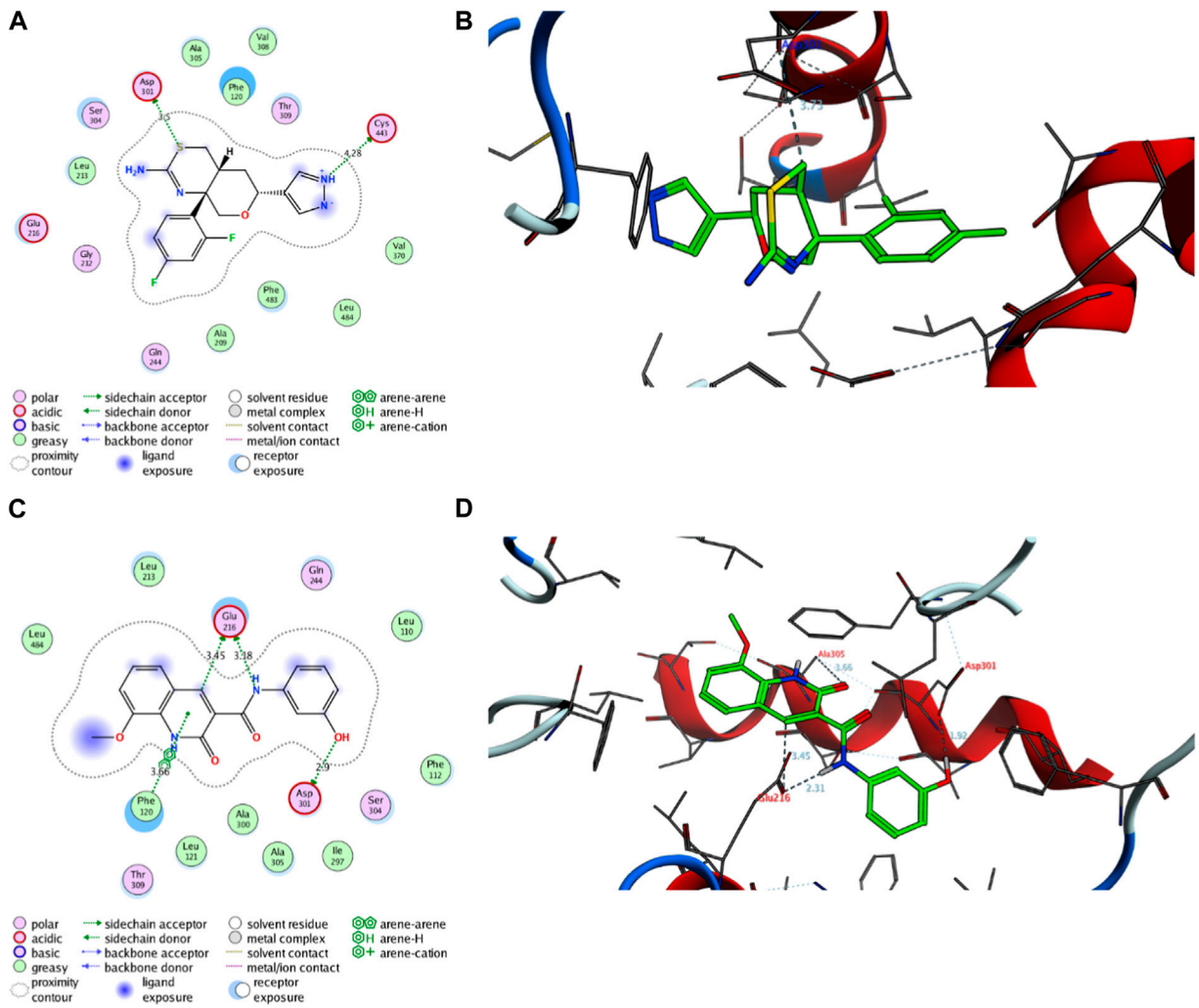

FIGURE 9
Representative binding modes of BACE1 Inhibitor 6 **(A,B)** and compound **7 (C,D)** inside the active site of CYP2D6 (PDB code: *4xrz*) protein through 2D and 3D molecular docking simulations.

staurosporine, have a considerable permeability to gastrointestinal tract. Further, in agreement with our *in vitro* analysis, all compounds showed the ability to be inhibitors for CYP2D6 protein. Taken together, our *in silico* analysis indicates that compound **7** possesses a promising pharmacokinetic and drug likeness properties to be considered in the development of anticancer drugs.

The assessment of toxicity indicated that all compounds belong to class IV with an oral lethal dose for rats ranging from 2.077–2.464 mol/kg (Table 5). The maximum tolerated dose for humans was relatively low for sorafenib and staurosporine (0.253 and 0.271 log mg/kg/d, respectively), while compound 7 displayed a considerable higher dose (0.615 log mg/kg/d). Further, all tested compounds did not show features for AMES toxicity (except for staurosporine), and skin sensitization. The tested compounds did not display ability to inhibit human ether-a-go-go-related gene 1 (hERG 1), while they showed to be inhibitors for (hERG 2).

As indicated in Table 5, all tested compounds displayed inactivity toward carcinogenicity mutagenicity, and heat shock factor response element with high probability values. The analysis further revealed that all tested compounds, except for sorafenib, exhibit no activity toward tumor suppressor phosphoprotein p53, and mitochondrial membrane potential with probability values ranging from 0.68–0.96. On the other hand, all compounds displayed considerable probability values toward immunotoxicity and hepatotoxicity (except for staurosporine). Interestingly, compound 7 showed inactivity to cytotoxicity with high probability value (0.93), while sorafenib and staurosporine exhibited activity to cytotoxicity with considerable probability. In conclusion, considering the toxicity profile observed, it can be inferred that compound **7** displayed a favorable safety profile. This profile was characterized by its non-carcinogenic, non-mutagenic, and non-cytotoxic properties, along with a satisfactory LD_{50} value.

TABLE 4 ***In silico*** **assessment of drug likeness, pharmacokinetics, and chemical properties of compound 7, sorafenib, and staurosporine.**

Assessment	Parameter	Compound 7	Sorafenib	Staurosporine
Chemical properties	M.Wt (Da)	310.30	464.82	466.53
	TPSA (Å^2)	91.42	92.35	69.45
	No. of H-bond acceptors	4	7	4
	No. of H-bond donors	3	3	2
	No. of rotatable bonds	4	9	2
	Fraction Csp3	0.06	0.10	0.32
Solubility	Log S (ESOL)	−3.27	−5.11	−5.06
	Solubility class	Soluble	Moderate	Moderate
Lipophilicity	Log $P_{o/w}$ (XLogP3)	1.99	4.07	3.24
	Log $P_{o/w}$ (MLogP)	1.61	2.91	2.60
Pharmacokinetics	skin permeation (Log K_p, cm/s)	−6.78	−6.25	−6.85
	BBB permeant	No	No	Yes
	GI absorption	High	Low	High
	P- glycoprotein substrate	No	No	Yes
	CYP2D6 inhibitor	Yes	Yes	Yes
Drug likeness	Drug-score*	0.86	0.2	0.37
	Bioavailability Score	0.55	0.55	0.55
	PAINS	0, alert	0, alert	0, alert
	Veber rule (violation)	Yes	Yes	Yes
	Lipinski rule (violation)	Yes	Yes	Yes
	Leadlikeness	Yes	No	No
	Synthetic accessibility	2.35	2.87	4.93

Taken together, our findings indicate that compound **7** demonstrates extraordinary cytotoxic properties against liver cancer cells by interfering with DNA replication, initiating programmed cell death, and displaying dual inhibitory activity against VEGFR-2 and CYP450 enzymes, showcasing its effectiveness. Further, *in silico* pharmacokinetic analysis indicated that compound **7** possesses promising pharmacokinetic and drug-likeness properties to be considered in the development of anticancer drugs (Figure 10). Therefore, the presented findings indicate that compound **7** could be a potential lead compound for the further development of potent anti-liver cancer agents.

3 Materials and methods

3.1 General information (instruments, analysis, and reagents)

All the chemicals and solvents employed in this study were acquired from reputable commercial sources and possessed a high level of purity, meeting analytical grade standards. Rigorous quality control protocols were meticulously implemented to guarantee the precision and reproducibility of the experimental data. Proper calibration of instruments, careful sample preparation, and appropriate reference standards were used to ensure reliable and accurate results in the characterization and analysis of the compounds. The 1H and 13C nuclear magnetic resonance (NMR) spectra were recorded on a Bruker avance 400 MHz spectrometer for ^{1}H NMR and 100 MHz spectrometer for ^{13}C NMR, respectively, using DMSO-d_6 solvent containing tetramethylsilane as an internal standard. The NMR measurements allowed for the characterization and structural elucidation of the compounds by analyzing the chemical shifts in δ (parts per million). Microanalytical data, including the determination of carbon, hydrogen, and nitrogen content, were obtained using a Perkin-Elmer 2,400 series CHN analyzer, which provides accurate elemental analysis and helps in determining the molecular formula of the compounds. The electron ionization mass spectrometry (EI-MS) was carried out using an Agilent Technologies 6890N gas chromatograph (GC) with a selective detector 5,973 mass spectrometer. The EI-MS analysis provided information about the mass-to-charge ratio of the compounds, allowing for the identification and confirmation of their molecular weights and molecular ions. Melting points of

TABLE 5 ***In silico*** **toxicity assessment for compound 7, sorafenib, and staurosporine.**

Assessment parameter	Compound 7	Sorafenib	Staurosporine
Toxicity class	IV	IV	IV
Rat Acute Toxicity (LD_{50}), mol/kg	2.077	2.14	2.464
AMES toxicity	No	No	Yes
Max. dose (human), (log mg/kg/d)	0.615	0.253	0.271
Skin Sensitization	No	No	No
hERG I inhibitor	No	No	No
hERG II inhibitor	Yes	Yes	Yes
Phosphoprotein p53, probability	Inactive, 0.96	Active, 0.57	Inactive, 0.68
Mitochondrial membrane potential, probability	Inactive, 0.70	Active, 0.79	Inactive, 0.70
Heat shock factor response element, probability	Inactive, 0.88	Inactive, 0.96	Inactive, 0.94
Immunotoxicity, probability	Active, 0.96	Active, 0.92	Active, 0.92
Carcinogenicity, probability	Inactive, 0.62	Inactive, 0.50	Inactive, 0.61
Hepatotoxicity, probability	Active, 0.69	Active, 0.82	Inactive, 0.73
Cytotoxicity, probability	Inactive, 0.93	Active, 0.77	Active, 0.79
Mutagenicity, probability	Inactive, 0.97	Inactive, 0.79	Inactive, 0.52

crystalline compounds were measured using an electrothermal melting point apparatus without any correction applied. The melting point, which is the temperature at which a solid compound changes from a solid to a liquid state, is a critical physical property that can provide insights into the purity, crystallinity, and identity of the compounds. The melting point data were carefully recorded and compared with literature values or reference standards to confirm the identity and purity of the compounds. Infrared (IR) spectra were recorded using a Bruker FT-8000 spectrometer, which allows for the analysis of molecular vibrations and functional groups in the infrared region. The IR spectra provides information about the presence of various chemical bonds and functional groups in the compounds, helping in the identification and characterization of the compounds.

3.2 Synthetic protocols and analytical assessments

3.2.1 Synthesis of ethyl 8-methoxycoumarin-3-carboxylate (**1**)

Compound **1** was obtained by fusion of a mixture of 3-methoxy-2-hydroxybenzaldehyde (0.01 mol) and diethylmalonate (0.01 mol) on a hot-plate in the presence of piperidine (1 mL) for 5 min. Subsequently, ethanol (20 mL) was inserted to the reaction mixture and the resulting mixture was heated for 2 h under reflux. After the TLC analysis demonstrated a complete reaction, the reaction mixture was cooled, and poured into ice-water while stirring. The mixture was then neutralized with dilute HCl (2%), and the resulting solid was collected with filtration. The obtained crude solid was washed with water and dried. Finally, the product was re-crystallized from ethanol to give **2** as colorless crystals. Yield 86%, m.p. 105°C, IR (KBr) υ_{max}: 1735, 1715 (C=O), 1,605, 1,583 (C=C), 1,125, 1,083 (C-O) cm^{-1}.^{1}H-NMR (DMSO-d_6, ppm) δ: 1.32 (t, 3H, CH_3), 3.92 (s, 3H, OCH_3), 4.31 (q, 2H, OCH_2), 7.30–7.45 (m, 3H, Ar-H), 8.71 (s, 1H, H-4 of coumarin ring). ^{13}C-NMR (DMSO-d_6, ppm) δ: 164.45, 163.04 (C=O), 157.15, 154.41 (C-O), 149.14 (C-4 of pyranone ring), 134.95, 130.73, 125.30, 118.76, 118.24, 116.60 (C-aromatic and C-3 of pyranone ring), 61.72 (OCH_2), 57.10 (OCH_3), 14.53 (CH_3). Anal. Calcd for $C_{13}H_{12}O_5$ (M. wt. = 248): C, 62.90; H, 4.84. Found: C, 62.61; H, 4.54.

3.2.2 Synthesis of 8-methoxycoumarin-3-carboxylic acid (**2**)

A solution containing (1, 0.01 mol) of coumarin ester dissolved in 25 mL of ethanoic acid was subjected to a reaction with HCl (4N, 20 mL). The resulting mixture was heated under reflux for 2 h, and the progress of the reaction was monitored using TLC analysis. Once complete hydrolysis had occurred, the reaction mixture was carefully poured into crushed ice and left at room temperature for 18 h. The solid product that formed was separated by filtration, thoroughly washed with water, and subsequently dried. Recrystallization of the crude product utilizing ethanol as a solvent afforded compound 2 as colorless crystals. Yield 57%, m.p. 186 °C. IR (KBr) υ_{max}: 3,355–2,951 (br. OH), 1726–1703 (br. C=O), 1,610, 1,580 (C=C), 1,036, 1,025 (C-O) cm^{-1}.^{1}H-NMR ((DMSO-d_6, ppm) δ: 3.93 (s, 3H, OCH_3), 7.31–7.45 (m, 3H, Ar-H), 8.71 (s, 1H, H-4 of coumarin ring). ^{13}C-NMR (DMSO-d_6, ppm) δ: 164.49, 156.90 (C=O), 148.95, 146.67 (C-O), 144.24 (C-4 of coumarin ring), 125.18, 121.52, 119.07, 118.96, 116.61 (C-aromatic and C-3 of pyranone ring), 56.60 (OCH_3). MS: *m/z* (%) = 221 (M^++1, 16.00), 220 (M^+, 96.36), 203 (22.34), 177 (8.93), 176 (100), 161 (15.58), 149 (7.22), 148 (38.72), 147 (20.17), 146 (6.35), 141 (7.33), 139 (34.97), 133 (61.14), 131 (4.08), 120 (17.92),

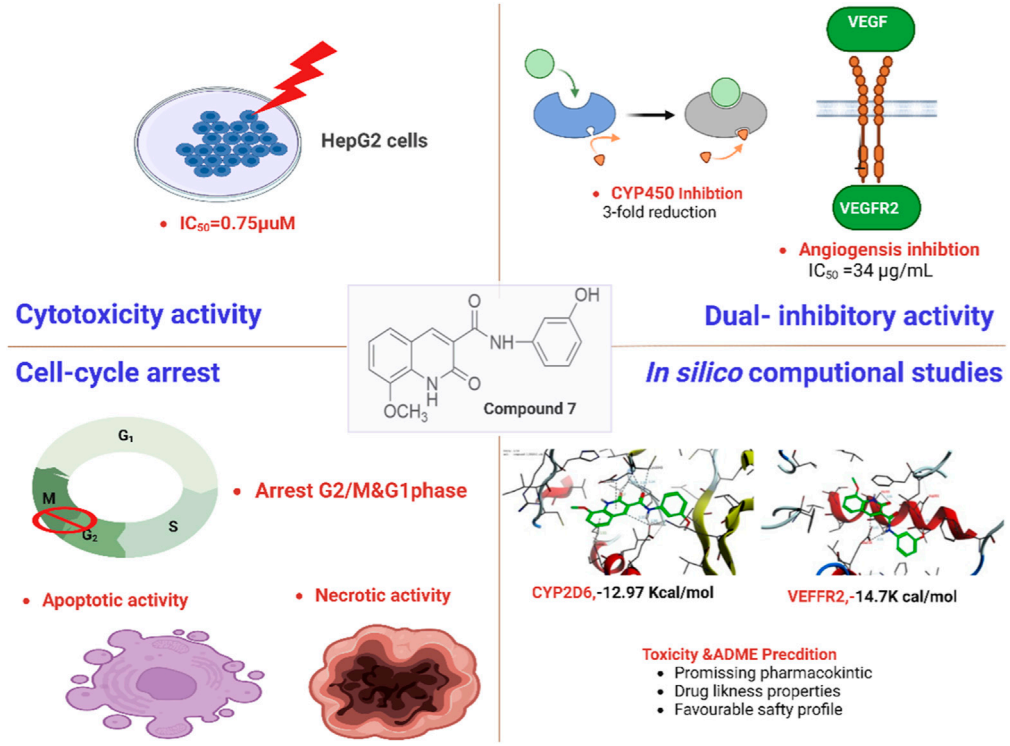

FIGURE 10
Representative graph for the antitumor potential of compound **7** against liver cancer.

119 (12.91), 118 (18.20), 117 (2.41), 111 (7.98), 105 (52.55), 104 (7.43), 103 (12.87), 102 (10.13), 91 (17.12), 90 (12.72), 89 (24.94), 88 (5.49), 77 (33.45), 76 (16.34), 75 (7.56), 65 (7.99), 63 (5.95), 62 (1.90), 51 (13.66). Anal. Calcd for $C_{11}H_8O_5$ (M. wt. = 220): C, 60.00; H, 3.64. Found: C, 59.81; H, 3.33.

3.2.3 Synthesis of *N*-(3-hydroxy)-phenyl 8-methoxycoumarin-3-carboxamide (**3**)

Treatment of coumarin-3-carboxlic acid (**2**, 0.01 mol) with thionyl chloride (25 mL) afforded a clear solution which was subsequently heated for 2 h under reflux. After excess thionyl chloride was removed under reduced pressure, the resulting mixture was treated with 3-aminophenol (0.01 mol) and dimethyl formamide (20 mL). The obtained reaction mixture was subjected to reflux conditions for an additional 2 h, during which it was heated. The reflux continued until the TLC analysis confirmed that the reaction had fully completed. Following this, the reaction mixture was cooled to room temperature and carefully introduced into ice-water while maintaining continuous stirring. The resulting mixture was allowed to stand overnight at ambient temperature. The afforded crude solid was collected by filtration, washed with water, and dried. Purification of obtained crude product by recrystallization from ethanol as a solvent provided compound **3** as yellow crystals. Yield 71%, m.p. 256 °C. IR (KBr) υ_{max}: 3,410 (OH), 3,225 (NH), 1725–1,690 (br. C=O), 1,610, 1,580 (C=C), 1,121, 1,081, 1,035 (C-O) cm^{-1}.^{1}H-NMR (DMSO-d_6, ppm) δ: 3.96 (s, 3H, OCH_3), 6.57–7.54 (m, 7H, Ar-H), 8.87 (s, 1H, H-4 of pyranone ring), 9.60 (s, 1H, OH), 10.59 (s, 1H, NH) ppm. ^{13}C-NMR (DMSO-d_6, ppm) δ: 160.72, 160.14 (C=O), 158.28, 147.97, 146.78 (C-O), 143.61 (C-4 of pyranone ring), 139.38, 130.25, 125.72, 121.63, 120.60, 119.53, 116.64, 111.94, 111.00, 107.32 (C-aromatic and C-3 of pyranone ring), 56.70 (OCH_3) ppm. MS: *m/z* (%) = 311 (M^+, 7.38), 310 (M^+-1, 1.34), 283 (2.12), 249 (11.46), 248 (95.82), 247 (6.97), 220 (1.08), 204 (9.87), 203 (45.49), 202 (64.10), 192 (1.54), 188 (1.34), 177 (9.93), 176 (100), 175 (14.60), 161 (1.76), 160 (1.43), 148 (7.16), 147 (3.32), 146 (2.22), 133 (7.17), 120 (5.39), 119 (21.69), 118 (7.91), 117 (12.18), 116 (3.07), 115 (3.56), 105 (26.27), 104 (9.63), 103 (3.69), 91 (11.09), 90 (4.29), 89 (16.53), 88 (10.24), 77 (22.00), 76 (28.07), 75 (9.02), 65 (7.02), 63 (8.37), 62 (3.50), 51 (5.96), 50 (9.40). Anal. Calcd for $C_{17}H_{13}NO_5$ (M. wt. = 311): C, 65.59; H, 4.18; N, 4.50. Found: C, 65.33; H, 3.89; N, 4.22.

3.2.4 General procedure for the halogenation reactions (formation of compounds **4** and **8**)

A solution containing 0.01 mol of either Compound **3** or Compound **7** was prepared by dissolving it in 20 mL of glacial acetic acid at ambient temperature. The resulting solution was then gradually treated with a bromine solution (0.01 mol) in 15 mL of glacial acetic acid through dropwise addition. After the reaction mixture was placed under reflux at 60°C, it was allowed to stir for 20 min, the characteristic color of bromine faded away, giving rise to the formation of a solution with a distinct yellow color. Subsequently, at room temperature, a new aliquot of bromine-ethanoic acid solution (1 mL) was gradually introduced to the reaction mixture, followed by stirring for an additional duration of 45–60 min. Once the TLC analysis confirmed that the reaction

had reached completion, the reaction mixture was carefully transferred into ice-water while vigorously stirring. The resulting solid product was subsequently collected through filtration. The crude solid was finally washed with water, dried, and purified by recrystallization utilizing a proper solvent to furnish the desired compound **4** or **8**.

3.2.4.1 Synthesis of N-(3-hydroxy)phenyl 5-bromo-8-methoxycoumarin-3-carboxamide (**4**)

The entitled compound was synthesized following the abovementioned procedure to provide compound **4** as yellow crystals after recrystallization using ethanol as a solvent. Yield 63%, m.p. 289°C. IR (KBr) υ_{max}: 3,420 (br. OH), 3,218 (br. NH_2), 1725–1,695 (br. C=O), 1,605, 1,588 (C=C), 1,087, 1,031 (C-O) cm^{-1}.^{1}H-NMR and ^{13}C-NMR: no data because compound **4** was insoluble in the available solvent. MS: *m/z* (%) = 389 (M^+, unstable), 348 (2.23), 346 (3.66), 328 (21.03), 327 (1.44), 326 (20.14), 283 (8.30), 281 (6.72), 257 (2.64), 256 (12.79), 255 (2.54), 254 (11.80), 219 (6.33), 213 (5.05), 211 (2.13), 199 (6.90), 197 (8.45), 191 (4.86), 185 (3.68), 183 (5.18), 175 (6.34), 173 (2.71), 169 (6.55), 168 (2.42), 167 (5.34), 162 (21.60), 161 (10.57), 160 (28.21), 158 (14.23), 157 (8.58), 152 (10.37), 147 (12.72), 137 (8.60), 135 (5.03), 134 (3.79), 133 (6.74), 131 (4.62), 129 (10.63), 127 (2.91), 119 (10.63), 117 (6.85), 111 (12.25), 110 (9.70), 109 (8.37), 107 (5.02), 105 (29.52), 103 (30.71), 98 (16.26), 97 (25.78), 96 (9.50), 95 (36.29), 91 (21.71), 89 (7.52), 88 (12.00), 87 (11.72), 86 (53.76), 85 (40.86), 84 (100), 83 (42.82), 82 (22.22), 81 (38.44), 79 (22.44), 77 (28.80), 76 (9.01), 75 (37.90), 74 (21.29), 73 (24.16), 71 (43.36), 70 (18.86), 69 (71.40), 67 (16.58), 65 (3.53), 63 (8.64), 60 (19.13), 57 (70.84), 56 (18.66), 55 (57.24), 51 (38.23), 50 (11.91). Anal. Calcd for $C_{17}H_{12}BrNO_5$ (M. wt. = 389): C, 52.44; H, 3.08; N, 3.60. Found: C, 52.18; H, 2.96; N, 3.33.

3.2.4.2 Synthesis of N-(3-hydroxy)phenyl 5-bromo-8-methoxy-azacoumarin-3-carboxamide (**8**)

The entitled compound **8** was obtained as yellow crystals following the abovementioned procedure after recrystallization using ethanol as a solvent. Yield 64%, m.p. 255°C. IR (KBr) υ_{max}: 3,421 (OH), 3,221 (br. NH), 1705, 1,693 (C=O), 1,605, 1,583 (C=C), 1,117, 1,063 (C-O) cm^{-1}.^{1}H-NMR ((DMSO-d_6, ppm) δ: 3.96 (s, 3H, OCH_3), 7.06–7.98 (m, 7H, Ar-H and NH), 8.80 (s, 1H, H-4 of pyridinone ring), 10.38, 10.39 (s, 1H, NH of two isomers) ppm. ^{13}C-NMR (DMSO-d_6, ppm) δ: 160.39, 160.15, 159.71, 159.51 (C=O), 151.88, 146.74 (C-O and C-N), 144.98 (C-4 of azacoumarin ring), 136.07, 135.92, 134.22, 129.10, 125.79, 121.87, 120.23, 119.32, 118.88, 118.45, 115.39, 113.56, 112.80, 111.80 (C-aromatic and C-3 of azacoumarin of two isomers), 57.03, 56.76 ($COCH_3$ of two isomers) ppm. MS: *m/z* (%) = 390 (M^++2, 2.68), 389 (M^++1, 0.55), 388 (M^+, 1.20), 312 (1.01), 311 (20.55), 310 (1.99), 283 (0.12), 282 (3.66), 281 (2.43), 256 (2.51), 213 (1.62), 212 (1.12), 211 (1.12), 204 (14.93), 203 (74.99), 202 (100), 167 (14.24), 157 (1.14), 149 (53.52), 133 (2.43), 132 (1.61), 131 (1.91), 121 (1.90), 119 (16.31), 117 (3.23), 116 (3.88), 115 (1.93), 113 (5.05), 111 (6.42), 109 (3.02), 104 (3.10), 103 (2.20), 97 (13.60), 96 (32.38), 95 (11.09), 94 (23.27), 93 (9.77), 91 (6.42), 89 (9.62), 85 (12.08), 83 (24.20), 82 (21.35), 81 (31.25), 80 (18.10), 79 (13.90), 77 (12.47), 76 (23.50), 75 (7.95), 74 (10.01), 73 (33.71), 71 (41.11), 70 (23.99), 69 (49.86), 68 (12.51), 65 (8.58), 63 (5.44), 62 (3.72), 60 (20.51), 57 (59.16), 56 (21.39), 55 (46.43), 51 (2.84), 50 (3.25). Anal. Calcd for $C_{17}H_{13}BrN_2O_4$ (M. wt. = 388): C, 52.58; H, 3.35; N, 7.22. Found: C, 52.33; H, 3.18; N, 7.07.

3.2.5 General procedure for the synthesis of acetoxy derivatives **5** and **6**

Compound **3** or Compound **4** (0.01 mol) was reacted with 20 mL of acetic anhydride, and the resulting mixture was refluxed for 2 h. After stirring for an additional 2 h under the same conditions, the reaction was stopped by adding it to an ice-water mixture. The resulting reaction mixture was allowed to settle for 24 h at room temperature, and the precipitate formed was separated, rinsed with water, and dried. The crude final products were subjected to recrystallization step utilizing a suitable solvent to afford the desired product (compounds **5** and **6**).

3.2.5.1 Synthesis of N-(2-acetoxy)phenyl 8-methoxycoumarin-3-carboxamide (**5**)

The entitled compound was obtained as yellow crystals following the abovementioned protocol after recrystallization from ethanol. Yield 62%, m.p. 184 °C. IR (KBr) υ_{max}: 3,225 (NH), 1746, 1728, 1,698 (C=O), 1,605, 1,588 (C=C), 1,121, 1,078, 1,038 (C-O) cm^{-1}.^{1}H-NMR ((DMSO-d_6, ppm) δ: 2.30 (s, 3H, $COCH_3$), 3.97 (s, 3H, OCH_3), 6.92–7.67 (m, 7H, Ar-H), 8.88 (s, 1H, H-4 of coumarin ring), 10.77 (s, 1H, NH) ppm. ^{13}C-NMR (DMSO-d_6, ppm) δ: 169.67, 160.62, 160.49 (C=O), 151.24, 148.09, 146.81 (C-O), 143.66 (C-4 of coumarin ring), 139.37, 130.33, 125.76, 121.67, 120.61, 119.47, 118.15, 117.63, 116.76, 113.86 (C-aromatic and C-3 of coumarin ring), 56.73 (OCH_3), 21.35 ($COCH_3$) ppm. MS: *m/z* (%) = 353 (M^+, 9.25), 312 (5.14), 311 (30.57), 310 (10.92), 294 (1.73), 283 (19.16), 282 (4.74), 204 (9.94), 203 (100), 202 (26.96), 175 (2.08), 160 (1.19), 144 (2.31), 120 (1.81), 119 (28.94), 118 (4.03), 117 (19.12), 116 (12.54), 110 (1.24), 109 (10.30), 105 (7.49), 104 (8.01), 103 (3.21), 101 (3.33), 91 (6.37), 90 (2.97), 89 (20.78), 88 (4.76), 83 (3.19), 80 (1.86), 79 (3.40), 77 (17.65), 76 (21.01), 75 (4.90), 65 (10.16), 64 (3.25), 63 (8.47), 57 (7.75), 56 (2.76), 55 (6.31), 51 (7.34). Anal. Calcd for $C_{19}H_{15}NO_6$ (M. wt. = 353): C, 64.59; H, 4.25; N, 3.96. Found: C, 64.33; H, 4.04; N, 3.68.

3.2.5.2 Synthesis of N-(3-acetoxy)phenyl 5-bromo-8-methoxycoumarin-3-carboxamide (**6**)

The desired compound was obtained as pale-yellow crystals following the abovementioned protocol after recrystallization utilizing ethanol as a solvent. Yield 67%, m.p. 205 °C. IR (KBr) υ_{max}: 3,222 (NH), 1749, 1723, 1,691 (C=O), 1,610, 1,589 (C=C), 1,121, 1,083, 1,027 (C-O) cm^{-1}.^{1}H-NMR ((DMSO-d_6, ppm) δ: 2.38, 2.44 (s, 3H, $COCH_3$ of two isomers), 3.96 (s, 3H, OCH_3), 7.37–8.45 (m, 6H, Ar-H), 8.99, 9.01 (s, 1H, H-4 of coumarin of two isomers), 11.19, 11.30 (s, 1H, NH of two isomers) ppm. ^{13}C-NMR (DMSO-d_6, ppm) δ: 168.64, 161.39, 160.42 (C=O), 149.94, 147.94, 146.80 (C-O), 143.84 (C-4 of coumarin ring), 136.92, 135.97, 125.90, 122.06, 119.54, 118.47, 117.90, 117.70, 117.34, 117.14, 111.39, 111.17 (C-aromatic and C-4 of coumarin ring), 56.90, 56.79 (OCH_3 of two isomers), 20.98, 20.71 ($COCH_3$ of two isomers) ppm. MS: *m/z* (%) = 431 (M^+, unstable), 390 (5.25), 389 (3.09), 388 (5.93), 350 (11.40), 349 (4.51), 348 (36.89), 347 (11.70), 346 (40.57), 345 (9.86), 344 (12.37), 329 (13.70), 328 (98.51), 327 (26.31), 326 (52.57), 325 (64.80), 311 (9.49), 310 (3.09), 308 (1.50), 300 (3.41), 299 (2.87), 298 (5.58), 284 (3.27), 283 (49.71), 282 (14.45), 281 (46.58), 280 (7.54),

279 (3.65), 266 (2.45), 265 (1.59), 257 (59.69), 256 (59.69), 255 (23.44), 254 (31.31), 253 (47.79), 247 (8.86), 241 (4.19), 240 (3.60), 239 (9.86), 238 (2.99), 228 (6.33), 227 (3.87), 226 (7.09), 219 (24.54), 218 (7.07), 213 (9.13), 212 (4.53), 211 (13.74), 210 (3.75), 204 (3.14), 203 (41.84), 201 (3.74), 199 (16.31), 198 (4.61), 197 (19.61), 196 (2.77), 191 (11.35), 185 (9.45), 184 (3.55), 183 (8.88), 176 (3.08), 175 (15.90), 174 (3.77), 173 (8.81), 169 (10.80), 168 (3.18), 167 (18.34), 157 (8.74), 156 (8.94), 155 (7.12), 154 (6.52), 153 (5.99), 149 (21.30), 147 (6.61), 141 (4.04), 132 (5.77), 131 (7.36), 129 (4.00), 120 (5.96), 119 (14.24), 118 (8.41), 117 (13.97), 116 (4.57), 105 (6.05), 104 (11.41), 103 (49.99), 108 (9.96), 101 (7.64), 98 (3.85), 97 (11.62), 96 (6.12), 95 (7.34), 93 (5.75), 92 (5.72), 91 (14.41), 90 (19.51), 89 (25.94), 88 (21.28), 87 (29.66), 86 (14.27), 85 (16.58), 84 (13.10), 83 (15.95), 82 (14.14), 81 (21.73), 80 (11.27), 79 (18.76), 78 (12.60), 77 (29.91), 76 (36.39), 75 (100), 74 (74.60), 73 (20.19), 69 (25.38), 65 (9.45), 63 (23.34), 62 (20.53), 61 (15.90), 60 (15.02), 57 (32.74), 55 (31.69), 53 (22.11), 51 (12.14), 50 (12.23). Anal. Calcd for $C_{19}H_{14}BrNO_6$ (M. wt. = 431): C, 52.90; H, 3.25; N, 3.25. Found: C, 52.73; H, 3.01; N, 3.11.

3.2.6 Synthesis of N-(3-hydroxy)phenyl 8-methoxy-azacoumarin-3-carboxamide (**7**)

Compound **3** (0.01 mol) was dissolved in 40 ml of absolute ethanol, and then reacted with 0.03 mol of anhydrous potassium carbonate. Before adding the ammonia solution (35%, 10 mL), the prepared liquid was allowed to heat through reflux for 30 min. The resulting reaction mixture was left to reflux for a further 4 h while TLC analysis monitored the reaction's development. After TLC analysis indicated a complete reaction, the mixture was cooled to room temperature and then carefully transferred into an ice-water mixture to rapidly halt the reaction. The obtained mixture was then carefully neutralized with dilute HCl (2%) till pH~7. the solid obtained from the reaction was isolated through filtration, rinsed with water, and dried. The crude product obtained was then subjected to recrystallization using ethanol as the solvent, resulting in the formation of yellow crystals of compound **7**. Yield 63%, m.p. 225 °C. IR (KBr) υ_{max}: 3,428 (br. OH), 3,228 (NH), 1705–1,695 (br. C=O), 1,605, 1890 (C=C), 1,093, 1,063, 1,032 (C-O) cm^{-1}.^{1}H-NMR (DMSO-d_6, ppm) δ: 3.96 (s, 3H, OCH_3), 6.56–7.55 (m, 7H, Ar-H), 8.87 (s, 1H, H-4 of coumarin ring), 9.60 (s, 1H, OH), 10.60 (s, 1H, NH) ppm. ^{13}C-NMR (DMSO-d_6, ppm) δ: 160.73, 160.12 (C=O), 158.29, 147.98, 146.78 (C-O), 143.61 (C-4 of azacoumarin ring), 139.38, 130.25, 125.71, 121.63, 120.57, 119.52, 116.63, 111.94, 111.00, 107.32 (C-aromatic and C-3 of pyridinone ring), 56.70, 56.51 (OCH_3 of two isomers). MS: *m/z* (%) = 310 (M^+, 1.18), 283 (4.83), 282 (1.39), 250 (1.02), 243 (5.97), 242 (2.76), 227 (4.30), 226 (5.74), 220 (2.63), 219 (23.78), 212 (2.18), 211 (1.36), 205 (2.18), 204 (9.74), 203 (60.89), 202 (3.26), 201 (1.13), 200 (1.04), 196 (1.09), 183 (1.62), 178 (2.85), 177 (12.73), 176 (19.36), 175 (6.98), 174 (2.71), 173 (2.36), 172 (2.49), 162 (2.84), 161 (3.71), 160 (1.50), 155 (2.14), 154 (2.79), 152 (1.12), 151 (2.97), 150 (8.62), 149 (2.90), 148 (10.18), 147 (7.00), 146 (3.68), 145 (2.35), 144 (2.34), 137 (4.92), 136 (13.70), 135 (12.16), 134 (5.76), 133 (17.64), 131 (2.47), 130 (1.79), 128 (1.46), 127 (2.38), 124 (10.66), 123 (2.20), 122 (5.39), 121 (4.42), 120 (8.99), 119 (14.22), 118 (8.09), 117 (9.10), 116 (6.37), 115 (4.04), 111 (1.30), 110 (8.19), 109 (100), 108 (12.86), 107 (10.10), 106 (8.98), 105 (22.58), 104 (10.45), 103 (6.88), 102 (6.27), 101 (4.07), 98 (1.71), 94 (3.59), 93 (6.52), 92 (6.79), 91 (17.02), 90 (8.86), 89 (26.52), 88 (6.74), 87 (4.26), 85 (3.85), 84 (2.71), 82 (4.90), 81 (31.30), 80 (46.18), 79 (11.60), 78 (11.49), 77 (37.03), 76 (29.15), 75 (11.74), 72 (3.15), 69 (3.74), 68 (5.75), 67 (2.65), 66 (5.81), 65 (25.88), 64 (10.80), 63 (23.86), 62 (12.46), 61 (3.81), 57 (2.45), 55 (7.37), 54 (7.86), 53 (22.56), 52 (17.37), 51 (27.99), 50 (14.41). Anal. Calcd for $C_{17}H_{14}N_2O_4$ (M. wt. = 310): C, 65.80; H, 4.55; N, 9.03. Found: C, 65.64; H, 4.29; N, 8.89.

3.3 Cell viability assay

HepG2 and HL-7702 cells were seeded in a 96-well plate at a density of 1 × 104 cells/well. The plate was subsequently placed in a humidified incubator with 5% CO2 at 37°C for 48 h to allow the cells to adhere and proliferate. Following this initial incubation period, the cells were exposed to varying concentrations of the synthesized compounds. The concentrations may have ranged from a lower to higher dose, depending on the experimental design. The molecules were dissolved in an appropriate solvent, DMSO, to obtain the desired concentrations. Control wells with no drug treatment were also included. Following the addition of the molecules, the plate was further incubated for 24 h at 37°C to allow the cells to respond to the drug treatment. The duration of the incubation may have varied depending on the specific experimental requirements. At the end of the 24-h treatment, (3-(4,5-dimethylthiazol-2-yl)-2,5-diphenyltetrazolium bromide) MTT dye was added to each well. MTT is a yellow tetrazolium salt that is utilized by metabolically active cells and converted into purple formazan crystals by mitochondrial enzymes in viable cells. After a further incubation of 4 h at 37°C, the medium in each well was carefully aspirated, and 100 μL of DMSO was added to dissolve the purple formazan crystals formed by viable cells. DMSO is a common solvent used to dissolve the formazan crystals and extract the intracellular purple product. The plate was then subjected to colorimetric measurement using an ELISA plate reader at a wavelength of 570 nm. The intensity of the purple color is proportional to the number of viable cells and reflects the growth condition of the cells in each well. The results were analyzed by calculating the percentage of cell viability or cell growth inhibition compared to the control wells. The data were typically presented as a dose-response curve, and the concentration of the drug that caused a 50% inhibition of cell growth (IC50) was determined as a measure of the drug's potency. The experiments were performed with at least three replicates for each concentration, and the entire experiment was repeated at least three times to ensure the reliability of the results. Statistical analysis may have been performed to determine the significance of differences between the treated groups and the control group, using appropriate statistical tests.

3.4 DNA flow cytometry assay

HepG-2 cells were seeded in 96-well plates at a density of 3.0 × 105 cells per well and incubated at 37°C for 12 h to allow cell attachment and growth. After the initial incubation, the cells were treated with compound 7 at its IC50 concentration dose value for 24 h. Following the treatment period, the cells were collected and fixed with 75% ethanol at 20°C overnight to arrest the cell cycle and

preserve the cellular morphology. The fixed cells were then washed with phosphate-buffered saline (PBS) and centrifuged to remove the ethanol. Next, the cells were incubated with a solution containing ribonuclease (Rnase) at a concentration of 10 mg/mL and propidium iodide (PI) at a concentration of 5 mg/mL. Rnase is an enzyme that digests RNA, while PI is a fluorescent dye that stains DNA. The incubation with Rnase and PI allows for the detection of DNA content in the cells by flow cytometry analysis. After the incubation, the cells were subjected to flow cytometry analysis using a FACS Calibur cytometer with Cellquest software (BD Bioscience, USA). Flow cytometry analysis measures the fluorescence emitted by the cells stained with PI, which correlates with the DNA content. This analysis provides information about the cell cycle distribution of the treated cells, including the percentage of cells in different phases of the cell cycle (e.g., G0/G1, S, and G2/M phases), and allows for the assessment of any changes in the cell cycle profile induced by compound 7 treatment. To ensure the reliability of the results, the experimental conditions were repeated at least three times, and the cells were treated with compound 7 at its IC50 concentration dose value to ensure the cells were exposed to an effective concentration of the compound. This experimental method provided valuable information on the mechanism of action of compound 7 and its potential as an anticancer agent.

3.5 Annexin-V-FITC/PI assay for apoptosis assessment

The experimental method involved seeding HepG-2 cells at a density of 1.5 × 105 cells per well in a 6-well plate and incubating the cells for 12 h to allow for cell attachment and growth. Following this, the cells were treated with compound 7 at its IC50 concentration for 24 h to induce apoptosis. Apoptosis, a programmed cell death process, was detected by staining the cells with Annexin-V conjugated to fluorescein isothiocyanate (FITC) and Propidium Iodide (PI), and the stained cells were analyzed using a FACSCalibur cytometer and Cellquest software (BD Bioscience). Annexin-V is a protein that binds specifically to phosphatidylserine, a phospholipid that is externalized on the outer surface of the plasma membrane during early stages of apoptosis. FITC, a green-fluorescent dye conjugated to Annexin-V, is used to label the apoptotic cells. PI, a red-fluorescent DNA intercalating agent, is used to distinguish between apoptotic and necrotic cells based on their DNA content. The FACSCalibur cytometer is a flow cytometer used to analyze and quantify fluorescently labeled cells. The experimental method likely allowed for the quantification of apoptotic cells by analyzing the Annexin-V-FITC and PI staining patterns using flow cytometry. The results obtained from this method provided information on the induction of apoptosis by compound 7 in HepG-2 cells, further elucidating the mechanism of action of this compound as a potential anticancer agent. To ensure the reliability of the results, the experimental conditions were repeated at least three times, and the cells were exposed to therapeutically effective concentration of the compound, they were treated with compound 7 at a dose corresponding to its IC_{50} concentration. This ensured that the cells were subjected to an optimal concentration of the compound during the experiment. This experimental method yielded crucial information on the mechanism by which it exerts its anticancer effects.

3.6 Assessment of VEGFR-2 kinase activity

The VEGFR-2 inhibitory activity of compound 7 and Sorafenib was evaluated using human VEGFR-2 ELISA (enzyme-linked immunosorbent assay) kits, according to the manufacturer's instructions. A 96-well plate was used for the assay, and each well was filled with a specific volume of the tested molecules and standard concentrations. The wells were coated with an immobilized antibody that specifically binds to VEGFR-2. After incubation, the wells were washed to remove unbound molecules, and biotinylated anti-human VEGFR-2 antibody was added to the wells. This biotinylated antibody specifically binds to VEGFR-2 that is captured by the immobilized antibody. Following another round of washing, a solution of conjugated streptavidin, which binds to the biotinylated antibody, was added to the wells. After washing to remove excess streptavidin, a solution of 3,3′,5,5′-tetramethylbenzidine (TMB) substrate was added to the wells and incubated for 30 min at 37°C. During this incubation, the bound conjugated streptavidin transformed the substrate into a colorful product. After terminating the reaction with an inhibitor solution, the optical density of the produced color was instantly determined at 450 nm with a spectrophotometer. The optical density values were used to quantify the inhibitory activity of compound 7 and Sorafenib against VEGFR-2, with higher inhibition resulting in lower optical density values. This assay provided a quantitative assessment of the inhibitory activity of compound 7 and Sorafenib against VEGFR-2 using an ELISA-based approach.

3.7 Assessment of cytochrome P450 (CYP2D6) activity

Human cells, obtained from the American Type Culture Collection (ATCC), were cultivated in RPMI medium (Invitrogen/Life Technologies). The medium was supplemented with 1% penicillin-streptomycin, 10 μg/ml of insulin (Sigma), and to support cell growth and 10% Fetal Bovine Serum (FBS) (Hyclone) viability. The cells were maintained at 37°C in a humidified atmosphere with 5% CO2. Cells were seeded into a 96-well plate at a density of 1.2–1.8 × 10,000 cells/well in a volume of 100 μL of complete growth medium. Compound 7 and SOR were added to the wells at various concentrations, ranging from low to high concentrations, to create a concentration-response curve. Each concentration was tested in triplicate. A control well with only complete growth medium was included as a negative control. The plate was incubated for 18–24 h at 37°C to allow the cells to adhere and grow in the presence of compound 7 and SOR. After the incubation period, the CYP inhibitory effect of compound 7 and SOR was evaluated using the Cytochrome P450 2D6 (CYP2D6) Inhibitor Screening Kit, following the manufacturer's guidelines. The culture media was quickly withdrawn, and the cultured cells were rinsed with PBS. Then, 100 μL of the CYP2D6 enzyme substrate solution was added to each well, and the plate was incubated for a specified period of time (as recommended by the manufacturer) at 37°C. After the incubation, the fluorescence intensity of the converted product was measured using a FLx800™ Fluorescence Microplate Reader at the excitation

wavelength of 390 nm and the emission wavelength of 488 nm. The fluorescence intensity data was used to generate concentration-response curves for compound 7 and SOR. The concentration that induced 50% maximal inhibition of CYP2D6 enzyme activity (IC50 value) was determined from the concentration-response curves using appropriate software or statistical methods. The IC50 values were calculated and used to quantify the inhibitory activity of compound 7 and SOR against CYP2D6 enzyme. The data were analyzed for statistical significance and presented as mean ± standard deviation (SD) from triplicate measurements.

3.8 Molecular docking study

Extensive *in silico* molecular docking investigations was conducted using MOE software to assess the affinity for attachment of this chemical class to the function sites of VEGFR2 and CYP2D6 proteins. Molecular docking enables the assessment of the binding affinity between small molecules and the binding site of the targeted protein, providing valuable insights into the mode of action of pharmacological compounds. To evaluate the binding mode of the designed N-(substituted-phenyl)-8-methoxycoumarin-3-carboxamide analogues, compound **7** was particularly selected to investigate its binding affinity towards the functional pocket of VEGFR-2 and CYP2D6 proteins. The 2D structure of compound **7** was acquired using Chem.Draw software, allowing for additional computer investigation of the chemical compound. The Protein Data Bank (PDB) provides a wealth of crystallographic structures for both VEGFR2 and CYP2D6 proteins, facilitating our study. Specifically, we selected the crystal structure of VEGFR2 protein co-crystallized with Sorafenib (PDB code: *4asd*) and the crystal structure of CYP2D6 protein co-crystallized with BACE1 inhibitor 6 (PDB code: *4xrz*) (McTigue et al., 2012; Brodney et al., 2015). These structures offer detailed insights into the three-dimensional arrangement of the proteins, enabling a comprehensive analysis of their structural features and potential binding sites. To prepare the 3D structures of VEGFR2 and CYP2D6 proteins for docking simulations, several steps were taken. First, the structures were protonated to account for the ionization states of amino acid residues at a specific pH. Next, partial charges were assigned to the atoms, and any additional chains and water molecules were removed from the structures to focus solely on the protein of interest. The MMFF94X force field was used to represent the distribution of charges within proteins, and energy minimization was carried out to optimize their conformations. To ensure the reliability and accuracy of the docking process, adjustments were made to the docking protocol. These adjustments involved employing Triangle Matcher placement and the London dG scoring function. The customized protocol aimed to improve the accuracy of predicting ligand binding. To confirm the effectiveness of the modified protocol, the binding affinity and interaction mode of the original co-crystallized ligand were carefully analyzed and compared to the reported data. This comparison served as a benchmark to assess the reliability of the docking results. Following the docking simulations, a thorough evaluation was performed on the resulting data. The binding modes exhibiting significantly strong binding affinity were specifically identified and chosen for subsequent analysis, taking into consideration their potential enlightenment to the desired targets. These selected binding modes were then used to estimate the corresponding docking scores and binding energies, providing quantitative measurements of the ligand-receptor interactions. By employing this rigorous docking approach, incorporating Triangle Matcher placement and the London dG scoring function, the validity and accuracy of the docking predictions were enhanced. The evaluation of the original ligand's binding interactions and the subsequent selection of high-affinity binding modes allowed for a comprehensive analysis of the ligand's potential binding affinity and energetics. In our analysis, we generated a total of 50 conformations crossponding to each protein, which were further assessed to examine the interactions between the ligand (compound 7) and amino acid residues. Additionally, the binding energy of each pose was assessed to quantify the strength of the ligand-protein interactions and provide insights into the stability and potential affinity of the compound within the binding site.

3.9 *In silico* ADME and toxicity prediction

In order to comprehensively assess the pharmacokinetic properties, drug-likeness, and potential toxicity of compound 7, an *in silico* computational evaluation and prediction were conducted. This evaluation involved comparing compound 7 with the reference drugs sorafenib and staurosporine. To perform these assessments, several computational tools were employed, including SwissADME, Protox II, OSIRIS Property Explorer, and pkCSM (Alzahrani et al., 2022; Abdelgalil et al., 2023; Hassan et al., 2023; Ragab et al., 2023). These tools have been widely used and established in the field for predicting various pharmacological and physicochemical properties of small molecules. SwissADME was employed to forecast essential pharmacokinetic variables, encompassing absorption, distribution, metabolism, excretion, and toxicity (ADMET). Protox II was employed to predict the potential toxicity of compound 7 by analyzing its interaction with various protein targets. OSIRIS Property Explorer was utilized to evaluate drug-likeness and predict the likelihood of compound 7 possessing specific toxicological, physicochemical, and environmental properties. Lastly, pkCSM was employed to assess the compound's potential to bind to different proteins and predict its pharmacokinetic properties. By utilizing these computational tools, a comprehensive evaluation of compound 7 was conducted, considering its pharmacokinetic properties, drug-likeness, and potential toxicity. The comparison with the reference drugs sorafenib and staurosporine allowed for a relative assessment of compound 7's profile. These computational predictions contribute to the initial characterization of compound 7 and provide valuable insights into its potential as a therapeutic agent (Alzahrani et al., 2022; Abdelgalil et al., 2023; Hassan et al., 2023; Ragab et al., 2023).

4 Conclusion

Liver cancer continues to be a prominent issue in global health, representing the sixth most frequently diagnosed cancer and the fourth

highest contributor to cancer-related fatalities on a global scale. The current study focused on investigating the antitumor potency of a novel class of compounds, specifically N-(substituted-phenyl)-8-methoxycoumarin-3-carboxamides, against liver cancer. The compounds were designed, synthesized, and characterized to assess their potential as effective anticancer agents. The assessment of antitumor activity revealed that the synthesized class of compounds exhibited significant cytotoxicity against Hep-G2 cells, a liver cancer cell line, surpassing the efficacy of the drug staurosporine while exhibiting minimal impact on normal cells. Compound **7** exhibited the highest cytotoxic activity against Hep-G2 cells among the synthesized compounds, displaying an IC_{50} value of 0.75 μM, which outperformed staurosporine's cytotoxicity (IC_{50} = 8.37 μM). Further investigation into the mechanism of action of compound **7** unveiled its ability to interfere with DNA replication, induce DNA damage, and consequently lead to cell cycle arrest. Specifically, compound **7** significantly reduced the percentage of cells in the G1 and G2/M phases while increasing the percentage of cells in the S phase. Additionally, flow cytometric analysis indicated that compound **7** triggered programmed cell death through the induction of necrosis and apoptosis in HepG-2 cells. Moreover, compound **7** exhibited a dual-inhibitory activity towards vascular endothelial growth factor receptor-2 (VEGFR-2) and cytochrome P450 enzymes, surpassing the activity of the drug sorafenib. Computational studies provided further insights by revealing a substantial binding affinity of compound **7** towards the binding cavity of VEGFR-2 and CYP450 enzymes. The study findings strongly indicate that the presented class of compounds, notably compound **7**, presents an exciting opportunity as a scaffold for developing exceptionally efficacious agents against liver cancer. These compounds exhibit immense potential for advancing novel therapeutics that can effectively combat liver cancer. The synthesized compounds exhibited remarkable cytotoxic effects on liver cancer cells by disrupting DNA replication, triggering programmed cell death, and demonstrating dual-inhibitory efficacy against VEGFR-2 and CYP450 enzymes. These findings emphasize the potential of these compounds as innovative therapeutic candidates for the treatment of liver cancer. Future research can focus on further optimizing the structure of compound **7** and conducting *in vivo* studies to validate its efficacy and safety profile as a potential liver cancer treatment option.

Data availability statement

The original contributions presented in the study are included in the article/Supplementary Material, further inquiries can be directed to the corresponding authors.

Author contributions

Conceptualization, ER, EA-E, AAE-B, and ES; methodology, ER, EA-E, HA, RA, II, and ES; validation, ER, EA-E, HA, RA, GA, AA, SA, and ES; investigation, ER, EA-E, RA, II, AA, MJ, and SA; resources, ER, EA-E, AAE-B, HA, RA, GA, II, and ES; data curation, ER, EA-E, AAE-B, HA, II, AA, MJ, and SA; writing—original draft preparation, ER, EA-E, AAE-B, and ES; writing—review and editing, ER, EA-E, AAEB, HA, RA, GA, II, AA, MJ, SA, and ES; visualization, ER, EA-E, HA, RA, GA, AA, MJ, and SA; supervision, ER, AAE-B, MJ, SA, and ES; project administration, ER, EA-E, AAE-B, and ES; and funding acquisition, MJ and SA. All authors contributed to the article and approved the submitted version.

Acknowledgments

The authors extend their appreciation to Princess Nourah bint Abdulrahman University Researchers Supporting Project number (PNURSP2023R165), Princess Nourah bint Abdulrahman University, Riyadh, Saudi Arabia.

Conflict of interest

The authors declare that the research was conducted in the absence of any commercial or financial relationships that could be construed as a potential conflict of interest.

Publisher's note

Supplementary material

The Supplementary Material for this article can be found online at: https://www.frontiersin.org/articles/10.3389/fchem.2023.1231030/full#supplementary-material

References

Abdelgalil, M. M., Ammar, Y. A., Elhag Ali, G. A. M., Ali, A. Kh., and Ragab, A. (2023). A novel of quinoxaline derivatives tagged with pyrrolidinyl scaffold as a new class of antimicrobial agents: Design, synthesis, antimicrobial activity, and molecular docking simulation. *J. Mol. Struct.* 1274, 134443. doi:10.1016/j.molstruc.2022.134443

Ahmed, S., Khan, H., Aschner, M., Mirzae, H., Küpeli Akkol, E., and Capasso, R. (2020). Anticancer potential of furanocoumarins: Mechanistic and therapeutic aspects. *Int. J. Mol. Sci.* 21, 5622. doi:10.3390/ijms21165622

Alfayomy, A. M., Abdel-Aziz, S. A., Marzouk, A. A., Shaykoon, M. S. A., Narumi, A., Konno, H., et al. (2021). Design and synthesis of pyrimidine-5-carbonitrile hybrids as COX-2 inhibitors: Anti-inflammatory activity, ulcerogenic liability, histopathological and docking studies. *Bioorg Chem.* 108, 104555. doi:10.1016/j.bioorg.2020.104555

Alzahrani, A. Y., Ammar, Y. A., Abu-Elghait, M., Salem, M. A., Assiri, M. A., Ali, T. E., et al. (2022). Development of novel indolin-2-one derivative incorporating thiazole moiety as DHFR and quorum sensing inhibitors: Synthesis, antimicrobial, and antibiofilm activities with molecular modelling study. *Bioorg Chem.* 119, 105571. doi:10.1016/j.bioorg.2021.105571

Amin, K. M., Abou-Seri, S. M., Awadallah, F. M., Eissa, A. A. M., Hassan, G. S., and Abdulla, M. M. (2015). Synthesis and anticancer activity of some 8-substituted-7-methoxy-2H-Chromen-2-One derivatives toward hepatocellular carcinoma HepG2 cells. *Eur. J. Med. Chem.* 90, 221–231. doi:10.1016/j.ejmech.2014.11.027

Annunziata, F., Pinna, C., Dallavalle, S., Tamborini, L., and Pinto, A. (2020). An overview of coumarin as a versatile and readily accessible scaffold with broad-ranging biological activities. *Int. J. Mol. Sci.* 21, 4618. doi:10.3390/ijms21134618

Antika, L. D., Tasfiyati, A. N., Hikmat, H., and Septama, A. W. (2022). Scopoletin: A Review of its source, biosynthesis, methods of extraction, and pharmacological activities. *Z Naturforsch C J. Biosci.* 77, 303–316. doi:10.1515/znc-2021-0193

Apte, R. S., Chen, D. S., and Ferrara, N. (2019). VEGF in signaling and disease: Beyond discovery and development. *Cell.* 176, 1248–1264. doi:10.1016/j.cell.2019.01.021

Arora, R., Sawney, S., Saini, V., Steffi, C., Tiwari, M., and Saluja, D. (2016). Esculetin induces antiproliferative and apoptotic response in pancreatic cancer cells by directly binding to KEAP1. *Mol. Cancer* 15, 64. doi:10.1186/s12943-016-0550-2

Ayala-Aguilera, C. C., Valero, T., Lorente-Macías, Á., Baillache, D. J., Croke, S., and Unciti-Broceta, A. (2022). Small molecule kinase inhibitor drugs (1995–2021): Medical indication, pharmacology, and synthesis. *J. Med. Chem.* 65 (2), 1047–1131. doi:10.1021/acs.jmedchem.1c00963

Bakare, S. B. (2021). Synthesis and anticancer evaluation of some coumarin and azacoumarin derivatives. *Pol. J. Chem. Technol.* 23, 27–34. doi:10.2478/pjct-2021-0013

Banhart, S., Saied, E. M., Martini, A., Koch, S., Aeberhard, L., Madela, K., et al. (2014). Improved plaque assay identifies a novel anti-Chlamydia ceramide derivative with altered intracellular localization. *Antimicrob. Agents Chemother.* 58, 5537–5546. doi:10.1128/AAC.03457-14

Brodney, M. A., Beck, E. M., Butler, C. R., Barreiro, G., Johnson, E. F., Riddell, D., et al. (2015). Utilizing structures of CYP2D6 and BACE1 complexes to reduce risk of drug–drug interactions with a novel series of centrally efficacious BACE1 inhibitors. *J. Med. Chem.* 58, 3223–3252. doi:10.1021/acs.jmedchem.5b00191

Bruix, J., Qin, S., Merle, P., Granito, A., Huang, Y.-H., Bodoky, G., et al. (2017). Regorafenib for patients with hepatocellular carcinoma who progressed on sorafenib treatment (resorce): A randomised, double-blind, placebo-controlled, phase 3 trial. *Lancet* 389, 56–66. doi:10.1016/S0140-6736(16)32453-9

Bruni, R., Barreca, D., Protti, M., Brighenti, V., Righetti, L., Anceschi, L., et al. (2019). Botanical sources, Chemistry, analysis, and biological activity of furanocoumarins of pharmaceutical interest. *Molecules* 24, 2163. doi:10.3390/molecules24112163

Chaudhary, D., Bedi, P., Santra, S., and Pramanik, T. (2022). Synthesis and biological properties of coumarin analogue: A brief Review. *Lett. Org. Chem.* 19, 362–387. doi:10.2174/1570178618666210202152452

Chen, C.-K., Yu, W.-H., Cheng, T.-Y., Chen, M.-W., Su, C.-Y., Yang, Y.-C., et al. (2016). Inhibition of vegf165/VEGFR2-dependent signaling by LECT2 suppresses hepatocellular carcinoma angiogenesis. *Sci. Rep.* 6, 31398. doi:10.1038/srep31398

Chidambaram, S., El-Sheikh, M. A., Alfarhan, A. H., Radhakrishnan, S., and Akbar, I. (2021). Synthesis of novel coumarin analogues: Investigation of molecular docking interaction of SARS-CoV-2 proteins with natural and synthetic coumarin analogues and their pharmacokinetics studies. *Saudi J. Biol. Sci.* 28, 1100–1108. doi:10.1016/j.sjbs.2020.11.038

Cullen, J. J., Hinkhouse, M. M., Grady, M., Gaut, A. W., Liu, J., Zhang, Y. P., et al. (2003). Dicumarol inhibition of NADPH:quinone oxidoreductase induces growth inhibition of pancreatic cancer via a superoxide-mediated mechanism. *Cancer Res.* 63, 5513–5520.

Dean, L., and Kane, M. (2021). "Codeine therapy and CYP2D6 genotype," in *Medical genetics summaries [internet]* (Bethesda, Maryland: National Center for Biotechnology Information US).

El Azab, I. H., Saied, E. M., Osman, A. A., Mehana, A. E., Saad, H. A., and Elkanzi, N. A. A. (2021). Novel N-bridged pyrazole-1-carbothioamides with potential antiproliferative activity: Design, synthesis, *in vitro* and *in silico* studies. *Future Med. Chem.* 13, 1743–1766. doi:10.4155/fmc-2021-0066

Fayed, E. A., Sabour, R., Harras, M. F., and Mehany, A. B. M. (2019). Design, synthesis, biological evaluation and molecular modeling of new coumarin derivatives as potent anticancer agents. *Med. Chem. Res.* 28, 1284–1297. doi:10.1007/s00044-019-02373-x

Ferlay, J., Colombet, M., Soerjomataram, I., Mathers, C., Parkin, D. M., Piñeros, M., et al. (2019). Estimating the global cancer incidence and mortality in 2018: GLOBOCAN sources and methods. *Int. J. Cancer* 144, 1941–1953. doi:10.1002/ijc.31937

Francisco, C. S., Javarini, C. L., de S Barcelos, I., Morais, P. A. B., de Paula, H., de S Borges, W., et al. (2020). Synthesis of coumarin derivatives as versatile scaffolds for GSK-3β enzyme inhibition. *Curr. Top. Med. Chem.* 20, 153–160. doi:10.2174/1568026619666191019105349

Gaber, A., Alsanie, W. F., Kumar, D. N., Refat, M. S., and Saied, E. M. (2020). Novel papaverine metal complexes with potential anticancer activities. *Molecules* 25, 5447. doi:10.3390/molecules25225447

Galluzzi, L., Vitale, I., Aaronson, S. A., Abrams, J. M., Adam, D., Agostinis, P., et al. (2018). Molecular mechanisms of cell death: Recommendations of the nomenclature committee on cell death 2018. *Cell. Death Differ.* 25, 486–541. doi:10.1038/s41418-017-0012-4

Garg, S. S., Gupta, J., Sahu, D., and Liu, C.-J. (2022). Pharmacological and therapeutic applications of esculetin. *Int. J. Mol. Sci.* 23, 12643. doi:10.3390/ijms232012643

Goel, H. L., and Mercurio, A. M. (2013). VEGF targets the tumour cell. *Nat. Rev. Cancer* 13, 871–882. doi:10.1038/nrc3627

Hakkola, J., Hukkanen, J., Turpeinen, M., and Pelkonen, O. (2020). Inhibition and induction of CYP enzymes in humans: An update. *Arch. Toxicol.* 94, 3671–3722. doi:10.1007/s00204-020-02936-7

Hassan, A. S., Morsy, N. M., Aboulthana, W. M., and Ragab, A. (2023). *In vitro* enzymatic evaluation of some pyrazolo[1,5- *a*]pyrimidine derivatives: Design, synthesis, antioxidant, anti-diabetic, anti-Alzheimer, and anti-arthritic activities with molecular modeling simulation. *Drug Dev. Res.* 84, 3–24. doi:10.1002/ddr.22008

Healey, R. D., Saied, E. M., Cong, X., Karsai, G., Gabellier, L., Saint-Paul, J., et al. (2022). Discovery and mechanism of action of small molecule inhibitors of ceramidases. *Angew. Chem.* 134, e202109967. doi:10.1002/anie.202109967

Hicklin, D. J., and Ellis, L. M. (2005). Role of the vascular endothelial growth factor pathway in tumor growth and angiogenesis. *JCO* 23, 1011–1027. doi:10.1200/JCO.2005.06.081

Hu, G., Gao, F., Wang, G., Fang, Y., Guo, Y., Zhou, J., et al. (2021a). Use of proteomics to identify mechanisms of hepatocellular carcinoma with the CYP2D6*10 polymorphism and identification of ANGPTL6 as a new diagnostic and prognostic biomarker. *J. Transl. Med.* 19, 359. doi:10.1186/s12967-021-03038-3

Hu, Y., Hu, C., Pan, G., Yu, C., Ansari, M. F., Yadav Bheemanaboina, R. R., et al. (2021b). Novel chalcone-conjugated, multi-flexible end-group coumarin thiazole hybrids as potential antibacterial repressors against methicillin-resistant Staphylococcus aureus. *Eur. J. Med. Chem.* 222, 113628. doi:10.1016/j.ejmech.2021.113628

Huang, A., Yang, X.-R., Chung, W.-Y., Dennison, A. R., and Zhou, J. (2020). Targeted therapy for hepatocellular carcinoma. *Sig Transduct. Target Ther.* 5, 146–213. doi:10.1038/s41392-020-00264-x

Kaur, M., Kohli, S., Sandhu, S., Bansal, Y., and Bansal, G. (2015). Coumarin: A promising scaffold for anticancer agents. *Anti-Cancer Agents Med. Chem.* 15, 1032–1048. doi:10.2174/1871520615666150101125503

Khamis, Z. I., Pang, X., Cui, Z., Sang, Q.-X. A., and Zhang, J. (2021). Cytochrome P450-2D6: A novel biomarker in liver cancer health disparity. *PLoS One* 16, e0257072. doi:10.1371/journal.pone.0257072

Khirallah, S. M., Ramadan, H. M. M., Aladl, H. A. A., Ayaz, N. O., Kurdi, L. A. F., Jaremko, M., et al. (2022a). Antidiabetic potential of novel 1,3,5-trisubstituted-2-thioxoimidazloidin-4-one analogues: Insights into α-glucosidase, α-amylase, and antioxidant activities. *Pharmaceuticals* 15, 1576. doi:10.3390/ph15121576

Khirallah, S. M., Ramadan, H. M. M., Shawky, A., Qahl, S. H., Baty, R. S., Alqadri, N., et al. (2022b). Development of novel 1,3-disubstituted-2-thiohydantoin analogues with potent anti-inflammatory activity; *in vitro* and in silico assessments. *Molecules* 27, 6271. doi:10.3390/molecules27196271

Kocarnik, J. M., Compton, K., Dean, F. E., Fu, W., Gaw, B. L., Harvey, J. D., et al. (2022). Global burden of disease 2019 cancer collaboration, cancer incidence, mortality, years of life lost, years lived with disability, and disability-adjusted life years for 29 cancer groups from 2010 to 2019: A systematic analysis for the global burden of disease study 2019. *JAMA Oncol.* 8, 420–444. doi:10.1001/jamaoncol.2021.6987

Konkoľová, E., Hudáčová, M., Hamuľaková, S., Jendželovský, R., Vargová, J., Ševc, J., et al. (2021). Tacrine-coumarin derivatives as topoisomerase inhibitors with antitumor effects on A549 human lung carcinoma cancer cell lines. *Molecules* 26, 1133. doi:10.3390/molecules26041133

Küpeli Akkol, E., Genç, Y., Karpuz, B., Sobarzo-Sánchez, E., and Capasso, R. (2020). Coumarins and coumarin-related compounds in pharmacotherapy of cancer. *Cancers (Basel)* 12, 1959. doi:10.3390/cancers12071959

Li, W.-B., Qiao, X.-P., Wang, Z.-X., Wang, S., and Chen, S.-W. (2020). Synthesis and antioxidant activity of conjugates of hydroxytyrosol and coumarin. *Bioorg Chem.* 105, 104427. doi:10.1016/j.bioorg.2020.104427

Liang, H., Shi, Y., Zeng, K., Zhao, M., Tu, P., and Jiang, Y. (2020). Coumarin derivatives from the leaves and twigs of murraya exotica L. And their anti-inflammatory activities. *Phytochemistry* 177, 112416. doi:10.1016/j.phytochem.2020.112416

Liu, C.-Y., Chen, K.-F., and Chen, P.-J. (2015). Treatment of liver cancer. *Cold Spring Harb. Perspect. Med.* 5, a021535. doi:10.1101/cshperspect.a021535

Liu, G.-L., Liu, L., and Shan, L.-P. (2020b). Evaluation on the antiviral effect of a hydroxycoumarin against infectious hematopoietic necrosis virus infection *in vitro* and *in vivo*. *Fish Shellfish Immunol.* 102, 389–399. doi:10.1016/j.fsi.2020.04.048

Liu, H., Xia, D.-G., Chu, Z.-W., Hu, R., Cheng, X., and Lv, X.-H. (2020a). Novel coumarin-thiazolyl ester derivatives as potential DNA gyrase inhibitors: Design, synthesis, and antibacterial activity. *Bioorg Chem.* 100, 103907. doi:10.1016/j.bioorg.2020.103907

Liu, Y., Li, Y., Wang, Y., Lin, C., Zhang, D., Chen, J., et al. (2022). Recent progress on vascular endothelial growth factor receptor inhibitors with dual targeting capabilities for tumor therapy. *J. Hematol. Oncol.* 15, 89. doi:10.1186/s13045-022-01310-7

Llovet, J. M., Kelley, R. K., Villanueva, A., Singal, A. G., Pikarsky, E., Roayaie, S., et al. (2021). Hepatocellular carcinoma. *Nat. Rev. Dis. Prim.* 7, 6–28. doi:10.1038/s41572-020-00240-3

Lu, P.-H., Liao, T.-H., Chen, Y.-H., Hsu, Y.-L., Kuo, C.-Y., Chan, C.-C., et al. (2022). Coumarin derivatives inhibit ADP-induced platelet activation and aggregation. *Molecules* 27, 4054. doi:10.3390/molecules27134054

Luo, X.-Y., Wu, K.-M., and He, X.-X. (2021). Advances in drug development for hepatocellular carcinoma: Clinical trials and potential therapeutic targets. *J. Exp. Clin. Cancer Res.* 40, 172. doi:10.1186/s13046-021-01968-w

McTigue, M., Murray, B. W., Chen, J. H., Deng, Y.-L., Solowiej, J., and Kania, R. S. (2012). Molecular conformations, interactions, and properties associated with drug efficiency and clinical performance among VEGFR TK inhibitors. *Proc. Natl. Acad. Sci.* 109, 18281–18289. doi:10.1073/pnas.1207759109

Medavaram, S., and Zhang, Y. (2018). Emerging therapies in advanced hepatocellular carcinoma. *Exp. Hematol. Oncol.* 7, 17. doi:10.1186/s40164-018-0109-6

Meleddu, R., Deplano, S., Maccioni, E., Ortuso, F., Cottiglia, F., Secci, D., et al. (2021). Selective inhibition of carbonic anhydrase IX and XII by coumarin and psoralen derivatives. *J. Enzyme Inhib. Med. Chem.* 36, 685–692. doi:10.1080/14756366.2021.1887171

Miao, Y., Yang, J., Yun, Y., Sun, J., and Wang, X. (2021). Synthesis and anti-rheumatoid arthritis activities of 3-(4-aminophenyl)-coumarin derivatives. *J. Enzyme Inhib. Med. Chem.* 36, 450–461. doi:10.1080/14756366.2021.1873978

Modi, S. J., and Kulkarni, V. M. (2019). Vascular endothelial growth factor receptor (VEGFR-2)/KDR inhibitors: Medicinal Chemistry perspective. *Med. Drug Discov.* 2, 100009. doi:10.1016/j.medidd.2019.100009

Mohamed, D. I., Abou-Bakr, D. A., Ezzat, S. F., El-Kareem, H. F. A., Nahas, H. H. A., Saad, H. A., et al. (2021). Vitamin D3 prevents the deleterious effects of testicular torsion on testis by targeting MiRNA-145 and ADAM17: *In silico* and *in vivo* study. *Pharmaceuticals* 14, 1222. doi:10.3390/ph14121222

Mohamed, D. I., Alaa El-Din Aly El-Waseef, D., Nabih, E. S., El-Kharashi, O. A., Abd El-Kareem, H. F., Abo Nahas, H. H., et al. (2022b). Acetylsalicylic acid suppresses alcoholism-induced cognitive impairment associated with atorvastatin intake by targeting cerebral MiRNA155 and NLRP3: *In vivo*, and in silico study. *Pharmaceutics* 14, 529. doi:10.3390/pharmaceutics14030529

Mohamed, D. I., Ezzat, S. F., Elayat, W. M., El-Kharashi, O. A., El-Kareem, H. F. A., Nahas, H. H. A., et al. (2022a). Hepatoprotective role of carvedilol against ischemic hepatitis associated with acute heart failure via targeting MiRNA-17 and mitochondrial dynamics-related proteins: An *in vivo* and in silico study. *Pharmaceuticals* 15, 832. doi:10.3390/ph15070832

Mohammed, F. Z., Rizzk, Y. W., Abdelhamid, M. S., and El-Deen, I. M. (2020). *In vivo* biological evaluation of ethyl 4-(7-hydroxy-4-methyl-2-oxoquinolin-1- ylamino)-coumarin-3-carboxylate as an antitumor agent. *Anti-Cancer Agents Med. Chem.* 20, 2246–2266. doi:10.2174/1871520620666200728131219

Nayeli, M.-B., Maribel, H.-R., Enrique, J.-F., Rafael, B.-P., Margarita, A.-F., Macrina, F.-M., et al. (2020). Anti-inflammatory activity of coumarins isolated from Tagetes lucida cav. *Nat. Prod. Res.* 34, 3244–3248. doi:10.1080/14786419.2018.1553172

Niu, M., Yi, M., Li, N., Wu, K., and Wu, K. (2021). Advances of targeted therapy for hepatocellular carcinoma. *Front. Oncol.* 11, 719896. doi:10.3389/fonc.2021.719896

Ozalp, L., Danış, Ö., Yuce-Dursun, B., Demir, S., Gündüz, C., and Ogan, A. (2020). Investigation of HMG-CoA reductase inhibitory and antioxidant effects of various hydroxycoumarin derivatives. *Arch. Pharm.* 353, 1900378. doi:10.1002/ardp.201900378

Özdemir, M., Köksoy, B., Ceyhan, D., Sayın, K., Erçağ, E., Bulut, M., et al. (2022). Design and *in silico* study of the novel coumarin derivatives against SARS-CoV-2 main enzymes. *J. Biomol. Struct. Dyn.* 40, 4905–4920. doi:10.1080/07391102.2020.1863263

Parvin, K., Hasanuzzaman, M., Mohsin, S. M., Nahar, K., and Fujita, M. (2021). Coumarin improves tomato plant tolerance to salinity by enhancing antioxidant defence, glyoxalase system and ion homeostasis. *Plant Biol. (Stuttg)* 23, 181–192. Suppl 1. doi:10.1111/plb.13208

Peter Guengerich, F., Waterman, M. R., and Egli, M. (2016). Recent structural insights into cytochrome P450 function. *Trends Pharmacol. Sci.* 37, 625–640. doi:10.1016/j.tips.2016.05.006

Pfeffer, C. M., and Singh, A. T. K. (2018). Apoptosis: A target for anticancer therapy. *Int. J. Mol. Sci.* 19, 448. doi:10.3390/ijms19020448

Phutdhawong, W., Chuenchid, A., Taechowisan, T., Sirirak, J., and Phutdhawong, W. S. (2021). Synthesis and biological activity evaluation of coumarin-3-carboxamide derivatives. *Molecules* 26, 1653. doi:10.3390/molecules26061653

Qin, H.-L., Zhang, Z.-W., Ravindar, L., and Rakesh, K. P. (2020). Antibacterial activities with the structure-activity relationship of coumarin derivatives. *Eur. J. Med. Chem.* 207, 112832. doi:10.1016/j.ejmech.2020.112832

Ragab, A., Fouad, S. A., Ammar, Y. A., Aboul-Magd, D. S., and Abusaif, M. S. (2023). Antibiofilm and anti-quorum-sensing activities of novel pyrazole and pyrazolo[1,5-a] Pyrimidine derivatives as carbonic anhydrase I and II inhibitors: Design, synthesis, radiosterilization, and molecular docking studies. *Antibiot. (Basel)* 12, 128. doi:10.3390/antibiotics12010128

Rawat, A., and Vijaya Bhaskar Reddy, A. (2022). Recent advances on anticancer activity of coumarin derivatives. *Eur. J. Med. Chem. Rep.* 5, 100038. doi:10.1016/j.ejmcr.2022.100038

Rumgay, H., Arnold, M., Ferlay, J., Lesi, O., Cabasag, C. J., Vignat, J., et al. (2022). Global burden of primary liver cancer in 2020 and predictions to 2040. *J. Hepatology* 77, 1598–1606. doi:10.1016/j.jhep.2022.08.021

Sabeel, Z., Liang, Y., Hao, M., Ying, L., Guo, R., Chen, R., et al. (2023). A comprehensive Review of antitumor properties of Angelica species and their antitumor-responsible constituents and the underlying molecular mechanisms involved in tumor inhibition. *Phytotherapy Res.* 37, 2187–2211. doi:10.1002/ptr.7841

Saied, E. M., and Arenz, C. (2021). Stereoselective synthesis of novel sphingoid bases utilized for exploring the secrets of sphinx. *Int. J. Mol. Sci.* 22, 8171. doi:10.3390/ijms22158171

Saied, E. M., Banhart, S., Bürkle, S. E., Heuer, D., and Arenz, C. (2015). A series of ceramide analogs modified at the 1-position with potent activity against the intracellular growth of Chlamydia trachomatis. *Future Med. Chem.* 7, 1971–1980. doi:10.4155/fmc.15.126

Saied, E. M., Diederich, S., and Arenz, C. (2014). Facile synthesis of the CERT inhibitor HPA-12 and some novel derivatives. *Chem. – Asian J.* 9, 2092–2094. doi:10.1002/asia.201402241

Saied, E. M., El-Maradny, Y. A., Osman, A. A., Darwish, A. M. G., Abo Nahas, H. H., Niedbała, G., et al. (2021). A comprehensive Review about the molecular structure of severe acute respiratory syndrome coronavirus 2 (SARS-CoV-2): Insights into natural products against COVID-19. *Pharmaceutics* 13, 1759. doi:10.3390/pharmaceutics13111759

Saied, E. M., Le, T. L.-S., Hornemann, T., and Arenz, C. (2018). Synthesis and characterization of some atypical sphingoid bases. *Bioorg. Med. Chem.* 26, 4047–4057. doi:10.1016/j.bmc.2018.06.031

Salehian, F., Nadri, H., Jalili-Baleh, L., Youseftabar-Miri, L., Abbas Bukhari, S. N., Foroumadi, A., et al. (2021). A Review: Biologically active 3,4-heterocycle-fused coumarins. *Eur. J. Med. Chem.* 212, 113034. doi:10.1016/j.ejmech.2020.113034

Salem, M. G., El-Maaty, D. M. A., El-Deen, Y. I. M., Elesawy, B. H., Askary, A. E., Saleh, A., et al. (2022). Novel 1,3-thiazole analogues with potent activity against breast cancer: A design, synthesis, *in vitro*, and in silico study. *Molecules* 27, 4898. doi:10.3390/molecules27154898

Sanches, K., Dias, R. V. R., da Silva, P. H., Fossey, M. A., Caruso, Í. P., de Souza, F. P., et al. (2019). Grb2 dimer interacts with coumarin through SH2 domains: A combined experimental and molecular modeling study. *Heliyon* 5, e02869. doi:10.1016/j.heliyon.2019.e02869

Sarmah, M., Chutia, K., Dutta, D., and Gogoi, P. (2021). Overview of coumarin-fused-coumarins: Synthesis, photophysical properties and their applications. *Org. Biomol. Chem.* 20, 55–72. doi:10.1039/D1OB01876K

Schoenleber, S. J., Kurtz, D. M., Talwalkar, J. A., Roberts, L. R., and Gores, G. J. (2009). Prognostic role of vascular endothelial growth factor in hepatocellular carcinoma: Systematic Review and meta-analysis. *Br. J. Cancer* 100, 1385–1392. doi:10.1038/sj.bjc.6605017

Shahzadi, I., Ali, Z., Baek, S. H., Mirza, B., and Ahn, K. S. (2020). Assessment of the antitumor potential of umbelliprenin, a naturally occurring sesquiterpene coumarin. *Biomedicines* 8, 126. doi:10.3390/biomedicines8050126

Shan, L.-P., Zhou, Y., Yan, M.-C., Liu, L., Chen, J., and Chen, J.-P. (2021). A novel antiviral coumarin derivative as a potential agent against WSSV infection in shrimp seedling culture. *Virus Res.* 297, 198387. doi:10.1016/j.virusres.2021.198387

Sharma, D., Dhayalan, V., et al. Sharma, D., Dhayalan, V., Manikandan, C., Dandela, R. (2022). *Recent methods for synthesis of coumarin derivatives and their new applications.* London, UK: IntechOpen. ISBN 978-1-83768-242-3.

Shibuya, M. (2011). Vascular endothelial growth factor (VEGF) and its receptor (VEGFR) signaling in angiogenesis: A crucial target for anti- and pro-angiogenic therapies. *Genes. Cancer* 2, 1097–1105. doi:10.1177/1947601911423031

Silva, V. L. M., Silva-Reis, R., Moreira-Pais, A., Ferreira, T., Oliveira, P. A., Ferreira, R., et al. (2022). Dicoumarol: From Chemistry to antitumor benefits. *Chin. Med.* 17, 145. doi:10.1186/s13020-022-00699-0

Song, J., Ham, J., Hong, T., Song, G., and Lim, W. (2021). Fraxetin suppresses cell proliferation and induces apoptosis through mitochondria dysfunction in human hepatocellular carcinoma cell lines Huh7 and Hep3B. *Pharmaceutics* 13, 112. doi:10.3390/pharmaceutics13010112

Stefanachi, A., Leonetti, F., Pisani, L., Catto, M., and Carotti, A. (2018). Coumarin: A natural, privileged and versatile scaffold for bioactive compounds. *Molecules* 23, 250. doi:10.3390/molecules23020250

Supuran, C. T. (2020). Coumarin carbonic anhydrase inhibitors from natural sources. *J. Enzyme Inhib. Med. Chem.* 35, 1462–1470. doi:10.1080/14756366.2020.1788009

Szwaczko, K. (2022). Coumarins synthesis and transformation via C–H bond activation—a Review. *Inorganics* 10, 23. doi:10.3390/inorganics10020023

Tarantino, G., Di Minno, M. N. D., and Capone, D. (2009). Drug-induced liver injury: Is it somehow foreseeable? *World J. Gastroenterol.* 15, 2817–2833. doi:10.3748/wjg.15.2817

Taylor, C., Crosby, I., Yip, V., Maguire, P., Pirmohamed, M., and Turner, R. M. (2020). A Review of the important role of CYP2D6 in pharmacogenomics. *Genes.* 11, 1295. doi:10.3390/genes11111295

Tong, X., Tang, R., Xiao, M., Xu, J., Wang, W., Zhang, B., et al. (2022). Targeting cell death pathways for cancer therapy: Recent developments in necroptosis,

pyroptosis, ferroptosis, and cuproptosis research. *J. Hematol. Oncol.* 15, 174. doi:10.1186/s13045-022-01392-3

Tran, K. B., Lang, J. J., Compton, K., Xu, R., Acheson, A. R., Henrikson, H. J., et al. (2022). The global burden of cancer attributable to risk factors, 2010–19: A systematic analysis for the global burden of disease study 2019. *Lancet* 400, 563–591. doi:10.1016/S0140-6736(22)01438-6

Viana, C. C., Praxedes, M. F. D. S., de Sousa, W. J. F. N., Bartolazzi, F., Vianna, M. S., Silva, J. L. P. da, et al. (2021). Influence of sex-based differences on oral anticoagulation control in patients taking coumarin derivatives: A systematic Review protocol. *JBI Evid. Synth.* 19, 477–483. doi:10.11124/JBIES-20-00168

Wang, G., Zhang, J., Liu, L., Sharma, S., and Dong, Q. (2012). Quercetin potentiates doxorubicin mediated antitumor effects against liver cancer through P53/bcl-xl. *PLOS ONE* 7, e51764. doi:10.1371/journal.pone.0051764

Wang, J., Lu, M. L., Dai, H. L., Zhang, S. P., Wang, H. X., and Wei, N. (2015). Esculetin, a coumarin derivative, exerts *in vitro* and *in vivo* antiproliferative activity against hepatocellular carcinoma by initiating a mitochondrial-dependent apoptosis pathway. *Braz J. Med. Biol. Res.* 48, 245–253. doi:10.1590/1414-431X20144074

Wang, T., Peng, T., Wen, X., Wang, G., Liu, S., Sun, Y., et al. (2020). Design, synthesis and evaluation of 3-substituted coumarin derivatives as anti-inflammatory agents. *Chem. Pharm. Bull. (Tokyo)* 68, 443–446. doi:10.1248/cpb.c19-01085

Wu, X.-Q., Huang, C., Jia, Y.-M., Song, B.-A., Li, J., and Liu, X.-H. (2014). Novel coumarin-dihydropyrazole thio-ethanone derivatives: Design, synthesis and anticancer activity. *Eur. J. Med. Chem.* 74, 717–725. doi:10.1016/j.ejmech.2013.06.014

Wu, Y., Xu, J., Liu, Y., Zeng, Y., and Wu, G. (2020). A Review on anti-tumor mechanisms of coumarins. *Front. Oncol.* 10, 592853. doi:10.3389/fonc.2020.592853

Xu, X.-T., Deng, X.-Y., Chen, J., Liang, Q.-M., Zhang, K., Li, D.-L., et al. (2020). Synthesis and biological evaluation of coumarin derivatives as α-glucosidase inhibitors. *Eur. J. Med. Chem.* 189, 112013. doi:10.1016/j.ejmech.2019.112013

Zanger, U. M., and Schwab, M. (2013). Cytochrome P450 enzymes in drug metabolism: Regulation of gene expression, enzyme activities, and impact of genetic variation. *Pharmacol. Ther.* 138, 103–141. doi:10.1016/j.pharmthera.2012.12.007

Zengin Kurt, B., Sonmez, F., Ozturk, D., Akdemir, A., Angeli, A., and Supuran, C. T. (2019). Synthesis of coumarin-sulfonamide derivatives and determination of their cytotoxicity, carbonic anhydrase inhibitory and molecular docking studies. *Eur. J. Med. Chem.* 183, 111702. doi:10.1016/j.ejmech.2019.111702

Zhang, J., Tan, Y., Li, G., Chen, L., Nie, M., Wang, Z., et al. (2021). Coumarin sulfonamides and amides derivatives: Design, synthesis, and antitumor activity *in vitro*. *Molecules* 26, 786. doi:10.3390/molecules26040786

Zhao, M., Ma, J., Li, M., Zhang, Y., Jiang, B., Zhao, X., et al. (2021). Cytochrome P450 enzymes and drug metabolism in humans. *Int. J. Mol. Sci.* 22, 12808. doi:10.3390/ijms222312808

Zhu, X.-D., Tang, Z.-Y., and Sun, H.-C. (2020). Targeting angiogenesis for liver cancer: Past, present, and future. *Genes. Dis.* 7, 328–335. doi:10.1016/j.gendis.2020.03.010

frontiers | Frontiers in Chemistry

TYPE Mini Review
PUBLISHED 10 August 2023
DOI 10.3389/fchem.2023.1247805

OPEN ACCESS

EDITED BY
Ramadan M. Ramadan,
Ain Sham University, Egypt

REVIEWED BY
Wilton Rogério Lustri,
University of Araraquara, Brazil
Fatma Elantabli,
Fayoum University, Egypt

*CORRESPONDENCE
Lozan Todorov,
ltodorov@pharmfac.mu-sofia.bg
Irena Kostova,
irenakostova@yahoo.com

RECEIVED 26 June 2023
ACCEPTED 31 July 2023
PUBLISHED 10 August 2023

CITATION
Todorov L and Kostova I (2023), 1,2,3-Triazoles and their metal chelates with antimicrobial activity.
Front. Chem. 11:1247805.
doi: 10.3389/fchem.2023.1247805

1,2,3-Triazoles and their metal chelates with antimicrobial activity

Lozan Todorov* and Irena Kostova*

Department of Chemistry, Faculty of Pharmacy, Medical University—Sofia, Sofia, Bulgaria

The emergence of drug-resistant bacterial and fungal pathogens has highlighted the urgent need of innovative antimicrobial therapeutics. Transition metal complexes with biologically active ligands (coumarins, terpyridines, triazoles, uracils, etc.) have long been investigated for antimicrobial activity. 1,2,3-Triazoles and their molecular derivatives are well known for a plethora of physiological activities, including antibacterial and antifungal. The aim of the present mini-review is to inform the reader about research conducted on potential antimicrobial 1,2,3-triazole complexes with transition metals. What the authors find surprising is how little such research and experimentation has actually been performed and reported in scientific literature. The goal is to highlight research efforts up to now and impress upon the reader the vast perspectives for novel, effective medicinal substances hidden in this yet unexplored field.

KEYWORDS

antimicrobial, transition metal, coordination complex, molecular hybrid, 1,2,3-triazoles

1 Introduction

Nitrogen heterocycles have been extensively studied for their overall medicinal properties (Heravi and Zadsirjan, 2020; Kerru et al., 2020) and in particular—antimicrobial activity, both antibacterial and antifungal. 1,2,3-Triazoles, in particular, have gained attention due to their structural versatility and potential for diverse biological activities—antimicrobial (Banu et al., 1999; Yadav et al., 2023), antiviral (Viegas et al., 2020; Chopade and Shaikh, 2022), anticancer (Slavova et al., 2020; Alam, 2022), anti-inflammatory (Kuntala et al., 2021; Matin et al., 2022), central nervous system (Silalai et al., 2022; Khan et al., 2023), anti-SARS-CoV-2 (Hamadi et al., 2022) to name a few. A vast amount of experimentation and literature reports on novel antimicrobial 1,2,3-triazoles has been accumulated over the years and the pace of research efforts seems to only accelerate. For example,'s sake, the authors of this article present several very detailed reviews on antimicrobial triazoles, published just over the past few years (Zhang, 2019; Xu, 2020; Deng et al., 2022; Li and Zhang, 2022; Rammohan et al., 2023). Transition metals have played a part in medicine for millenia now. Gold (Parish, 1992), silver (Barillo and Marx, 2014) and mercury (Norn et al., 2008), for example, have historically been applied as disinfectant, anti-inflammatory and antimicrobial agents. The accidental discovery of cisplatin (Alderden et al., 2006) and its anticancer effect introduced transition metals to modern, science-based medicine. Ruthenium, gold, silver and lanthanum, to name a few (Todorov and Kostova, 2023), followed suit. A number of biological activities of transition metal complexes have been reported over the years.

- Anticancer activity, manifested through apoptosis, tumor growth inhibition and reduction of drug resistance. Different mechanisms of action have been observed -DNA binding and intra-strand adduct formation (Tchounwou et al., 2021) (platinum complexes), DNA groove binding and possible subsequent DNA cleavage (Lee et al., 2020) (ruthenium complexes), interaction of thiol-containing biomolecules like thioredoxin reductase (Zou et al., 2015) (gold complexes), etc;
- Antimicrobial activity against bacteria, fungi and protozoa, including some drug-resistant strains (Frei et al., 2023);
- Antioxidant activity (Rodríguez-Arce and Saldías, 2021; Abd El-Lateef et al., 2023; Todorov et al., 2023), scavenging reactive oxygen species (ROS) thus protecting healthy cells from oxidative stress-related damage;
- Photodynamic therapy (PDT)—some transition metal complexes with organic ligands act as photosensitizers in PDT, generating ROS upon light irradiation (McKenzie et al., 2019). This allows for localized cytotoxicity against cancer cells and pathogenic microorganisms;
- Anti-inflammatory activity (Mucha et al., 2021; Obaleye et al., 2021) by impacting inflammatory pathways (e.g., cyclooxygenase inhibition (Deb et al., 2020)) and suppression of pro-inflammatory molecules (e.g., cytokine suppression (Lin et al., 2022)), showing potential as possible future treatment agents for inflammatory diseases;
- Bioimaging and phototherapeutic agents (Lee and Lo, 2022; Palacio et al., 2022), based on the intrinsic luminescent properties of the transition metals and the "antenna effect" of the coordinated ligands.

Transition metal complexes have been gaining more and more popularity over the past decades as potential antimicrobial agents. Recent increases in the number of drug-resistant pathogens (Waclaw, 2016) have opened a new door for research of transition metal coordination compounds, characterized with novel mechanisms of action and reduced sensitivity to microbial defenses. With that consideration in mind, the authors ventured to review the available scientific literature on the subject of coordination compounds, containing a transition metal ion and 1,2,3-triazole bearing ligands. Considering the large number of 1,2,3-triazoles with reported antimicrobial activity, their complexes with transition metals have sparsely undergone such research. The authors present herewith all currently available data on the subject, revealing a wide field of opportunity for future investigations.

2 1,2,3-Triazole complexes with antimicrobial activity

A series of Ni(II) and Co.(II) mixed-ligand complexes with 1,2,3-triazole and thiocyanate were synthesized (Olagboye et al., 2013). These relatively simple structures allow for a more "immediate" observation of the impact of the 1,2,3-triazole ligand on antimicrobial activity. The novel complexes and the respective ligands were tested against bacteria (*Staphylococcus aureus, Escherichia coli, Klebsiella aerogenes, Bacillus subtilis* and *Salmonella typhi*) and fungi (*Aspergillus niger*, *Colletotrichum falcatum*, *Alternaria solani*, *Fusarium oxysporum*, and *Rhizoctonia solani*). Exposure time was 24 h, 37 centigrade, agar pour plate technique at 2.5% and 5.0% concentrations of the tested compounds. Streptomycin sulphate (0.2%) was used as a positive standard for bacteria and benlate—for the fungi. Zone of inhibition radii were used to measure the effect. While all complexes, ligands and simple metal salts were weaker antimicrobials, compared to the positive standards, the authors noted that Co.(II)-1,2,3-triazole complexes were more potent antifungal and antibacterial agents, compared to their Ni(II) counterparts. Coordinating the metal ions with 1,2,3-triazole improves antimicrobial activity, the zone of inhibition of 5.0% $CoCl_2$ was 5–12 mm (fungal experiments), coordinating the ion with one molecule 1,2,3-triazole increases the radius to 32–56 mm. 5.0% $NiSO_4$ had a zone inhibition radius of 1–16 mm (fungi), coordinating it with one 1,2,3-triazole increases the radius to 61–76 mm. Coordinating a second 1,2,3-triazole causes a further increase to 70–77 mm. Similar observations were made in the bacterial experiments. The aforementioned experiment serves as a simple demonstration how complexation of a transition metal with the 1,2,3-triazole pharmacophore leads to improvement of the biological activity.

Kumar and coworkers (Kumar et al., 2015a) reveals that a Ru(II) triply-stranded helicate complex, involving a pyridyl-1,2,3-triazole ligand and $RuCl_3$. The complex was stable over a period of 72 h both in DMSO solution (50 centigrade heating) and in presence of the biological ligand histidine. The ligand itself and the corresponding helicate complex were tested for antimicrobial activity against *Staphylococcus aureus* (Gram-positive) and *Escherichia coli* (Gram-negative), Gentamicin being the positive control. Disk diffusion assays demonstrated that both compounds possess modest activity with Minimum Inhibitory Concentration (MIC) > 256 μg/mL. The authors proposed that dinuclear complexes with increased lipophilicity could improve antibacterial action.

Another study involved the synthesis of a series of tris (homoleptic) Ru (II) 2-pyridyl-1,2,3-triazole complexes (Kumar et al., 2016). Ligands were synthesized by way of "click" chemistry and contained various aliphatic butyl, hexyl, octyl, dodecyl, hexadecyl) and aromatic (phenyl, benzyl) moieties. Their antibacterial activities were tested against *S. aureus* (methicillin-resistant (MRSA), strains MR4393 and MR4595 and non-resistant ATCC 25923) and *E. coli* ATCC 25923 by way of disk diffusion, disk dilution and broth microdilution. Gentamicin was used as positive control. Due to limited water solubility, all compounds were tested as DMSO solutions, DMSO having been established to not have biological activity. The most active compounds (Figure 1—compounds 1 and 2) were tested against additional types of pathogenic bacteria—*Acinetobacter calcoaceticus*, and *Mycobacterium smegmatis*. All synthesized ligands did not manifest antimicrobial activity. Complexes bearing an alkyl substituent (6-8 carbon atoms length) at the triazole ring manifested significant antimicrobial activity against non-resistant gram-positive *S. aureus* with MIC between 4 and 8 μg/mL. Promising MICs (4–16 μg/mL) were observed in the resistant *S. aureus* strains, the same or an improved value, compared to Gentamicin (MIC = 16 μg/mL against these same strains). All complexes did not perform well against gram-positive *E. coli*, no effect having been observed within tested concentration ranges.

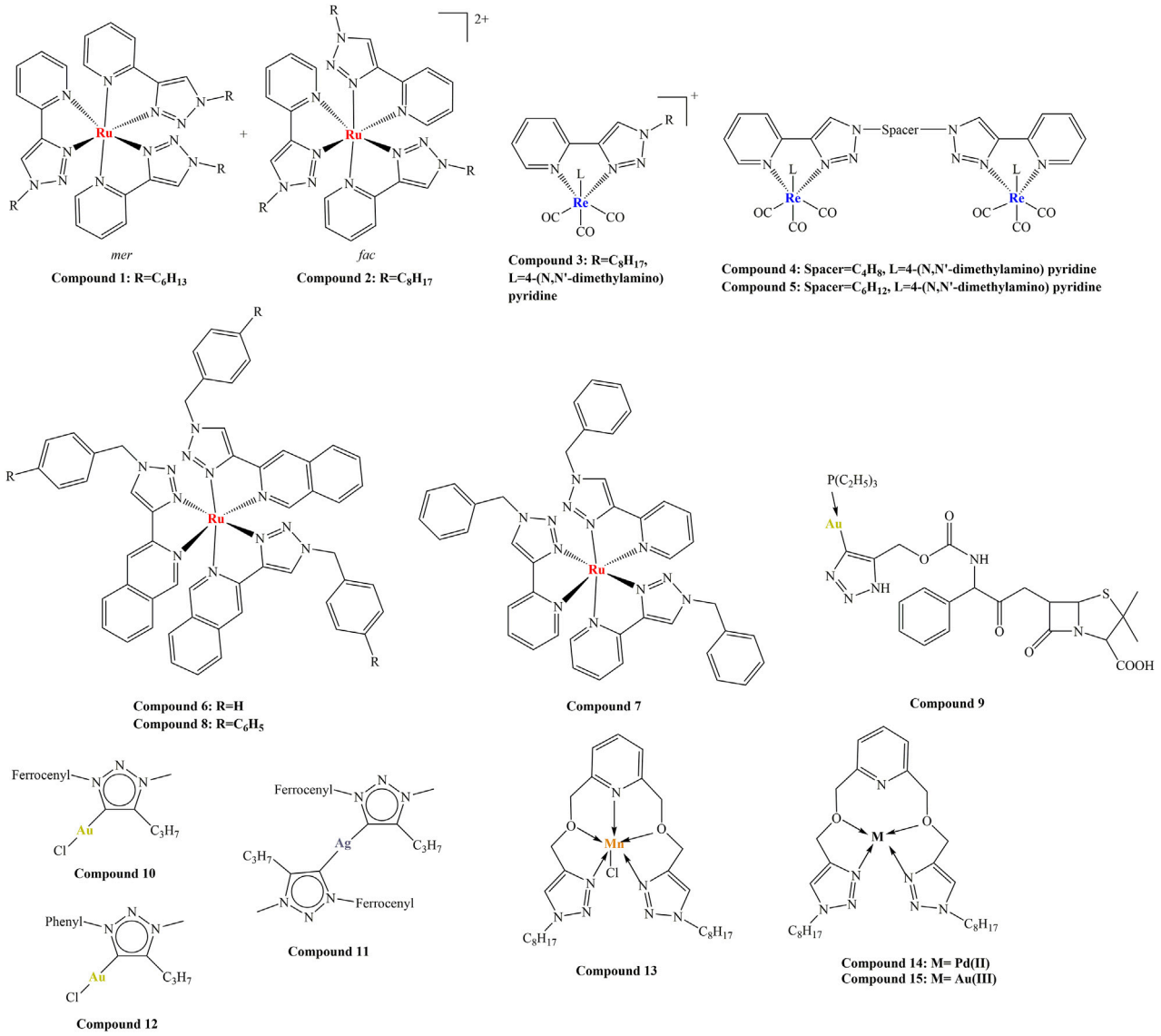

FIGURE 1
Some of the compounds, reported herein.

Longer side chains or aromatic substituents were associated with moderate activity. Increased lipophilicity was discovered to be associated with an improved effect, however, the correlation was observed up to a point. The type of geometric isomer (*mer*-or *fac*-) did not impact biological activity. The main mode of action was suggested to be cell wall/cell membrane disruption (1 h incubation in presence of varying concentrations of the complexes, together with fluorescent propidium iodide, followed by fluorescence measurement). The authors dismissed the redox properties of the Ru (II) ion to be involved in the observed biological activity. Cytotoxicity against healthy human dermal keratinocytes and Vero cells showed cytotoxicity well above MIC against the pathogenic bacteria tested. It was noted that stereochemistry did not significantly impact antimicrobial properties.

Similar mono- and di-*fac*-rhenium (I) tricarbonyl 2-pyridyl-1,2,3-triazole complexes with a variety of aliphatic and aromatic substituents were synthesized (Kumar et al., 2015b). None of the ligands exhibited antibacterial activity *versus E. coli* (ATCC 25922) and *S. aureus* (ATCC 25923). None of the mono-*fac*-tricarbonyl complexes, neutral and cationic, exhibited any activity against Gram-negative *E. coli*. Only one of them exhibited significant activity against *S. aureus* with MIC = 16 μg/mL (Figure 1, compound 3). The positive control, Gentamicin, had MIC< 0.5 μg/mL. The cationic and neutral di-*fac*-tricarbonyl complexes behaved in a similar manner. Only two of them (Figure 1, compounds 4 and 5) exhibited MIC = 16 μg/mL against *S. aureus*, significantly greater than that of Gentamicin. All but two were inactive against *E. coli*. Both active complexes manifested greater activity against *E. coli* MIC = 9 and 15 μg/mL, compared to the positive control Gentamicin MIC = 23 μg/mL. The highest activity is observed in cationic di-rhenium complexes with greater lipophilicity. The authors noted that their Ru (II) analogues are

much more active, thus more appropriate as potential antibacterial agents.

Kreofsky and coworkers generated series of Ru(II) coordination compounds of N-N bidentate chelators with 1,2,3-triazole and isoquinoline subunits (Kreofsky et al., 2020): 1-(1-substituted-1,2,3-triazol-4-yl) isoquinolines and 3-(1-substituted-1,2,3-triazol-4-yl) isoquinolines. Each chelator formed 3:1 coordination compound with Ru (II) as a mixture of stereoisomers with the common formula $[RuL_3]Cl_2$. The antimicrobial properties of these compounds were tested against Gram-positive *Bacillus subtilis* and *Staphylococcus epidermidis* as well as Gram-negative *Escherichia coli* and *Enterobacter aerogenes*. None of the ligands manifested inhibition at concentrations up to 250 uM. Coordinating them with Ru (II) caused dramatic improvement in antimicrobial activity. Isoquinoline stereochemistry did not impact antimicrobial properties. Incorporation of isoquinoline (Figure 1, compound 6), instead of pyridine (Figure 1, compound 7) improved activity 3-6 fold. In benzyl-containing (position 1 of the 1,2,3-triazole ring) compounds, isoquinoline groups improved potency against both gram-positive (20 to 40-fold) and gram-negative (8-fold) bacteria. Improving hydrophobicity by way of phenylbenzyl groups (Figure 1, compound 8) instead of benzyl groups (Figure 1, compound 6) caused a diminishment of activity (15-fold against all tested microorganisms). Replacement of the pyridine N-N chelator unit with isoquinoline caused up to 32-fold improvement in MIC values against both Gram-positive (MIC decreased from 16 μM to 0.4–0.8 μM) and Gram-negative bacteria (MIC decreased from more than 250 μM–31 μM). Gram-positive microorganisms were more sensitive to the Ru(II) complexes, compared to the Gram-negative ones. The eukaryotic C. albicans manifested very high MIC values (more than 250 μM with all tested compounds), demonstrating good selectivity against prokaryotes.

Michaut and coworkers synthesized organogold(I) antibacterial compounds by click chemistry with triethylphosphine-gold(I) azides and an alkyne derivative. They reported a novel series of metallo-antibiotics (chryso-lactams), containing penam-scaffolds, a 1,2,3-triazole and a gold(I) ion (Michaut et al., 2020). The novel compounds were tested against a range of Gram-positive (*Staphylococcus aureus, Staphylococcus epidermis, Enterococcus faecalis and E. faecium*) and one Gram-negative (*Escherichia coli*) bacteria. *E. coli* turned out to be resistant to the novel metallo-antibiotics, due to the low permeability of its outer membrane. All novel compounds were more active than their organic, antibiotic precursors. The size of the phosphine ligand of the gold (I) coordination center seemed to significantly impact biological activity. Triphenylphosphine resulted in lower activity, compared to ampicillin. Dimethylphosphine, a ligand with a significantly decreased size, improved activity, compared to triphenylphosphine. Trimethylphosphine did not further improve activity against Gram-positive bacteria, but caused moderate anti *E. coli* activity. The research team noted that smaller phosphine ligands tended to improve activity. The most active compound, (Figure 1, compound 9), bearing a triethylphposphine, was more effective than ampicillin against *Staphylococcus* species and *Enterococcus* strains. It exhibited MIC values of less than 0.05 μg/mL up to 1 μg/mL in the tested Gram-positive strains. Its toxicity against normal human hepatocytes was presented as EC_{50} = 16.39 μg/mL and at concentrations of up to 7.9 μg/mL cell viability was unaffected. Further study by the same team (Michaut et al., 2021) on the impact of the penam scaffold on antibacterial activity against the same bacterial strains showed that chirality of the phenyl-glycine core appeared to have no effect. The penam scaffold was dispensable, according to the authors, since antibacterial activity of the investigated substances relied on the gold (I) ion, thus reducing the risk of emergence of cross-resistance with other antibiotic families.

Hoyer and coworkers (Hoyer et al., 2021) synthesized series of silver (I) and gold (I) complexes with mesoionic carbenes of 1,2,3-triazole-5-ylidene type. Antibacterial activity was investigated with Gram-negative *Salmonella typhimurium* (liquid microdilution assay) and *Escherichia coli*. Initial steps of the experiment involved the synthesis of triazoles and triazolium salts that bore no significant antibacterial activity. Contrary to previous observations, addition of a ferrocene functionality to position 1 of the triazole ring (Figure 1, compounds 10 and 11) decreased the antibacterial effect, compared to a phenyl functionality in the same position (Figure 1, compound 12). Complexation with Ag (I) and Au (I) improved activity, the silver complexes being more active than the gold ones.

Abdulameer et al synthesized complexes of Mn (II), Pd (II) and Au (III) with 6-bis (((1-octyl-1H-1,2,3-triazol-4-yl) methoxy) methyl) pyridine (Abdulameer and Alias, 2022). As a result of rigorous analysis, involving a variety of analytical methods, the authors concluded that the ligand can behave as a tetradentate and pentadentate chelator. The Mn complex had octahedral geometry, while the Pd and Au had square planarl geometry (Figure 1, compounds 13–15). They were tested for antimicrobial activity against *S. aureus, E. coli* and *C. albicans*. Their potency was measured as width of the inhibition zone, associated with the compound's presence at three different concentrations (10, 50, and 200 ppm). At all investigated concentrations and with all microbes tested, the observed activity increased in the following order: ligand < Mn complex < Pd complex < Au complex. The most potent compound, the Au (III) complex, at the highest dose of 200 ppm manifested inhibition diameters of 35 mm (*E. coli*), 26 mm (*S. aureus*) and 18 mm (*C. albicans*). The researchers did not provide results from a positive control in their article.

Aljohani et al. (2022) and coworkers synthesized 1,2,3-triazole-sulfadiazine-ZnO hybrids and tested them against three carbapenem-resistant metallo-β-lactamase producing *K. pneumoniae* (Kp1, Kp5 and Kp8). The synthesized novel sulfadiazines exhibited MIC values between 128 and 256 μg/mL against all three strains. The ZnO nanoparticles, used in the hybrids, had MIC between 16 and 32 μg/mL. Combining the novel sulfadiazines with the ZnO nanoparticles caused a significant synergistic effect (MIC between 2 and 18 μg/mL). Cell viability assays with normal lung cells (CEAS-2Bs) showed IC_{50} values between 160 and 620 μg/mL. These results demonstrated potential excellent activity *versus* resistant microbial strains, combined with comparatively low toxicity against healthy tissues. Endotracheal aerosolization of the most potent substance revealed its presence in rat's lungs after 24 h (residence duration up to 85.3%). That is combined with notable ability to control pneumonia infection in rats, revealed by histopathological investigations.

Smitten and coworkers synthesized 1,2,3-triazole-based Os(II) complex as prospective cellular imaging agents, testing their red/near-IR luminescence and antimicrobial activity (Smitten et al.,

TABLE 1 Antimicrobial activities of the compounds, described herein, that manifest significant antimicrobial activity.

Compound number	Microbial strain	Activity—tested compound	Activity—control substance (if tested)
1	*S. aureus* (ATCC 25923)	MIC	Gentamicin (MIC)
		8 μg/mL	< 0.125 μg/mL
	S. aureus (NZRM 9653)	1 μg/mL	0.5 μg/mL
	MRSA (MR 9519)	4 μg/mL	0.125 μg/mL
	MRSA (MR 4393)	4 μg/mL	16 μg/mL
	MRSA (MR 4549)	8 μg/mL	16 μg/mL
	M. smegmatis	4 μg/mL	0.125 μg/mL
	A. calcoaceticus	128 μg/mL	64 μg/mL
2	*S. aureus* (ATCC 25923)	MIC	Gentamicin (MIC)
		8 μg/mL	< 0.125 μg/mL
	S. aureus (NZRM 9653)	2 μg/mL	0.5 μg/mL
	MRSA (MR 9519)	8 μg/mL	0.125 μg/mL
	MRSA (MR 4393)	4 μg/mL	16 μg/mL
	MRSA (MR 4549)	8 μg/mL	16 μg/mL
	M. smegmatis	8 μg/mL	0.125 μg/mL
	A. calcoaceticus	16 μg/mL	64 μg/mL
3	*S. aureus* (ATCC 25923)	MIC	Gentamicin (MIC)
		16 μg/mL	< 0.5 μg/mL
	E. coli (ATCC 25922)	none	< 0.5 μg/mL
4	*S. aureus* (ATCC 25923)	MIC	Gentamicin (MIC)
		16 μg/mL	< 0.5 μg/mL
	E. coli (ATCC 25922)	none	< 0.5 μg/mL
5	*S. aureus* (ATCC 25923)	MIC	Gentamicin (MIC)
		32 μg/mL	< 0.5 μg/mL
	E. coli (ATCC 25922)	none	< 0.5 μg/mL
6	*B. subtilis* (ATCC 6051)	MIC	No control tested
		0.8 μM	
	S. epidermidis (ATCC 14990)	0.4 μM	
	E. coli (ATCC 25922)	31 μM	
	E. aerogenes (ATCC 13048)	31 μM	
	C. albicans (ATCC 90028)	250 μM	
7	*B. subtilis* (ATCC 6051)	MIC	No control tested
		>250 μM	
	S. epidermidis (ATCC 14990)	>250 μM	
	E. coli (ATCC 25922)	>250 μM	
	E. aerogenes (ATCC 13048)	>250 μM	
	C. albicans (ATCC 90028)	>250 μM	
8	*B. subtilis* (ATCC 6051)	MIC	No control tested

(Continued on following page)

TABLE 1 (*Continued*) Antimicrobial activities of the compounds, described herein, that manifest significant antimicrobial activity.

Compound number	Microbial strain	Activity—tested compound	Activity—control substance (if tested)
		16 μM	
	S. epidermidis (ATCC 14990)	16 μM	
	E. coli (ATCC 25922)	>250 μM	
	E. aerogenes (ATCC 13048)	>250 μM	
	C. albicans (ATCC 90028)	>250 μM	
9	*S. aureus* (ATCC 25923)	MIC	Ampicillin (MIC)
		0.125 μg/mL	0.5 μg/mL
	S. aureus (ATCC 700699)	0.25 μg/mL	>8 μg/mL
	S. aureus (ATCC 29213)	0.125 μg/mL	0.5 μg/mL
	S. aureus (ST20131,365)	0.25 μg/mL	4 μg/mL
	S. epidermidis (ATCC 14990)	≤ 0.06 μg/mL	1 μg/mL
	S. epidermidis (ATCC 35984)	≤ 0.06 μg/mL	>8 μg/mL
	S. epidermidis (ST20140436)	≤ 0.06 μg/mL	4 μg/mL
	S. epidermidis (ST20150446)	0.125 μg/mL	8 μg/mL
	E. faecalis (JH2-2)	0.5 μg/mL	0.5 μg/mL
	E. faecalis (UCN41)	1 μg/mL	0.5 μg/mL
	E. faecalis (V583)	1 μg/mL	0.5 μg/mL
	E. faecium (ATCC 19434T)	1 μg/mL	0.5 μg/mL
	E. faecium (BM 4147)	2 μg/mL	8 μg/mL
	E. faecium (AUS0004)	1 μg/mL	>8 μg/mL
	E. coli (ATCC 25922)	>8 μg/mL	2 μg/mL
10	*S. typhimurium* (strain not indicated)	Relative growth[1]	No control tested
		≈0.4 a.u	
11	*S. typhimurium* (strain not indicated)	Relative growth[1]	Kanamycin (OD_{600}[2], 50 μM)
		≈0.15 a.u	
		OD_{600}[2] at 50 μM	≈0
		≈0.35	
12	*S. typhimurium* (strain not indicated)	Relative growth[1]	Kanamycin (OD_{600}[2], 50 μM)
		< 0.1 a.u	
		OD_{600}[2] at 50 μM	≈0
		≈0.30	
13	*E. coli* (strain not indicated)	Growth inhibition[3]	No control tested
		25 mm	
	S. aureus (strain not indicated)	22 mm	
	C. albicans (strain not indicated)	16 mm	
14	*E. coli* (strain not indicated)	Growth inhibition[3]	No control tested
		32 mm	
	S. aureus (strain not indicated)	24 mm	

(Continued on following page)

TABLE 1 (*Continued*) **Antimicrobial activities of the compounds, described herein, that manifest significant antimicrobial activity.**

Compound number	Microbial strain	Activity—tested compound	Activity—control substance (if tested)
	C. albicans (strain not indicated)	17 mm	
15	*E. coli* (strain not indicated)	Growth inhibition[3]	No control tested
		35 mm	
	S. aureus (strain not indicated)	26 mm	
	C. albicans (strain not indicated)	18 mm	

[1]Relative growth was described by the original authors as follows.
Relative growth= OD_{600} (*bacterium + compound*)—OD_{600} (*compound*), where OD_{600} is the optical density of the sample at 600 nm. Results are presented for 4 μg/mL. No MICs, were presented.
[2]OD_{600} was used by the original authors as a signal for biological activity when comparing compounds 11 and 12 to Kanamycin. No such comparison was performed for Compound 10. No MICs, were presented. Results shown are for 50 μM concentration.
[3]Presented as width of the inhibition zone in millimeters. Results presented are for the highest concentration tested (200 ppm).

2020). The novel, water-soluble complexes were tested against a panel or resistant cell lines—methicillin resistant *Staphylococcus aureus* (MRSA), uropathogenic, multidrug resistant EC958 ST131 strain of *Escherichia coli*, a multidrug resistant clinical isolate strain of *Pseudomonas aeruginosa*—PA2017 and a multidrug resistant clinical isolate strain of *Acinetobacter baumannii*—AB184. MICs were obtained in nutrient rich media Mueller–Hinton-II (MH-II) and defined media—Glucose Defined Minimal Media (GDMM) for Gram-negative strains and Chemical Defined Media (CDM) for Gram-positive strains. All complexes manifested no activity (same as the positive control Ampicillin) against almost all pathogenic strains. The only exception being MRSA, with which some mild activity was observed (MIC = 48 μg/mL and 96 μg/mL) by two of the complexes. It was noted that *mer*-complexes possessed higher antibacterial effect than their *fac*-isomers. Potential phototoxicity was also investigated. The researchers discovered that light irradiation (48 J/cm^{-2}, 30 min) does improve antibacterial activity compared to the control in dark conditions.

A summary of the data on antimicrobial activities of the most active compounds, described herein, can be viewed in Table 1.

3 Discussion and conclusion

From the published material the authors were able to gather, several tentative conclusions could be derived.

- Combining transition metal ions with low, or even nonexistent, antimicrobial activity with otherwise inactive 1,2,3-triazoles can produce active complexes. Such effects of complexation have previously been observed in transition metal complexes with anticancer properties (Todorov et al., 2023);
- In all works reported herein, synergistic effects between the ligand and the metal ion/nanoparticle have been observed;
- 1,2,3-Triazoles can be utilized as molecular "bridges", connecting transition metal ions to biologically active molecules (e.g., antibiotics, antifungal). This could yield novel antimicrobial agents, with new mechanisms of action, associated with the metal ion, thus overcoming microbial resistance mechanisms;
- Gram-positive bacteria seem to be more sensitive to transition metal complexes, compared to gram-negative. Lipophilicity of the complexes seems to play an important role for the antibacterial effect. There seems to be some kind of a lipophilic "goldilocks zone", where effectiveness is optimal;
- Results reported herein demonstrate the possibility of creating selective antibacterial agents, that are well tolerated by healthy human tissues, i.e., medicinal substances with favorable therapeutic indices.

The authors of the present article would like to emphasize the gap in research when it comes to antimicrobial transition metal complexes with 1,2,3-triazoles. Given the extensive investigational work that has been done in the field of 1,2,3-triazole molecules/molecular hybrids with antibacterial and antifungal properties, it is highly unusual that their coordination compounds have been somewhat "left behind" in that respect until now. One possible reason might be that most investigations, associated with these types of compounds, are directed at cancer research, with antibacterial/antifungal assays being left as somewhat of an afterthought. The ever-increasing number of multidrug-resistant pathogens, resulting from the ubiquitous application of antimicrobial agents in the fields of human medicine, animal husbandry and agriculture, presents a clear and present threat to human society. The aforementioned research gap could provide a perspective path to the discovery of novel, antimicrobial medicinal compounds that are effective against what the general public might call "superbugs". It is the authors' opinion that significantly more research into this matter would be beneficial to all. Synthesis of novel 1,2,3-triazole complexes with platinum, ruthenium, gold and their subsequent testing not only for anticancer, but also for antimicrobial properties could be carried out. In addition, certain other transition metals, like members of the lanthanide series, are known to suppress bacteria (Balusamy et al., 2012). Such metals that are characterized by comparatively low toxicities (Kajjumba et al., 2021) and are relatively abundant in nature which makes them good candidates for novel antimicrobial agents.

Author contributions

IK contributed to the conceptualization of the present work. LT wrote the first draft of the manuscript. All authors contributed to the article and approved the submitted version.

Funding

This study is financed by the European Union-NextGenerationEU, through the National Recovery and Resilience Plan of the Republic of Bulgaria, project No. BG-RRP-2.004-0004-C01.

Acknowledgments

This is a short text to acknowledge the contributions of specific colleagues, institutions, or agencies that aided the efforts of the authors.

Conflict of interest

The authors declare that the research was conducted in the absence of any commercial or financial relationships that could be construed as a potential conflict of interest.

Publisher's note

All claims expressed in this article are solely those of the authors and do not necessarily represent those of their affiliated organizations, or those of the publisher, the editors and the reviewers. Any product that may be evaluated in this article, or claim that may be made by its manufacturer, is not guaranteed or endorsed by the publisher.

References

Abd El-Lateef, H. M., El-Dabea, T., Khalaf, M. M., and Abu-Dief, A. M. (2023). Recent overview of potent antioxidant activity of coordination compounds. *Antioxidants* 12 (2), 213. doi:10.3390/antiox12020213

Abdulameer, J. H., and Alias, M. F. (2022). Synthesis and characterization of some metal complexes with 2, 6-bis (((1-octyl-1H-1, 2, 3-triazol-4-yl) methoxy) methyl) pyridine and the study of their biological activities. *Eurasian Chem. Commun.* 4, 1266–1284. doi:10.22034/ecc.2022.348852.1494

Alam, M. M. (2022). 1, 2, 3-triazole hybrids as anticancer agents: A review. *Arch. Pharm.* 355 (1), 2100158. doi:10.1002/ardp.202100158

Alderden, R. A., Hall, M. D., and Hambley, T. W. (2006). The discovery and development of cisplatin. *J. Chem. Educ.* 83 (5), 728. doi:10.1021/ed083p728

Aljohani, F. S., Rezki, N., Aouad, M. R., Hagar, M., Bakr, B. A., Shaaban, M. M., et al. (2022). Novel 1, 2, 3-Triazole-sulphadiazine-ZnO hybrids as potent antimicrobial agents against carbapenem resistant bacteria. *Antibiotics* 11 (7), 916. doi:10.3390/antibiotics11070916

Balusamy, B., Kandhasamy, Y. G., Senthamizhan, A., Chandrasekaran, G., Subramanian, M. S., and Kumaravel, T. S. (2012). Characterization and bacterial toxicity of lanthanum oxide bulk and nanoparticles. *J. Rare Earths* 30 (12), 1298–1302. doi:10.1016/s1002-0721(12)60224-5

Banu, K. M., Dinakar, A., and Ananthanarayanan, C. (1999). Synthesis, characterization, antimicrobial studies and pharmacological screening of some substituted 1, 2, 3-triazoles. *Indian J. Pharm. Sci.* 61 (4), 202.

Barillo, D. J., and Marx, D. E. (2014). Silver in medicine: A brief history BC 335 to present. *Burns* 40, S3–S8. doi:10.1016/j.burns.2014.09.009

Chopade, P., and Shaikh, A. (2022). Advancements and future perspectives of 1, 2, 3 triazole scaffold as promising antiviral agent in drug discovery. *Int. J. Pharm. Sci. Res.* 13, 4805–4818. doi:10.13040/IJPSR.0975-8232.13(12).4805-18

Deb, J., Lakshman, T. R., Ghosh, I., Jana, S. S., and Paine, T. K. (2020). Mechanistic studies of *in vitro* anti-proliferative and anti-inflammatory activities of the Zn (ii)–NSAID complexes of 1, 10-phenanthroline-5, 6-dione in MDA-MB-231 cells. *Dalton Trans.* 49 (32), 11375–11384. doi:10.1039/d0dt01721c

Deng, C., Yan, H., Wang, J., Liu, K., Liu, B-S., and Shi, Y-M. (2022). 1, 2, 3-Triazole-containing hybrids with potential antibacterial activity against ESKAPE pathogens. *Eur. J. Med. Chem.* 244, 114888. doi:10.1016/j.ejmech.2022.114888

Frei, A., Verderosa, A. D., Elliott, A. G., Zuegg, J., and Blaskovich, M. A. (2023). Metals to combat antimicrobial resistance. *Nat. Rev. Chem.* 7 (3), 202–224. doi:10.1038/s41570-023-00463-4

Hamadi, N. B., Guesmi, A., Algathami, F. K., Khezami, L., Nouira, W., and El-Fattah, W. A. (2022). Synthesis and molecular docking of new 1,2,3-triazole carbohydrates withCOVID-19 proteins. *Curr. Org. Synth.* 20, 238–245. doi:10.2174/1570179419666220414095602

Heravi, M. M., and Zadsirjan, V. (2020). Prescribed drugs containing nitrogen heterocycles: An overview. *RSC Adv.* 10 (72), 44247–44311. doi:10.1039/d0ra09198g

Hoyer, C., Schwerk, P., Suntrup, L., Beerhues, J., Nössler, M., Albold, U., et al. (2021). Synthesis, characterization, and evaluation of antibacterial activity of ferrocenyl-1, 2, 3-triazoles, triazolium salts, and triazolylidene complexes of gold (i) and silver (i). *Eur. J. Inorg. Chem.* 2021 (14), 1373–1382. doi:10.1002/ejic.202100024

Kajjumba, G. W., Attene-Ramos, M., and Marti, E. J. (2021). Toxicity of lanthanide coagulants assessed using four *in vitro* bioassays. *Sci. Total Environ.* 800, 149556. doi:10.1016/j.scitotenv.2021.149556

Kerru, N., Gummidi, L., Maddila, S., Gangu, K. K., and Jonnalagadda, S. B. (2020). A review on recent advances in nitrogen-containing molecules and their biological applications. *Molecules* 25 (8), 1909. doi:10.3390/molecules25081909

Khan, S. A., Akhtar, M. J., Gogoi, U., Meenakshi, D. U., and Das, A. (2023). An overview of 1, 2, 3-triazole-Containing hybrids and their potential anticholinesterase activities. *Pharmaceuticals* 16 (2), 179. doi:10.3390/ph16020179

Kreofsky, N. W., Dillenburg, M. D., Villa, E. M., and Fletcher, J. T. (2020). Ru (II) coordination compounds of NN bidentate chelators with 1, 2, 3 triazole and isoquinoline subunits: Synthesis, spectroscopy and antimicrobial properties. *Polyhedron* 177, 114259. doi:10.1016/j.poly.2019.114259

Kumar, S. V., Lo, W. K., Brooks, H. J., and Crowley, J. D. (2015a). Synthesis, structure, stability and antimicrobial activity of a ruthenium (II) helicate derived from a bis-bidentate "click" pyridyl-1, 2, 3-triazole ligand. *Inorganica Chim. Acta* 425, 1–6. doi:10.1016/j.ica.2014.10.011

Kumar, S. V., Lo, W. K., Brooks, H. J., Hanton, L. R., and Crowley, J. D. (2015b). Antimicrobial properties of mono-and di-fac-rhenium tricarbonyl 2-pyridyl-1, 2, 3-triazole complexes. *Aust. J. Chem.* 69 (5), 489–498. doi:10.1071/ch15433

Kumar, S. V., Scottwell, S. Ø., Waugh, E., McAdam, C. J., Hanton, L. R., Brooks, H. J., et al. (2016). Antimicrobial properties of tris (homoleptic) ruthenium (II) 2-Pyridyl-1, 2, 3-triazole "click" complexes against pathogenic bacteria, including methicillin-resistant staphylococcus aureus (MRSA). *Inorg. Chem.* 55 (19), 9767–9777. doi:10.1021/acs.inorgchem.6b01574

Kuntala, N., Mareddy, J., Telu, J. R., Banothu, V., Pal, S., and Anireddy, J. S. (2021). Nonsteroidal anti-inflammatory drugs based new 1, 2, 3-triazole derivatives: Their design, one-pot synthesis and *in vitro* evaluation. *J. Heterocycl. Chem.* 58 (10), 2018–2032. doi:10.1002/jhet.4328

Lee, L. C-C., and Lo, K. K-W. (2022). Luminescent and photofunctional transition metal complexes: From molecular design to diagnostic and therapeutic applications. *J. Am. Chem. Soc.* 144 (32), 14420–14440. doi:10.1021/jacs.2c03437

Lee, S. Y., Kim, C. Y., and Nam, T-G. (2020). <p>Ruthenium complexes as anticancer agents: A brief history and perspectives</p>. *Drug Des. Dev. Ther.* 14, 5375–5392. doi:10.2147/dddt.s275007

Li, J., and Zhang, J. (2022). The antibacterial activity of 1, 2, 3-triazole-and 1, 2, 4-triazole-containing hybrids against *Staphylococcus aureus*: An updated review (2020-present). *Curr. Top. Med. Chem.* 22 (1), 41–63. doi:10.2174/1568026621666211111160332

Lin, R-K., Venkatesan, P., Yeh, C-H., Chien, C-M., Lin, T-S., Lin, C-C., et al. (2022). Effective topical treatments using innovative NNO-tridentate vanadium (iv) complexes-mediated photodynamic therapy in a psoriasis-like mouse model. *J. Mater. Chem. B* 10 (25), 4759–4770. doi:10.1039/d2tb00344a

Matin, M. M., Matin, P., Rahman, M. R., Ben Hadda, T., Almalki, F. A., Mahmud, S., et al. (2022). Triazoles and their derivatives: Chemistry, synthesis, and therapeutic applications. *Front. Mol. Biosci.* 9, 864286. doi:10.3389/fmolb.2022.864286

McKenzie, L. K., Bryant, H. E., and Weinstein, J. A. (2019). Transition metal complexes as photosensitisers in one-and two-photon photodynamic therapy. *Coord. Chem. Rev.* 379, 2–29. doi:10.1016/j.ccr.2018.03.020

Michaut, M., Steffen, A., Contreras, J-M., Morice, C., Paulen, A., Schalk, I. J., et al. (2020). Chryso-lactams: Gold (I) derivatives of ampicillin with specific activity against Gram-positive pathogens. *Bioorg. Med. Chem. Lett.* 30 (9), 127098. doi:10.1016/j.bmcl.2020.127098

Michaut, M., Steffen, A., Contreras, J-M., Morice, C., Schalk, I. J., Plésiat, P., et al. (2021). 1, 2, 3-Triazole-gold (I)-triethylposphine derivatives active against resistant

Gram-positive pathogens. *Bioorg. Med. Chem. Lett.* 40, 127879. doi:10.1016/j.bmcl.2021.127879

Mucha, P., Skoczyńska, A., Małecka, M., Hikisz, P., and Budzisz, E. (2021). Overview of the antioxidant and anti-inflammatory activities of selected plant compounds and their metal ions complexes. *Molecules* 26 (16), 4886. doi:10.3390/molecules26164886

Norn, S., Permin, H., Kruse, E., and Kruse, P. R. (2008). Mercury--a major agent in the history of medicine and alchemy. *Dan. Med. Arb.* 36, 21–40.

Obaleye, J., Aliyu, A., Rajee, A., and Bello, K. (2021). Synthesis, characterization, *in-vitro* anti-inflammatory and antimicrobial screening of metal (II) mixed diclofenac and acetaminophen complexes. *Bull. Chem. Soc. Ethiop.* 35 (1), 77–86. doi:10.4314/bcse.v35i1.6

Olagboye, S., Okoronkwo, A., and Lajide, L. (2013). Synthesis, characterization and antimicrobial evaluation of mixed ligand complexes of Ni (II) and Co (II) 1, 2, 3-Triazole with thiocyanate. *Res. Rev. J. Chem.* 2 (1), 25–31.

Palacio, I., Moreno, M., Náñez, A., Purwidyantri, A., Domingues, T., Cabral, P., et al. (2022). *Attomolar detection of hepatitis C virus core protein powered by molecular antenna-like graphene effect*. Durham, NC: Research Square.

Parish, R. (1992). Gold in medicine-chrysotherapy. *Interdiscip. Sci. Rev.* 17 (3), 221–228. doi:10.1179/isr.1992.17.3.221

Rammohan, A., Venkatesh, B. C., Basha, N. M., Zyryanov, G. V., and Nageswararao, M. (2023). Comprehensive review on natural pharmacophore tethered 1, 2, 3-triazoles as active pharmaceuticals. *Chem. Biol. Drug Des.* 101 (5), 1181–1203. doi:10.1111/cbdd.14148

Rodríguez-Arce, E., and Saldías, M. (2021). Antioxidant properties of flavonoid metal complexes and their potential inclusion in the development of novel strategies for the treatment against neurodegenerative diseases. *Biomed. Pharmacother.* 143, 112236. doi:10.1016/j.biopha.2021.112236

Silalai, P., Jaipea, S., Tocharus, J., Athipornchai, A., Suksamrarn, A., and Saeeng, R. (2022). New 1, 2, 3-Triazole-genipin analogues and their anti-alzheimer's activity. *ACS omega* 7 (28), 24302–24316. doi:10.1021/acsomega.2c01593

Slavova, K. I., Todorov, L. T., Belskaya, N. P., Palafox, M. A., and Kostova, I. P. (2020). Developments in the application of 1, 2, 3-triazoles in cancer treatment. *Recent Pat. Anti-Cancer Drug Discov.* 15 (2), 92–112. doi:10.2174/1574892815666200717164457

Smitten, K. L., Scattergood, P. A., Kiker, C., Thomas, J. A., and Elliott, P. I. (2020). Triazole-based osmium (II) complexes displaying red/near-IR luminescence: Antimicrobial activity and super-resolution imaging. *Chem. Sci.* 11 (33), 8928–8935. doi:10.1039/d0sc03563g

Tchounwou, P. B., Dasari, S., Noubissi, F. K., Ray, P., and Kumar, S. (2021). Advances in our understanding of the molecular mechanisms of action of cisplatin in cancer therapy. *J. Exp. Pharmacol.* 13, 303–328. doi:10.2147/jep.s267383

Todorov, L., and Kostova, I. (2023). Recent trends in the development of novel metal-based antineoplastic drugs. *Molecules* 28 (4), 1959. doi:10.3390/molecules28041959

Todorov, L., Saso, L., and Kostova, I. (2023). Antioxidant activity of coumarins and their metal complexes. *Pharmaceuticals* 16 (5), 651. doi:10.3390/ph16050651

Viegas, D. J., da Silva, V. D., Buarque, C. D., Bloom, D. C., and Abreu, P. A. (2020). Antiviral activity of 1, 4-disubstituted-1, 2, 3-triazoles against HSV-1 *in vitro*. *Antivir. Ther.* 25 (8), 399–410. doi:10.3851/imp3387

Waclaw, B. (2016). Evolution of drug resistance in bacteria. *Biophysics Infect.* 915, 49–67. doi:10.1007/978-3-319-32189-9_5

Xu, Z. (2020). 1, 2, 3-Triazole-containing hybrids with potential antibacterial activity against methicillin-resistant *Staphylococcus aureus* (MRSA). *Eur. J. Med. Chem.* 206, 112686. doi:10.1016/j.ejmech.2020.112686

Yadav, P., Kaushik, C. P., Yadav, A., Yadav, J., and Singh, D. (2023). Piperazine-1, 2, 3-triazole scaffolds: Design, synthesis, anticancer and antimicrobial evaluation. *Future Med. Chem.* 15 (8), 679–697. doi:10.4155/fmc-2022-0316

Zhang, B. (2019). Comprehensive review on the anti-bacterial activity of 1, 2, 3-triazole hybrids. *Eur. J. Med. Chem.* 168, 357–372. doi:10.1016/j.ejmech.2019.02.055

Zou, T., Lum, C. T., Lok, C-N., Zhang, J-J., and Che, C-M. (2015). Chemical biology of anticancer gold (III) and gold (I) complexes. *Chem. Soc. Rev.* 44 (24), 8786–8801. doi:10.1039/c5cs00132c

frontiers | Frontiers in Chemistry

TYPE Perspective
PUBLISHED 31 January 2024
DOI 10.3389/fchem.2024.1358539

OPEN ACCESS

EDITED BY
Calvin Omolo,
United States International University—Africa, Kenya

REVIEWED BY
Mohammed Salih,
University of Medical Sciences and Technology, Sudan
Madeline E. Kavanagh,
Leiden University, Netherlands

*CORRESPONDENCE
Jean Leandro Dos Santos,
jean.santos@unesp.br

RECEIVED 19 December 2023
ACCEPTED 22 January 2024
PUBLISHED 31 January 2024

CITATION
Bonjorno AF, Pavan AR, Fernandes GFS, Scarim CB, Castagnolo D and Dos Santos JL (2024), BacPROTACs targeting Clp protease: a promising strategy for anti-mycobacterial drug discovery.
Front. Chem. 12:1358539.
doi: 10.3389/fchem.2024.1358539

BacPROTACs targeting Clp protease: a promising strategy for anti-mycobacterial drug discovery

Andressa Francielli Bonjorno[1], Aline Renata Pavan[1,2], Guilherme F. S. Fernandes[3], Cauê Benito Scarim[1], Daniele Castagnolo[3] and Jean Leandro Dos Santos[1]*

[1]School of Pharmaceutical Sciences, São Paulo State University (UNESP), Araraquara, Brazil, [2]Institute of Chemistry, São Paulo State University (UNESP), Araraquara, Brazil, [3]Department of Chemistry, University College London, London, United Kingdom

Tuberculosis (TB) has claimed more lives over the course of two millennia than any other infectious disease worldwide. In 2021, the World Health Organization (WHO) estimated that 10.6 million people were diagnosed with TB, resulting in the deaths of 1.4 million HIV-negative individuals. The emergence of multidrug-resistant TB (MDR-TB), defined as resistance to at least rifampicin (RIF) and isoniazid (INH), and extensively drug-resistant TB (XDR-TB), poses the primary challenge to overcome in the coming years. We have recently conducted an extensive analysis of investments and research endeavours in the field, with the overarching objective of achieving the established milestone of TB eradication by the year 2030. Over the past several years, there has been notable progress in advancing a multitude of promising compounds, each possessing distinct mechanisms of action, into clinical phases of development. However, it is worth noting that strains of mycobacteria resistant to current antitubercular drugs have already emerged for some of these compounds The exploration of the innovative Proteolytic Target Chimeras (PROTACs) protein degradation approach has emerged as a viable avenue for the discovery of novel antimicrobials. While the ubiquitin system is exclusive to eukaryotic cells, certain bacteria use a similar degradation system that relies on the recognition of phosphorylated arginine residues (pArg) by the ClpC:ClpP (ClpCP) protease, thereby leading to protein degradation. In this opinion article, we have described and analized the advances in the use of PROTACs that leverage bacterial proteolytic machinery (BacPROTACs) to design new antitubercular agents. Scope Statement. The development of novel pharmaceuticals for tuberculosis treatment is deemed urgently necessary due to the emergence of resistant strains. In this context, the introduction of new technologies capable of alleviating the disease and attaining the objectives outlined by the World Health Organization is imperative. Among the innovative strategies, the degradation of proteins that are crucial for the survival of the *bacillus* holds promise for generating new medications, particularly those that are effective at treating latent (non-replicating) *Mycobacterium tuberculosis*. Within this perspective, we present the advancements and obstacles encountered in the

exploration of new BacPROTAC compounds, with the intention of encouraging research and illuminating challenges associated with the implementation of BacPROTACs to address to the global tuberculosis crisis.

KEYWORDS

Mycobacterium tuberculosis, tuberculosis, Bac-PROTAC, ClpC1P1P2, protein degradation, new drugs, drug discovery

1 Introduction

Tuberculosis (TB) has claimed more lives over the course of two millennia than any other infectious disease worldwide. In 2021, the World Health Organization (WHO) estimated that 10.6 million people were diagnosed with TB, resulting in the deaths of 1.4 million HIV-negative individuals. Additionally, TB claimed the lives of 214,000 HIV-positive individuals. The emergence of multidrug-resistant TB (MDR-TB), defined as resistance to at least rifampicin (RIF) and isoniazid (INH), and extensively drug-resistant TB (XDR-TB), poses the primary challenge to overcome in the coming years. The latest data from WHO regarding drug-resistant TB is alarming, with an estimated 450,000 new cases and 182,000 deaths from MDR- or RIF-resistant TB in 2021, reflecting a 3.1% increase compared to 2020 (WHO, 2022).

We have recently conducted an extensive analysis of investments and research endeavours in the field to assess whether we are on course to achieve the overarching objective of TB eradication by 2030. (Stop TB partnership, 2019; Treatment Action Group, 2020; Fernandes et al., 2022).

Over the past several years, there has been notable progress in advancing a multitude of promising compounds, each possessing distinct mechanisms of action, into clinical phases of development. However, it is worth noting that strains of mycobacteria that are resistant of these compounds have already emerged (Fernandes et al., 2022). This underscores the urgency of identifying novel antitubercular strategies, particularly those active against infections caused by XDR-TB. Within this context, proteolysis-targeting chimeras (PROTACs) protein degradation approach have emerged as an innovative approach for the discovery of novel antimicrobials, as noted by Békés (2022).

Targeted Protein Degradation (TPD) approach has been extensively investigated in the realm of anticancer agents. PROTACs induce a ternary complex between a protein of interest (POI) and an E3 ligase, facilitating polyubiquitination and subsequent degradation of the POI (Békés et al., 2022). This procedure relies on the covalent attachment of ubiquitin molecules to specific lysine residues of the POI, which enables it to be recruited to, and degraded by, the proteosome (Sakamoto, 2001). The catalytic and event-driven mechanism of action of PROTACS provide the potential for the compounds to be used in lower doses than conventional drugs, which represents a pharmacological gain by reducing the adverse effects. Furthermore, PROTACs only need to attach to, and not modulate the targets to exerts its action. Thus, it expands the range of the druggable targets that can be explored, including non-enzymatic proteins. The engagement of two different macromolecules as long as the proper formation of a ternary complex between them improves the selectivity of these molecules, highlighting the advantages in using PROTACs (Pettersson, 2019; Sun, 2019; Burslem, 2020; Bekes, 2022; Liu, 2022; Sincere, 2023). Therefore, the applicability of the PROTAC technology in the field of antimicrobials emerge as a powerful strategy (Grohmann, 2023).

While the ubiquitin system is exclusive to eukaryotic cells, certain bacteria use a similar degradation system that relies on the recognition of phosphorylated arginine residues (pArg) by the ClpC:ClpP (ClpCP) protease, thereby leading to protein degradation (Trentini, 2016). This unique bacterial pathway hinges upon the critical role played by the ClpC subunit, particularly its $ClpC_{NTD}$ protomer, in facilitating pArg recognition and the subsequent translocation of the target protein into the ClpP compartment for degradation (Wang, 2011).

Mycobacteria harbour an analogous protease system known as ClpC1P1P2, which plays a pivotal role in cellular survival, even within macrophages (Rengarajan, 2005). For mycobacteria, the caseinolytic protease (Clp) complexes is composed by ClpP1 and ClpP2 subunits, which associate with the unfoldase ClpC1 or ClpX to form the active protease complex (Taylor et al., 2023). Recently, Morreale and others demonstrated that PROTACs could similarly harness this mycobacterial protein degradation machinery to target neo-substrates in bacteria (Morreale, 2022) The researchers engineered a bifunctional molecule comprising a phosphorylated arginine moiety, at one end, which served to mimic the degradation tag, a linker, and a POI-specific binder at the other end. These innovative molecules were coined BacPROTACs (Morreale, 2022).

In the initial phase of their study, the authors selected monomeric streptavidin (mSA) as their POI and proceeded with the synthesis of BacPROTAC-1 (Figure 1), incorporating biotin as a ligand for the POI. They employed isothermal titration calorimetry (ITC) to confirm that the compound maintained its ability to bind to both mSA and $ClpC_{NTD}$ individually, with dissociation constants (Kd) of 3.9 and 2.8 mM, respectively. Additionally, analytical size-exclusion chromatography (SEC) demonstrated the formation of a stable ternary complex, underscoring the molecule's capacity to simultaneously engage with the POI and Clp_{NTD}. Subsequently, *in vitro* investigations involving the treatment of a reconstituted CplCP from *B. subtilis* with BacPROTAC-1led to the selective degradation of mSA, notably observable at a concentration of 100 μM. To further probe the substrate specificity of this innovative PROTAC, the authors cloned four fusion proteins in *Bacillus subtilis* (NdrI, TagD, NusA, and Kre) and subjected them to BacPROTAC-1 treatment. Significant differences in degradation efficiency were observed between the 4 substrates, with mSA-KRE degraded at as low as 1 μM, shedding light on the nuanced impact of structural variations within the substrate on the degradation pattern (Morreale, 2022).

When utilizing PROTAC technology, it is crucial to validate that observed outcomes are inherently linked to the activity of the

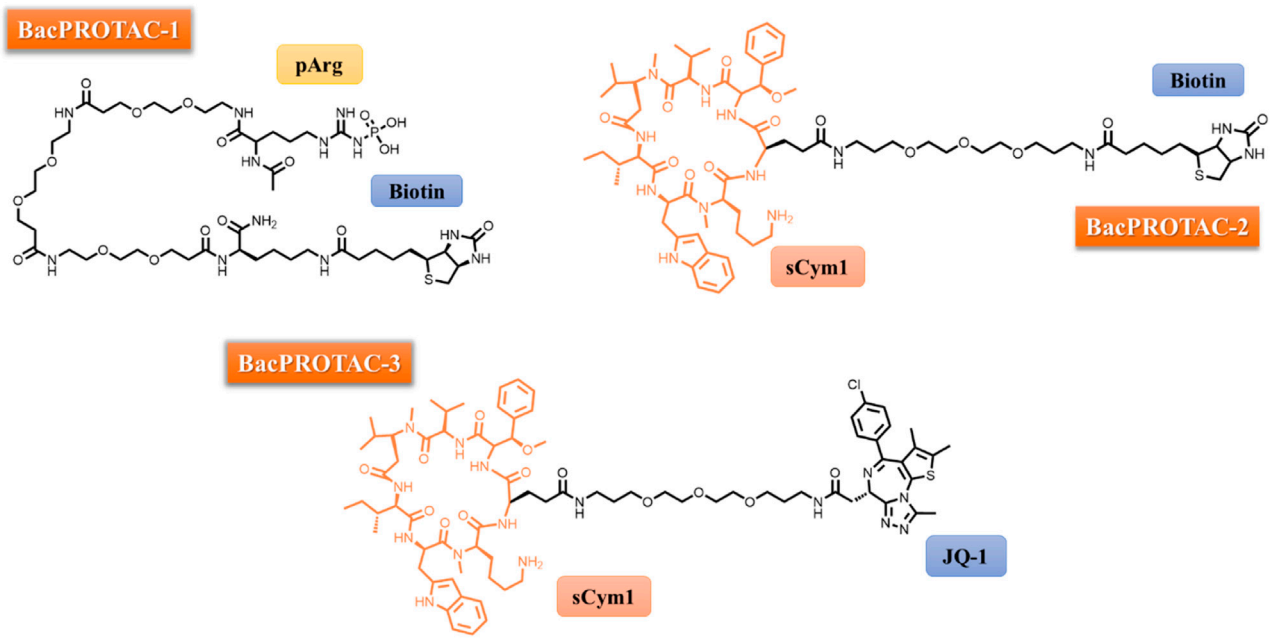

FIGURE 1
Chemical structure of BacPROTACs-1, -2 and -3.

designed molecule. To address this critical aspect, BacPROTAC-1 was meticulously applied to treat ClpCP in tandem with both pArg and biotin in isolation. This approach effectively resulted in the inhibition of mSA-Kre degradation, as the binding sites crucial for the formation of a ternary complex were preoccupied by these molecules. A parallel series of experiments yielded akin results when a non-phosphorylated arginine moiety was integrated into the BacPROTAC structure. Notably, the linker length did not exert a significant influence on the degradation process, which contrasts with the significant impact of linkers observed in other TPD studies (Troup et al., 2020; Bemis et al., 2021).

As part of the ongoing research, BacPROTAC-1 was subsequently assessed within the reconstituted ClpC1P1P2 complex derived from *Mycobacterium smegmatis*. This evaluation unveiled the molecule's capacity for high-affinity binding to the $ClpC1_{NTD}$, with a Kd of 0.69 mM. Importantly, this interaction facilitated the formation of a ternary complex involving mSA and $ClpC1_{NTD}$, culminating in the selective degradation of mSA. These findings not only underscored the suitability of ClpC1P1P2 from mycobacteria for the advancement of PROTAC technology but also opened avenues for overcoming the limitations associated with the pharmacokinetics of pArg, as expounded by Schmidt in 2014. In response to this challenge, BacPROTAC-2 was designed, in which the pArg subunit was substituted with cyclomarin A (CymA), a cyclic peptide renowned for its robust binding affinity to $ClpC1_{NTD}$ and enhanced permeability across the mycobacterial envelope (Schmitt, 2011a). It is noteworthy that ClpC1 serves as the target for an array of effectors, encompassing diverse natural products such as cyclomarin A, ecumicin, lassomycin, and rufomycin (Hoi, 2023). Cyclomarin and ecumicin exhibit comparable affinities for both ClpC2 and ClpC3, two small Clp proteins, and this interaction may lead to the upregulation of proteins (Hoi, 2023).

Subsequently, BacPROTAC-2 (Figure 1) was synthesized and its efficacy in degrading mSA was assessed. BacPROTAC-2 displayed a degradation pattern akin to that observed with pArg derivatives, underscoring its potency in TPD. To further establish the versatility of the mycobacterial protease in targeting various proteins, BacPROTAC-3 (Figure 1) was designed to incorporate JQ-1, a ligand for bromodomain-1 of BRDT ($BRDT_{BD1}$), a human protein with no structural analogues in mycobacteria. When *M. smegmatis*, genetically modified to express $BRDT_{BD1}$, was subjected to treatment with BacPROTAC-3 at a concentration of 10 μM, a substantial reduction of nearly 50% in target protein levels was observed. Notably, individual components of BacPROTAC-3, namely Cym and JQ-1, exhibited no discernible impact on the target protein levels and co-incubation of JQ-1 and BacPROTAC-3 competitively inhibited protein degradation. Furthermore, a new compound (BacPROTAC-3a) containing the distomer of JQ-1 showed no effect on the target protein levels, confirming that productive engagement of $BRDT_{BD1}$ is required for the mechanisms of action of BacPROTAC-3 (Morreale, 2022).

CymA, a natural product known for its high binding affinity to $ClpC1_{NTD}$, exerts a pronounced inhibitory effect on ClpC1 activity, an unfoldase that interacts with the ClpP1P2 protease to assemble a confined degradation chamber (Vasudevan et al., 2013). Phenotypic assays against *Mycobacterium tuberculosis* showed that CymA was active against several MDR-TB clinical isolates and hypoxic non replicating *bacillus*, without effects against Gram-negative and Gram-positive bacteria (Schimitt et al., 2011b). Using molecular modification approach, it was synthesized a cyclic peptide with a slightly simplified structure, named desoxycyclomarin C (dCym) (Junk et al., 2023).

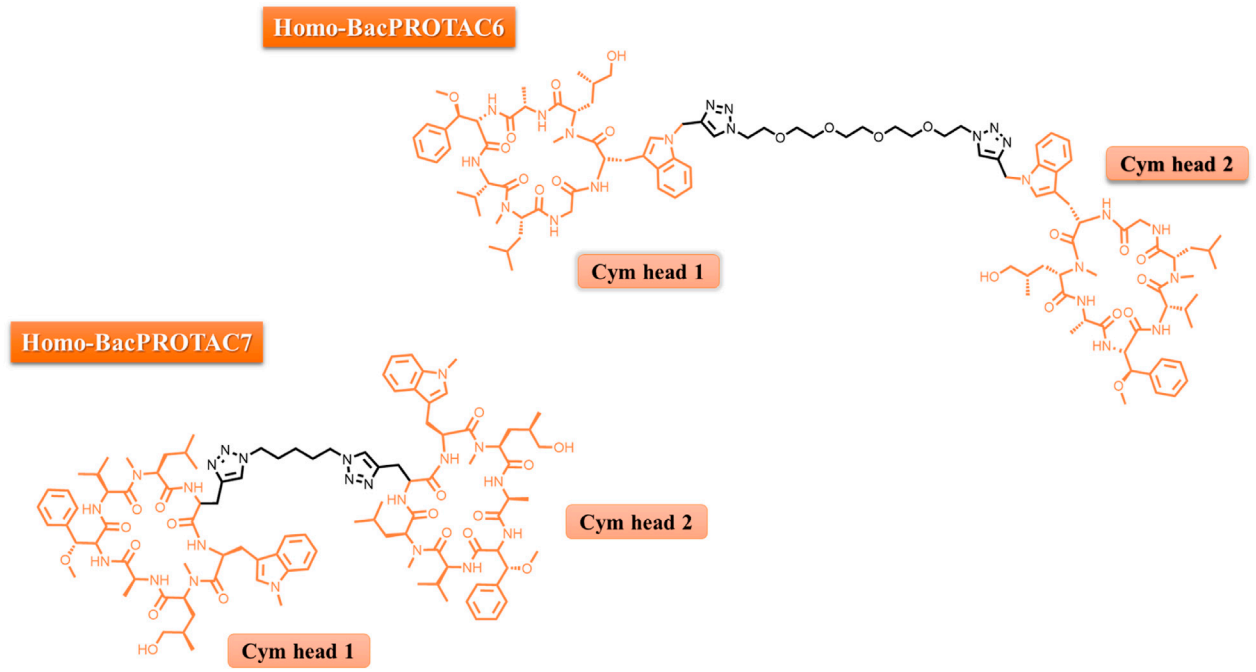

FIGURE 2
Chemical representation of HBPs 6 and 7.

Compound dCym, an analogue of CymA, has the capability to disrupt the proteome of mycobacteria, notably characterized by a 600-fold increase in ClpC2 levels (Hoi, 2023). ClpC2 is a protease protector striking similarity to the receptor domain of ClpC1. This similarity enables ClpC2 to bind to dCym, thereby preventing its interference with ClpC1, ultimately mitigating dCym's toxicity by a factor of 4 in *M. smegmatis*. ClpC2, as well as the recent described ClpC3, serve as regulatory components within the Clp complexes, sharing the same ligand-binding site as observed in ClpC1. In doing so, they operate by engaging in competition for substrate binding (Hoi et al., 2023; Taylor et al., 2023). However, while ClpP2 is crucial for delivering substrates to the proteolytic complex, the proteolytic activity of ClpP1 alone is both necessary and sufficient for the degradation of at least some Clp substrates (D'Andrea et al., 2022).

To disrupt the "protective" effect against dCym and CymA mediated through the competitive binding to ClpC2/ClpC3, Hoi and others synthesized cyclic peptides dimers, which was named Homo-BacPROTACs (HBP). These HBP were synthesized to feature the dCym moiety at both ends connected by a different linker length (Figure 2). The goal was to simultaneously degrade both ClpC1, ClpC2 and the complex ClpC1P1P2. By using a *M. smegmatis* model system, it was found that these Homo-BacPROTACs were able to reduce the levels of ClpC1 and ClpC2 up to 40% and 45%–60%, respectively, in comparison with the monomeric dCym, after 24 h of treatment. The antimycobacterial effects was evaluated using *M. tuberculosis* H37Rv. In this phenotypic assay, the MIC_{50} values for HSP-6 and HSP-7 were 0.34 and 0.26 μM, respectively. In this experiment the MIC_{50} value for dCym was 39 μM. Both compounds were able to reduce ClpC1 and ClpC2 levels, and was active against dormant state of the *M. tuberculosis* (Hoi et al., 2023).

Figure 3 presents a summary of the mechanism of the proteolytic machinery, as well as the BacPROTACs and HBPs.

Although advances have been achieved in the last years, the range of known small molecule ligands for the ClpP1P2, ClpC1, and ClpC2 complex remains relatively limited. Yang and others described that the anticancer cediranib, a potent inhibitor of the VEGF family receptor tyrosine kinases, is a potent ClpP1P2 inhibitor in *M. tuberculosis*. Cediranib was identified through a screening of a vast library of compounds. *In vitro*, this drug inhibited the complex ClpP1P2 with IC_{50} value of 2.8 μM and a selective index of 13.3 in comparison with human peptidase/protease. Through structural and mutational studies, it has been revealed that cediranib binds to MtbClpP1P2 by interacting with an allosteric pocket located in the equatorial handle domain of the MtbClpP1 subunit. Notably, phenotypic assays conducted with *M. tuberculosis* revealed MIC_{50} values against H37Ra and H37Rv of 14.1 and 28.2 μM, respectively. Minimal growth inhibition was noted in other species, including *E. coli*, *S. aureus*, and *P. aeruginosa* (Yang et al., 2023).

Another example of ClpP1P2 inhibitor is the proteasome inhibitor bortezomib. This drug was approved by US FDA for the treatment of multiple myeloma and mantle cell lymphoma, and it was identified in a fluorescence-based assay as a potent ClpP1P2 inhibitor. Whole-cell phenotypic assays carried out with *M. tuberculosis* H37Rv showed by using bortezomib MIC_{50} values of 0.8 μM (Moreira et al., 2015). To mitigate the effects on human proteasome, a series of peptide boronic compounds were described by Moreira and others. After a vast structure activity relationship (SAR) study, the researchers have found compounds that exhibited up to a 100-fold reduction in activity against the human proteasome yet retained both ClpP1P2 inhibition and effectiveness in inhibiting

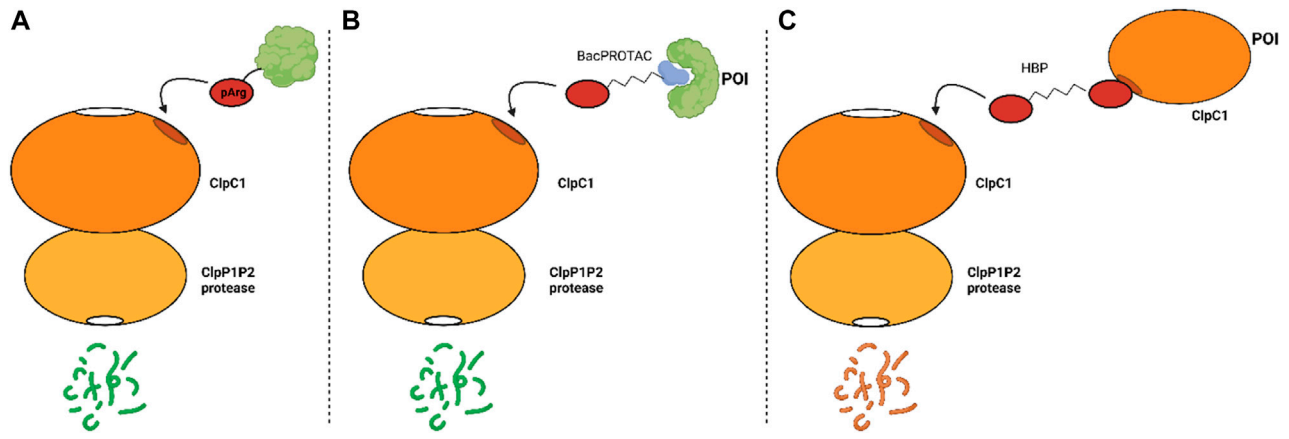

FIGURE 3
Mechanism of proteolysis mediated, or not, by synthetic compounds. **(A)** natural occurring protein degradation mediated by the recognition of pArg by ClpC1; **(B)** protein degradation induced by the BacPROTAC and **(C)** degradation of ClpC1 induced by HBPs.

mycobacterial growth (Moreira et al., 2017). Therefore, while the human proteasome inhibitor bortezomib presents itself as a compelling scaffold for BacPROTAC design, it is imperative to eliminate its effects on the human proteasome and optimize interactions with ClpP1P2.

The outcomes stemming from the implementation of PROTAC technology in the quest for novel antimicrobials represent a beacon of hope, particularly in light of the escalating challenges posed by antibiotic resistance. The proliferation of antibiotic-resistant strains, including the MDR and XDR variants, as exemplified in the context of TB, has accentuated the urgency of innovative approaches. PROTAC technology, by enable the design of degraders, now stands as a formidable driver in expanding the realm of druggable targets. Such approach is a promising tool by targeting biomolecules that need not harbour traditional active sites and exhibits several advantages, including: reduction of pressure to evolve resistance; improve the selectivity, as require engagement of two distinct targets and formation of ternary complexes; BacPROTACs are catalytic and event driven, which enables lower drug concentrations that could improve the therapeutic index of a drug, and by reducing side effects; BacPROTACs only require to bind (not modulate the function) of their target, which could increase the proportion of the bacterial proteome that can be pharmacologically modulated. Thus, these adaptable degraders can be tailored for a diverse range of targets, including structural proteins and protein aggregates, thereby transcending the conventional confines of target selectivity (Bekes, 2022). In essence, this emergent avenue furnishes the scientific community with an ever-expanding arsenal of tools to be used to overcome the problems we are facing nowadays in the drug discovery of antimicrobials.

Data availability statement

The original contributions presented in the study are included in the article/supplementary material, further inquiries can be directed to the corresponding author.

Author contributions

AB: Data curation, Formal Analysis, Investigation, Methodology, Writing–original draft, Writing–review and editing. AP: Conceptualization, Data curation, Formal Analysis, Investigation, Methodology, Visualization, Writing–original draft, Writing–review and editing. GF: Conceptualization, Data curation, Formal Analysis, Investigation, Methodology, Supervision, Visualization, Writing–original draft, Writing–review and editing. CS: Conceptualization, Formal Analysis, Funding acquisition, Investigation, Methodology, Resources, Writing–original draft, Writing–review and editing. DC: Conceptualization, Investigation, Methodology, Resources, Supervision, Visualization, Writing–original draft, Writing–review and editing. JdS: Conceptualization, Data curation, Formal Analysis, Funding acquisition, Investigation, Supervision, Writing–original draft.

Funding

The author(s) declare financial support was received for the research, authorship, and/or publication of this article. This study was supported by Fundação de Amparo à Pesquisa do Estado de São Paulo (FAPESP) process numbers: 2018/19523-7 (AP), 2020/13279-7 (JdS), 2021/14973-7 (AB), 2022/15844-9 (AB) and 2023/05739-6 (JdS). Pro-reitoria de Pós-Graduação UNESP—PROPG edital 69/2023.

Acknowledgments

We thank the National Council for Scientific and Technological Development (CNPq) and the Fundação de Amparo à Pesquisa do Estado de São Paulo (FAPESP) process numbers 2018/19523-7, 2020/13279-7, 2021/14973-7, 2022/15844-9 and 2023/05739-6.

Conflict of interest

The authors declare that the research was conducted in the absence of any commercial or financial relationships that could be construed as a potential conflict of interest.

The author(s) declared that they were an editorial board member of Frontiers, at the time of submission. This had no impact on the peer review process and the final decision.

Publisher's note

All claims expressed in this article are solely those of the authors and do not necessarily represent those of their affiliated organizations, or those of the publisher, the editors and the reviewers. Any product that may be evaluated in this article, or claim that may be made by its manufacturer, is not guaranteed or endorsed by the publisher.

References

Bekes, M., Langley, D. R., and Crews, C. M. (2022). PROTAC targeted protein degraders: the past is prologue. *Nat. Rev. Drug Disc* 21, 181–200. doi:10.1038/s41573-021-00371-6

Bemis, T. A., La Clair, J. J., and Burkart, M. D. (2021). Unraveling the role of linker design in proteolysis targeting chimeras. *J. Med. Chem.* 64, 8042–8052. doi:10.1021/acs.jmedchem.1c00482

Burslem, G. M., and Crews, C. M. (2020). Proteolysis-Targeting Chimeras as therapeutics and tools for biological discovery. *Cell.* 181, 102–114. doi:10.1016/j.cell.2019.11.031

Cook, M. A., and Wright, G. D. (2022). The past, present, and future of antibiotics. *Sci. Transl. Med.* 14, eabo7793. doi:10.1126/scitranslmed.abo7793

D'Andrea, F. B., Poulton, N. C., Froom, R., Tam, K., Campbell, E. A., and Rock, J. M. (2022). The essential *M. tuberculosis* Clp protease is functionally asymmetric *in vivo*. *Sci. Adv.* 8, eabn7943. doi:10.1126/sciadv.abn7943

Fernandes, G. F. S., Thompson, A. M., Castagnolo, D., Denny, W. A., and Dos Santos, J. L. (2022). Tuberculosis drug discovery: challenges and new horizons. *J. Med. Chem.* 65, 7489–7531. doi:10.1021/acs.jmedchem.2c00227

Grohmann, C., Marapana, D. S., and Ebert, G. (2023). Targeted protein degradation at the host-pathogen interface. *Mol. Microbiol.* 117, 670–681. doi:10.1111/mmi.14849

Hoi, D. M., Junker, S., Junk, L., Schwechel, K., Fischel, K., Podlesainski, D., et al. (2023). Clp-targeting BacPROTACs impair mycobacterial proteostasis and survival. *Cell.* 186, 2176–2192.e22. doi:10.1016/j.cell.2023.04.009

Hu, Z., and Crews, C. M. (2022). Recent developments in PROTAC-mediated protein degradation: from bench to clinic. *Chembiochem* 23, e202100270. doi:10.1002/cbic.202100270

Junk, L., Schmiedel, V. M., Guha, S., Greb, P., Fischel, K., Rumpel, K., et al. (2023). BacPROTAC-induced degradation of ClpC1 as a new strategy against drug-resistant mycobacteria. *ChemRxiv*. doi:10.26434/chemrxiv-2022-8hnrh-v2

Liu, Z., Hu, M., Yang, Y., Du, C., Zhou, H., Liu, C., et al. (2022). An overview of PROTACs: a promising drug discovery paradigm. *Mol. Biomed.* 3, 46. doi:10.1186/s43556-022-00112-0

Moreira, W., Ngan, G. J., Low, J. L., Poulsen, A., Chia, B. C., Ang, M. J., et al. (2015). Target mechanism-based whole-cell screening identifies bortezomib as an inhibitor of caseinolytic protease in mycobacteria. *mBio* 6, 002533–e315. doi:10.1128/mBio.00253-15

Moreira, W., Santhanakrishnan, S., Ngan, G. J. Y., Low, C. B., Sangthongpitag, K., Poulsen, A., et al. (2017). Towards selective mycobacterial ClpP1P2 inhibitors with reduced activity against the human proteasome. *Antimicrob. Agents Chemother.* 61, e02307–e02316. doi:10.1128/AAC.02307-16

Morreale, F. E., Kleine, S., Leodolter, J., Junker, S., Hoi, D. M., Ovchinnikov, S., et al. (2022). BacPROTACs mediate targeted protein degradation in bacteria. *Cell.* 185, 2338–2353.e18. doi:10.1016/j.cell.2022.05.009

Munita, J. M., and Arias, C. A. (2016). Mechanisms of antibiotic resistance. *Microbiol. Spectr.* 4. VMBF-0016–2015. doi:10.1128/microbiolspec.VMBF-0016-2015

Pettersson, M., and Crews, C. M. (2019). PROteolysis targeting chimeras (PROTACs) – past, present and future. *Drug Discov. Today Technol.* 31, 15–27. doi:10.1016/j.ddtec.2019.01.002

Rengarajan, J., Bloom, B. R., and Rubin, E. J. (2005). Genome-wide requirements for *Mycobacterium tuberculosis* adaptation and survival in macrophages. *Proc. Natl. Acad. Sci.* 102, 8327–8332. doi:10.1073/pnas.0503272102

Sakamoto, K. M., Kim, K. B., Kumagai, A., Deshaies, R. J., and Crews, C. M. (2001). Protacs: chimeric molecules that target proteins to the Skp1-Cullin-F box complex for ubiquitination and degradation. *Proc. Natl. Acad. Sci. U. S. A.* 98, 8554–8559. doi:10.1073/pnas.141230798

Sarathy, J. P., Aldrich, C. C., Go, M. L., and Dick, T. (2023). PROTAC antibiotics: the time is now. *Expert Opin. Drug Disc* 18, 363–370. doi:10.1080/17460441.2023.2178413

Schimdt, A., Trentini, D. B., Spiess, S., Fuhrmann, J., Ammerer, G., Mechter, K., et al. (2014). Quantitative phosphoproteomics reveals the role of protein arginine phosphorylation in the bacterial stress response. *Mol. Cell. Proteomics* 13, 537–550. doi:10.1074/mcp.M113.032292

Schmitt, E. K., Riwanto, M., Sambandamurthy, V., Roggo, S., Miault, C., Zwingelstein, C., et al. (2011b). The natural product cyclomarin kills *Mycobacterium tuberculosis* by targeting the ClpC1 subunit of the caseinolytic protease. *Angew. Chem. Int. Ed. Engl.* 50, 5889–5891. doi:10.1002/anie.201101740

Schmitt, K. E., Riwanto, M., Sambandamurthy, V., Roggo, S., Miault, C., Zwingesltein, C., et al. (2011a). The natural product cyclomarin kills *Mycobacterium tuberculosis* by targeting the ClpC1 subunit of the caseinolytic protease. *Angew. Chem. Int.* 50, 5889–5891. doi:10.1002/anie.201101740

Sincere, N. I., Anand, K., Ashique, S., Yang, J., and You, C. (2023). PROTACs: emerging targeted protein degradation approaches for advanced druggable strategies. *Molecules* 28, 4014. doi:10.3390/molecules28104014

Stop TB Partnership (2019). *The paradigm shift: global plan to end TB 2018–2022.* Geneva.

Sun, X., Gao, H., Yang, Y., He, M., Wu, Y., Song, Y., et al. (2019). Protacs: great opportunities for academia and industry. *Signal Transduc Target Ther.* 4, 64. doi:10.1038/s41392-019-0101-6

Taylor, G., Cui, H., Leodolter, J., Giese, C., and Weber-Ban, E. (2023). ClpC2 protects mycobacteria against a natural antibiotic targeting ClpC1-dependent protein degradation. *Commun. Biol.* 6, 301. doi:10.1038/s42003-023-04658-9

Treatment Action Group (2020). *Tuberculosis research funding trends, 2005–2019.* New York City.

Trentini, D. B., Suskiewicz, M. J., Heuck, A., Kurzbauer, R., Deszcz, L., Mechtler, K., et al. (2016). Arginine phosphorylation marks proteins for degradation by a Clp protease. *Nature* 539, 48–53. doi:10.1038/nature20122

Troup, R. I., Fallan, C., and Baud, M. G. J. (2020). Current strategies for the design of PROTAC linkers: a critical review. *Explor Target Antitumor Ther.* 1, 273–312. doi:10.37349/etat.2020.00018

Vasudevan, D., Rao, S. P., and Noble, C. G. (2013). Structural basis of mycobacterial inhibition by cyclomarin A. *J. Biol. Chem.* 288, 30883–30891. doi:10.1074/jbc.M113.493767

Wang, F., Mei, Z., Qi, Y., Yan, C., Hu, Q., Wang, J., et al. (2011). Structure and mechanism of the hexameric MecA-ClpC molecular machine. *Nature* 471, 331–335. doi:10.1038/nature09780

World Health Organization (2022). *Global tuberculosis report 2022.* Geneva: WHO, 1–68.

Yang, Y., Zhao, N., Xu, X., Zhou, Y., Luo, B., Zhang, J., et al. (2023). Discovery and mechanistic study of novel *Mycobacterium tuberculosis* ClpP1P2 inhibitors. *J. Med. Chem.* 66, 16597–16614. doi:10.1021/acs.jmedchem.3c01054

frontiers | Frontiers in Chemistry

TYPE Original Research
PUBLISHED 18 March 2024
DOI 10.3389/fchem.2024.1384301

OPEN ACCESS

EDITED BY
Mehlika Dilek Altıntop,
Anadolu University, Türkiye

REVIEWED BY
Mohamed Radwan,
Kumamoto University, Japan
Sevil Şenkardeş,
Marmara University, Türkiye

*CORRESPONDENCE
Faqing Ye,
yfq664340@163.com
Huijun Chen,
chjtzs@163.com
Xiaojiao Yang,
yxj9597@wmu.edu.cn

†These authors have contributed equally to this work

RECEIVED 09 February 2024
ACCEPTED 28 February 2024
PUBLISHED 18 March 2024

CITATION
Xu X, Zhu Z, Chen S, Fu Y, Zhang J, Guo Y, Xu Z, Xi Y, Wang X, Ye F, Chen H and Yang X (2024), Synthesis and biological evaluation of novel benzothiazole derivatives as potential anticancer and antiinflammatory agents. *Front. Chem.* 12:1384301.
doi: 10.3389/fchem.2024.1384301

Synthesis and biological evaluation of novel benzothiazole derivatives as potential anticancer and antiinflammatory agents

Xuemei Xu[1†], Zhaojingtao Zhu[2†], Siyu Chen[2†], Yanneng Fu[2], Jinxia Zhang[2], Yangyang Guo[2], Zhouyang Xu[2], Yingying Xi[2], Xuebao Wang[2], Faqing Ye[2]*, Huijun Chen[3]* and Xiaojiao Yang[4]*

[1]Department of Pharmacy, Wenzhou Hospital of Integrated Traditional Chinese and Western Medicine, Wenzhou, China, [2]School of Pharmaceutical Science, Wenzhou Medical University, Wenzhou, China, [3]Department of Pharmacy, The First People's Hospital of Taizhou, Taizhou, China, [4]Scientific Research Center, Wenzhou Medical University, Wenzhou, China

Introduction: Cancer, a significant global health concern, necessitates innovative treatments. The pivotal role of chronic inflammation in cancer development underscores the urgency for novel therapeutic strategies. Benzothiazole derivatives exhibit promise due to their distinctive structures and broad spectrum of biological effects. This study aims to explore new anti-tumor small molecule drugs that simultaneously anti-inflammatory and anticancer based on the advantages of benzothiazole frameworks.

Methods: The compounds were characterized by nuclear magnetic resonance (NMR), liquid chromatograph-mass spectrometer (LC-MS) and high performance liquid chromatography (HPLC) for structure as well as purity and other related physicochemical properties. The effects of the compounds on the proliferation of human epidermoid carcinoma cell line (A431) and human non-small cell lung cancer cell lines (A549, H1299) were evaluated by MTT method. The effect of compounds on the expression levels of inflammatory factors IL-6 and TNF-α in mouse monocyte macrophages (RAW264.7) was assessed using enzyme-linked immunosorbent assay (ELISA). The effect of compounds on apoptosis and cell cycle of A431 and A549 cells was evaluated by flow cytometry. The effect of compounds on A431 and A549 cell migration was evaluated by scratch wound healing assay. The effect of compounds on protein expression levels in A431 and A549 cells was assessed by Western Blot assay. The physicochemical parameters, pharmacokinetic properties, toxicity and drug similarity of the active compound were predicted using Swiss ADME and admetSAR web servers.

Results: Twenty-five novel benzothiazole compounds were designed and synthesized, with their structures confirmed through spectrogram verification. The active compound 6-chloro-*N*-(4-nitrobenzyl) benzo[d] thiazol-2-amine (compound **B7**) was screened through a series of bioactivity assessments, which significantly inhibited the proliferation of A431, A549 and H1299 cancer cells, decreased the activity of IL-6 and TNF-α, and hindered cell migration. In addition, at concentrations of 1, 2, and 4 μM, **B7** exhibited apoptosis-promoting and cell cycle-arresting effects similar to those of the lead compound 7-chloro-*N*-(2, 6-dichlorophenyl) benzo[d] thiazole-2-amine (compound **4i**). Western blot analysis confirmed that **B7** inhibited both AKT and ERK signaling pathways in A431 and A549 cells. The prediction results of ADMET indicated that **B7** had good drug properties.

Discussion: This study has innovatively developed a series of benzothiazole derivatives, with a focus on compound **B7** due to its notable dual anticancer and anti-inflammatory activities. **B7** stands out for its ability to significantly reduce cancer cell proliferation in A431, A549, and H1299 cell lines and lower the levels of inflammatory cytokines IL-6 and TNF-α. These results position **B7**B7 as a promising candidate for dual-action cancer therapy. The study's mechanistic exploration, highlighting **B7**'s simultaneous inhibition of the AKT and ERK pathways, offers a novel strategy for addressing both the survival mechanisms of tumor cells and the inflammatory milieu facilitating cancer progression.

KEYWORDS

organic synthesis, benzothiazole derivatives, anticancer, antiinflammatory, biological evaluation

1 Introduction

Cancer is a formidable disease that poses a significant threat to human health and has been a persistent challenge in the global public health domain (Ferlay et al., 2015; Fitzmaurice et al., 2015; Bray et al., 2021; Sung et al., 2021). Despite notable advances in the medical field, cancer treatment still confronts various limitations and challenges (Chang et al., 2021; Craig et al., 2021; Ghanbar and Suresh, 2024). Drug therapy stands out as a widely employed approach in cancer treatment (Wu et al., 2022), where the effectiveness and side effects of drugs are pivotal factors influencing treatment outcomes (Dinić et al., 2020; Steinbrueck et al., 2020; Li et al., 2024b). Consequently, the quest for novel anticancer drugs has emerged as a central focus of contemporary research.

Chronic inflammation is increasingly recognized as a critical factor in cancer development. This complex interplay facilitates tumor initiation and progression. IL-6 and TNF-α are key inflammatory cytokines known for their roles in immune regulation, inflammation, and cell proliferation. Their involvement in tumor development and progression is a subject of ongoing research (Hastir et al., 2020; Park et al., 2020; Cowan et al., 2022). These research underscores the multifaceted roles of IL-6 and TNF-α in tumor development. These cytokines not only contribute to the pro-inflammatory tumor microenvironment but also interact with various signaling pathways and immune cells, influencing both local tumor growth and systemic inflammatory responses. Their impact on tumor development and progression highlights their potential as targets for therapeutic intervention in cancer treatment (Meza et al., 2021).

Over the past two decades, benzothiazole compounds have attracted considerable research attention due to their distinctive structure and diverse biological activities, including anti-tumor (Kamal et al., 2010; Kamal et al., 2011; El-Helby et al., 2019; Makowska et al., 2019; Mokesch et al., 2020), anti-inflammatory (Lee et al., 2011; Kumar and Singh, 2021), neuroprotective (Choi et al., 2007), antibacterial (Al-Tel et al., 2011; Racané et al., 2020), and antiparasitic (Awadh, 2023) activities, etc. In recent years, extensive research has focused on modifying the benzothiazole nucleus to enhance its anti-tumor activities. Among the modified structures, benzothiazole derivatives exhibiting specificity towards various anti-tumor receptors have consistently emerged. This includes compounds interacting with receptor tyrosine kinases such as C-Met and EGFR (Noolvi et al., 2012), those influencing the PI3K/Akt/mTOR pathway (D'Angelo et al., 2011), and those exhibiting antimicrobial properties, as illustrated in Scheme 1. Additionally, two compounds have garnered special attention for their excellent anti-tumor effects: **PMX610** [2-(3,4-dimethoxyphenyl)-5-fluorobenzothiazole] (Mortimer et al., 2006) and compound **4i** (Noolvi et al., 2012) (Figure 1). **PMX610** has been reported to possess potent and selective *in vitro* anti-tumor properties in human cancer cell lines, particularly against non-small cell lung, colon, and breast cancer lines from 60 human cancer cell line screen. Compound **4i** demonstrated promising anticancer activity against the non-small cell lung cancer cell line HOP-92, with substitutions at the 2,6-positions displayed significant anticancer potential in initial cytotoxicity screening across three human cancer cell lines. These findings underscore the significance of benzothiazole as a core structure in drug synthesis, with modifications to the benzothiazole nucleus enhancing its anticancer activity. The importance of benzothiazole and its derivatives in anticancer research is progressively becoming apparent.

Based on the above analysis, this study is to explore new anti-tumor small molecule drugs that simultaneously anti-inflammatory and anticancer based on the advantages of benzothiazole frameworks. Based on compounds **PMX610** and **4i** as lead compounds, we attempted to design A, B, C, and D four series of compounds. Series A of benzothiazoles has been designed by incorporating diverse substituted phenyl groups at the 2-phenyl position of 2-phenyl benzothiazole, drawing inspiration from existing literature and undergoing further optimization (Kumbhare et al., 2012). Series B and C of benzothiazoles have been meticulously designed by introducing an additional carbon atom or carbonyl groups between two rings, compared to compound **4i**. Series D of benzothiazoles has been designed as a further replacement of Series B (Figure 1). The compounds designed in this study exhibit a distinct departure in structure from classical small molecule anti-tumor compounds. This structural variation enables the exploration of the relationship between activity and structure, with the intention of leading to the derivation of more advantageous molecular architectures. We anticipate that these compounds will emerge as promising candidates for anticancer prospects, providing scientific evidence for future anticancer drug development and introducing new possibilities to clinical treatment.

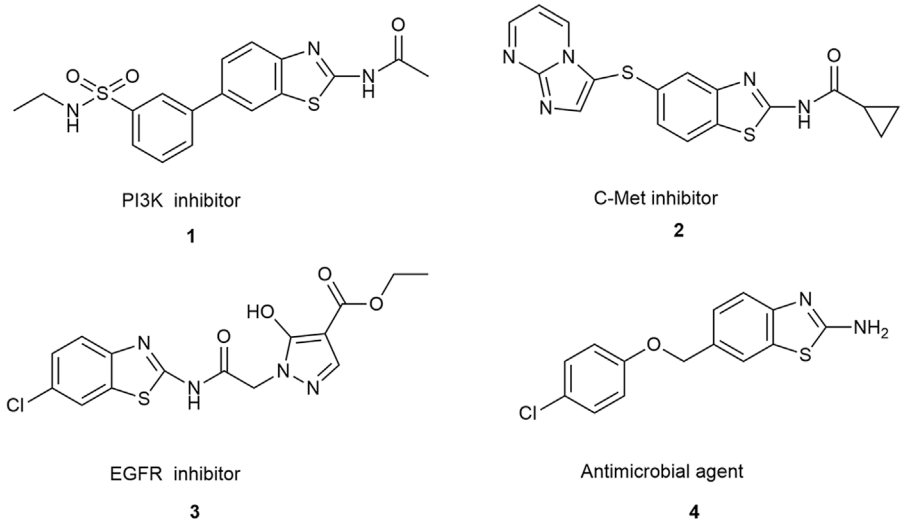

FIGURE 1
Benzothiazole as anticancer agents and antimicrobial agents.

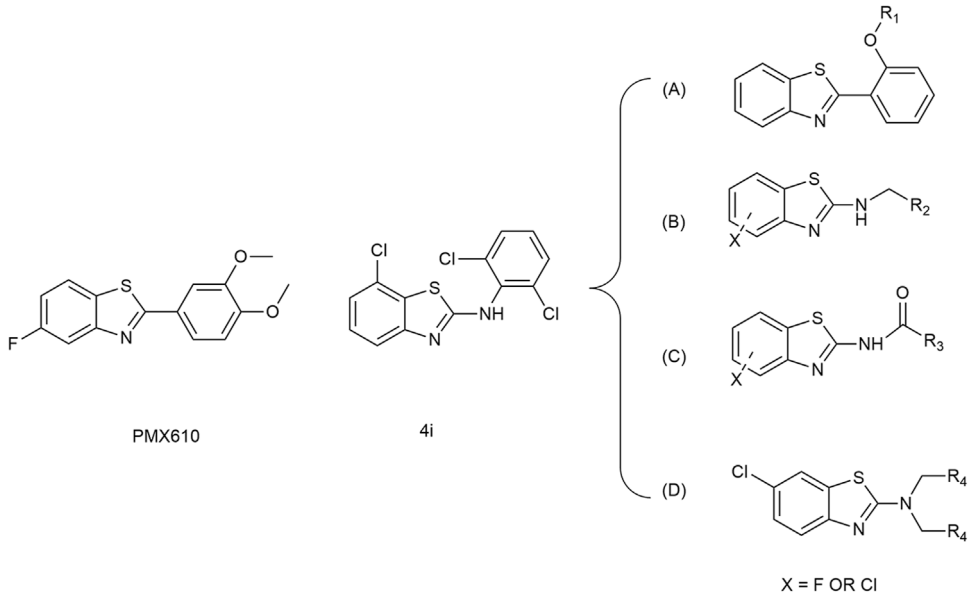

SCHEME 1
Design principle of target compounds.

2 Materials and methods

2.1 Chemical reagents and instruments

The reagents and alkoxyamine intermediates employed in chemical synthesis were procured directly from reputable suppliers such as Macklin, Aladdin, and Energy Chemical. All solvents utilized possessed high chemical purity and underwent no further treatment. These included petroleum ether (PE), ethyl acetate (EA), dichloromethane (DCM), dimethyl sulfoxide (DMSO), and 1,4-Dioxane. The progression of the reaction was tracked through analytical thin-layer chromatography (TLC) utilizing a silica gel GF254 plate (Qingdao Haiyang Chemical Plant, China), with spot observations made under UV light at 254 nm or 365 nm. Column chromatography was conducted using silica gel (90–150 μm; Qingdao Ocean Chemical Co., Ltd.). The melting points were determined using the XT-4 micromelting point apparatus without correction. ^{1}H NMR and ^{13}C NMR spectra were acquired using a Bruker 400/600 MHz Avance NMR spectrometer, employing $CDCl_3$ or DMSO-d_6 as solvents. Mass spectra were generated using an ACQUITY I-Class UPLC and a XEVO TQD triple quadrupole Mass Spectrometer (Waters, USA).

HPLC (Agilent 1260, USA) assessed the purity of the compounds, all of which exhibited purity levels surpassing 96%. Elemental analysis for C, H, and N was conducted via an elemental analyzer (Flash EA1112, United States) and found to be within ± 0.3% of the theoretical values.

2.2 Synthesis method of 2-phenol-benzothiazole

A substantial quantity of 2-phenol-benzothiazole must be synthesized. Benzothiazole (1 mmol), 2-hydroxyiodobenzene (1 mmol), and K_2CO_3 (2 mmol) as a binding agent were combined in 2 mL of DMSO. The resulting mixture is magnetically stirred at 120°C for 6 h, with the reaction progress monitored via TLC. Upon completion, the reaction mixture was cooled to room temperature, and the solvent is evaporated under reduced pressure. Following this, water (8 mL) and an equivalent volume of ethyl acetate were introduced for extraction through multiple iterations of small-volume extractions (3 times). The aqueous layer was discarded, and the organic layer was desiccated with Na_2SO_4. Subsequent to drying, the organic layer underwent evaporation under reduced pressure, and the resulting residue was subjected to column chromatography. Intermediate 1 was extracted through column chromatography using a mobile phase of petroleum ether: ethyl acetate = 2:1. The yield is 50%, and the product was dried in an oven for subsequent use.

2.3 General synthesis method of A1-A8

To attain the desired A-type final product, 2-phenol-benzothiazole (1 mmol) was combined with various brominated compounds (1.2 mmol) and K_2CO_3 (2 mmol) as a binding agent, within of acetonitrile (6 mL). The resulting mixture underwent stirring at room temperature for a duration of 3 h. Throughout the reaction, the solution underwent a noticeable transition from a pale-yellow suspension to a white suspension, with progress monitored through TLC. Following the completion of the reaction, solvent evaporation was conducted under reduced pressure. Subsequently, water (6 mL) was introduced to dissolve K_2CO_3, followed by the addition of an equivalent volume of ethyl acetate for extraction. This extraction process was iteratively performed in three steps, employing small aliquots. The aqueous layer was discarded, and the organic layers were consolidated and desiccated using solid Na_2SO_4. Following desiccation, the organic layer underwent evaporation under reduced pressure to eliminate excess ethyl acetate. The resultant product was subjected to recrystallization using petroleum ether. Yield determination took place after the drying process, and subsequent characterization of the product was performed.

2.4 General synthesis method of B1-B8

In a 100 mL three-necked flask, either 2-amino-6-chlorobenzothiazole (3.4 mmol) or 2-amino-5-fluorobenzothiazole (3.4 mmol), along with 2 mmol of K_2CO_3 as a binding agent, were introduced. Subsequently, acetonitrile (6 mL) was added, and the mixture underwent sonication. Concurrently, benzyl bromide (1 mmol) was dissolved in acetonitrile (15 mL). The benzyl bromide solution was then meticulously introduced dropwise into the three-necked flask using a constant pressure dropping funnel, with a controlled rate of 1 drop every 5 s. The ensuing reaction mixture underwent reflux for a duration of 6–7 h, with the progression monitored via TLC. Upon completion, the reaction mixture was gradually cooled to room temperature, and the solvent was then evaporated under reduced pressure. Extraction ensued by introducing saturated NaCl (8 mL) and an equivalent volume of ethyl acetate, followed by multiple iterations for thorough extraction. The resultant organic layer was separated, and solid Na_2SO_4 was incorporated for desiccation. The desiccated organic layer underwent further evaporation under reduced pressure, and the resultant residue underwent purification through column chromatography. The elution solvent comprised a blend of petroleum ether and ethyl acetate in a 9:1 ratio. Fractions collected during chromatography were concentrated under reduced pressure, yielding the final solid product. The overall yield was determined post-drying.

2.5 General synthesis method of C1-C7

In the reaction involving 2-amino-6-chlorobenzothiazole (1 mmol) or 2-amino-5-fluorobenzothiazole (1 mmol), acyl chloride (4 mmol), and triethylamine (1 mL) as a binding agent, dioxane (10 mL) was employed as the solvent. The reaction mixture underwent reflux for 3–4 h, with TLC used to monitor the reaction progress. After completion, the reaction mixture was cooled to room temperature, and saturated Na_2CO_3, in a molar ratio equivalent to the acyl chloride, was added. The resulting mixture was stirred overnight. The precipitated product was filtered, followed by drying. The yield was determined post-drying.

2.6 General synthesis method of D1-D2

In a 100 mL three-necked flask, either **B6** (3.4 mmol) or **B8** (3.4 mmol), along with K_2CO_3 (2 mmol) as a binding agent, was introduced. Following this, acetonitrile (6 mL) was added, and the resulting mixture underwent sonication. Concurrently, benzyl bromide (1 mmol) was dissolved in acetonitrile (15 mL). The benzyl bromide solution was subsequently added dropwise to the three-necked flask using a constant-pressure dropping funnel at a rate of 1 drop every 5 s. The reaction mixture underwent reflux for 6–7 h, with TLC monitoring the reaction progress. Upon completion, the reaction mixture was cooled to room temperature, and the solvent was evaporated under reduced pressure. Extraction was carried out by adding saturated NaCl (8 mL) and an equal volume of ethyl acetate in multiple iterations. The organic layer was separated, and solid Na_2SO_4 was added for drying. The dried organic layer was evaporated under reduced pressure, and the resulting residue underwent

purification via column chromatography. The elution solvent, a mixture of petroleum ether and ethyl acetate in a 15:1 ratio, was employed. The collected fractions were concentrated under reduced pressure to obtain the solid product, with yield determination following the drying process.

2.7 Structural characterization data of target compounds

Ethyl 2-(2-(benzo[d]thiazol-2-yl)phenoxy)acetate (**A1**) White solid; Yield/%: 78%; Mp/°C: 73.4~75.4; ESI-MS [M + H]$^+$: 314.6; ^{1}H NMR (600 MHz, $CDCl_3$) δ ppm: 8.556 (d, *J* = 7.8 Hz, 1H, Ph-H), 8.096 (d, *J* = 8.2 Hz, 1H, Ph-H), 7.935 (d, *J* = 8.0 Hz, 1H, Ph-H), 7.491 (t, *J* = 7.68 Hz, 1H, Ph-H), 7.439 (t, *J* = 7.86 Hz, 1H, Ph-H), 7.377 (t, *J* = 7.62 Hz, 1H, Ph-H), 7.199 (t, *J* = 7.56 Hz, 1H, Ph-H), 6.969 (d, *J* = 8.28 Hz, 1H, Ph-H), 4.866 (s, 2H, -OCH_2), 4.299–4.335 (m, 2H, CH_2), 1.316 (t, *J* = 7.14 Hz, 3H, CH_3). ^{13}C NMR (150 MHz, $CDCl_3$) δ ppm: 168.2 (-C=O), 163.1 (thiazole-C), 155.6 (benzothiazole-C), 136.3 (benzothiazole-C), 131.9 (Ph-C), 130.2 (Ph-C), 126.1 (Ph-C), 124.9 (Ph-C), 122.9 (Ph-C), 122.4 (Ph-C), 121.4 (Ph-C), 112.6 (Ph-C), 66.1 (-$OCH_2COOCH_2CH_3$), 61.7(-$OCH_2COOCH_2CH_3$), 14.3(-$OCH_2COOCH_2CH_3$). Anal. Calcd for $C_{17}H_{15}NO_3S$: C, 65.16%; H, 4.82%; N, 4.47%; Found: C, 65.18%; H, 4.83%; N, 4.46%.

2-(2-((2-nitrobenzyl)oxy)phenyl)benzo[d]thiazole (**A2**) White solid; Yield/%: 81%; Mp/°C: 115.6~117.6; ESI-MS [M + H]$^+$: 363.2; ^{1}H NMR (600 MHz, $CDCl_3$) δ ppm: 8.502 (d, *J* = 7.8 Hz, 1H, Ph-H), 8.231 (d, *J* = 8.22 Hz, 1H, Ph-H), 8.115 (d, *J* = 8.16 Hz, 1H, Ph-H), 7.971 (d, *J* = 7.86 Hz, 1H, Ph-H), 7.905 (d, *J* = 7.92 Hz, 1H, Ph-H), 7.687 (t, *J* = 7.5 Hz, 1H, Ph-H), 7.496–7.547 (m, 2H, Ph-H), 7.373–7.440 (m, 2H, Ph-H), 7.182 (t, *J* = 7.5 Hz, 1H, Ph-H), 7.036 (d, *J* = 8.34 Hz, 1H, Ph-H), 5.792 (s, 2H, -OCH_2). ^{13}C NMR (150 MHz, $CDCl_3$) δ ppm: 163.1 (thiazole-C), 155.8 (benzothiazole-C), 152.3 (Ph-C), 147.1 (Ph-C), 136.0 (Ph-C), 134.3 (Ph-C), 133.3 (benzothiazole-C), 132.0 (Ph-C), 130.4 (Ph-C), 129.1 (Ph-C), 128.8 (Ph-C), 126.2 (Ph-C), 125.3 (Ph-C), 125.0 (Ph-C), 123.0 (Ph-C), 122.2 (Ph-C), 121.4 (Ph-C), 113.4 (Ph-C), 68.2(-OCH_2-). Anal. Calcd for $C_{20}H_{14}N_2O_3S$: C, 66.29%; H, 3.89%; N, 7.73%; Found: C, 66.31%; H, 3.88%; N, 7.74%.

2-(3-(2-(benzo[d]thiazol-2-yl)phenoxy)propyl)isoindoline-1,3-dione (**A3**) Pale yellow solid; Yield/%: 67%; Mp/°C: 141.6~143.6; ESI-MS[M + H]$^+$: 415.1; ^{1}H NMR (600 MHz, $CDCl_3$) δ ppm: 8.476 (dd, *J* = 7.8, 1.8 Hz, 1H, Ph-H), 8.033 (d, *J* = 8.4 Hz, 1H, Ph-H), 7.978 (d, *J* = 8.4 Hz, 1H, Ph-H), 7.721–7.735 (m, 2H, Ph-H), 7.585–7.599 (m, 2H Ph-H), 7.421–7.486 (m, 2H, Ph-H), 7.374 (t, *J* = 7.8 Hz, 1H, Ph-H), 7.115 (t, *J* = 7.68 Hz, 1H, Ph-H), 7.033 (d, *J* = 8.4 Hz, 1H, Ph-H), 4.319 (t, *J* = 5.88 Hz, 2H, -OCH_2), 4.080 (t, *J* = 6.84 Hz, 2H, -CH_2), 2.418–2.460 (m, 2H, -CH_2). ^{13}C NMR (150 MHz, $CDCl_3$) δ ppm: 168.5 (-C=O), 163.3 (thiazole-C), 156.5 (benzothiazole-C), 135.9 (benzothiazole-C), 133.9 (Ph-C), 132.1 (Ph-C), 129.8 (Ph-C), 126.1 (Ph-C), 124.8 (Ph-C), 123.1 (Ph-C), 122.6 (Ph-C), 121.6 (Ph-C), 112.2 (Ph-C), 67.3 (-$OCH_2CH_2CH_2$-), 36.1 (-$OCH_2CH_2CH_2$-), 28.8 (-$OCH_2CH_2CH_2$-). Anal. Calcd for $C_{24}H_{18}N_2O_3S$: C, 69.55%; H, 4.38%; N, 6.76%; Found: C,69.51%; H, 4.37%; N, 6.75%.

2-(2-((4-nitrobenzyl)oxy)phenyl)benzo[d]thiazole (**A4**) White solid; Yield/%: 70%; Mp/°C: 135.5~137.5; ESI-MS [M + H]$^+$: 363.2; ^{1}H NMR (600 MHz, $CDCl_3$) δ ppm: 8.535 (dd, *J* = 8.16, 2.4 Hz, 1H, Ph-H), 8.287 (d, *J* = 8.58 Hz, 2H, Ph-H), 8.101 (d, *J* = 8.16 Hz, 1H, Ph-H), 7.897 (d, *J* = 7.98 Hz, 1H, Ph-H), 7.733 (d, *J* = 8.58 Hz, 2H, Ph-H), 7.503 (t, *J* = 7.86 Hz, 1H, Ph-H), 7.370–7.454 (m, 2H, Ph-H), 7.184 (t, *J* = 7.62 Hz, 1H, Ph-H), 7.057 (d, *J* = 8.28 Hz, 1H, Ph-H), 5.426 (s, 2H,-OCH_2). ^{13}C NMR (150 MHz, $CDCl_3$) δ ppm: 162.9 (thiazole-C), 155.8 (benzothiazole-C), 148.0 (Ph-C), 143.4 (Ph-C), 135.8 (Ph-C), 132.1 (benzothiazole-C), 130.4 (Ph-C), 128.3 (Ph-C), 126.3 (Ph-C), 125.1 (Ph-C), 124.1 (Ph-C), 122.9 (Ph-C), 122.2 (Ph-C), 121.4 (Ph-C), 113.0 (Ph-C), 69.9 (-OCH_2-). Anal. Calcd for $C_{20}H_{14}N_2O_3S$: C, 66.29%; H, 3.89%; N, 7.73%; Found: C, 66.30%; H, 3.90%; N, 7.75%.

2-(2-((3-chlorobenzyl)oxy)phenyl)benzo[d]thiazol (**A5**) White solid; Yield/%: 65%; Mp/°C: 53.4~55.4; ESI-MS [M + H]$^+$: 352.1; ^{1}H NMR (600 MHz, $CDCl_3$) δ ppm: 8.546 (dd, *J* = 7.68, 1.38 Hz, 1H, Ph-H), 8.098 (d, *J* = 8.10 Hz, 1H, Ph-H), 7.899 (d, *J* = 7.92 Hz, 1H, Ph-H), 7.567 (s, 1H, Ph-H), 7.491 (t, *J* = 8.04 Hz, 1H, Ph-H), 7.347–7.429 (m, 5H, Ph-H), 7.158 (t, *J* = 7.74 Hz, 1H, Ph-H), 7.069 (d, *J* = 8.34 Hz, 1H, Ph-H), 5.311 (s, 2H, -OCH_2). ^{13}C NMR (150 MHz, $CDCl_3$) δ ppm: 156.1 (thiazole-C), 138.3 (Ph-C) (benzothiazole-C), 136.1 (Ph-C), 134.7 (benzothiazole-C), 131.9 (Ph-C), 130.1 (Ph-C), 128.5 (Ph-C), 127.9 (Ph-C), 126.1 (Ph-C), 125.9 (Ph-C), 124.8 (Ph-C), 122.9 (Ph-C), 121.8 (Ph-C), 121.4 (Ph-C), 113.0 (Ph-C), 70.4 (-OCH_2-). Anal. Calcd for $C_{20}H_{14}ClNOS$: C, 68.27%; H, 4.01%; N, 3.98%; Found: C, 68.28%; H, 4.02%; N, 3.99%.

2-(2-((4-methylbenzyl)oxy)phenyl)benzo[d]thiazole (**A6**) White solid; Yield/% 77%; Mp/°C: 57.3~59.3; ESI-MS [M + H]$^+$: 332.0; ^{1}H NMR (600 MHz, $CDCl_3$) δ ppm: 8.555 (dd, *J* = 7.98, 1.32 Hz, 1H, Ph-H), 8.082 (d, *J* = 8.16Hz, 1H, Ph-H), 7.883 (d, *J* = 7.92Hz, 1H, Ph-H), 7.402–7.489 (m, 4H, Ph-H), 7.351 (t, *J* = 7.38 Hz, 1H, Ph-H), 7.225 (d, *J* = 7.8 Hz, 2H, Ph-H), 7.124 (dd, *J* = 7.56, 5.58 Hz, 2H, Ph-H), 5.309 (s, 2H, -OCH_2), 2.390 (s, 3H, -CH_3). ^{13}C NMR (150 MHz, $CDCl_3$) δ ppm: 163.2 (thiazole-C), 156.3 (Ph-C), (benzothiazole-C), 138.0 (Ph-C), 136.1 (Ph-C), 133.0 (benzothiazole-C), 131.7 (Ph-C), 129.3 (Ph-C), 127.9 (Ph-C), 125.9 (Ph-C), 124.5 (Ph-C), 122.7 (Ph-C), 121.3 (Ph-C), 121.3 (Ph-C), 113.0 (Ph-C), 70.9 (-OCH_2-), 21.2 (-CH_3). Anal. Calcd for $C_{21}H_{17}NOS$: C, 76.10%; H, 5.17%; N, 4.23%; Found: C, 76.08%; H, 5.16%; N, 4.22%.

2-(2-(benzyloxy)phenyl)benzo[d]thiazole (**A7**) Gray solid; Yield/%: 70%; Mp/°C: 89.7~91.7; ESI-MS [M + H]$^+$: 318.4; ^{1}H NMR (600 MHz, $CDCl_3$) δ ppm: 8.557 (dd, *J* = 7.98, 1.50 Hz, 1H, Ph-H), 8.089 (d, *J* = 8.22 Hz, 1H, Ph-H), 7.879 (d, *J* = 7.98 Hz, 1H, Ph-H), 7.546 (d, *J* = 7.32 Hz, 2H, Ph-H), 7.481 (t, *J* = 8.04 Hz, 1H, Ph-H), 7.342–7.435 (m, 5H, Ph-H), 7.102–7.151 (m, 2H, Ph-H), 5.352(s, 2H, -OCH_2). ^{13}C NMR (150 MHz, $CDCl_3$) δ ppm: 163.3 (thiazole-C), 156.3 (benzothiazole-C), 136.0 (Ph-C), 131.9 (Ph-C), (benzothiazole-C), 129.9 (Ph-C), 128.6 (Ph-C), 128.3 (Ph-C), 127.8 (Ph-C), 126.0 (Ph-C), 124.7 (Ph-C), 122.6 (Ph-C), 121.5 (Ph-C), 121.3 (Ph-C), 113.0 (Ph-C), 71.0 (-OCH_2-). Anal. Calcd for $C_{20}H_{15}NOS$: C, 75.68%; H, 4.76%; N, 4.41%; Found: C, 75.70%; H, 4.77%; N, 4.42%.

4-((2-(benzo[d]thiazol-2-yl)phenoxy)methyl)benzonitrile (**A8**) Gray solid; Yield/%: 66%; Mp/°C: 131.8~133.8; ESI-MS [M + H]$^+$: 343.1; ^{1}H NMR (600 MHz, $CDCl_3$) δ ppm: 8.546 (d, *J* = 7.8 Hz, 1H, Ph-H), 8.098 (d, *J* = 8.16 Hz, 1H, Ph-H), 7.894 (d, *J* = 7.92 Hz, 1H, Ph-H), 7.717 (d, *J* = 8.1Hz, 2H, Ph-H), 7.660 (d, *J* = 8.04 Hz, 2H, Ph-H), 7.501 (t, *J* = 7.74 Hz, 1H, Ph-H), 7.431 (t, *J* = 8.1 Hz,1H, Ph-H), 7.381 (t, *J* = 7.68Hz, 1H, Ph-H), 7.175 (t, *J* = 7.56 Hz, 1H, Ph-H), 7.041 (d, *J* = 8.34 Hz, 1H, Ph-H), 5.380 (s, 2H, -OCH_2). ^{13}C NMR

(150 MHz, $CDCl_3$) δ ppm: 155.7 (thiazole-C), 141.4 (benzothiazole-C), 132.5 (benzothiazole-C), 131.9 (Ph-C), 130.2 (Ph-C), 128.1 (Ph-C), 126.2 (Ph-C), 124.9 (Ph-C), 122.8 (Ph-C), 122.0 (Ph-C), 121.3 (Ph-C), 118.5 (-CN), 112.8 (Ph-C), 112.2 (Ph-C), 70.1 (-OCH_2-). Anal. Calcd for $C_{21}H_{14}N_2OS$: C, 73.66%; H, 4.12%; N, 8.18%; Found: C, 73.64%; H, 4.11%; N, 8.17%.

6-fluoro-*N*-phenethylbenzo[d]thiazol-2-amine (**B1**) White solid; Yield/%: 86%; Mp/°C: 132.4~134.6; ESI-MS [M + H]$^+$: 273.1; ^{1}H NMR (400 MHz, DMSO-d_6) δ ppm: 12.85 (s, 1H, -NH), 8.07–8.04 (m, 1H, Ph-H), 7.85–7.79 (m, 3H, Ph-H), 7.60 (dd, *J* = 9.9, 2.5 Hz, 1H, Ph-H), 7.25–7.13 (m, 3H, Ph-H), 3.89 (s, 2H, -CH_2), 3.87 (s, 2H, -CH_2). ^{13}C NMR (101 MHz, DMSO-d_6) δ ppm: 165.6 (thiazole-C), 163.0 (Ph-C), 161.9 (Ph-C), 160.6 (Ph-C), 153.2 (Ph-C), 148.9 (benzothiazole-C), 123.4 (C, d, $J_{C-C-C-F}$ = 10.10 Hz), 122.9 (Ph-C), 112.2 (Ph-C), 111.9 (Ph-C), 111.6 (C, d, $J_{C-C-C-C-F}$ = 4.04 Hz), 106.8 (C, d, J_{C-C-F} = 24.24 Hz), 56.2 (-CH_2CH_2-), 56.1 (-CH_2CH_2-). Anal. Calcd for $C_{15}H_{13}FN_2S$: C, 66.15%; H, 4.81%; N, 10.29%; Found: C, 66.16%; H, 4.82%; N, 10.30%.

N-(2,6-dichlorobenzyl)-6-fluorobenzo[d]thiazol-2-amine (**B2**) Gray solid; Yield/%: 77%; Mp/°C: 156.8~158.2; ESI-MS [M + H]$^+$: 327.0; ^{1}H NMR (400 MHz, DMSO-d_6) δ ppm: 8.57 (d, *J* = 4.5 Hz, 1H, Ph-H), 7.70 (dd, *J* = 8.6, 5.6 Hz, 1H, Ph-H), 7.55 (d, *J* = 8.1 Hz, 2H, Ph-H), 7.43 (dd, *J* = 8.7, 7.5 Hz, 1H, Ph-H), 7.28 (dd, *J* = 10.4, 2.5 Hz, 1H, Ph-H), 6.99–6.85 (m, 1H, Ph-H), 4.83 (s, 2H, -CH_2). ^{13}C NMR (101 MHz, DMSO-d_6) δ ppm: 168.1 (thiazole-C), 163.0 (Ph-C), 160.6 (benzothiazole-C), 136.2 (Ph-C), 132.9 (Ph-C), 131.2 (Ph-C), 129.1 (Ph-C), 126.0 (benzothiazole-C), 122.5 (C, d, $J_{C-C-C-F}$ = 10.1 Hz), 109.1(C, d, J_{C-C-F} = 24.24 Hz), 105.1(C, d, J_{C-C-F} = 24.25 Hz), 44.1 (-CH_2-). Anal. Calcd for $C_{14}H_9Cl_2FN_2S$: C, 51.39%; H, 2.77%; N, 8.56%; Found: C, 51.37%; H, 2.76%; N, 8.55%.

N-(3,4-dimethoxybenzyl)-6-fluorobenzo[d]thiazol-2-amine (**B3**) Gray solid; Yield/%: 79%; Mp/°C: 135.5~137.4; ESI-MS [M + H]$^+$: 319.1; ^{1}H NMR (400 MHz, DMSO-d_6) δ(ppm): 8.56 (s, 1H, -NH), 7.43 (dd, *J* = 8.3, 5.5 Hz, 1H, Ph-H), 7.11 (s, 1H, Ph-H), 6.99–6.75 (m, 4H, Ph-H), 5.08 (s, 2H, -CH_2). 3.73 (d, *J* = 5.1 Hz, 6H, -OCH_3). ^{13}C NMR (101 MHz, DMSO-d_6) δ ppm: 163.0 (thiazole-C), 160.6 (Ph-C), 160.0 (Ph-C), 149.2 (benzothiazole-C), 148.5 (Ph-C), 141.9 (Ph-C), 141.8 (Ph-C), 129.2 (benzothiazole-C), 123.1 (C, d, $J_{C-C-C-F}$ = 9.09 Hz), 119.8 (Ph-C), 117.9 (Ph-C), 112.1 (C, d, J_{C-C-F} = 18.18 Hz), 108.1 (C, d, J_{C-C-F} = 23.23 Hz), 98.6 (Ph-C), 98.3 (Ph-C), 55.9 (-OCH_3), 45.1 (-CH_2-). Anal. Calcd for $C_{16}H_{15}FN_2O_2S$: C, 60.36%; H, 4.75%; N, 8.80%; Found: C, 60.38%; H, 4.76%; N, 8.81%.

6-fluoro-*N*-(4-nitrobenzyl)benzo[d]thiazol-2-amine (**B4**) White solid; Yield/%: 65%; Mp/°C: 142.5~144.7; ESI-MS [M + H]$^+$: 304.1; ^{1}H NMR (400 MHz, DMSO-d_6) δ ppm: 8.86 (t, *J* = 5.9 Hz, 1H, -NH), 8.27–8.21 (m, 2H, Ph-H), 7.70 (dd, *J* = 8.6, 5.6 Hz, 1H, Ph-H), 7.66–7.59 (m, 2H, Ph-H), 7.20 (dd, *J* = 10.5, 2.5 Hz, 1H, Ph-H), 6.91 (td, *J* = 9.3, 2.6 Hz, 1H, Ph-H), 4.76 (d, *J* = 5.9 Hz, 2H, -CH_2). ^{13}C NMR (101 MHz, DMSO-d_6) δ ppm: 168.8 (thiazole-C), 153.9 (C, d, $J_{C-C-C-F}$ = 12.12 Hz), 147.2 (C, d, J_{C-C-F} = 40.40 Hz), 128.6 (Ph-C), 127.5 (Ph-C), 126.4 (benzothiazole-C), 124.1 (Ph-C), 122.4 (C, d, J_{C-C-F} = 10.10 Hz), 109.1 (Ph-C), 105.5 (Ph-C), 46.9 (-CH_2-). Anal. Calcd for $C_{14}H_{10}FN_3O_2S$: C, 55.44%; H, 3.32%; N, 13.85%; Found: C, 55.47%; H, 3.33%; N, 13.86%.

6-chloro-*N*-(3-fluorobenzyl)benzo[d]thiazol-2-amine (**B5**) White solid; Yield/%: 45%; Mp/°C: 145.6~147.6; ESI-MS [M + H]$^+$: 293.5; ^{1}H NMR (600 MHz, $CDCl_3$) δ ppm:7.545 (d, *J* = 2.1 Hz, 1H, Ph-H),7.429 (d, *J* = 8.64 Hz, 1H, Ph-H), 7.103–7.246 (m, 5H, Ph-H), 5.149 (s, 1H, -NH), 4.646 (s, 2H, -OCH_2). ^{13}C NMR (150 MHz, $CDCl_3$) δ ppm: 130.4 (benzothiazole-C), 130.4 (Ph-C), 127.0 (Ph-C), 126.5 (Ph-C), 123.1 (Ph-C), 123.1 (Ph-C), 120.5 (Ph-C), 119.8 (Ph-C), 114.9 (Ph-C), 114.8 (Ph-C), 114.6 (Ph-C), 114.4 (Ph-C), 48.6 (-CH_2-). Anal. Calcd for $C_{14}H_{10}ClFN_2S$: C, 57.44%; H, 3.44%; N, 9.57%; Found: C, 57.48%; H, 3.45%; N, 9.58%.

6-chloro-*N*-(3,5-dimethoxybenzyl)benzo[d]thiazol-2-amine (**B6**) Pale yellow solid; Yield/%: 58%; Mp/°C: 101.3~103.3; ESI-MS [M + H]$^+$: 335.1; ^{1}H NMR (600 MHz, $CDCl_3$) δ ppm: 7.539 (d, *J* = 1.98 Hz, 1H, Ph-H), 7.427 (d, *J* = 8.58 Hz, 1H, Ph-H), 7.236 (s, 1H, Ph-H), 6.342–6.528 (m, 3H, Ph-H), 5.083 (s, 1H, -NH), 4.557(s, 2H, -CH_2), 3.746 (s, 6H, -OCH_3). ^{13}C NMR (150 MHz, $CDCl_3$) δ ppm: 167.5 (thiazole-C), 161.3 (Ph-C),151.0 (benzothiazole-C), 139.6 (Ph-C), 131.8 (benzothiazole-C), 126.5 (Ph-C), 121.5 (Ph-C), 120.6 (Ph-C), 119.7 (Ph-C), 110.7 (Ph-C), 107.0 (Ph-C), 107.0 (Ph-C), 105.7 (Ph-C), 99.8 (Ph-C), 99.1 (Ph-C), 55.5 (-CH_3), 49.5 (-CH_2-). Anal. Calcd for $C_{16}H_{15}ClN_2O_2S$: C, 57.40%; H, 4.52%; N, 8.37%; Found: C, 57.36%; H, 4.51%; N, 8.36%.

6-chloro-*N*-(4-nitrobenzyl)benzo[d]thiazol-2-amine (**B7**) Pale yellow solid; Yield/%: 31%; Mp/°C: 148.4~150.8; ESI-MS [M + H]$^+$: 320.4; ^{1}H NMR (600 MHz, $CDCl_3$) δ ppm: 8.412 (d, *J* = 8.4 Hz, 1H, Ph-H), 8.216 (d, *J* = 8.4 Hz, 2H, Ph-H), 8.199 (s, 1H, Ph-H), 8.145 (d, *J* = 8.4 Hz, 1H, Ph-H), 7.451 (d, *J* = 8.4 Hz, 2H, Ph-H), 4.850 (s, 2H, -CH_2), 3.077 (s, 1H, -NH). ^{13}C NMR (150 MHz, $CDCl_3$) δ ppm: 167.5 (thiazole-C), 158.7 (benzothiazole-C),151.1 (Ph-C), 129.6 (Ph-C), 129.5 (benzothiazole-C), 126.6 (Ph-C), 121.6 (Ph-C), 115.8 (Ph-C), 110.5 (Ph-C), 48.7 (-CH_2-). Anal. Calcd for $C_{14}H_{10}ClN_3O_2S$: C, 52.59%; H, 3.15%; N, 13.14%; Found: C, 52.61%; H, 3.14%; N, 13.13%.

N-benzyl-6-chlorobenzo[d]thiazol-2-amine (**B8**) Pale yellow solid; Yield/%: 50%; Mp/°C: 123.5~125.5; ESI-MS [M + H]$^+$: 275.1; ^{1}H NMR (600 MHz, $CDCl_3$) δ ppm: 7.540 (d, *J* = 2.04 Hz, 1H, Ph-H), 7.357–7.394 (m, 3H, Ph-H), 7.305–7.332 (m, 3H, Ph-H), 7.243 (d, *J* = 2.04 Hz, 1H, Ph-H), 5.160 (s, 1H, -NH), 4.631(s, 2H, -CH_2). ^{13}C NMR (125 MHz, DMSO-d_6) δ ppm: 166.9 (thiazole-C), 151.2 (benzothiazole-C), 138.5 (Ph-C), 131.9 (benzothiazole-C), 128.6 (Ph-C), 128.3 (Ph-C), 127.3 (Ph-C), 127.1 (Ph-C), 126.8 (Ph-C), 125.7 (Ph-C), 124.7 (Ph-C), 120.5 (Ph-C), 118.9 (Ph-C), 47.2 (-CH_2-). Anal. Calcd for $C_{14}H_{11}ClN_2S$: C, 61.20%; H, 4.04%; N, 10.20%; Found: C, 61.17%; H, 4.03%; N, 10.19%.

N-(6-fluorobenzo[d]thiazol-2-yl)benzamide (**C1**) Gray solid; Yield/%: 45%; Mp/°C: >300; ESI-MS [M + H]$^+$: 273.1; ^{1}H NMR (400 MHz, DMSO-d_6) δ ppm: 12.99 (s, 1H, -CONH), 8.21–8.11 (m, 2H, Ph-H), 8.06 (dd, *J* = 8.7, 5.5 Hz, 1H, Ph-H), 7.68 (t, *J* = 7.4 Hz, 1H, Ph-H), 7.65–7.53 (m, 3H, Ph-H), 7.23 (td, *J* = 9.1, 2.4 Hz, 1H, Ph-H). ^{13}C NMR (101 MHz, DMSO-d_6) δ 166.4 (thiazole-C), 163.0 (Ph-C), 161.6 (Ph-C), 160.6 (Ph-C), 133.4 (Ph-C), 132.1 (Ph-C), 129.1 (Ph-C), 128.8 (Ph-C), 127.8 (benzothiazole-C), 123.5 (C, d, $J_{C-C-C-F}$ = 10.10 Hz), 112.2 (C, d, J_{C-C-F} = 24.24 Hz), 107.0 (C, d, J_{C-C-F} = 24.24 Hz). Anal. Calcd for $C_{14}H_9FN_2OS$: C, 61.75%; H, 3.33%; N, 10.29%; Found: C, 61.73%; H, 3.32%; N, 10.28%.

2,6-dichloro-*N*-(6-fluorobenzo[d]thiazol-2-yl) benzamide (**C2**) White solid; Yield/%: 51%; Mp/°C: >300; ESI-MS [M + H]$^+$: 341.0; ^{1}H NMR (400 MHz, DMSO-d_6) δ ppm: 13.32 (s, 1H, -CONH), 8.09 (dd, *J* = 8.8, 5.5 Hz, 1H, Ph-H), 7.73–7.48 (m, 4H, Ph-H), 7.26 (td, *J* = 9.1, 2.5 Hz, 1H, Ph-H). ^{13}C NMR (101 MHz, DMSO-d_6) δ ppm: 163.8 (thiazole-C), 163.1 (Ph-C), 160.7 (Ph-C), 160.1 (Ph-C), 150.0

(C, d, $J_{C-C-C-F}$ = 12.12 Hz), 134.6 (Ph-C), 132.8 (Ph-C), 131.6 (Ph-C), 128.8 (benzothiazole-C), 127.8 (Ph-C), 123.7 (C, d, $J_{C-C-C-F}$ = 10.10 Hz), 112.7 (C, d, J_{C-C-F} = 24.24 Hz), 107.6 (C, d, J_{C-C-F} = 24.24 Hz). Anal. Calcd for $C_{14}H_7Cl_2FN_2OS$: C, 49.29%; H, 2.07%; N, 8.21%; Found: C, 49.31%; H, 2.08%; N, 8.22%.

N-(6-fluorobenzo[d]thiazol-2-yl)-3,4-dimethoxybenzamide (**C3**) White solid; Yield/%: 46%; Mp/°C: >300; ESI-MS [M + H]$^+$: 333.1; ^{1}H NMR (400 MHz, DMSO-d_6) δ ppm: 12.86 (s, 1H, -CONH), 8.05 (dd, *J* = 8.7, 5.5 Hz, 1H, Ph-H), 7.93–7.74 (m, 2H, Ph-H), 7.60 (dd, *J* = 10.0, 2.2 Hz, 1H, Ph-H), 7.22 (td, *J* = 9.1, 2.4 Hz, 1H, Ph-H), 7.14 (d, *J* = 8.5 Hz, 1H, Ph-H), 3.88 (d, *J* = 7.1 Hz, 6H, -OCH_3). ^{13}C NMR (101 MHz, DMSO-d_6) δ ppm: 165.6 (thiazole-C), 163.0 (Ph-C), 161.9 (Ph-C), 160.6 (Ph-C), 153.2 (Ph-C), 150.1 (benzothiazole-C), 148.8 (Ph-C), 127.8 (Ph-C), 123.7 (C, d, $J_{C-C-C-F}$ = 55.55 Hz), 122.8 (Ph-C), 111.8 (C, d, J_{C-C-F} = 32.32 Hz), 111.6, 106.9 (C, d, J_{C-C-F} = 25.25 Hz), 56.2 (-OCH_3). Anal. Calcd for $C_{16}H_{13}FN_2O_3S$: C, 57.82%; H, 3.94%; N, 8.43%; Found: C, 57.79%; H, 3.93%; N, 8.42%.

N-(6-fluorobenzo[d]thiazol-2-yl)-4-nitrobenzamide (**C4**) White solid; Yield/%: 60%; Mp/°C:187.7~189.4; ESI-MS [M + H]$^+$: 319.1; ^{1}H NMR (400 MHz, CF_3COOD) δ ppm: δ 8.61 (dd, *J* = 63.9, 8.5 Hz, 4H, Ph-H), 8.21 (dd, *J* = 9.2, 4.4 Hz, 1H, Ph-H), 7.89 (d, *J* = 7.7 Hz, 1H, Ph-H), 7.64 (t, *J* = 8.9 Hz, 1H, Ph-H). ^{13}C NMR (101 MHz, CF_3COOD) δ ppm: 165.44 (thiazole-C), 151.2 (benzothiazole-C), 136.0 (C, d, $J_{C-C-C-F}$ = 13.13 Hz), 134.8 (Ph-C), 129.8 (benzothiazole-C), 124.4 (Ph-C), 121.1 (Ph-C), 118.6 (Ph-C), 116.7 (C, d, J_{C-C-F} = 25.25 Hz), 115.8 (Ph-C), 113.0 (Ph-C), 110.18 (Ph-C), 103.3 (C, d, J_{C-C-F} = 28.28 Hz). Anal. Calcd for $C_{14}H_8FN_3O_3S$: C, 53.00%; H, 2.54%; N, 13.24%; Found: C, 53.03%; H, 2.55%; N, 13.22%.

N-(6-chlorobenzo[d]thiazol-2-yl)-4-methoxybenzamide (**C5**) Gray solid; Yield/%: 70%; Mp/°C: >300, ESI-MS [M + H]$^+$: 319.1; ^{1}H NMR (600 MHz, $CDCl_3$) δ ppm: 10.081 (s, 1H, -NH), 7.947 (d, *J* = 8.3 Hz, 2H, Ph-H), 7.813 (s, 1H, Ph-H), 7.376 (d, *J* = 8.6 Hz, 1H, Ph-H), 7.291 (d, *J* = 8.6 Hz, 1H, Ph-H), 3.862 (s, 3H, -OCH_3). ^{13}C NMR (150 MHz, DMSO-d_6) δ ppm: 166.1 (thiazole-C), 163.3 (-C=O), 160.7 (Ph-C), 147.8 (benzothiazole-C), 133.7 (benzothiazole-C), 130.9 (Ph-C), 127.9 (Ph-C), 126.8 (Ph-C), 124.4 (Ph-C), 121.8 (Ph-C), 121.7 (Ph-C), 114.4 (Ph-C), 56.0 (-OCH_3). Anal. Calcd for $C_{15}H_{11}ClN_2O_2S$: C, 56.52%; H, 3.48%; N, 8.79%; Found: C, 56.59%; H, 3.47%; N, 8.78%.

N-(6-chlorobenzo[d]thiazol-2-yl)benzamide (**C6**) Gray solid; Yield/%: 82%; Mp/°C: >300; ESI-MS [M + H]$^+$: 289.1; ^{1}H NMR (600 MHz, $CDCl_3$) δ ppm: 11.011 (s, 1H, -NH), 7.985 (d, *J* = 7.86 Hz, 2H, Ph-H), 7.819 (s, 1H, Ph-H), 7.610 (t, *J* = 7.1 Hz, 2H, Ph-H), 7.481 (d, *J* = 7.5 Hz, 2H, Ph-H), 7.273 (s, 1H, Ph-H). ^{13}C NMR (150 MHz, DMSO-d_6) δ ppm: 166.9 (thiazole-C), 160.6 (-C=O), 147.7 (benzothiazole-C), 133.7 (Ph-C), 133.3 (benzothiazole-C), 132.5 (Ph-C), 129.1 (Ph-C), 128.7 (Ph-C), 128.0 (Ph-C), 126.9 (Ph-C), 121.9 (Ph-C), 121.7 (Ph-C). Anal. Calcd for $C_{14}H_9ClN_2OS$: C, 58.24%; H, 3.14%; N, 9.70%; Found: C, 58.20%; H, 3.13%; N, 9.71%.

N-(6-chlorobenzo[d]thiazol-2-yl)-2-fluorobenzamide (**C7**) White solid; Yield/%: 77%; Mp/°C: >300; ESI-MS [M + H]$^+$: 307.0; ^{1}H NMR (600 MHz, $CDCl_3$) δ ppm: 11.755 (s, 1H, -NH), 9.562 (s, 1H, Ph-H), 9.444 (d, *J* = 8.58 Hz, 1H, Ph-H), 9.350–9.385 (m, 1H, Ph-H), 9.105–9.155 (m, 2H, Ph-H), 9.006 (s, 1H, Ph-H), 8.971 (s, 1H, Ph-H). ^{13}C NMR (1500 MHz, DMSO-d_6) δ ppm: 166.0 (thiazole-C), 165.9 (-C=O), 164.2(benzothiazole-C), 133.4(benzothiazole-C), 131.7 (Ph-C), 131.6 (Ph-C), 128.2 (Ph-C), 127.0 (Ph-C), 122.0 (Ph-C), 121.8 (Ph-C), 116.2 (Ph-C), 116.1 (Ph-C). Anal. Calcd for $C_{14}H_8ClFN_2OS$: C, 54.82%; H, 2.63%; N, 9.13%; Found: C, 54.79%; H, 2.62%; N, 9.14%.

6-chloro-*N*,*N*-bis(3,5-dimethoxybenzyl)benzo[d]thiazol-2-amine (**D1**) White solid; Yield/%: 20%; Mp/°C: 83.4~85.3; ESI-MS [M + H]$^+$: 485.1; ^{1}H NMR (600 MHz, $CDCl_3$) δ ppm: 7.533 (d, *J* = 2.04 Hz, 1H, Ph-H), 7.311 (d, *J* = 2.04 Hz, 1H, Ph-H), 6.331–6.549 (m, 7H, Ph-H), 4.663 (s, 4H, -CH_2), 3.743 (s, 12H, -OCH_3). ^{13}C NMR (150 MHz, $CDCl_3$) δ ppm: 169.2 (thiazole-C), 161.2 (Ph-C), 151.6 (benzothiazole-C), 138.6 (Ph-C), 132.3 (benzothiazole-C), 126.5 (Ph-C), 123.9 (Ph-C), 122.2 (Ph-C), 120.4 (Ph-C), 119.7 (Ph-C), 100.0 (Ph-C), 99.6 (Ph-C), 55.4 (-CH_2-, -OCH_3). Anal. Calcd for $C_{25}H_{25}ClN_2O_4S$: C, 61.91%; H, 5.20%; N, 5.78%; Found: C, 61.93%; H, 5.21%; N, 5.79%.

N,*N*-dibenzyl-6-chlorobenzo[d]thiazol-2-amine (**D2**) Gray solid; Yield/%: 21%; Mp/°C: 134.4~136.4; ESI-MS [M + H]$^+$: 365.1; ^{1}H NMR (600 MHz, $CDCl_3$) δ ppm: 7.321–7.360 (m, 10H, Ph-H), 7.282 (d, *J* = 2.34 Hz, 1H, Ph-H), 7.059 (dd, J = 8.7, 2.34 Hz, 1H, Ph-H), 6.962 (d, *J* = 8.52 Hz, 1H, Ph-H), 4.484 (s, 2H, -CH_2), 4.178 (s, 2H, -CH_2). ^{13}C NMR (150 MHz, DMSO-d_6) δ ppm: 136.1 (benzothiazole-C), 134.1 (Ph-C), 133.0 (Ph-C), 129.0 (Ph-C), 128.9 (Ph-C), 128.6 (Ph-C), 128.5 (Ph-C), 127.6 (Ph-C), 127.4 (Ph-C), 126.4 (Ph-C), 56.6 (-CH_2-). Anal. Calcd for $C_{21}H_{17}ClN_2S$: C, 69.13%; H, 4.70%; N, 7.68%; Found: C, 69.16%; H, 4.71%; N, 7.69%.

2.8 Oil-water partition coefficient (log P) measurement experiment

The partition coefficient between n-octanol and water (log Po/w) is the classical descriptor for Lipophilicity (Daina et al., 2017). The test methodology followed previously published protocols (Wang et al., 2021). At room temperature, two large Erlenmeyer flasks were taken and filled with n-octanol and water, respectively. The flasks were placed in a constant temperature shaker at 150 rpm for 24 h to saturate the solvents. The mixtures were then transferred to separating funnels under normal pressure to obtain water-saturated n-octanol and n-octanol-saturated water for subsequent use. The target compound (2 mg) was accurately weighed and placed in a 2 mL brown volumetric flask. Anhydrous methanol was added to ultrasonically dissolve the compound, and the mixture was diluted to volume and thoroughly shaken to prepare a 1 mg/mL stock solution. The stock solution was further diluted to obtain 1, 1.5, 2, 2.5, 5 and 10 μg/mL reference solutions for construction of a standard curve using a UV-visible spectrophotometer. An excess amount of the analyte was dissolved in water-saturated n-octanol, and the mixture was shaken at 150 rpm for 24 h at constant temperature to obtain a saturated solution. The saturated solution was allowed to stand, centrifuged, and 1 mL of the supernatant was transferred to a 4 mL centrifuge tube. N-octanol saturated water (1 mL) was added, and the mixture was shaken at 150 rpm for 24 h at constant temperature. After standing for 8 h, the mixture was centrifuged. Appropriate amounts of the n-octanol phase before and after equilibration were diluted with methanol, and concentrations were determined from the standard curve to obtain C_0 and C_1. The concentration in the n-octanol saturated aqueous phase, C_w, was calculated as $C_w = C_0 - C_1$. Thus, log $P_{o/w} = \log_{10} C_0/C_w$.

2.9 Cell lines and cell culture

Mouse monocyte macrophage leukemia cells RAW 264.7, human lung epithelial cells Beas-2b, human epidermoid carcinoma cells A431, non-small cell lung cancer cells A549 and H1299 were purchased from the Shanghai Cell Bank of the Chinese Academy of Sciences Committee. Beas-2b, A549 cells were cultured in DMEM/F12 (11330032, Gibco), and RAW264.7, A431, H1299 cells were cultured in high sugar DMEM (11965092, Gibco). Both media were supplemented with 10% FBS (12484028, Gibco) and 1% penicillin-streptomycin mixture (100×) (10378016, Gibco). Cells were grown in 37°C thermostat incubator (Thermo Fisher, United States) containing 5% CO_2 and stored in −80°C for short-term storage, and in liquid nitrogen for long-term storage. None of the cell resuscitation passages used in the experiments herein exceeded 20 generations.

2.10 Cell proliferation and toxicity assay

Beas-2b, A431, A549 and H1299 cells were cultured in 96-well plates (5×10^3 cells/well) for 16 h, respectively. Subsequently, positive compound **4i** and 25 newly synthesized compounds were added at a final concentration of 10 μM or gradient concentrations (0.01, 0.1, 0.5, 1, 5 and 10 μM), co-incubated with the cells for 48 h. MTT (M8180, Solarbio) solutions (5 mg/mL) were then added and incubated for 4 h in the dark. Then, formazan crystals were dissolved with DMSO (D8371, Solarbio), followed by shaking on a shaker (DRAGONLAB, China) for 10 min. Finally, absorbance at 490 nm wavelength for each well was measured with Microplate reader (Molecular Devices, United States) (Tang et al., 2020; Lee et al., 2021). The results are expressed as mean ± SD from three independent experiments. Cells inhibition rates or IC_{50} values were calculated using GraphPad Prism 9.5.0.

2.11 Anti-inflammation activity assay

RAW264.7 cells were cultured in 6-well plates (2×10^5 cells/well) for 24 h and treated with 25 newly synthesized compounds (final concentration at 10 μM) for 30 min, respectively. Subsequently, the cells were stimulated with 1 μL of LPS (500 ng/mL) (L8880, Solarbio). After 24 h, the supernatant was collected and analyzed using an ELISA kit (EK206 and EK182, MULTISCIENCES) to quantify the levels of inflammatory cytokines IL-6 and TNF-α (Li et al., 2021).

2.12 Flow cytometry analysis of cell apoptosis

The A431 and A549 cells were cultured in 6-well plates (1×10^5 cells/mL) for 16 h. Subsequently, cells were treated with different concentrations (1, 2 and 4 μM) of either **B7** or **4i** for 24 h. Then, the cells were collected, washed, and stained with the FITC Annexin V Apoptosis Detection Kit I (556547, BD) (Jiang et al., 2017). Sample testing was performed using a FACS Calibur Flow Cytometer (BD, United States), and subsequent data analysis was performed using FlowJo 10.6.2.

2.13 Flow cytometry analysis of cell cycle

The A431 and A549 cells were cultured in 6-well plates (1×10^5 cells/mL) for 16 h. Subsequently, they were treated with different concentrations (1, 2 and 4 μM) of either **B7** or **4i** (4 μM) for 24 h. Cells were collected, mixed by adding 75% ethanol with shaking on a vortex shaker, and placed in the refrigerator at 4°C for overnight fixation. The cells were incubated with PI-Raze solution for 15 min at room temperature, protected from light, according to the instructions of BD Cycletest Plus DNA Reagent Kit (340242, BD), and detected by FACS Calibur flow cytometry (Oh et al., 2023), and subsequent data analysis was performed using FlowJo 10.6.2.

2.14 Wound healing analysis of cell migration

The A431 and A549 cells were cultured in 6-well plates (5×10^5 cells/well). When the cell confluency reached approximately 90%, used a sterile 10 μL pipette tip to create three parallel scratches evenly. Subsequently, rinsed with PBS to remove floating cells, and then treated with **B7** and **4i** at final concentrations of 4 μM. Captured images using a microscope camera system (Nikon, JPN) at 0 and 48 h post-treatment (Xu et al., 2023).

2.15 Western blot analysis

The A431 and A549 cells were cultured in 6-well plates (2×10^5 cells/well) for 2 h and treated with different concentrations of **B7**(1, 5, and 10 μM) or **4i** (10 μM). The corresponding cells were collected, washed with PBS (P1020, Solarbio), and lysed with RIPA buffer (R0010, Solarbio) to extract the total proteins. The extracted protein was loaded, subjected to SDS-PAGE electrophoresis (Bio-Rad) (Xu et al., 2023), and then the protein was transferred to a PDVF membrane (IPVH00010, Millipore) and incubated in the corresponding Primary Antibody AKT (9272, Cell Signaling Technology), phospho-AKT (4058, Cell Signaling Technology), ERK (A4782, ABclonal Technology), phospho-ERK (AP0974, ABclonal Technology) and GAPDH (AB0037, Abways Technology) overnight. Then, the Primary Antibody was recovered and enzyme-labeled secondary antibodies Goat Anti-Rabbit IgG HRP (H + L) (A0208, Beyotime Technology) were used. Finally, Imaging was performed on a gel Imaging System (Bio-Rad, United States) using the Ultra-sensitive ECL Chemiluminescence Assay Kit (P0018AS, Beyotime Technology).

2.16 ADMET analysis

The physicochemical parameters, pharmacokinetic properties and drug similarity of the active compound B7 were predicted using Swiss ADME web server (http://www.swissadme.ch/) (Daina et al., 2017). The toxicity associated with compound B7 was predicted by admetSAR web server (http://lmmd.ecust.edu.cn/admetsar2) (Cheng et al., 2012).

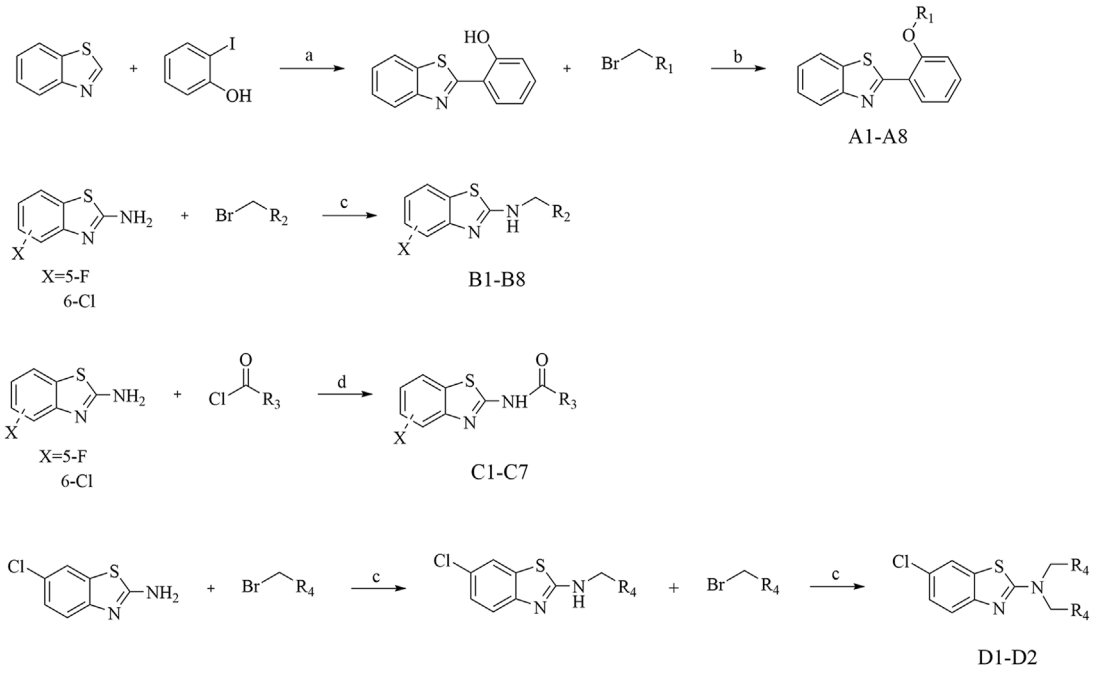

SCHEME 2
Synthesis of A Series, B Series, C Series, and D Series. Reagents and conditions: **(A)** K_2CO_3, DMSO, 120°C, 6 h; **(B)** K_2CO_3, acetonitrile, rt, 3 h; **(C)** K_2CO_3, acetonitrile, 65°C, 6 h; **(D)** Et_3N, dioxane, 100°C, 3 h.

2.17 Statistical analysis

For the statistical analysis, Microsoft Excel 2016 and GraphPad Prism 9.5.0 software were used. The results were presented as the mean ± standard error of the mean. Statistical analyses were conducted via Student's t-test. A value of $p < 0.05$ is defined as statistically significant. Statistical significance differences (compared to control group) are defined as follows: $p > 0.05$ (not significant, ns), $p \leq 0.05$ (*), $p \leq 0.01$ (**) and $p \leq 0.001$ (***).

3 Results

3.1 Chemistry

The synthetic pathways for the compounds in series A, B, C, and D were elucidated in Scheme 2. Commencing with benzothiazole and 2-hydroxyiodobenzene, and utilizing DMSO as the solvent, 2-phenol-benzothiazole was synthesized through nucleophilic substitution reactions. Subsequent steps involved the use of 2-phenol-benzothiazole and various substituted benzyl bromides as initial reactants, leading to the formation of eight compounds in the A series through the Williamson synthesis method. The B series is created by employing 2-amino-halogenated benzothiazole and diverse substituted benzyl bromides, resulting in the synthesis of eight compounds via amine halogenation reactions. The synthesis of the C series involved the use of 2-amino-halogenated benzothiazole and various substituted acyl chlorides, resulting in the production of seven compounds via amide formation reactions. Similarly, the synthetic procedure for the D series compounds closely resembled that of the B series. To validate the synthesized compounds in this study, thorough analyses utilizing ^{1}H NMR, ^{13}C NMR, ESI-MS, HPLC and elemental analysis were conducted, confirming the accuracy of their structures (Supplementary Material).

3.2 Biological evaluation

3.2.1 Anti-proliferation assay *in vitro*

To assess the anti-proliferative effects of the compounds on cells, we employed the MTT method to analyze the impact of all 2-amino-benzo[d] thiazole derivatives, along with the lead compound **4i**, at a concentration of 10 μM across Beas-2b, A431, A549, and H1299 cells (Tables 1–3). At the same time, we tested the log *p* values of 25 new compounds. According to Lipinski's rule of five (Ro5), the calculated log *p*-value should be < 5 for compounds intended for oral administration (Lipinski et al., 2001; Danalev et al., 2023). As shown in Tables 1–3, almost all of the compounds had log $p < 5$, which indicates that our newly synthesized compounds have good lipid solubility and have the conditions for drug formation.

The results indicated that following treatment with various compounds, the cell viability of Beas-2b cells remained consistently above 70%, underscoring the safety and reliability of the synthesized compounds at this concentration. The inhibitory rates of A series compounds on A431, A549, and H1299 cancer cells were consistently below 50%. Conversely, compounds from the B series (**B5**, **B7**, and **B8**) as well as those from the C and D series (**C5** and **C6**) demonstrated notable inhibitory effects on these cancer cells, surpassing 50% inhibition rates. Notably, compound **B7** exhibited a potent anti-proliferative effect, with inhibition rates exceeding 75% for all three cancer cell lines.

TABLE 1 Structure-activity relationship of A series and cells inhibition rate (%).

Comp.	R_1	log P	A431 (%)	A549 (%)	H1299 (%)	Beas-2b (%)
A1	ethyl acetate	2.35 ± 0.21	45.64 ± 1.21	42.34 ± 1.15	49.53 ± 0.84	10.22 ± 0.92
A2	2-nitrobenzyl	3.51 ± 0.19	35.84 ± 2.03	33.15 ± 2.34	42.37 ± 1.26	17.33 ± 3.26
A3	2-butylisoindoline-1,3-dione	3.63 ± 0.16	34.23 ± 1.15	28.54 ± 2.21	30.92 ± 0.77	5.25 ± 0.39
A4	4-nitrobenzyl	3.74 ± 0.35	35.81 ± 1.02	33.32 ± 1.36	39.43 ± 1.20	10.34 ± 0.64
A5	3-chlorobenzyl	4.51 ± 0.24	45.67 ± 0.87	47.62 ± 1.24	35.26 ± 2.24	18.25 ± 2.23
A6	4-methylbenzyl	4.72 ± 0.28	27.66 ± 1.62	20.73 ± 2.31	33.91 ± 0.68	15.11 ± 3.28
A7	benzyl	3.95 ± 0.15	15.31 ± 2.21	12.24 ± 3.42	26.53 ± 1.11	11.36 ± 2.65
A8	4-ethylbenzonitrile	3.44 ± 0.22	28.56 ± 1.24	24.35 ± 1.22	37.29 ± 2.30	14.21 ± 3.65

TABLE 2 Structure-activity relationship of B series and cells inhibition rate (%).

Comp.	X	R_2	log P	A431 (%)	A549 (%)	H1299 (%)	Beas-2b (%)
B1	5-F	N-phenethyl	3.47 ± 0.27	21.13 ± 2.03	18.34 ± 0.93	26.31 ± 0.91	23.12 ± 1.52
B2	5-F	N-(2,6-dichlorobenzyl)	4.25 ± 0.16	27.48 ± 2.42	30.25 ± 2.13	31.29 ± 1.14	18.62 ± 1.67
B3	5-F	N-(3,4-dimethoxybenzyl)	2.56 ± 0.12	32.36 ± 2.92	22.35 ± 1.34	44.63 ± 1.75	25.37 ± 2.01
B4	5-F	N-(4-nitrobenzyl)	2.67 ± 0.25	24.33 ± 1.87	19.62 ± 1.32	25.02 ± 1.62	21.35 ± 2.21
B5	6-Cl	N-(3-fluorobenzyl)	3.58 ± 0.11	59.69 ± 3.62	58.64 ± 1.01	51.34 ± 3.03	20.65 ± 1.85
B6	6-Cl	N-(3,5-dimethoxybenzyl)	3.36 ± 0.18	43.42 ± 1.61	35.23 ± 2.86	32.84 ± 0.74	20.58 ± 1.32
B7	6-Cl	N-(4-nitrobenzyl)	3.25 ± 0.24	78.67 ± 1.75	80.88 ± 1.03	75.72 ± 1.37	16.64 ± 1.36
B8	6-Cl	N-benzyl	3.56 ± 0.16	57.43 ± 3.64	65.75 ± 0.96	55.22 ± 2.49	18.12 ± 3.22

TABLE 3 Structure-activity relationship of C and D series and cells inhibition rate (%).

Comp.	X	R_3, R_4	log P	A431 (%)	A549 (%)	H1299 (%)	Beas-2b (%)
C1	5-F	N-benzamide	2.56 ± 0.14	17.52 ± 1.35	19.31 ± 1.07	28.34 ± 1.25	16.31 ± 1.82
C2	5-F	N-(2,6-dichlorobenzyl)	2.93 ± 0.11	5.61 ± 0.26	0.27 ± 0.12	6.80 ± 0.22	12.82 ± 1.76
C3	5-F	N-(3,4-dimethoxybenzyl)	2.49 ± 0.39	12.35 ± 1.51	4.38 ± 0.35	17.99 ± 2.52	21.29 ± 1.62
C4	5-F	N-(4-nitrobenzyl)	3.06 ± 0.23	43.11 ± 1.45	35.26 ± 1.82	45.22 ± 0.55	13.45 ± 1.65
C5	6-Cl	N-(4-methoxybenzamide)	2.87 ± 0.15	55.67 ± 2.34	56.33 ± 2.96	51.98 ± 0.24	17.21 ± 1.24
C6	6-Cl	N-benzamide	3.05 ± 0.17	57.73 ± 2.12	55.56 ± 2.78	59.72 ± 1.84	20.56 ± 0.52
C7	6-Cl	N-(2-fluorobenzamide)	2.90 ± 0.32	40.36 ± 1.33	44.64 ± 0.94	48.28 ± 0.37	21.36 ± 2.25
D1	Cl	N, N-bis(3,5-dimethoxybenzyl)	5.69 ± 0.25	38.66 ± 1.56	15.45 ± 3.46	32.66 ± 1.25	19.32 ± 1.31
D2	Cl	N, N-dibenzyl	5.82 ± 0.22	43.63 ± 1.39	40.34 ± 1.06	46.89 ± 2.71	24.31 ± 3.10

In summary, the data suggested that the recently synthesized compounds (**B5**, **B7**, **B8**, **C5**, and **C6**) exhibit promising anti-cancer properties without causing notable toxicity. Subsequent research and exploration are deemed necessary.

Then compounds **B5**, **B7**, **B8**, **C5**, and **C6** were assessed at gradient concentrations (0.01, 0.1, 0.5, 1, 5 and 10 μM), revealing significant inhibitory effects on A431, A549, and H1299 cell lines. Subsequently, the IC_{50} tests for A431, A549, and H1299 cells were conducted on the six selected compounds (Table 4). Notably, among these compounds, **B7** exhibited superior inhibitory effects across all three cancer cell lines, with IC_{50} values of 1.51 ± 0.20 μM for A431, 0.96 ± 0.24 μM for A549, and 1.68 ± 1.32 μM for H1299 cells. Remarkably, **B7** surpassed the efficacy of the other five compounds and demonstrated marginally superior inhibitory activity compared to the reference compound **4i**. Determining the IC_{50} values for **B7** lays the groundwork for further biological experiments, offering crucial insights for conducting experiments at specific dosage concentrations.

TABLE 4 IC_{50} (mean ± SD) (μM) values of some designed compounds and 4i.

Cell lines	B5 (μM)	B7 (μM)	B8 (μM)	C5 (μM)	C6 (μM)	4i (μM)
A431	10.79 ± 0.56	1.51 ± 0.20	5.36 ± 1.00	4.35 ± 0.90	8.40 ± 1.06	2.00 ± 0.41
A549	5.44 ± 1.00	0.96 ± 0.24	6.25 ± 0.99	9.82 ± 0.98	8.17 ± 0.40	1.09 ± 0.32
H1299	9.26 ± 1.34	1.68 ± 0.12	6.69 ± 0.54	8.94 ± 1.21	9.02 ± 0.37	2.48 ± 0.53

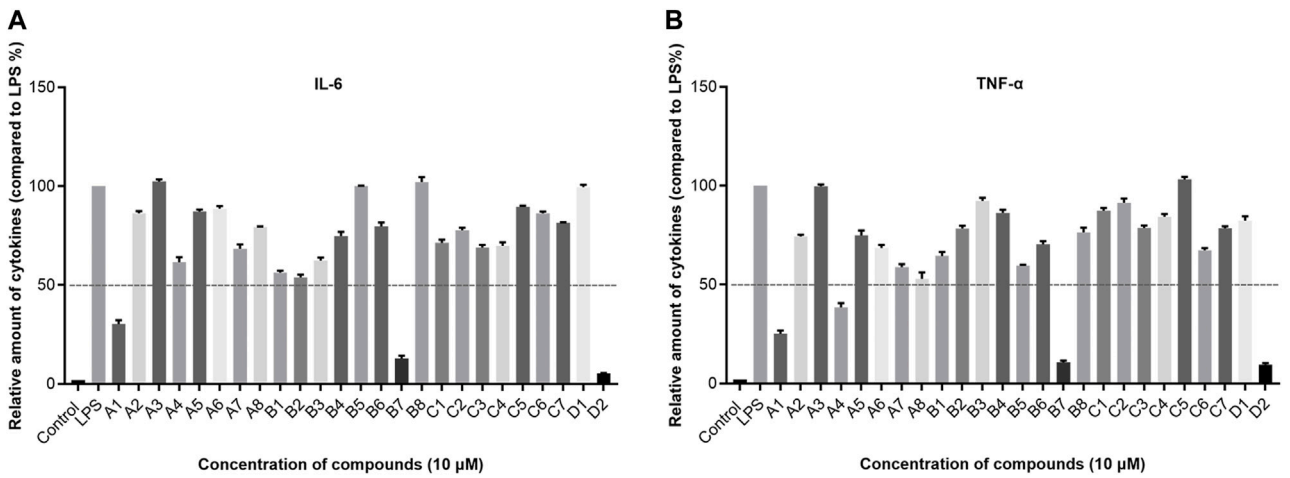

FIGURE 2
The expression levels of IL-6 and TNF-α *in vitro*. **(A)** The expression of IL-6 after compounds treatment; **(B)** The expression of TNF-α after compounds treatment.

3.2.2 Anti-inflammatory activity assay *in vitro*

In consideration of the interconnected development of inflammation and tumors, we undertook an initial screening of recently synthesized compounds to assess their anti-inflammatory activity. The parameters under scrutiny encompassed IL-6 and TNF-α, both serving as representative cytokines expressed significantly post-stimulation (Lee et al., 2011; Kumar and Singh, 2021). The down-regulatory effects of each compound on IL-6 and TNF-α were evaluated using ELISA Kit. Specifically, the ELISA method was employed to examine the impact of all recently synthesized compounds on the expression of IL-6 and TNF-α inflammatory factors at a concentration of 10 μM (Figure 2). Combining the expression levels of both inflammatory factors, in comparison to the blank control, compounds **A1**, **B7**, and **D2** demonstrated significant inhibitory effects on IL-6 and TNF-α expression at 10 μM, suggesting potent anti-inflammatory activity. Particularly, **D2** exhibited the most favorable effects, followed by **B7**, which showed efficacy comparable to that of **D2**.

3.2.3 B7 promoted apoptosis of A431 and A549 cells

In subsequent experiments, a concise mechanistic exploration was undertaken on the optimized compound **B7**. The objective was to examine whether **B7** induces apoptosis in A431 and A549 cells. Flow cytometry was employed to assess the impact of **B7** on cancer cell apoptosis 24 h post-treatment (Figure 3). The findings unveiled a gradual increase in the apoptosis rate of both A431 and A549 cells with the escalating concentration of **B7**. Notably, at a concentration of 4 μM, the pro-apoptotic effect of **B7** equaled that of the lead compound **4i** and, indeed, surpassed the efficacy of **4i**.

3.2.4 B7 blocked the cycle of A431 and A549 cells

In a parallel fashion, concentrations of 1, 2, and 4 μM were utilized for the application of flow cytometry to evaluate the cell cycle arrest induced by compound **B7** in A431 and A549 cells. As shown in Figure 4, compound **B7** and **4i** manifested a G2 phase cell cycle arrest effect on cancer cells, with **B7** exhibiting a noteworthy dose-dependent response. Notably, the cell cycle arrest induced by **B7** in both A431 and A549 cells surpassed that of **4i** at 4 μM.

3.2.5 B7 inhibited the migration of A431 and A549 cells

Tumor cells are recognized for their capacity for unrestricted proliferation and resistance to apoptosis, accompanied by a proclivity for facile metastasis (Khan et al., 2023). Consequently, we employed the wound healing assay to assess the migratory inhibitory effects of **B7** and **4i** on A431 and A549 cells across 4 μM for 48 h (Figure 5). The findings indicated that in A431 cells, the migration inhibitory effect of **B7** slightly surpassed that of **4i**. However, as none of the groups exhibited complete healing, extending the experiment duration until full healing is observed could yield more precise conclusions. It is noteworthy that in A549 cells, scratches in the DMSO blank control group had fully healed, highlighting the stronger inhibitory effect of **B7** on cell migration compared to **4i**. In conclusion, **B7** demonstrated superior efficacy in inhibiting cancer cell migration.

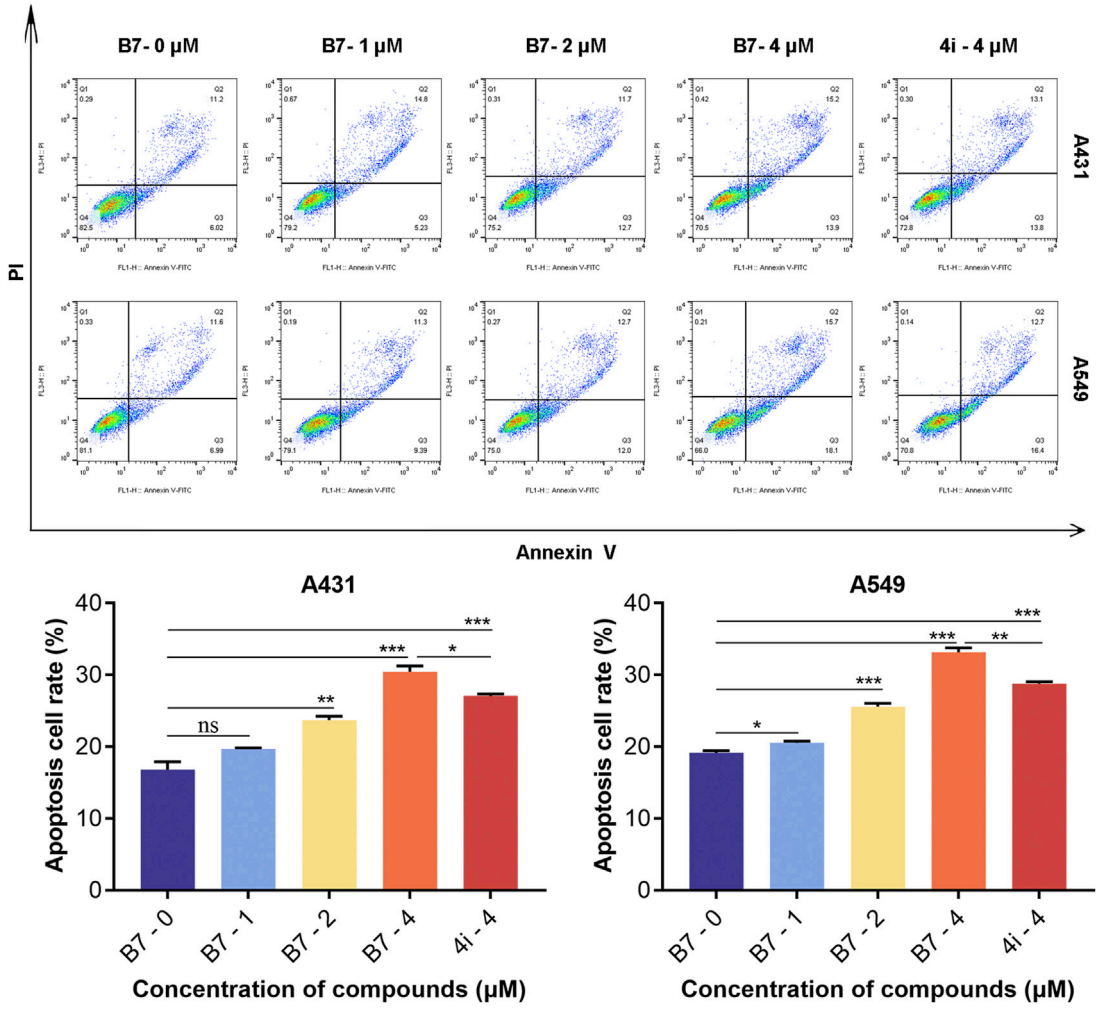

FIGURE 3
Apoptosis of A431 and A549 cells treated with B7 or 4i. Statistical significance differences were set to $p > 0.05$ (ns), $p \leq 0.05$ (*), $p \leq 0.01$ (**) and $p \leq 0.001$ (***).

3.2.6 B7 inhibited the phosphorylation of AKT and ERK

The anticipated experimental findings underscored the significant anti-promotion, pro-apoptotic, cell cycle arrest effects, and anti-inflammatory properties of **B7** on A431 and A549 cells. A psychological inquiry into the pathways or key mechanisms through which **B7** manifests its remarkable anti-cancer and anti-inflammatory activity prompted investigation. To this end, we examined the activity of common anti-tumor receptor kinases, revealing that **B7** had minimal impact on them. Furthermore, employing Western blot analysis to scrutinize prevalent anti-tumor and anti-inflammatory signaling pathways, we observed that **B7** can markedly inhibit both AKT and ERK protein phosphorylation simultaneously, surpassing the inhibitory effect observed with **4i** (Figure 6). The synergistic effects of the AKT and ERK pathways in cancer therapy have garnered considerable attention. Some studies propose that co-inhibiting these two pathways may be more effective than inhibiting either one alone, as it can concurrently disrupt multiple biological processes in cells, thereby enhancing the overall effectiveness of treatment (Dimri et al., 2020; Wu et al., 2023). The concurrent inhibition of the AKT and ERK pathways by compound **B7** may elucidate its efficacy in both anti-inflammatory and anticancer capacities.

3.2.7 In silico ADMET assessment of compound B7

The results of ADME and toxicity prediction were shown in Table 5. Based on the ADME prediction results, it could be seen that the physicochemical properties, ADME indexes and pharmacokinetic properties of B7 were within the permissible parameters (Ogbodo et al., 2023). From the toxicity prediction results, B7 had certain hepatotoxicity, but it was not irritating and corrosive to eyes and skin, and was not carcinogenic (Melo et al., 2022). Based on the above results, it was clear that B7 was a compound with better drug-like properties and deserved further studies.

4 Discussion

In this study, a series of novel benzothiazole derivatives was synthesized, and their anti-proliferative and anti-inflammatory

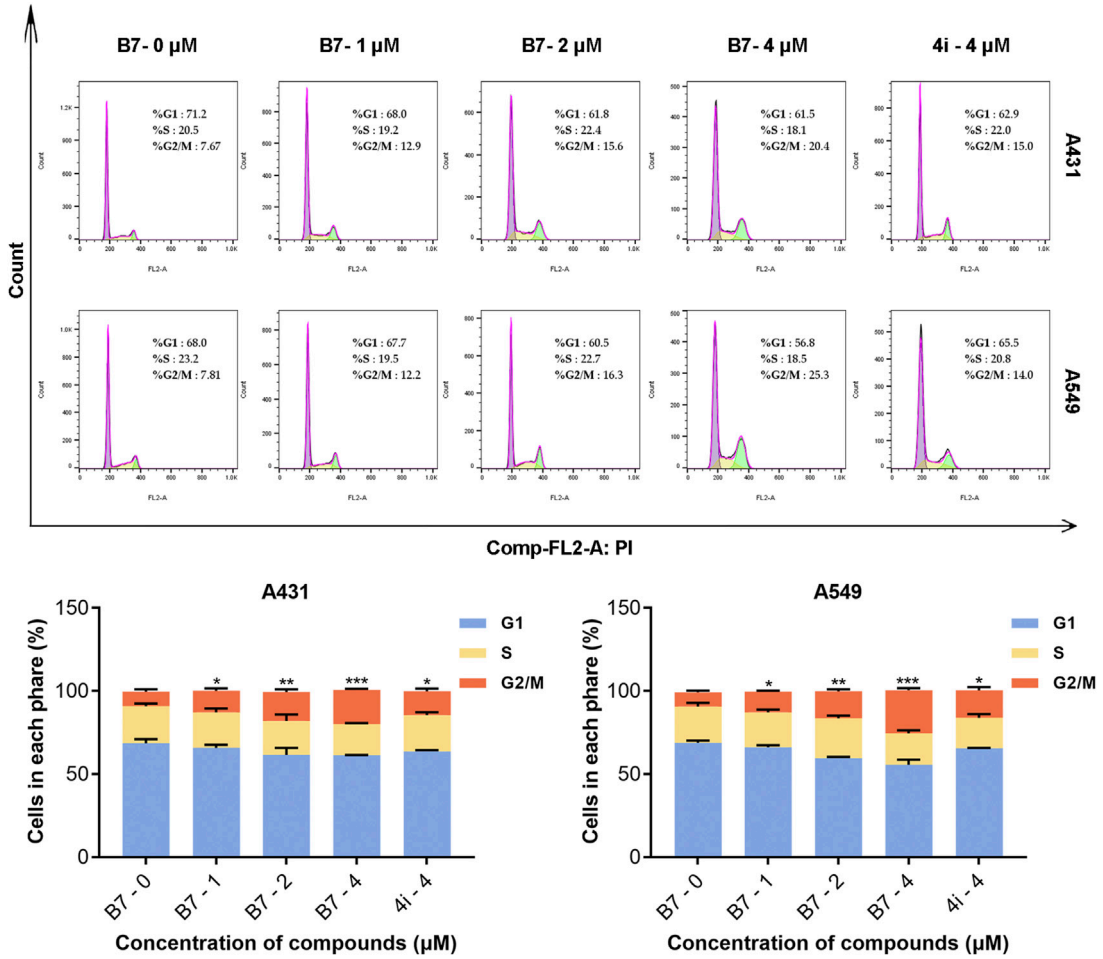

FIGURE 4
Cycle block of A431 and A549 cells treated with B7 or 4i. Statistical significance differences were set to $p > 0.05$ (ns), $p \leq 0.05$ (*), $p \leq 0.01$ (**) and $p \leq 0.001$ (***).

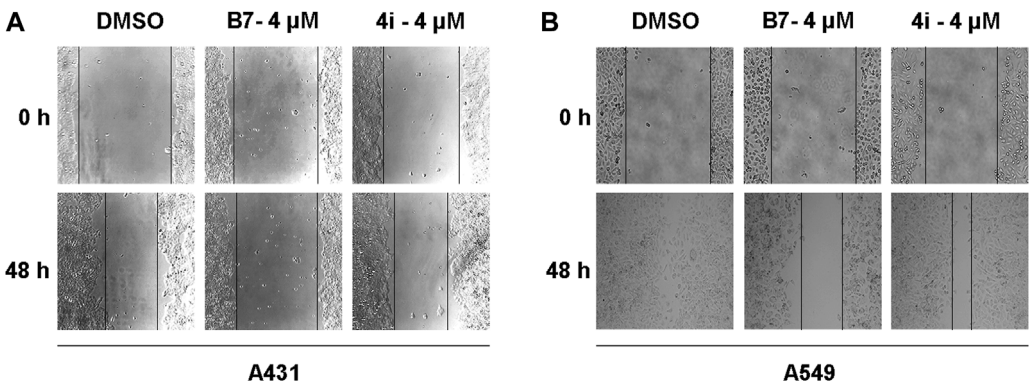

FIGURE 5
Migration of A431 and A549 cells treated with B7 or 4i. **(A)** The migration of A431 cells treated with B7 or 4i for 48 h; **(B)** The migration of A549 cells treated with B7 or 4i for 48 h.

activities were systematically assessed in cellular contexts. The results delineate variable inhibitory effects of these compounds on the A431, A549, and H1299 cell lines. Notably, compound **B7** exhibits superior inhibitory effects across all three cancer cell lines. Furthermore, these compounds demonstrate a capacity to downregulate the expression of inflammatory factors IL-6 and

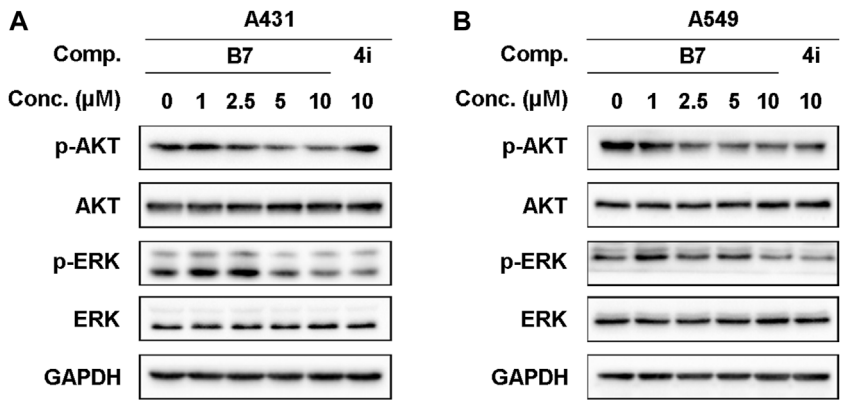

FIGURE 6
The protein expression levels of A431 and A549 cells treated with B7 or 4i. **(A)** The protein expression levels of A431 cells treated with B7 or 4i for 2 h; **(B)** The protein expression levels of A549 cells treated with B7 or 4i for 2 h.

TABLE 5 In silico ADMET properties of compound B7.

Properties	Prediction	Properties	Prediction
Physicochemical Properties		Pharmacokinetic	
Formula	$C_{14}H_{10}ClN_3O_2S$	GI absorption	High
Molecular weight	319.77 g/mol	BBB permeant	No
Num. heavy atoms	21	P-gp substrate	No
Num. arom. heavy atoms	15	CYP1A2 inhibitor	Yes
Fraction Csp3	0.07	CYP2C19 inhibitor	Yes
Num. rotatable bonds	4	CYP2C9 inhibitor	Yes
Num. H-bond acceptors	3	CYP2D6 inhibitor	No
Num. H-bond donors	1	CYP3A4 inhibitor	No
Molar Refractivity	87.24	Druglikeness	
TPSA	98.98 $Å^2$	Lipinski	Yes; 0 violation
Lipophilicity		Ghose	Yes
Log *Po*/w (iLOGP)	2.52	Veber	Yes
Log *Po*/w (XLOGP)	4.65	Egan	Yes
Log *Po*/w (WLOGP)	4.13	Muegge	Yes
Log *Po*/w (MLOGP)	3.33	Bioavailability Score	0.55
Log *Po*/w (SILICOS-IT)	2.64	Toxicity	
Consensus Log *Po*/w	3.45	Carcinogenicity	-
Water Solubility		Eye corrosion/irritation	-
Log *S* (ESOL)	−5.02	Skin corrosion/irritation	-
Solubility	3.08e-03 mg/mL	Hepatotoxicity	+
Class	Moderately soluble	Acute oral toxicity (c)	III

Legend: + (toxic); - (non-toxic); acute oral toxicity (c) level category—category I and II (toxic compound) and category III and IV (non-toxic compound), based on U.S. Environmental Protection Agency (EPA) criteria (Melo et al., 2022).

TNF-α to varying extents. Specifically, compounds **B7** and **D2** significantly suppress the expression of IL-6 and TNF-α.

In light of the anti-tumor and anti-inflammatory activities of the target compounds, we conducted a comprehensive Structure-Activity Relationship (SAR) analysis on a novel series of 2-aminobenzothiazole compounds. The A-series compounds demonstrated inhibition rates below 50% for A549, A431, and H1299 cells, whereas the B, C, and D-series exhibited pronounced inhibitory effects on these cancer cells. It can be deduced that the benzylamine moiety, tethered to the benzothiazole ring in this compound class, serves as an indispensable pharmacophore and a pivotal pharmacophoric group. This necessity arises from the requirement for a larger substituent at this position to occupy, thereby promoting a more stable conformation. Upon comparison of the bioactivity between B-series and C-series compounds, it was observed that the overall bioactivity of B-series compounds surpasses that of the C-series. This observation implies that the introduction of a carbonyl group to form an amide bond did not yield an enhancement in anti-tumor and anti-inflammatory activities. Further scrutiny of various substituents on the benzothiazole ring unveiled a notable increase in bioactivity when chlorine is situated at the 6th position on the benzothiazole ring, in contrast to fluorine substitution at the 5th position. Exploring additional substituents on benzothiazole may hold promise for optimizing the activity of these compounds. The compound D2 exhibits significant advantages in anti-inflammatory aspects, which may be related to its unique bisubstituted structure, worthy of further study.

Additionally, the presence of a nitro group on compound **B7** has captured our attention. The nitro group is a common and distinctive functional group in medicinal chemistry, prevalent in various classes of drugs including anticancer agents, antibiotics, antituberculosis medications, antiparasitic agents, sedatives, insecticides, and herbicides. This moiety exhibits a potent electron-withdrawing capacity, leading to the formation of localized electron-deficient sites within the molecule. It engages with nucleophilic reagents present in biological systems such as proteins, amino acids, nucleic acids, and enzymes through processes like nucleophilic addition, electron transfer, or complexation. Consequently, compounds containing nitro groups have been extensively studied in medicinal chemistry research. For instance, Nifurtimox (Rolon et al., 2022; Xin et al., 2022; Eslin et al., 2023), utilized in the treatment of Chagas disease and recurrent neuroblastoma, and Venetoclax (Li et al., 2024a), a Bcl-2 inhibitor used for managing chronic lymphocytic leukemia, both feature nitro structures. However, it is imperative to acknowledge that drugs incorporating nitro groups often elicit severe adverse reactions and toxicity, including carcinogenicity, hepatotoxicity, mutagenicity, and bone marrow suppression. Consequently, the nitro group is frequently considered a red flag structural motif, which somewhat impedes the exploration of its therapeutic potential. Nevertheless, in our study, the investigated compounds demonstrated negligible inhibitory effects on Beas-2b cells, indicating a lack of cytotoxicity *in vitro*. However, further investigation is warranted to evaluate their toxicity *in vivo*.

A key mechanism underlying **B7**'s anticancer efficacy appears to be its dual inhibition of the AKT and ERK signaling pathways. The AKT and ERK cascades play pivotal roles in tumor cell proliferation, survival, and metastasis (Chen et al., 2023; Cui et al., 2023). While previous benzothiazole-based inhibitors have targeted single pathways, **B7** is unique in concurrently suppressing both AKT and ERK phosphorylation. This dual targeting likely contributes to **B7**'s potent induction of apoptosis, cell cycle arrest, and inhibition of cell migration in our experiments.

Additionally, **B7** significantly reduces the production of the inflammatory cytokines IL-6 and TNF-α. As highlighted in the Introduction, chronic inflammation driven by these factors can create microenvironments conducive to tumor growth and progression. Therefore, **B7**'s anti-inflammatory properties may further augment its anticancer effects.

Future studies should focus on elucidating the precise molecular interactions enabling **B7**'s dual pathway inhibition. Testing **B7**'s efficacy in animal models will also be crucial to assess its potential for clinical translation. Limitations of this initial study include the narrow range of cancer cell lines examined. Expanding the panel of cell lines could provide further insights into **B7**'s spectrum of anticancer activity.

5 Conclusion

In summary, this study has innovatively developed a series of benzothiazole derivatives, with a focus on compound **B7** due to its notable dual anticancer and anti-inflammatory activities. **B7** stands out for its ability to significantly reduce cancer cell proliferation in A431, A549, and H1299 cell lines and lower the levels of inflammatory cytokines IL-6 and TNF-α. These results position B7 as a promising candidate for dual-action cancer therapy. The study's mechanistic exploration, highlighting **B7**'s simultaneous inhibition of the AKT and ERK pathways, offers a novel strategy for addressing both the survival mechanisms of tumor cells and the inflammatory milieu facilitating cancer progression.

Data availability statement

The original contributions presented in the study are included in the article/Supplementary Material, further inquiries can be directed to the corresponding authors.

Author contributions

XX: Writing–original draft, Conceptualization, Data curation, Funding acquisition. ZZ: Conceptualization, Investigation, Writing–original draft, Software. SC: Conceptualization, Investigation, Writing–original draft. YF: Methodology, Writing–original draft. JZ: Formal Analysis, Writing–original draft. YG: Resources, Writing–original draft. ZX: Data curation, Writing–original draft. YX: Supervision, Writing–original draft. XW: Funding acquisition, Supervision, Writing–original draft. FY: Writing–review and editing, Conceptualization. HC: Funding acquisition, Writing–review and editing. XX: Funding acquisition, Writing–review and

editing. XY: Conceptualization, Formal Analysis, Investigation, Software, Writing–review and editing.

Funding

The author(s) declare that financial support was received for the research, authorship, and/or publication of this article. This research was funded by the Basic social development science and technology projects of Wenzhou (grant no. Y20210214, Y20220206); The Basic social development science and technology projects of Taizhou (grant no. 20ywb67) and the scientific research projects of Zhejiang Provincial Education Department (grant no. Y202249707).

Acknowledgments

The authors extend their appreciation to the Analysis and Testing Center of Wenzhou Medical University for generously providing the essential equipment utilized in this study.

Conflict of interest

The authors declare that the research was conducted in the absence of any commercial or financial relationships that could be construed as a potential conflict of interest.

Publisher's note

All claims expressed in this article are solely those of the authors and do not necessarily represent those of their affiliated organizations, or those of the publisher, the editors and the reviewers. Any product that may be evaluated in this article, or claim that may be made by its manufacturer, is not guaranteed or endorsed by the publisher.

Supplementary material

The Supplementary Material for this article can be found online at: https://www.frontiersin.org/articles/10.3389/fchem.2024.1384301/full#supplementary-material

References

Al-Tel, T. H., Al-Qawasmeh, R. A., and Zaarour, R. (2011). Design, synthesis and *in vitro* antimicrobial evaluation of novel Imidazo[1,2-a]pyridine and imidazo[2,1-b][1,3]benzothiazole motifs. *Eur. J. Med. Chem.* 46, 1874–1881. doi:10.1016/j.ejmech.2011.02.051

Awadh, A. A. A. (2023). Biomedical applications of selective metal complexes of indole, benzimidazole, benzothiazole and benzoxazole: A review (from 2015 to 2022). *Saudi Pharm J.* 31, 101698. doi:10.1016/j.jsps.2023.101698

Bray, F., Laversanne, M., Weiderpass, E., and Soerjomataram, I. (2021). The ever-increasing importance of cancer as a leading cause of premature death worldwide. *Cancer* 127, 3029–3030. doi:10.1002/cncr.33587

Chang, L., Ruiz, P., Ito, T., and Sellers, W. R. (2021). Targeting pan-essential genes in cancer: challenges and opportunities. *Cancer Cell* 39, 466–479. doi:10.1016/j.ccell.2020.12.008

Cheng, F., Li, W., Zhou, Y., Shen, J., Wu, Z., Liu, G., et al. (2012). admetSAR: a comprehensive source and free tool for assessment of chemical ADMET properties. *J. Chem. Inf. Model* 52, 3099–3105. doi:10.1021/ci300367a

Chen, L., Zhu, S., Liu, T., Zhao, X., Xiang, T., Hu, X., et al. (2023). Aberrant epithelial cell interaction promotes esophageal squamous-cell carcinoma development and progression. *Signal Transduct. Target Ther.* 8, 453. doi:10.1038/s41392-023-01710-2

Choi, M. M., Kim, E. A., Hahn, H. G., Nam, K. D., Yang, S. J., Choi, S. Y., et al. (2007). Protective effect of benzothiazole derivative KHG21834 on amyloid β-induced neurotoxicity in PC12 cells and cortical and mesencephalic neurons. *Toxicology* 239, 156–166. doi:10.1016/j.tox.2007.07.010

Cowan, A. J., Green, D. J., Kwok, M., Lee, S., Coffey, D. G., Holmberg, L. A., et al. (2022). Diagnosis and management of multiple myeloma: a review. *Jama* 327, 464–477. doi:10.1001/jama.2022.0003

Craig, M., Jenner, A. L., Namgung, B., Lee, L. P., and Goldman, A. (2021). Engineering in medicine to address the challenge of cancer drug resistance: from micro- and nanotechnologies to computational and mathematical modeling. *Chem. Rev.* 121, 3352–3389. doi:10.1021/acs.chemrev.0c00356

Cui, Y., Wu, X., Jin, J., Man, W., Li, J., Li, X., et al. (2023). CircHERC1 promotes non-small cell lung cancer cell progression by sequestering FOXO1 in the cytoplasm and regulating the miR-142-3p-HMGB1 axis. *Mol. Cancer* 22, 179. doi:10.1186/s12943-023-01888-7

Daina, A., Michielin, O., and Zoete, V. (2017). SwissADME: a free web tool to evaluate pharmacokinetics, drug-likeness and medicinal chemistry friendliness of small molecules. *Sci. Rep.* 7, 42717. doi:10.1038/srep42717

Danalev, D., Iliev, I., Dobrev, S., Angelova, S., Petrin, S., Dzimbova, T., et al. (2023). Synthesis, antiproliferative effect and *in silico* LogP prediction of BIM-23052 analogs containing tyr instead of phe. *Pharmaceutics* 15, 1123. doi:10.3390/pharmaceutics15041123

D'Angelo, N. D., Kim, T. S., Andrews, K., Booker, S. K., Caenepeel, S., Chen, K., et al. (2011). Discovery and optimization of a series of benzothiazole phosphoinositide 3-kinase (PI3K)/mammalian target of rapamycin (mTOR) dual inhibitors. *J. Med. Chem.* 54, 1789–1811. doi:10.1021/jm1014605

Dimri, M., Humphries, A., Laknaur, A., Elattar, S., Lee, T. J., Sharma, A., et al. (2020). NAD(P)H quinone dehydrogenase 1 ablation inhibits activation of the phosphoinositide 3-kinase/akt serine/threonine kinase and mitogen-activated protein kinase/extracellular signal-regulated kinase pathways and blocks metabolic adaptation in hepatocellular carcinoma. *Hepatology* 71, 549–568. doi:10.1002/hep.30818

Dinić, J., Efferth, T., GarcíA-Sosa, A. T., Grahovac, J., PadróN, J. M., Pajeva, I., et al. (2020). Repurposing old drugs to fight multidrug resistant cancers. *Drug Resist Updat* 52, 100713. doi:10.1016/j.drup.2020.100713

El-Helby, A. A., Sakr, H., Eissa, I. H., Al-Karmalawy, A. A., and El-Adl, K. (2019). Benzoxazole/benzothiazole-derived VEGFR-2 inhibitors: design, synthesis, molecular docking, and anticancer evaluations. *Arch. Pharm. Weinh.* 352, e1900178. doi:10.1002/ardp.201900178

Eslin, D., Zage, P. E., Bergendahl, G., Lewis, E., Roberts, W., Kraveka, J., et al. (2023). A phase II trial of nifurtimox combined with topotecan and cyclophosphamide for refractory or relapsed neuroblastoma and medulloblastoma. *Int. J. Cancer* 153, 1026–1034. doi:10.1002/ijc.34569

Ferlay, J., Soerjomataram, I., Dikshit, R., Eser, S., Mathers, C., Rebelo, M., et al. (2015). Cancer incidence and mortality worldwide: sources, methods and major patterns in GLOBOCAN 2012. *Int. J. Cancer* 136, E359–E386. doi:10.1002/ijc.29210

Fitzmaurice, C., Dicker, D., Pain, A., Hamavid, H., Moradi-Lakeh, M., Macintyre, M. F., et al. (2015). The global burden of cancer 2013. *JAMA Oncol.* 1, 505–527. doi:10.1001/jamaoncol.2015.0735

Ghanbar, M. I., and Suresh, K. (2024). Pulmonary toxicity of immune checkpoint immunotherapy. *J. Clin. Invest.* 134, e170503. doi:10.1172/jci170503

Hastir, J. F., Delbauve, S., Larbanoix, L., Germanova, D., Goyvaerts, C., Allard, J., et al. (2020). Hepatocarcinoma induces a tumor necrosis factor-dependent kupffer cell death pathway that favors its proliferation upon partial hepatectomy. *Front. Oncol.* 10, 547013. doi:10.3389/fonc.2020.547013

Jiang, S. X., Qi, B., Yao, W. J., Gu, C. W., Wei, X. F., Zhao, Y., et al. (2017). Berberine displays antitumor activity in esophageal cancer cells *in vitro*. *World J. Gastroenterol.* 23, 2511–2518. doi:10.3748/wjg.v23.i14.2511

Kamal, A., Reddy, K. S., Khan, M. N., Shetti, R. V., Ramaiah, M. J., Pushpavalli, S. N., et al. (2010). Synthesis, DNA-binding ability and anticancer activity of benzothiazole/benzoxazole-pyrrolo[2,1-c] [1,4]benzodiazepine conjugates. *Bioorg Med. Chem.* 18, 4747–4761. doi:10.1016/j.bmc.2010.05.007

Kamal, A., Srikanth, Y. V., Naseer Ahmed Khan, M., Ashraf, M., Kashi Reddy, M., Sultana, F., et al. (2011). 2-Anilinonicotinyl linked 2-aminobenzothiazoles and [1,2,4]triazolo[1,5-b] [1,2,4]benzothiadiazine conjugates as potential mitochondrial apoptotic inducers. *Bioorg Med. Chem.* 19, 7136–7150. doi:10.1016/j.bmc.2011.09.060

Khan, S. U., Fatima, K., Malik, F., Kalkavan, H., and Wani, A. (2023). Cancer metastasis: molecular mechanisms and clinical perspectives. *Pharmacol. Ther.* 250, 108522. doi:10.1016/j.pharmthera.2023.108522

Kumar, G., and Singh, N. P. (2021). Synthesis, anti-inflammatory and analgesic evaluation of thiazole/oxazole substituted benzothiazole derivatives. *Bioorg Chem.* 107, 104608. doi:10.1016/j.bioorg.2020.104608

Kumbhare, R. M., Kosurkar, U. B., Janaki Ramaiah, M., Dadmal, T. L., Pushpavalli, S. N., and Pal-Bhadra, M. (2012). Synthesis and biological evaluation of novel triazoles and isoxazoles linked 2-phenyl benzothiazole as potential anticancer agents. *Bioorg Med. Chem. Lett.* 22, 5424–5427. doi:10.1016/j.bmcl.2012.07.041

Lee, H. J., Pham, P. C., Pei, H., Lim, B., Hyun, S. Y., Baek, B., et al. (2021). Development of the phenylpyrazolo[3,4-d]pyrimidine-based, insulin-like growth factor receptor/Src/AXL-targeting small molecule kinase inhibitor. *Theranostics* 11, 1918–1936. doi:10.7150/thno.48865

Lee, Y. R., Jin, G. H., Lee, S. M., Park, J. W., Ryu, J. H., Jeon, R., et al. (2011). Inhibition of TNF-α-mediated inflammatory responses by a benzodioxolylacetylamino-linked benzothiazole analog in human fibroblast-like synoviocytes. *Biochem. Biophys. Res. Commun.* 408, 625–629. doi:10.1016/j.bbrc.2011.04.073

Li, F., Liu, J., Liu, C., Liu, Z., Peng, X., Huang, Y., et al. (2024a). Cyclic peptides discriminate BCL-2 and its clinical mutants from BCL-XL by engaging a single-residue discrepancy. *Nat. Commun.* 15, 1476. doi:10.1038/s41467-024-45848-1

Li, L., Yu, M., Li, Y., Li, Q., Yang, H., Zheng, M., et al. (2021). Synergistic anti-inflammatory and osteogenic n-HA/resveratrol/chitosan composite microspheres for osteoporotic bone regeneration. *Bioact. Mater* 6, 1255–1266. doi:10.1016/j.bioactmat.2020.10.018

Lipinski, C. A., Lombardo, F., Dominy, B. W., and Feeney, P. J. (2001). Experimental and computational approaches to estimate solubility and permeability in drug discovery and development settings. *Adv. Drug Deliv. Rev.* 46, 3–25. doi:10.1016/s0169-409x(96)00423-1

Li, X., Shen, M., Yang, J., Liu, L., and Yang, Y. W. (2024b). Pillararene-based stimuli-responsive supramolecular delivery systems for cancer therapy. *Adv. Mater*, e2313317. doi:10.1002/adma.202313317

Makowska, A., Wolff, L., Sączewski, F., Bednarski, P. J., and Kornicka, A. (2019). Synthesis and cytotoxic evaluation of benzoxazole/benzothiazole-2-imino-coumarin hybrids and their coumarin analogues as potential anticancer agents. *Pharmazie* 74, 648–657. doi:10.1691/ph.2019.9664

Melo, D. S., Nery Neto, J. A. O., Santos, M. S. D., Pimentel, V. D., Carvalho, R. C. V., Sousa, V. C., et al. (2022). Isopropyl gallate, a gallic acid derivative: *in silico* and *in vitro* investigation of its effects on leishmania major. *Pharmaceutics* 14, 2701. doi:10.3390/pharmaceutics14122701

Meza, K., Biswas, S., Zhu, Y. S., Gajjar, A., Perelstein, E., Kumar, J., et al. (2021). Tumor necrosis factor-alpha is associated with mineral bone disorder and growth impairment in children with chronic kidney disease. *Pediatr. Nephrol.* 36, 1579–1587. doi:10.1007/s00467-020-04846-3

Mokesch, S., Cseh, K., Geisler, H., Hejl, M., Klose, M. H. M., Roller, A., et al. (2020). Investigations on the anticancer potential of benzothiazole-based metallacycles. *Front. Chem.* 8, 209. doi:10.3389/fchem.2020.00209

Mortimer, C. G., Wells, G., Crochard, J. P., Stone, E. L., Bradshaw, T. D., Stevens, M. F., et al. (2006). Antitumor benzothiazoles. 26. 2-(3,4-Dimethoxyphenyl)-5-fluorobenzothiazole (GW 610, NSC 721648), a simple fluorinated 2-arylbenzothiazole, shows potent and selective inhibitory activity against lung, colon, and breast cancer cell lines. *J. Med. Chem.* 49, 179–185. doi:10.1021/jm050942k

Noolvi, M. N., Patel, H. M., and Kaur, M. (2012). Benzothiazoles: search for anticancer agents. *Eur. J. Med. Chem.* 54, 447–462. doi:10.1016/j.ejmech.2012.05.028

Ogbodo, U. C., Enejoh, O. A., Okonkwo, C. H., Gnanasekar, P., Gachanja, P. W., Osata, S., et al. (2023). Computational identification of potential inhibitors targeting cdk1 in colorectal cancer. *Front. Chem.* 11, 1264808. doi:10.3389/fchem.2023.1264808

Oh, E. T., Kim, H. G., Kim, C. H., Lee, J., Kim, C., Lee, J. S., et al. (2023). NQO1 regulates cell cycle progression at the G2/M phase. *Theranostics* 13, 873–895. doi:10.7150/thno.77444

Park, J. W., Chang, H. J., Yeo, H. Y., Han, N., Kim, B. C., Kong, S. Y., et al. (2020). The relationships between systemic cytokine profiles and inflammatory markers in colorectal cancer and the prognostic significance of these parameters. *Br. J. Cancer* 123, 610–618. doi:10.1038/s41416-020-0924-5

Racané, L., Ptiček, L., Fajdetić, G., Tralić-Kulenović, V., Klobučar, M., Kraljević Pavelić, S., et al. (2020). Green synthesis and biological evaluation of 6-substituted-2-(2-hydroxy/methoxy phenyl)benzothiazole derivatives as potential antioxidant, antibacterial and antitumor agents. *Bioorg Chem.* 95, 103537. doi:10.1016/j.bioorg.2019.103537

Rolon, M., Hanna, E., Vega, C., Coronel, C., Dea-Ayuela, M. A., Serrano, D. R., et al. (2022). Solid nanomedicines of nifurtimox and benznidazole for the oral treatment of Chagas disease. *Pharmaceutics* 14, 1822. doi:10.3390/pharmaceutics14091822

Steinbrueck, A., Sedgwick, A. C., Brewster, J. T., Yan, K. C., Shang, Y., Knoll, D. M., et al. (2020). Transition metal chelators, pro-chelators, and ionophores as small molecule cancer chemotherapeutic agents. *Chem. Soc. Rev.* 49, 3726–3747. doi:10.1039/c9cs00373h

Sung, H., Ferlay, J., Siegel, R. L., Laversanne, M., Soerjomataram, I., Jemal, A., et al. (2021). Global cancer statistics 2020: GLOBOCAN estimates of incidence and mortality worldwide for 36 cancers in 185 countries. *CA Cancer J. Clin.* 71, 209–249. doi:10.3322/caac.21660

Tang, L., Hamid, Y., Liu, D., Shohag, M. J. I., Zehra, A., He, Z., et al. (2020). Foliar application of zinc and selenium alleviates cadmium and lead toxicity of water spinach - bioavailability/cytotoxicity study with human cell lines. *Environ. Int.* 145, 106122. doi:10.1016/j.envint.2020.106122

Wang, X., Wu, K., Fang, L., Yang, X., Zheng, N., Du, Z., et al. (2021). Discovery of N-substituted sulfamoylbenzamide derivatives as novel inhibitors of STAT3 signaling pathway based on Niclosamide. *Eur. J. Med. Chem.* 218, 113362. doi:10.1016/j.ejmech.2021.113362

Wu, Q., Qian, W., Sun, X., and Jiang, S. (2022). Small-molecule inhibitors, immune checkpoint inhibitors, and more: FDA-approved novel therapeutic drugs for solid tumors from 1991 to 2021. *J. Hematol. Oncol.* 15, 143. doi:10.1186/s13045-022-01362-9

Wu, Q., Tan, L., Ren, X., Fu, C., Chen, Z., Ren, J., et al. (2023). Metal-organic framework-based nano-activators facilitating microwave combined therapy via a divide-and-conquer tactic for triple-negative breast cancer. *ACS Nano* 17, 25575–25590. doi:10.1021/acsnano.3c09734

Xin, Y., Chen, S., Tang, K., Wu, Y., and Guo, Y. (2022). Identification of nifurtimox and chrysin as anti-influenza virus agents by clinical transcriptome signature reversion. *Int. J. Mol. Sci.* 23, 2372. doi:10.3390/ijms23042372

Xu, P., Yang, J., Chen, Z., Zhang, X., Xia, Y., Wang, S., et al. (2023). N6-methyladenosine modification of CENPF mRNA facilitates gastric cancer metastasis via regulating FAK nuclear export. *Cancer Commun. (Lond)* 43, 685–705. doi:10.1002/cac2.12443

frontiers | Frontiers in Chemistry

TYPE Original Research
PUBLISHED 25 July 2024
DOI 10.3389/fchem.2024.1447831

OPEN ACCESS

EDITED BY
Manuel Aureliano,
University of Algarve, Portugal

REVIEWED BY
Cristina Maccallini,
University of Studies G. d'Annunzio Chieti and Pescara, Italy
Custódia Fonseca,
University of Algarve, Portugal

*CORRESPONDENCE
Chao Wang,
wangchao20086925@126.com
Dongming Xing,
xdm_tsinghua@163.com

RECEIVED 12 June 2024
ACCEPTED 10 July 2024
PUBLISHED 25 July 2024

CITATION
Xiu Y, Zhang Y, Yang S, Shi L, Xing D and Wang C (2024), Design, synthesis, and bioevaluation of diarylpyrimidine derivatives as novel microtubule destabilizers.
Front. Chem. 12:1447831.
doi: 10.3389/fchem.2024.1447831

Design, synthesis, and bioevaluation of diarylpyrimidine derivatives as novel microtubule destabilizers

Yutao Xiu[1,2], Yujing Zhang[3], Shanbo Yang[1,2], Lingyu Shi[1,2], Dongming Xing[1,2,4]* and Chao Wang[1,2]*

[1]Cancer Institute, The Affiliated Hospital of Qingdao University, Qingdao University, Qingdao, Shandong, China, [2]Qingdao Cancer Institute, Qingdao University, Qingdao, Shandong, China, [3]The Affiliated Cardiovascular Hospital of Qingdao University, Qingdao University, Qingdao, Shandong, China, [4]School of Life Sciences, Tsinghua University, Beijing, China

In this work, a series of new diarylpyrimidine derivatives as microtubule destabilizers were designed, synthesized, and evaluated for anticancer activities. Based on restriction configuration strategy, we introduced the pyrimidine moiety containing the hydrogen-bond acceptors as *cis*-olefin bond of CA-4 analogs to improve structural stability. Compounds **11a-t** exerted antiproliferative activities against three human cancer cell lines (SGC-7901, HeLa, and MCF-7), due to tubulin polymerization inhibition, showing high selectivity toward cancer cells in comparison with non-tumoral HSF cells, as evidenced by MTT assays. In mechanistic investigations, compound **11s** remarkably inhibited tubulin polymerization and disorganized microtubule in SGC-7901 cells by binding to tubulin. Moreover, **11s** caused G2/M phase cell cycle arrest in SGC-7901 cells in a concentration-dependent manner. Furthermore, molecular modeling analysis revealed that **11s** interacts with tubulin through binding to the colchicine site. In addition, the prediction of physicochemical properties disclosed that **11s** conformed well to the Lipinski's rule of five. This work offered a fresh viewpoint for the discovery of new tubulin-targeting anticancer drugs.

KEYWORDS

microtubule destabilizer, combretastatin A-4, antiproliferative activity, pyrimidine, molecular docking

1 Introduction

Microtubules have been identified as an essential target for anticancer drug development. They play an important role in a variety of fundamental cell functions, including shape maintenance, intracellular transport, and cell division (Dumontet and Jordan, 2010; Steinmetz and Prota, 2018; Čermák et al., 2020). Microtubule targeting agents have been classified as microtubule stabilizers (taxanes and epothilones) and microtubule destabilizers (alkaloids and colchicine) according to the mechanism of interference with microtubule dynamics (Chen et al., 2010; Cao et al., 2018; Wang et al., 2021). The microtubule destabilizers have attracted considerable interest from medicinal chemists due to the largely successful clinical use of vinca alkaloids (Lu et al., 2012; Wang et al., 2018). In the past decades, many excellent microtubule destabilizers have been reported, such as combretastatin A-4 (CA-4, **1**, Figure 1), CA-4P (**2**, Figure 1), BNC-105P (**3**, Figure 1), SMART (**4**, Figure 1), VERU-111 (**5**, Figure 1), and

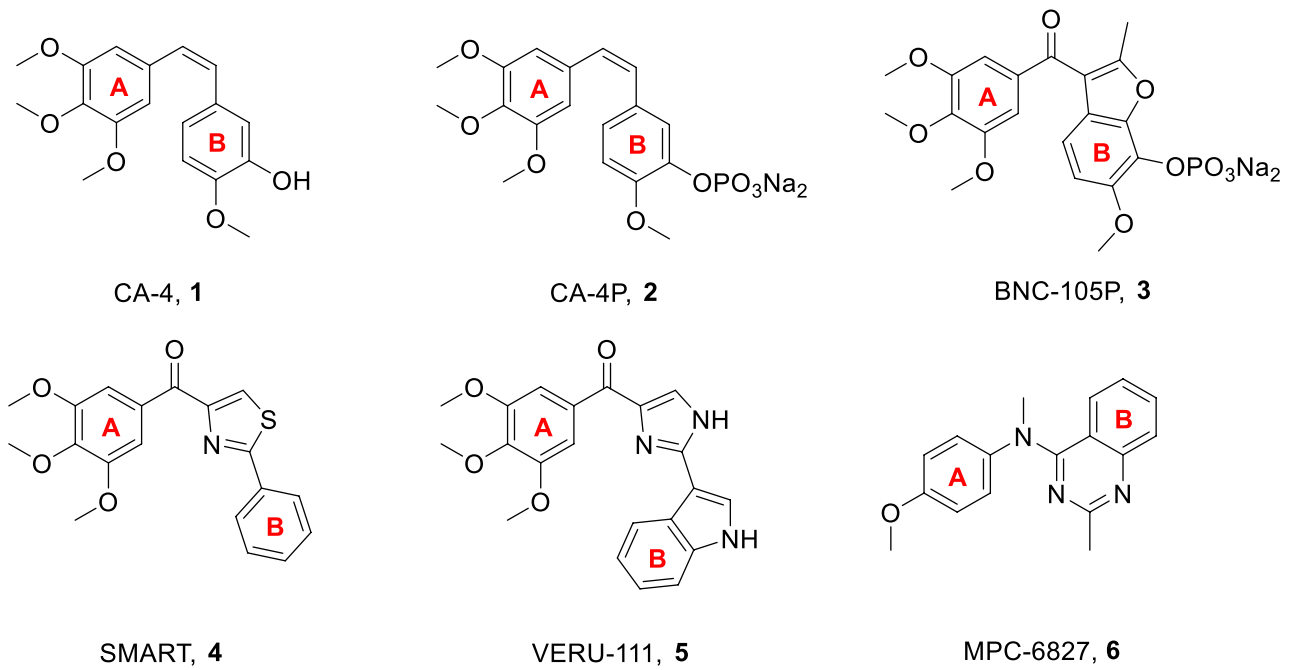

FIGURE 1
Chemical structures of some microtubule destabilizers.

MPC-6827 (**6**, Figure 1) (Pettit et al., 1989; Kasibhatla et al., 2007; Grossmann et al., 2012; Pal et al., 2015; Pérez-Pérez et al., 2016; Wu et al., 2018; Mahmud et al., 2020).

CA-4, a natural product that inhibits tubulin polymerization by interacting with the colchicine binding site on tubulin, was first isolated in 1989 from the bark of the South African willow tree, *Combretum caffrum* (Pettit et al., 1989). This *cis*-stilbene has been shown to exhibit excellent cytotoxicity against a variety of human cancer cell lines, including multi-drug resistant cancer cell lines (Mustafa et al., 2019; Paidakula et al., 2022). CA-4P (2, Figure 1), which is the soluble prodrug of CA-4, is now undergoing clinical trials as a combination therapy for several multi-drug resistant solid cancers (Pérez-Pérez et al., 2016). Owing to the structural simplicity of CA-4, many academic and industrial groups have carried out numerous structure-activity relationship (SAR) studies on this compound and its analogs. SAR studies have indicated that the presence of a *cis*-olefin bond and 3,4,5-trimethoxyphenyl as A-ring are crucial for producing potent potency (Hamze et al., 2020). CA-4 and other olefinic analogs tend to isomerize into inactive *trans*-forms during administration and storage. Thus, stabilizing the *cis*-olefin in the CA-4 structure is a key trend (Jian et al., 2020). In recent years, to improve structural stability, leading researchers have sought to replace the *cis*-olefin in the CA-4 structure with a heterocyclic ring to be used as a lead compound, while simultaneously creating a *cis* conformation for both the A-and B-ring. To date, different cyclic structures, such as three-, four-, five-, and six-membered heterocyclic rings, have been utilized to replace the *cis*-olefin structure of CA-4, producing favorable outcomes.

Pyrimidine is an aromatic heterocycle with six members that comprises of two nitrogen atoms. Pyrimidine derivatives show great advantages due to the presence of nitrogen atoms, such as the ability to increase the basicity of the molecule, due to their basic properties and the possibility of the nitrogen atom to form strong hydrogen bonds with the target. In addition, pyrimidine derivatives are a topic of continuing research due to their ease of preparation and a wide range of potential pharmacological properties, which include bactericidal effect (Tan et al., 2022), anti-inflammatory activities (Shukla et al., 2016), and antitumor activities (Sana et al., 2021; Kang et al., 2023). Several pyrimidine-based microtubule destabilizers, including arylpyrimidine derivative (**7**, Figure 2), diarylpyrimidine derivative (**8**, Figure 2), arylpyrimidine-indole derivative (**9**, Figure 2), and indole-pyrimidine hybrid (**10**, Figure 2), had been produced and tested (Xie et al., 2009; Xie et al., 2011; Zhang et al., 2014; Hu et al., 2015).

The primary aim of this work was to design, synthesize, and biologically evaluate new diarylpyrimidine derivatives (**11**, Figure 3) with high binding affinity to tubulin, which can trigger antimitotic effect on cancer cells. To this end, we successfully replaced the *cis*-olefin linker of CA-4 with a pyrimidine moiety. We further explored the incorporation of the following different aromatic B-ring: aryl, thienyl, pyridine, indole, and naphthalene. Some of the newly synthesized compounds are with more structural stability than the reference CA-4. Their antiproliferative activities were studied in three human tumor cell lines. Normal skin fibroblast (HSF) cells were used to study toxicity in healthy tissues. Moreover, a specific compound, **11s**, was evaluated for tubulin polymerization, immunofluorescence staining, cell cycle analysis, induction of cell apoptosis, and molecular docking analysis.

2 Result and discussion

2.1 Chemistry

The target compounds diarylpyrimidine derivatives **11a-t** were synthesized according to the procedure described in Scheme 1.

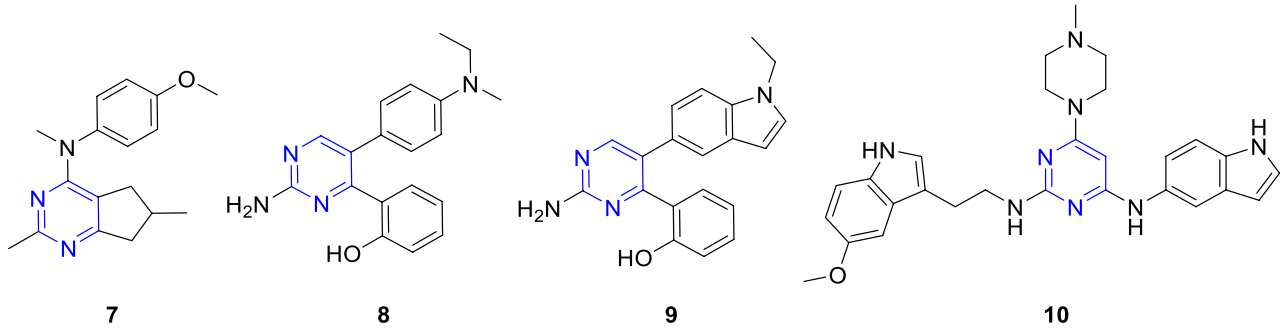

FIGURE 2
Chemical structures of some pyrimidine-based microtubule destabilizers.

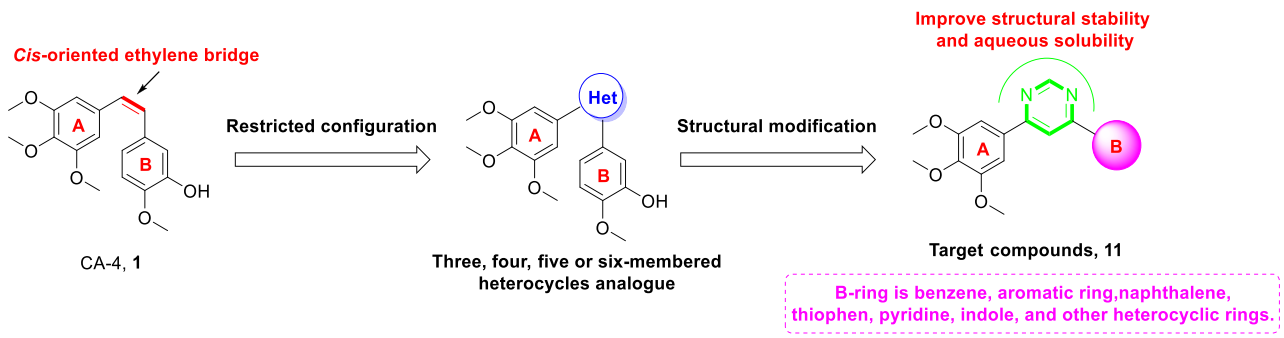

FIGURE 3
The rational design of target compounds.

Previous literature outlines that the 4,6-dichloropyrimidine (**13**) was synthesized using 4,6-dihydroxypyrimidine (**12**) as the starting material (Yang et al., 2022; Wang et al., 2023). The synthesis of 4-chloro-6-(3,4,5-trimethoxyphenyl) pyrimidine (**14**) was achieved through the Suzuki cross-coupling reaction between **13** and 3,4,5-trimethoxyphenylboric acid, in the presence of potassium carbonate and tetrakis (triphenylphosphine) palladium (Shi et al., 2022). Target compounds **11a-t** were obtained by Suzuki cross-coupling reaction between **14** and the corresponding arylboronic acids (Dufresne et al., 2007).

2.2 Biological evaluation

2.2.1 *In vitro* antiproliferative activity

The MTT assay with CA-4 as a positive control was used to evaluate the antiproliferative activities of the newly synthesized compounds **11a-t** against three representative cancer cell lines (SGC-7901, HeLa, and MCF-7). Some target compounds with IC_{50} values in the micromolar range showed moderate potency against three cancer cell lines. Out of the tested compounds, **11s**, which contained an indole moiety as the B-ring, displayed the most potent antiproliferative activities against SGC-7901, HeLa, and MCF-7 cell lines with IC_{50} values of 12.0, 15.3, and 16.7 μM, respectively.

The SAR of the 20 target compounds have been summarized (Table 1). With phenyl or aryl moieties as the B-ring, **11a-11o** showed moderate to weak activities, and the introduction of electron-donating groups (EDGs), such as -CH_3 (**11d**), -3-CH_3-4-CH_3 (**11e**) -OCH_3 (**11g** and **11h**), -OCH_2CH_3 (**11i**), -3-OH-4-OCH_3 (**11j**), on the para-substitution of B-ring, led to maintaining or increasing in antiproliferative activities. However, when electron-withdrawing groups (EWGs), such as -F (**11n**), -Cl (**11o**), and -NO_2 (**11l**), were introduced on the para-substitution of B-ring, the antiproliferative activities were decreased, and the results indicated that EDGs located on the para-substitution of B-ring had better activities. We next introduced different rigid aromatic groups such as thienyl (**11p**), pyridyl (**11q** and **11r**), indolyl (**11s**), naphthyl (**11t**) into the B-ring to explore the effect of different skeletons on antiproliferative activities against three different cell lines. Amongst these, **11s** showed the best antiproliferative activity against SGC-7901 cells (IC_{50} value of 12.0 μM), suggesting that the volume and electronegativity of B-ring may be the important factors affecting activity.

Next, cytotoxicity test was performed with HSF to assess the cytotoxicity of **11s**, and CA-4 was used as the positive control. As can be seen in Table 2, the cytotoxicity of **11s** (IC_{50} value >100 μM) on HSF was significantly weaker than that of CA-4 (IC_{50} value 0.77 μM). The result showed that the cytotoxicity of **11s** was lower than that of CA-4.

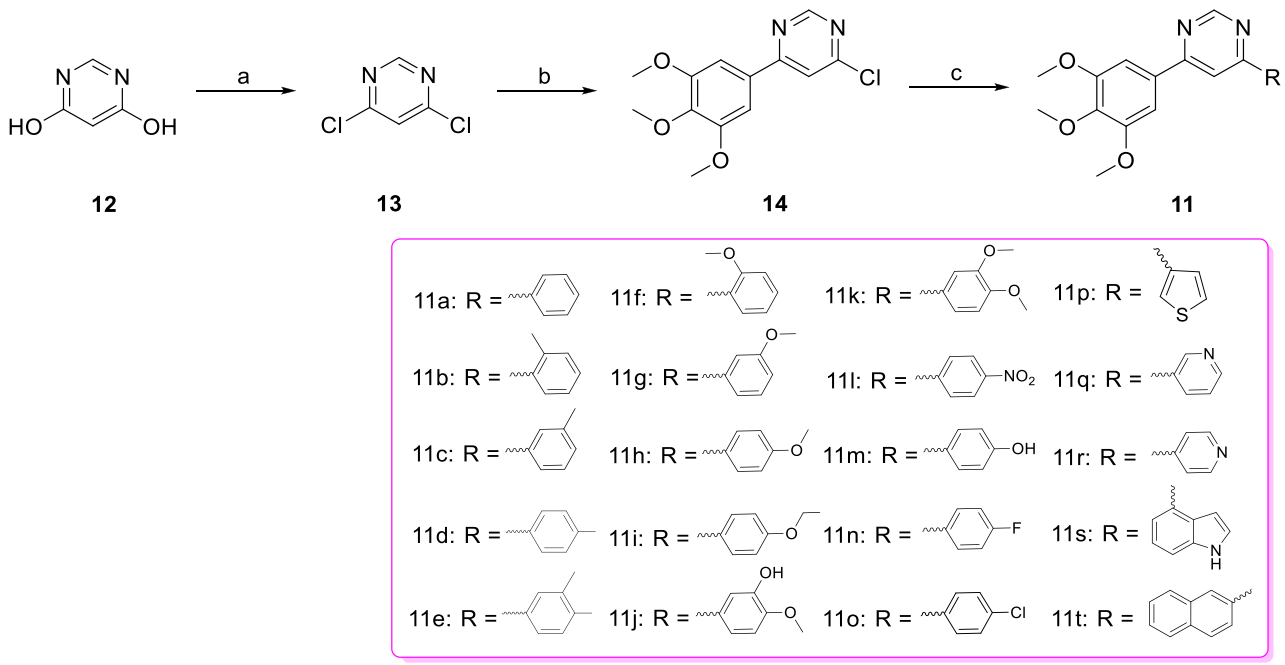

SCHEME 1
Reagents and conditions (a) $POCl_3$, NEt_3, reflux; (b) 3,4,5-trimethoxyphenylboric acid, $Pd(PPh_3)_4$, K_2CO_3, 1,4-dioxane/H_2O, N_2 atmosphere,110°C, M.W.; (c) Substituted phenylboronic acid, $Pd(PPh_3)_4$, K_2CO_3, 1,4-dioxane/H_2O, N_2 atmosphere,126°C, M.W.

2.2.2 Effect on tubulin polymerization

For clarification of whether these 3-aryl-4-(3,4,5-trimethoxyphenyl) pyridines target the tubulin-microtubule system, we assessed the inhibition of tubulin polymerization using the most active compound, **11s**, alongside the negative control paclitaxel and the positive control CA-4. Figure 4 indicates that both **11s** and CA-4 were effective inhibitors of tubulin polymerization in comparison to the negative control, paclitaxel. Furthermore, **11s** was found to inhibit tubulin polymerization in a concentration-dependent manner. These results illustrated that **11s** inhibited tubulin polymerization in a manner similar to CA-4.

2.2.3 Analysis of immunofluorescence staining

Using CA-4 (0.10 μM) as a reference, we tested whether compound **11s** could destabilize microtubule dynamics in SGC-7901 cells using an immunofluorescence assay to verify the direct effects of **11s** on tubulin. Indirect immunofluorescence was also used to observe cellular microtubule structures. As shown in Figure 5, the cells treated with **11s** (12.0 μM) showed changes in the shape of the nucleus (blue) and the microtubule network (green) was constricted and disorganized in comparison with the control group. The results suggested that **11s** disrupted the cytoskeleton and inhibited microtubule assembly in a similar way to CA-4.

2.2.4 Cell cycle analysis

The effects of the most promising compound **11s** on the cell cycle were investigated to further explore the biological target. SGC-7901 cells were treated with 12.0 μM, 24.0 μM, and 36.0 μM of **11s**, and the percentage of SGC-7901 cells in different cell cycle phases after treatment was analyzed by flow cytometry. As revealed in Figure 6, the percentage of SGC-7901 cells arrested in G2/M phase increased from 15.75% to 23.23% after treatment with the three concentrations of **11s** compared to the control (9.68%). Thus, **11s** could induce G2/M phase arrest in SGC-7901 cells in a concentration-dependent manner. The cell cycle distribution demonstrated that **11s** was able to induce a G2/M phase arrest and subsequent apoptosis in SGC-7901 cells.

2.2.5 Induction of cell apoptosis

Annexin VFITC/PI assay was performed to investigate whether compound **11s** induced apoptosis. The total percentage of early (Annexin-V+/PI-) and late (Annexin-V+/PI-) apoptotic cells was only 1.50% in the control group after 48 h of treatment, as shown in Figure 7. However, after 48 h of treatment with 12.0 μM of **11s**, 3.61% of the total number of apoptotic cells was obtained. In addition, the percentage of apoptotic cells increased to 7.09% and 7.93% when SGC-7901 cells were incubated with higher concentrations of **11s** at 24.0 μM and 36.0 μM. These results revealed that **11s** was an effective, concentration-dependent inducer of apoptosis in SGC-7901 cells.

2.2.6 Molecular docking analysis

Molecular docking studies of CA-4 and the most potent compound, **11s**, with the tubulin crystal structure (PDB: 5LYJ) were also performed to further investigate the binding interactions. Both compounds were docked to tubulin in order to compare the binding properties of **11s** with those of CA-4. The binding orientations of **11s** (magenta) and CA-4 (cyan) overlapped well in the binding models shown in Figure 8A. As depicted in Figures 8A–C hydrogen bond is

TABLE 1 Antiproliferative activities of all compounds.

Compounds	(IC_{50}, μM)[a]		
	SGC-7901	HeLa	MCF-7
11a	70.2	81.1	>100
11b	96.6	>100	>100
11c	>100	79.3	>100
11d	39.9	42.3	48.4
11e	61.2	66.8	73.5
11f	>100	>100	>100
11g	46.5	62.3	76.0
11h	24.8	31.3	35.7
11i	44.3	50.3	64.6
11j	19.4	21.5	27.9
11k	>100	76.9	>100
11l	>100	>100	>100
11m	84.9	>100	87.3
11n	>100	>100	>100
11o	>100	>100	>100
11p	40.2	31.9	60.5
11q	>100	>100	>100
11r	>100	>100	>100
11s	**12.0**	**15.3**	**16.7**
11t	>100	>100	>100
CA-4[b]	0.098	0.87	0.12

[a]IC_{50}: the half maximal inhibitory concentration.
[b]Used as positive controls.

TABLE 2 Cytotoxicity test of 11s and CA-4 against HSF.

Compounds	(IC_{50}, μM)[a]
11s	>100
CA-4	0.77

[a]IC_{50}: the half maximal inhibitory concentration.
[b]Used as positive controls.

present between Cysβ241 and the oxygen of the methoxy group (A-ring) of **11s** and CA-4. Another hydrogen bond is also observed between Valβ315 with the nitrogen of the indole group (**11s**, B-ring). In addition, the nitrogen of the pyrimidine group (**11s**) forms an extra hydrogen bond with the residue Thrα179. The docking score of CA-4 (Docking score: −9.2 kcal/mol) in the 5LYJ was lower than that of **11s** (Docking score: −8.8 kcal/mol), which might be the reason why CA-4 has stronger antiproliferative activities than **11s**. These molecular docking results were in support of the biological assay data above and suggested that **11s** may be a potential microtubule destabilizer.

2.2.7 Physicochemical properties

To examine the drug-like properties of diarylpyrimidine derivatives, conventional physicochemical properties of CA-4, **11j**, and **11s** were predicted using a free online website (http://www.swissadme.ch/index.php) or ChemBioDraw Ultra 14.0 software for their fit with Lipinski's five rule. As summarized in Table 3, CA-4, **11j**, and **11s** fit well with the Lipinski's five rule.

3 Conclusion

Overall, based on the analysis of the X-ray crystal structure of tubulin in complex with DMAM-CA-4, we reported the design and discovery of a new set of diarylpyrimidine derivatives on the cis-orientation of the olefin bond of CA-4 as the novel microtubule destabilizers with improved structural stability.

The MTT assay results proved that target compounds 11a-t exhibited moderate antiproliferative potencies against three human tumor cells (SGC-7901, HeLa, and MCF-7) *in vitro*. Studies on the mechanism of action of the most promising compound showed that **11s** inhibits tubulin polymerization, disrupts the microtubule network of the SGC-7901 cells and arrests the cell cycle in G2/M phase, subsequently inducing apoptosis. **11s** was highly selective for cancer cells compared to non-tumour HSF cells. Molecular docking analysis revealed that the most biologically active compound **11s** binds very favourably to the colchicine site and provided a structural explanation for the SAR. Lastly, the prediction of physicochemical properties indicated that **11s** fits well with five Lipinski's rule. This work provides a new perspective for the discovery of new microtubule destabilizers.

4 Experimental

4.1 Chemistry

4.1.1 Materials and methods

All solvents and reagents were purchased from reputable chemical companies, ensuring the highest quality for our experiments. The ^{1}H NMR and ^{13}C NMR spectra were conducted in $CDCl_3$ using TMS as an internal reference on a Bruker AVANCE spectrometer, operating at frequencies of 500 MHz for proton nuclei and 126 MHz for carbon nuclei. This advanced instrumentation allowed us to obtain precise structural information about the compounds under investigation. For accurate determination of molecular weights and elemental compositions, high resolution mass spectra (HRMS) were recorded using an Agilent Accurate-Mass Q-TOF 6530 instrument in electrospray ionization (ESI) mode. This technology provided us with highly accurate mass measurements, enabling confident identification of the analyzed compounds. To efficiently carry out our reactions, microwave synthesis was employed utilizing a single mode cavity microwave synthesizer manufactured by CEM Corporation based in North Carolina, United States. This innovative equipment allowed us to rapidly heat reaction mixtures under controlled conditions, resulting in improved yields and reduced reaction times compared to conventional heating methods. In order to monitor the progress of our reactions visually, thin-layer chromatography (TLC) analysis was performed under both UV light wavelengths: 365 nm and 254 nm. By comparing the migration

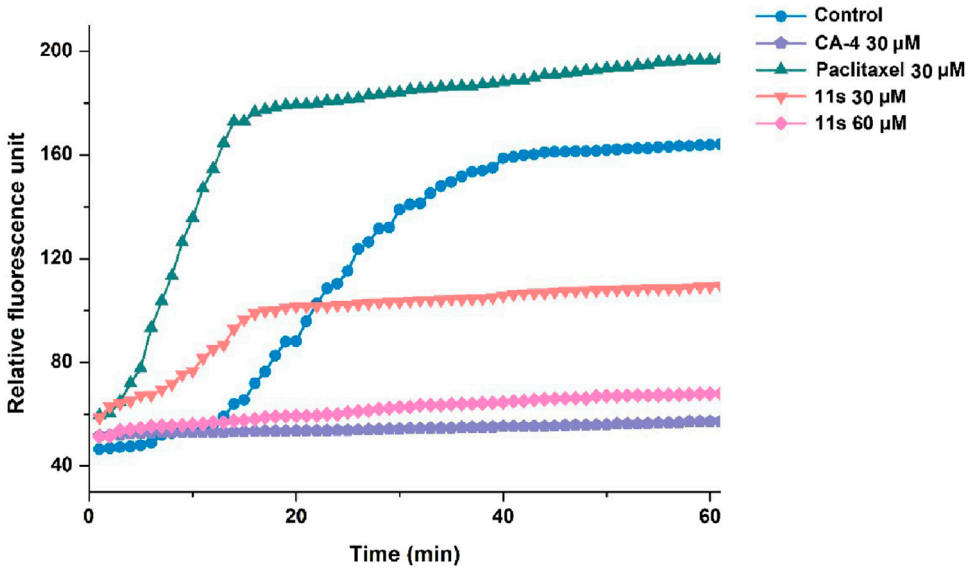

FIGURE 4
Effects of compound **11s** on tubulin polymerization.

distances of reactants and products on TLC plates coated with appropriate stationary phases, we could assess the extent of conversion during each step of our synthetic procedures.

4.1.2 General synthetic procedure for 4,6-dichloropyrimidine (13)

Triethylamine (4 mmol) and phosphorus oxychloride (15.8 mmol) were mixed dropwise in a 50 mL round-bottomed flask. Then 4,6-dihydroxypyrimidine (2.3 mmol) was added dropwise. The reaction was refluxed for 1 h and then poured onto crushed ice. The precipitate was filtered and then purified by flash chromatography eluted with hexanes/ethyl acetate (1:1) to give the title compound as a light yellow solid.

4.1.3 General synthetic procedure for 4-chloro-6-(3,4,5-trimethoxyphenyl)pyrimidine (14)

To the mixture of THF and water, 3,4,5-trimethoxyphenyl boric acid (1 mmol) was added under argon protection. 4,6-dichloropyrimidine (1 mmol), $Pd(PPh_3)_4$ (0.05 mmol), and K_2CO_3 (2 mmol) were added and reacted for 20 min at 110°C in a microwave reactor. As soon as the TLC monitoring reaction was finished, the system cooled, the solvent was removed, and water was added. The ethyl acetate extraction was then combined with the organic phase, washed the organic phase with saturated brine, then dried anhydrous Na_2SO_4, filtered, vacuum evaporated, column chromatography, and obtained the target compound.

4.1.4 General synthetic procedure for diarylpyrimidine derivatives (**11a-t**)

A mixture of $Pd(PPh_3)_4$ (0.010 mmol), 4-chloro-6-(3,4,5-trimethoxyphenyl) pyrimidine (**14**, 0.15 mmol), K_2CO_3 (0.60 mmol), and the corresponding substituted phenylboronic acid (0.16 mmol) in a solution of 1,4-dioxane/H_2O (8 mL, 3:1) was subjected to degassing and purging with N_2 for three cycles. Subsequently, the reaction mixture was stirred under an N_2 atmosphere at 126°C for 25 min in a microwave reactor until completion as indicated by TLC analysis. Upon completion, H_2O (50 mL) was added to the reaction mixture followed by extraction with ethyl acetate. The combined organic layers were then washed with brine solution and dried over anhydrous Na_2SO_4 before filtration and concentration under vacuum to yield a residue that underwent purification via column chromatography using a *n*-hexane/ethyl acetate eluent mixture in a ratio of 4:1 to afford the desired diarylpyrimidine derivatives (**11a-t**).

4.1.4.1 4-Phenyl-6-(3,4,5-trimethoxyphenyl) pyrimidine (**11a**)

White solid; yield: 65%; Mp: 88°C–89°C; ^{1}H NMR (500 MHz, $CDCl_3$) δ 9.29 (d, *J* = 1.3 Hz, 1H), 8.14 (dd, *J* = 6.5, 3.3 Hz, 2H), 8.02 (d, *J* = 1.3 Hz, 1H), 7.55 (dd, *J* = 5.1, 1.9 Hz, 3H), 7.40 (s, 2H), 4.00 (s, 6H), 3.94 (s, 3H); ^{13}C NMR (126 MHz, $CDCl_3$) δ 164.73, 164.24, 159.04, 153.70 (2C), 140.78, 137.05, 132.39, 130.94, 129.02 (2C), 127.19 (2C), 112.52, 104.51 (2C), 61.00, 56.39 (2C); HRMS calcd for $C_{19}H_{19}N_2O_3$ $[M + H]^+$ 323.1396, found 323.1390.

4.1.4.2 4-(o-tolyl)-6-(3,4,5-trimethoxyphenyl) pyrimidine (**11b**)

White solid; yield: 82%; Mp: 93°C–95°C; ^{1}H NMR (500 MHz, $CDCl_3$) δ 9.30 (d, *J* = 1.3 Hz, 1H), 7.75 (d, *J* = 1.3 Hz, 1H), 7.51 - 7.47 (m, 1H), 7.44 - 7.36 (m, 3H), 7.34 (dd, *J* = 9.0, 4.7 Hz, 2H), 3.97 (s, 6H), 3.93 (s, 3H), 2.46 (s, 3H); ^{13}C NMR (126 MHz, $CDCl_3$) δ 167.95, 163.57, 158.52, 153.70 (2C), 140.78, 138.21, 136.07, 132.12, 131.15, 129.52, 129.38, 126.17, 116.53, 104.41 (2C), 60.99, 56.33 (2C), 20.29; HRMS calcd for $C_{20}H_{21}N_2O_3$ $[M + H]^+$ 337.1552, found 337.1541.

4.1.4.3 4-(m-tolyl)-6-(3,4,5-trimethoxyphenyl) pyrimidine (**11c**)

White solid; yield: 56%; Mp: 80°C–82°C; ^{1}H NMR (500 MHz, $CDCl_3$) δ 9.28 (d, *J* = 0.8 Hz, 1H), 8.00 (d, *J* = 1.0 Hz, 1H), 7.97 (s, 1H), 7.91 (d, *J* = 7.7 Hz, 1H), 7.43 (t, *J* = 7.6 Hz, 1H), 7.40 (s, 2H), 7.35 (d, *J* = 7.5 Hz, 1H), 4.00 (s, 6H), 3.94 (s, 3H), 2.48 (s, 3H); ^{13}C NMR (126 MHz, $CDCl_3$) δ 164.90, 164.19, 158.98, 153.69 (2C),

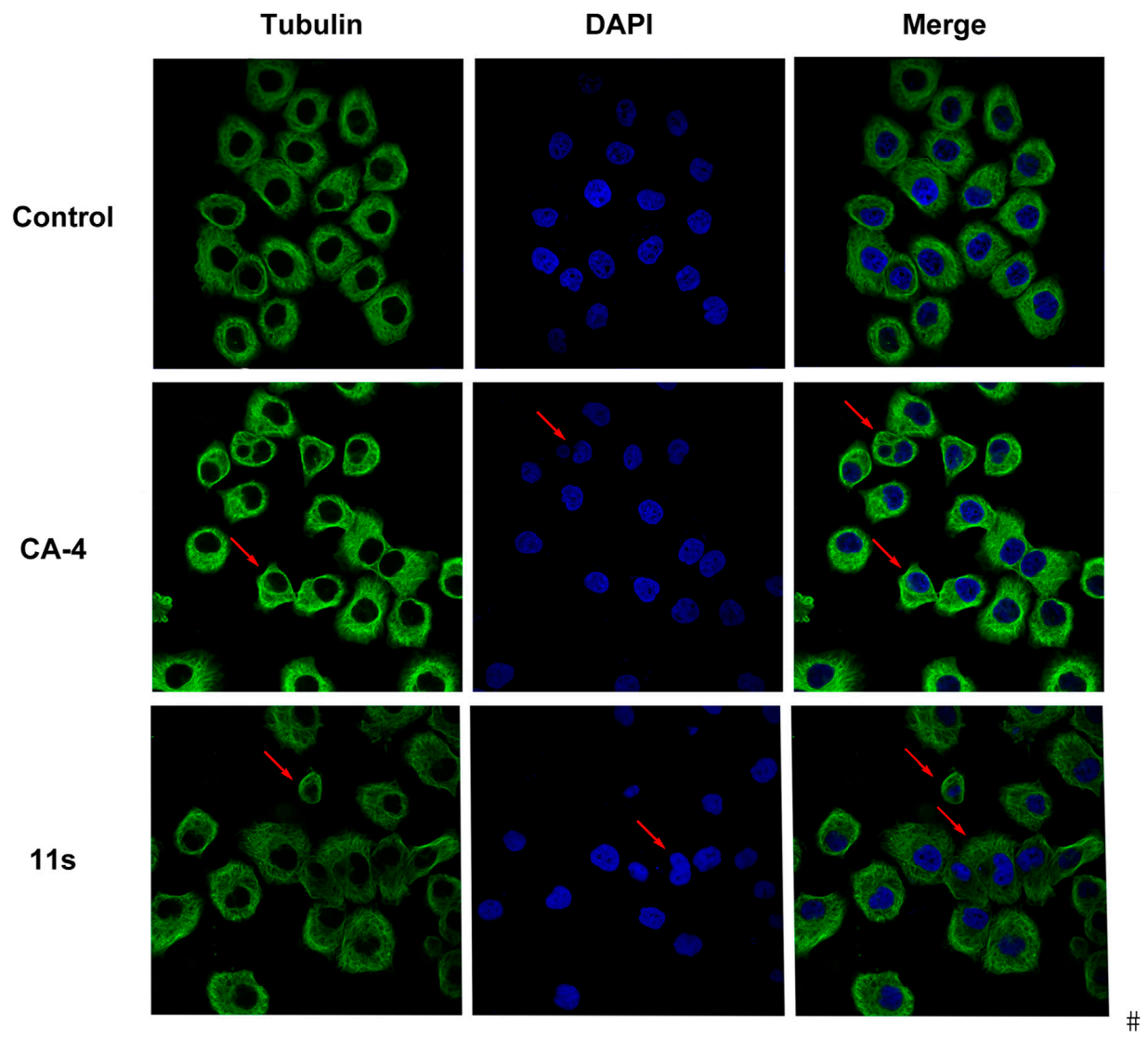

FIGURE 5
Effects of compound **11s** and CA-4, on the cellular microtubule network and microtubule reassemble by immunofluorescence.

140.77, 138.84, 137.01, 132.43, 131.72, 128.90, 127.82, 124.30, 112.59, 104.55 (2C), 60.99, 56.41 (2C), 21.50; HRMS calcd for $C_{20}H_{21}N_2O_3$ $[M + H]^+$ 337.1552, found 337.1540.

4.1.4.4 4-(p-tolyl)-6-(3,4,5-trimethoxyphenyl) pyrimidine (**11d**)

White solid; yield: 91%; Mp: 133°C–134°C; ^{1}H NMR (500 MHz, $CDCl_3$) δ 9.26 (d, *J* = 1.3 Hz, 1H), 8.05 (d, *J* = 8.2 Hz, 2H), 7.99 (d, *J* = 1.3 Hz, 1H), 7.39 (s, 2H), 7.35 (d, *J* = 7.9 Hz, 2H), 4.00 (s, 6H), 3.94 (s, 3H), 2.45 (s, 3H); ^{13}C NMR (126 MHz, $CDCl_3$) δ 164.64, 164.10, 158.99, 153.67 (2C), 141.39, 140.71, 134.20, 132.52, 129.75 (2C), 127.08 (2C), 112.14, 104.50 (2C), 60.99, 56.39 (2C), 21.46; HRMS calcd for $C_{20}H_{21}N_2O_3$ $[M + H]^+$ 337.1552, found 337.1576.

4.1.4.5 4-(3,4-dimethylphenyl)-6-(3,4,5-trimethoxyphenyl) pyrimidine (**11e**)

White solid; yield: 58%; Mp: 93°C–95°C; ^{1}H NMR (500 MHz, $CDCl_3$) δ 9.26 (d, *J* = 1.2 Hz, 1H), 7.98 (d, *J* = 1.2 Hz, 1H), 7.94 (s, 1H), 7.85 (dd, *J* = 7.8, 1.6 Hz, 1H), 7.39 (s, 2H), 7.30 (d, *J* = 7.9 Hz, 1H), 4.00 (s, 6H), 3.94 (s, 3H), 2.39 (s, 3H), 2.35 (s, 3H); ^{13}C NMR (126 MHz, $CDCl_3$) δ 164.80, 164.06, 158.94, 153.67 (2C), 140.70, 140.11, 137.42, 134.55, 132.57, 130.28, 128.24, 124.58, 112.21, 104.54 (2C), 60.99, 56.41 (2C), 19.90, 19.82; HRMS calcd for $C_{21}H_{23}N_2O_3$ $[M + H]^+$ 351.1709, found 351.1708.

4.1.4.6 4-(2-methoxyphenyl)-6-(3,4,5-trimethoxyphenyl) pyrimidine (**11f**)

White solid; yield: 70%; Mp: 104°C–106°C; ^{1}H NMR (500 MHz, $CDCl_3$) δ 9.29 (d, *J* = 1.3 Hz, 1H), 8.26 (d, *J* = 1.3 Hz, 1H), 7.99 (dd, *J* = 7.7, 1.8 Hz, 1H), 7.47 (ddd, *J* = 8.3, 7.4, 1.8 Hz, 1H), 7.37 (s, 2H), 7.13 (td, *J* = 7.6, 1.0 Hz, 1H), 7.06 (d, *J* = 8.9 Hz, 1H), 3.98 (s, 6H), 3.93 (s, 3H), 3.92 (s, 3H); ^{13}C NMR (126 MHz, $CDCl_3$) δ 163.48, 163.15, 158.70, 157.72, 153.62 (2C), 140.52, 132.78, 131.69, 131.00, 126.49, 121.26, 117.45, 111.61, 104.55 (2C), 60.98, 56.30 (2C), 55.73; HRMS calcd for $C_{20}H_{21}N_2O_4$ $[M + H]^+$ 353.1501, found 353.1499.

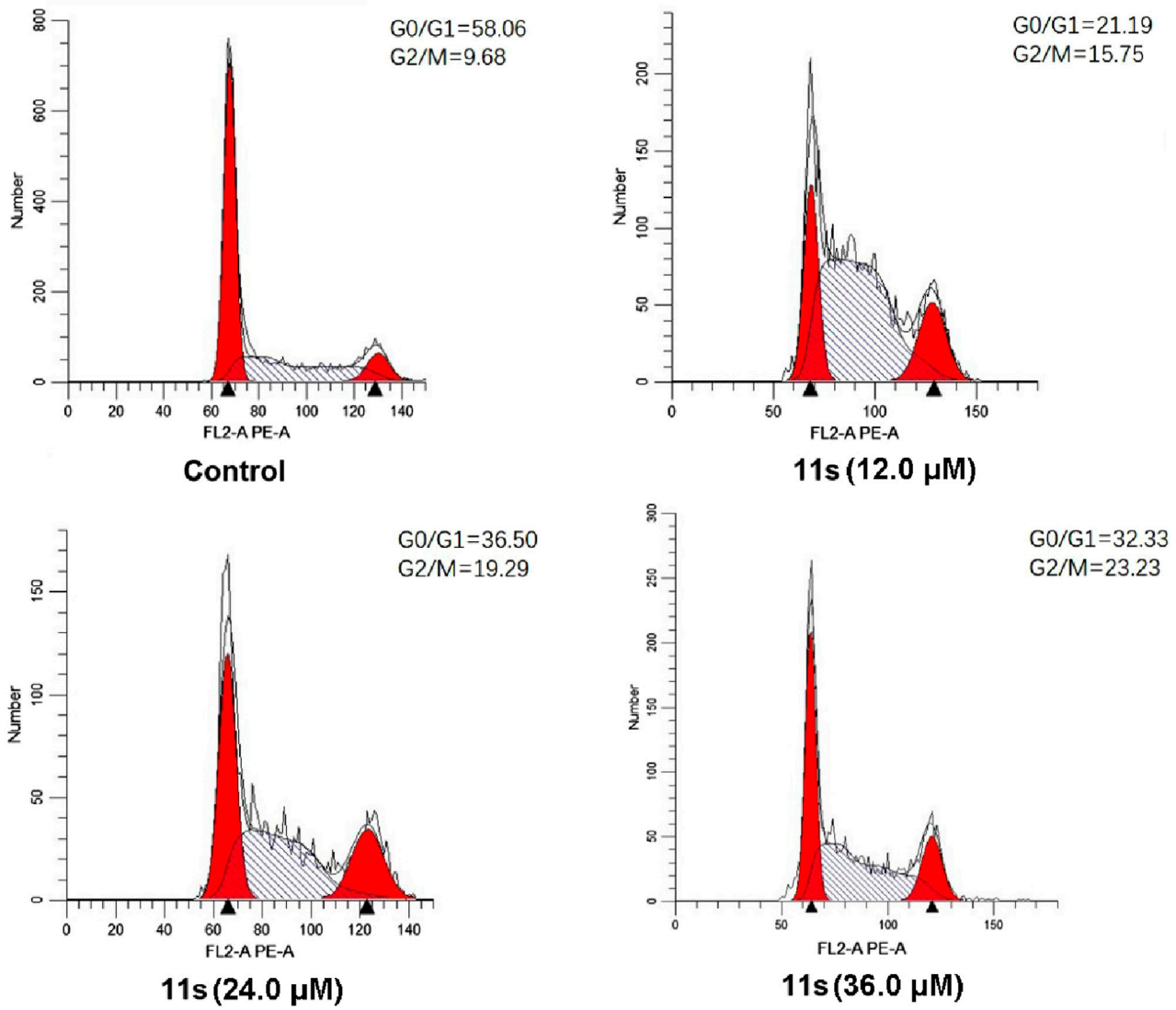

FIGURE 6
Effects of compound **11s** on cell cycle. SGC-7901 cell lines were treated with compound **11s** for 24 h.

4.1.4.7 4-(3-methoxyphenyl)-6-(3,4,5-trimethoxyphenyl) pyrimidine (**11g**)

Light yellow solid; yield: 53%; Mp: 121°C–122°C; ^{1}H NMR (500 MHz, $CDCl_3$) δ 9.28 (d, *J* = 1.2 Hz, 1H), 8.00 (d, *J* = 1.2 Hz, 1H), 7.73 (dd, *J* = 2.3, 1.8 Hz, 1H), 7.71 - 7.66 (m, 1H), 7.45 (t, *J* = 8.0 Hz, 1H), 7.39 (s, 2H), 7.08 (dd, *J* = 8.2, 2.6 Hz, 1H), 4.00 (s, 6H), 3.94 (s, 3H), 3.92 (s, 3H); ^{13}C NMR (126 MHz, $CDCl_3$) δ 164.50, 164.25, 160.22, 158.97, 153.70 (2C), 140.79, 138.50, 132.34, 130.02, 119.50, 116.76, 112.64, 112.49, 104.51 (2C), 60.99, 56.40 (2C), 55.49; HRMS calcd for $C_{20}H_{21}N_2O_4$ [M + H]$^+$ 353.1501, found 353.1502.

4.1.4.8 4-(4-methoxyphenyl)-6-(3,4,5-trimethoxyphenyl) pyrimidine (**11h**)

Light yellow solid; yield: 78%; Mp: 99°C–101°C; ^{1}H NMR (500 MHz, $CDCl_3$) δ 9.23 (s, 1H), 8.13 (d, *J* = 8.9 Hz, 2H), 7.95 (d, *J* = 1.1 Hz, 1H), 7.38 (s, 2H), 7.05 (d, *J* = 8.9 Hz, 2H), 4.00 (s, 6H), 3.94 (s, 3H), 3.90 (s, 3H); ^{13}C NMR (126 MHz, $CDCl_3$) δ 164.15, 163.96, 162.08, 158.90, 153.67 (2C), 140.68, 132.56, 129.34, 128.73 (2C), 114.38 (2C), 111.59, 104.49 (2C), 60.99, 56.39 (2C), 55.45; HRMS calcd for $C_{20}H_{21}N_2O_4$ [M + H]$^+$ 353.1501, found 353.1525.

4.1.4.9 4-(4-ethoxyphenyl)-6-(3,4,5-trimethoxyphenyl) pyrimidine (**11i**)

Light yellow solid; yield: 84%; Mp: 149°C–151°C; ^{1}H NMR (500 MHz, $CDCl_3$) δ 9.22 (d, *J* = 1.2 Hz, 1H), 8.11 (d, *J* = 8.9 Hz, 2H), 7.94 (d, *J* = 1.1 Hz, 1H), 7.37 (s, 2H), 7.03 (d, *J* = 8.9 Hz, 2H), 4.12 (q, *J* = 7.0 Hz, 2H), 3.99 (s, 6H), 3.93 (s, 3H), 1.46 (t, J = 7.0 Hz, 3H); ^{13}C NMR (126 MHz, $CDCl_3$) δ 164.18, 163.93, 161.47, 158.92, 153.65 (2C), 140.64, 132.60, 129.14, 128.70 (2C), 114.85 (2C), 111.54, 104.47 (2C), 63.68, 60.98, 56.38 (2C), 14.74; HRMS calcd or $C_{21}H_{23}N_2O_4$ [M + H]$^+$ 367.1658, found 367.1650.

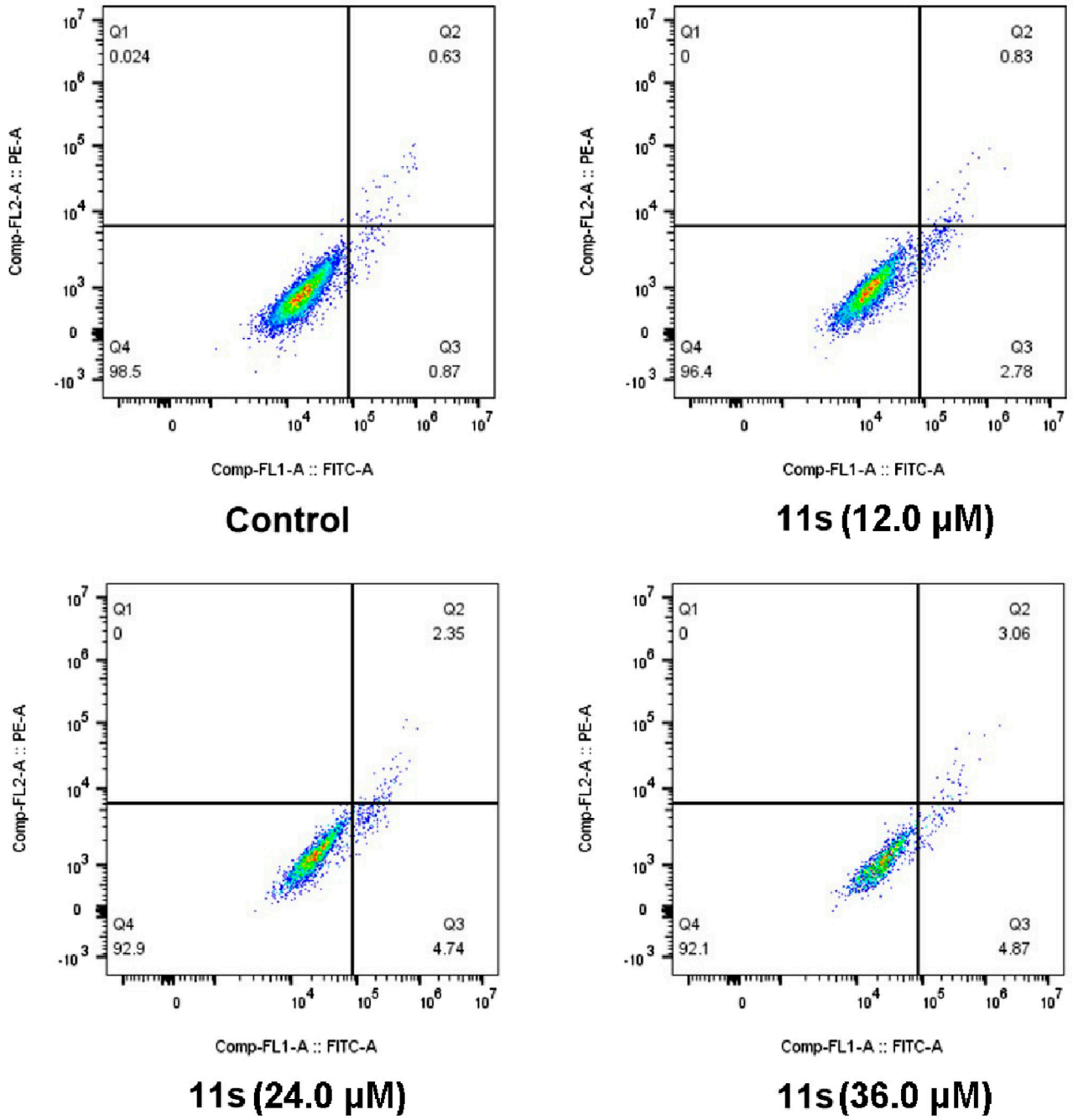

FIGURE 7
Analyses of apoptosis induction in SGC-7901 cells. Cells were harvested and stained with Annexin-V/PI for analysis after treatment with different concentrations of compound **11s** and control for 48 h. The diverse cell stages were given as live (Q4), early apoptotic (Q3), late apoptotic (Q2), and necrotic cells (Q1).

4.1.4.10 2-Methoxy-5-(6-(3,4,5-trimethoxyphenyl) pyrimidin-4-yl)phenol (**11j**)

Yellow solid; yield: 79%; Mp: 117°C–118°C; ^{1}H NMR (500 MHz, $CDCl_3$) δ 9.22 (d, *J* = 1.1 Hz, 1H), 7.92 (d, *J* = 1.1 Hz, 1H), 7.75 (dt, *J* = 5.8, 2.9 Hz, 1H), 7.72 (dd, *J* = 10.4, 1.7 Hz, 1H), 7.37 (s, 2H), 6.98 (d, *J* = 8.4 Hz, 1H), 6.28 (s, 1H), 3.98 (s, 6H), 3.95 (s, 3H), 3.93 (s, 3H); ^{13}C NMR (126 MHz, $CDCl_3$) δ 164.11, 163.94, 158.86, 153.65 (2C), 149.24, 146.13, 140.61, 132.53, 130.16, 119.69, 113.29, 111.76, 110.83, 104.40 (2C), 60.98, 56.36 (2C), 56.02; HRMS calcd for $C_{20}H_{21}N_2O_5$ [M + H]$^+$ 369.1450, found 369.1459.

4.1.4.11 4-(3,4-dimethoxyphenyl)-6-(3,4,5-trimethoxyphenyl)pyrimidine (**11k**)

Light yellow solid; yield: 54%; Mp: 127°C–128°C; ^{1}H NMR (500 MHz, $CDCl_3$) δ 9.24 (d, *J* = 1.2 Hz, 1H), 7.96 (d, *J* = 1.2 Hz, 1H), 7.82 (d, *J* = 2.0 Hz, 1H), 7.69 (dd, *J* = 8.4, 2.1 Hz, 1H), 7.38 (s, 2H), 7.00 (d, *J* = 8.4 Hz, 1H), 4.02 (s, 3H), 3.99 (s, 6H),

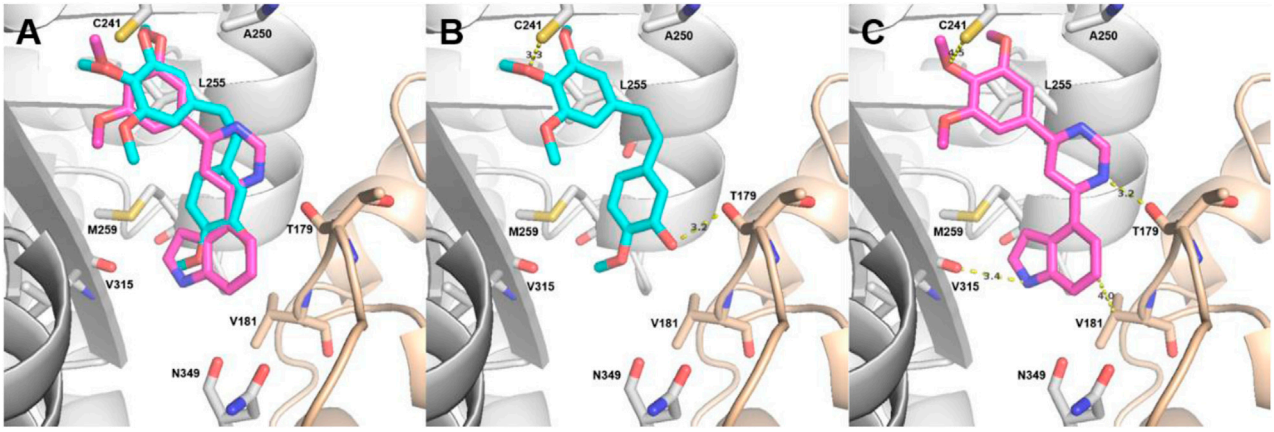

FIGURE 8
Proposed binding modes for 11s **(A, C)** in comparison with CA-4 **(A, B)** at the colchicine site. Carbon atoms are shown in cyan for CA-4 and in magenta for **11s**. The residues from the α-tubulin chain are shown in pale yellow, whereas residues from β-tubulin are colored in gray.

TABLE 3 Prediction of physicochemical properties of CA-4, 11j, and 11s[a].

Compounds	cLogP	TPSA	Natoms	MW	HBA	HBD
Standard	<5	<140		<500	<10	<5
CA-4	3.32	57.15	43	316.35	4	1
11j	2.73	81.87	47	368.39	6	1
11s	3.32	64.44	46	361.40	5	1

[a]cLogP: calculated logarithm of the octanol-water partition coefficient; TPSA: topological polar surface area; Natoms: No. of atoms; MW: molecular weight; HBA: hydrogen-bond acceptor atoms. HBD: hydrogen-bond donor atoms.

3.97 (s, 3H), 3.93 (s, 3H); ^{13}C NMR (126 MHz, $CDCl_3$) δ 164.13, 164.01, 158.89, 153.67 (2C), 151.67, 149.51, 140.72, 132.57, 129.72, 120.17, 111.77, 111.03, 110.05, 104.56 (2C), 60.99, 56.42 (2C), 56.12, 56.04; HRMS calcd for $C_{21}H_{23}N_2O_5$ [M + H]$^+$ 383.1607, found 383.1603.

4.1.4.12 4-(4-nitrophenyl)-6-(3,4,5-trimethoxyphenyl) pyrimidine (**11l**)

Yellow solid; yield: 50%; Mp: 156°C–158°C; ^{1}H NMR (500 MHz, $CDCl_3$) δ 9.35 (d, *J* = 1.3 Hz, 1H), 8.41 (d, *J* = 9.0 Hz, 2H), 8.33 (d, *J* = 9.0 Hz, 2H), 8.07 (d, *J* = 1.3 Hz, 1H), 7.42 (s, 2H), 4.01 (s, 6H), 3.95 (s, 3H); ^{13}C NMR (126 MHz, $CDCl_3$) δ 164.96, 162.25, 159.25, 153.80 (2C), 149.31, 142.91, 131.74, 128.43, 128.21 (2C), 124.17 (2C), 113.02, 104.67 (2C), 61.03, 56.46 (2C); HRMS calcd for $C_{19}H_{18}N_3O_5$ [M + H]$^+$ 368.1246, found 368.1253.

4.1.4.13 4-(6-(3,4,5-trimethoxyphenyl)pyrimidin-4-yl) phenol (**11m**)

Light yellow solid; yield: 51%; Mp: 224°C–226°C; ^{1}H NMR (500 MHz, $CDCl_3$) δ 9.23 (d, *J* = 1.3 Hz, 1H), 8.09 (d, *J* = 8.8 Hz, 2H), 7.95 (d, *J* = 1.3 Hz, 1H), 7.38 (s, 2H), 6.99 (d, *J* = 8.8 Hz, 2H), 5.52 (s, 1H), 4.00 (s, 6H), 3.94 (s, 3H); ^{13}C NMR (126 MHz, $CDCl_3$) δ 164.12, 164.03, 158.91, 158.37, 153.67 (2C), 140.69, 132.54, 130.00, 129.01 (2C), 115.94 (2C), 111.62, 104.50 (2C), 61.00, 56.40 (2C); HRMS calcd for $C_{19}H_{19}N_2O_4$ [M + H]$^+$ 339.1345, found 339.1368.

4.1.4.14 4-(4-fluorophenyl)-6-(3,4,5-trimethoxyphenyl) pyrimidine (**11n**)

White solid; yield: 91%; Mp: 133°C–135°C; ^{1}H NMR (500 MHz, $CDCl_3$) δ 9.25 (s, 1H), 8.15 (dd, *J* = 8.6, 5.4 Hz, 2H), 7.96 (s, 1H), 7.38 (s, 2H), 7.21 (t, *J* = 8.6 Hz, 2H), 3.99 (s, 6H), 3.93 (s, 3H); ^{13}C NMR (126 MHz, $CDCl_3$) δ 164.63, 164.30, 163.54, 159.00, 153.69 (2C), 140.85, 133.15, 132.25, 129.25 (2C), 116.06 (2C), 112.05, 104.51 (2C), 60.99, 56.38 (2C); HRMS calcd for $C_{19}H_{18}FN_2O_3$ [M + H]$^+$ 341.1301, found 341.1302.

4.1.4.15 4-(4-chlorophenyl)-6-(3,4,5-trimethoxyphenyl) pyrimidine (**11o**)

Yellow solid; yield: 55%; Mp: 136°C–137°C; ^{1}H NMR (500 MHz, $CDCl_3$) δ 9.28 (d, *J* = 1.3 Hz, 1H), 8.10 (d, *J* = 8.6 Hz, 2H), 7.98 (d, *J* = 1.3 Hz, 1H), 7.52 (d, *J* = 8.7 Hz, 2H), 7.39 (s, 2H), 4.00 (s, 6H), 3.94 (s, 3H); ^{13}C NMR (126 MHz, $CDCl_3$) δ 164.45, 163.46, 159.07, 153.72 (2C), 140.92, 137.23, 135.45, 132.19, 129.26 (2C), 128.48 (2C), 112.18, 104.56 (2C), 61.00, 56.42 (2C); HRMS calcd for $C_{19}H_{18}ClN_2O_3$ [M + H]$^+$ 357.1006, found 357.1010.

4.1.4.16 4-(thiophen-3-yl)-6-(3,4,5-trimethoxyphenyl) pyrimidine (**11p**)

Light yellow solid; yield: 87%; Mp: 106°C–108°C; ^{1}H NMR (500 MHz, $CDCl_3$) δ 9.20 (d, *J* = 1.3 Hz, 1H), 8.19 (dd, *J* = 3.0, 1.3 Hz, 1H), 7.85 (d, *J* = 1.3 Hz, 1H), 7.76 (dd, *J* = 5.1, 1.2 Hz, 1H), 7.45 (dd, *J* = 5.1, 3.0 Hz, 1H), 7.36 (s, 2H), 3.98 (s, 6H), 3.93 (s, 3H);

^{13}C NMR (126 MHz, $CDCl_3$) δ 164.20, 160.24, 159.06, 153.66 (2C), 140.77, 140.10, 132.33, 127.02, 126.85, 125.93, 112.15, 104.48 (2C), 60.98, 56.38 (2C); HRMS calcd for $C_{17}H_{17}N_2O_3S$ [M + H]$^+$ 329.0960, found 329.0955.

4.1.4.17 4-(pyridin-3-yl)-6-(3,4,5-trimethoxyphenyl) pyrimidine (**11q**)

Light yellow solid; yield: 97%; Mp: 120°C–121°C; ^{1}H NMR (500 MHz, $CDCl_3$) δ 9.33 (s, 1H), 9.30 (d, *J* = 1.2 Hz, 1H), 8.76 (d, *J* = 4.0 Hz, 1H), 8.46 (d, *J* = 8.0 Hz, 1H), 8.04 (d, *J* = 1.2 Hz, 1H), 7.48 (dd, *J* = 7.9, 4.7 Hz, 1H), 7.40 (s, 2H), 3.99 (s, 6H), 3.93 (s, 3H); ^{13}C NMR (126 MHz, $CDCl_3$) δ 164.56, 162.27, 159.24, 153.73 (2C), 151.65, 148.44, 141.03, 134.75, 132.79, 131.88, 123.83, 112.44, 104.52 (2C), 61.00, 56.39 (2C); HRMS calcd for $C_{18}H_{18}N_3O_3$ [M + H]$^+$ 324.1348, found 324.1340.

4.1.4.18 4-(pyridin-4-yl)-6-(3,4,5-trimethoxyphenyl) pyrimidine (**11r**)

Light yellow solid; yield: 67%; Mp: 124°C–126°C; ^{1}H NMR (500 MHz, $CDCl_3$) δ 9.34 (d, *J* = 1.3 Hz, 1H), 8.83 (d, *J* = 5.7 Hz, 2H), 8.06 (d, *J* = 1.3 Hz, 1H), 8.01 (dd, *J* = 4.5, 1.6 Hz, 2H), 7.41 (s, 2H), 4.00 (s, 6H), 3.94 (s, 3H); ^{13}C NMR (126 MHz, $CDCl_3$) δ 164.96, 162.27, 159.32, 153.78 (2C), 150.77 (2C), 144.33, 141.19, 131.76, 121.09 (2C), 112.78, 104.62 (2C), 61.02, 56.43 (2C); HRMS calcd for $C_{18}H_{18}N_3O_3$ [M + H]$^+$ 324.1348, found 324.1346.

4.1.4.19 4-(6-(3,4,5-trimethoxyphenyl)pyrimidin-4-yl)-1H-indole (**11s**)

Light yellow solid; yield: 84%; Mp: 84°C–86°C; ^{1}H NMR (500 MHz, $CDCl_3$) δ 9.38 (d, *J* = 1.3 Hz, 1H), 8.97 (s, 1H), 8.15 (d, *J* = 1.3 Hz, 1H), 7.73 (dd, *J* = 7.4, 0.8 Hz, 1H), 7.53 (d, *J* = 8.1 Hz, 1H), 7.42 (s, 2H), 7.36 - 7.31 (m, 2H), 7.15 (s, 1H), 3.98 (s, 6H), 3.94 (s, 3H); ^{13}C NMR (126 MHz, $CDCl_3$) δ 166.59, 163.71, 158.89, 153.67 (2C), 140.56, 136.85, 132.69, 129.69, 126.05, 126.02, 121.93, 120.51, 114.93, 113.73, 104.50 (2C), 102.39, 61.00, 56.35 (2C); HRMS calcd for $C_{21}H_{20}N_3O_3$ [M + H]$^+$ 362.1505, found 362.1495.

4.1.4.20 4-(naphthalen-2-yl)-6-(3,4,5-trimethoxyphenyl) pyrimidine (**11t**)

Light yellow solid; yield: 86%; Mp: 135°C–137°C; ^{1}H NMR (500 MHz, $CDCl_3$) δ 9.33 (d, *J* = 1.2 Hz, 1H), 8.67 (s, 1H), 8.22 (dd, *J* = 8.6, 1.8 Hz, 1H), 8.14 (d, *J* = 1.2 Hz, 1H), 8.00 (dd, *J* = 8.8, 4.2 Hz, 2H), 7.90 (dd, *J* = 6.1, 3.0 Hz, 1H), 7.61 - 7.51 (m, 2H), 7.43 (s, 2H), 4.01 (s, 6H), 3.95 (s, 3H); ^{13}C NMR (126 MHz, $CDCl_3$) δ 164.56, 164.29, 159.06, 153.71 (2C), 140.82, 134.58, 134.23, 133.26, 132.42, 128.99, 128.83, 127.77, 127.50, 127.47, 126.72, 123.90, 112.68, 104.60 (2C), 61.01, 56.43 (2C); HRMS calcd for $C_{23}H_{21}N_2O_3$ [M + H]$^+$ 373.1552, found 373.1557.

4.2 Biological evaluation

4.2.1 Cell culture

All cell lines were derived from the American Type Culture Collection (ATCC, Manassas, VA) or our own laboratory. In order to maintain the viability and growth of HeLa, SGC-7901, MCF-7, and HSF cells, they were cultured in RPMI-1640 medium supplemented with 100 U/mL streptomycin, 100 U/mL penicillin, and 10% FBS. The use of antibiotics was necessary to prevent bacterial contamination while the addition of FBS provided essential nutrients for cell growth. The culture conditions were maintained at a temperature of 37°C in a humidified atmosphere containing 5% CO_2 which mimicked physiological conditions within the body. Careful attention was paid to maintaining optimal culture conditions for each cell line throughout the duration of our experiments to ensure reliable results. This standardized culturing protocol ensures consistent conditions for growing HeLa, SGC-7901, MCF-7, and HSF cells under controlled laboratory settings. By following these guidelines and using reliable sources for obtaining cell lines like ATCC's collection guarantees reproducibility across different experiments conducted by researchers globally.

4.2.2 *In vitro* antiproliferative activity

The MTT assay was employed to determine the *in vitro* antiproliferative activity of all target compounds and CA-4 (Shi et al., 2022). Cells were seeded at a density of 2×10^4/well in 96-well plates, taking into account the growth rate of the cell line. After 24 h, triplicate wells were treated with the compounds and media under investigation. Following 72 h of incubation at 37°C in a CO_2-enriched environment (5%), the medium containing drugs was replaced with fresh medium containing a solution of MTT (5 mg/mL) for subsequent analysis. After an additional incubation period of 4 h, dimethyl sulfoxide (100 μL) was added to each well and gently vortexed until complete dissolution of purple formazan crystals occurred. The optical density values at OD_{490} were determined using a microplate reader. The resulting data were calculated and plotted as percentage viability relative to control samples. IC_{50} values represented drug concentrations that caused absorption by untreated wells in MTT assays to reach 50%.

4.2.3 Effect on tubulin polymerization

A fluorescence-based tubulin polymerization assay kit (Cytoskeleton-Cat.#BK011P) was employed in this study to investigate the effects of CA-4 and compound **11s** on tubulin polymerization. The experimental procedures were conducted following the manufacturer's protocol (Dufresne et al., 2007). To initiate the assay, tubulin was resuspended in ice-cold G-PEM buffer and then added to 96-well plates containing different concentrations of the indicated drugs or vehicle control. Thorough mixing of samples ensured proper distribution of the compounds within each well. To monitor tubulin assembly, a plate reader was utilized to measure fluorescence at regular intervals of 1 min for a total duration of 90 min at a temperature maintained at 37°C. This allowed us to observe any changes in tubulin polymerization over time induced by CA-4 and compound **11s**. After obtaining the data from these measurements, IC_{50} values were calculated using SPSS software specifically after a period of 20 min. These IC_{50} values provide valuable information about the concentration required for CA-4 and compound **11s** to inhibit half of the tubulin polymerization process.

4.2.4 Analysis of immunofluorescence staining

Immunostaining was conducted to identify the presence of tubulin protein associated with microtubules after exposure to compound **11s** and CA-4 (Shi et al., 2022). SGC-7901 cells were seeded at a density of 1×10^4 in a 24-well plate and incubated for 24 h. Subsequently, the cells

were treated with either **11s**, CA-4, or the vehicle for a duration of 24 h. The control and treated cells were fixed using PBS containing 4% formaldehyde at −20°C for half an hour, followed by two washes with PBS. To enable permeabilization, the cells were exposed to PBS containing 0.1% (v/v) Triton X-100 for 5 min. Following this step, blocking was performed using PBS supplemented with 5% bovine serum albumin for 10 min. A solution consisting of primary α-tubulin antibody diluted at a ratio of 1/100 in PBS containing 2% bovine serum albumin was prepared. The plates were incubated overnight at a temperature of 4°C. After removing any unbound primary antibody using PBS, the cells were exposed to FITC-conjugated anti-mouse secondary antibody. A dilution of 1/1,000 was prepared for the anti-mouse secondary antibody using a solution of 2% BSA in PBS, and the cells were then incubated at a temperature of 37°C for a duration of 3 h. To eliminate any remaining unbound secondary antibody, the cells were rinsed with PBS solution. Following this step, DAPI dye was used to stain the nuclei. Finally, immunofluorescence was observed through a fluorescence microscope.

4.2.5 Cell cycle analysis

The SGC-7901 cell line (8×10^4 cells) was subjected to culture with specified concentrations of compound **11s** or a solution containing 0.05% DMSO for the indicated durations (Khazir et al., 2020). The cells were harvested through centrifugation, followed by PBS washing and fixation in ice-cold 70% ethanol. After another round of centrifugation, the fixed cells were resuspended in 500 mL of PBS supplemented with RNase at a concentration of 1 mg/mL. Subsequently, incubation at 37°C for 30 min was performed before staining the cells with propidium iodide at a concentration of 50 mg/mL under dark conditions at 4°C for half an hour. Flow cytometry analysis using FACS was then conducted on the samples. This experimental procedure was repeated no less than three times.

4.2.6 Induction of cell apoptosis

An Annexin-Van-FITC/PI assay was conducted to assess the potential of the target compound in inducing apoptosis (Wang et al., 2024). SGC-7901 cells were cultured in 6-well plates (3×10^5 cells/well) and treated with varying concentrations of compound **11s** or a control solution for 48 h. Subsequently, the cells were collected through centrifugation, rinsed with PBS, and suspended in binding buffer. Following this, a cell suspension was prepared by adding 10 μL of PI staining solution and 5 μL of Annexin V-FITC, which were then incubated at room temperature in darkness for 15 min. Finally, the samples were analyzed using a CytoFLEX flow cytometer and Flowjo 10.8 software was utilized to calculate the percentage of apoptotic cells.

4.3 Molecular docking analysis

The ligands used for molecular docking were generated in.sdf format using ChemBioDrawUltra 13.0 and processed with LigPrep in the Schrödinger package (Wang et al., 2024). The Tubulin crystal structure in complex with **11s** and CA-4 was obtained from the RCSB PDB Bank and processed using the Protein Preparation Wizard within the Schrödinger package. The ligands were also prepared using LigPrep Wizard in the Schrödinger package, including adding hydrogen atoms to residues and assigning bond orders. Subsequently, the OPLS3 force field was applied to minimize protein energy and remove steric hindrance. During docking, a grid box measuring 15 Å × 15 Å × 15 Å was generated around the protein's active site. Docking procedures were carried out using Ligand Docking in the Schrödinger package, and the results were analyzed utilizing PyMOL.

Data availability statement

The original contributions presented in the study are included in the article/Supplementary Material, further inquiries can be directed to the corresponding authors.

Author contributions

YX: Data curation, Formal Analysis, Writing–original draft. YZ: Data curation, Formal Analysis, Software, Validation, Writing–original draft. SY: Resources, Software, Validation, Visualization, Writing–review and editing. LS: Data curation, Formal Analysis, Investigation, Software, Visualization, Writing–review and editing. DX: Conceptualization, Project administration, Writing–review and editing. CW: Conceptualization, Funding acquisition, Project administration, Resources, Supervision, Writing–review and editing.

Funding

The author(s) declare that financial support was received for the research, authorship, and/or publication of this article. This work was supported by grants from the National Natural Science Foundation of China (82303590), the Natural Science Foundation of Shandong (ZR2021QH156), the Natural Science Foundation of Qingdao (23-2-1-141-zyyd-jch), the Youth Innovation Team Development Program of Shandong Province (2023KJ227), the China Postdoctoral Science Foundation (2023M741867), and the Qingdao Postdoctoral Application Project (QDBSH20230202076).

Conflict of interest

The authors declare that the research was conducted in the absence of any commercial or financial relationships that could be construed as a potential conflict of interest.

Publisher's note

Supplementary material

The Supplementary Material for this article can be found online at: https://www.frontiersin.org/articles/10.3389/fchem.2024.1447831/full#supplementary-material

References

Cao, Y. N., Zheng, L. L., Wang, D., Liang, X. X., Gao, F., and Zhou, X. L. (2018). Recent advances in microtubule-stabilizing agents. *Eur. J. Med. Chem.* 143, 806–828. doi:10.1016/j.ejmech.2017.11.062

Čermák, V., Dostál, V., Jelínek, M., Libusová, L., Kovář, J., Rösel, D., et al. (2020). Microtubule-targeting agents and their impact on cancer treatment. *Eur. J. Cell Biol.* 99 (4), 151075. doi:10.1016/j.ejcb.2020.151075

Chen, S. M., Meng, L. H., and Ding, J. (2010). New microtubule-inhibiting anticancer agents. *Expert Opin. Inv. Drug.* 19 (3), 329–343. doi:10.1517/13543780903571631

Dufresne, S., Hanan, G. S., and Skene, W. G. (2007). Preparation, photophysics, and electrochemistry of segmented comonomers consisting of thiophene and pyrimidine units: new monomers for hybrid copolymers. *J. Phys. Chem. B* 111 (39), 11407–11418. doi:10.1021/jp075259j

Dumontet, C., and Jordan, M. A. (2010). Microtubule-binding agents: a dynamic field of cancer therapeutics. *Nat. Rev. Drug Discov.* 9, 790–803. doi:10.1038/nrd3253

Grossmann, K. F., Colman, H., Akerley, W. A., Glantz, M., Matsuoko, Y., Beelen, A. P., et al. (2012). Phase I trial of verubulin (MPC-6827) plus carboplatin in patients with relapsed glioblastoma multiforme. *J. Neuro-Oncol.* 110 (2), 257–264. doi:10.1007/s11060-012-0964-7

Hamze, A., Alami, M., and Provot, O. (2020). Developments of isoCombretastatin A-4 derivatives as highly cytotoxic agents. *Eur. J. Med. Chem.* 190, 112110. doi:10.1016/j.ejmech.2020.112110

Hu, M., Zhang, B., Yang, H., Liu, Y., Chen, Y., Ma, T., et al. (2015). Design, Synthesis and molecular docking studies of novel indole–pyrimidine hybrids as tubulin polymerization inhibitors. *Chem. Biol. Drug Des.* 86, 1491–1500. doi:10.1111/cbdd.12616

Jian, X. E., Yang, F., Jiang, C. S., You, W. W., and Zhao, P. L. (2020). Synthesis and biological evaluation of novel pyrazolo[3,4-b]pyridines as cis-restricted Combretastatin A-4 analogues. *Bioorg. Med. Chem. Lett.* 30 (8), 127025. doi:10.1016/j.bmcl.2020.127025

Kang, Y., Pei, Y., Qin, J., Zhang, Y., Duan, Y., Yang, H., et al. (2023). Design, synthesis, and biological activity evaluation of novel tubulin polymerization inhibitors based on pyrimidine ring skeletons. *Bioorg. Med. Chem. Lett.* 84, 129195. doi:10.1016/j.bmcl.2023.129195

Kasibhatla, S., Baichwal, V., Cai, S. X., Roth, B., Skvortsova, I., Skvortsov, S., et al. (2007). MPC-6827: a small-molecule inhibitor of microtubule formation that is not a substrate for multidrug resistance pumps. *Cancer Res.* 67 (12), 5865–5871. doi:10.1158/0008-5472.can-07-0127

Khazir, J., Ahmad Mir, B., Chashoo, G., Maqbool, T., Riley, D., and Pilcher, L. (2020). Design, synthesis, and anticancer evaluation of acetamide and hydrazine analogues of pyrimidine. *J. Heterocycl. Chem.* 57, 1306–1318. doi:10.1002/jhet.3867

Lu, Y., Chen, J., Xiao, M., Li, W., and Miller, D. D. (2012). An overview of tubulin inhibitors that interact with the colchicine binding site. *Pharm. Res-Dordr.* 29 (11), 2943–2971. doi:10.1007/s11095-012-0828-z

Mahmud, F., Deng, S., Chen, H., Miller, D. D., and Li, W. (2020). Orally available tubulin inhibitor VERU-111 enhances antitumor efficacy in paclitaxel-resistant lung cancer. *Cancer Lett.* 495, 76–88. doi:10.1016/j.canlet.2020.09.004

Mustafa, M., Anwar, S., Elgamal, F., Ahmed, E. R., and Aly, O. M. (2019). Potent Combretastatin A-4 analogs containing 1,2,4-triazole: synthesis, antiproliferative, anti-tubulin activity, and docking study. *Eur. J. Med. Chem.* 183, 111697. doi:10.1016/j.ejmech.2019.111697

Paidakula, S., Nerella, S., Kankala, S., and Kankala, R. K. (2022). Recent trends in tubulin-binding Combretastatin A-4 analogs for anticancer drug development. *Curr. Med. Chem.* 29 (21), 3748–3773. doi:10.2174/0929867328666211202101641

Pal, S., Azad, A., Bhatia, S., Drabkin, H., Costello, B., Sarantopoulos, J., et al. (2015). A phase I/II trial of BNC105P with everolimus in metastatic renal cell carcinoma. *Clin. Cancer Res.* 21 (15), 3420–3427. doi:10.1158/1078-0432.ccr-14-3370

Pérez-Pérez, M. J., Priego, E. M., Bueno, O., Martins, M. S., Canela, M. D., and Liekens, S. (2016). Blocking blood flow to solid tumors by destabilizing tubulin: an approach to targeting tumor growth. *J. Med. Chem.* 59 (19), 8685–8711. doi:10.1021/acs.jmedchem.6b00463

Pettit, G. R., Singh, S. B., Hamel, E., Lin, C. M., Alberts, D. S., and Garcia-Kendall, D. (1989). Isolation and structure of the strong cell growth and tubulin inhibitor combretastatin A-4. *Experientia* 45 (2), 209–211. doi:10.1007/bf01954881

Sana, S., Reddy, V. G., Srinivasa Reddy, T., Tokala, R., Kumar, R., Bhargava, S. K., et al. (2021). Cinnamide derived pyrimidine-benzimidazole hybrids as tubulin inhibitors: synthesis, *in silico* and cell growth inhibition studies. *Bioorg. Chem.* 110, 104765. doi:10.1016/j.bioorg.2021.104765

Shi, L., Yang, S., Chang, J., Zhang, Y., Liu, W., Zeng, J., et al. (2022). Design, synthesis and biological evaluation of 9-aryl-5H-pyrido[4,3-b]indole derivatives as potential tubulin polymerization inhibitors. *Front. Chem.* 10, 1004835. doi:10.3389/fchem.2022.1004835

Shukla, L., Ajram, L. A., Begg, M., Evans, B., Graves, R. H., Hodgson, S. T., et al. (2016). 2,8-Diazaspiro[4.5]decan-8-yl pyrimidin-4-amine potent CCR4 antagonists capable of inducing receptor endocytosis. *Eur. J. Med. Chem.* 115, 14–25. doi:10.1016/j.ejmech.2016.02.058

Steinmetz, M. O., and Prota, A. E. (2018). Microtubule-targeting agents: strategies to hijack the cytoskeleton. *Trends Cell Biol.* 28, 776–792. doi:10.1016/j.tcb.2018.05.001

Tan, Y. M., Li, D., Li, F. F., Fawad Ansari, M., Fang, B., and Zhou, C. H. (2022). Pyrimidine-conjugated fluoroquinolones as new potential broad-spectrum antibacterial agents. *Bioorg. Med. Chem. Lett.* 73, 128885. doi:10.1016/j.bmcl.2022.128885

Wang, C., Li, Y., Liu, Z., Wang, Z., Liu, Z., Man, S., et al. (2021). Design, synthesis and biological evaluation of 1-Aryl-5-(4-arylpiperazine-1-carbonyl)-1H-tetrazols as novel microtubule destabilizers. *J. Enzym. Inhib. Med. Ch.* 36 (1), 549–560. doi:10.1080/14756366.2020.1759582

Wang, C., Zhang, Y., Yang, S., Shi, L., Xiu, Y., Wu, Y., et al. (2024). 3-aryl-4-(3,4,5-trimethoxyphenyl)pyridines inhibit tubulin polymerisation and act as anticancer agents. *J. Enzyme Inhib. Med. Chem.* 39 (1), 2286939. doi:10.1080/14756366.2023.2286939

Wang, C., Zhang, Y., Yang, S., Xiu, Y., Chen, W., Wang, Y., et al. (2023). Design, synthesis, and biological evaluation of 4-aryl-9H-carbazoles as tubulin polymerization inhibitors with potent anticancer activities. *Arab. J. Chem.* 16, 105146. doi:10.1016/j.arabjc.2023.105146

Wang, Q., Arnst, K. E., Wang, Y., Kumar, G., Ma, D., Chen, H., et al. (2018). Structural modification of the 3,4,5-trimethoxyphenyl moiety in the tubulin inhibitor VERU-111 leads to improved antiproliferative activities. *J. Med. Chem.* 61 (17), 7877–7891. doi:10.1021/acs.jmedchem.8b00827

Wu, Y., Guan, Q., Zheng, D., Yan, P., Feng, D., Du, J., et al. (2018). Conformation impacts on the bioactivities of SMART analogues. *Eur. J. Med. Chem.* 158, 733–742. doi:10.1016/j.ejmech.2018.09.045

Xie, F., Zhao, H., Li, D., Chen, H., Quan, H., Shi, X., et al. (2011). Synthesis and biological evaluation of 2,4,5-substituted pyrimidines as a new class of tubulin polymerization inhibitors. *J. Med. Chem.* 54, 3200–3205. doi:10.1021/jm101388d

Xie, F., Zhao, H., Zhao, L., Lou, L., and Hu, Y. (2009). Synthesis and biological evaluation of novel 2,4,5-substituted pyrimidine derivatives for anticancer activity. *Bioorg. Med. Chem. Lett.* 19, 275–278. doi:10.1016/j.bmcl.2008.09.067

Yang, S., Wang, C., Shi, L., Chang, J., Zhang, Y., Meng, J., et al. (2022). Design, synthesis and biological evaluation of novel diarylpyridine derivatives as tubulin polymerisation inhibitors. *J. Enzym. Inhib. Med. Ch.* 37 (1), 2755–2764. doi:10.1080/14756366.2022.2130284

Zhang, X., Raghavan, S., Ihnat, M., Thorpe, J. E., Disch, B. C., Bastian, A., et al. (2014). The design and discovery of water soluble 4-substituted-2,6-dimethylfuro [2,3-d] pyrimidines as multitargeted receptor tyrosine kinase inhibitors and microtubule targeting antitumor agents. *Bioorg. Med. Chem.* 22, 3753–3772. doi:10.1016/j.bmc.2014.04.049

frontiers | Frontiers in Chemistry

TYPE Review
PUBLISHED 26 September 2024
DOI 10.3389/fchem.2024.1465459

OPEN ACCESS

EDITED BY
Daniela Rigano,
University of Naples Federico II, Italy

REVIEWED BY
Lee James Byrne,
Canterbury Christ Church University, United Kingdom
Bibiana Monson De Souza,
São Paulo State University, Brazil
Christian W. Gruber,
Medical University of Vienna, Austria

*CORRESPONDENCE
Loïc Quinton,
loic.quinton@uliege.be
Jean-Pierre Gillet,
jean-pierre.gillet@unamur.be

†These authors share first authorship

‡These authors share last authorship

RECEIVED 16 July 2024
ACCEPTED 04 September 2024
PUBLISHED 26 September 2024

CITATION
Freuville L, Matthys C, Quinton L and Gillet J-P (2024) Venom-derived peptides for breaking through the glass ceiling of drug development. *Front. Chem.* 12:1465459.
doi: 10.3389/fchem.2024.1465459

Venom-derived peptides for breaking through the glass ceiling of drug development

Lou Freuville[1†], Chloé Matthys[2†], Loïc Quinton[1*‡] and Jean-Pierre Gillet[2*‡]

[1]Laboratory of Mass Spectrometry, MolSys Research Unit, University of Liège, Liège, Belgium, [2]Laboratory of Molecular Cancer Biology, URPhyM, NARILIS, University of Namur, Namur, Belgium

Venoms are complex mixtures produced by animals and consist of hundreds of components including small molecules, peptides, and enzymes selected for effectiveness and efficacy over millions of years of evolution. With the development of venomics, which combines genomics, transcriptomics, and proteomics to study animal venoms and their effects deeply, researchers have identified molecules that selectively and effectively act against membrane targets, such as ion channels and G protein-coupled receptors. Due to their remarkable physico-chemical properties, these molecules represent a credible source of new lead compounds. Today, not less than 11 approved venom-derived drugs are on the market. In this review, we aimed to highlight the advances in the use of venom peptides in the treatment of diseases such as neurological disorders, cardiovascular diseases, or cancer. We report on the origin and activity of the peptides already approved and provide a comprehensive overview of those still in development.

KEYWORDS

venomics, venom peptides, biologically active molecules, drug development, therapy, cancer

1 Introduction

Venomous animals are widely distributed taxonomically, represented in both invertebrates (annelids, arthropods, mollusks, nematodes, cnidarians . . .) and vertebrates (platypus, snakes, lizards, fish, shrews . . .), as shown in Figure 1 (Morsy et al., 2023). Venomous species are ubiquitous, having colonized many aquatic and terrestrial biotopes, in temperate, tropical, and equatorial areas. Fry *et al.* have defined venom as "a secretion, produced in a specialized gland in an animal, and delivered to a target animal through the infliction of a wound" (Fry et al., 2009). However, in addition to predation and defense, venom serves various functional roles including communication, mating, and offspring care (Schendel et al., 2019). Animal venoms are complex chemical cocktails composed of hundreds of molecules, mostly peptides, and proteins, but also small molecules and salts. Peptides and proteins from venoms are commonly referred to as toxins, but enzymes have also been identified among them (Simoes-Silva et al., 2018). The main families of venom enzymes are L-amino oxidases (LAAOs), phospholipases A2 (PLA2s), proteinases (especially snake venom metalloproteinases (SVMPs), and snake venom serine proteinases (SVSPs) in snake venoms), acetylcholinesterases, and hyaluronidases. Even if they have a deleterious effect on the prey, such enzymes are not (always) considered to be toxins (Utkin, 2015).

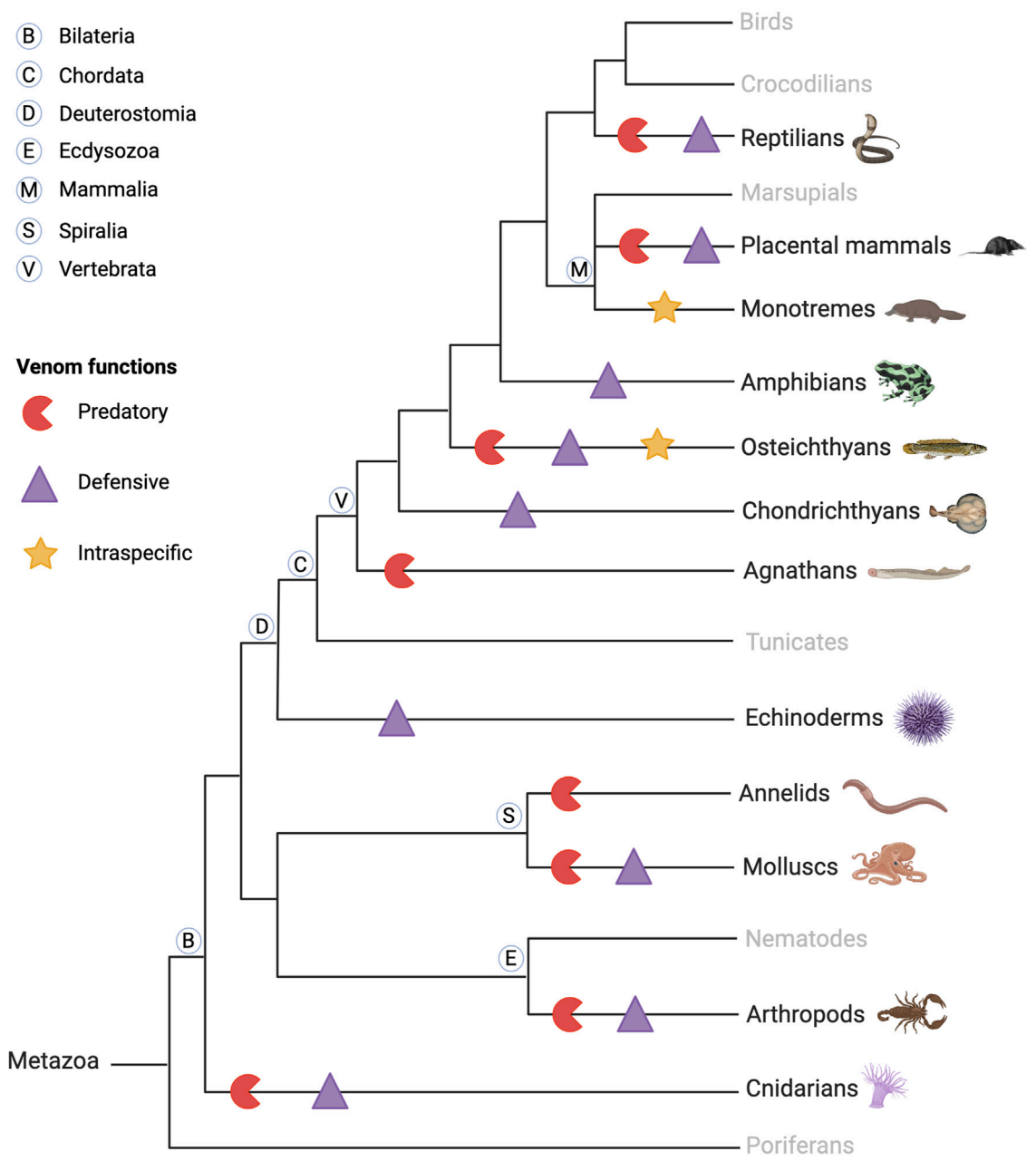

FIGURE 1
Schematic phylogenetic tree of venomous animal diversity and key venom functions. Venomous animals are found in invertebrates and vertebrates, aquatic and terrestrial animals, and predators and prey. They use their venom for predation and defense, and some use their venom against conspecifics, intraspecifically, in competition for reproduction, as in the platypus. Created with BioRender.com (2024) and inspired by Schendel et al. (2019).

Venomous animals have evolved highly complex venoms over millions of years of evolution. Based on recent transcriptomic and proteomic studies, it is generally accepted that an average of a few hundred toxins are present in each venom. Knowing that hundreds of thousands of venomous species have been identified to date, animal venoms can be seen as an incredibly diverse molecular toolbox composed of tens of millions of bioactive peptides and proteins (Herzig et al., 2020). Biologically active venom peptides and proteins act selectively and efficiently against molecular targets, such as ion channels (ICs) and G protein-coupled receptors (GPCRs) but also enzyme-linked receptors (Ghosh et al., 2019; Utkin et al., 2019). Venom toxins have the incredible ability to activate, inhibit, or modulate their functions paving the way for the elucidation of critical physiological processes. From a molecular structural point of view, venom toxins are mostly highly structured peptides with disulfide bridges, providing the molecule with the perfect conformation to bind to the receptors and conferring high stability and resistance to proteases (King, 2013).

Venoms exhibit high chemical diversity and exert a wide range of pharmacological activities. Their toxins act at low doses with high selectivity for receptors, and even for specific subtypes of receptors. From this simple point of view, toxins are extremely attractive for

developing therapeutic drugs. However, some of them are not as selective and may target not only a single (sub)type of receptor but a variety of them. In that context, the development of innovative pharmacological drugs appears tricky, if not possible, as the new tool acts on the receptor of interest, without activating additional receptors that may be involved in critical physiological functions (Smith et al., 2015). As these requirements are never met, such polypharmacological toxins are usually discarded from the pool of interest. In the development of toxin-based therapies, the blood-brain barrier passage remains another major obstacle that researchers are actively trying to overcome. It has been shown that adding positively charged amino acids to the terminal ends of the peptide improves its delivery to the target (Teesalu et al., 2009). Although such modification generally reduces potency, it increases the half-life of the active venom-derived peptide drugs. Another critical parameter to explore is oral bioavailability, which depends on the mass and hydrophobicity of the drug candidates. This is not necessarily limiting, depending on the target site of action. Intravenous or local administration is a credible option to circumvent this difficulty (Stepensky, 2018). While toxins can be valuable in therapeutic research, understanding their pharmacological properties, including pharmacokinetics and pharmacodynamics is critical to the successful development of a lead peptide.

Despite these challenges, the potential for venom peptides in developing therapeutic molecules remains significant. Therefore, venom peptides are ideal candidates for developing novel therapeutic molecules due to their high potency, selectivity, and stability (Holford et al., 2018). To date, eleven venom-derived molecules have been approved and marketed for the treatment of disease from lizard (exenatide and lixisenatide), cone snail (ziconotide), leech (bivalirudin and desirudin), and snake (captopril, enalapril, tirofiban, eptifibatide, batroxobin, and cobratide) venoms. These drugs are used: as anticoagulants for bivariludin and desirudin, as antithrombotics for eptifibatide and tirofiban, as defibrinogenating agents for batroxobin, in case of hypertension for captopril and enalapril, to reduce pain for cobratide and ziconotide, and to treat type 2 diabetes for exenatide and lixisenatide. These drugs are synthetic toxins or molecules derived from natural toxins (Bordon et al., 2020). Many studies are underway in preclinical and clinical settings for treating chronic pain, certain cancers, depression, or diabetes (Miljanich, 2004; Mamelak et al., 2006; Osteen et al., 2016). In this context, this review proposes a journey in the recent advances of venom toxins exploited in potential treatments for both cancer and non-cancer diseases. For the reader's information, this review will not discuss the antimicrobial activity of toxins. More information can be obtained from the review *Antimicrobials from Venomous Animals: An Overview* by Yacoub et al. (2020).

2 Snakes: pioneers in the use of venom toxins as medicine. What's next?

Venomous snakes cause up to 2.7 million cases of envenomation worldwide each year (WHO, 2021). Venom toxins and enzymes disrupt the victim's physiological systems and cause morbidity or even death if left untreated. The therapeutic use of snake venom was documented in Ayurveda as early as the 7th century and was also mentioned by ancient Greek philosophers and physicians for its pharmacological properties (King, 2013). More recently, technological advances have allowed researchers to transform these potentially deadly toxins into life-saving therapeutics. Components of snake venom have shown potential for the development of new drugs, from the development of captopril, the first drug derived from the bradykinin-potentiating peptide of *Bothrops jararaca* (southeast coast of South America), to disintegrins with potent activity against certain types of cancer. Snake venom exhibits cytotoxic, neurotoxic, and hemotoxic activities, making it the focus of many research projects. The study of the cytotoxic properties of venoms for cancer treatment is ongoing. Despite extensive research on the neurotoxicity of snake venoms for neuronal diseases, no drug derived from snake toxin has been marketed for this purpose. Due to the complexity of the neuronal system, this area of research is still in progress (Oliveira et al., 2022).

2.1 Composition of snake venoms

The classification proposed by Tasoulis and Isbister in 2017 identifies four primary (see Table 1) and six secondary protein families (see Table 2) (Tasoulis and Isbister, 2017), which can be respectively associated with enzymatic and non-enzymatic bioactivities (Kang et al., 2011). Several toxins and enzymes exhibit species-specific properties, including defensins, waglerin, maticotoxin, and cystatins. In contrast, PLA2 is the most abundant protein family detected in snake venoms and is present in nearly all snake species (Tasoulis and Isbister, 2023). The PLA2s family is followed in prevalence by the three-finger toxins (3FTxs), a family of non-enzymatic toxins named as such due to the three loops formed by the peptide chain constrained by a conserved disulfide-bond pattern. Beyond these general considerations, it is important to keep in mind that the composition of snake venom is highly species-dependent. It is also influenced by the gender, age, geographic area, and feeding habits of the snake (Gopal et al., 2023). For example, elapid venoms consist mainly of PLA2s and 3FTxs. In contrast, viper venoms are mostly devoid of 3FTxs and contain more snake venom metalloproteinases, PLA2s, and snake venom serine proteases. Crotal venoms also lack 3FTxs, except for *Atropoides nummifer* (Tasoulis and Isbister, 2017).

2.2 Drugs derived from snake toxins currently in clinical use

As early as 1981, the US Food and Drug Administration (FDA) approved the first venom-based treatment, a toxin isolated from the venom of the Brazilian pit viper, *Bothrops jararaca* (see Figure 2). Captopril (Capoten®) is a derivative of bradykinin potentiating peptides (BPPs), which lower blood pressure and reduce cardiac hypertrophy (Kini and Koh, 2020). BPPs, which belong to the natriuretic peptide family, inactivate bradykinin and catalyze the conversion of Angiotensin I to the vasoconstrictor Angiotensin II, by inhibiting the proteolytic Angiotensin-Converting Enzyme (ACE) (Ferreira et al., 1970). Captopril mimics the BPP Pro-Ala-Trp

TABLE 1 Dominant protein families.

Toxin family names	Information	Examples	References for more details
Phospholipases A2 (PLA2s) Group I *Elapidae* and *Hydropidae*	13–18.5 kDa Enzymatic 7 disulfide bridges Presence of a calcium-binding loop	Notexin (*Notechis scutatus*): 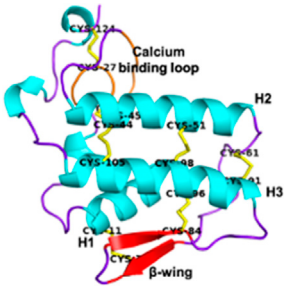 PDB 1AE7	Westerlund et al. (1992) Ponce-Soto et al. (2007) Castro-Amorim et al. (2023)
Phospholipases A2 (PLA2s) Group II *Crotalidae* and *Viperidae*		Crotoxin (*Crotalus durissus*):  PDB 3R0L	
Snake Venom Metalloproteinases (SVMPs) P-I *Viperidae*	20–30 kDa Enzymatic Metalloproteinase (M) domain only	Adamalysin-II (*Crotalus adamenteus*): 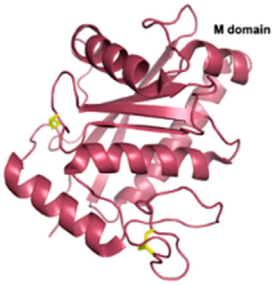 PDB 4AIG	Gomis-Ruth et al. (1993) Igarashi et al. (2007) Olaoba et al. (2020)
Snake Venom Metalloproteinases (SVMPs) P-II *Viperidae*	30–60 kDa Enzymatic Pro-domain, M domain, and disintegrins domain (D) Presence of a RGD (Arg-Gly-Asp) motif	Salmosin (*Gloydius brevicaudus*): 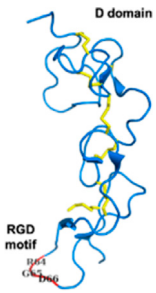 PDB 1L3X	

(Continued on following page)

TABLE 1 (*Continued*) Dominant protein families.

Toxin family names	Information	Examples	References for more details
Snake Venom Metalloproteinases (SVMPs) P-III *Viperidae, Elapidae, Atractaspididae*, and *Colubridae*	60–100 kDa Enzymatic Pro-domain, M domain, D domain and cysteine-rich (C) domain	VAPB2 (*Crotalus atrox*): 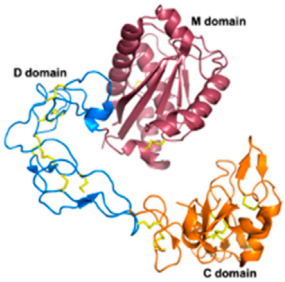 PDB 2DW0	
Snake venom serine proteases (SVSPs) *Viperidae, Elapidae*	26–250 kDa Enzymatic Extend C-terminal tail Active site is constituted of the canonical catalytic triad His-Asp-Ser	Dav-PA (*Deinagkistrodon acutus*): 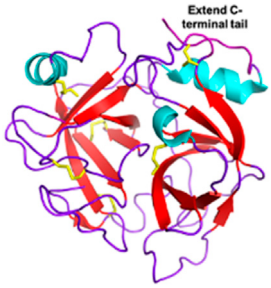 PDB 1OP0	Serrano and Maroun (2005)
Three-finger toxins (3FTxs) *Elapidae*	6–9 kDa Non-enzymatic Named after a highly conserved folding pattern: 3 β-stranded loops (fingers) and a central core stabilized by 4 disulfide bridges Possibility to present a RGD motif	Mambalgin-1 (*Dendroaspis polylepis*): 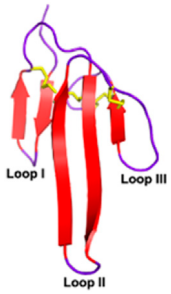 PDB 7ULB	Utkin (2019)

triad, the recognition motif for ACE, and binds strongly to the enzyme's active site (Ki = 1.7 nM) (Cushman and Ondetti, 1991). Captopril is hydrophilic and has a low molecular weight (Stepensky, 2018). However, its main disadvantage is the presence of a thiol group, which has been reported to cause side effects, such as skin rash and loss of taste. To circumvent this drawback, this reactive thiol has been replaced by a carboxylate function in the first step, resulting in a new molecule called enalaprilat. This replacement induced a lack of oral bioavailability, but replacing the carboxylate with an ethylic ester greatly improved it, resulting in enalapril (Patchett, 1984). Based on these initial developments, many drugs have been commercialized (lisinopril, quinapril, ramipril, etc.) (Acharya et al., 2003).

Snake toxins and enzymes have also been described as potent antithrombotic drugs. For instance, echistatin (49 residues) from *Echis carinatus* venom and barbourin (74 residues) from *Sistrurus miliarius* belong to the disintegrin family, due to their potency to bind to integrins. Integrins αIIbβ3 are membrane receptors found on the surface of blood platelets. These receptors play a critical role in platelet aggregation (Casewell et al., 2013). In arterial thrombosis, rupture of the atherosclerotic plaque triggers platelet adhesion and aggregation, leading to clot formation in the arteries, obstructing blood flow to the brain and heart. Ligands for integrins, such as fibronectin, fibrinogen, and von Willebrand factor, interact in the final step of platelet aggregation, via a common recognition motif: a tripeptide sequence RGD (Arg, Gly, Glu) (Lebreton et al., 2016). This motif is commonly found in many PII-type SVMPs. It is unsurprisingly present in echistatin, and a similar sequence, KGD (Lys, Gly, Gluc), is also found in the barbourin. The advantage of the KGD sequence is that it does not block the adhesive functions of other RGD-dependent integrins, and therefore specifically inhibits platelet-dependent thrombus formation. Echistatin and barbourin have led to the development of two αIIbβ3 inhibitors, called tirofiban (Aggrastat®) and eptifibatide (Integrilin®), respectively, both of which were approved by the FDA in 1998 (Bledzka et al., 2013).

Another target of snake toxins is fibrinogen for anticoagulation purposes (Kini, 2006). For example, consider

TABLE 2 Secondary protein families discussed in the review.

Toxin family names	Information	Examples	References for more details
L-amino acid oxidases (LAAOs) *Viperidae, Elapidae*	Monomeric mass: 50–70 kDa Enzymatic Homodimer with FAD (Flavine Adenine Dinucleotide) or FMN (Flavin Mononucleotide) cofactors	LAAO (*Calloselasma rhodostoma*): 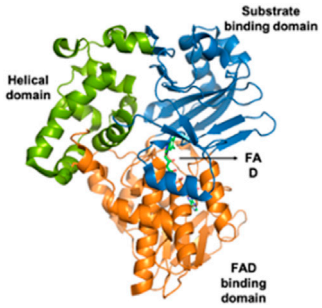 PDB 2IID	Ullah (2020) Izidoro et al. (2014)
Cysteine-rich secretory proteins (CRiSPs) *Viperidae, Elapidae*	20–30 kDa Non-enzymatic Pathogenesis related group 1 (PR-1) domain, a short hinge region and a cysteine rich (CR) domain	CRiSP (*Trimeresurus Stejnegeri*): 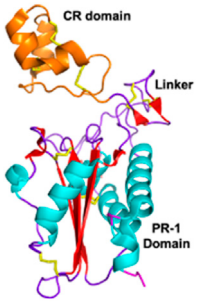 PDB 1RC9	Tadokoro et al. (2020) Urra et al. (2015) Guo et al. (2005)
Disintegrins *Viperidae*, *Atractaspididae* and *Colubridae*	5–10 kDa Non-enzymatic Four subfamilies ranging from 4 to 7 disulfide bridges Result of the proteolytic process of P-II SVMPs	Echistatin (*Echis carinatus*):  PDB 6LSQ	Chen et al. (2020) Calvete et al. (2005) Vasconcelos et al. (2021)
Natriuretic peptides (NPs) *Viperidae, Elapidae*	5–10 kDa	Bradykinin-potentiating and C-type natriuretic peptides (*Bothrops insularis*): Not available in PDB AFDB accession: AF-P68515-F1	Potter et al. (2009)

batroxobin, a 231-residue serine protease isolated from *Bothrops moojeni* venom. Batroxobin is a snake venom thrombin-like serine protease (svTLEs) that catalyzes the cleavage of the Arg16-Gly17 bond of the Aα chain of fibrinogen. By catalyzing this cleavage, it reduces plasma levels of fibrinogen, making clots more fragile and easier to dissolve (Vu et al., 2013). The advantage of this substitute over the well-known thrombin is double as it is more stable and not inhibited by heparin and hirudin (Funk et al., 1971). Treatment with Defibrase®, the drug derived from batroxobin and marketed in China and Japan, is used in ischemia caused by vascular occlusive disease, peripheral and microcirculatory dysfunction, and acute cerebral infarction (D'Amelio et al., 2021).

In the venom of the lancehead pit viper, *Bothrops atrox*, an enzymatic system has been discovered and demonstrated a powerful anti-hemorrhagic activity. This system, composed of batroxobin and a thromboplastin-like enzyme, has been derived into a pharmaceutical specialty called Reptilase®, which plays the role of haemocoagulase (Oliveira et al., 2022). The thromboplastin-like enzyme is a metalloprotein that activates Factor X to fXa, which converts prothrombin into thrombin. Combining the two activities, forming haemocoagulase, accelerates the hemostasis process, reducing bleeding and clotting times (Pentapharm).

The sixth drug based on a snake venom toxin is α-cobrotoxin (cobratide), purified from the venom of *Naja naja atra*, a cobra found in China. α-Cobrotoxin is a 3FTx

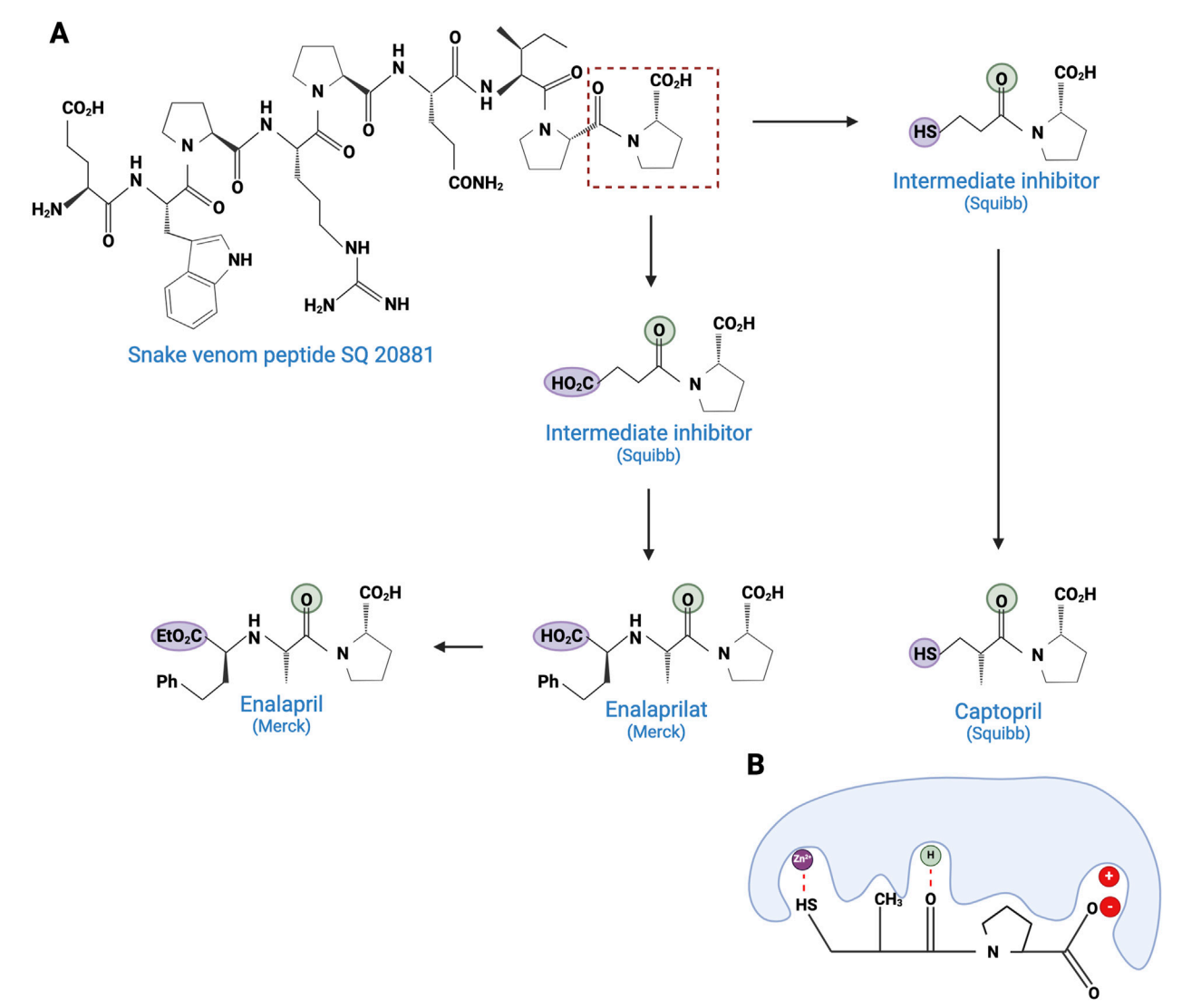

FIGURE 2
Development of captopril and next ACE inhibitors. **(A)** The natural peptide SQ 20881 (sequence EWPRPQIPP), discovered in *Bothrops jararaca* venom, is an inhibitor of ACE, inducing a drop in blood pressure. Squibb company synthetized a derivative which led, after optimization, to the captopril (1981). Because of the side effects of the thiol group, Merck replaced the latter with a carboxylate, resulting in the enalaprilat molecule (1985). However, as this modification resulted in the loss of oral bioavailability, the esterification of the enalaprilat was considered by Merck to solve the problem successfully and created the enalapril (1985). The conserved zinc binder is shown in purple. The H-bond acceptor is shown in green. **(B)** Interaction between captopril and ACE. By preventing the binding of the inert Angiotensin I to ACE, captopril inhibits the formation of Angiotensin II. Created with BioRender.com (2024).

α-neurotoxin, known to act selectively and with high affinity on muscle type α1 nicotinic acetylcholine receptors (nAChRs). α-Cobrotoxin exhibits analgesic activity without opiate dependence and can therefore substitute for morphine (Gazerani and Cairns, 2014).

2.3 Snake toxins in drug development

Other snake toxins are currently under development in the pharmaceutical field, to play a role in the treatment of cardiovascular diseases as antiplatelet or anticoagulant agents, and potentially even in the treatment of certain types of cancer (Kini and Koh, 2020; da Rocha et al., 2023).

2.3.1 Antiplatelet and anticoagulant agents

As noted above, some drugs have already been developed as antiplatelet agents (tirofiban and eptifibatide). Still, many more toxins with similar activities are being discovered, reinforcing the great potential of toxins used as antiplatelet drugs. Like the drugs already on the market, some 3FTxs share the same RGD motif, which is a key for binding to platelet receptors. This is the case of dendroaspin (also known as mambin) (McDowell et al., 1992), S5C1 (Joubert and Taljaard, 1979), both isolated from the venom of *Dendroaspis jamesoni kaimosae* and thrombostatin from *Dendroaspis angusticeps* (Prieto et al., 2002). They possess the RGD motif in loop III (see Table 1). Dendroaspin targets the most abundant platelet integrin αIIbβ3 and thus prevents the binding of fibrinogen. When

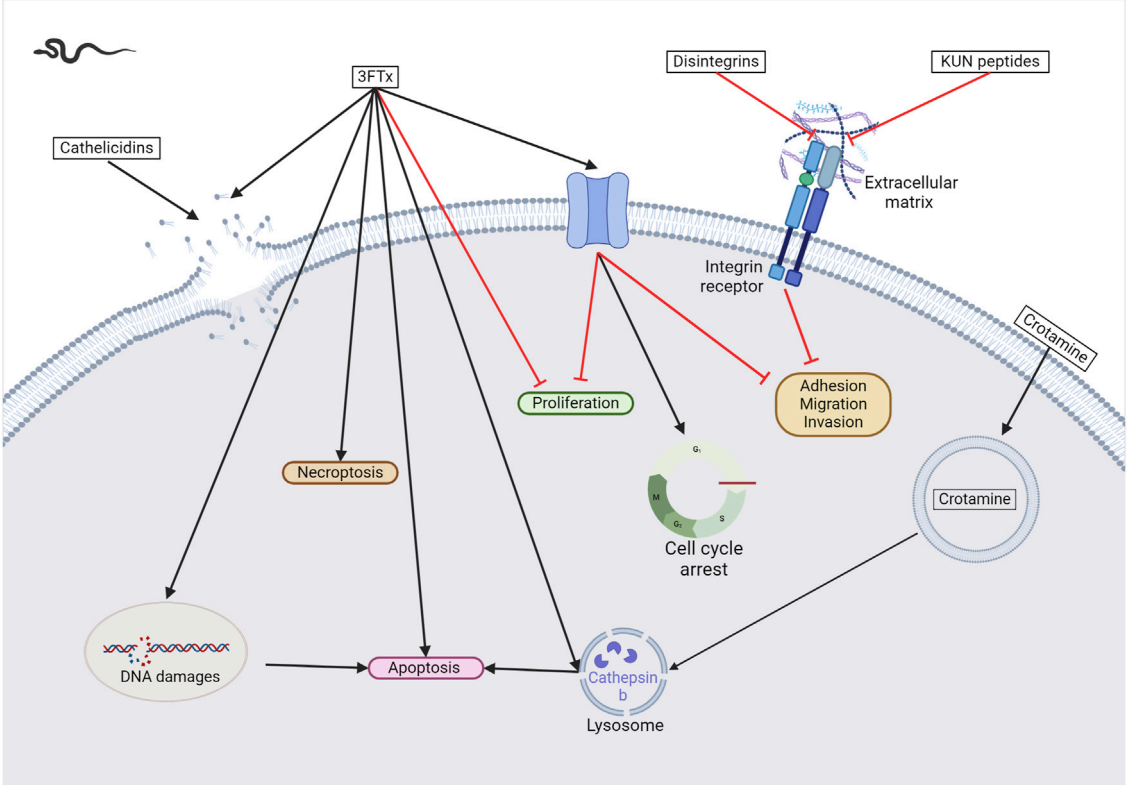

FIGURE 3
Snake venom toxins as potential anticancer agents. In various cancer cell lines, 3FTx have been demonstrated to have a lytic activity by disrupting cell membranes, inducing DNA damage, and/or the release of lysosomal cathepsin B that further leads to apoptosis, to induce necroptosis and/or to stop cell proliferation (Abdel-Ghani et al., 2019; Wu et al., 2013; Liu et al., 2019). Moreover, these toxins can also target ion channels, halting cancer cell proliferation, adhesion, migration, and invasion, and inducing cell cycle arrest (Bychkov et al., 2021; Sudarikova et al., 2022). Cathelicidins are mainly described to form pores in cancer cell membranes ((Wang et al., 2013). Finally, disintegrins and Kunitz-type serine protease inhibitors (KUN) peptides primarily affect the interactions between the extracellular matrix and cell membrane receptors, reducing cancer cell adhesion, migration, and invasion (Zhou et al., 2000a; Brown et al., 2008; Minea et al., 2010; Zhang et al., 2021; Bhattacharya et al., 2023). Created with BioRender.com (2024).

the RGD motif is mutated in RYD or RCD, the binding becomes selective for β1 and β3 integrins. Toxin binding inhibits ADP-induced platelet aggregation (Wattam et al., 2001). Another 3FTx, γ-bungarotoxin, isolated from *Bungarus multicinctus*, also shares the RGD motif. In γ-bungarotoxin, the motif is located in loop II, which is less accessible and induces a lower activity for the receptor than in loop III (IC_{50} = 34 μM) (Shiu et al., 2004). All these 3FTxs exhibit anticoagulant properties, making them interesting as potential antithrombotic agents. Other 3FTxs present anticoagulant potential. Hemetexin AB, exactin, and ringhalexin, all from the venom of *Hemachatus haemachatus*, target specific coagulation factors or complexes with inhibitory activity (Banerjee et al., 2005; Barnwal et al., 2016; Girish and Kini, 2016). The disadvantage of exactin and ringhalexin for therapeutic use is that they are also slightly neurotoxic. However, their high selectivity would allow the development of interesting molecular probes or diagnostic tools (Kini and Koh, 2020).

2.3.2 Cytotoxic activity in cancer

Snake toxins also present an interest in the cancer field (see Figure 3). Indeed, some 3FTxs are strongly cytotoxic. In that context, cytotoxins have been the focus of numerous studies investigating various cancer cell types. For instance, sumaCTX, a cytotoxin extracted from the venom of *Naja sumatrana*, has received much attention from the community due to its cytotoxic activity against MCF-7 breast cancer cells (Teoh and Yap, 2020). It induces membrane hyperpolarization and apoptosis via activation of the two caspases 3 and 7. Changes in the secretome of cells treated with high doses of sumaCTX were later observed (Hiu and Yap, 2021). Most of the expressed proteins were involved in carbon metabolism, immune response, and necroptosis. *Naja sumatrana* cytotoxin was also tested on two types of cancer cells, lung adenocarcinoma and prostate cancer (Chong et al., 2020). The results showed significant differences in cellular behavior, with an increase in late apoptotic and necrotic cells compared to untreated cells. However, the specific mechanisms involved remain unclear.

Other cytotoxins in snake venoms are being extensively studied for their potential anticancer properties. The NKCT1 (purified *Naja kaouthia* protein toxin) was first extracted from *Naja kaouthia* venom in 2010 and showed cardiotoxic and cytotoxic properties against two leukemia cell lines (U937 and K561) (Debnath et al., 2010). Recently, a growing interest in conjugating this toxin with gold nanoparticles to target leukemia, glioblastoma, hepatocarcinoma, and breast cancer cells emerged (Bhowmik et al., 2013; Bhowmik and Gomes, 2017; Bhowmik et al., 2017).

A synergistic effect of administering gold nanoparticle-NKCT1 conjugates was then observed. Indeed, while the conjugation induces apoptosis of cancer cells through caspase activation, it also reduces cytotoxicity against non-cancerous cells. Treatment with GNP-NKCT1 induces autophagy in leukemia cells (Bhowmik and Gomes, 2016). In breast cancer cells, it induces cell cycle arrest by inactivating CDK4 and reduces migration and invasion by inhibiting MMP-9 (Bhowmik and Gomes, 2017).

Naja atra cytotoxins (CTX) have also been studied in various cancer cell types. In leukemia cells, CTX1 treatment led to the initiation of necroptosis and the activation of the FasL/Fas-mediated death signaling pathway (Liu et al., 2019; Chiou et al., 2021). Notably, the venom of *Naja atra* contains numerous CTX isoforms, of which only CTX1 can induce this type of cell death whereas CTX3 induces autophagy-dependent apoptosis in leukemia cells (Chiou et al., 2019). This result suggests that different mechanisms may mediate CTX cytotoxicity. In addition, CTX can cause the loss of the lysosomal membrane integrity in breast cancer cells, leading to the release of lysosomal enzymes, including cathepsin B, which induces necrosis or apoptosis (Wu et al., 2013). Intramuscular administration of CTX1 in mice currently results in skeletal muscle necrosis, making its clinical use impossible, without sequence optimization or improved delivery (Ownby et al., 1993).

Another cobra species, *Naja nubiae*, caught the scientific community's attention by providing the cytotoxin nubein 6.8 (Abdel-Ghani et al., 2019). This peptide shows similarities with other cytotoxins identified in different cobra species and shares the first 6 N-terminal amino acids. In addition, it shows cytotoxic effects against several types of cancer cells, including melanoma and ovarian carcinoma. Cytotoxin nubein 6.8 has been shown to cause DNA damage leading to apoptosis. However, the precise mechanisms underlying this cytotoxicity have not been fully elucidated yet.

NN-32 is a peptide isolated from the cobra *Naja naja* that shows strong homology to other cytotoxins from *Naja* species (Das et al., 2011). When treated with NN-32, leukemia, and breast cancer cells show a reduction in cell viability and proliferation, with a concomitant decrease in lysosomal activity and induction of apoptosis (Das et al., 2013; Attarde and Pandit, 2017). More recently, nanogold particles have been conjugated with the NN-32 peptide, resulting in GNP-NN-32. The goal of developing GNP-NN-32 was the same as for NKCT1, *i.e.*, to increase the selective cytotoxicity against breast cancer cells. The results showed lower IC_{50} values (Attarde and Pandit, 2020).

Dendroaspis polylepis polylepis, the famous Black mamba, produces mambalgins that inhibit acid-sensing ion channels (ASICs). ASICs are voltage-insensitive receptors that are activated by extracellular protons. By selectively and potently inhibiting the ASIC1a and ASIC1b subtypes, with an IC_{50} between 11 and 300 nM, mambalgin-1 showed a potent analgesic effect, while mambalgin-2 is a powerful and reversible inhibitor of ASIC1a (Diochot et al., 2012). In the context of cancer, this channel has recently been described to be overexpressed in breast, melanoma, lung, and liver cancers (Jin et al., 2015; Bychkov et al., 2020; Yang et al., 2020; Wang et al., 2021; Sudarikova et al., 2022). The mambalgin-2 application to leukemia cells reduces their growth and induces cell cycle arrest (Bychkov et al., 2020). In glioma cells, the constant cation current required for cell growth and migration was shown to be mediated by ASIC1a (Rooj et al., 2012). Their treatment with mambalgin-2 induces cell cycle arrest and apoptosis. Acidification, which promotes cell proliferation, migration, and invasiveness, is facilitated by this channel in melanoma (Bychkov et al., 2021). Treatment with mambalgin-2 reduces this phenotype. The same conclusion has recently been drawn for lung adenocarcinoma (Sudarikova et al., 2022).

Kunitz-type serine protease inhibitors (KUN) are small proteins that contain a Kunitz domain. These domains are approximately 50–60 amino acid residues with alpha and beta-fold structures stabilized by three conserved disulfide bridges and inhibit the enzymatic activity of serine proteases (Munawar et al., 2018). KUNs have also been investigated for their promising anticancer activity. Vipegrin, extracted from *Daboia russelli* (Russell's viper) venom, is cytotoxic against breast cancer cells while showing no significant effect on non-cancerous cells (Bhattacharya et al., 2023). This property suggests that vipegrin may follow a specific pathway for killing cancer cells, but unfortunately, it has not been identified to date. Another example is PIVL, a peptide derived from the venom of *Macrovipera lebetina,* which possesses an anti-tumor activity by primarily blocking integrin receptor function, resulting in reduced adhesion of cancer cells. This suggests that PIVL's anticancer activity is not related to cell viability but affects cancer cell migration and invasion (Morjen et al., 2013).

Crotoxin, derived from the venom of *Crotalus durissus terrificus*, is a complex of two subunits, namely phospholipase A2 (crotactin) and a non-enzymatic subunit (crotapotin) that enhances the activity of the first subunit (Faure et al., 1993). This β-neurotoxin activates both autophagic and apoptotic pathways in leukemia, breast, and lung cancer cells (Yan et al., 2006; Yan et al., 2007; Han et al., 2014). Crotoxin has also been shown to enhance the efficacy of gefitinib in lung adenocarcinoma cells (Wang et al., 2012; Wang et al., 2014). Gefitinib is an inhibitor of the epidermal growth factor receptor (EGFR), which is used to treat lung cancer. One hypothesis explaining the synergistic effect is based on the observation that crotoxin modulates EGFR signaling (Donato et al., 1996). Recent studies show that crotoxin also exhibits cytotoxic effects against several cancer cell types, including esophageal, brain, cervical, and pancreatic cancer (Muller et al., 2018). Further evidence shows that crotoxin may have an anti-tumor effect on estrogen-positive (ER+) breast cancer by decreasing the phosphorylation of the ERK1/2 protein, with the antiproliferative effect then being related to the inhibition of the MAPK pathway (Almeida et al., 2021). Crotoxin treatment (10 μg/kg) did not induce any changes in body weight or biochemical parameters in mice (He et al., 2013; da Rocha et al., 2023). However, it was still effective in reducing tumor growth in transplanted esophageal and oral cancer mice. A phase 1 clinical trial was initiated to evaluate the pharmacokinetics of the toxin in patients with advanced breast cancer (Cura et al., 2002), and an open-label phase 1 clinical trial in patients with advanced cancer using intravenous administration was more recently initiated in 2018 and has shown promising results for the efficacy of the toxin in cancer treatment (see Table 3).

The Caspian cobra, *Naja naja oxiana*, is considered the most venomous species among the *Naja sp*. This cobra secretes a specific cytotoxin called oxineur (Sadat et al., 2023). Oxineur shows cytotoxic activity against colon cancer cells while not affecting normal cells. However, more extensive testing is required to evaluate the effects of its administration on animals.

TABLE 3 Summary table of venom-derived molecules mentioned in clinical trials.

Tested molecule	Specie	Molecular mechanism	Target disease	Phase	Status	Trial number	References	Comment
Crotoxin	*Crotalus durissus terrificus*	Cytotoxic	Advanced solid tumors	Phase 1 part 3 (tolerability of intra-patient dose escalation with i.v. administration, confirmation of induction of drug tolerance and assessment of drug efficacy)	Not recruiting yet (08/2024)	NCT01481532	Cura et al. (2002)	
BLZ-100	*Leiurus quinquestriatus quinquestriatus*	Binding to cancer cells	Soft tissue sarcoma	Phase 1	Withdrawn	NCT02464332		
			Skin cancer	Phase 1 dose escalation/expansion study	Completed	NCT02097875	Yamada et al. (2021)	
			Glioma	Phase 1 dose escalation/expansion study	Completed	NCT02234297	Patil et al. (2019)	
			Pediatric subjects with primary central nervous system tumor	Phase 1 dose escalation/expansion study	Completed	NCT02462629		
			Solid tumors (surgical excision)	Phase 1 exploratory study of the safety	Completed	NCT02496065	Dintzis et al. (2019)	
			Pediatric subjects with primary central nervous system tumor	Phase 2/3	Completed	NCT03579602		
			Oral cavity squamous cell carcinoma and high-grade dysplasia	Phase 1/2	Recruiting	NCT05316688		
Xen2174	*Conus marmoreus*	Norepinephrine transporter inhibitor	Cancer patients with chronic pain	Phase 2b	Completed	EUCTR 2010-019109-40BG	Okkerse et al. (2017)	Discontinuation due to dose-limiting toxicity
Contulakin-G	*Conus geographus*	Neurotensin receptor subunit of the NMDA receptor (hNTR1) agonist	Central neuropathic pain following spinal cord injury	Phase 1	Completed		Sang et al. (2016)	Discontinuation due to financial issues
Vc1.1 (ACV-1)	*Conus victoriae*	α9α10 nAChR antagonist	Healthy volunteers	Phase 1 multiple ascending dose study of the safety, tolerability and pharmacokinetics	Completed	ACTRN12605000408684		
			Diabetic peripheral neuropathic pain or post-herpetic neuralgia	Phase 2a study of the safety, tolerability, pharmacodynamics and pharmacokinetics	Stopped early	ACTRN12607000201471		Discontinuation due to lack of efficacy
ShK-186 (dalazatide)	*Stichodactyla helianthus*	$K_V1.3$ channel antagonist	Healthy volunteers	Phase 1 multiple ascending dose study of the safety, tolerability and pharmacokinetics	Completed	NCT02446340		
			Plaque psoriasis	Phase 1 study of the safety, tolerability and pharmacodynamics	Completed	NCT02435342	Tarcha et al. (2017)	
SOR-C13	*Blarina brevicauda*	TRPV6 calcium channel inhibitor	Advanced solid tumors	Phase 1 dose escalation study	Completed	NCT01578564	Fu et al. (2017)	
			Advanced solid tumors	Phase 1	Completed	NCT03784677		

Disintegrins are components of snake venoms that interact with integrins through the RGD domain (see Table 2). Because integrins are involved in angiogenesis and metastasis, integrin ligands are potentially potent anticancer reagents. For instance, obtustatin, a disintegrin inhibitor of the α1β1 integrin isolated from the venom of *Macrovipera lebetina obtusa* venom, inhibits melanoma growth in mice (Brown et al., 2008). The inhibition mechanisms are mainly due to obtustatin's anti-angiogenic activity, which activates apoptosis in endothelial cells. Obtustatin also reduces tumor size in sarcoma-bearing mice, via angiogenesis inhibition (Ghazaryan et al., 2015; Ghazaryan et al., 2019). Contortrostatin, a disintegrin homodimer derived from the venom of *Agkistrodon contortrix contortrix*, is another potent integrin inhibitor, that is selective for β1, β3, and β5 integrins (Zhou et al., 2000a). Contortrostatin, although non-cytotoxic, inhibits the adhesion and invasion of breast cancer cells *in vitro* (Zhou et al., 2000b). This anti-invasive effect was attributed to the blockage of αvβ3, an integrin highly expressed in metastatic cells. Interestingly, migration and invasion are also reduced in prostate cancer. However, this effect cannot be attributed to αvβ3 inhibition as this prostate cancer cell line (PC-3) does not express this integrin but αvβ5 may be an alternative target (Lin et al., 2010). Furthermore, encapsulation of contortrostatin in liposomes prevents potential clinical side effects such as platelet binding and immunogenicity (Swenson et al., 2004). These findings are promising for the long-term use of the compound in clinical trials. According to a recent review published in 2020, the next step will be to submit an investigational new drug application to initiate a phase 1 clinical trial (Schonthal et al., 2020). In addition, Zhang and co-workers have recently developed a recombinant fusion protein known as IL-24-CN, a tumor suppressor protein (Zhang et al., 2021). Overexpression of IL-24 can inhibit cancer cell proliferation and induce apoptosis. The study successfully demonstrated the growth-suppressive and apoptosis-inducing effects of IL-24-CN on melanoma cells.

Vicrostatin is a disintegrin produced by recombination of the C-terminal tail of echistatin with contortrostatin (Minea et al., 2010). Despite its immunogenicity, this construct not only retains the native binding properties of contortrostatin but also shows an innovative binding to the integrin α5β1. Intravenous administration of vicrostatin in mice showed no side effects. As previously demonstrated for other disintegrins, vicrostatin can inhibit angiogenesis, thereby reducing both tumor vascular density and metastasis (Minea et al., 2010). In the context of glioma treatment, brachytherapy is an emerging method in which radioactive material is delivered to the tumor to minimize damage to healthy tissue. Radioiodinated vicrostatin (^{131}I-VCN) has been developed to treat glioma, a tumor type expressing high levels of integrins. ^{131}I-VCN has been successfully tested in glioma animal models and has been shown to prolong survival (Swenson et al., 2018). Moreover, Jadvar and colleagues have recently developed a ^{64}Cu-labeled vicrostatin probe for PET imaging of tumor angiogenesis in prostate cancer, suggesting that venom components can be used as both diagnostic and therapeutic tools (Jadvar et al., 2019). Other disintegrins found in snake venom are also listed in Table 4.

Cathelicidins are a class of antimicrobial peptides found in insects, fish, amphibians, and mammals. They are effective against a wide range of bacteria, fungi, viruses, and protozoa (Wang et al., 2013). Interestingly, these peptides have also shown cytotoxic activity against cancer cells. More specifically, BF-30 is a cathelicidin-like polypeptide, extracted from *Bungarus fasciatus*. BF30 inhibits the proliferation of metastatic melanoma cells without affecting normal cells (Wang et al., 2013). *In vivo*, this compound effectively reduces cell proliferation and has low toxicity in mice. Furthermore, BF30 reduces angiogenesis by decreasing VEGF gene expression levels. BF-30 derivatives have been developed to improve the pharmacokinetic and pharmacodynamic parameters of BF-30 (Qi et al., 2020).

In the venom of *Crotalus durissus terrificus,* crotamine is a β-defensin that possesses cell-penetrating properties by efficiently translocating into cells (Pereira et al., 2011). Crotamine exhibits targeted cytotoxicity against melanoma cell lines, with a specificity of 5 times higher than normal cells. Interestingly, no toxicity was observed in treated animals. The precise mechanisms underlying the cytotoxic effects of crotamine are not well understood. One hypothesis is that crotamine is endocytosed and transported to the lysosome, resulting in an increase in lysosomal content and the leakage of content into the cytosol. Furthermore, lysosomes have been shown to trigger intracellular Ca^{2+} transients and affect mitochondrial membrane potential (Nascimento et al., 2012). In addition, crotamine has been found to accumulate in tumor cells, suggesting that it could act as a diagnostic tool like vicrostatin (Kerkis et al., 2014). To facilitate the advancement of crotamine in clinical trials, an oral administration of the molecule was assessed in animals (Campeiro et al., 2018). Small changes in glucose clearance, total cholesterol, triglyceride, and lipoprotein levels were measured but were considered harmless. No other adverse toxic effects were observed. Synthetic crotamine has since been produced with similar properties to the native peptide, allowing for improved analogs with fewer potential side effects and better properties (de Carvalho Porta et al., 2020). This provides an opportunity for further research into developing new applications for these analogs.

2.3.3 Neurological disorders

Snake venom contains other toxins that may have potential in the treatment of neurodegenerative diseases, such as Alzheimer's and Parkinson's (see Figure 4). For instance, interesting bioactivity in the context of Alzheimer's disease comes from fasciculin, a 61-residue 3FTx isolated from *Dendroaspis angusticeps* (Waqar and Batool, 2015). By inhibiting the acetylcholinesterase (AChE), fasciculin restores normal levels of acetylcholine (Harel et al., 1995). Since a reduction in this neurotransmitter leads to cognitive impairment, particularly the memory loss associated with Alzheimer's disease (Winblad and Jelic, 2004), the effect of fasciculin may be beneficial. In parallel, RVV-V, a peptide discovered in the venom of *Daboia russelli russelli* is a procoagulant enzyme activator of factor V that destabilizes β-amyloid (Aβ) aggregates. Alzheimer's disease is characterized by insoluble plaques composed of Aβ peptide fibrils. Destabilizing these aggregates would help prevent amyloidosis (Bhattacharjee and Bhattacharyya, 2013).

Ionotropic γ-aminobutyric acid type A ($GABA_A$) receptors are massively present in the central nervous system. They modulate Cl^- conductance across the cell membrane and thus shape synaptic transmission (Sieghart, 2006). These receptors have been implicated in many diseases including epilepsy, schizophrenia, and chronic pain. Some snake toxins (α-bungarotoxin and α-cobratoxin)

TABLE 4 Other snake toxins with a potential interest in drug discovery.

Name	Species	Demonstrated effects	References
Leberagin-C (Leb-C)	*Macrovipera lebetina transmediterrannea*	- Reduction of adhesion, migration and invasion of breast cancer cells - Angiogenesis inhibition *in vitro* and *in vivo* - Reduction in tumor size *in vivo*	Limam et al. (2023)
r-viridistatin 2	*Crotalus viridis viridis*	- Inhibition of platelet aggregation - Inhibition of adhesion, migration and invasion of cancer cells - Inhibition of lung colonization of melanoma cells (B16F10) *in vivo*	Lucena et al. (2012)
Crotalicidin	*Crotalus durissus terrificus*	- Anti-tumoral effects - Anti-microbial effects - Anti-fungal activity - Antichagastic activity	Falcao et al. (2015) Perez-Peinado et al. (2020) Klaiss-Luna et al. (2023) Cavalcante et al. (2017) Aguiar et al. (2020) Bandeira et al. (2018)
Micrurotoxin-1 and 2	*Micrurus mipartitus*	$GABA_A$ receptor activity modulation	Rosso et al. (2015)

show activity for $GABA_A$ receptors, but unfortunately also act on nAChRs avoiding any easy use of these toxins for medical purposes.

The venom of the Eastern green mamba, *Dendroaspis angusticeps*, but also the black mamba *Dendroaspis polylepis polylepis* (black mamba), contains muscarinic toxins that selectively target muscarinic acetylcholine receptors (mAChRs; M1 – M5). These toxins exhibit high affinity, selectivity, and low reversibility for their receptors (for a table with the inhibition constants of each toxin for each channel subtype, see the review by Servent et al. (2011)). M1, M4, and M5 are mainly found in the central nervous system, whereas M2 and M3 are found in the central and peripheral nervous systems. Muscarinic toxins offer the possibility to regulate dysfunctional receptors and thus provide solutions for neurological diseases as well as diseases related to the peripheral system, such as chronic obstructive pulmonary disease, incontinence, overactive bladder, etc. (Servent et al., 2011). The Eastern green mamba venom is a rich source of drug candidates as another toxin, called mambaquaretin-1 (MQ-1) shows high affinity and selectivity for the vasopressin type 2 receptor (V2R), with a Ki = 2.81 nM (Ciolek et al., 2017). Interestingly, MQ-1 does not interact with the other subtypes of the vasopressin receptors (V1a, V1b) and with the oxytocin receptor OT (Ki > 1 mM), making it a true molecular tool for the specific study of the V2R. From a therapeutic point of view, this Kunitz-type venom protein has the potential to treat polycystic kidney disease (PKDs), a genetic disorder characterized by the formation of numerous cysts in the kidneys, leading to end-stage renal failure. Selective inhibition of the V2 receptor reduces cAMP levels. This molecule stimulates chloride-induced cell proliferation and fluid secretion into the cyst lumen in polycystic kidneys. Since the discovery of MQ-1, eight other mambaquaretin-like toxins have been discovered in mamba's venoms. All of them are antagonists of V2R, interacting with the receptor with nanomolar affinity (Droctove et al., 2022).

3 Harnessing the power of arthropod venom for next-generation therapies

Arthropods are the largest group of animals on Earth, comprising approximately 80% of the 1.5 million described animal species (according to the IUCN Red List in 2023). This phylum includes insects, arachnids, crustaceans, and myriapods, such as bees, scorpions, and spiders (Soltan-Alinejad et al., 2022).

3.1 Scorpion venoms, champions ion channel targeting

Scorpions have evolved over 400 million years to produce powerful toxins that affect various targets, especially localized in the nervous system (Estrada-Gomez et al., 2017). Scorpion venoms include peptides, enzymes, and non-protein compounds, such as salts, free amino acids, lipids, nucleotides, and neurotransmitters (Almaaytah and Albalas, 2014). Peptides are divided into two main classes according to their structural and functional properties: disulfide-bridged peptides (DBPs), and non-disulfide-bridged peptides (NDBPs). Five families comprise the DBPs, sodium channel toxins (NaTx), potassium channel toxins (KTx), chloride channel toxins (ClTx), calcium channel toxins (CaTx), and transient receptor potential channel toxins (TRPTx), all described in Table 5. Among the NDBPs, short antimicrobial peptides (AMPs) and bradykinin potentiating peptides (BPPs) are commonly found (Hmed et al., 2013). As seen in the case of the snakes, scorpions produce L-amino acid oxidases (LAAOs), serine proteases, hyaluronidases, metalloproteinases, nucleotidases, and phospholipases A2 (Soltan-Alinejad et al., 2022). Although NDBPs do not have specific ion channel targets, they are increasingly studied for their potential as antimicrobial, antiviral, and anticancer agents (Almaaytah and Albalas, 2014).

Overall, scorpion DBP toxins primarily target ion channels (ICs). Because ICs modulate essential functions in the body, their dysfunction can lead to the development of neurological disorders such as chronic pain, depression, autoimmune diseases, epilepsy, and cancer, as well as metabolic diseases such as diabetes. These dysfunctions, known as channelopathies, can be caused by the deregulation of channel opening/closing, changes in current amplitude, or problems regulating protein activity (Mendes et al., 2023). Neurotoxins of arthropods targeting these channels with

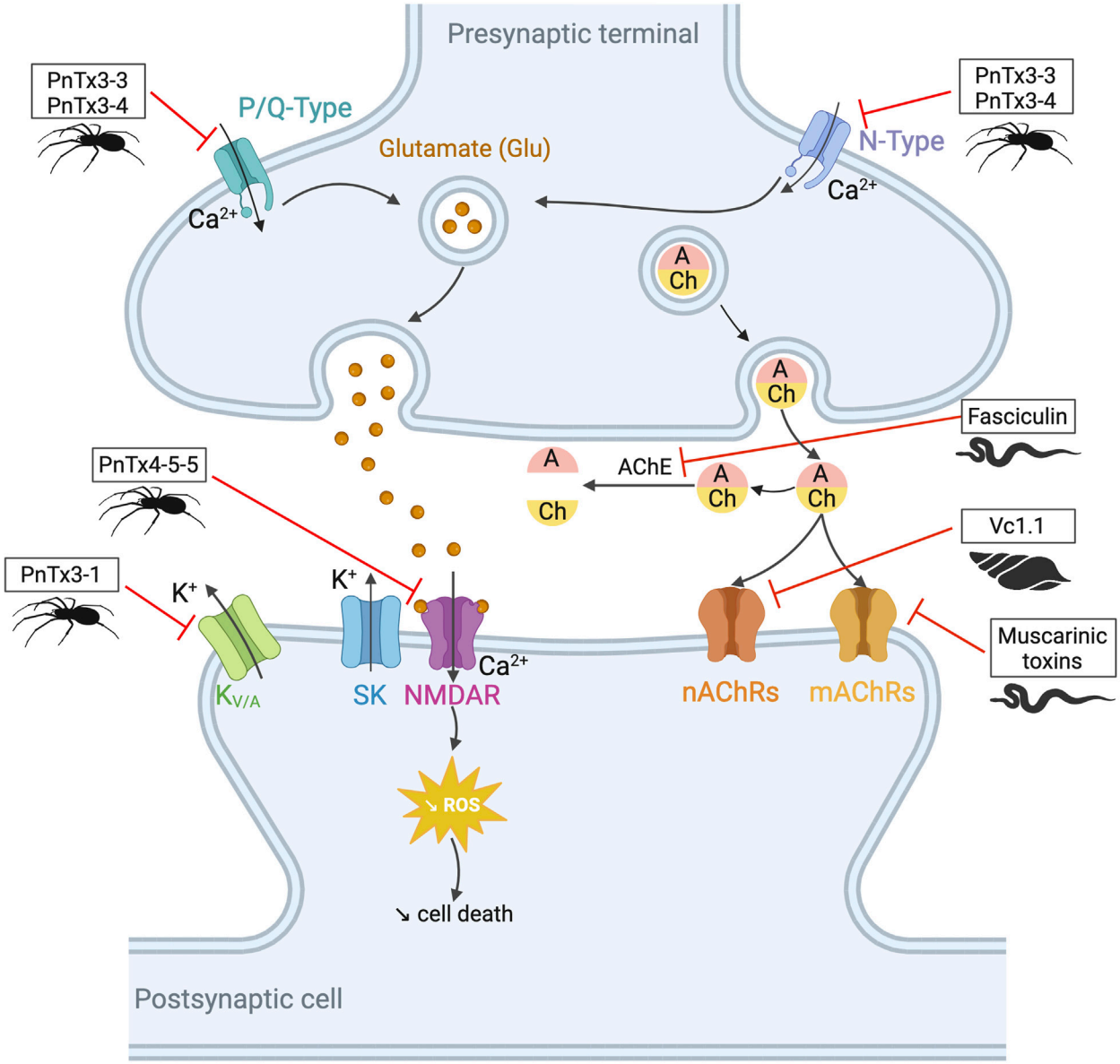

FIGURE 4
Potential toxin inhibitors involved in neurological disorders, such as Alzheimer's disease, Parkinson's disease, and chronic pain. Vc1.1 has antagonistic activity on neuronal nAChRs involved in neuropathic pain (Sandall et al., 2003; Bordon et al., 2020). Inhibition of AChE by fasciculin helps to counteract the acetylcholine deficiency seen in disorders such as Alzheimer's disease. Blocking $K_{V/A}$ channels with PnTx3-1 reduces memory deficits (Gomes et al., 2013). PnTx4-5-5 has a neuroprotective effect by blocking the NMDA receptors by reducing glutamate release (Silva et al., 2016). N- and P/Q-type channels also release glutamate by controlling the calcium flux. PnTx3-3 and PnTx3-4 have inhibitory activity on these two channels (Vieira et al., 2005; Dalmolin et al., 2011; Souza et al., 2012; Pedron et al., 2021). The reduction of glutamate prevents ROS formation. Muscarinic toxins can regulate mAChRs when they are dysfunctional. Adapted from "NMDAR-dependent long-term depression (LTD)," Created with BioRender.com (2023).

remarkable specificity and potency constitute true molecular scalpels for studying IC distributions, functions, structures, and real candidates for tomorrow's drugs. This review section is divided into five parts corresponding to the sodium, potassium, chloride, and calcium channels targeted, as well as other potential activities of scorpion venom.

3.1.1 Sodium channels toxins (NaTxs)

Voltage-gated sodium channels (Na_v) play an essential role in pain transmission, especially with $Na_v1.7$, $Na_v1.8$, and $Na_v1.9$ subtypes, the most expressed in sensory neurons. Scorpion-derived peptides exert analgesic effects by regulating various Na_v channels, especially $Na_v1.1$, $Na_v1.6$, $Na_v1.7$, $Na_v1.8$, and $Na_v1.9$ (Cummins et al., 2007; Eagles et al., 2022). Many NaTxs possess analgesic potency. Among them, BmK AS, BmK AS1, and BmK IT2 act on $Na_v1.8$, $Na_v1.9$, and $Na_v1.3$ by reducing the peak Na^+ conductance in dorsal root ganglia (DRG) neurons. Others like BmKM9, BmK AGAP, and AGP-SYPU1 inhibit the inactivation of the activated $Na_v1.4$, $Na_v1.5$, and $Na_v1.7$. All these peptides are derived from *Buthus martensii* Karsch. BmK AGAP alleviates inflammatory pain by inhibiting the expression of peripheral and spinal mitogen-activated protein kinases and induces long-lasting

TABLE 5 DBPs scorpion families.

Toxin family names	Information	Examples	References
NaTx	Major component of scorpion venom 13–56 residues 3–4 disulfide bridges Two subgroups: α-NaTx (bind to receptor site 3) and β-NaTx (bind to the receptor site 4)	α-toxin OD1 (*Odontobuthus doriae*):  PDB 4HHF	Xia et al. (2023)
KTx	23–64 residues 2–4 disulfide bridges Six subgroups depending on their sequence and structural folds: α-KTx, β-KTx, γ-KTx, κ-KTx, δ-KTx, λ-KTx, and ε-KTx	Charybdotoxin (*Leiurus quinquestriatus*): 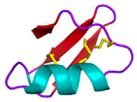 PDB 2CRD	
CaTx	33–36 residues 2–3 disulfide bridges Two subgroups with an ICK motif or a disulfide-directed β-hairpin (DDH) fold	ICK motif - Imperatoxin (*Pandinus imperator*): 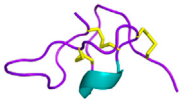 PDB 1IE6	
		DDH motif - U1-liotoxin-Lw1a (*Liocheles australasiae*): 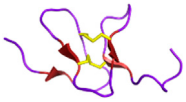 PDB 2KYJ	
ClTx	35–38 residues 4 disulfide bridges	Chlorotoxin (*Leiurus quinquestriatus*): 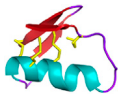 PDB 1CHL	
TRPTx	2–3 disulfide bridges Recently discovered	Wasabi receptor toxin (*Urodacus manicatus*): 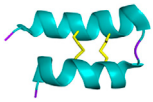 PDB 6OFA	

analgesia by blocking TRPV1 currents when injected with lidocaine. It is considered a promising analgesic due to its multitarget capabilities (Kampo et al., 2021). Despite the discovery of numerous potent and selective Na_v channel inhibitors, which are pharmacologically interesting, very few of these inhibitors have resulted in effective pain relief in preclinical models or human clinical trials (Eagles et al., 2022).

3.1.2 Potassium channels toxins (KTxs)

Potassium channels are divided into four groups according to their activation mode and the number of transmembrane segments (TM). Inwardly rectifying K^+ (KIR) channels have 2 TM and two pore domains, whereas potassium channels (K2P) consist of 4 TM and two pores, K_{Ca} are calcium-activated potassium channels with 6 or 7 TM, and K_V are voltage-gated potassium channels with 6 TM (Wulff et al., 2009). K_V channels have been implicated in several diseases including cancer, autoimmune, neurological, and cardiovascular diseases.

In 1984, patch-clamp studies highlighted the role of the voltage-gated K_V channels in the activation of thymus-derived lymphocytes (T cells). Therefore, ion channels are involved in the immune response (Matteson and Deutsch, 1984). $K_V1.3$ (KCNA3) and calcium-activated $K_{Ca}3.1$ channels are primarily responsible for K^+ efflux and are important therapeutic targets in various autoimmune diseases, such as multiple sclerosis, rheumatoid arthritis, and type-1 diabetes (Chandy and Norton, 2017). Charydbotoxin (ChTX), identified from the venom of *Leiurus quinquestriatus*, is a blocker of K_V channels (Kd = 3 nM) but also of intermediate conductance calcium-activated channels ($IK_{Ca}1$) (Kd = 5 nM). Other inhibitors of the $K_V1.3$ channel are margatoxin (MgTX), from *Centruroides margaritatus*, and HsTX1 from *Heterometrus spinnifer* venom. They are both potent blockers in the picomolar range of $K_V1.3$. HsTX1 is a potentially attractive candidate for the treatment of $K_V1.3$-related diseases due to its selectivity ($IC_{50}(K_V1.3)$ = 29 ± 3 pM; $IC_{50}(K_V1.1)$ = 11,330 ± 1,329 pM). To further improve selectivity, analogs of this toxin (HsTX1[R14A] and HsTX1 [R14Abu]) have been developed. The arginine at position 14 is replaced by a neutral residue to prevent ionic interaction with $K_V1.1$. This toxin binds to the E353 amino acid of this potassium channel

but does not bind to $K_V1.3$. Thus, the affinity for $K_V1.1$ is reduced without affecting the affinity for $K_V1.3$. The selectivity of HsTX1 [R14A] is then more than 2,000-fold for $K_V1.3$ over $K_V1.1$ (Rashid et al., 2014). Other synthetic analogs of scorpion toxins show potent activity against $K_V1.3$. Among them, OSK-1[E16K, K20D] has a five-fold higher IC_{50} than the native peptide OSK-1 (α-KTx3.7) from *Orthochirus scrobiculosus*: 3 pM versus 14 pM, respectively (Mouhat et al., 2005). Other peptides are listed in Table 6.

Scorpion venom also contains several peptides with anticancer activity (see Figure 5). For instance, κ-hefutoxin-1, a peptide isolated from the venom of *Heterometrus fulvipes*, is a potassium channel inhibitor. Specifically, it can inhibit the oncogenic $K_V10.1$ channel, which is overexpressed in several types of cancer (Pardo et al., 1999; Moreels et al., 2017). However, the effects of this peptide on cancer cells remain to be determined. Interestingly, P01-toxin, extracted and purified from the venom of *Androctonus australis* is a potent inhibitor of the SK2 potassium channel (Mlayah-Bellalouna et al., 2023). While the peptide was shown to reduce cell viability, adhesion, and migration in glioma cells, no such effects were observed in breast and colon cancer cells. These results suggest that SK2 channels are involved in the formation of glioma tumors. Another peptide toxin derived from the same species, AaTs-1, shares more than 80% homology with chlorotoxin (Aissaoui-Zid et al., 2021). Like chlorotoxin, AaTs-1 binds to chloride channels, MMP-2, and annexin 2, leading to a reduction in glioma cell proliferation and migration. In terms of anticancer activity, the effects of *Buthus martensii Karsh* antitumor analgesic peptide (BmK AGAP) on breast cancer cells have been studied, revealing its ability to inhibit cancer cell stemness, epithelial-mesenchymal transition, migration, and invasion (Kampo et al., 2019). The mechanisms underlying these effects have been investigated, and it has been found that the downregulation of PTX3 via NF-κB and Wnt/β-catenin signaling is critical.

3.1.3 Chloride channels toxins (ClTxs)

ClTxs are divided into two subgroups. The vast majority have an inhibitory cystine knot (ICK) motif, characterized by two disulfide bonds pierced by a third to form a pseudoknot. The second motif, the disulfide-directed hairpin (DDH), would result from a simplification of the ICK motif to only two bonds (Smith et al., 2013). The best-known toxin targeting chloride channels is chlorotoxin, isolated from the venom of *Leiurus quinquestriatus*. Chlorotoxin can also bind to matrix metalloproteinase-2, annexin A2, estrogen receptor α, and neuropilin-1 receptor. This peptide has been extensively studied in the context of glioblastoma and neuroblastoma where those proteins are all involved in cell migration and invasion, as recently reviewed by Boltman and colleagues (Boltman et al., 2023). In addition, chlorotoxin has a wide range of applications, including tumor imaging and combination with other therapeutics or molecules as this peptide can cross the blood-brain barrier (Veiseh et al., 2007; Formicola et al., 2019; Vannini et al., 2021; Dardevet et al., 2022). Numerous clinical trials are underway to establish the safety and pharmacokinetic properties of BLZ-100, a chlorotoxin-based imaging agent containing indocyanine green as a fluorophore (Patil et al., 2019) (see Table 3). The efficacy of chlorotoxin in the treatment of other cancers has also been investigated. Efficacy against cervical cancer cells is significantly improved when coupled with a platinum complex (Graf et al., 2012). In breast cancer, chlorotoxin has the potential to inhibit cell proliferation, migration, and invasion by either directly binding to the estrogen receptor (ER) or by preventing estrogen binding to its receptor. This thereby inhibits the ER signaling pathway (Wang et al., 2019).

3.1.4 Calcium channels toxins (CaTxs)

Because calcium channels are involved in pain pathways, Parkinson's disease, epilepsy, seizures, migraine, and ataxia, they are promising and interesting targets (Zamponi, 2016). As scorpion venoms are a rich source of toxins that act on Ca^{2+} channels, they may have therapeutic potential. Such scorpion toxins include calcins, a family of cell-penetrating peptides composed of 33 residues (35 for hadrucalcin) and three disulfide bridges. They have an ICK motif and potently target Ryanodine receptors (RyRs), intracellular ion channels that regulate the Ca^{2+} release from the endoplasmic and sarcoplasmic reticulum, thereby triggering myocardial contraction (Vargas-Jaimes et al., 2017). Imperacalcin (formerly imperatoxin A), identified from the venom of *Pandinus imperator*, is the first member of the calcium-targeting toxins to bind to RyR1 with nanomolar affinities (Valdivia et al., 1992). Subsequently, maurocalcin, from the venom of *Scorpio maurus palmatus*, was isolated based on sequence similarity to imperacalcin (82% sequence identity). Both increase skeletal RyR (RyR1) activity but also have a nanomolar affinity for cardiac RyR (RyR2) (De Waard et al., 2020). Other toxins of interest are listed in Table 6.

CPP-Ts, isolated from *Tityus serrulatus* venom, is a cell-penetrating peptide, that crosses both cellular and nuclear membranes. This peptide increases the contractile frequency of cardiomyocytes by activating the inositol 1,4,5-trisphosphate receptor (InsP3R), a ligand-gated Ca^{2+} release channel. This activation leads to a transient change in intracellular calcium levels. CPP-Ts can be internalized by cancer cells and not by normal cell lines, making it a potential intranuclear delivery tool to target cancer cells (Oliveira-Mendes et al., 2018).

3.1.5 Other targets

Scorpion venom also contains antimicrobial peptides (AMPs), which belong to the group of non-disulfide-bridged peptides (NDBPs) (Almaaytah and Albalas, 2014). Their role in venom and their molecular target remains to be elucidated. However, the antimicrobial peptides Smp43 and Smp24 from the Egyptian scorpion *Scorpio maurus palmatus* were studied in different cancer cell types including hepatocellular, non-small cell lung, and leukemia cancer cell lines. Smp43 exhibits antitumor properties in hepatocellular carcinoma by inducing apoptosis, autophagy, necrosis, and arresting cell cycle progression (Chai et al., 2021). In addition, both peptides stimulate pyroptosis, a regulated cell death mechanism that recruits the inflammasome, which subsequently activates caspases (Elrayess et al., 2021). These two peptides also induce a loss of mitochondrial membrane potential, leading to the accumulation of reactive oxygen species in lung and hepatocellular cancer cells (Guo et al., 2022; Nguyen T. et al., 2022; Deng et al., 2023). Interestingly, Smp43 only has minor effects on a lung fibroblast cell line, MRC-5 (Deng et al., 2023).

Scorpion peptides have also been investigated for the treatment of malaria. This disease, caused by *Plasmodium falciparum* infection,

TABLE 6 Other scorpion toxins with a potential interest in drug discovery.

Name	Species	Demonstrated effects	References
ADWX-1	Modification of BmKTX (from *Buthus martensi*)	$K_V1.3$ inhibition	Han et al. (2008)
Maurotoxin	*Scorpio maurus*	$IK_{Ca}1$ channel inhibition	Kharrat et al. (1996) Castle et al. (2003)
Hemicalcin	*Hemiscorpius lepturus*	Stimulation of ryanodine binding to ryanodin receptor type 1 (RyR1)	Shahbazzadeh et al. (2007)
Opicalcin 1 and 2	*Opistophthalmus carinatus*	Stimulation of ryanodine binding to RyR	Zhu et al. (2003)
Hadrucalcin	*Hadrurus gertschi*	Stimulation of ryanodine binding to RyR1 and 2	Schwartz et al. (2009)
Urocalcin	*Urodacus yaschenkoi*	Stimulation of ryanodine binding to RyR	Luna-Ramirez et al. (2013)
Vejocalcin	*Vaejovis mexicanus*	Stimulation of ryanodine binding to RyR	Xiao et al. (2016)

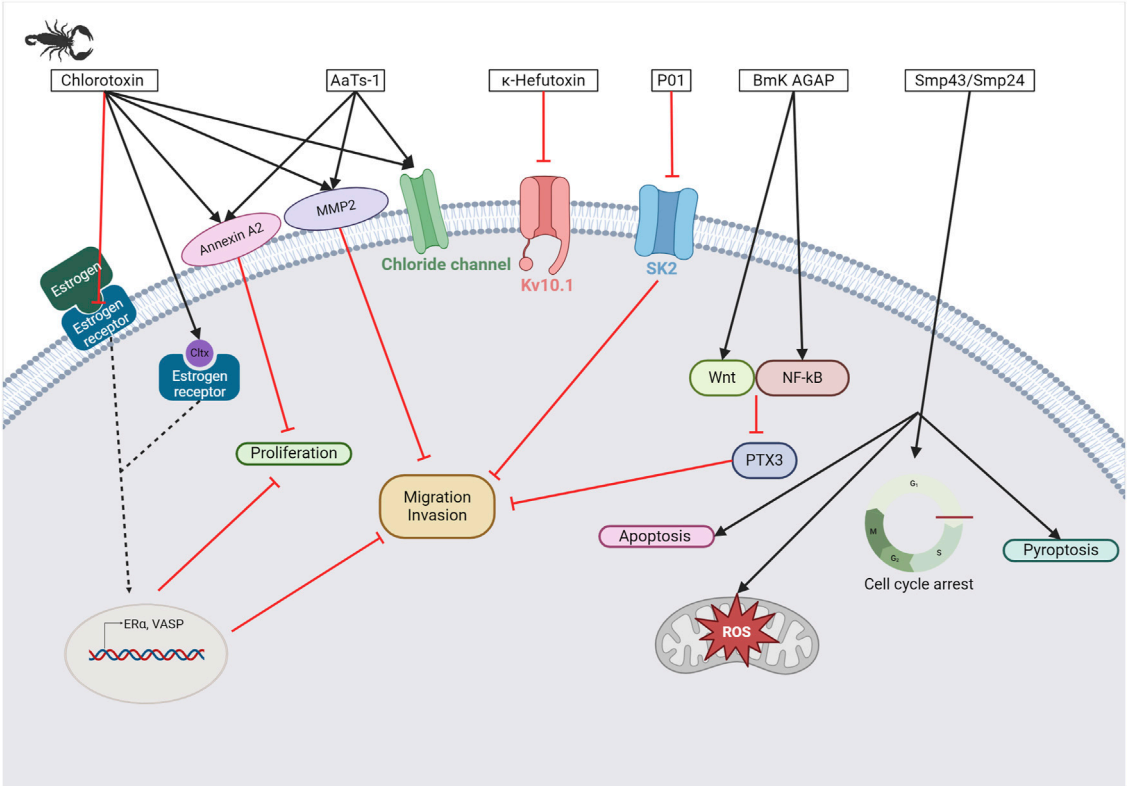

FIGURE 5
Scorpion toxins as potential anticancer therapy. Chlorotoxin has four cellular targets: estrogen receptor (ERα), annexin A2, MMP2, and chloride channel. Overall, the binding of chlorotoxin to these targets leads to inhibiting cell proliferation and/or reducing cancer cell migration and invasion (Boltman et al., 2023). Binding to chloride channels can also help to visualize tumor sites in brain tumors. Sharing 80% of homology with chlorotoxin, AaTs-1 binds annexin A2, MMP2, and chloride channels (Aissaoui-Zid et al., 2021). κ-hefutoxin-1 is a $K_V10.1$ inhibitor, a potassium channel known to be overexpressed in several cancer types (Pardo et al., 1999; Moreels et al., 2017). P01 is a potent SK2 channel inhibitor that leads to the inhibition of cancer cell migration and invasion (Mlayah-Bellalouna et al., 2023). BmK AGAP has been shown to reduce cancer cell migration and invasion by the downregulation of PTX3 via NF-κB and Wnt/β-catenin (Kampo et al., 2019). Finally, Smp43 and Smp24 are two antimicrobial peptides that can trigger apoptosis, pyroptosis, an accumulation of reactive oxygen species, or a cell cycle arrest in cancer cells (Chai et al., 2021; Elrayess et al., 2021). Created with BioRender.com (2024).

occurs in more than one hundred countries and can be fatal, especially in children (Murray et al., 2012). Scorpine, isolated from *Pandinus imperator*, shows activity in the ookinete and gamete stages of the development of the parasite *Plasmodium berghei*. Since the developmental stages of the two parasites are the same, scorpine could represent a promising model for malaria treatment (Conde et al., 2000). Lastly, some peptides with antimicrobial activities are also important antimalarial candidates, such as meucin-24, meucin-25, and hadrurin (Ortiz et al., 2015).

3.2 Spider venoms, on the way to a new drug for heart attack and beyond

Spiders, like scorpions, have evolved over more than 400 million years. Although about 50,000 species have been described so far, the diversity is estimated to be more than 100,000 (Agnarsson et al., 2013; World Spider Catalog, 2023). Spider venoms consist of proteins, peptides, nucleotides, and small molecular weight organic molecules, such as organic acids, nucleotides, amino acids, amines . . ., and salts (Smith et al., 2015). Peptides without disulfide bonds, often antimicrobial peptides, are represented in these venoms but their major components are disulfide-rich peptides, which possess an ICK motif, in most cases, or a DDH fold, a Kunitz motif, a colipase-like fold or a helical arthropod-neuropeptide-derived (HAND) motif (for more information on these motifs, see the review by Langenegger et al. (2019). Ion channels are the main targets of spider toxins and, more precisely voltage-dependent sodium and calcium channels (Na_V and Ca_V) representing up to 75% of the total number of receptors targeted. Various enzymes, such as hyaluronidase, phospholipase A2, and proteases, are the primary protein families found in spider venom. Therefore, they contain a valuable collection of biologically active peptides of interest for drug discovery (King and Hardy, 2013). Unfortunately, spider venom has long remained unexplored. For a long time, venom research focused only on certain species of venomous animals, primarily snakes (King, 2011). "The limited availability of venom from species that produce small amounts or are rare was due to unsuitable techniques uses. The development of omics techniques like transcriptomics and proteomics has opened up opportunities for the study of these long-neglected species" (Holford et al., 2018).

3.2.1 Regulation of insulin secretion

As mentioned above, arthropod venom contains toxins with activities on ion channels. These channels are involved in physiological mechanisms, including the regulation of insulin secretion by glucose. They allow membrane depolarization and trigger an action potential that induces the release of insulin granules. The channels involved in this process are ATP-sensitive potassium (K_{ATP}) channels. Their closure leads to the depolarization of the cell, which opens voltage-dependent calcium (Ca_V) channels, triggering the action potential that allows insulin granules to be released from the pancreas (Ashcroft and Rorsman, 1989). This is followed by repolarization of the cell with activation of large conductance calcium-activated K^+ (BK) and voltage-gated potassium ($K_V2.1$ and $K_V1.7$) channels (Herrington, 2007). κ-theraphotoxin-Gr1a (hanatoxin-1, HaTx1), a toxin with inhibitory activity on these $K_V2.1$ channels, was isolated from the venom of the Chilean pink tarantula, *Grammostola rosea* (Swartz and MacKinnon, 1995). By blocking them, the HaTx1 increases glucose-stimulated insulin secretion (see Figure 6) (Herrington et al., 2005). Unfortunately, this peptide, as well as guangxitoxin-1 (GxTx1E, κ-theraphotoxin-Pg1a), isolated from the venom of the Chinese tiger tarantula (*Chilobrachys guangxiensis*), also shows an affinity for other various channels, such as $K_V4.2$ and $Ca_V2.1$ and $K_V2.2$ and 4.3 respectively. This lack of selectivity prevents its use as a treatment (Herrington, 2007).

3.2.2 Chronic pain and neurological disorders

The ion channel activity of spider venom peptides may lead to potential treatments for chronic pain (see Figure 4). Acid-sensing ion channels (ASICs), transient receptor potential (TRP), and Na_V and Ca_V channels are involved in the transduction of stimuli into depolarization of the cell membrane and are therefore important in the development of analgesics (King and Vetter, 2014). Among the ion channels, voltage-gated calcium channels are the main target of spider toxins. For instance, the venom of *Phoneutria nigriventer,* one of the most studied with not less than 41 neurotoxins identified, is a rich source of potential analgesic drugs due to its activity on Ca_V channels (Peigneur et al., 2018). ω-ctenitoxin-Pn2a (also known as PnTx3-3) and ω-ctenitoxin-Pn4a (PnTx3-6 or Phα1β), two toxins identified from this venom, both block $Ca_V2.1$, $Ca_V2.2$, and $Ca_V2.3$ channels, as well as Ca_V1 and $Ca_V1.2$. Despite the apparent lack of selectivity, the peptides show analgesic activity in mouse models without side effects (Vieira et al., 2005; Dalmolin et al., 2011). As PnTx3-3 reduces pain and depressive symptoms, it is a credible drug candidate for fibromyalgia (Pedron et al., 2021). In addition to opioid treatment, PnTx3-6 potentiates the analgesic effect of morphine and reduces the adverse effects of regular morphine use, such as tolerance, constipation, and withdrawal symptoms (de Souza et al., 2011). *Phoneutria nigriventer* venom is also being studied for Huntington's disease, a fatal neurodegenerative disorder, as Joviano-Santos and colleagues recently demonstrated the neuroprotective effect of PnTx3-6 (Joviano-Santos et al., 2021). Indeed, neuronal survival was improved, and the release of L-glutamate was reduced in mice treated with the toxin. Huntington's disease is associated with the formation of insoluble aggregates and glutamatergic excitotoxicity associated with progressive neuronal death. This led to an improvement in behavioral and morphological parameters related to motor tests (Joviano-Santos et al., 2021). PnTx3-6 may have important potential in various diseases. Compared to current drugs (morphine and ziconotide), the spider toxin is more effective and has fewer side effects (Rigo et al., 2013). The inconvenience is the limitation of administration, as it is unlikely to be available orally (Tonello et al., 2014).

Other toxins inhibiting $Ca_V2.2$ (N-type) channels are of primary interest because of their involvement in pain pathways (for review see Sousa et al., 2013). In addition to chronic pain, $Ca_V2.1$ (or P/Q type) channels have been implicated in many neurological disorders including migraine, Alzheimer's disease, and epilepsy (Nimmrich and Gross, 2012; Inan et al., 2024). ω-Agatoxin-Aa4a (ω-agatoxin IVA) and ω-agatoxin-Aa4b (IVB), from the venom of the American funnel-web spider *Agelenopsis aperta*, are the most selective blockers of this calcium channel subtype, with an IC_{50} of about 2 and 3 nM, respectively. The remaining problem for this type of peptide is the poor permeability of the blood-brain barrier (Smith et al., 2015).

$Na_V1.7$ – $Na_V1.9$ voltage-gated sodium channels are expressed in nociceptive neurons and therefore play a critical role in pain signaling. $Na_V1.7$ is by far the most important target for analgesic development (Alexandrou et al., 2016). All spider toxins identified to bind to this channel come from theraphosid spiders (tarantulas) and share the ICK motif. These include huwentoxin-IV (*Haplopelma schmidti*), GpTX-1 (*Grammostola portei*), ceratotoxin-1 (*Ceratogyrus cornuatus*), Pn3a (*Phamphobeteus nigricolor*), β-theraphotoxin-Tp2a/ProTx-II (*Thrixopelma pruriens*), and

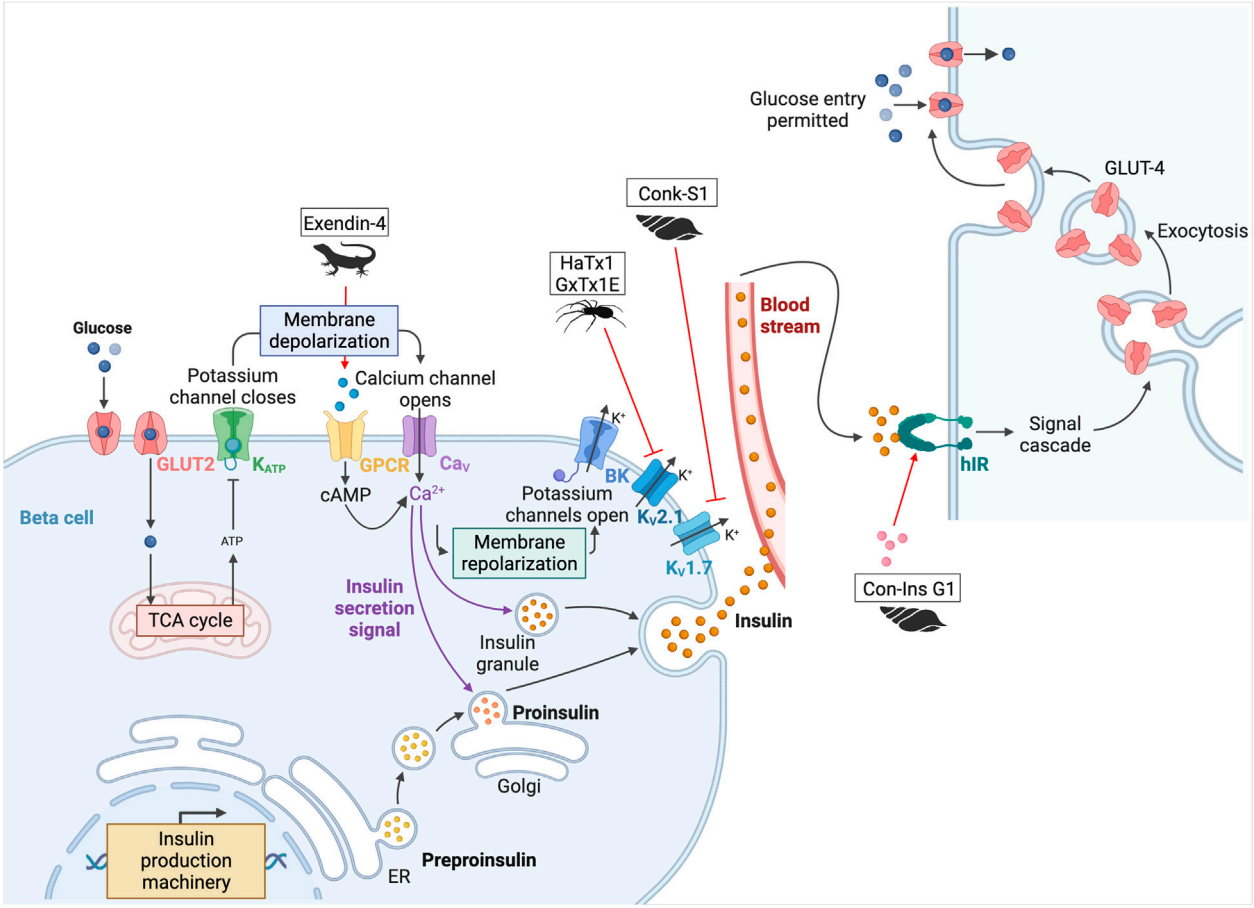

FIGURE 6
Potential toxins involved in the insulin pathway. Glucose is transported into pancreatic beta cells by facilitated diffusion through GLUT2 glucose transporters. Once inside the cell, glucose is converted to ATP by glycolysis and oxidative phosphorylation. When the ATP/ADP ratio is high, K^+ channels are inhibited, leading to cell membrane depolarization. Closure of the K_{ATP} channels leads to the depolarization of the cell, which opens the Ca_V channels and triggers the action potential that allows insulin granules to be released from the pancreas. This is followed by repolarization of the cell with activation of BK, $K_V2.1$, and $K_V1.7$. Once produced, insulin is delivered to target tissues, such as the liver, adipocytes, muscle, and brain. Insulin binds to hIR, initiating a phosphorylation cascade that ultimately leads to glucose uptake and storage in glycogen, thereby lowering blood glucose levels. HaTx1 and GxTx1E are two spider peptides, and Conk-S1 is a cone snail peptide that inhibits $K_V2.1$ and $K_V1.7$ respectively (Herrington et al., 2005; Herrington, 2007; Finol-Urdaneta et al., 2012). Inactivation of these channels leads to an increase in glucose-stimulated insulin secretion. Another cone snail toxin, Con-Ins G1 is an insulin-like peptide that can activate hIR (Xiong et al., 2020). Finally, the most famous one is exenatide-4, from the Gila monster, which led to the development of the drug exenatide (Byetta©) (Nadkarni et al., 2014). This peptide binds to the incretin hormone GLP-1 receptor. This GPCR stimulates adenylyl cyclase activity and cAMP accumulation, leading to insulin secretion. Adapted from "Insulin production pathway" and "Insulin pathway," created with BioRender.com (2024).

β-theraphotoxin-Cj2a/JzTX-V (*Chilobrachys jingzhao*). ProTx-II is the most potent $Na_V1.7$ blocker (IC_{50} = 0.3 nM) of the six currently known, but none is sufficiently selective to be developed as a therapeutic drug. The recent review from Neff and his co-workers describes the peptide engineering of each toxin to achieve better selectivity and highlights some interesting analogs (Neff and Wickenden, 2021). JNJ-63955918, derived from the ProTx-II, increases the selectivity for $Na_V1.7$ from 100- to 1000-fold compared to other Na_V channels, but unfortunately, the affinity is altered by ~10-fold (Flinspach et al., 2017). AM-6120, derived from JzTX-V, was designed as a potent and selective peptide with >750-fold potency against $Na_V1.5$, 1.6, and 1.8. Similarly, ProTx-II analogs optimized for the ability to cross the blood-nerve barrier *in vivo* have recently been successfully developed (Adams et al., 2022; Nguyen P. T. et al., 2022).

Spider toxins targeting Na_V channels are not only interesting for pain treatment. $Na_V1.1$ channels are involved in Dravet syndrome, a form of infantile epilepsy with ataxia and loss of motor skills. Hm1a, identified from *Heteroscodra maculata* venom, selectively inhibits these $Na_V1.1$ channels and constitutes a promising candidate for treating the disease as its administration improved seizure inhibition and reduced the number of seizures per day in mouse models (Richards et al., 2018).

Spider venom has also been extensively studied in stroke. During cerebral ischemia, which occurs in most strokes (>80%), oxygen is depleted and the brain switches from oxidative phosphorylation to anaerobic glycolysis (Duggan et al., 2021). The pH drops from ~7.3 to 6.0–6.5 and even below 6.0 in severe ischemia. This low pH activates the acid-sensing ion channels 1a which are the main acid sensors in the brain. Some studies have shown that removing or

inhibiting ASIC1a by genetic ablation reduces neuronal death (Xiong et al., 2004). More recently, in 2017, Hi1a, isolated from the Australian funnel-web spider *Hadronyche infensa*, was shown to be a potent inhibitor of ASIC1a. The real revolution of this peptide is its protection of the brain from neuronal damage for 8 h after a stroke event, instead of "only" 2–4 h for other potential drugs such as psalmotoxin 1 (PcTx1) from *Psalmopoeus cambridgei* (Chassagnon et al., 2017). Hi1a has a high sequence similarity to PcTx1, but is a more potent inhibitor, and is more selective with no effect on ASIC2a and ASIC3 channels. As a brief aside, in addition to its neuroprotective activity, PcTx1 is also of interest for reducing cartilage destruction in rheumatoid arthritis, in which ASIC1 plays a key role (Saez and Herzig, 2019). Hi1a has the ideal characteristics to be a therapeutic candidate. Very recently, the Australian government announced the next steps for the development of this peptide as the first spider-based drug. The search for other ASIC inhibitors continues with the Hm3a (*Heteroscodra maculata*) identification, which shows some similarities to PcTx-1. Both completely block ASIC1a with high potency (IC_{50} PcTx-1 ≃ 0.9 nM and IC_{50} Hm3a ≃ 1.3 nM) and have a lower activity for ASIC1b (EC_{50} ≃ 46.5 nM for both). A key advantage of Hm3a over the other drug candidates is its better biological stability (Er et al., 2017).

3.2.3 Cancer

The potential of spider toxins has also been explored in cancer treatment (see Figure 7). Indeed, the venom of *Chilobrachys jingzhao* has been shown to have the ability to inhibit voltage-gated sodium channels. This is the case of JZTx-14, which was first reported by Zhang in 2018, who demonstrated its ability to block current flow in voltage-gated sodium ($Na_V1.2$–1.8) channels (Zhang et al., 2018). Having observed the pro-metastatic effects of $Na_V1.5$ and knowing that inhibitors of $Na_V1.5$ are seen as emerging therapeutic candidates for breast cancer, Wu and colleagues conducted tests to analyze the potential of the peptide as an inhibitor of this channel in triple-negative breast cancer cells (Luo et al., 2020; Wu et al., 2023). Although this peptide did not reduce cancer cell proliferation, an inhibition of cancer cell migration by affecting the extracellular matrix and cell adhesion molecules was observed.

It has also been shown that ASIC1a expression is altered in gliomas. Consequently, inhibition of ASIC1a with PcTx-1 can reduce the proliferation and migration of glioma cells (Rooj et al., 2012). Notably, reducing ASIC1a expression in other types of cancer cells can also limit proliferation, migration, and invasion (Jin et al., 2015). Due to its remarkable selectivity, PcTx-1 has also recently been used as a true pharmacological tool to identify the ASIC1 subtype associated with breast cancer progression (Yang et al., 2020).

With more than 200 species described to date, spiders of the genus *Lycosa* have been extensively studied for this purpose. Lycosin-I peptide, derived from a toxin identified in the venom of *Lycosa singorensis*, a spider found in Central and Eastern Europe, has shown promise as a potential treatment option. Lycosin-I inhibits cancer cell growth *in vitro* by inducing programmed cell death (Liu et al., 2012). It sensitizes cancer cells to apoptosis and inhibits their proliferation by upregulating the cyclin-dependent kinase inhibitor 1B, p27, whose major function is to stop the cell cycle at the G1 phase. The mechanisms through which this peptide interacts with membrane cancer cells were investigated by Tan and colleagues (Tan et al., 2016). Furthermore, in 2018, Shen and colleagues demonstrated that lycosin-I inhibits the invasion and metastasis of prostate cancer cells (Shen et al., 2018). To improve the delivery of lycosin-I to cancer cells, the amino acid sequence of the peptide was modified by replacing a lysine with an arginine (Zhang et al., 2017). This change improved the interaction between R-lycosin I and the cancer cell membrane. The selectivity against cancer cells was then improved, while the IC_{50} against non-cancerous cells remained stable. In addition to amino acid modifications, various fatty acids were incorporated at the N-terminus of the R-lycosin I peptide to enhance its anticancer activity (Jian et al., 2018). The cytotoxicity of the obtained lipopeptide R-C16 with a 16-carbon fatty acid chain was three times higher for cancer cells than that of the original peptide. This was mainly due to the increased hydrophobicity, which enhanced the interaction between the peptide and the cell membrane. In 2017, Tan and colleagues created lycosin-I-modified spherical gold nanoparticles to improve intracellular delivery and were shown to accumulate in cancer cells, *in vitro* and *in vivo* (Tan et al., 2017). This suggests a high potential for clinical application in cancer therapy. Gold nanoparticles have been developed for selective targeting of cancer cells, as they can accumulate at tumor sites via non-specific receptor-mediated endocytosis. These particles can be applied locally and activated by laser light via the hyperthermia principle to penetrate directly into the tumor (Vines et al., 2019). Recently, the same team successfully developed lycosin-I-inspired fluorescent gold nanoparticles for tumor cell bioimaging (Tan et al., 2021). In parallel, a lycosin-I peptide coupled to HCPT, a DNA topoisomerase I inhibitor, has been developed (Zhang Q. et al., 2020). This conjugate forms in-solution nanospheres that enhance its antitumor and antimetastatic activity both *in vitro* and *in vivo*.

Another peptide, LyeTx I, from another species of the genus *Lycosa*, *Lycosa erythrognatha*, was synthesized and evaluated already in 2009 (Santos et al., 2010). This peptide was initially assessed for its antimicrobial properties, against *Staphylococcus aureus*, *Escherichia coli*, and *Candida krusei*. Despite a mild hemolytic activity, LyeTx I is a promising candidate for potential clinical applications. In 2018, an optimized peptide known as LyeTx I-b was prepared by incorporating a deletion of the His at position 16 and acetylating the N-terminus (Reis et al., 2018). The new compound exhibits antimicrobial activity that is 10 times higher than the native peptide. LyeTx I-b is not only interesting for its antimicrobial activity but also for its antitumor activity on brain tumor cells (Abdel-Salam et al., 2019). Interestingly, the IC_{50} values are lower for cancer cells (U-87 MG, glioblastoma cells) than for normal cells (<30 μM *versus* >100 μM), indicating a selectivity for the cancer cells. Notably, there was no effect on either apoptosis or autophagy in normal cells. However, exposure to IC_{50} treatment for a short period (approximately 15 min) degrades the integrity of cell membranes. This observation was confirmed by electron microscopy, which revealed pores, holes, and slits indicative of necrotic cell death (Abdel-Salam et al., 2019). The LyeTx I-b peptide has also been studied for its selectivity in degrading breast cancer cells (Abdel-Salam et al., 2021; de Avelar Junior et al., 2022). Exposure to this peptide induced apoptotic death in breast cancer cells but not in

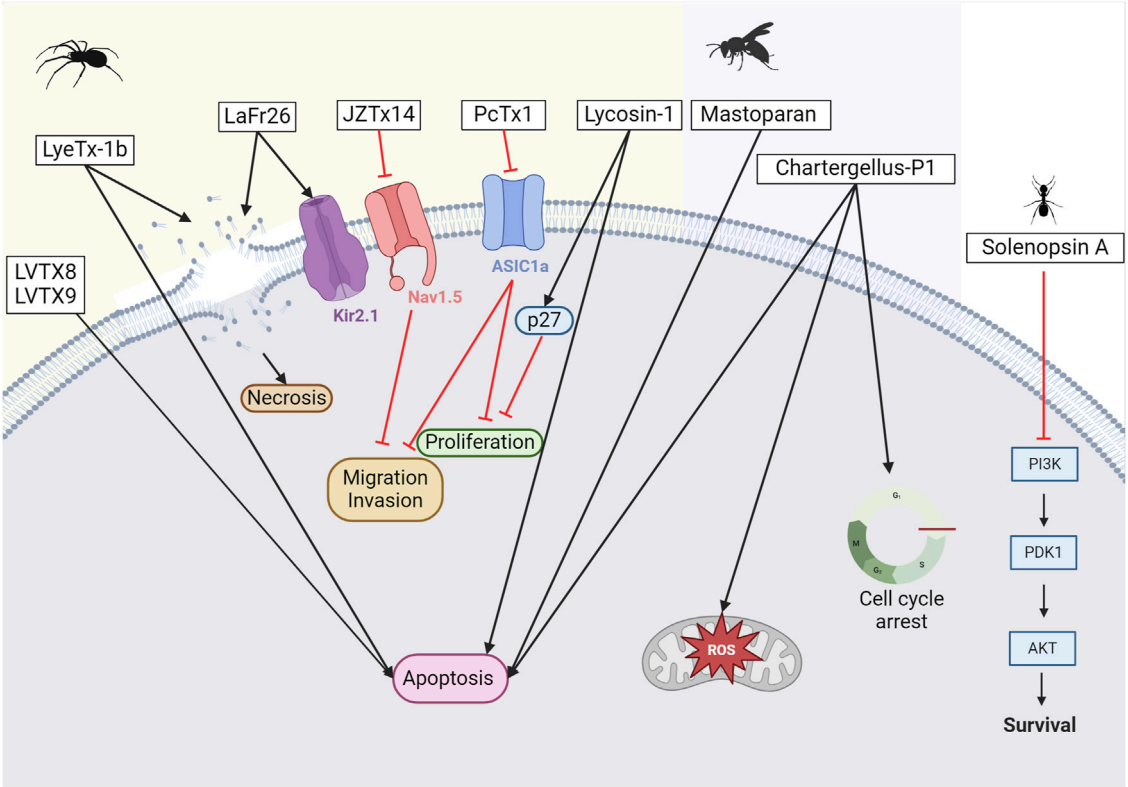

FIGURE 7
Potential anticancer toxins from other Arthropods. From left to right, an overview of some toxins with anti-cancer activity from spiders, wasps, and ants. From spider venoms, LVTX8 and LVTX9 can trigger apoptosis in some cancer cells (Zhang P. et al., 2020). LyeTx-1b has been demonstrated to either create pores leading to necrosis or trigger apoptosis (Abdel-Salam et al., 2019). LaFr26 is a pore-forming peptide specific to the Kir2 channel (Okada et al., 2019). JZTx14 is an inhibitor of the $Na_V1.5$ channel. Inhibiting this channel leads to a reduction in the migration and invasion of cancer cells (Zhang et al., 2018). PcTx1 is an inhibitor of the ASIC1a channel. Its inhibition reduces cell proliferation (Rooj et al., 2012). Lycosin-1 can upregulate the p27 protein, which reduces cancer cell proliferation (Liu et al., 2012; Tan et al., 2016). However, it can also trigger apoptosis. From wasp venoms, mastoparan induces apoptosis, while chartergellus-P1 can increase reactive oxygen species and induce cell cycle arrest (de Azevedo et al., 2015; Soares et al., 2022). From ant venom, solenopsin A blocks PI3k and its downstream pathway (Arbiser et al., 2007). Created with BioRender.com (2024).

glioblastoma ones. Interestingly, systemic injection of the peptide into mice did not result in toxicity to the liver, kidneys, brain, spleen, or heart. Hematological parameters remained normal. *In vitro* studies confirmed that the peptide has antitumor activity and reduces tumor size. In addition, the peptide was found to have an immunomodulatory effect, reducing the number of monocytes, lymphocytes, neutrophils, and eosinophils. This discovery was significant because it demonstrated the involvement of leukocytes in tumor migration and metastasis. Moreover, the combined use of LyeTx-Ib and the chemotherapeutic agent cisplatin showed an increase in selectivity and a synergistic effect in a triple-negative breast cancer cell line, MDA-MB-231(de Avelar Junior et al., 2022). The combination of LyeTx-Ib and cisplatin showed reduced nephrotoxicity compared to cisplatin alone. Cisplatin treatment is associated with significant side effects, with nephrotoxicity occurring in more than 20%–30% of patients. These recent positive results are promising for future clinical trials.

The last *Lycosa* species under review is *Lycosa vittata*, mainly found in Southwestern China. Two interesting peptides have been described from its venom, LVTX-8 and LVTX-9. Both showed cytotoxic activity and the ability to induce apoptosis in lung carcinoma cells (A549 and H460) (Zhang P. et al., 2020). Furthermore, RNA sequencing analysis of treated and control samples showed that regulation of the p53 pathway inhibited cancer cell growth and migration. These findings were further validated in a mouse model of metastasis. More recently, analogs of LVTX-8 were shown to increase stability and resistance to protease degradation (Chi et al., 2023). Similarly, LVTX-9 was derived from the *Lycosa vittata* venom gland cDNA library (Li et al., 2021). However, this peptide exhibits lower levels of cytotoxicity against cancer cells. Chemical modifications involving the addition of fatty acids of different lengths to the N-terminus of LVTX-9 significantly increased the hydrophobicity of the peptides and, in turn, their cytotoxicity. LVTX-9-C18 showed the highest cytotoxicity due to an 18-carbon fatty acid inclusion in its sequence.

The potential effects of tarantula venom on cancer cells have been extensively studied. Of particular note is SNX-482, derived from the African tarantula *Hysterocrates gigas*. The 41 amino acids peptide, first reported in 1998 (Newcomb et al., 1998), is known to affect the influx of ion channels, specifically, the $Ca_V2.3$ subunit-containing R-type calcium channel. However, the role of this channel in cancer initiation and progression is not fully understood. A study investigating the effects of SNX-482 on

macrophages has shown that the peptide activates M0-macrophages, and increases molecules involved in antigen presentation, unraveling its potential for cancer immunotherapy (Munhoz et al., 2021).

So far, *Lachesana* spiders have revealed two peptides of interest: LaFr26 and latarcin-3a. LaFr26 is a pore-forming peptide that can conduct ions, like ionophores (Okada et al., 2015). Notably, this peptide was revealed to be specific for HEK293T cells overexpressing the inwardly rectifying K^+ (Kir2.1) channel. Therefore, LaFr26 may be a remarkable choice for hyperpolarized K^+ channel expressing cancer cells. This has been demonstrated later and confirmed for two lung cancer cell lines, LX22 and BEN (Okada et al., 2019). The second peptide, latarcin-3a, was first described in 2006 (Kozlov et al., 2006). Various latarcins have been discovered in the venom of *Lachesana tarabaevi*, with numerous effects noted (for a detailed review, see Dubovskii et al. (2015). For its anticancer properties, the amino acids of the latarcin-3a peptide have recently been modified to increase its hydrophobicity and net charge, resulting in increased antitumor activity (de Moraes et al., 2022).

3.2.4 Muscular dystrophy

GsMTx4, a modulator of mechanosensitive ion channels (MSCs), was isolated from the tarantula *Grammostola rosea* (Gnanasambandam et al., 2017). This peptide has great potential for the treatment of Duchenne Muscular Dystrophy (DMD), a fatal orphan muscle disease for which there is currently no treatment. DMD is caused by a mutation in the gene encoding the dystrophin protein, resulting in a reduction or an absence of this protein and increased activation of MSCs (Ward et al., 2018). Interestingly, GsMTx4 can modulate the MSCs associated with dystrophin deficiency without affecting the MSCs involved in hearing and touch. This clear advantage, combined with its non-toxicity, non-immunogenicity, and high stability, makes it a good therapeutic candidate for DMD (Sachs, 2015). GsMTx4 has been in clinical development since 2014 and has been renamed AT-300 (Saez and Herzig, 2019).

3.3 Hymenoptera venoms, beyond melittin

Hymenoptera is an order that includes several species of bees, ants, and wasps and contains over 150,000 species. Hymenoptera venoms are composed of toxins and non-toxic components, such as inorganic salts, sugars, formic acid, free amino acids, hydrocarbons, peptides, and proteins (Guido-Patino and Plisson, 2022). Honeybee (*Apis mellifera*) venom has been widely studied for many years for its potential in a wide range of treatments, particularly for its antimicrobial activity. The venom consists of peptides, with melittin being the major compound, bioactive amines, non-peptide compounds, and enzymes such as hyaluronidase and PLA2 (group III) (Son et al., 2007).

3.3.1 Neurological disorders

Group III PLA2s have real potential in the treatment of neurodegenerative diseases, such as prion, Parkinson's, and Alzheimer's diseases. Prion disease involves the accumulation of a misfolded, β-sheet-enriched isoform (PrPSc) of cellular prion protein (PrPC). The misfolded isoform is partially resistant to protease digestion, and forms aggregated and detergent-insoluble polymers in the CNS (Saverioni et al., 2013). Neuronal cell death caused by prion peptides can be prevented by PLA2s, which reduce PrP (106–126)-mediated neurotoxicity (Jeong et al., 2011). In Alzheimer's disease, an Aβ peptide aggregation occurs, leading to neuroinflammation with microgliosis. PLA2s, found in bee venom, aid in suppressing microglial activation, leading to reduced cognitive and neuroinflammatory responses (Ye et al., 2016). PLA2s also offer therapeutic potential for Parkinson's disease. This neurodegenerative disorder is characterized by a progressive degeneration of dopaminergic neurons in the substantia nigra. As in Alzheimer's disease, neuroinflammatory mechanisms are involved in neuronal degeneration (Hirsch and Hunot, 2009) and PLA2s have a beneficial neuroprotective effect by increasing the survival of dopaminergic neurons. They can also induce the activation of regulatory T cells (Tregs) (Chung et al., 2015).

3.3.2 Cancers

While bee venom products, such as melittin, have been extensively studied for their effects on cancer cells, this review will focus on other Hymenoptera species that possess anticancer activities (Pandey et al., 2023). Ant venom has received limited attention in cancer treatment. The red imported fire ant (RIFA), *Solenopsis invicta Buren*, is a widely distributed invasive species responsible for painful stings annually reported. The venom of this species consists primarily of non-peptide piperidine alkaloids called solenopsins and other noxious substances (Mo et al., 2023). Studies have shown that solenopsin A can reduce angiogenesis in a zebrafish model (Arbiser et al., 2007). Treatment *in vitro* appears to block the activation of Akt and PI3k, thereby regulating their downstream pathway. This PI3k/Akt pathway is well known to play a role in cancer cell growth, survival, and carcinogenesis (see Figure 7).

Wasp venoms additionally contain various small bioorganic molecules including amines (such as histamine and dopamine), proteins, and peptides (such as mastoparan and waspkinin) (Souza et al., 2005). Two peptides, polybia-MPI, and polybia-CP, have been isolated from the venom of the *Polybia paulista* wasp. Both have demonstrated cytotoxic effects against prostate and bladder cancer cells (see Figure 7) (Souza et al., 2005; Wang et al., 2008; Wang et al., 2011). More recently, a couple of groups attempted to improve polybia-MPI by mutating an amino acid or by engineering bacterial outer membrane vesicles to enhance its delivery to the tumor site (Phuong et al., 2023; Ren et al., 2023). Mastoparan is a small peptide discovered in wasp venom. Since then, more than 40 different mastoparan sequences have been identified (de Santana et al., 2022). Mastoparan from *Vespa* wasps and *Vespula* hornets has been shown to have cytotoxic effects against various cancer cells, including melanoma, breast adenocarcinoma, and glioblastoma (de Azevedo et al., 2015). It has also been observed to act synergistically with the chemotherapeutic agent gemcitabine in a mouse model of breast cancer (Hilchie et al., 2016). The mechanisms involved are related to mitochondrial-dependent apoptosis. Finally, chartergellus-P1 was isolated from the wasp *Chartergellus communis* and shares more than 90% homology with the polybia-CP peptide (Soares et al., 2022). As expected, the peptide exhibits cytotoxicity against two breast cancer cell lines (MCF-7 and MDA-MB-231), primarily by inducing cell cycle arrest, promoting apoptosis, and increasing intracellular reactive oxygen species levels.

4 Cone snail venom, an incredible pharmacological toolbox

Cone snails are specialized sea and ocean predators that use their venom to paralyze and hunt fishes, mollusks, and worms. Cone snail venoms represent a rich source of potent pharmacological compounds. It is reasonably estimated that more than 100 different peptides are produced in each venom. With 800 species, the cone snail venom library can be considered as a source of more than 80,000 bioactive peptides (Terlau and Olivera, 2004; Kohn, 2018). Cone snail venoms contain hundreds of small neurotoxic peptides (usually less than 5 kDa) that can be divided into two main groups based on the number of disulfide bonds: disulfide-poor (sometimes called conopeptides), with one or fewer disulfide bonds, and disulfide-rich, with two or more disulfide bonds (Mohan et al., 2020). Disulfide-poor peptides are usually less abundant in venom than disulfide-rich peptides, and include various subgroups with various targets, as shown in Table 7 (Lebbe and Tytgat, 2016). Disulfide-rich conotoxins are highly structured and often have high affinity for membrane receptors and ion channels, see Table 8 and Figure 8. Structural properties such as the number of disulfide bridges and the cysteine backbone, are important for the target interaction. Conotoxins are named following a convention of first the Greek letter related to their pharmacological target, second the initials of the conus species, next a Roman number related to the cysteine framework, and finally a capital letter for the order of discovery (Morales Duque et al., 2019; Ratibou et al., 2024). Cone snail venom has a rich pharmacological potential. However, only a small percentage (0.2%) of the components of these venoms have been studied so far, leaving much to be discovered (Peigneur et al., 2019).

4.1 Chronic pain

Cone snail venom is well-known because it gave birth to the development of a famous drug called ziconotide (Prialt©). The latter, approved by the FDA in 2004, is used to treat chronic pain (as an analgesic). This venom-derived drug has the same sequence and structure as the ω-conotoxin MVIIA isolated and characterized from *Conus magus* venom (McIntosh et al., 1982; Miljanich, 2004). MVIIA is a blocker of the N-type $Ca_v2.2$ voltage-gated calcium channel. $Ca_v2.2$ is a validated target for the treatment of neuropathic pain. They are highly expressed in primary somatosensory afferent neurons, and the ventral horn and are then involved in synaptic transmission in ascending pain pathways (Kutzsche et al., 2024). α-RgIA (*Conus regius*) also shows an inhibitory activity on N-type $Ca_v2.2$ channels with the same mechanism of action as MVIIA, explaining why this conotoxin could also be a promising treatment for neuropathic pain (Margiotta et al., 2022). Conotoxins, like many peptides, often cannot cross the blood-brain barrier, as is the case with ziconotide. Although it cannot then be administered systemically, but rather intrathecally, it has the advantage that its efficacy does not diminish over time, unlike opioid analgesics (morphine) (Gazerani and Cairns, 2014).

The χ-conotoxin family is known to target norepinephrine transporters (NETs) involved in neurological disorders, including neuropathic pain. χ-MrIA analog (Xen2174), isolated from *Conus marmoreus*, is an inhibitor of the norepinephrine transporter (NET) and shows high selectivity for this transporter (IC_{50} χ-MrIA = 645 nM). The synthetic analog has been tested for the treatment of chronic neuropathic pain in post-operative and cancer patients (Nielsen et al., 2005). Although the phase 2 clinical trial showed promising results, it did not pass phase 2b due to dose-limiting toxicity (Coulter-Parkhill et al., 2021) (see Table 3). The compound contulakin-G (16 residues), found in the venom of *Conus geographus*, entered clinical trials but was ultimately discontinued (see Table 3). It acts as an agonist of the neurotensin receptor subunit of the NMDA receptor (hNTR1) (Craig et al., 1999; Coulter-Parkhill et al., 2021).

4.2 Type-2 diabetes

Con-Ins G1 is an insulin-like peptide isolated from the venom of *Conus geographus*. This insulin molecule can activate the human insulin receptor (hIR) (see Figure 6). Unlike human insulin, Con-Ins G1 has a lower affinity for the primary binding site of the hIR and instead has a preferential affinity for the secondary binding site. This suggests a different mode of activation of the hIR (Safavi-Hemami et al., 2015; Xiong et al., 2020). The main problem with type-2 diabetes treatments (sulfonylureas, meglitinides, thiazolidines, GLP-1 mimetics, etc.) is that they are all associated with side effects, such as weight gain and hypoglycemia (Dobrica et al., 2019). Con-Ins G1 has led to the development of new recombinant analogs with a rapid onset of action due to their smaller size. The small size of the peptide makes chemical synthesis less complex, making it a strong candidate for a new human insulin treatment. Con-Ins G1 could become an important option among clinically approved insulin analogs (Xiong et al., 2020). The identification of conotoxin-like insulins opens the way to the study of cones and other marine species venoms. The comparison of sequence and structural features of human, zebrafish, and cone insulin provides a solid basis for exploring the diversity of conotoxin-like insulins to advance drug development efforts (Guo et al., 2024).

Conk-S1, isolated from the venom of *Conus striatus*, has shown a selective inhibitory activity for $K_V1.7$ beta-cell channels. Insulin secretion is directly related to the electrical activity of the beta cell. Inhibition of this channel allows an increase in glucose-stimulated insulin secretion. Notably, the Conk-S1 inhibits the $K_V1.7$ channel without causing hypoglycemia. Therefore, this conotoxin is of interest as a potential new therapeutic option, or at least to help characterize the mechanism of $K_V1.7$ channels involved in insulin secretion, as this is still little understood (Finol-Urdaneta et al., 2012).

4.3 Channelopathies

Among ligand-gated ion channels, nicotinic acetylcholine receptors (nAChRs) and N-methyl-D-aspartate NMDA receptors have the greatest potential as lead compounds for new receptor therapies. nAChRs are found in both the peripheral and central

TABLE 7 Disulfide-poor peptide families.

Family	Disulfide bond	Target	Examples	References for more details
Contulakins	0	Neurotensin receptors	Contulakin-G (*Conus geographus*): Not available in PDB AFDB accession: AF-Q9XYR5-F1	Robinson and Norton (2014) Lebbe and Tytgat (2016)
Conantokins	0	N-methyl-D-aspartate receptors	Conantokin-G (*Conus geographus*):  PDB 1AD7	
Conorfamides	0	RFamide receptors	CNF-Tx2 (*Conus textile*): 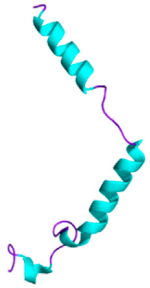 PDB 8JGB	
Conolysins	0	Cellular membranes	Conopressin (*Conus monile*): Not available in PDB AFDB accession: AF-Q9XYR5-F1	
Conopressins	1	Vasopressin receptors	Contulakin-G (*Conus geographus*): Not available in PDB AFDB accession: AF-A0A4Y5X186-F1	
Contryphans	1	Ca_V or K_V channels	Contryphan-R (*Conus radiatus*):  PDB 1QFB	
Conophans	0	Unknown	Conophan mus-V (*Conus mus*): Not available in PDB or AF	
Conomarphins	0	Unknown	Conomaprhin (*Conus marmoreus*):  PDB 2JQB	
Conomaps	0	Unknown	Conomap-Vt (*Conus planorbis*): Not available in PDB or AF	
ConoCAPs	1	Unknown	ConoCAP-a (*Conus villepinii*): Not available in PDB AFDB accession: AF-E3PQQ8 -F1	
Cono-NPYs	0	Unknown	Cono-NPY (*Conus betulinus*): Not available in PDB or AF	
CONOGAYs	1	Unknown	ConoGAY-AusB (*Conus australis*): Not available in PDB AFDB accession: AF-P0DOZ2 -F1	

nervous systems. They regulate the flow of sodium, potassium, and calcium ions across the cell membrane. These receptors mediate various cognitive processes and synaptic transmission from nerves to muscles (Hurst et al., 2013). As such, they play many important roles in the nervous system. There are 17 subtypes identified according to the combination of the five transmembrane subunits: α1 to α10, β1 to β4, γ, δ, and ε. Depending on the receptor subtype, and its localization, different disorders can be associated with them (Colombo et al., 2013). The main disorders are neurological, such as Alzheimer's disease, schizophrenia, Parkinson's disease, and depression, but nAChRs are also involved in nicotine addiction, and nicotine-induced behaviors, and are associated with small cell lung cancer (Ho et al., 2020). Cone venoms have evolved numerous classes of conopeptides that selectively target these channels. Among all the conotoxin families, no less than seven target the nAChR. The most abundant are the α-conotoxins (Lebbe et al., 2014). Within this family of conotoxins, the α3/5 targets muscle subtype nAChRs while α4/3, α4/4, α4/5, α4/6, and α4/7 conotoxins target neuronal nAChRs (Bekbossynova et al., 2021). For example, α-GI, an α3/5 targeting muscle nAChR subunit, isolated from *Conus geographus*, could be used as an alternative to a muscle relaxant administered during surgery (Tuba et al., 2002). The data show that α-GI targets the α/δ interface of the muscle nAChR with over 10,000 times higher affinity than the α/γ interface in mouse muscle. However, for the Torpedo nAChR, α-GI has a much higher affinity for the α/γ interface compared to the α/δ interface (Bekbossynova et al., 2021). Vc1.1 (ACV-1), from *Conus victoriae*, is a neuronal antagonist of α9α10 nAChRs, it was of interest as an analgesic for the treatment of neuropathic pain, but its efficacy did not reach the expected level, and phase II clinical trials were discontinued (see Figure 4; Table 3) (Sandall et al., 2003; Bordon et al., 2020). Another conotoxin MilIA, derived from *Conus milneedwardsi*, also shows activity for nAChR. MilIA is an α-conotoxin with a 3/5 framework. The potency against the muscle-type nAChR composed of α1β1γδ or α1β1εδ subunits, depending on the stage of development, fetal or adult, is rather low (IC_{50} fetal = 13,130 ± 1,125 nM and IC_{50} adult = 1,118 ± 78,891 nM). Synthetic analogs, MilIA [M9G] and MilIA [N10K], were then generated with a 23-fold and 3-fold improvement in potency, respectively. These analogs show selectivity for the fetal muscle type nAChR (Peigneur et al., 2019).

4.4 Cancers

The conopeptide Cs68, discovered in the venom of *Conus spurius*, inhibits the oncogenic voltage-gated potassium $K_V10.1$ channel, suggesting its potential as a therapeutic option (see Figure 9) (Martinez-Hernandez et al., 2023). It is worth noting that the efficacy of the peptide on cancer cells has not yet been investigated. Noteworthy, this peptide was also shown to inhibit $K_V11.1$ and $K_V1.5$. Similarly, three conotoxins (Vi14b, Mr3e.1, and Tx3a.1) isolated from *Conus virgo*, *Conus marmoreus*, and *Conus textile* exhibit anti-ovarian cancer activity and inhibit two voltage-gated sodium channels ($Na_V1.4$ and $Na_V1.8$) (Ju et al., 2022). This observation is directly related to the overexpression of voltage-gated sodium channels in ovarian cancer cells (Gao et al., 2010). However, the mechanisms by which these conotoxins reduce ovarian cancer cell viability are currently unknown and require further investigation.

4.5 Another conoidea member with anticancer activity

Terebridae belong to the same superfamily as Conidae. Its venom is understudied. Tv1, a peptide from the marine snail *Terebra variegate*, shows anticancer properties on hepatocellular carcinoma cells. Its efficacy is based on the modulation of the activity of TRPC6 and/or TRPV6 channels (Anand et al., 2019), which are involved in carcinogenesis. Administration of Tv1 to mice resulted in a reduction in tumor size.

5 Other venomous species of interest

5.1 Leeches

Leeches belong to the *Hirudinae* family. They are hematophagous, predatory, or parasitic feeders. There are over 700 species found worldwide, except Antarctica (Phillips et al., 2020). Their saliva -so not literally a venom- contains proteins with anticoagulant properties that prevent blood clotting and allow them to feed for long periods.

Hirudin, a protein isolated from the saliva of the leech *Hirudo medicinalis*, is a direct thrombin inhibitor (DTI). This peptide has an anticoagulant effect, but its irreversible inactivation of thrombin causes more bleeding than heparin (Warkentin, 2004). To improve the interaction with the active site of thrombin, some analogs have been designed based on the structure of hirudin. As a result, bivalirudin (Hirulog®), a 20 amino acid peptide, was developed and used as a clinical drug as it can reversibly bind to thrombin (Lee and Ansell, 2011).

5.2 Heloderma

There are only five known species of Heloderma. This family of venomous animals is found in the Southwestern United States, Mexico, and Central America. The venom of these venomous lizards is produced by their pre-mandibular glands and released through specialized grooved teeth. These animals use their venom for defense and for hunting small animals (Russell and Bogert, 1981). Proteomic studies of *Heloderma* venoms have highlighted various proteins and peptides such as hyaluronidase, CRiSP, exendin, helokinestatin, helofensin, kallikrein-like proteases, PLA_2 (type III), and B-type natriuretic peptide (Koludarov et al., 2014). Helokinestatin and helofensin, which release toxic bioactive peptides after proteolytic degradation, are specific to venomous lizards (Sanggaard et al., 2015).

The venom of the Gila monster, *Heloderma suspectum*, contains a peptide homologous to the mammalian glucagon-like peptide 1 (GLP-1), exendin-4, which then binds to the incretin hormone GLP-1 receptor, a GPCR (Ki 0.46 nM). Because GLP-1 plays an important role in maintaining healthy blood glucose levels, a synthetic homolog of exendin-4, called exenatide (Byetta®), was developed in 2005 for type-2 diabetes treatment (see Figure 6). Exenatide

TABLE 8 Disulfide-rich peptide families.

Family	Disulfide bond number	Pharmacological target	Examples	References for more details
α-conotoxins	2	nAChRs	PnIA (*Conus pennaceus*): 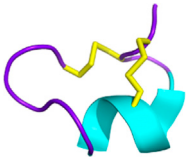 PDB 7N1Z	Lluisma et al. (2008) Robinson and Norton (2014) Ratibou et al. (2024)
	3	nAChRs	SII (*Conus striatus*):  PDB 6OTB	
γ-conotoxins	3	Neuronal pacemaker cation currents	Gamma-conotoxin-like TEA53 (*Conus textile*): Not available in PDB AFDB accession: AF-AFQ3YEG0-F1	
δ-conotoxins	3	Na^+ channels	TXVIA (*Conus textile*): 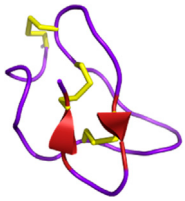 PDB 1FU3	
ε-conotoxins	2	G-Protein coupled receptors or Ca^{2+} channels	TxIX (*Conus textile*): 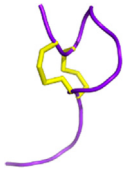 PDB 1WCT	
ι-conotoxins	4	Na^+ channels	RXIA (*Conus radiatus*):  PDB 2JTU	
κ-conotoxins	3	K^+ channels	PVIIA (*Conus purpurascens*): 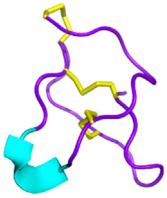 PDB 1AV3	

(Continued on following page)

TABLE 8 (*Continued*) Disulfide-rich peptide families.

Family	Disulfide bond number	Pharmacological target	Examples	References for more details
μ-conotoxins	3	Na^+ channels	GIIIA (*Conus geographus*): 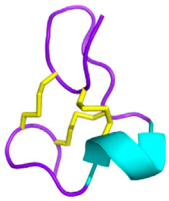 PDB 1TCG	
ρ-conotoxins	2	α-adrenoceptors	TIA (*Conus tulipa*): 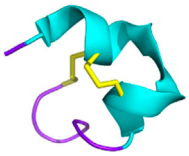 PDB 2LR9	
σ-conotoxins	5	Serotonin gated ion channels 5-HT_3	GVIIIA (*Conus geographus*): Not available in PDB AFDB accession: AF-P58924-F1	
τ-conotoxins	2	Somatostatin receptors	CnVA (*Conus consors*): Not available in PBD or AF	
χ-conotoxins	2	Norepinephrine (NE) transporters	MrIA (*Conus marmoreus*):  PDB 2EW4	
ψ-conotoxins	3	nAChRs	PIIIE (*Conus purpurascens*): 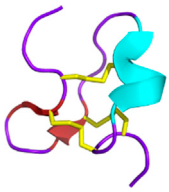 PDB 1JLO	
ω-conotoxins	3	Ca^{2+} channels	MVIIA (*Conus striatus*): 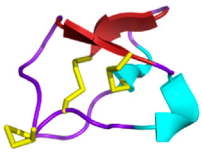 PDB 1MVJ	
φ-conotoxins	4	Granulin activity	MiXXVIIA (*Conus miles*):  PDB 6PPC	

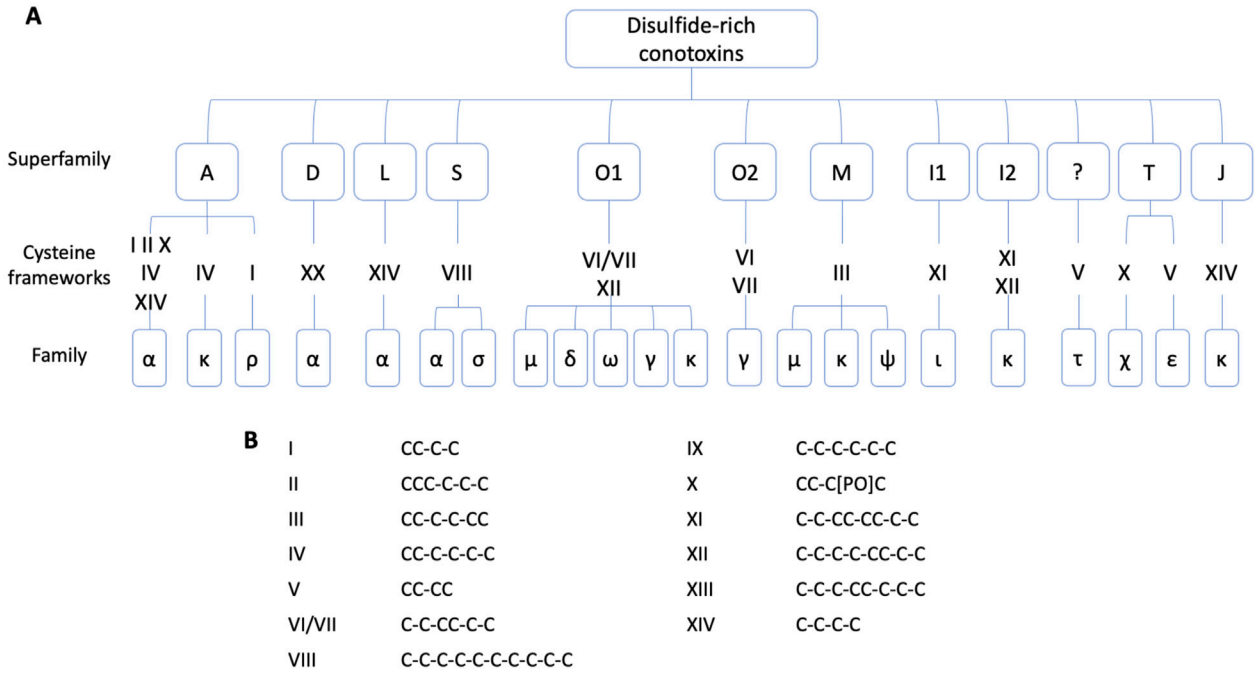

FIGURE 8
Classification of disulfide-rich conotoxins according to their cysteine frameworks. **(A)** Conotoxins are classified according to their pharmacological family, defined by a Greek letter, their cysteine framework, and their gene superfamily, represented by an Arabic capital letter (Akondi et al., 2014; Ratibou et al., 2024). **(B)** Conotoxin cysteine frameworks and their cysteine pattern.

induces insulin release, inhibits glucagon secretion, delays gastric emptying, and then suppresses appetite (Nadkarni et al., 2014). The first marketed drug derived from these observations, although effective, had an increased risk of pancreatitis. Therefore, other drugs have been developed to compensate for this problem (Lyxumia® and Bydureon®) (Nauck et al., 2021). The development of these peptides is particularly interesting because it is the first treatment to target a metabolic function.

5.3 Cnidaria

Cnidaria includes sea anemones, sea pens, corals, jellyfish, and hydra, all of which are venomous and use their venom for predation and defense. There are about 10,000 aquatic species worldwide. They contain a collagen-filled capsule with venom and a thread-like tubule. This latter expands upon external mechanical or chemical stimulation. Most of the tubules can penetrate the skin and inject the venom contained in the capsule. Cnidaria venom is composed of enzymes, such as phospholipase A2 and metalloproteases, pore-forming toxins with actinoporins and perforin, and some neurotoxins that target potassium (KTxs) and sodium (NaTxs) channels, inhibitors of ASIC and transient receptor potential cation channel subfamily V member 1 (TRPV1), and Kunitz peptides (Jouiaei et al., 2015).

5.3.1 Cancer

Sea anemone venoms are a rich source of peptides with exceptional pharmacological properties. Several peptides have been identified as useful for cancer research (see Figure 9). U-AITx-Ate1, isolated from the Australian sea anemone *Actinia tenebrosa*, is one of them. This peptide shows cytotoxicity against two breast cancer cell lines (MCF-7 and MDA-MB-231) (Elnahriry et al., 2019). However, the underlying mechanisms responsible for this cytotoxicity have not yet been investigated. Among the sea anemone toxins, the actinoporins are of particular interest. These toxins have been shown to reduce the proliferation and migration of several cancer cells, including leukemia, cervical cancer, breast cancer, and colon cancer. It can also induce apoptosis and reduce colony formation. The results show the potential of this toxin for cancer treatment (Kvetkina et al., 2020). However, since actinoporins are cytolytic by forming pores in cell membranes, their implementation in the clinic will require adaptations to reduce potential systemic toxicity.

5.3.2 Channelopathies

As mentioned in the scorpion section, $K_V1.3$ channels are implicated in several autoimmune diseases, such as multiple sclerosis, type 1 diabetes mellitus, and rheumatoid arthritis, where the ion channel plays a role in T-cell activation. *Stichodactyla helianthus*, a Caribbean Sea anemone, presents a toxin, ShK, that binds to this receptor at picomolar concentrations (Kd 11 pM) (Chandy et al., 2004). This potency is attractive for drug development, but a lack of selectivity reduces this interest. Indeed, ShK also presents an affinity for $K_V1.1$ and $K_V1.6$ at subnanomolar concentrations and for $K_V1.2$, $K_V3.2$, and $K_{Ca}3.1$ in the nanomolar range. As a result, nearly 400 analogs have been produced (Chandy et al., 2023). ShK-186, called dalazatide, is the most promising of these analogs and has reached phase 2 clinical trials for psoriasis treatment (Olsen et al., 2016) (see Table 3).

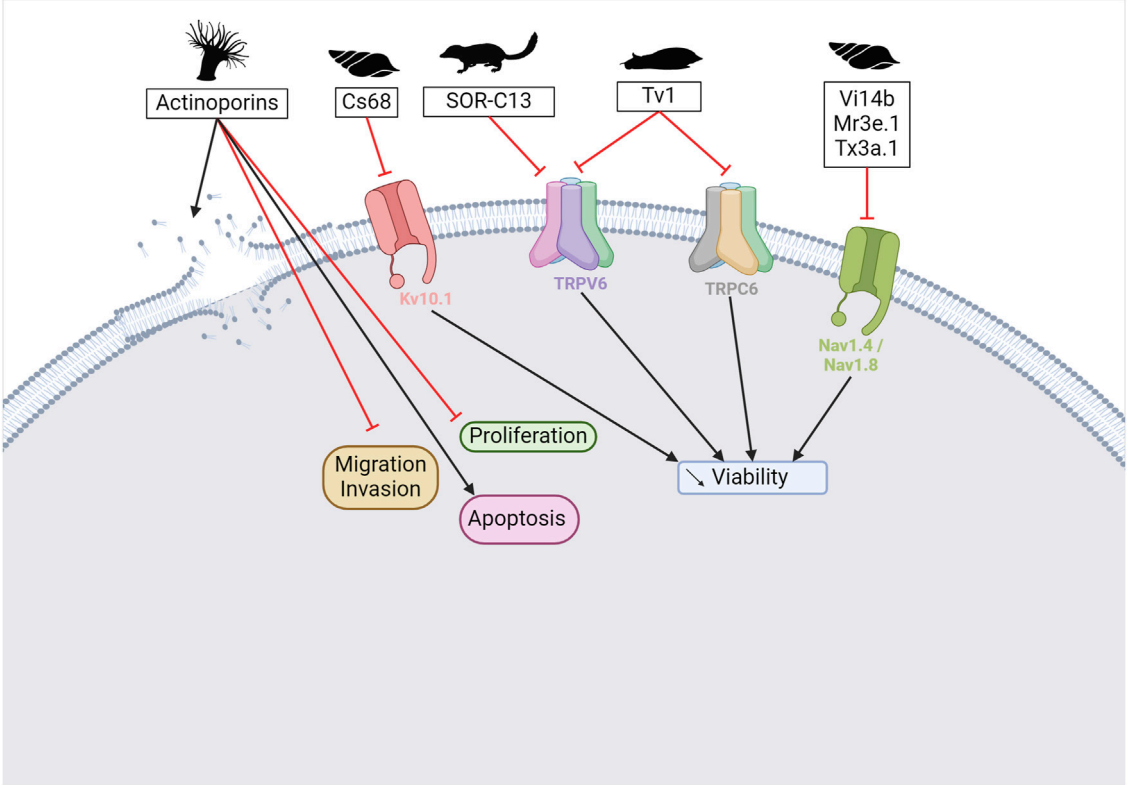

FIGURE 9
Potential anticancer peptides from cone snails and other species. Actinoporins from sea anemone venoms can form pores in cancer cell membranes but also reduce migration, invasion, and proliferation and trigger apoptosis (Kvetkina et al., 2020). Cs68 from *Conus spurius* inhibits the K_V10.1 channel, leading to a reduction in cell viability—same observation for Vi14b, Mr3e.1, and Tx3a.1 that inhibit Na_V1.4 and Na_V1.8 channels (Martinez-Hernandez et al., 2023; Ju et al., 2022). SOR-C13 extracted from soricidin inhibits the TRPV6 channel (Stewart, 2018). Tv1 from the marine snail *Terebra variegate* can modulate the activity of TRPV6 and/or TRPC6 channels (Anand et al., 2019). Overall, specific mechanisms of action from those peptides remain to be elucidated. Created with BioRender.com (2024).

Cnidaria venom contains various toxins that target ion channels, such as Na_V, K_V, and ASIC, which are involved in neurodegenerative diseases. According to Liao *et al.*, the use of cnidaria toxins is underexploited, although this venom is a rich source of ion channel blockers, as presented in this review (Liao et al., 2019).

5.4 Mammalia

It is a recurring mistake to forget that venomous animals are also found among mammals, including monotremes (platypuses), eulipotyphla (shrews), chiropterans (vampire bats), and primates (pygmy lorises).

The monotreme order includes the platypus and four species of echidna. The male platypus (*Ornithorhynchus anatinus*) has a venom gland located on its hind leg. During the breeding season, the venom is used against competing males (Wong et al., 2012). The purpose of echidna venom is not yet understood. This venom is composed of C-type natriuretic peptides, defensin-like peptides, nerve growth factors, hyaluronidase, protease, and uncharacterized proteins (Ligabue-Braun et al., 2012). Monotreme venom also contains an analog of glucagon-like peptide-1 (pGLP-1) (Tsend-Ayush et al., 2016).

Soricidin is a peptide derived from the northern short-tailed shrew, *Blarina brevicauda* that has been shown to bind to the TRPV6 calcium channel (Stewart et al., 2006; Bowen et al., 2013). Two peptides, SOR-C13 and SOR-C17, extracted from soricidin, exhibit an affinity for ovarian and prostate tumors, enriched in TRPV6 channels (see Figure 9) (Stewart, 2018). These peptides' conjugation with chemotherapeutics or contrast agents could further expand their use in diagnostic and therapeutic applications. SOR-C13 is in phase 1 of clinical development for the treatment of solid tumors (NCT01578564, NCT03784677) (Fu et al., 2017).

6 Limitations and future of venom-based drug discovery

Despite the large number of toxins with affinity for receptors involved in a variety of problems, and therefore a definite therapeutic potential, it can be observed that few venom-derived toxins are transformed into therapeutic successes. Many clinical trials are discontinued for lack of specificity, bioavailability, or efficacy (see Table 3). The difficulties in translating the *in vitro* pharmacological performance of Na_V1.7 channels into effective *in vivo* analgesic outcomes were described in 2022 (Eagles et al., 2022). The challenge arises from the complexity of biological systems and the differences between controlled cellular environments and whole living

organisms (Kim et al., 2020; Eagles et al., 2022). Indeed, the predictability of preclinical models is one of the causes explaining clinical trial failure (Gerard et al., 2021). Furthermore, research on receptors as therapeutic targets has highlighted the importance of understanding complex molecular interactions and specific mechanisms of action.

However, new possibilities are emerging now that artificial intelligence (AI) overturns how we work and think. Deep learning techniques like Molecular Contrastive Learning (MolCLR) and AlphaFold 3 can help predict molecular properties, protein structures, and how proteins interact with other molecules with high precision, thereby facilitating the discovery of new drugs (Jumper et al., 2021; Wang et al., 2022; Desai et al., 2024). These advanced technologies have the potential to discover venom-peptide analogs that efficiently target receptors, thus overcoming the limitation of *in vitro* testing. Moreover, 3D modeling applications could facilitate the development of toxins as therapeutics, enabling them to mimic the desired toxin activity without associated toxicity or to mitigate "off-target" effects. A data augmentation method, combining Generative Adversarial Networks (GAN) and Convolutional Neural Networks (CNN), was used recently to predict novel spider neurotoxic peptides (Lee et al., 2021). Deep learning tools, such as Graph Neural Networks (GNN) and Variational Autoencoders (VAE), can model the interaction between the peptide and the target at a granular level, providing valuable insights for designing more effective molecules (Seo et al., 2021; Li et al., 2022). In the context of venom-based drug discovery, these same technologies can create new chemical compounds inspired by venom with optimal pharmacological properties. DeepLPI, using Bidirectional Long Short-Term Memory (BiLSTM) can predict crucial protein-ligand interactions for therapeutic efficacy (Wei et al., 2022). The application of deep learning and AI tools in venom research provides a comprehensive understanding of intricate biological interactions and accelerates the drug discovery process. These technologies can overcome existing barriers by providing precise predictions and enabling faster, cost-effective testing (Bedraoui et al., 2024). The limitations in venom-based drug discovery highlight the importance of *in vivo* validation and the integration of advanced technologies to overcome obstacles in biomedical research.

7 Conclusion

In summary, venomous animals have evolved complex venom systems over millions of years, creating an extensive molecular arsenal that serves multiple biological functions beyond predation and defense. These venoms, rich in peptides and proteins, have proven highly effective in targeting specific molecular mechanisms, making them valuable candidates for drug development. The structural properties of venom peptides, such as their stability and selective binding capabilities, highlight their potential to create novel therapeutic agents. With 11 venom-derived drugs already approved for the treatment of various diseases and numerous studies underway, the potential of venom in medical applications is becoming increasingly evident. As research continues to explore the diverse bioactive compounds within venom, we can expect significant advances in the treatment of both cancer and non-cancer diseases by exploiting the unique properties of these naturally evolved molecules.

Author contributions

LF: Conceptualization, Writing–original draft. CM: Conceptualization, Writing–original draft. LQ: Conceptualization, Writing–review and editing. J-PG: Conceptualization, Writing–review and editing.

Funding

The author(s) declare that no financial support was received for the research, authorship, and/or publication of this article.

Conflict of interest

The authors declare that the research was conducted in the absence of any commercial or financial relationships that could be construed as a potential conflict of interest.

Publisher's note

References

Abdel-Ghani, L. M., Rahmy, T. R., Tawfik, M. M., Kaziri, I., Al-Obaidi, A., Rowan, E. G., et al. (2019). Cytotoxicity of Nubein6.8 peptide isolated from the snake venom of Naja nubiae on melanoma and ovarian carcinoma cell lines. *Toxicon* 168, 22–31. doi:10.1016/j.toxicon.2019.06.220

Abdel-Salam, M. A. L., Carvalho-Tavares, J., Gomes, K. S., Teixeira-Carvalho, A., Kitten, G. T., Nyffeler, J., et al. (2019). The synthetic peptide LyeTxI-b derived from Lycosa erythrognatha spider venom is cytotoxic to U-87 MG glioblastoma cells. *Amino Acids* 51 (3), 433–449. doi:10.1007/s00726-018-2678-4

Abdel-Salam, M. A. L., Pinto, B., Cassali, G., Bueno, L., Pegas, G., Oliveira, F., et al. (2021). LyeTx I-b peptide attenuates tumor burden and metastasis in a mouse 4T1 breast cancer model. *Antibiot. (Basel)* 10 (9), 1136. doi:10.3390/antibiotics10091136

Acharya, K. R., Sturrock, E. D., Riordan, J. F., and Ehlers, M. R. (2003). Ace revisited: a new target for structure-based drug design. *Nat. Rev. Drug Discov.* 2 (11), 891–902. doi:10.1038/nrd1227

Adams, G. L., Pall, P. S., Grauer, S. M., Zhou, X., Ballard, J. E., Vavrek, M., et al. (2022). Development of ProTx-II analogues as highly selective peptide blockers of Na(v)1.7 for

the treatment of pain. *J. Med. Chem.* 65 (1), 485–496. doi:10.1021/acs.jmedchem.1c01570

Agnarsson, I., Coddington, J. A., and Kuntner, M. (2013). "Systematics: progress in the study of spider diversity and evolution," in *Spider research in the 21st century: trends and perspectives* (Siri Scientific Press), 58–111. P. D.

Aguiar, F. L. L., Santos, N. C., de Paula Cavalcante, C. S., Andreu, D., Baptista, G. R., and Goncalves, S. (2020). Antibiofilm activity on Candida albicans and mechanism of action on biomembrane models of the antimicrobial peptide ctn[15-34]. *Int. J. Mol. Sci.* 21 (21), 8339. doi:10.3390/ijms21218339

Aissaoui-Zid, D., Saada, M. C., Moslah, W., Potier-Cartereau, M., Lemettre, A., Othman, H., et al. (2021). AaTs-1: a tetrapeptide from Androctonus australis scorpion venom, inhibiting U87 glioblastoma cells proliferation by p53 and FPRL-1 up-regulations. *Molecules* 26 (24), 7610. doi:10.3390/molecules26247610

Akondi, K. B., Muttenthaler, M., Dutertre, S., Kaas, Q., Craik, D. J., and Lewis, R. J. (2014). Discovery, synthesis, and structure-activity relationships of conotoxins. *Chem. Rev.* 114 (11), 5815–5847. doi:10.1021/cr400401e

Alexandrou, A. J., Brown, A. R., Chapman, M. L., Estacion, M., Turner, J., Mis, M. A., et al. (2016). Subtype-selective small molecule inhibitors reveal a fundamental role for Nav1.7 in nociceptor electrogenesis, axonal conduction and presynaptic release. *PLoS One* 11 (4), e0152405. doi:10.1371/journal.pone.0152405

Almaaytah, A., and Albalas, Q. (2014). Scorpion venom peptides with no disulfide bridges: a review. *Peptides* 51, 35–45. doi:10.1016/j.peptides.2013.10.021

Almeida, C. F., Amaral, C., Augusto, T. V., Correia-da-Silva, G., Marques de Andrade, C., Torqueti, M. R., et al. (2021). The anti-cancer potential of crotoxin in estrogen receptor-positive breast cancer: its effects and mechanism of action. *Toxicon* 200, 69–77. doi:10.1016/j.toxicon.2021.07.003

Anand, P., Filipenko, P., Huaman, J., Lyudmer, M., Hossain, M., Santamaria, C., et al. (2019). Selective inhibition of liver cancer cells using venom peptide. *Mar. Drugs* 17 (10), 587. doi:10.3390/md17100587

Arbiser, J. L., Kau, T., Konar, M., Narra, K., Ramchandran, R., Summers, S. A., et al. (2007). Solenopsin, the alkaloidal component of the fire ant (*Solenopsis invicta*), is a naturally occurring inhibitor of phosphatidylinositol-3-kinase signaling and angiogenesis. *Blood* 109 (2), 560–565. doi:10.1182/blood-2006-06-029934

Ashcroft, F. M., and Rorsman, P. (1989). Electrophysiology of the pancreatic β-cell. *Prog. Biophys. Mol. Biol.* 54 (2), 87–143. doi:10.1016/0079-6107(89)90013-8

Attarde, S. S., and Pandit, S. V. (2017). Cytotoxic activity of NN-32 toxin from Indian spectacled cobra venom on human breast cancer cell lines. *BMC Complement. Altern. Med.* 17 (1), 503. doi:10.1186/s12906-017-2018-3

Attarde, S. S., and Pandit, S. V. (2020). Anticancer potential of nanogold conjugated toxin GNP-NN-32 from Naja naja venom. *J. Venom. Anim. Toxins Incl. Trop. Dis.* 26, e20190047. doi:10.1590/1678-9199-JVATITD-2019-0047

Bandeira, I. C. J., Bandeira-Lima, D., Mello, C. P., Pereira, T. P., De Menezes, R., Sampaio, T. L., et al. (2018). Antichagasic effect of crotalicidin, a cathelicidin-like vipericidin, found in *Crotalus durissus* terrificus rattlesnake's venom gland. *Parasitology* 145 (8), 1059–1064. doi:10.1017/S0031182017001846

Banerjee, Y., Mizuguchi, J., Iwanaga, S., and Kini, R. M. (2005). Hemextin AB complex, a unique anticoagulant protein complex from Hemachatus haemachatus (African Ringhals cobra) venom that inhibits clot initiation and factor VIIa activity. *J. Biol. Chem.* 280 (52), 42601–42611. doi:10.1074/jbc.M508987200

Barnwal, B., Jobichen, C., Girish, V. M., Foo, C. S., Sivaraman, J., and Kini, R. M. (2016). Ringhalexin from Hemachatus haemachatus: a novel inhibitor of extrinsic tenase complex. *Sci. Rep.* 6, 25935. doi:10.1038/srep25935

Bedraoui, A., Suntravat, M., El Mejjad, S., Enezari, S., Oukkache, N., Sanchez, E. E., et al. (2024). Therapeutic potential of snake venom: toxin distribution and opportunities in deep learning for novel drug discovery. *Med. Drug Discov.* 21, 100175. doi:10.1016/j.medidd.2023.100175

Bekbossynova, A., Zharylgap, A., and Filchakova, O. (2021). Venom-derived neurotoxins targeting nicotinic acetylcholine receptors. *Molecules* 26 (11), 3373. doi:10.3390/molecules26113373

Bhattacharjee, P., and Bhattacharyya, D. (2013). Factor V activator from Daboia russelli russelli venom destabilizes β-amyloid aggregate, the hallmark of alzheimer disease. *J. Biol. Chem.* 288 (42), 30559–30570. doi:10.1074/jbc.M113.511410

Bhattacharya, N., Kolvekar, N., Mondal, S., Sarkar, A., and Chakrabarty, D. (2023). Biological activities of Vipegrin, an anti-adhesive Kunitz-type serine proteinase inhibitor purified from Russell's viper venom. *Toxicon* 232, 107213. doi:10.1016/j.toxicon.2023.107213

Bhowmik, T., and Gomes, A. (2016). NKCT1 (purified Naja kaouthia protein toxin) conjugated gold nanoparticles induced Akt/mTOR inactivation mediated autophagic and caspase 3 activated apoptotic cell death in leukemic cell. *Toxicon* 121, 86–97. doi:10.1016/j.toxicon.2016.08.004

Bhowmik, T., and Gomes, A. (2017). Down-regulation of cyclin-dependent kinase-4 and MAPK through estrogen receptor mediated cell cycle arrest in human breast cancer induced by gold nanoparticle tagged toxin protein NKCT1. *Chem. Biol. Interact.* 268, 119–128. doi:10.1016/j.cbi.2017.03.009

Bhowmik, T., Saha, P. P., Dasgupta, A., and Gomes, A. (2013). Antileukemic potential of PEGylated gold nanoparticle conjugated with protein toxin (NKCT1) isolated from Indian cobra (Naja kaouthia) venom. *Cancer Nanotechnol.* 4 (1-3), 39–55. doi:10.1007/s12645-013-0036-5

Bhowmik, T., Saha, P. P., Sarkar, A., and Gomes, A. (2017). Evaluation of cytotoxicity of a purified venom protein from Naja kaouthia (NKCT1) using gold nanoparticles for targeted delivery to cancer cell. *Chem. Biol. Interact.* 261, 35–49. doi:10.1016/j.cbi.2016.11.007

Bledzka, K., Smyth, S. S., and Plow, E. F. (2013). Integrin alphaIIbbeta3: from discovery to efficacious therapeutic target. *Circ. Res.* 112 (8), 1189–1200. doi:10.1161/CIRCRESAHA.112.300570

Boltman, T., Meyer, M., and Ekpo, O. (2023). Diagnostic and therapeutic approaches for glioblastoma and neuroblastoma cancers using chlorotoxin nanoparticles. *Cancers (Basel)* 15 (13), 3388. doi:10.3390/cancers15133388

Bordon, K. C. F., Cologna, C. T., Fornari-Baldo, E. C., Pinheiro-Junior, E. L., Cerni, F. A., Amorim, F. G., et al. (2020). From animal poisons and venoms to medicines: achievements, challenges and perspectives in drug discovery. *Front. Pharmacol.* 11, 1132. doi:10.3389/fphar.2020.01132

Bowen, C. V., DeBay, D., Ewart, H. S., Gallant, P., Gormley, S., Ilenchuk, T. T., et al. (2013). *In vivo* detection of human TRPV6-rich tumors with anti-cancer peptides derived from soricidin. *PLoS One* 8 (3), e58866. doi:10.1371/journal.pone.0058866

Brown, M. C., Staniszewska, I., Del Valle, L., Tuszynski, G. P., and Marcinkiewicz, C. (2008). Angiostatic activity of obtustatin as α1β1 integrin inhibitor in experimental melanoma growth. *Int. J. Cancer* 123 (9), 2195–2203. doi:10.1002/ijc.23777

Bychkov, M. L., Kirichenko, A. V., Shulepko, M. A., Mikhaylova, I. N., Kirpichnikov, M. P., and Lyukmanova, E. N. (2021). Mambalgin-2 inhibits growth, migration, and invasion of metastatic melanoma cells by targeting the channels containing an ASIC1a subunit whose up-regulation correlates with poor survival prognosis. *Biomedicines* 9 (10), 1324. doi:10.3390/biomedicines9101324

Bychkov, M. L., Shulepko, M. A., Vasileva, V. Y., Sudarikova, A. V., Kirpichnikov, M. P., and Lyukmanova, E. N. (2020). ASIC1a inhibitor mambalgin-2 suppresses the growth of leukemia cells by cell cycle arrest. *Acta Naturae* 12 (2), 111–116. doi:10.32607/actanaturae.11158

Calvete, J. J., Marcinkiewicz, C., Monleon, D., Esteve, V., Celda, B., Juarez, P., et al. (2005). Snake venom disintegrins: evolution of structure and function. *Toxicon* 45 (8), 1063–1074. doi:10.1016/j.toxicon.2005.02.024

Campeiro, J. D., Marinovic, M. P., Carapeto, F. C., Dal Mas, C., Monte, G. G., Carvalho Porta, L., et al. (2018). Oral treatment with a rattlesnake native polypeptide crotamine efficiently inhibits the tumor growth with no potential toxicity for the host animal and with suggestive positive effects on animal metabolic profile. *Amino Acids* 50 (2), 267–278. doi:10.1007/s00726-017-2513-3

Casewell, N. R., Wuster, W., Vonk, F. J., Harrison, R. A., and Fry, B. G. (2013). Complex cocktails: the evolutionary novelty of venoms. *Trends Ecol. Evol.* 28 (4), 219–229. doi:10.1016/j.tree.2012.10.020

Castle, N. A., London, D. O., Creech, C., Fajloun, Z., Stocker, J. W., and Sabatier, J. M. (2003). Maurotoxin: a potent inhibitor of intermediate conductance Ca2+-activated potassium channels. *Mol. Pharmacol.* 63 (2), 409–418. doi:10.1124/mol.63.2.409

Castro-Amorim, J., Novo de Oliveira, A., Da Silva, S. L., Soares, A. M., Mukherjee, A. K., Ramos, M. J., et al. (2023). Catalytically active snake venom PLA(2) enzymes: an overview of its elusive mechanisms of reaction. *J. Med. Chem.* 66 (8), 5364–5376. doi:10.1021/acs.jmedchem.3c00097

Cavalcante, C. S., Falcao, C. B., Fontenelle, R. O., Andreu, D., and Radis-Baptista, G. (2017). Anti-fungal activity of Ctn[15-34], the C-terminal peptide fragment of crotalicidin, a rattlesnake venom gland cathelicidin. *J. Antibiot. (Tokyo)* 70 (3), 231–237. doi:10.1038/ja.2016.135

Chai, J., Yang, W., Gao, Y., Guo, R., Peng, Q., Abdel-Rahman, M. A., et al. (2021). Antitumor effects of scorpion peptide Smp43 through mitochondrial dysfunction and membrane disruption on hepatocellular carcinoma. *J. Nat. Prod.* 84 (12), 3147–3160. doi:10.1021/acs.jnatprod.1c00963

Chandy, K. G., and Norton, R. S. (2017). Peptide blockers of K(v)1.3 channels in T cells as therapeutics for autoimmune disease. *Curr. Opin. Chem. Biol.* 38, 97–107. doi:10.1016/j.cbpa.2017.02.015

Chandy, K. G., Sanches, K., and Norton, R. S. (2023). Structure of the voltage-gated potassium channel K(V)1.3: insights into the inactivated conformation and binding to therapeutic leads. *Channels (Austin)* 17 (1), 2253104. doi:10.1080/19336950.2023.2253104

Chandy, K. G., Wulff, H., Beeton, C., Pennington, M., Gutman, G. A., and Cahalan, M. D. (2004). K+ channels as targets for specific immunomodulation. *Trends Pharmacol. Sci.* 25 (5), 280–289. doi:10.1016/j.tips.2004.03.010

Chassagnon, I. R., McCarthy, C. A., Chin, Y. K., Pineda, S. S., Keramidas, A., Mobli, M., et al. (2017). Potent neuroprotection after stroke afforded by a double-knot spider-venom peptide that inhibits acid-sensing ion channel 1a. *Proc. Natl. Acad. Sci. U. S. A.* 114 (14), 3750–3755. doi:10.1073/pnas.1614728114

Chen, Z., Tran, D., Li, T., Arias, K., Griffith, B. P., and Wu, Z. J. (2020). The role of a disintegrin and metalloproteinase proteolysis and mechanical damage in

nonphysiological shear stress-induced platelet receptor shedding. *ASAIO J.* 66 (5), 524–531. doi:10.1097/MAT.0000000000001028

Chi, Q. N., Jia, S. X., Yin, H., Wang, L. E., Fu, X. Y., Ma, Y. N., et al. (2023). Efficient synthesis and anticancer evaluation of spider toxin peptide LVTX-8-based analogues with enhanced stability. *Bioorg Chem.* 134, 106451. doi:10.1016/j.bioorg.2023.106451

Chiou, J. T., Shi, Y. J., Wang, L. J., Huang, C. H., Lee, Y. C., and Chang, L. S. (2019). Naja atra cardiotoxin 3 elicits autophagy and apoptosis in U937 human leukemia cells through the Ca(2+)/PP2A/AMPK Axis. *Toxins (Basel)* 11 (9), 527. doi:10.3390/toxins11090527

Chiou, J. T., Wang, L. J., Lee, Y. C., and Chang, L. S. (2021). Naja atra cardiotoxin 1 induces the FasL/fas death pathway in human leukemia cells. *Cells* 10 (8), 2073. doi:10.3390/cells10082073

Chong, H. P., Tan, K. Y., and Tan, C. H. (2020). Cytotoxicity of snake venoms and cytotoxins from two southeast asian cobras (Naja sumatrana, Naja kaouthia): exploration of anticancer potential, selectivity, and cell death mechanism. *Front. Mol. Biosci.* 7, 583587. doi:10.3389/fmolb.2020.583587

Chung, E. S., Lee, G., Lee, C., Ye, M., Chung, H. S., Kim, H., et al. (2015). Bee venom phospholipase A2, a novel Foxp3+ regulatory T cell inducer, protects dopaminergic neurons by modulating neuroinflammatory responses in a mouse model of Parkinson's disease. *J. Immunol.* 195 (10), 4853–4860. doi:10.4049/jimmunol.1500386

Ciolek, J., Reinfrank, H., Quinton, L., Viengchareun, S., Stura, E. A., Vera, L., et al. (2017). Green mamba peptide targets type-2 vasopressin receptor against polycystic kidney disease. *Proc. Natl. Acad. Sci. U. S. A.* 114 (27), 7154–7159. doi:10.1073/pnas.1620454114

Colombo, S. F., Mazzo, F., Pistillo, F., and Gotti, C. (2013). Biogenesis, trafficking and up-regulation of nicotinic ACh receptors. *Biochem. Pharmacol.* 86 (8), 1063–1073. doi:10.1016/j.bcp.2013.06.023

Conde, R., Zamudio, F. Z., Rodriguez, M. H., and Possani, L. D. (2000). Scorpine, an anti-malaria and anti-bacterial agent purified from scorpion venom. *FEBS Lett.* 471 (2-3), 165–168. doi:10.1016/s0014-5793(00)01384-3

Coulter-Parkhill, A., McClean, S., Gault, V. A., and Irwin, N. (2021). Therapeutic potential of peptides derived from animal venoms: current views and emerging drugs for diabetes. *Clin. Med. Insights Endocrinol. Diabetes* 14, 117955142110060. doi:10.1177/11795514211006071

Craig, A. G., Norberg, T., Griffin, D., Hoeger, C., Akhtar, M., Schmidt, K., et al. (1999). Contulakin-G, an O-glycosylated invertebrate neurotensin. *J. Biol. Chem.* 274 (20), 13752–13759. doi:10.1074/jbc.274.20.13752

Cummins, T. R., Sheets, P. L., and Waxman, S. G. (2007). The roles of sodium channels in nociception: implications for mechanisms of pain. *Pain* 131 (3), 243–257. doi:10.1016/j.pain.2007.07.026

Cura, J. E., Blanzaco, D. P., Brisson, C., Cura, M. A., Cabrol, R., Larrateguy, L., et al. (2002). Phase I and pharmacokinetics study of crotoxin (cytotoxic PLA(2), NSC-624244) in patients with advanced cancer. *Clin. Cancer Res.* 8 (4), 1033–1041.

Cushman, D. W., and Ondetti, M. A. (1991). History of the design of captopril and related inhibitors of angiotensin converting enzyme. *Hypertension* 17 (4), 589–592. doi:10.1161/01.hyp.17.4.589

Dalmolin, G. D., Silva, C. R., Rigo, F. K., Gomes, G. M., do Nascimento Cordeiro, M., Richardson, M., et al. (2011). Antinociceptive effect of Brazilian armed spider venom toxin Tx3-3 in animal models of neuropathic pain. *Pain* 152 (10), 2224–2232. doi:10.1016/j.pain.2011.04.015

D'Amelio, F., Vigerelli, H., de Brandao Prieto da Silva, A. R., and Kerkis, I. (2021). Bothrops moojeni venom and its components - an overview. *J. Venom. Res.* 11, 26–33.

Dardevet, L., Najlaoui, F., Aroui, S., Collot, M., Tisseyre, C., Pennington, M. W., et al. (2022). A conjugate between lqh-8/6, a natural peptide analogue of chlorotoxin, and doxorubicin efficiently induces glioma cell death. *Biomedicines* 10 (10), 2605. doi:10.3390/biomedicines10102605

da Rocha, R. G., Santos, E. M. S., Tanaka-Azevedo, A. M., Serino-Silva, C., Souza, M. G., Gomes, E. S. B., et al. (2023). The antineoplastic potential of crotoxin isolated from *Crotalus durissus* terrificus snake venom on oral squamous cell carcinoma. *Toxicon* 221, 106965. doi:10.1016/j.toxicon.2022.106965

Das, T., Bhattacharya, S., Biswas, A., Gupta, S. D., Gomes, A., and Gomes, A. (2013). Inhibition of leukemic U937 cell growth by induction of apoptosis, cell cycle arrest and suppression of VEGF, MMP-2 and MMP-9 activities by cytotoxin protein NN-32 purified from Indian spectacled cobra (Naja naja) venom. *Toxicon* 65, 1–4. doi:10.1016/j.toxicon.2013.01.004

Das, T., Bhattacharya, S., Halder, B., Biswas, A., Das Gupta, S., Gomes, A., et al. (2011). Cytotoxic and antioxidant property of a purified fraction (NN-32) of Indian Naja naja venom on Ehrlich ascites carcinoma in BALB/c mice. *Toxicon* 57 (7-8), 1065–1072. doi:10.1016/j.toxicon.2011.04.012

de Avelar Junior, J. T., Lima-Batista, E., Castro Junior, C. J., Pimenta, A. M. C., Dos Santos, R. G., Souza-Fagundes, E. M., et al. (2022). LyeTxI-b, a synthetic peptide derived from a spider venom, is highly active in triple-negative breast cancer cells and acts synergistically with cisplatin. *Front. Mol. Biosci.* 9, 876833. doi:10.3389/fmolb.2022.876833

de Azevedo, R. A., Figueiredo, C. R., Ferreira, A. K., Matsuo, A. L., Massaoka, M. H., Girola, N., et al. (2015). Mastoparan induces apoptosis in B16F10-Nex2 melanoma cells via the intrinsic mitochondrial pathway and displays antitumor activity *in vivo*. *Peptides* 68, 113–119. doi:10.1016/j.peptides.2014.09.024

Debnath, A., Saha, A., Gomes, A., Biswas, S., Chakrabarti, P., Giri, B., et al. (2010). A lethal cardiotoxic-cytotoxic protein from the Indian monocellate cobra (Naja kaouthia) venom. *Toxicon* 56 (4), 569–579. doi:10.1016/j.toxicon.2010.05.016

de Carvalho Porta, L., Fadel, V., D'Arc Campeiro, J., Oliveira, E. B., Godinho, R. O., and Hayashi, M. A. F. (2020). Biophysical and pharmacological characterization of a full-length synthetic analog of the antitumor polypeptide crotamine. *J. Mol. Med. Berl.* 98 (11), 1561–1571. doi:10.1007/s00109-020-01975-y

de Moraes, L., Silva, P. S. E., Pereira, T., Almeida Rodrigues, T. A., Farias Frihling, B. E., da Costa, R. A., et al. (2022). First generation of multifunctional peptides derived from latarcin-3a from Lachesana tarabaevi spider toxin. *Front. Microbiol.* 13, 965621. doi:10.3389/fmicb.2022.965621

Deng, Z., Gao, Y., Nguyen, T., Chai, J., Wu, J., Li, J., et al. (2023). The potent antitumor activity of Smp43 against non-small-cell lung cancer A549 cells via inducing membranolysis and mitochondrial dysfunction. *Toxins (Basel)* 15 (5), 347. doi:10.3390/toxins15050347

Desai, D., Kantliwala, S. V., Vybhavi, J., Ravi, R., Patel, H., and Patel, J. (2024). Review of AlphaFold 3: transformative advances in drug design and therapeutics. *Cureus* 16 (7), e63646. doi:10.7759/cureus.63646

de Santana, C. J. C., Pires Junior, O. R., Fontes, W., Palma, M. S., and Castro, M. S. (2022). Mastoparans: a group of multifunctional α-helical peptides with promising therapeutic properties. *Front. Mol. Biosci.* 9, 824989. doi:10.3389/fmolb.2022.824989

de Souza, A. H., Lima, M. C., Drewes, C. C., da Silva, J. F., Torres, K. C., Pereira, E. M., et al. (2011). Antiallodynic effect and side effects of Phα1β, a neurotoxin from the spider Phoneutria nigriventer: comparison with ω-conotoxin MVIIA and morphine. *Toxicon* 58 (8), 626–633. doi:10.1016/j.toxicon.2011.09.008

De Waard, S., Montnach, J., Cortinovis, C., Chkir, O., Erfanian, M., Hulin, P., et al. (2020). Maurocalcin and its analog MCaE12A facilitate Ca2+ mobilization in cardiomyocytes. *Biochem. J.* 477 (20), 3985–3999. doi:10.1042/BCJ20200206

Dintzis, S. M., Hansen, S., Harrington, K. M., Tan, L. C., Miller, D. M., Ishak, L., et al. (2019). Real-time visualization of breast carcinoma in pathology specimens from patients receiving fluorescent tumor-marking agent tozuleristide. *Arch. Pathol. Lab. Med.* 143 (9), 1076–1083. doi:10.5858/arpa.2018-0197-OA

Diochot, S., Baron, A., Salinas, M., Douguet, D., Scarzello, S., Dabert-Gay, A. S., et al. (2012). Black mamba venom peptides target acid-sensing ion channels to abolish pain. *Nature* 490 (7421), 552–555. doi:10.1038/nature11494

Dobrica, E. C., Gaman, M. A., Cozma, M. A., Bratu, O. G., Pantea Stoian, A., and Diaconu, C. C. (2019). Polypharmacy in type 2 diabetes mellitus: insights from an internal medicine department. *Med. Kaunas.* 55 (8), 436. doi:10.3390/medicina55080436

Donato, N. J., Martin, C. A., Perez, M., Newman, R. A., Vidal, J. C., and Etcheverry, M. (1996). Regulation of epidermal growth factor receptor activity by crotoxin, a snake venom phospholipase A2 toxin. *Biochem. Pharmacol.* 51 (11), 1535–1543. doi:10.1016/0006-2952(96)00097-4

Droctove, L., Ciolek, J., Mendre, C., Chorfa, A., Huerta, P., Carvalho, C., et al. (2022). A new Kunitz-type snake toxin family associated with an original mode of interaction with the vasopressin 2 receptor. *Br. J. Pharmacol.* 179 (13), 3470–3481. doi:10.1111/bph.15814

Dubovskii, P. V., Vassilevski, A. A., Kozlov, S. A., Feofanov, A. V., Grishin, E. V., and Efremov, R. G. (2015). Latarcins: versatile spider venom peptides. *Cell Mol. Life Sci.* 72 (23), 4501–4522. doi:10.1007/s00018-015-2016-x

Duggan, N. M., Saez, N. J., Clayton, D., Budusan, E., Watson, E. E., Tucker, I. J., et al. (2021). Total synthesis of the spider-venom peptide Hi1a. *Org. Lett.* 23 (21), 8375–8379. doi:10.1021/acs.orglett.1c03112

Eagles, D. A., Chow, C. Y., and King, G. F. (2022). Fifteen years of Na(V) 1.7 channels as an analgesic target: why has excellent *in vitro* pharmacology not translated into *in vivo* analgesic efficacy? *Br. J. Pharmacol.* 179 (14), 3592–3611. doi:10.1111/bph.15327

Elnahriry, K. A., Wai, D. C. C., Krishnarjuna, B., Badawy, N. N., Chittoor, B., MacRaild, C. A., et al. (2019). Structural and functional characterisation of a novel peptide from the Australian sea anemone Actinia tenebrosa. *Toxicon* 168, 104–112. doi:10.1016/j.toxicon.2019.07.002

Elrayess, R. A., Mohallal, M. E., Mobarak, Y. M., Ebaid, H. M., Haywood-Small, S., Miller, K., et al. (2021). Scorpion venom antimicrobial peptides induce caspase-1 dependant pyroptotic cell death. *Front. Pharmacol.* 12, 788874. doi:10.3389/fphar.2021.788874

Er, S. Y., Cristofori-Armstrong, B., Escoubas, P., and Rash, L. D. (2017). Discovery and molecular interaction studies of a highly stable, tarantula peptide modulator of acid-sensing ion channel 1. *Neuropharmacology* 127, 185–195. doi:10.1016/j.neuropharm.2017.03.020

Estrada-Gomez, S., Gomez-Rave, L., Vargas-Munoz, L. J., and van der Meijden, A. (2017). Characterizing the biological and biochemical profile of six different scorpion venoms from the Buthidae and Scorpionidae family. *Toxicon* 130, 104–115. doi:10.1016/j.toxicon.2017.02.007

Falcao, C. B., Perez-Peinado, C., de la Torre, B. G., Mayol, X., Zamora-Carreras, H., Jimenez, M. A., et al. (2015). Structural dissection of crotalicidin, a rattlesnake venom

cathelicidin, retrieves a fragment with antimicrobial and antitumor activity. *J. Med. Chem.* 58 (21), 8553–8563. doi:10.1021/acs.jmedchem.5b01142

Faure, G., Harvey, A. L., Thomson, E., Saliou, B., Radvanyi, F., and Bon, C. (1993). Comparison of crotoxin isoforms reveals that stability of the complex plays a major role in its pharmacological action. *Eur. J. Biochem.* 214 (2), 491–496. doi:10.1111/j.1432-1033.1993.tb17946.x

Ferreira, S. H., Bartelt, D. C., and Greene, L. J. (1970). Isolation of bradykinin-potentiating peptides from *Bothrops jararaca* venom. *Biochemistry* 9 (13), 2583–2593. doi:10.1021/bi00815a005

Finol-Urdaneta, R. K., Remedi, M. S., Raasch, W., Becker, S., Clark, R. B., Struver, N., et al. (2012). Block of Kv1.7 potassium currents increases glucose-stimulated insulin secretion. *EMBO Mol. Med.* 4 (5), 424–434. doi:10.1002/emmm.201200218

Flinspach, M., Xu, Q., Piekarz, A. D., Fellows, R., Hagan, R., Gibbs, A., et al. (2017). Insensitivity to pain induced by a potent selective closed-state Nav1.7 inhibitor. *Sci. Rep.* 7, 39662. doi:10.1038/srep39662

Formicola, B., Dal Magro, R., Montefusco-Pereira, C. V., Lehr, C. M., Koch, M., Russo, L., et al. (2019). The synergistic effect of chlorotoxin-mApoE in boosting drug-loaded liposomes across the BBB. *J. Nanobiotechnology* 17 (1), 115. doi:10.1186/s12951-019-0546-3

Fry, B. G., Roelants, K., Champagne, D. E., Scheib, H., Tyndall, J. D., King, G. F., et al. (2009). The toxicogenomic multiverse: convergent recruitment of proteins into animal venoms. *Annu. Rev. Genomics Hum. Genet.* 10, 483–511. doi:10.1146/annurev.genom.9.081307.164356

Fu, S., Hirte, H., Welch, S., Ilenchuk, T. T., Lutes, T., Rice, C., et al. (2017). First-in-human phase I study of SOR-C13, a TRPV6 calcium channel inhibitor, in patients with advanced solid tumors. *Invest. New Drugs* 35 (3), 324–333. doi:10.1007/s10637-017-0438-z

Funk, C., Gmur, J., Herold, R., and Straub, P. W. (1971). Reptilase®-R—a new reagent in blood coagulation. *Br. J. Haematol.* 21 (1), 43–52. doi:10.1111/j.1365-2141.1971.tb03415.x

Gao, R., Shen, Y., Cai, J., Lei, M., and Wang, Z. (2010). Expression of voltage-gated sodium channel alpha subunit in human ovarian cancer. *Oncol. Rep.* 23 (5), 1293–1299. doi:10.3892/or_00000763

Gazerani, P., and Cairns, B. E. (2014). Venom-based biotoxins as potential analgesics. *Expert Rev. Neurother.* 14 (11), 1261–1274. doi:10.1586/14737175.2014.962518

Gerard, L., Duvivier, L., and Gillet, J. P. (2021). Targeting tumor resistance mechanisms. *Fac. Rev.* 10, 6. doi:10.12703/r/10-6

Ghazaryan, N., Movsisyan, N., Macedo, J. C., Vaz, S., Ayvazyan, N., Pardo, L., et al. (2019). The antitumor efficacy of monomeric disintegrin obtustatin in S-180 sarcoma mouse model. *Invest. New Drugs* 37 (5), 1044–1051. doi:10.1007/s10637-019-00734-2

Ghazaryan, N. A., Ghulikyan, L. A., Kishmiryan, A. V., Kirakosyan, G. R., Nazaryan, O. H., Ghevondyan, T. H., et al. (2015). Anti-tumor effect investigation of obtustatin and crude *Macrovipera lebetina* obtusa venom in S-180 sarcoma bearing mice. *Eur. J. Pharmacol.* 764, 340–345. doi:10.1016/j.ejphar.2015.07.011

Ghosh, A., Roy, R., Nandi, M., and Mukhopadhyay, A. (2019). Scorpion venom-toxins that aid in drug development: a review. *Int. J. Pept. Res. Ther.* 25 (1), 27–37. doi:10.1007/s10989-018-9721-x

Girish, V. M., and Kini, R. M. (2016). Exactin: a specific inhibitor of Factor X activation by extrinsic tenase complex from the venom of Hemachatus haemachatus. *Sci. Rep.* 6, 32036. doi:10.1038/srep32036

Gnanasambandam, R., Ghatak, C., Yasmann, A., Nishizawa, K., Sachs, F., Ladokhin, A. S., et al. (2017). GsMTx4: mechanism of inhibiting mechanosensitive ion channels. *Biophys. J.* 112 (1), 31–45. doi:10.1016/j.bpj.2016.11.013

Gomes, G. M., Dalmolin, G. D., Cordeiro, M. doN., Gomez, M. V., Ferreira, J., and Rubin, M. A. (2013). The selective A-type K+ current blocker Tx3-1 isolated from the Phoneutria nigriventer venom enhances memory of naïve and Aβ25-35-treated mice. *Toxicon official J. Int. Soc. Toxinology* 76, 23–27. doi:10.1016/j.toxicon.2013.08.059

Gomis-Ruth, F. X., Kress, L. F., and Bode, W. (1993). First structure of a snake venom metalloproteinase: a prototype for matrix metalloproteinases/collagenases. *EMBO J.* 12 (11), 4151–4157. doi:10.1002/j.1460-2075.1993.tb06099.x

Gopal, G., Muralidar, S., Prakash, D., Kamalakkannan, A., Indhuprakash, S. T., Thirumalai, D., et al. (2023). The concept of Big Four: road map from snakebite epidemiology to antivenom efficacy. *Int. J. Biol. Macromol.* 242 (Pt 1), 124771. doi:10.1016/j.ijbiomac.2023.124771

Graf, N., Mokhtari, T. E., Papayannopoulos, I. A., and Lippard, S. J. (2012). Platinum(IV)-chlorotoxin (CTX) conjugates for targeting cancer cells. *J. Inorg. Biochem.* 110, 58–63. doi:10.1016/j.jinorgbio.2012.02.012

Guido-Patino, J. C., and Plisson, F. (2022). Profiling hymenopteran venom toxins: protein families, structural landscape, biological activities, and pharmacological benefits. *Toxicon X* 14, 100119. doi:10.1016/j.toxcx.2022.100119

Guo, M., Teng, M., Niu, L., Liu, Q., Huang, Q., and Hao, Q. (2005). Crystal structure of the cysteine-rich secretory protein stecrisp reveals that the cysteine-rich domain has a K+ channel inhibitor-like fold. *J. Biol. Chem.* 280 (13), 12405–12412. doi:10.1074/jbc.M413566200

Guo, Q., Huang, M., Li, M., Chen, J., Cheng, S., Ma, L., et al. (2024). Diversity and evolutionary analysis of venom insulin derived from cone snails. *Toxins (Basel)* 16 (1), 34. doi:10.3390/toxins16010034

Guo, R., Chen, X., Nguyen, T., Chai, J., Gao, Y., Wu, J., et al. (2022). The strong anti-tumor effect of Smp24 in lung adenocarcinoma A549 cells depends on its induction of mitochondrial dysfunctions and ROS accumulation. *Toxins (Basel)* 14 (9), 590. doi:10.3390/toxins14090590

Han, R., Liang, H., Qin, Z. H., and Liu, C. Y. (2014). Crotoxin induces apoptosis and autophagy in human lung carcinoma cells *in vitro* via activation of the p38MAPK signaling pathway. *Acta Pharmacol. Sin.* 35 (10), 1323–1332. doi:10.1038/aps.2014.62

Han, S., Yi, H., Yin, S. J., Chen, Z. Y., Liu, H., Cao, Z. J., et al. (2008). Structural basis of a potent peptide inhibitor designed for Kv1.3 channel, a therapeutic target of autoimmune disease. *J. Biol. Chem.* 283 (27), 19058–19065. doi:10.1074/jbc.M802054200

Harel, M., Kleywegt, G. J., Ravelli, R. B., Silman, I., and Sussman, J. L. (1995). Crystal structure of an acetylcholinesterase-fasciculin complex: interaction of a three-fingered toxin from snake venom with its target. *Structure* 3 (12), 1355–1366. doi:10.1016/s0969-2126(01)00273-8

He, J. K., Wu, X. S., Wang, Y., Han, R., Qin, Z. H., and Xie, Y. (2013). Growth inhibitory effects and molecular mechanisms of crotoxin treatment in esophageal Eca-109 cells and transplanted tumors in nude mice. *Acta Pharmacol. Sin.* 34 (2), 295–300. doi:10.1038/aps.2012.156

Herrington, J. (2007). Gating modifier peptides as probes of pancreatic β-cell physiology. *Toxicon* 49 (2), 231–238. doi:10.1016/j.toxicon.2006.09.012

Herrington, J., Sanchez, M., Wunderler, D., Yan, L., Bugianesi, R. M., Dick, I. E., et al. (2005). Biophysical and pharmacological properties of the voltage-gated potassium current of human pancreatic β-cells. *J. Physiol.* 567 (Pt 1), 159–175. doi:10.1113/jphysiol.2005.089375

Herzig, V., Cristofori-Armstrong, B., Israel, M. R., Nixon, S. A., Vetter, I., and King, G. F. (2020). Animal toxins - nature's evolutionary-refined toolkit for basic research and drug discovery. *Biochem. Pharmacol.* 181, 114096. doi:10.1016/j.bcp.2020.114096

Hilchie, A. L., Sharon, A. J., Haney, E. F., Hoskin, D. W., Bally, M. B., Franco, O. L., et al. (2016). Mastoparan is a membranolytic anti-cancer peptide that works synergistically with gemcitabine in a mouse model of mammary carcinoma. *Biochim. Biophys. Acta* 1858 (12), 3195–3204. doi:10.1016/j.bbamem.2016.09.021

Hirsch, E. C., and Hunot, S. (2009). Neuroinflammation in Parkinson's disease: a target for neuroprotection? *Lancet Neurol.* 8 (4), 382–397. doi:10.1016/S1474-4422(09)70062-6

Hiu, J. J., and Yap, M. K. K. (2021). The effects of Naja sumatrana venom cytotoxin, sumaCTX on alteration of the secretome in MCF-7 breast cancer cells following membrane permeabilization. *Int. J. Biol. Macromol.* 184, 776–786. doi:10.1016/j.ijbiomac.2021.06.145

Hmed, B., Serria, H. T., and Mounir, Z. K. (2013). Scorpion peptides: potential use for new drug development. *J. Toxicol.* 2013, 1–15. doi:10.1155/2013/958797

Ho, T. N. T., Abraham, N., and Lewis, R. J. (2020). Structure-function of neuronal nicotinic acetylcholine receptor inhibitors derived from natural toxins. *Front. Neurosci.* 14, 609005. doi:10.3389/fnins.2020.609005

Holford, M., Daly, M., King, G. F., and Norton, R. S. (2018). Venoms to the rescue. *Science* 361 (6405), 842–844. doi:10.1126/science.aau7761

Hurst, R., Rollema, H., and Bertrand, D. (2013). Nicotinic acetylcholine receptors: from basic science to therapeutics. *Pharmacol. Ther.* 137 (1), 22–54. doi:10.1016/j.pharmthera.2012.08.012

Igarashi, T., Araki, S., Mori, H., and Takeda, S. (2007). Crystal structures of catrocollastatin/VAP2B reveal a dynamic, modular architecture of ADAM/adamalysin/reprolysin family proteins. *FEBS Lett.* 581 (13), 2416–2422. doi:10.1016/j.febslet.2007.04.057

Inan, S. Y., Yildirim, S., Tanriover, G., and Ilhan, B. (2024). P/Q type (Ca(v)2.1) calcium channel blocker omega-agatoxin IVA alters cleaved caspase-3 and BDNF expressions in the rat brain and suppresses seizure activity. *Mol. Neurobiol.* 61 (4), 1861–1872. doi:10.1007/s12035-023-03678-0

Izidoro, L. F., Sobrinho, J. C., Mendes, M. M., Costa, T. R., Grabner, A. N., Rodrigues, V. M., et al. (2014). Snake venom L-amino acid oxidases: trends in pharmacology and biochemistry. *Biomed. Res. Int.* 2014, 1–19. doi:10.1155/2014/196754

Jadvar, H., Chen, K., Park, R., Yap, L. P., Vorobyova, I., Swenson, S., et al. (2019). Preclinical evaluation of a (64)Cu-labeled disintegrin for PET imaging of prostate cancer. *Amino Acids* 51 (10-12), 1569–1575. doi:10.1007/s00726-019-02794-3

Jeong, J. K., Moon, M. H., Bae, B. C., Lee, Y. J., Seol, J. W., and Park, S. Y. (2011). Bee venom phospholipase A2 prevents prion peptide induced-cell death in neuronal cells. *Int. J. Mol. Med.* 28 (5), 867–873. doi:10.3892/ijmm.2011.730

Jian, C., Zhang, P., Ma, J., Jian, S., Zhang, Q., Liu, B., et al. (2018). The roles of fatty-acid modification in the activity of the anticancer peptide R-lycosin-I. *Mol. Pharm.* 15 (10), 4612–4620. doi:10.1021/acs.molpharmaceut.8b00605

Jin, C., Ye, Q. H., Yuan, F. L., Gu, Y. L., Li, J. P., Shi, Y. H., et al. (2015). Involvement of acid-sensing ion channel 1α in hepatic carcinoma cell migration and invasion. *Tumour Biol.* 36 (6), 4309–4317. doi:10.1007/s13277-015-3070-6

Joubert, F. J., and Taljaard, N. (1979). Some properties and the complete primary structures of two reduced and S-carboxymethylated polypeptides (S5C1 and S5C10) from Dendroaspis jamesoni kaimosae (Jameson's mamba) venom. *Biochim. Biophys. Acta* 579 (1), 228–233. doi:10.1016/0005-2795(79)90101-6

Jouiaei, M., Yanagihara, A. A., Madio, B., Nevalainen, T. J., Alewood, P. F., and Fry, B. G. (2015). Ancient venom systems: a review on Cnidaria toxins. *Toxins (Basel)* 7 (6), 2251–2271. doi:10.3390/toxins7062251

Joviano-Santos, J. V., Valadao, P. A. C., Magalhaes-Gomes, M. P. S., Fernandes, L. F., Diniz, D. M., Machado, T. C. G., et al. (2021). Protective effect of a spider recombinant toxin in a murine model of Huntington's disease. *Neuropeptides* 85, 102111. doi:10.1016/j.npep.2020.102111

Ju, S., Zhang, Y., Guo, X., Yan, Q., Liu, S., Ma, B., et al. (2022). Anti-ovarian cancer conotoxins identified from Conus venom. *Molecules* 27 (19), 6609. doi:10.3390/molecules27196609

Jumper, J., Evans, R., Pritzel, A., Green, T., Figurnov, M., Ronneberger, O., et al. (2021). Highly accurate protein structure prediction with AlphaFold. *Nature* 596 (7873), 583–589. doi:10.1038/s41586-021-03819-2

Kampo, S., Ahmmed, B., Zhou, T., Owusu, L., Anabah, T. W., Doudou, N. R., et al. (2019). Scorpion venom analgesic peptide, BmK AGAP inhibits stemness, and epithelial-mesenchymal transition by down-regulating PTX3 in breast cancer. *Front. Oncol.* 9, 21. doi:10.3389/fonc.2019.00021

Kampo, S., Cui, Y., Yu, J., Anabah, T. W., Falagan, A. A., Bayor, M. T., et al. (2021). Scorpion Venom peptide, AGAP inhibits TRPV1 and potentiates the analgesic effect of lidocaine. *Heliyon* 7 (12), e08560. doi:10.1016/j.heliyon.2021.e08560

Kang, T. S., Georgieva, D., Genov, N., Murakami, M. T., Sinha, M., Kumar, R. P., et al. (2011). Enzymatic toxins from snake venom: structural characterization and mechanism of catalysis. *FEBS J.* 278 (23), 4544–4576. doi:10.1111/j.1742-4658.2011.08115.x

Kerkis, I., Hayashi, M. A., Prieto da Silva, A. R., Pereira, A., De Sa Junior, P. L., Zaharenko, A. J., et al. (2014). State of the art in the studies on crotamine, a cell penetrating peptide from South American rattlesnake. *Biomed. Res. Int.* 2014, 1–9. doi:10.1155/2014/675985

Kharrat, R., Mabrouk, K., Crest, M., Darbon, H., Oughideni, R., Martin-Eauclaire, M. F., et al. (1996). Chemical synthesis and characterization of maurotoxin, a short scorpion toxin with four disulfide bridges that acts on K+ channels. *Eur. J. Biochem.* 242 (3), 491–498. doi:10.1111/j.1432-1033.1996.0491r.x

Kim, J., Koo, B. K., and Knoblich, J. A. (2020). Human organoids: model systems for human biology and medicine. *Nat. Rev. Mol. Cell Biol.* 21 (10), 571–584. doi:10.1038/s41580-020-0259-3

King, G. F. (2011). Venoms as a platform for human drugs: translating toxins into therapeutics. *Expert Opin. Biol. Ther.* 11 (11), 1469–1484. doi:10.1517/14712598.2011.621940

King, G. F. (2013). Venoms to drugs: translating venom peptides into therapeutics. *Aust. Biochem.* 44 (3), 13–15.

King, G. F., and Hardy, M. C. (2013). Spider-venom peptides: structure, pharmacology, and potential for control of insect pests. *Annu. Rev. Entomol.* 58, 475–496. doi:10.1146/annurev-ento-120811-153650

King, G. F., and Vetter, I. (2014). No gain, no pain: NaV1.7 as an analgesic target. *ACS Chem. Neurosci.* 5 (9), 749–751. doi:10.1021/cn500171p

Kini, R. M. (2006). Anticoagulant proteins from snake venoms: structure, function and mechanism. *Biochem. J.* 397 (3), 377–387. doi:10.1042/BJ20060302

Kini, R. M., and Koh, C. Y. (2020). Snake venom three-finger toxins and their potential in drug development targeting cardiovascular diseases. *Biochem. Pharmacol.* 181, 114105. doi:10.1016/j.bcp.2020.114105

Klaiss-Luna, M. C., Giraldo-Lorza, J. M., Jemiola-Rzeminska, M., Strzalka, K., and Manrique-Moreno, M. (2023). Biophysical insights into the antitumoral activity of crotalicidin against breast cancer model membranes. *Int. J. Mol. Sci.* 24 (22), 16226. doi:10.3390/ijms242216226

Kohn, A. J. (2018). Conus envenomation of humans: in fact and fiction. *Toxins (Basel)* 11 (1), 10. doi:10.3390/toxins11010010

Koludarov, I., Jackson, T. N., Sunagar, K., Nouwens, A., Hendrikx, I., and Fry, B. G. (2014). Fossilized venom: the unusually conserved venom profiles of Heloderma species (beaded lizards and gila monsters). *Toxins (Basel)* 6 (12), 3582–3595. doi:10.3390/toxins6123582

Kozlov, S. A., Vassilevski, A. A., Feofanov, A. V., Surovoy, A. Y., Karpunin, D. V., and Grishin, E. V. (2006). Latarcins, antimicrobial and cytolytic peptides from the venom of the spider Lachesana tarabaevi (Zodariidae) that exemplify biomolecular diversity. *J. Biol. Chem.* 281 (30), 20983–20992. doi:10.1074/jbc.M602168200

Kutzsche, J., Guzman, G. A., Willuweit, A., Kletke, O., Wollert, E., Gering, I., et al. (2024). An orally available Ca(v)2.2 calcium channel inhibitor for the treatment of neuropathic pain. *Br. J. Pharmacol.* 181 (12), 1734–1756. doi:10.1111/bph.16309

Kvetkina, A., Malyarenko, O., Pavlenko, A., Dyshlovoy, S., von Amsberg, G., Ermakova, S., et al. (2020). Sea anemone heteractis crispa actinoporin demonstrates *in vitro* anticancer activities and prevents HT-29 colorectal cancer cell migration. *Molecules* 25 (24), 5979. doi:10.3390/molecules25245979

Langenegger, N., Nentwig, W., and Kuhn-Nentwig, L. (2019). Spider venom: components, modes of action, and novel strategies in transcriptomic and proteomic analyses. *Toxins (Basel)* 11 (10), 611. doi:10.3390/toxins11100611

Lebbe, E. K., Peigneur, S., Wijesekara, I., and Tytgat, J. (2014). Conotoxins targeting nicotinic acetylcholine receptors: an overview. *Mar. Drugs* 12 (5), 2970–3004. doi:10.3390/md12052970

Lebbe, E. K., and Tytgat, J. (2016). In the picture: disulfide-poor conopeptides, a class of pharmacologically interesting compounds. *J. Venom. Anim. Toxins Incl. Trop. Dis.* 22, 30. doi:10.1186/s40409-016-0083-6

Lebreton, L., Tuffigo, M., Pillois, X., and Fiore, M. (2016). L'intégrine $\alpha_{IIb}\beta_3$: Une actrice insoupçonnée dans la formation des plaquettes sanguines. *Med. Sci. Paris.* 32 (3), 290–296. doi:10.1051/medsci/20163203014

Lee, B., Shin, M. K., Hwang, I. W., Jung, J., Shim, Y. J., Kim, G. W., et al. (2021). A deep learning approach with data augmentation to predict novel spider neurotoxic peptides. *Int. J. Mol. Sci.* 22 (22), 12291. doi:10.3390/ijms222212291

Lee, C. J., and Ansell, J. E. (2011). Direct thrombin inhibitors. *Br. J. Clin. Pharmacol.* 72 (4), 581–592. doi:10.1111/j.1365-2125.2011.03916.x

Li, F., Wu, S., Chen, N., Zhu, J., Zhao, X., Zhang, P., et al. (2021). Fatty acid modification of the anticancer peptide LVTX-9 to enhance its cytotoxicity against malignant melanoma cells. *Toxins (Basel)* 13 (12), 867. doi:10.3390/toxins13120867

Li, T., Zhao, X. M., and Li, L. (2022). Co-VAE: drug-target binding affinity prediction by Co-regularized variational Autoencoders. *IEEE Trans. Pattern Anal. Mach. Intell.* 44 (12), 8861–8873. doi:10.1109/TPAMI.2021.3120428

Liao, Q., Feng, Y., Yang, B., and Lee, S. M. (2019). Cnidarian peptide neurotoxins: a new source of various ion channel modulators or blockers against central nervous systems disease. *Drug Discov. Today* 24 (1), 189–197. doi:10.1016/j.drudis.2018.08.011

Ligabue-Braun, R., Verli, H., and Carlini, C. R. (2012). Venomous mammals: a review. *Toxicon* 59 (7-8), 680–695. doi:10.1016/j.toxicon.2012.02.012

Limam, I., Abdelkarim, M., El Ayeb, M., Crepin, M., Marrakchi, N., and Di Benedetto, M. (2023). Disintegrin-like protein strategy to inhibit aggressive triple-negative breast cancer. *Int. J. Mol. Sci.* 24 (15), 12219. doi:10.3390/ijms241512219

Lin, E., Wang, Q., Swenson, S., Jadvar, H., Groshen, S., Ye, W., et al. (2010). The disintegrin contortrostatin in combination with docetaxel is a potent inhibitor of prostate cancer *in vitro* and *in vivo*. *Prostate* 70 (12), 1359–1370. doi:10.1002/pros.21173

Liu, Y., Ming, W., Wang, Y., Liu, S., Qiu, Y., Xiang, Y., et al. (2019). Cytotoxin 1 from Naja atra Cantor venom induced necroptosis of leukemia cells. *Toxicon* 165, 110–115. doi:10.1016/j.toxicon.2019.04.012

Liu, Z., Deng, M., Xiang, J., Ma, H., Hu, W., Zhao, Y., et al. (2012). A novel spider peptide toxin suppresses tumor growth through dual signaling pathways. *Curr. Mol. Med.* 12 (10), 1350–1360. doi:10.2174/156652412803833643

Lluisma, A. O., Lopez-Vera, E., Bulaj, G., Watkins, M., and Olivera, B. M. (2008). Characterization of a novel psi-conotoxin from Conus parius Reeve. *Toxicon* 51 (2), 174–180. doi:10.1016/j.toxicon.2007.07.009

Lucena, S. E., Jia, Y., Soto, J. G., Parral, J., Cantu, E., Brannon, J., et al. (2012). Anti-invasive and anti-adhesive activities of a recombinant disintegrin, r-viridistatin 2, derived from the Prairie rattlesnake (Crotalus viridis viridis). *Toxicon* 60 (1), 31–39. doi:10.1016/j.toxicon.2012.03.011

Luna-Ramirez, K., Quintero-Hernandez, V., Vargas-Jaimes, L., Batista, C. V., Winkel, K. D., and Possani, L. D. (2013). Characterization of the venom from the Australian scorpion Urodacus yaschenkoi: molecular mass analysis of components, cDNA sequences and peptides with antimicrobial activity. *Toxicon* 63, 44–54. doi:10.1016/j.toxicon.2012.11.017

Luo, Q., Wu, T., Wu, W., Chen, G., Luo, X., Jiang, L., et al. (2020). The functional role of voltage-gated sodium channel Nav1.5 in metastatic breast cancer. *Front. Pharmacol.* 11, 1111. doi:10.3389/fphar.2020.01111

Mamelak, A. N., Rosenfeld, S., Bucholz, R., Raubitschek, A., Nabors, L. B., Fiveash, J. B., et al. (2006). Phase I single-dose study of intracavitary-administered iodine-131-TM-601 in adults with recurrent high-grade glioma. *J. Clin. Oncol.* 24 (22), 3644–3650. doi:10.1200/JCO.2005.05.4569

Margiotta, F., Micheli, L., Ciampi, C., Ghelardini, C., McIntosh, J. M., and Di Cesare Mannelli, L. (2022). Conus regius-derived conotoxins: novel therapeutic opportunities from a marine organism. *Mar. Drugs* 20 (12), 773. doi:10.3390/md20120773

Martinez-Hernandez, L., Lopez-Vera, E., Aguilar, M. B., Rodriguez-Ruiz, X. C., and Ortiz-Arellano, M. A. (2023). κO-SrVIA conopeptide, a novel inhibitor peptide for two members of the human EAG potassium channel family. *Int. J. Mol. Sci.* 24 (14), 11513. doi:10.3390/ijms241411513

Matteson, D. R., and Deutsch, C. (1984). K channels in T lymphocytes: a patch clamp study using monoclonal antibody adhesion. *Nature* 307 (5950), 468–471. doi:10.1038/307468a0

McDowell, R. S., Dennis, M. S., Louie, A., Shuster, M., Mulkerrin, M. G., and Lazarus, R. A. (1992). Mambin, a potent glycoprotein IIb-IIIa antagonist and platelet aggregation inhibitor structurally related to the short neurotoxins. *Biochemistry* 31 (20), 4766–4772. doi:10.1021/bi00135a004

McIntosh, M., Cruz, L. J., Hunkapiller, M. W., Gray, W. R., and Olivera, B. M. (1982). Isolation and structure of a peptide toxin from the marine snail Conus magus. *Arch. Biochem. Biophys.* 218 (1), 329–334. doi:10.1016/0003-9861(82)90351-4

Mendes, L. C., Viana, G. M. M., Nencioni, A. L. A., Pimenta, D. C., and Beraldo-Neto, E. (2023). Scorpion peptides and ion channels: an insightful review of mechanisms and drug development. *Toxins (Basel)* 15 (4), 238. doi:10.3390/toxins15040238

Miljanich, G. P. (2004). Ziconotide: neuronal calcium channel blocker for treating severe chronic pain. *Curr. Med. Chem.* 11 (23), 3029–3040. doi:10.2174/0929867043363884

Minea, R. O., Helchowski, C. M., Zidovetzki, S. J., Costa, F. K., Swenson, S. D., and Markland, F. S., Jr. (2010). Vicrostatin - an anti-invasive multi-integrin targeting chimeric disintegrin with tumor anti-angiogenic and pro-apoptotic activities. *PLoS One* 5 (6), e10929. doi:10.1371/journal.pone.0010929

Mlayah-Bellalouna, S., Aissaoui-Zid, D., Chantome, A., Jebali, J., Souid, S., Ayedi, E., et al. (2023). Insights into the mechanisms governing P01 scorpion toxin effect against U87 glioblastoma cells oncogenesis. *Front. Pharmacol.* 14, 1203247. doi:10.3389/fphar.2023.1203247

Mo, Y., Shi, Q., Qi, G., and Chen, K. (2023). Potential anti-tumor effects of *Solenopsis invicta* venom. *Front. Immunol.* 14, 1200659. doi:10.3389/fimmu.2023.1200659

Mohan, M. K., Abraham, N., R, P. R., Jayaseelan, B. F., Ragnarsson, L., Lewis, R. J., et al. (2020). Structure and allosteric activity of a single-disulfide conopeptide from Conus zonatus at human alpha3beta4 and alpha7 nicotinic acetylcholine receptors. *J. Biol. Chem.* 295 (20), 7096–7112. doi:10.1074/jbc.RA119.012098

Morales Duque, H., Campos Dias, S., and Franco, O. L. (2019). Structural and functional analyses of cone snail toxins. *Mar. Drugs* 17 (6), 370. doi:10.3390/md17060370

Moreels, L., Peigneur, S., Yamaguchi, Y., Vriens, K., Waelkens, E., Zhu, S., et al. (2017). Expanding the pharmacological profile of kappa-hefutoxin 1 and analogues: a focus on the inhibitory effect on the oncogenic channel K(v)10.1. *Peptides* 98, 43–50. doi:10.1016/j.peptides.2016.08.008

Morjen, M., Kallech-Ziri, O., Bazaa, A., Othman, H., Mabrouk, K., Zouari-Kessentini, R., et al. (2013). PIVL, a new serine protease inhibitor from *Macrovipera lebetina* transmediterranea venom, impairs motility of human glioblastoma cells. *Matrix Biol.* 32 (1), 52–62. doi:10.1016/j.matbio.2012.11.015

Morsy, M. A., Gupta, S., Dora, C. P., Jhawat, V., Dhanawat, M., Mehta, D., et al. (2023). Venoms classification and therapeutic uses: a narrative review. *Eur. Rev. Med. Pharmacol. Sci.* 27 (4), 1633–1653. doi:10.26355/eurrev_202302_31408

Mouhat, S., Visan, V., Ananthakrishnan, S., Wulff, H., Andreotti, N., Grissmer, S., et al. (2005). K+ channel types targeted by synthetic OSK1, a toxin from Orthochirus scrobiculosus scorpion venom. *Biochem. J.* 385 (Pt 1), 95–104. doi:10.1042/BJ20041379

Muller, S. P., Silva, V. A. O., Silvestrini, A. V. P., de Macedo, L. H., Caetano, G. F., Reis, R. M., et al. (2018). Crotoxin from *Crotalus durissus* terrificus venom: *in vitro* cytotoxic activity of a heterodimeric phospholipase A(2) on human cancer-derived cell lines. *Toxicon* 156, 13–22. doi:10.1016/j.toxicon.2018.10.306

Munawar, A., Ali, S. A., Akrem, A., and Betzel, C. (2018). Snake venom peptides: tools of biodiscovery. *Toxins (Basel)* 10 (11), 474. doi:10.3390/toxins10110474

Munhoz, J., Thome, R., Rostami, A., Ishikawa, L. L. W., Verinaud, L., and Raposo, C. (2021). The SNX-482 peptide from Hysterocrates gigas spider acts as an immunomodulatory molecule activating macrophages. *Peptides* 146, 170648. doi:10.1016/j.peptides.2021.170648

Murray, C. J., Rosenfeld, L. C., Lim, S. S., Andrews, K. G., Foreman, K. J., Haring, D., et al. (2012). Global malaria mortality between 1980 and 2010: a systematic analysis. *Lancet* 379 (9814), 413–431. doi:10.1016/S0140-6736(12)60034-8

Nadkarni, P., Chepurny, O. G., and Holz, G. G. (2014). Regulation of glucose homeostasis by GLP-1. *Prog. Mol. Biol. Transl. Sci.* 121, 23–65. doi:10.1016/B978-0-12-800101-1.00002-8

Nascimento, F. D., Sancey, L., Pereira, A., Rome, C., Oliveira, V., Oliveira, E. B., et al. (2012). The natural cell-penetrating peptide crotamine targets tumor tissue *in vivo* and triggers a lethal calcium-dependent pathway in cultured cells. *Mol. Pharm.* 9 (2), 211–221. doi:10.1021/mp2000605

Nauck, M. A., Quast, D. R., Wefers, J., and Meier, J. J. (2021). GLP-1 receptor agonists in the treatment of type 2 diabetes - state-of-the-art. *Mol. Metab.* 46, 101102. doi:10.1016/j.molmet.2020.101102

Neff, R. A., and Wickenden, A. D. (2021). Selective targeting of Nav1.7 with engineered spider venom-based peptides. *Channels (Austin)* 15 (1), 193–207. doi:10.1080/19336950.2020.1860382

Newcomb, R., Szoke, B., Palma, A., Wang, G., Chen, X., Hopkins, W., et al. (1998). Selective peptide antagonist of the class E calcium channel from the venom of the tarantula Hysterocrates gigas. *Biochemistry* 37 (44), 15353–15362. doi:10.1021/bi981255g

Nguyen, P. T., Nguyen, H. M., Wagner, K. M., Stewart, R. G., Singh, V., Thapa, P., et al. (2022a). Computational design of peptides to target Na(V)1.7 channel with high potency and selectivity for the treatment of pain. *Elife* 11, e81727. doi:10.7554/eLife.81727

Nguyen, T., Guo, R., Chai, J., Wu, J., Liu, J., Chen, X., et al. (2022b). Smp24, a scorpion-venom peptide, exhibits potent antitumor effects against hepatoma HepG2 cells via multi-mechanisms *in vivo* and *in vitro*. *Toxins (Basel)* 14 (10), 717. doi:10.3390/toxins14100717

Nielsen, C. K., Lewis, R. J., Alewood, D., Drinkwater, R., Palant, E., Patterson, M., et al. (2005). Anti-allodynic efficacy of the chi-conopeptide, Xen2174, in rats with neuropathic pain. *Pain* 118 (1-2), 112–124. doi:10.1016/j.pain.2005.08.002

Nimmrich, V., and Gross, G. (2012). P/Q-type calcium channel modulators. *Br. J. Pharmacol.* 167 (4), 741–759. doi:10.1111/j.1476-5381.2012.02069.x

Okada, M., Corzo, G., Romero-Perez, G. A., Coronas, F., Matsuda, H., and Possani, L. D. (2015). A pore forming peptide from spider Lachesana sp. venom induced neuronal depolarization and pain. *Biochim. Biophys. Acta* 1850 (4), 657–666. doi:10.1016/j.bbagen.2014.11.022

Okada, M., Ortiz, E., Corzo, G., and Possani, L. D. (2019). Pore-forming spider venom peptides show cytotoxicity to hyperpolarized cancer cells expressing K+ channels: a lentiviral vector approach. *PLoS One* 14 (4), e0215391. doi:10.1371/journal.pone.0215391

Okkerse, P., Hay, J. L., Sitsen, E., Dahan, A., Klaassen, E., Houghton, W., et al. (2017). Pharmacokinetics and pharmacodynamics of intrathecally administered Xen2174, a synthetic conopeptide with norepinephrine reuptake inhibitor and analgesic properties. *Br. J. Clin. Pharmacol.* 83 (4), 751–763. doi:10.1111/bcp.13176

Olaoba, O. T., Karina Dos Santos, P., Selistre-de-Araujo, H. S., and Ferreira de Souza, D. H. (2020). Snake venom metalloproteinases (SVMPs): a structure-function update. *Toxicon X* 7, 100052. doi:10.1016/j.toxcx.2020.100052

Oliveira, A. L., Viegas, M. F., da Silva, S. L., Soares, A. M., Ramos, M. J., and Fernandes, P. A. (2022). The chemistry of snake venom and its medicinal potential. *Nat. Rev. Chem.* 6 (7), 451–469. doi:10.1038/s41570-022-00393-7

Oliveira-Mendes, B. B. R., Horta, C. C. R., do Carmo, A. O., Biscoto, G. L., Sales-Medina, D. F., Leal, H. G., et al. (2018). CPP-Ts: a new intracellular calcium channel modulator and a promising tool for drug delivery in cancer cells. *Sci. Rep.* 8 (1), 14739. doi:10.1038/s41598-018-33133-3

Olsen, C., Tarcha, E., Probst, P., Peckham, D., and Iadonato, S. (2016). LB779 Dalazatide (ShK-186), a first-in-class peptide inhibitor of Kv1.3 potassium channels, demonstrates safety, tolerability and proof of concept of efficacy in patients with active plaque psoriasis. *J. Investigative Dermatology* 136 (8), B5. doi:10.1016/j.jid.2016.05.029

Ortiz, E., Gurrola, G. B., Schwartz, E. F., and Possani, L. D. (2015). Scorpion venom components as potential candidates for drug development. *Toxicon* 93, 125–135. doi:10.1016/j.toxicon.2014.11.233

Osteen, J. D., Herzig, V., Gilchrist, J., Emrick, J. J., Zhang, C., Wang, X., et al. (2016). Selective spider toxins reveal a role for the Nav1.1 channel in mechanical pain. *Nature* 534 (7608), 494–499. doi:10.1038/nature17976

Ownby, C. L., Fletcher, J. E., and Colberg, T. R. (1993). Cardiotoxin 1 from cobra (Naja naja atra) venom causes necrosis of skeletal muscle *in vivo*. *Toxicon* 31 (6), 697–709. doi:10.1016/0041-0101(93)90376-t

Pandey, P., Khan, F., Khan, M. A., Kumar, R., and Upadhyay, T. K. (2023). An updated review summarizing the anticancer efficacy of melittin from bee venom in several models of human cancers. *Nutrients* 15 (14), 3111. doi:10.3390/nu15143111

Pardo, L. A., del Camino, D., Sanchez, A., Alves, F., Bruggemann, A., Beckh, S., et al. (1999). Oncogenic potential of EAG K(+) channels. *EMBO J.* 18 (20), 5540–5547. doi:10.1093/emboj/18.20.5540

Patchett, A. A. (1984). The chemistry of enalapril. *Br. J. Clin. Pharmacol.* 18 (Suppl. 2), 201S–207S. doi:10.1111/j.1365-2125.1984.tb02599.x

Patil, C. G., Walker, D. G., Miller, D. M., Butte, P., Morrison, B., Kittle, D. S., et al. (2019). Phase 1 safety, pharmacokinetics, and fluorescence imaging study of tozuleristide (BLZ-100) in adults with newly diagnosed or recurrent gliomas. *Neurosurgery* 85 (4), E641–E649. doi:10.1093/neuros/nyz125

Pedron, C., Antunes, F. T. T., Rebelo, I. N., Campos, M. M., Correa, A. P., Klein, C. P., et al. (2021). Phoneutria nigriventer Tx3-3 peptide toxin reduces fibromyalgia symptoms in mice. *Neuropeptides* 85, 102094. doi:10.1016/j.npep.2020.102094

Peigneur, S., de Lima, M. E., and Tytgat, J. (2018). Phoneutria nigriventer venom: a pharmacological treasure. *Toxicon* 151, 96–110. doi:10.1016/j.toxicon.2018.07.008

Peigneur, S., Devi, P., Seldeslachts, A., Ravichandran, S., Quinton, L., and Tytgat, J. (2019). Structure-function elucidation of a new α-conotoxin, MilIA, from Conus milneedwardsi. *Mar. Drugs* 17 (9), 535. doi:10.3390/md17090535

Pereira, A., Kerkis, A., Hayashi, M. A., Pereira, A. S., Silva, F. S., Oliveira, E. B., et al. (2011). Crotamine toxicity and efficacy in mouse models of melanoma. *Expert Opin. Investig. Drugs* 20 (9), 1189–1200. doi:10.1517/13543784.2011.602064

Perez-Peinado, C., Valle, J., Freire, J. M., and Andreu, D. (2020). Tumor cell attack by crotalicidin (ctn) and its fragment ctn[15-34]: insights into their dual membranolytic and intracellular targeting mechanism. *ACS Chem. Biol.* 15 (11), 2945–2957. doi:10.1021/acschembio.0c00596

Phillips, A. J., Govedich, F. R., and Moser, W. E. (2020). Leeches in the extreme: morphological, physiological, and behavioral adaptations to inhospitable habitats. *Int. J. Parasitol. Parasites Wildl.* 12, 318–325. doi:10.1016/j.ijppaw.2020.09.003

Phuong, H. B. T., Tran, V. A., Ngoc, K. N., Huu, V. N., Thu, H. N., Van, M. C., et al. (2023). Effect of substituting glutamine with lysine on structural and biological properties of antimicrobial peptide Polybia-MP1. *Amino Acids* 55 (7), 881–890. doi:10.1007/s00726-023-03276-3

Ponce-Soto, L. A., Lomonte, B., Gutierrez, J. M., Rodrigues-Simioni, L., Novello, J. C., and Marangoni, S. (2007). Structural and functional properties of BaTX, a new Lys49 phospholipase A2 homologue isolated from the venom of the snake Bothrops alternatus. *Biochim. Biophys. Acta* 1770 (4), 585–593. doi:10.1016/j.bbagen.2006.11.015

Potter, L. R., Yoder, A. R., Flora, D. R., Antos, L. K., and Dickey, D. M. (2009). Natriuretic peptides: their structures, receptors, physiologic functions and therapeutic applications. *Handb. Exp. Pharmacol.* 191, 341–366. doi:10.1007/978-3-540-68964-5_15

Prieto, A. R., Ma, H., Huang, R., Khan, G., Schwartz, K. A., Hage-Korban, E. E., et al. (2002). Thrombostatin, a bradykinin metabolite, reduces platelet activation in a model of arterial wall injury. *Cardiovasc Res.* 53 (4), 984–992. doi:10.1016/s0008-6363(01)00514-4

Qi, J., Wang, W., Lu, W., Chen, W., Sun, H., and Shang, A. (2020). Design and biological evaluation of novel BF-30 analogs for the treatment of malignant melanoma. *J. Cancer* 11 (24), 7184–7195. doi:10.7150/jca.47549

Rashid, M. H., Huq, R., Tanner, M. R., Chhabra, S., Khoo, K. K., Estrada, R., et al. (2014). A potent and Kv1.3-selective analogue of the scorpion toxin HsTX1 as a potential therapeutic for autoimmune diseases. *Sci. Rep.* 4, 4509. doi:10.1038/srep04509

Ratibou, Z., Inguimbert, N., and Dutertre, S. (2024). Predatory and defensive strategies in cone snails. *Toxins (Basel)* 16 (2), 94. doi:10.3390/toxins16020094

Reis, P. V. M., Boff, D., Verly, R. M., Melo-Braga, M. N., Cortes, M. E., Santos, D. M., et al. (2018). LyeTxI-b, a synthetic peptide derived from Lycosa erythrognatha spider venom, shows potent antibiotic activity *in vitro* and *in vivo*. *Front. Microbiol.* 9, 667. doi:10.3389/fmicb.2018.00667

Ren, C., Li, Y., Cong, Z., Li, Z., Xie, L., and Wu, S. (2023). Bioengineered bacterial outer membrane vesicles encapsulated Polybia-mastoparan I fusion peptide as a promising nanoplatform for bladder cancer immune-modulatory chemotherapy. *Front. Immunol.* 14, 1129771. doi:10.3389/fimmu.2023.1129771

Richards, K. L., Milligan, C. J., Richardson, R. J., Jancovski, N., Grunnet, M., Jacobson, L. H., et al. (2018). Selective Na(V)1.1 activation rescues Dravet syndrome mice from seizures and premature death. *Proc. Natl. Acad. Sci. U. S. A.* 115 (34), E8077–E8085. doi:10.1073/pnas.1804764115

Rigo, F. K., Trevisan, G., Rosa, F., Dalmolin, G. D., Otuki, M. F., Cueto, A. P., et al. (2013). Spider peptide Phα1β induces analgesic effect in a model of cancer pain. *Cancer Sci.* 104 (9), 1226–1230. doi:10.1111/cas.12209

Robinson, S. D., and Norton, R. S. (2014). Conotoxin gene superfamilies. *Mar. Drugs* 12 (12), 6058–6101. doi:10.3390/md12126058

Rooj, A. K., McNicholas, C. M., Bartoszewski, R., Bebok, Z., Benos, D. J., and Fuller, C. M. (2012). Glioma-specific cation conductance regulates migration and cell cycle progression. *J. Biol. Chem.* 287 (6), 4053–4065. doi:10.1074/jbc.M111.311688

Rosso, J. P., Schwarz, J. R., Diaz-Bustamante, M., Ceard, B., Gutierrez, J. M., Kneussel, M., et al. (2015). MmTX1 and MmTX2 from coral snake venom potently modulate GABAA receptor activity. *Proc. Natl. Acad. Sci. U. S. A.* 112 (8), E891–E900. doi:10.1073/pnas.1415488112

Russell, F. E., and Bogert, C. M. (1981). Gila monster: its biology, venom and bite--a review. *Toxicon* 19 (3), 341–359. doi:10.1016/0041-0101(81)90040-4

Sachs, F. (2015). Mechanical transduction by ion channels: a cautionary tale. *World J. Neurol.* 5 (3), 74–87. doi:10.5316/wjn.v5.i3.74

Sadat, S. N., Bagheri, K. P., Maghsoudi, H., and Shahbazzadeh, D. (2023). Oxineur, a novel peptide from Caspian cobra Naja naja oxiana against HT-29 colon cancer. *Biochim. Biophys. Acta Gen. Subj.* 1867 (2), 130285. doi:10.1016/j.bbagen.2022.130285

Saez, N. J., and Herzig, V. (2019). Versatile spider venom peptides and their medical and agricultural applications. *Toxicon* 158, 109–126. doi:10.1016/j.toxicon.2018.11.298

Safavi-Hemami, H., Gajewiak, J., Karanth, S., Robinson, S. D., Ueberheide, B., Douglass, A. D., et al. (2015). Specialized insulin is used for chemical warfare by fish-hunting cone snails. *Proc. Natl. Acad. Sci. U. S. A.* 112 (6), 1743–1748. doi:10.1073/pnas.1423857112

Sandall, D. W., Satkunanathan, N., Keays, D. A., Polidano, M. A., Liping, X., Pham, V., et al. (2003). A novel α-conotoxin identified by gene sequencing is active in suppressing the vascular response to selective stimulation of sensory nerves *in vivo*. *Biochemistry* 42 (22), 6904–6911. doi:10.1021/bi034043e

Sang, C. N., Barnabe, K. J., and Kern, S. E. (2016). Phase ia clinical trial evaluating the tolerability, pharmacokinetics, and analgesic efficacy of an intrathecally administered neurotensin A analogue in central neuropathic pain following spinal cord injury. *Clin. Pharmacol. Drug Dev.* 5 (4), 250–258. doi:10.1002/cpdd.253

Sanggaard, K. W., Dyrlund, T. F., Thomsen, L. R., Nielsen, T. A., Brondum, L., Wang, T., et al. (2015). Characterization of the gila monster (*Heloderma suspectum* suspectum) venom proteome. *J. Proteomics* 117, 1–11. doi:10.1016/j.jprot.2015.01.004

Santos, D. M., Verly, R. M., Pilo-Veloso, D., de Maria, M., de Carvalho, M. A., Cisalpino, P. S., et al. (2010). LyeTx I, a potent antimicrobial peptide from the venom of the spider Lycosa erythrognatha. *Amino Acids* 39 (1), 135–144. doi:10.1007/s00726-009-0385-x

Saverioni, D., Notari, S., Capellari, S., Poggiolini, I., Giese, A., Kretzschmar, H. A., et al. (2013). Analyses of protease resistance and aggregation state of abnormal prion protein across the spectrum of human prions. *J. Biol. Chem.* 288 (39), 27972–27985. doi:10.1074/jbc.M113.477547

Schendel, V., Rash, L. D., Jenner, R. A., and Undheim, E. A. B. (2019). The diversity of venom: the importance of behavior and venom system morphology in understanding its ecology and evolution. *Toxins (Basel)* 11 (11), 666. doi:10.3390/toxins11110666

Schonthal, A. H., Swenson, S. D., Chen, T. C., and Markland, F. S. (2020). Preclinical studies of a novel snake venom-derived recombinant disintegrin with antitumor activity: a review. *Biochem. Pharmacol.* 181, 114149. doi:10.1016/j.bcp.2020.114149

Schwartz, E. F., Capes, E. M., Diego-Garcia, E., Zamudio, F. Z., Fuentes, O., Possani, L. D., et al. (2009). Characterization of hadrucalcin, a peptide from Hadrurus gertschi scorpion venom with pharmacological activity on ryanodine receptors. *Br. J. Pharmacol.* 157 (3), 392–403. doi:10.1111/j.1476-5381.2009.00147.x

Seo, S., Choi, J., Park, S., and Ahn, J. (2021). Binding affinity prediction for protein-ligand complex using deep attention mechanism based on intermolecular interactions. *BMC Bioinforma.* 22 (1), 542. doi:10.1186/s12859-021-04466-0

Serrano, S. M., and Maroun, R. C. (2005). Snake venom serine proteinases: sequence homology vs. substrate specificity, a paradox to be solved. *Toxicon* 45 (8), 1115–1132. doi:10.1016/j.toxicon.2005.02.020

Servent, D., Blanchet, G., Mourier, G., Marquer, C., Marcon, E., and Fruchart-Gaillard, C. (2011). Muscarinic toxins. *Toxicon* 58 (6-7), 455–463. doi:10.1016/j.toxicon.2011.08.004

Shahbazzadeh, D., Srairi-Abid, N., Feng, W., Ram, N., Borchani, L., Ronjat, M., et al. (2007). Hemicalcin, a new toxin from the Iranian scorpion Hemiscorpius lepturus which is active on ryanodine-sensitive Ca2+ channels. *Biochem. J.* 404 (1), 89–96. doi:10.1042/BJ20061404

Shen, H., Xie, Y., Ye, S., He, K., Yi, L., and Cui, R. (2018). Spider peptide toxin lycosin-I induces apoptosis and inhibits migration of prostate cancer cells. *Exp. Biol. Med. (Maywood)* 243 (8), 725–735. doi:10.1177/1535370218772802

Shiu, J. H., Chen, C. Y., Chang, L. S., Chen, Y. C., Chen, Y. C., Lo, Y. H., et al. (2004). Solution structure of gamma-bungarotoxin: the functional significance of amino acid residues flanking the RGD motif in integrin binding. *Proteins* 57 (4), 839–849. doi:10.1002/prot.20269

Sieghart, W. (2006). Structure, pharmacology, and function of GABAA receptor subtypes. *Adv. Pharmacol.* 54, 231–263. doi:10.1016/s1054-3589(06)54010-4

Silva, F. R., Batista, E. M., Gomez, M. V., Kushmerick, C., Da Silva, J. F., Cordeiro, M. N., et al. (2016). The Phoneutria nigriventer spider toxin, PnTx4-5-5, promotes neuronal survival by blocking NMDA receptors. *Toxicon official J. Int. Soc. Toxinology* 112, 16–21. doi:10.1016/j.toxicon.2016.01.056

Simoes-Silva, R., Alfonso, J., Gomez, A., Holanda, R. J., Sobrinho, J. C., Zaqueo, K. D., et al. (2018). Snake venom, A natural library of new potential therapeutic molecules: challenges and current perspectives. *Curr. Pharm. Biotechnol.* 19 (4), 308–335. doi:10.2174/1389201019666180620111025

Smith, J. J., Lau, C. H. Y., Herzig, V., Ikonomopoulou, M. P., Rash, L. D., and King, G. F. (2015). "Therapeutic applications of spider-venom peptides," in *Venoms to drugs: therapeutic applications of spider-venom peptides*, 221–244.

Smith, J. J., Vetter, I., Lewis, R. J., Peigneur, S., Tytgat, J., Lam, A., et al. (2013). Multiple actions of phi-LITX-Lw1a on ryanodine receptors reveal a functional link between scorpion DDH and ICK toxins. *Proc. Natl. Acad. Sci. U. S. A.* 110 (22), 8906–8911. doi:10.1073/pnas.1214062110

Soares, S., Lopes, K. S., Mortari, M., Oliveira, H., and Bastos, V. (2022). Antitumoral potential of Chartergellus-CP1 peptide from Chartergellus communis wasp venom in two different breast cancer cell lines (HR+ and triple-negative). *Toxicon* 216, 148–156. doi:10.1016/j.toxicon.2022.07.004

Soltan-Alinejad, P., Alipour, H., Meharabani, D., and Azizi, K. (2022). Therapeutic potential of bee and scorpion venom phospholipase A2 (PLA2): a narrative review. *Iran. J. Med. Sci.* 47 (4), 300–313. doi:10.30476/IJMS.2021.88511.1927

Son, D. J., Lee, J. W., Lee, Y. H., Song, H. S., Lee, C. K., and Hong, J. T. (2007). Therapeutic application of anti-arthritis, pain-releasing, and anti-cancer effects of bee venom and its constituent compounds. *Pharmacol. Ther.* 115 (2), 246–270. doi:10.1016/j.pharmthera.2007.04.004

Sousa, S. R., Vetter, I., and Lewis, R. J. (2013). Venom peptides as a rich source of cav2.2 channel blockers. *Toxins (Basel)* 5 (2), 286–314. doi:10.3390/toxins5020286

Souza, B. M., Mendes, M. A., Santos, L. D., Marques, M. R., Cesar, L. M., Almeida, R. N., et al. (2005). Structural and functional characterization of two novel peptide toxins isolated from the venom of the social wasp Polybia paulista. *Peptides* 26 (11), 2157–2164. doi:10.1016/j.peptides.2005.04.026

Souza, I. A., Cino, E. A., Choy, W. Y., Cordeiro, M. N., Richardson, M., Chavez-Olortegui, C., et al. (2012). Expression of a recombinant Phoneutria toxin active in calcium channels. *Toxicon official J. Int. Soc. Toxinology* 60 (5), 907–918. doi:10.1016/j.toxicon.2012.05.026

Stepensky, D. (2018). Pharmacokinetics of toxin-derived peptide drugs. *Toxins (Basel)* 10 (11), 483. doi:10.3390/toxins10110483

Stewart, J. M. (2018). *Peptide composition for cancer treatment by inhibiting TRPV6 calcium channel activity United States of America patent application 15/088,993*.

Stewart, J. M., Steeves, B. J., and Vernes, K. (2006). *Paralytic peptide for use in neuromuscular therapy United States of America patent application 10/858,233*.

Sudarikova, A. V., Bychkov, M. L., Kulbatskii, D. S., Chubinskiy-Nadezhdin, V. I., Shlepova, O. V., Shulepko, M. A., et al. (2022). Mambalgin-2 inhibits lung adenocarcinoma growth and migration by selective interaction with ASIC1/α-ENaC/γ-ENaC heterotrimer. *Front. Oncol.* 12, 904742. doi:10.3389/fonc.2022.904742

Swartz, K. J., and MacKinnon, R. (1995). An inhibitor of the Kv2.1 potassium channel isolated from the venom of a Chilean tarantula. *Neuron* 15 (4), 941–949. doi:10.1016/0896-6273(95)90184-1

Swenson, S., Costa, F., Minea, R., Sherwin, R. P., Ernst, W., Fujii, G., et al. (2004). Intravenous liposomal delivery of the snake venom disintegrin contortrostatin limits breast cancer progression. *Mol. cancer Ther.* 3 (4), 499–511. doi:10.1158/1535-7163.499.3.4

Swenson, S., Minea, R. O., Tuan, C. D., Thein, T. Z., Chen, T. C., and Markland, F. S. (2018). A novel venom-derived peptide for brachytherapy of glioblastoma: preclinical studies in mice. *Molecules* 23 (11), 2918. doi:10.3390/molecules23112918

Tadokoro, T., Modahl, C. M., Maenaka, K., and Aoki-Shioi, N. (2020). Cysteine-rich secretory proteins (CRISPs) from venomous snakes: an overview of the functional diversity in A large and underappreciated superfamily. *Toxins (Basel)* 12 (3), 175. doi:10.3390/toxins12030175

Tan, H., Huang, Y., Xu, J., Chen, B., Zhang, P., Ye, Z., et al. (2017). Spider toxin peptide lycosin-I functionalized gold nanoparticles for *in vivo* tumor targeting and therapy. *Theranostics* 7 (12), 3168–3178. doi:10.7150/thno.19780

Tan, H., Liu, S., He, Y., Cheng, G., Zhang, Y., Wei, X., et al. (2021). Spider toxin peptide-induced NIR gold nanocluster fabrication for GSH-responsive cancer cell imaging and nuclei translocation. *Front. Bioeng. Biotechnol.* 9, 780223. doi:10.3389/fbioe.2021.780223

Tan, H., Luo, W., Wei, L., Chen, B., Li, W., Xiao, L., et al. (2016). Quantifying the distribution of the stoichiometric composition of anticancer peptide lycosin-I on the lipid membrane with single molecule spectroscopy. *J. Phys. Chem. B* 120 (12), 3081–3088. doi:10.1021/acs.jpcb.5b12618

Tarcha, E. J., Olsen, C. M., Probst, P., Peckham, D., Munoz-Elias, E. J., Kruger, J. G., et al. (2017). Safety and pharmacodynamics of dalazatide, a Kv1.3 channel inhibitor, in the treatment of plaque psoriasis: a randomized phase 1b trial. *PLoS One* 12 (7), e0180762. doi:10.1371/journal.pone.0180762

Tasoulis, T., and Isbister, G. K. (2017). A review and database of snake venom proteomes. *Toxins (Basel)* 9 (9), 290. doi:10.3390/toxins9090290

Tasoulis, T., and Isbister, G. K. (2023). A current perspective on snake venom composition and constituent protein families. *Arch. Toxicol.* 97 (1), 133–153. doi:10.1007/s00204-022-03420-0

Teesalu, T., Sugahara, K. N., Kotamraju, V. R., and Ruoslahti, E. (2009). C-end rule peptides mediate neuropilin-1-dependent cell, vascular, and tissue penetration. *Proc. Natl. Acad. Sci. U. S. A.* 106 (38), 16157–16162. doi:10.1073/pnas.0908201106

Teoh, S., and Yap, M. (2020). Naja sumatrana venom cytotoxin, suma CTX exhibits concentration-dependent cytotoxicity via caspase-activated mitochondrial-mediated apoptosis without transitioning to necrosis. *Toxin Rev.* 40, 886–900. doi:10.1080/15569543.2020.1799408

Terlau, H., and Olivera, B. M. (2004). Conus venoms: a rich source of novel ion channel-targeted peptides. *Physiol. Rev.* 84 (1), 41–68. doi:10.1152/physrev.00020.2003

Tonello, R., Rigo, F., Gewehr, C., Trevisan, G., Pereira, E. M., Gomez, M. V., et al. (2014). Action of Phα1β, a peptide from the venom of the spider Phoneutria nigriventer, on the analgesic and adverse effects caused by morphine in mice. *J. Pain* 15 (6), 619–631. doi:10.1016/j.jpain.2014.02.007

Tsend-Ayush, E., He, C., Myers, M. A., Andrikopoulos, S., Wong, N., Sexton, P. M., et al. (2016). Monotreme glucagon-like peptide-1 in venom and gut: one gene - two very different functions. *Sci. Rep.* 6, 37744. doi:10.1038/srep37744

Tuba, Z., Maho, S., and Vizi, E. S. (2002). Synthesis and structure-activity relationships of neuromuscular blocking agents. *Curr. Med. Chem.* 9 (16), 1507–1536. doi:10.2174/0929867023369466

Ullah, A. (2020). Structure-function studies and mechanism of action of snake venom L-amino acid oxidases. *Front. Pharmacol.* 11, 110. doi:10.3389/fphar.2020.00110

Urra, F. A., Pulgar, R., Gutierrez, R., Hodar, C., Cambiazo, V., and Labra, A. (2015). Identification and molecular characterization of five putative toxins from the venom gland of the snake Philodryas chamissonis (Serpentes: dipsadidae). *Toxicon* 108, 19–31. doi:10.1016/j.toxicon.2015.09.032

Utkin, Y., Vassilevski, A., Kudryavtsev, D., and Undheim, E. A. B. (2019). Editorial: animal toxins as comprehensive pharmacological tools to identify diverse ion channels. *Front. Pharmacol.* 10, 423. doi:10.3389/fphar.2019.00423

Utkin, Y. N. (2015). Animal venom studies: current benefits and future developments. *World J. Biol. Chem.* 6 (2), 28–33. doi:10.4331/wjbc.v6.i2.28

Utkin, Y. N. (2019). Last decade update for three-finger toxins: newly emerging structures and biological activities. *World J. Biol. Chem.* 10 (1), 17–27. doi:10.4331/wjbc.v10.i1.17

Valdivia, H. H., Kirby, M. S., Lederer, W. J., and Coronado, R. (1992). Scorpion toxins targeted against the sarcoplasmic reticulum Ca(2+)-release channel of skeletal and cardiac muscle. *Proc. Natl. Acad. Sci. U. S. A.* 89 (24), 12185–12189. doi:10.1073/pnas.89.24.12185

Vannini, E., Mori, E., Tantillo, E., Schmidt, G., Caleo, M., and Costa, M. (2021). CTX-CNF1 recombinant protein selectively targets glioma cells *in vivo*. *Toxins (Basel)* 13 (3), 194. doi:10.3390/toxins13030194

Vargas-Jaimes, L., Xiao, L., Zhang, J., Possani, L. D., Valdivia, H. H., and Quintero-Hernandez, V. (2017). Recombinant expression of Intrepicalcin from the scorpion Vaejovis intrepidus and its effect on skeletal ryanodine receptors. *Biochim. Biophys. Acta Gen. Subj.* 1861 (4), 936–946. doi:10.1016/j.bbagen.2017.01.032

Vasconcelos, A. A., Estrada, J. C., David, V., Wermelinger, L. S., Almeida, F. C. L., and Zingali, R. B. (2021). Structure-function relationship of the disintegrin family: sequence signature and integrin interaction. *Front. Mol. Biosci.* 8, 783301. doi:10.3389/fmolb.2021.783301

Veiseh, M., Gabikian, P., Bahrami, S. B., Veiseh, O., Zhang, M., Hackman, R. C., et al. (2007). Tumor paint: a chlorotoxin:Cy5.5 bioconjugate for intraoperative visualization of cancer foci. *Cancer Res.* 67 (14), 6882–6888. doi:10.1158/0008-5472.CAN-06-3948

Vieira, L. B., Kushmerick, C., Hildebrand, M. E., Garcia, E., Stea, A., Cordeiro, M. N., et al. (2005). Inhibition of high voltage-activated calcium channels by spider toxin PnTx3-6. *J. Pharmacol. Exp. Ther.* 314 (3), 1370–1377. doi:10.1124/jpet.105.087023

Vines, J. B., Yoon, J. H., Ryu, N. E., Lim, D. J., and Park, H. (2019). Gold nanoparticles for photothermal cancer therapy. *Front. Chem.* 7, 167. doi:10.3389/fchem.2019.00167

Vu, T. T., Stafford, A. R., Leslie, B. A., Kim, P. Y., Fredenburgh, J. C., and Weitz, J. I. (2013). Batroxobin binds fibrin with higher affinity and promotes clot expansion to a greater extent than thrombin. *J. Biol. Chem.* 288 (23), 16862–16871. doi:10.1074/jbc.M113.464750

Wang, H., Ke, M., Tian, Y., Wang, J., Li, B., Wang, Y., et al. (2013). BF-30 selectively inhibits melanoma cell proliferation via cytoplasmic membrane permeabilization and DNA-binding *in vitro* and in B16F10-bearing mice. *Eur. J. Pharmacol.* 707 (1-3), 1–10. doi:10.1016/j.ejphar.2013.03.028

Wang, J., Qin, X., Zhang, Z., Chen, M., Wang, Y., and Gao, B. (2014). Crotoxin suppresses the tumorigenic properties and enhances the antitumor activity of Iressa® (gefinitib) in human lung adenocarcinoma SPCA-1 cells. *Mol. Med. Rep.* 10 (6), 3009–3014. doi:10.3892/mmr.2014.2620

Wang, J. H., Xie, Y., Wu, J. C., Han, R., Reid, P. F., Qin, Z. H., et al. (2012). Crotoxin enhances the antitumor activity of gefinitib (Iressa) in SK-MES-1 human lung squamous carcinoma cells. *Oncol. Rep.* 27 (5), 1341–1347. doi:10.3892/or.2012.1677

Wang, K., Yan, J., Liu, X., Zhang, J., Chen, R., Zhang, B., et al. (2011). Novel cytotoxity exhibition mode of polybia-CP, a novel antimicrobial peptide from the venom of the social wasp Polybia paulista. *Toxicology* 288 (1-3), 27–33. doi:10.1016/j.tox.2011.06.014

Wang, K. R., Zhang, B. Z., Zhang, W., Yan, J. X., Li, J., and Wang, R. (2008). Antitumor effects, cell selectivity and structure-activity relationship of a novel antimicrobial peptide polybia-MPI. *Peptides* 29 (6), 963–968. doi:10.1016/j.peptides.2008.01.015

Wang, Y., Li, K., Han, S., Tian, Y. H., Hu, P. C., Xu, X. L., et al. (2019). Chlorotoxin targets ERα/VASP signaling pathway to combat breast cancer. *Cancer Med.* 8 (4), 1679–1693. doi:10.1002/cam4.2019

Wang, Y., Wang, J., Cao, Z., and Barati Farimani, A. (2022). Molecular contrastive learning of representations via graph neural networks. *Nat. Mach. Intell.* 4, 279–287. doi:10.1038/s42256-022-00447-x

Wang, Y., Zhang, J., Jiang, P., Li, K., Sun, Y., and Huang, Y. (2021). ASIC1a promotes acidic microenvironment-induced HCC cells migration and invasion by inducing autophagy. *Eur. J. Pharmacol.* 907, 174252. doi:10.1016/j.ejphar.2021.174252

Waqar, M., and Batool, S. (2015). *In silico* analysis of binding of neurotoxic venom ligands with acetylcholinesterase for therapeutic use in treatment of Alzheimer's disease. *J. Theor. Biol.* 372, 107–117. doi:10.1016/j.jtbi.2015.02.028

Ward, C. W., Sachs, F., Bush, E. D., and Suchyna, T. M. (2018). GsMTx4-D provides protection to the D2.mdx mouse. *Neuromuscul. Disord.* 28 (10), 868–877. doi:10.1016/j.nmd.2018.07.005

Warkentin, T. E. (2004). Bivalent direct thrombin inhibitors: hirudin and bivalirudin. *Best. Pract. Res. Clin. Haematol.* 17 (1), 105–125. doi:10.1016/j.beha.2004.02.002

Wattam, B., Shang, D., Rahman, S., Egglezou, S., Scully, M., Kakkar, V., et al. (2001). Arg-Tyr-Asp (RYD) and Arg-Cys-Asp (RCD) motifs in dendroaspin promote selective inhibition of β1 and β3 integrins. *Biochem. J.* 356 (Pt 1), 11–17. doi:10.1042/0264-6021:3560011

Wei, B., Zhang, Y., and Gong, X. (2022). DeepLPI: a novel deep learning-based model for protein-ligand interaction prediction for drug repurposing. *Sci. Rep.* 12 (1), 18200. doi:10.1038/s41598-022-23014-1

Westerlund, B., Nordlund, P., Uhlin, U., Eaker, D., and Eklund, H. (1992). The three-dimensional structure of notexin, a presynaptic neurotoxic phospholipase A2 at 2.0 A resolution. *FEBS Lett.* 301 (2), 159–164. doi:10.1016/0014-5793(92)81238-h

WHO (2021). Snake antivenoms. Available at: http://www.who.int/mediacentre/factsheets/fs337/en/(Accessed August 22, 2023).

Winblad, B., and Jelic, V. (2004). Long-term treatment of Alzheimer disease: efficacy and safety of acetylcholinesterase inhibitors. *Alzheimer Dis. Assoc. Disord.* 18 (Suppl. 1), S2–S8. doi:10.1097/01.wad.0000127495.10774.a4

Wong, E. S., Morgenstern, D., Mofiz, E., Gombert, S., Morris, K. M., Temple-Smith, P., et al. (2012). Proteomics and deep sequencing comparison of seasonally active venom glands in the platypus reveals novel venom peptides and distinct expression profiles. *Mol. Cell Proteomics* 11 (11), 1354–1364. doi:10.1074/mcp.M112.017491

World Spider Catalog (2023). World Spider Catalog. Version 25.5. Natural History Museum Bern, Available at: http://wsc.nmbe.ch. (Accessed October 21, 2023).

Wu, M., Ming, W., Tang, Y., Zhou, S., Kong, T., and Dong, W. (2013). The anticancer effect of cytotoxin 1 from Naja atra Cantor venom is mediated by a lysosomal cell death pathway involving lysosomal membrane permeabilization and cathepsin B release. *Am. J. Chin. Med.* 41 (3), 643–663. doi:10.1142/S0192415X13500456

Wu, W., Yin, Y., Feng, P., Chen, G., Pan, L., Gu, P., et al. (2023). Spider venom-derived peptide JZTX-14 prevents migration and invasion of breast cancer cells via inhibition of sodium channels. *Front. Pharmacol.* 14, 1067665. doi:10.3389/fphar.2023.1067665

Wulff, H., Castle, N. A., and Pardo, L. A. (2009). Voltage-gated potassium channels as therapeutic targets. *Nat. Rev. Drug Discov.* 8 (12), 982–1001. doi:10.1038/nrd2983

Xia, Z., He, D., Wu, Y., Kwok, H. F., and Cao, Z. (2023). Scorpion venom peptides: molecular diversity, structural characteristics, and therapeutic use from channelopathies to viral infections and cancers. *Pharmacol. Res.* 197, 106978. doi:10.1016/j.phrs.2023.106978

Xiao, L., Gurrola, G. B., Zhang, J., Valdivia, C. R., SanMartin, M., Zamudio, F. Z., et al. (2016). Structure-function relationships of peptides forming the calcin family of ryanodine receptor ligands. *J. Gen. Physiol.* 147 (5), 375–394. doi:10.1085/jgp.201511499

Xiong, X., Menting, J. G., Disotuar, M. M., Smith, N. A., Delaine, C. A., Ghabash, G., et al. (2020). A structurally minimized yet fully active insulin based on cone-snail venom insulin principles. *Nat. Struct. Mol. Biol.* 27 (7), 615–624. doi:10.1038/s41594-020-0430-8

Xiong, Z. G., Zhu, X. M., Chu, X. P., Minami, M., Hey, J., Wei, W. L., et al. (2004). Neuroprotection in ischemia: blocking calcium-permeable acid-sensing ion channels. *Cell* 118 (6), 687–698. doi:10.1016/j.cell.2004.08.026

Yacoub, T., Rima, M., Karam, M., Fajloun, J., and Fajloun, Z. (2020). Antimicrobials from venomous animals: an overview. *Molecules* 25 (10), 2402. doi:10.3390/molecules25102402

Yamada, M., Miller, D. M., Lowe, M., Rowe, C., Wood, D., Soyer, H. P., et al. (2021). A first-in-human study of BLZ-100 (tozuleristide) demonstrates tolerability and safety in skin cancer patients. *Contemp. Clin. Trials Commun.* 23, 100830. doi:10.1016/j.conctc.2021.100830

Yan, C. H., Liang, Z. Q., Gu, Z. L., Yang, Y. P., Reid, P., and Qin, Z. H. (2006). Contributions of autophagic and apoptotic mechanisms to CrTX-induced death of K562 cells. *Toxicon* 47 (5), 521–530. doi:10.1016/j.toxicon.2006.01.010

Yan, C. H., Yang, Y. P., Qin, Z. H., Gu, Z. L., Reid, P., and Liang, Z. Q. (2007). Autophagy is involved in cytotoxic effects of crotoxin in human breast cancer cell line MCF-7 cells. *Acta Pharmacol. Sin.* 28 (4), 540–548. doi:10.1111/j.1745-7254.2007.00530.x

Yang, C., Zhu, Z., Ouyang, X., Yu, R., Wang, J., Ding, G., et al. (2020). Overexpression of acid-sensing ion channel 1a (ASIC1a) promotes breast cancer cell proliferation, migration and invasion. *Transl. Cancer Res.* 9 (12), 7519–7530. doi:10.21037/tcr-20-2115

Ye, M., Chung, H. S., Lee, C., Yoon, M. S., Yu, A. R., Kim, J. S., et al. (2016). Neuroprotective effects of bee venom phospholipase A2 in the 3xTg AD mouse model of Alzheimer's disease. *J. Neuroinflammation* 13, 10. doi:10.1186/s12974-016-0476-z

Zamponi, G. W. (2016). Targeting voltage-gated calcium channels in neurological and psychiatric diseases. *Nat. Rev. Drug Discov.* 15 (1), 19–34. doi:10.1038/nrd.2015.5

Zhang, J., Tang, D., Liu, S., Hu, H., Liang, S., Tang, C., et al. (2018). Purification and characterization of JZTx-14, a potent antagonist of mammalian and prokaryotic voltage-gated sodium channels. *Toxins (Basel)* 10 (10), 408. doi:10.3390/toxins10100408

Zhang, J., Zhang, K., Ren, Y., and Wei, D. (2021). The expression, purification, and functional evaluation of the novel tumor suppressor fusion protein IL-24-CN. *Appl. Microbiol. Biotechnol.* 105 (20), 7889–7898. doi:10.1007/s00253-021-11558-7

Zhang, P., Ma, J., Yan, Y., Chen, B., Liu, B., Jian, C., et al. (2017). Arginine modification of lycosin-I to improve inhibitory activity against cancer cells. *Org. Biomol. Chem.* 15 (44), 9379–9388. doi:10.1039/c7ob02233f

Zhang, P., Yan, Y., Wang, J., Dong, X., Zhang, G., Zeng, Y., et al. (2020a). An anti-cancer peptide LVTX-8 inhibits the proliferation and migration of lung tumor cells by regulating causal genes' expression in p53-related pathways. *Toxins (Basel)* 12 (6), 367. doi:10.3390/toxins12060367

Zhang, Q., Zhang, P., Jian, S., Li, J., Li, F., Sun, X., et al. (2020b). Drug-bearing peptide-based nanospheres for the inhibition of metastasis and growth of cancer. *Mol. Pharm.* 17 (9), 3165–3176. doi:10.1021/acs.molpharmaceut.0c00118

Zhou, Q., Hu, P., Ritter, M. R., Swenson, S. D., Argounova, S., Epstein, A. L., et al. (2000a). Molecular cloning and functional expression of contortrostatin, a homodimeric disintegrin from southern copperhead snake venom. *Arch. Biochem. Biophys.* 375 (2), 278–288. doi:10.1006/abbi.1999.1682

Zhou, Q., Sherwin, R. P., Parrish, C., Richters, V., Groshen, S. G., Tsao-Wei, D., et al. (2000b). Contortrostatin, a dimeric disintegrin from *Agkistrodon contortrix* contortrix, inhibits breast cancer progression. *Breast Cancer Res. Treat.* 61 (3), 249–260. doi:10.1023/a:1006457903545

Zhu, S., Darbon, H., Dyason, K., Verdonck, F., and Tytgat, J. (2003). Evolutionary origin of inhibitor cystine knot peptides. *FASEB J.* 17 (12), 1765–1767. doi:10.1096/fj.02-1044fje

Frontiers in Chemistry

Explores all fields of chemical science across the periodic table

Advances our understanding of how atoms, ions, and molecules come together and come apart. It explores the role of chemistry in our everyday lives - from electronic devices to health and wellbeing.

Discover the latest Research Topics

See more →

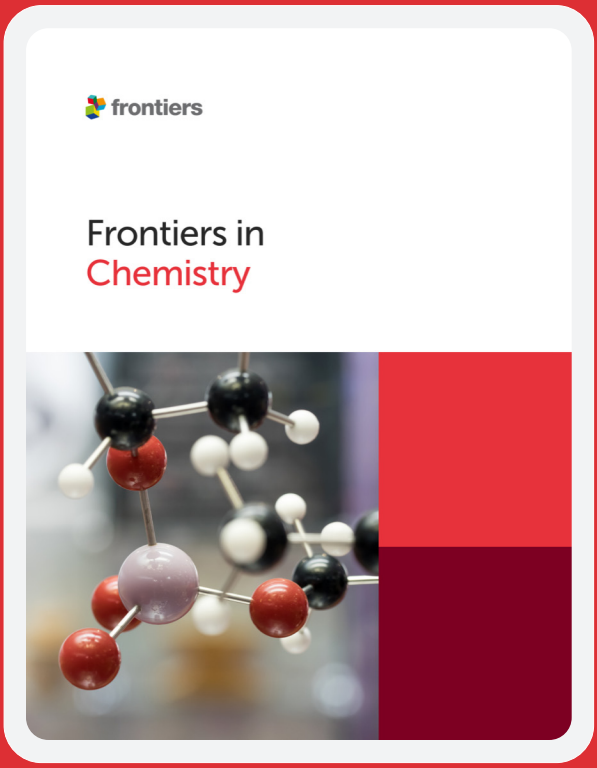

Frontiers

Avenue du Tribunal-Fédéral 34
1005 Lausanne, Switzerland
frontiersin.org

Contact us

+41 (0)21 510 17 00
frontiersin.org/about/contact